



Torrefaction and grinding of lignocellulosic biomass for its thermochemical valorization : influence of pretreatment conditions on powder flow properties

John Alexander Pachón-Morales

► To cite this version:

John Alexander Pachón-Morales. Torrefaction and grinding of lignocellulosic biomass for its thermochemical valorization : influence of pretreatment conditions on powder flow properties. Chemical and Process Engineering. Université Paris Saclay (COMUE), 2019. English. NNT : 2019SACLC051 . tel-02887096

HAL Id: tel-02887096

<https://theses.hal.science/tel-02887096>

Submitted on 2 Jul 2020

HAL is a multi-disciplinary open access archive for the deposit and dissemination of scientific research documents, whether they are published or not. The documents may come from teaching and research institutions in France or abroad, or from public or private research centers.

L'archive ouverte pluridisciplinaire **HAL**, est destinée au dépôt et à la diffusion de documents scientifiques de niveau recherche, publiés ou non, émanant des établissements d'enseignement et de recherche français ou étrangers, des laboratoires publics ou privés.

Torrefaction and grinding of lignocellulosic biomass for its thermochemical valorization: influence of pretreatment conditions on powder flow properties

Thèse de doctorat de l'Université Paris-Saclay
préparée à CentraleSupélec

École doctorale n°579 - Sciences mécaniques et énergétiques, matériaux et
géosciences (SMEMAG)

Spécialité de doctorat : Génie des Procédés

Thèse présentée et soutenue à Gif-sur-Yvette, le 11 Juin 2019, par

John Alexander Pachón-Morales

Composition du Jury :

M. Farhang Radjai DR CNRS, LMGC, Université de Montpellier – Research Affiliate, Massachusetts Institute of Technology	Rapporteur
M. Anthony Dufour CR CNRS, LRGP, Université de Lorraine	Rapporteur
Mme Dingena Schott Associate Professor, Delft University of Technology	Examinatrice
M. Geoffroy Lumay Associate Professor, Université de Liège	Examineur
Mme Véronique Aubin Professeure, MSSMat, CentraleSupélec	Présidente
M. Julien Colin Maître de Conférences, LGPM, CentraleSupélec	Co-encadrant de thèse
M. Patrick Perré Professeur, LGPM, CentraleSupélec	Co-directeur de thèse
M. François Puel Professeur, CentraleSupélec	Directeur de thèse

Titre : Torréfaction et broyage de biomasse lignocellulosique pour sa valorisation thermochimique : influence des conditions de prétraitement sur les propriétés d'écoulement des poudres

Mots clés : Biomasse lignocellulosique, BtL, torréfaction, DEM, test de cisaillement, coulabilité de poudres, distribution de taille et forme de particules

Résumé : Une technologie prometteuse pour répondre à la demande croissante en énergie renouvelable est la gazéification de biomasse lignocellulosique pour la production de biocarburants de deuxième génération. Ce procédé nécessite une alimentation en biomasse sous forme de poudre. Les problèmes de convoyage et de manipulation liés à la faible coulabilité de la biomasse broyée sont un verrou pour l'industrialisation des procédés BtL. La torréfaction comme procédé de prétraitement, en plus d'augmenter la densité énergétique de la biomasse, peut influencer également les propriétés des particules obtenues après broyage, et en conséquence, l'écoulement des poudres. L'évaluation de l'écoulement des poudres de biomasse sous différentes conditions de consolidation est essentielle pour concevoir des technologies de manipulation et de convoyage efficaces. L'objectif de ce travail est d'évaluer l'effet des conditions de torréfaction et de broyage sur l'écoulement de poudres de biomasse. Une première partie consiste en une étude expérimentale dans laquelle la coulabilité d'échantillons torréfiés sous différentes intensités a été évaluée à l'aide d'un appareil de cisaillement annulaire. La coulabilité est corrélée à l'intensité de la torréfaction (mesurée par la perte de masse globale) pour deux essences différentes. La forme des particules semble être le paramètre qui influence de manière prédominante la coulabilité des poudres à l'état consolidé.

La caractérisation de la coulabilité à l'état non consolidé a été effectuée à l'aide d'un tambour rotatif par l'analyse des avalanches des poudres. Des corrélations entre les caractéristiques des particules et la coulabilité sont ainsi établies. La modélisation de l'écoulement de la biomasse à l'aide de la Méthode des Éléments Discrets (DEM) constitue une deuxième partie de ces travaux de recherche. La taille submillimétrique des particules de biomasse, ainsi que leur faible densité, leur forme allongée et leur comportement cohésif sont des défis pour l'implémentation d'un modèle de réaliste d'écoulement particulaire en DEM. Un modèle DEM des particules de biomasse est mis en œuvre à l'aide d'une représentation simplifiée (assemblage de sphères) à gros grains de la forme des particules, ainsi que d'un modèle de force cohésif. Une procédure systématique de calibration des paramètres DEM permet d'obtenir un ensemble de paramètres ajustés. L'évolution expérimentale des contraintes de cisaillement d'une poudre dans un état consolidé peut alors être reproduite de façon réaliste. De même, le comportement d'avalanche des poudres dans un tambour tournant est également bien reproduit par les simulations, de façon qualitative et quantitative. Ces résultats mettent en évidence le potentiel des simulations DEM pour étudier l'effet des caractéristiques des particules, qui sont influencées par la torréfaction et les conditions de broyage, sur le comportement d'écoulement de la biomasse en poudre.

Title: Torrefaction and grinding of lignocellulosic biomass for its thermochemical valorization: influence of pretreatment conditions on powder flow properties

Keywords: Lignocellulosic biomass, BtL, torrefaction, DEM, shear testing, rotating drum, powder flowability, particle size and shape distribution

Abstract: Gasification of lignocellulosic biomass for production of second-generation biofuels is a promising technology to meet renewable energy needs. However, feeding and handling problems related to the poor flowability of milled biomass considerably hinder the industrial implementation of Biomass-to-Liquid processes. Torrefaction as pretreatment step, in addition to improving energy density of biomass, also affects the properties of the milled particles (namely size and shape) that significantly influence flow behavior. The evaluation of biomass flow characteristics under different flow conditions is essential to design efficient and trouble-free handling solutions. The aim of this work is to assess the effect of the torrefaction and grinding conditions on the biomass flow behavior. A first part consists of an experimental study in which the flow properties of samples torrefied under different intensities were obtained using a ring shear tester. Flowability is correlated to the intensity of torrefaction, as measured by the global mass loss, for two different wood species. Particle shape seems to be the predominant parameter influencing flowability of powders in a consolidated state.

Characterization of non-consolidated flowability through avalanching analysis using an in-house rotating drum was also conducted. Correlations between particle characteristics and flow behavior are thus established.

The modeling of biomass flow using the Discrete Element Method (DEM) constitutes a second major part of this research. Challenging aspects of biomass particle modeling are their submillimetric size, low density, elongated shape and cohesive behavior. A material DEM model is implemented using a simplified (multisphere) upscaled representation of particle shape, along with a cohesive contact model. A systematic calibration procedure results in an optimal set of DEM parameters. The experimental shear stress evolution and yield locus can then be realistically reproduced. The avalanching behavior of the powders is also well captured by simulations, both qualitatively and quantitatively. These results highlight the potential of DEM simulations to investigate the effect of particle characteristics, which are driven by torrefaction and grinding conditions, on the flow behavior of powdered biomass.

Acknowledgements

Throughout the process of completing this doctoral project I received a great deal of support and assistance. First of all, I would like to thank François Puel, whose technical but above all moral guidance was invaluable for the accomplishment of this work. I could not have imagined having a better advisor and mentor for my doctoral project.

I would like to express my sincere gratitude to Julien Colin. I will always admire your technical skills both experimentally and theoretically and your devotion to science with rigor and perseverance. I am very grateful to Joel Casalinho for all the help, especially during the design and set-up of the various experimental devices used in this work. I would like to thank Patrick Perré for welcoming me to the LGPM and for all the very valuable and high-level scientific exchanges we had during my stay at CentraleSupélec.

A very special gratitude goes out to all the LGPM team. It was great to have the opportunity to work majority of my research among you. Thanks to all those who made the environment friendly during these years, especially to my fellow Ph.D. candidates -too many to mention one by one- with whom I shared lots of doubts and uncertainties, but also lots of moments of entertainment and fulfilment. I would like to thank Imène and Mariska, who provided me with valuable help and to whom I hope I have been able to transmit a bit of passion for the world of research in general and for biomass valorization in particular.

My sincere thanks also goes to Dingena Schott for welcoming me at TU Delft. My stay in the Netherlands was one of the most fruitful and exciting phases of my doctorate. I am especially grateful to Huy, Javad and Hamid for their help with DEM simulations and their precious guidance during my stay in Delft.

I thank the members of the jury for their commitment to rigorously evaluate this work and to enrich it with valuable suggestions. Many thanks to Veronique Aubin for chairing the jury, to Anthony Dufour and Farhang Radjai for their thoughtful reading of this manuscript and their suggestions. I also thank Geoffroy Lumay and Dingena Schott for their comments and their active participation during the defence of this project.

I am grateful to my family members and friends who have patiently supported me along the way. A huge thank you to Julia for all her support and patience, particularly during the last stages which were not the easiest. I sincerely do not know how I could have made it through without your help. I hope to be able to give the help back to you soon.

General preamble

The work presented in this thesis manuscript was carried out at the LGPM laboratory (*Laboratoire de Génie des Procédés et Matériaux*), of CentraleSupélec (Université Paris-Saclay).

This manuscript is written in an article-based form. Five publications therefore constitute the chapters III, IV (two publications corresponding to sections 2 and 3), and V (two publications corresponding to sections 2 and 4), with unpublished complementary information included in the chapters. The content of publications has not been modified from the published versions, but the layout has been homogenized according to the general format of the manuscript. Due to the writing format chosen for this manuscript, some of the background information, mainly in the Introduction and Materials and Methods sections of the various articles, had to be reiterated and may seem redundant to the reader. We would like to emphasize that this apparent redundancy obeys a need for self-sufficiency of the articles in their published or submitted form.

The references to the publications are as follows:

- **Effect of torrefaction intensity on the flow properties of lignocellulosic biomass powders**
John Pachón-Morales, Julien Colin, Florian Pierre, François Puel, Patrick Perré
Biomass and Bioenergy
Volume 120, January 2019, Pages 301-312
DOI: <https://doi.org/10.1016/j.biombioe.2018.11.017>
- **Investigation on criteria for assessment of flowability of cohesive and non-cohesive powders using a rotating drum**
John Pachón-Morales, Julien Colin, Joel Casalinho, François Puel, Patrick Perré
To be submitted to *Advanced powder technology*
- **Flowability characterization of torrefied biomass powders: static and dynamic testing**
John Pachón-Morales, Julien Colin, Joel Casalinho, Patrick Perré, François Puel
Submitted to *Biomass and bioenergy* on January 2019
- **DEM modeling for flow of cohesive lignocellulosic biomass powders: Model calibration using bulk tests**
John Pachón-Morales, Huy Do, Julien Colin, François Puel, Patrick Perré, Dingena Schott
Advanced Powder Technology
Volume 30, Issue 4, April 2019, Pages 732-750
DOI: <https://doi.org/10.1016/j.appt.2019.01.003>
- **Potential of DEM for investigation of flow of cohesive and elongated biomass particles in a rotating drum**
John Pachón-Morales, Patrick Perré, Joel Casalinho, Huy Do, Dingena Schott, François Puel, Julien Colin
Submitted to *Advanced powder technology* on April 2019

This work was the subject of oral presentations at an international and a national scientific conference, which resulted in the publication of conference proceedings, as follows:

- 8th International Conference on Micromechanics of Granular Media (Powders and Grains) in Montpellier, France, on July 3-7, 2017.
Flowability of lignocellulosic biomass powders: influence of torrefaction intensity.
John Pachón-Morales, Julien Colin, Floran Pierre, Thibaut Champavert, François Puel, Patrick Perré
EPJ Web Conf. 140 13017 (2017)
DOI: <https://doi.org/10.1051/epjconf/201714013017>
- 16th Conference of the French Society of Process Engineers (SFGP) in Nancy, France, on July 11-13, 2017.
Influence de l'épaisseur de particule sur l'homogénéité de traitement thermique d'un bois de peuplier.
John Pachón-Morales, Julien Colin, Floran Pierre, François Puel, Patrick Perré
Récent Progrès en Génie des Procédés 2017
ISBN: 978-2-910239-85-5
HAL Id: hal-01661843

Part of this work was carried out in collaboration between the LGPM and the Transport Engineering and Logistics section, Department of Maritime & Transport Technology, Faculty of Mechanical, Maritime and Materials Engineering of the Delft University of Technology (Delft, the Netherlands). This collaboration resulted in a doctoral research stay in Delft between March and June 2018, partly funded by the French-Dutch Network as part of the 'Eole' scholarship program.

Résumé en Français

Introduction

Bien que les opinions sur la disponibilité des stocks de ressources fossiles puissent varier de 50 à 500 ans, il est largement admis que les réserves sont limitées et qu'il est essentiel de rechercher de nouvelles sources d'énergie renouvelables. Cette limitation, combinée aux effets observés sur le changement climatique, a stimulé l'intérêt pour la biomasse en tant que source d'énergie renouvelable neutre en CO₂. L'utilisation de carburants issus de la biomasse (biocarburants) est l'une des réponses technologiques prometteuses pour réduire les émissions de CO₂ et de gaz à effet de serre dans le secteur du transport.

Après une première génération de biocarburants qui utilise la partie comestible des plantes, une deuxième génération – qui utilise la totalité de la matière lignocellulosique – reste à développer à échelle industrielle. Bien qu'il existe plusieurs voies de transformation pour la valorisation de la biomasse, la conversion thermochimique par gazéification à flux entraîné est l'une des voies privilégiées pour la production de biocarburants de deuxième génération. L'utilisation d'une matière première de biomasse sous forme de poudre augmente sa réactivité pendant la gazéification et facilite son transport et son injection. Il est donc nécessaire de broyer en amont la biomasse solide pour obtenir une poudre. Cependant, en raison de la résilience mécanique de la lignocellulose notamment liée à sa nature fibreuse, cette étape est très consommatrice en énergie. Par ailleurs, les problèmes liés à la manipulation de biomasse sous forme broyée sont fréquents et entravent considérablement l'industrialisation des procédés 2G. La conception de technologies efficaces de stockage, de manipulation et d'alimentation nécessite une connaissance des propriétés d'écoulement du matériau sous différents états de conditionnement.

La torréfaction, en plus d'améliorer des caractéristiques de la biomasse telles que le contenu énergétique et de diminuer son hygroscopicité, est une étape de prétraitement qui peut améliorer la broyabilité de la biomasse et réduire la consommation énergétique de cette étape. Actuellement, les connaissances des propriétés d'écoulement des poudres de biomasse restent très limitées et très peu d'informations sont disponibles sur les effets de la torréfaction sur les caractéristiques des particules et leur aptitude à écoulement. Cependant, cette connaissance est essentielle pour la conception d'équipements et de procédés industriels de conversion de biomasse et pour la prévention des problèmes lors du transport ou du stockage.

L'objectif de ce projet doctoral est d'observer, quantifier et comprendre l'effet des étapes de prétraitement (torréfaction et broyage) sur les caractéristiques physiques des poudres de biomasse obtenues. Dans ce but, une combinaison d'approches expérimentales et numériques est utilisée pour étudier le comportement du matériau, ainsi que pour développer des outils qui peuvent être utilisés pour la conception et l'optimisation des systèmes de manipulation et convoyage industriels de la biomasse.

Questions de recherche

En résumé, l'objectif de ce travail peut être synthétisé comme une tentative de répondre aux suivantes questions de recherche:

- Comment la torréfaction et les conditions de broyage affectent-elles les propriétés particulières de la biomasse ?
- Quel est l'effet de ces caractéristiques de particules sur le comportement d'écoulement dans différentes conditions ?
- Les simulations par la méthode des éléments discrets peuvent-elles, dans un but prédictif, reproduire le comportement d'écoulement de matériaux de biomasse bruts et torréfiés ?

Méthodologie

Dans un premier temps, d'un point de vue expérimental, la compréhension du comportement macroscopique de la poudre nécessite l'évaluation des effets de torréfaction à l'échelle particulaire, notamment en termes de taille et de forme des particules. Comme les matériaux granulaires peuvent se comporter très différemment en fonction de leur conditionnement et de leur état de consolidation, leur caractérisation dans des conditions différentes est également nécessaire. Deuxièmement, d'un point de vue numérique, la modélisation des écoulements à l'aide de la méthode des éléments discrets (DEM) peut fournir un aperçu des effets des caractéristiques à l'échelle des particules (imposées par les conditions de prétraitement) sur le comportement macroscopique. De plus, l'évaluation de la nature prédictive des simulations, qui est toujours souhaitée et recherchée, peut renforcer leur valeur en tant que moyen d'optimiser le procédé de valorisation de biomasse.

Ce manuscrit est écrit sous forme d'articles. Cinq publications constituent donc les chapitres III, IV (deux publications correspondant aux sections 2 et 3) et V (deux publications correspondant aux sections 2 et 4), avec des informations complémentaires non publiées incluses dans ces chapitres. Le contenu des publications n'a pas été modifié par rapport aux versions publiées, mais la mise en page a été homogénéisée selon le format général du manuscrit. En raison du format d'écriture choisi pour ce travail, certaines des informations de base, principalement dans les sections Introduction et Matériel et Méthodes des divers articles, ont dû être répétées et peuvent sembler redondantes pour le lecteur. Nous tenons à souligner que cette redondance apparente obéit à un besoin d'autosuffisance des articles sous leur forme publiée ou soumise.

Révision bibliographique : bilan de l'état des connaissances

La majorité de la littérature s'est jusqu'à présent concentrée sur les modifications subies par la biomasse pendant la torréfaction d'un point de vue chimique et mécanique. Peu d'études ont abordé la question des effets du traitement thermique sur la coulabilité de la biomasse broyée. Aucune étude quantitative n'a été réalisée par rapport à l'effet couplé de la torréfaction et du broyage sur les caractéristiques des particules et les propriétés d'écoulement qui en découlent. Quelques recherches existent cependant, traitant de la coulabilité de poudres de biomasse native, notamment via des essais de cisaillement. Il y a donc un besoin explicite de plus de travaux qui permettent la compréhension du comportement de la biomasse traitée thermiquement.

À un niveau plus fondamental, il est nécessaire de poursuivre les recherches sur l'adéquation des différents descripteurs de taille et de forme des particules de biomasse, qui permettent d'établir des corrélations avec les propriétés d'écoulement. Ceci est particulièrement critique pour les poudres de biomasse où l'on peut obtenir des populations très polydispersées de particules allongées après broyage.

La simulation de ce type de particules nécessite également la définition de modèles de matériaux simplifiés qui doivent être basés sur des descripteurs de taille et de forme représentatifs.

Le potentiel des tests en tambour rotatif pour l'évaluation de l'écoulement non consolidé et dynamique n'a pas encore été évalué pour la biomasse. Ceci est principalement dû à l'absence d'un cadre robuste et fiable pour la caractérisation des matériaux cohésifs utilisant les résultats des tests d'avalanches dans des tambours rotatifs. Des corrélations ont été proposées entre les descripteurs d'écoulement obtenus à partir d'expériences dans des tambours rotatifs et le comportement dans des systèmes industriels de manipulation de poudres, mais des travaux supplémentaires sont encore nécessaires sur ce sujet. La possibilité d'extraire des paramètres utiles à la conception d'équipements, comme c'est le cas pour les tests de cisaillement, mérite également une recherche approfondie.

Peu d'attention a été accordée à la combinaison d'approches expérimentales et numériques pour étudier l'écoulement de poudres de biomasse. Jusqu'à présent, la plupart des recherches utilisant la Méthode des Eléments Discrets se concentrent sur l'étude des interactions particule-équipement pour des briquettes de bois, des granulés ou des copeaux de bois. Le développement de modèles DEM adaptés à la biomasse dont les caractéristiques des particules ne correspondent pas aux systèmes typiquement modélisés (sphériques, avec des tailles supérieures au centimètre et non cohésifs). L'établissement de tels modèles, qui doivent demeurer efficaces sur le plan des simulations, peut faire intervenir de nouvelles méthodes de représentation de la forme des particules, des approches d'*upscaling* ainsi que de nouveaux modèles de forces de contact. Enfin, d'avantage de recherches sont nécessaires sur des tests appropriés aux matériaux cohésifs permettant la calibration des paramètres DEM.

Principaux résultats et conclusions

Nous avons d'abord exploré les effets de la torréfaction sur les propriétés d'écoulement des poudres de biomasse en état consolidé à l'aide d'une cellule de cisaillement annulaire de Schulze. Des échantillons de deux essences de bois, peuplier (feuillu) et épicéa (résineux), ont ainsi été torréfiés et broyés. L'écoulement étant fortement influencé par les propriétés des particules, nous avons mesuré l'impact du traitement thermique sur les distributions de taille et de forme des particules. La perte de résilience de la structure du bois brut par torréfaction a été vérifiée par le déplacement progressif des distributions de taille et de forme vers des distributions plus larges de particules plus fines et plus rondes lorsque les échantillons étaient torréfiés de manière plus intense.

En même temps, nous avons observé une amélioration significative de la coulabilité avec l'intensité de torréfaction : la biomasse broyée passe d'un caractère cohésif pour les échantillons non-traités à un comportement presque fluide pour les poudres les plus fortement torréfiées. Selon les tendances générales des matériaux granulaires reportées dans la littérature, les échantillons intensément torréfiés, qui étaient composés d'une forte proportion de particules fines, devraient s'écouler difficilement en raison de l'augmentation des forces de cohésion interparticulaires par rapport au poids des particules. Nos résultats suggèrent que la diminution du chevauchement des particules (grâce notamment à des formes plus arrondies) a un effet dominant, ce qui se traduit par un meilleur écoulement. C'est donc l'évolution de la forme des particules plutôt que de leur taille qui est un paramètre décisif pour augmenter la coulabilité. L'amélioration de la coulabilité et les changements de taille et de forme des particules s'expliquent donc par le même effet : la perte de résilience de la structure fibreuse du bois natif par traitement thermique.

La perte de masse est un indicateur synthétique de l'intensité du traitement thermique en torréfaction, puisqu'elle inclut la température et le temps de séjour dans le réacteur. Cet indicateur a été corrélé avec succès dans des recherches antérieures aux propriétés physico-chimiques de la biomasse torréfiée. Nos résultats ont mis en évidence la possibilité de relier cette perte de masse à un facteur de coulabilité par une relation linéaire commune pour les deux espèces étudiées ici. Nous proposons donc de considérer la perte de masse comme un indicateur de la coulabilité à l'état consolidé. Ainsi, un indicateur unique, lié aux conditions de torréfaction, pourrait être utilisé pour la conception des étapes de prétraitement de la filière BtL.

Les propriétés d'écoulement déterminées pour la biomasse broyée native et torréfiée représentent des données précieuses qui peuvent être utilisées directement, grâce à la procédure de Jenike, pour la conception d'installations de stockage industriel telles que des trémies et des silos. Puisque la torréfaction suivie du broyage génère des poudres de biomasse composées de particules rondes et uniformes, avec l'avantage supplémentaire de réduire la consommation d'énergie pour le broyage, nos résultats indiquent que la torréfaction devrait être considérée comme un processus de prétraitement permettant d'améliorer l'écoulement de la biomasse en état consolidé. Des travaux supplémentaires sont toutefois nécessaires pour déterminer si le coût énergétique de la torréfaction compense la réduction du coût énergétique du broyage, en intégrant les bénéfices sur les opérations de manipulation des poudres.

Dans une deuxième étape de notre travail expérimental, nous nous sommes focalisés sur l'étude de l'écoulement des poudres de biomasse lorsqu'elles sont en surface libre, c'est-à-dire sans consolidation au-delà de la charge exercée par le propre poids du matériau. C'est le conditionnement du matériau que l'on trouve habituellement dans les systèmes de convoyage tels que les vis d'alimentation ou les pipelines. Le tambour rotatif est l'un des dispositifs expérimentaux le plus pertinents pour étudier l'écoulement des matériaux granulaires dans ces conditions. Nous avons donc conçu et construit un dispositif expérimental couplé à une procédure efficace de traitement d'image qui nous a permis d'évaluer, par analyse d'avalanches, le comportement dynamique des poudres de biomasse avec une intervention minimale de l'opérateur. En raison de l'absence dans la littérature de descripteurs de coulabilité standards pour des matériaux cohésifs obtenus avec des expériences en tambours rotatifs, nous avons d'abord étudié la pertinence d'un indicateur de mouvement de la poudre, « l'angle centroïde », qui est basé sur les changements du centre de gravité de la poudre pendant la rotation. Cet angle s'est avéré efficace pour capturer la dynamique de la poudre et nous a permis d'évaluer plusieurs descripteurs de coulabilité tels que l'angle supérieur de stabilité, la fraction de révolution nécessaire pour déclencher les événements et la taille des avalanches.

Outre les descripteurs de coulabilité mentionnés ci-dessus, l'irrégularité du profil de surface libre dans le tambour rotatif, caractérisé par le coefficient de détermination r^2 , nous a permis de distinguer le caractère non-cohésif d'un lot de billes du caractère cohésif des échantillons de biomasse. L'évaluation de la coulabilité à une vitesse de rotation relativement faible a donné lieu à des distributions de descripteurs dont on a pu tirer des conclusions fiables sur l'écoulement non confiné. Les descripteurs de coulabilité proposés sont complémentaires les uns des autres et doivent être considérés simultanément pour obtenir une conclusion plus précise sur les propriétés d'écoulement des matériaux testés.

Le cadre général établi pour l'étude de la coulabilité à l'aide d'un tambour rotatif nous a permis d'étudier l'écoulement de poudres de peuplier natif et torréfié et de comparer les résultats ainsi obtenus à ceux issus des mesures en état consolidé en cellule de cisaillement annulaire. L'étude de deux coupes de tamisage (« fin » et « grossier ») d'échantillons de biomasse native et torréfiée a montré que les poudres fines étaient toujours plus cohésives que les coupes de tamisage grossier. Nous avons établi deux grandes catégories de comportement des poudres de biomasse dans un conditionnement non consolidé. Les

poudres les plus cohésives avaient une plus grande tendance à former des amas de particules qui s'écoulaient mal, tandis que des phénomènes de glissement par cisaillement étaient caractéristiques d'un bon comportement d'écoulement. Nos résultats suggèrent que, par exemple, dans un système à vis d'alimentation, les poudres finement tamisées légèrement torréfiées seraient plus susceptibles d'avoir un débit intermittent et de présenter des problèmes de blocage, que les poudres natives grossières. Plusieurs corrélations empiriques ont permis d'éclaircir ces tendances à partir des caractéristiques des particules. Les descripteurs de coulabilité obtenus à partir d'essais de cisaillement et d'expériences de tambour rotatif ont donc été reliés à la taille, à la forme et à l'étendue des distributions. Les relations quantitatives établies indiquent que la coulabilité, telle que mesurée par le test de cisaillement annulaire, est directement liée à la taille moyenne des particules (Feret minimum) et au ratio d'aspect, et inversement proportionnelle à l'étendue de la distribution de taille. Dans un conditionnement non-consolidé à surface libre, les particules fines, rugueuses et allongées, ainsi que les poudres avec une distribution étroite, seraient plus cohésives. Contrairement à l'état consolidé, l'augmentation de la polydispersité des poudres semble donc améliorer l'écoulement en absence de consolidation.

Dans une deuxième phase de ce travail, afin de bénéficier de la puissance de la Méthode des Eléments Discrets pour la simulation de matériaux granulaires, nous avons développé un modèle de particules de biomasse à l'aide de LIGGGHTS®, un logiciel *open source* de simulation DEM. Afin de reproduire de manière réaliste le comportement des matériaux issus de la biomasse, des représentations simplifiées des particules ont été utilisées, ce qui a nécessité l'ajustement (« calibration ») des paramètres DEM. Aucune procédure de calibration de paramètres n'a pas encore été documentée dans la littérature pour les matériaux avec les caractéristiques de la biomasse, c'est-à-dire, avec des particules submillimétriques, allongées et cohésives. Par conséquent, comme première étape du travail de modélisation, nous avons développé et appliqué une procédure de calibration automatique pour obtenir des ensembles optimaux de paramètres d'interaction (coefficients de friction de glissement, coefficient de friction de roulement et densité énergétique de cohésion) qui reproduisent par simulation des réponses expérimentales telles que l'angle de repos d'un tas, la densité apparente et un taux de rétention. Une approche de représentation de la forme des particules par ensembles de sphères, ainsi qu'une mise en échelle de la taille des grains nous a permis de saisir, de manière simplifiée mais efficace sur le plan du temps de calcul, la nature allongée des particules de biomasse. L'utilisation d'une représentation *upscaled* (mise à l'échelle des particules d'un facteur 4) a en effet été nécessaire pour limiter le nombre de particules simulées et ainsi réduire le temps de calcul. La simulation d'une séquence de pré-cisaillement et de cisaillement dans une cellule annulaire appliquées à une coupe tamis grossière de biomasse native a fourni des contraintes tangentielles similaires à celles des expériences, montrant que les paramètres calibrés pouvaient en principe également être utilisés en conditions consolidées.

Nous avons évalué le potentiel de la méthode DEM pour la simulation de l'écoulement de poudres de biomasse par l'étude du système à tambour rotatif utilisé pour la détermination de la coulabilité en état non-consolidé. Ce faisant, nous avons pu, en même temps, tester les paramètres calibrés précédemment en utilisant des mesures expérimentales pour deux coupes de tamisage d'échantillons natifs, légèrement torréfiés et intensément torréfiés. Les simulations DEM du comportement en avalanches ont abouti à des résultats similaires aux résultats expérimentaux vis-à-vis de plusieurs indicateurs de coulabilité (angle supérieur de stabilité, fraction d'événements déclenchant les avalanches et taille d'avalanches), montrant que la Méthode des Eléments Discrets pouvait être utilisée comme un outil fiable pour analyser et prédire l'écoulement non consolidé des poudres de biomasse.

Globalement, la torréfaction semble améliorer les propriétés d'écoulement de biomasse en état consolidé. La biomasse torréfiée est donc moins susceptible de provoquer des problèmes de blocage

dans les unités de stockage. En revanche, puisque seuls des échantillons tamisés ont été testés dans des conditions non consolidées, il n'est pas facile de tirer des conclusions sur l'effet net de la torréfaction sur l'écoulement non consolidé à partir des résultats présentés dans ces travaux. Pour les échantillons tamisés, cependant, l'effet bénéfique de la torréfaction est mitigé et moins clair que dans des conditions consolidées. Bien que la torréfaction semble être un traitement efficace pour améliorer les caractéristiques de forme des particules et donc l'écoulement, nous sommes conscients que, dans un processus de gazéification, d'autres contraintes que l'optimisation de l'écoulement des poudres (notamment, la consommation énergétique globale du procédé et la densité énergétique du produit torréfié) peuvent influencer le choix général des conditions de torréfaction. Cependant, ces travaux ont mis en évidence que le choix des paramètres de prétraitement était crucial pour définir les propriétés physiques de la poudre et que ces effets devaient être pris en compte dans la conception générale et l'optimisation des procédés de prétraitement BtL.

Perspectives

Diverses perspectives pour des travaux futurs se dégagent de ces travaux. D'abord, d'un point de vue expérimental, l'évaluation des interactions de surface (forces électrostatiques, rugosité) et de leurs effets sur l'écoulement des poudres biomasse est un sujet majeur qui devrait être considéré dans la continuation de ce travail. L'évaluation de la pertinence des descripteurs moyens de taille et forme des particules pour caractériser l'écoulement doit également être approfondie. Par ailleurs, une progression naturelle de ces travaux devrait inclure des tests sur des échantillons non-tamisés en tambour rotatif.

Concernant les simulations DEM, l'utilisation d'approches autres que les ensembles de sphères pour la représentation de la forme allongée des particules est encouragée pour les travaux futurs. Par exemple, la dernière version de LIGGGHTS® (3.8.0) inclut la possibilité d'avoir des particules de forme « superquadrique ». L'utilisation des formes superquadriques pourrait mieux imiter la forme plate des particules de biomasse que les modèles à ensemble de sphères. Des modèles à fibres flexibles, qui commencent à être implémentés dans les codes de simulation DEM, sont également de grand intérêt pour la simulation des particules de biomasse qui peuvent se plier et inversement sous consolidation. D'autres travaux sont également nécessaires pour établir des tests de calibration, en plus de l'angle de repos utilisé dans ce travail, qui pourraient distinguer différents degrés de cohésion de poudre de biomasse.

Enfin, d'un point de vue plus global, à l'échelle du procédé, un dernier axe de travaux futurs concerne l'intégration des méthodologies et des résultats présentés dans ce travail à la conception et à l'évaluation des technologies de prétraitement de la biomasse dans la filière BtL. Nous avons montré comment les résultats de ces travaux peuvent être utilisés soit pour la conception d'équipements (par exemple silos et vis d'alimentation), soit pour ajuster le couple intensité de torréfaction/intensité de broyage, en termes de bilan énergétique et pour satisfaire les besoins de gazéification. D'autres travaux sont cependant nécessaires, notamment, pour confirmer la pertinence de la perte de masse comme indicateur de coulabilité, ainsi que pour valider l'extrapolation des conclusions des tests en tambour rotatifs à l'étude des performances ou au design d'unités de convoyage. Une évaluation, à l'échelle du procédé, des économies d'énergie générées par l'amélioration de l'écoulement de la biomasse par torréfaction serait importante pour confirmer l'intérêt global de la torréfaction comme étape de prétraitement.

Content

Résumé en Français.....	3
List of Figures	15
List of Tables.....	18
Abbreviations	20
Symbols	21
General Introduction	25
CHAPTER I. Literature review	29
A- From biomass to liquid fuels	31
1. Energetic, environmental and geopolitical context.....	31
1.1. First-generation biofuels.....	32
1.2. Second-generation biofuels.....	33
1.3. The French scenario: Futurol, BioTfuel and Syndièse projects	34
2. From biomass to liquid fuels.....	34
2.1. Biomass, its interest and limitations	34
2.1.1. Drivers for biomass use	35
2.1.2. Challenges for utilization of biomass.....	35
2.2. Wood as a model of lignocellulosic biomass: properties and structure.....	36
2.2.1. Anatomic structure	36
2.2.2. Biochemical composition	39
2.2.3. Poplar and Spruce: potential use as feedstock for BtL processes	41
2.3. Processes for biomass valorization into liquid fuels	43
2.3.1. Biochemical conversion of biomass	43
2.3.2. Thermochemical conversion and Biomass to Liquid processes.....	43
2.3.3. Feedstock pretreatment for gasification.....	49
2.4. Obstacles for the industrialization of BtL processes	56
2.5. Handling biomass and biomass powders: current issues and problematics.....	57
B- Flow behavior of biomass powders.....	59
1. Non-cohesive and cohesive granular materials	59
2. Methods for measuring bulk flow properties	59
2.1. Shear tests	59
2.1.1. Schulze ring shear tester.....	60
2.2. Other measurement methods for determination of flow properties of bulk solids	64
2.3. Rotating drum systems for measurements of flow properties	65
2.3.1. Commercial systems for flowability assessment using rotating drum principles.....	67
3. Linking flow properties and granulometry of granular materials	67
4. Flowability of biomass materials: state-of-the-art	68
4.1. Size and shape of biomass particles and effects on flowability.....	70
4.2. Effects of torrefaction on flow properties of biomass materials.....	71
C - Modeling flow of biomass materials	72
1. The Discrete Element Method (DEM)	73

1.1.	Governing equations.....	73
1.2.	Interparticle force models	74
1.2.1.	Contact models.....	74
1.3.	Numerical resolution and simulation aspects	78
1.3.1.	Integration scheme	78
1.3.2.	Velocity-Verlet Integration scheme	78
1.3.3.	Timestep.....	79
1.3.4.	Contact detection.....	80
1.4.	Particle shape in DEM: rolling friction model and multisphere representation	80
1.4.1.	Computational challenges of DEM	81
1.5.	Scaling approaches	82
1.6.	Calibration approaches	82
1.7.	DEM Software.....	83
1.7.1.	Overview	83
1.7.2.	LIGGGHTS®.....	83
2.	The Discrete Element Method applied to biomass systems	85
	Knowledge gap	86
CHAPTER II. Experimental facilities.....		87
1.	Preamble	89
2.	Torrefaction unit description	89
2.1.	The furnace.....	89
2.2.	Oxygen content control.....	89
2.3.	Cooling system.....	89
1.1.	Mass loss monitoring	90
1.2.	Temperature profiles.....	91
2.	Influence of particle thickness on the heat treatment homogeneity of poplar wood	91
3.	Grinding units.....	92
3.1.	<i>IKA M20</i> cutting mill.....	92
3.2.	<i>Retsch SM300</i> cutting mill	93
3.3.	Planetary ball mill.....	94
3.4.	Measurements of energy consumption required for grinding.....	95
4.	Particle size and shape characterization.....	95
4.1.	Size and shape descriptors	96
CHAPTER III. Flowability characterization of powdered biomass under consolidation: effects of torrefaction intensity.....		99
1.	Preamble	102
2.	Effect of torrefaction intensity on the flow properties of lignocellulosic biomass powders	103
	Abstract.....	103
2.1.	Introduction	103
2.2.	Materials and methods.....	105
2.2.1.	Biomass preparation.....	105
2.2.2.	Torrefaction.....	106
2.2.3.	Grinding procedure.....	107

2.2.4.	Particle size and shape analysis.....	107
2.2.5.	Flowability tests	107
2.3.	Results	108
2.3.1.	Effect of torrefaction intensity on particle size and shape distributions.....	108
2.3.2.	Effect of torrefaction intensity on flow properties of biomass powders	112
2.4.	Discussion on the combined effects of particle size/shape and treatment intensity.....	114
2.5.	Conclusions	118
2.6.	Acknowledgements.....	118
	APPENDIX: Additional flow properties: angles of friction, cohesion and bulk density	118
3.	Complementary investigation on the biomass flowability under consolidation	120
3.1.	Introduction	120
3.2.	Effects of torrefaction intensity on flowability of ball-milled poplar powders.....	120
3.2.1.	Torrefaction conditions.....	121
3.2.2.	Cutting milling: particle size and shape measurement.....	121
3.2.3.	Ball milling: particle size and shape measurement	122
3.2.4.	Flowability measurements	124
3.3.	Particle size and shape effects on flow properties for the same torrefaction intensity.....	126
3.3.1.	Sample preparation.....	126
3.3.2.	Particle size and shape	126
3.3.3.	Flowability measurements	127
3.4.	Conclusion.....	129

CHAPTER IV. Flowability characterization of powdered biomass in a non-consolidated – dynamic conditioning using a rotating drum 131

1.	Preamble	134
2.	Investigation on criteria for assessment of flowability of cohesive and non-cohesive powders using a rotating drum.....	135
	Abstract.....	135
2.1.	Introduction	135
2.1.1.	Criteria for assessing flowability inside a rotating drum.....	136
2.2.	Materials and methods.....	138
2.2.1.	Granular materials	138
2.2.2.	Rotating drum and avalanching tests.....	138
2.2.3.	Bulk motion indicator and flowability criteria	140
2.3.	Results and discussion	144
2.3.1.	Analysis under a range of rotational speeds	144
2.3.1.1.	Average α	144
2.3.1.2.	UAS and LAS	144
2.3.1.3.	Period between avalanches	144
2.3.1.4.	Duration of avalanches.....	145
2.3.1.5.	Load rate.....	145
2.3.1.6.	Avalanche rate.....	147
2.3.1.7.	f factor: fraction of revolution needed to trigger an avalanche	147
2.3.1.8.	Avalanches size $UAS-LAS$	147
2.3.1.9.	Cohesion index	148
2.3.2.	Analysis under a single rotational speed ($\omega = 0.5$ rpm).....	148
2.3.2.1.	UAS, f and avalanches size distributions	149
2.3.2.2.	Analysis of regularity of surface profile: Mean r^2 value at $\omega=0.5$ rpm	150

2.4. Conclusion.....	151
Acknowledgments	152
3. Flowability characterization of torrefied biomass powders: static and dynamic testing.....	153
Abstract	153
3.1. Introduction	153
3.2. Materials and methods.....	155
3.2.1. Biomass powder preparation	155
3.2.1.1. Torrefaction.....	155
3.2.1.2. Grinding and sieving.....	156
3.2.2. Particle size and shape measurements.....	156
3.2.3. Flowability tests	158
3.2.3.1. <i>Ring shear tester</i>	158
3.3. Results and discussion	160
3.3.1. Ring shear tests	160
3.3.2. Dynamic free-surface conditioning: Rotating drum tests	162
3.3.2.1. Categorization of events.....	162
3.3.2.2. <i>UAS</i> distributions.....	164
3.3.2.3. <i>f</i> distributions.....	165
3.3.2.4. Irregularity of powder bed profile r^2	166
3.3.3. Discussion on the effects of particle characteristics	167
3.4. Conclusion.....	169
Acknowledgments	169
Appendix A. Flow properties measurements using shear testers	170
Appendix B. Considerations on shear testing of biomass powders.....	170

CHAPTER V. Towards a Discrete Element Model for raw and torrefied milled biomass particles.....

1. Preamble	175
2. DEM modeling for flow of cohesive lignocellulosic biomass powders: Model calibration using bulk tests	177
Abstract.....	177
2.1. Introduction	177
2.2. Materials and methods.....	179
2.2.1. Sample preparation and particle size and shape characterization	179
2.2.2. Bulk behavior tests	180
2.2.2.1. Angle-of-Repose from bulk solid heaps	180
2.2.2.2. Bulk density	181
2.2.2.3. Rectangular container test.....	181
2.2.2.4. Ring shear tester	182
2.2.3. DEM simulations setup.....	182
2.2.3.1. DEM contact model	182
2.2.3.2. Particle representation	184
2.2.3.3. Time-step.....	186
2.2.3.4. Angle-of-Repose and bulk density determination from simulations	187
2.2.3.5. Ring shear tester simulations	187

2.2.4.	Calibration approach.....	188
2.2.4.1.	Selection and range of values of parameters to be calibrated	189
2.2.4.2.	Optimization problem setup (genetic algorithm).....	190
2.3.	Results and discussion	191
2.3.1.	Bulk behavior tests	191
2.3.1.1.	Bulk density	191
2.3.1.2.	Angle of Repose tests	191
2.3.1.3.	Rectangular container test.....	192
2.3.2.	DEM simulations.....	193
2.3.2.1.	Pareto chart analysis.....	193
2.3.2.2.	Heap angle of repose and bulk density	194
2.3.2.3.	Main effects of calibrated parameters	197
2.3.3.	Calibration and selection of optimal values.....	199
2.3.3.1.	Pareto fronts, 3D representation of optimal values.....	199
2.3.3.2.	Ring shear tester simulations.....	200
2.4.	Conclusion.....	201
	Acknowledgements	202
	Appendix A. Experimental plan	203
	Appendix B. Individual simulation results	203
3.	Implementation of the calibration procedure of DEM parameters for torrefied biomass powders	205
3.1.	Sample preparation and particle size and shape characteristics	205
3.2.	Bulk behavior tests	205
3.2.1.	Angle-of-repose from bulk solid heaps, bulk density and compressibility index.....	205
3.2.2.	Rectangular container test	209
3.3.	DEM simulations	209
3.4.	Calibration results using NSGA-II optimization	210
3.5.	Optimization without interpolation using Minitab®.....	212
4.	Potential of DEM for investigation of non-consolidated flow of cohesive and elongated biomass particles	215
	Abstract.....	215
4.1.	Introduction	215
4.2.	Granular materials and experimental setup.....	218
4.2.1.	Granular material preparation	218
4.2.2.	Rotating drum and avalanching tests.....	219
4.3.	DEM modeling.....	221
4.3.1.	Contact model.....	221
4.3.2.	Particle shape approximation.....	222
4.3.3.	Particle size upscaling and material model calibration.....	223
4.3.4.	Simulated system description.....	225
4.4.	Results and discussion	228
4.5.	Potential of DEM simulations for exploration of shape and cohesion effects on flow.....	233
4.6.	Conclusions	236
	Acknowledgments	237
	CONCLUSION AND PERSPECTIVES	239
	General conclusion.....	241

Perspectives and suggestions for future work	245
APPENDIXES	249
Appendix I. Influence of particle thickness on the heat treatment homogeneity of poplar wood	250
Appendix II. Measurements of energy consumption required for grinding	256
Appendix III. Automated calculation of avalanche angles in a rotating drum system	259
Appendix IV. Examples of LIGGGHTS® input scripts	272
References	279

List of Figures

Figure 1. Outline of the main parts of the manuscript.	27
Figure 2. Borregaard biorefinery.	33
Figure 3. The three principal axes of wood with respect to fibers direction and growth rings.	37
Figure 4. Schematic of cell organization of conifer and broad-leaved trees.	38
Figure 5. Schematic view of cell wall layers (MFA is the microfibril angle).	39
Figure 6. Plant cells, microfibril structure and cellulose chemical representation.	40
Figure 7. Chemical structure of hemicelluloses.	41
Figure 8. Lignins.	41
Figure 9. (a) Poplar plantation (b) Spruce plantation in Lanarce (France) (c) Geographic distribution of poplar plantations in France. (d) Spruce average volume per hectare.	42
Figure 10. Routes for biomass valorization.	44
Figure 11. Main stages of a biomass gasification process (BioTfuel project).	47
Figure 12. Gasification reactions at the particle scale.	47
Figure 13. Fischer-Tropsch synthesis process flowchart.	49
Figure 14. Hammer mill grinding woody biomass.	50
Figure 15. Thermogravimetry of a poplar sample.	52
Figure 16. SEM images of a transversal section of E. Saligna.	54
Figure 17. Comparison of power consumptions for milling of raw, dried and torrefied willow wood to final average size between 0.2 and 0.8 mm.	55
Figure 18. Optimized torrefaction process layout.	56
Figure 19. Flow problems in storage units.	57
Figure 20. Schematic of a Jenike's shear tester (A: Base, B: ring, C: lid, σ : normal force, τ : shear force).	60
Figure 21. Schulze ring shear tester RST-XS.	60
Figure 22. Shear stress procedure in a ring shear tester.	61
Figure 23. Flow function, lines of constant flowability and flowability classification.	62
Figure 24. (a). Flow regimes in silos. (b) Scheme of a conical hopper depicting the hopper outlet diameter (B) and the hopper half angle (β).	63
Figure 25. (a). Compressibility test in a tap volumeter. (b). Funnel for measuring time of discharge (t_M). (c). Measurement of poured angle-of-repose (α_M).	64
Figure 26. Flowability characterization methods. CI: compressibility index; RST: Ring shear tester; AoR: angle-of-repose.	65
Figure 27. Flow regimes in a rotating drum for non-cohesive powders.	66
Figure 28. Flow in a rotating drum.	66
Figure 29. Revolution powder analyzer.	67
Figure 30. Schematic representation of forces acting on particle i from contacting particle j and non-contacting particle k (capillary interaction).	74
Figure 31. General DEM algorithm.	75
Figure 32. Schematic representation of the Hertz-Mindlin spring dash-pot contact force model.	76
Figure 33. (a) Woodchip approximation using the multisphere approach and (b) actual woodchip particle. (c) Maize grain (d) DEM multisphere model.	81
Figure 34. Schematic representation of particle size scaling approaches	82
Figure 35. Example of LIGGGHTS® input file with its main sections highlighted.	84
Figure 36. Schematic representation of the torrefaction unit.	90
Figure 37. Typical temperature profile during a torrefaction test.	91
Figure 38. IKA M20 cutting mill.	92
Figure 39. Retsch SM300 cutting mill.	93
Figure 40. Retsch PM100 planetary ball mill.	94
Figure 41. QICPIC apparatus.	96

Figure 42. Particle size and shape descriptors. _____	97
Figure 43. Flow properties determination. _____	108
Figure 44. Influence of torrefaction intensity on circularity and size distributions for spruce and poplar powders. _____	109
Figure 45. Influence of torrefaction intensity (Mass Loss ML) on PSD. _____	110
Figure 46. Effect of torrefaction intensity on the mean particle size (left) and volume of fines (right) of poplar and spruce powders. _____	111
Figure 47. Effect of torrefaction intensity (ML) on flow properties. _____	113
Figure 48. Effect of the torrefaction intensity on the flowability factor of poplar and spruce powders. _____	114
Figure 49. Effect of particle size and shape on flow properties for poplar and spruce powders _____	116
Figure 50. Scanning Electronic Microscopic images for untreated and torrefied spruce and poplar powders. _____	117
Figure 51. Cumulative (left) and differential (right) size distributions in volume for the SM300 grinder outflow with a 1 mm hole bottom sieve. _____	121
Figure 52. (a) Median descriptors of particle size and PSD span for the five samples. (b) Cumulative size distributions in maximum (dotted curves) and minimum (solid curves) Feret diameters. _____	122
Figure 53. Particle size characteristics after ball milling. _____	123
Figure 54. Shape characteristics of the raw and torrefied samples. _____	124
Figure 55. Scanning Electronic Microscopy images for raw, slightly and intensively torrefied poplar powders. _____	124
Figure 56. Flowability of raw and torrefied ball-milled biomass samples. _____	125
Figure 57. Effect of grinding time on the aspect ratio and size distributions of the powder obtained after ball milling ($ML = 12.2\%$). _____	126
Figure 58. (a) Differential particle size distributions at different grinding times. (b) Differential aspect ratio distributions. (c) Average descriptors of particle size, shape (50 th centiles of the cumulative distributions) and span of the PSD as function of the grinding time. _____	127
Figure 59. SEM images of the powders obtained after different grinding times. _____	128
Figure 60. Flowability of torrefied biomass powder ($ML = 12.2\%$) at different grinding times. _____	128
Figure 61. Rotating drum system. _____	139
Figure 62. (a) Image processing flowchart. (b) Main stages of image processing. _____	140
Figure 63. Definitions the average angle of surface (θ) and the centroid angle (α). _____	141
Figure 64. (a) Typical evolution of α for a non-cohesive and two cohesive samples at $\omega = 0.2$ rpm. (b) Equivalence between θ and α motion descriptors for glass-beads. _____	141
Figure 65. Descriptors used for assessing flowability of non-cohesive and cohesive powders over a range of rotational speeds. _____	146
Figure 66. Flowability descriptors distributions for $\omega=0.5$ rpm. _____	149
Figure 67. Flow descriptor for the irregularity of surface profile (r^2). _____	150
Figure 68. Biomass size and shape characteristics. _____	157
Figure 69. Rotating drum system. _____	160
Figure 70. Yield loci at $\sigma_{pre} = 5$ kPa. _____	160
Figure 71. (a) (b). Flow functions and (c) flowability factor FFC for the biomass sieving cuts. _____	161
Figure 72. Typical evolution of the centroid angle for two examples of biomass powders and non-cohesive glass beads. _____	162
Figure 73. Flow inside the rotating drum for two biomass samples. _____	163
Figure 74. Events duration for coarse (a) and fine (b) biomass powders. _____	164
Figure 75. UAS distributions for both sieving fractions of raw, mildly and intensively torrefied samples. _____	165
Figure 76. Distributions of the fraction of revolution required to trigger events. _____	166
Figure 77. Coefficient of determination r^2 . _____	166
Figure 78. Experimental and calculated values of three flowability descriptors. _____	168
Figure 79. Shear stress testing for sample 1 at $\sigma_{pre} = 2$ kPa. _____	170
Figure 80. (a) Shear stress and lid displacement during shear test of Sample 1 at $\sigma_{pre} = 2$ kPa. (b) Shear stress evolution of Sample 6 at $\sigma_{pre} = 5$ kPa (note the presence of peak values when shearing to failure). _____	171
Figure 81. AoR setup. _____	181
Figure 82. Rectangular container device. _____	182

Figure 83. Schematic representation of the contact model used in this study. _____	184
Figure 84. Particle representation for biomass samples. _____	185
Figure 85. Influence of scaling particles size up for sample 1. _____	186
Figure 86. Geometry of the simulated ring shear tester. _____	188
Figure 87. Flowchart of the calibration procedure. _____	189
Figure 88. Examples of heaps obtained and rectangular container test from DEM simulations. _____	192
Figure 89. Pareto charts of the standardized effects. _____	193
Figure 90. Contour surface responses for sample 1. _____	195
Figure 91. Contour surface responses for sample 2. _____	196
Figure 92. Average coefficients of determination of heaps profiles. _____	197
Figure 93. Main effects plots. The dotted horizontal line represents the overall mean. _____	198
Figure 94. Pareto front evolution over 100 generations of NSGA-II optimization. _____	199
Figure 95. Sets of optimal calibrated parameters for sample 1 and 2. _____	200
Figure 96. Simulated (DEM) and experimental (Exp) evolution of shear (τ) and consolidation stresses (σ) for sample 1. _____	201
Figure 97. Simulation results of AoR, bulk density and p ratio for Sample 1 and 2. _____	204
Figure 98. Lifting cylinder preliminary tests. _____	206
Figure 99. Angle-of-repose experiments. _____	206
Figure 100. Compressibility index and angle-of-repose for the six biomass samples. _____	208
Figure 101. DEM particle representation of biomass samples (true relative size) using a multisphere approach. _____	209
Figure 102. Simulation results for the sample $ML = 24.5\%$. _____	210
Figure 103. Pareto fronts after 100 generations of NSGA-II optimization. _____	211
Figure 104. Sets of optimal parameters for torrefied samples. The size and color scale of the data points indicate the value of the sum O_1+O_2 for each set of μ_s , μ_r and CED. _____	212
Figure 105. Examples of optimization results from MINITAB for samples 1 and 2. _____	213
Figure 106. Typical SEM images of the granular materials used in this work. _____	219
Figure 107. Rotating drum system. _____	220
Figure 108. Multisphere particle representation. _____	224
Figure 109. Calibration bulk experiment (Heap formation). _____	225
Figure 110. Experimental and DEM-simulated motion inside the rotating drum for torrefied biomass and glass beads samples. _____	227
Figure 111. Typical experimental and simulated post-avalanche profiles after one rotation. _____	228
Figure 112. Experimental and DEM-modeled evolution of the 'centroid angle'. _____	229
Figure 113. Distributions of flowability descriptors. Left-side plots correspond to the experimental results, right-side are the results obtained from DEM simulations. _____	230
Figure 114. Irregularity of the free-surface profile as measured by the coefficient of determination (r^2). _____	232
Figure 115. Snapshots of DEM simulations showing the effect of particle shape and interparticle cohesion on flow. _____	234
Figure 116. Effect of particle characteristics on the flow behavior at two consecutive moments t_i and t_j . _____	235
Figure 117. Effect of particle characteristics on the temporal evolution of α during one drum revolution. _____	235
Figure 118. Comparison of DEM results between monodisperse raw biomass and a polydisperse sample. _____	236
Figure 119. (a) Sample conditioning (the core thermocouple is schematized). (b). Samples inside the torrefaction furnace. _____	252
Figure 120. Effect of sample thickness on core temperature at a torrefaction temperature of 280 °C for one-hour treatment. _____	253
Figure 121. Comparison of temperature overshoot for three treatment intensities. _____	253
Figure 122. Effect of particle thickness and torrefaction temperature on the overall mass loss (ML). _____	254
Figure 123. Elementary ratios of carbon and oxygen composition on the sample surface and core as a function of the torrefaction intensity for different thicknesses. _____	255
Figure 124. Power consumption profile for raw and torrefied wood chips in a SM300 grinder. _____	256
Figure 125. Power consumption in a planetary ball mill for an empty grinding jar ('no-load test') and filled with raw and torrefied biomass. _____	257

List of Tables

Table 1. Interest and challenges of utilization of lignocellulosic biomass within an energy context. _____	36
Table 2. Elementary approximated composition of wood. _____	39
Table 3. Average composition (mass %) of woody biomass. _____	40
Table 4. Classification of extractives in wood. _____	42
Table 5. Comparison of biochemical and thermochemical processing of biomass. _____	44
Table 6. Comparison of the main BtL processes. _____	45
Table 7. Main gasification reactor designs. _____	48
Table 8. Structural and chemical changes in biomass during drying and torrefaction.. _____	51
Table 9. Effects of torrefaction on biomass feedstock properties. _____	53
Table 10. Flowability classification according to FFC values. _____	62
Table 11. Flowability scale according to several indicators. _____	65
Table 12. Simulation approaches for granular materials. _____	72
Table 13. Soft-particle and hard-particle approaches of DEM. _____	73
Table 14. Approaches for DEM parameter calibration. _____	83
Table 15. IKA M20 technical data. _____	92
Table 16. Cutting mill SM300 main features. _____	93
Table 17. Main features of the PM100 ball mill. _____	94
Table 18. Torrefaction conditions and global mass loss for the 14 samples studied. _____	106
Table 19. Parameters of the exponential regressions of the form $x_{50} = a \cdot [b + \exp(-c \cdot ML)]$ for the mean particle size after grinding as a function of ML . _____	111
Table 20. Ground samples properties: Global mass loss, mean particle size, mean circularity and span values. _____	112
Table 21. Flow properties for milled poplar and spruce at different torrefaction intensities. _____	119
Table 22. Torrefaction temperature and global mass loss of the samples for a 1-hour treatment. _____	121
Table 23. Additional flow properties ($\sigma_{pre} = 5$ kPa) _____	125
Table 24. Additional flow properties ($\sigma_{pre} = 5$ kPa) _____	129
Table 25. Size and shape properties of the samples _____	138
Table 26. Synthetic values from flowability descriptors distributions. _____	150
Table 27. Powders size and shape descriptors. _____	157
Table 28. Values of the flowability descriptors from a rotating drum setup biomass powders. Span values are indicated in round brackets, flowability ranking is reported in square brackets. _____	164
Table 29. Parameters of the power law relationships (Eqs. (16) to (18)) for three flowability descriptors. _____	168
Table 30. Samples nomenclature and size/shape characteristics. _____	180
Table 31. Equations for calculations of forces and torques on particle i according to the Hertz-Mindlin model. _____	183
Table 32. Parameters of multisphere model for particles representation _____	185
Table 33. DEM simulation parameters for particles and walls _____	190
Table 34. Set of calibration parameters tested. _____	190
Table 35. Input parameters of NSGA-II _____	190
Table 36. Numerical precision of binary encoded factors. _____	191
Table 37. Bulk behavior experiments results (standard deviation is reported in parentheses). _____	192
Table 38. Optimized values of μ_s , μ_r and CED and comparison of simulated responses (Sim.) against experimental measurements (Exp.). e : relative error between experimental and DEM responses. _____	200
Table 39. Simulation (Sim.) and experimental (Exp.) results for ring shear tester tests. _____	201
Table 40. Sample nomenclature, size and shape characteristics. _____	205
Table 41. Results of bulk measurements for the biomass powders (the values in parentheses correspond to the standard deviation). _____	207
Table 42. Parameters for multisphere model representation of biomass samples. _____	209

Table 43. DEM features for simulations of heap formation. _____	210
Table 44. Optimized values of μ_s , μ_r and CED and comparison of simulated responses (Sim.) against experimental measurements (Exp.). e: relative error between the experimental and DEM responses. _____	212
Table 45. Optimized values using MINITAB. _____	214
Table 46. Sample size and shape characteristics. _____	219
Table 47. Equations for calculations of forces and torques on particle i according to the Hertz-Mindlin model. _____	222
Table 48. Characteristics of the multisphere model for representation of biomass particles (non-scaled). _____	223
Table 49. DEM simulation parameters for particles and walls. _____	226
Table 50. Characteristics of the simulated rotating drum system. _____	227
Table 51. Experimental and simulated results for several flowability indicators. Span values (Eq. 10) are indicated in round brackets, flowability ranking is reported in square brackets from I being the worst flowing material to IV the material with the best flowability. The relative error is referred to as e. _____	231

Abbreviations

1G	First generation (biofuels)
2G	Second generation (biofuels)
2D	Two-dimensional
3D	Three-dimensional
AoR	Angle-of-repose
ASTM	American Section of the International Association for Testing Materials,
BC	Biomass coarse sieving cut
BF	Biomass fine sieving cut
BtL	Biomass-to-Liquid
CAD	Computer Aid Design
CAS	Critical Applied Stress
Cat	Catalyst
CEA	French Alternative Energies and Atomic Energy Commission
CFD	Computational Fluid Dynamics
CGB	Confédération Générale des Planteurs de Betteraves
<i>CI</i>	Compressibility (Carr's) Index
CML	Compound Middle Lamella
DEM	Discrete Element Method
ECN	Energy Research Center (the Netherlands)
EPSD	Elastoplastic Spring-Dashpot Model
EU	European Union
FEM	Finite Element Method
<i>FFC</i>	Flow function coefficient
FTS	Fischer-Tropsch synthesis
GB	Glass beads
GHG	Greenhouse gas
IFPEN	Institut Français du Pétrole – Énergies Nouvelles
INRA	Institut National de la Recherche Agronomique
ISO	International Organization for Standardization
JKR	Johnson, Kendall, Roberts force model
LAMMPS	Large-scale Atomic/Molecular Massively Parallel Simulator
<i>LAS</i>	Lower Angle of Stability
LCA	Life cycle assessment
LED	Light-emitting diode
LIGGGHTS	LAMMPS Improved General Granular and Granular-heat transfer simulator
MRI	Magnetic Resonance Imaging
ONF	Office National des Forêts
NSGA	Non-dominated Sorting Genetic Algorithm
PSD	Particle size distribution
R&D	Research and Development
Ref.	Reference
RST	Ring shear tester
SD	Standard deviation
sJKR	Simplified JKR model
SRST	Schulze ring shear tester
<i>UAS</i>	Upper Angle of Stability
USA	United States of America
w.b.	Wet basis (for moisture content)

Symbols

		Units
A	Surface of contact	m^2
\mathbf{a}	Acceleration	$m \cdot s^{-2}$
a	Aspect ratio	
a_{50}	50 th centile of the aspect ratio distribution	
AoR	Angle-of-repose	degrees
A_p	Projected area of particle	m^2
A_v	Area of convex hull	m^2
B	Hopper outlet size	m
c	Overlapping factor	
C	Cohesion	kPa
C_x	Convexity	
CED	Cohesion energy density	$J \cdot m^3$
CI	Compressibility index	
D	Composite desirability	
d_i	Individual desirability	
d_{ij}	Distance between centers of particles i, j	m
d_p	Particle diameter	m (or μm)
d_{eq}	Equivalent diameter (of a sphere having the same volume than the clump of spheres)	m
d_{Fmax}	Maximum Feret Diameter	m (or μm)
d_{Fmin}	Minimum Feret Diameter	m (or μm)
d_{Fmean}	Mean Feret Diameter	m (or μm)
e	Relative error	%
e	Coefficient of restitution	
FF	Flow function	
FFC	Flow function coefficient	
\bar{f}	Flow factor (for hopper design)	
f	Fraction of revolution required to trigger events	
\bar{f}	Flow function	
F_1, F_2	Forces measured by the tie rods in a RST	N
\mathbf{F}_{ij}^c	Contact force between particles i and j	N
$\mathbf{f}_{ij}^{c,t}$	Tangential component of the normal contact force	N
$\mathbf{f}_{ij}^{c,n}$	Normal component of the normal contact force	N
$\mathbf{f}_{ij}^{c,n} \Big _s$	elastic deformation (spring) conservative force	N
$\mathbf{f}_{ij}^{c,n} \Big _r$	viscous dissipation (damping or dash-pot force)	N
\mathbf{g}	Gravity	$m \cdot s^{-2}$
G_{eff}	Effective shear modulus	Pa
HR	Hausner ratio	
I_i	Moment of inertia of particle i	$kg \cdot m^2$
k_n	Elastic constant for normal contact	$N \cdot m^{-1}$
k_t	Elastic constant for tangential contact	$N \cdot m^{-1}$
k_r	Rolling stiffness	$N \cdot m^{-1}$
L_i	Lower limit of possible values of Y_i	
m_i	Mass of particle i	kg
m_{eff}	Effective mass	kg
ML	Mass loss	%
m_r	Mass of powder retained (shear box)	g

m_0	Initial mass of powder (shear box)	g
N	Normal force	
n	Avalanche number, number of particles between endplates	
n_{sph}	Number of spheres in a clump	
O	Objective function	
P	Pressure	Pa
P	Perimeter	m
p	Retainment ratio (shear box)	
R	Particle radius	m
R_{eff}	Effective radius	m
r^2	Coefficient of determination of linear regression	
s	Skin parameter	m
S_x	Particle size span	
S_ψ	Circularity span	
S_ϵ	Span for flowability indicator ϵ distribution	
T	Temperature	°C
T	Period between avalanches	s
\mathbf{T}_{ij}^t	Torque acting in particle i by particle j	N·m
\mathbf{T}_{ij}^r	Rolling friction torque	N·m
$\mathbf{T}_{ij}^{r,k}$	Torque component modeled as a mechanical spring	N·m
t	Time	s
t_M	Time of discharge	s
U_i	Upper limit of possible values of Y_i	
\mathbf{v}_i	Velocity vector of the mass center of particle i	m·s ⁻¹
V_{clump}	Volume of a cluster of spheres	m ³
V_L	Loose volume	m ³
V_T	Tapped volume	
\mathcal{X}	Set of optimal individuals	
v_i	Tangential relative velocity	m·s ⁻¹
w	Rotating drum width	m
\mathbf{x}_i	Particle vectorial position	m
x_{50}	50 th centile of PSD	μm
Y_{eff}	Effective Young's modulus	kPa
Y	Young's modulus	kPa
Y_i	Response to be optimized	

Greek letters

		Units
α	Centroid angle	degrees
β	Hopper half angle	degrees
γ_n	Viscoelastic damping constant for normal contact	N·s·m ⁻¹
γ_t	Viscoelastic damping constant for tangential contact	N·s·m ⁻¹
δ_t	Tangential displacement	m
$\Delta\alpha$	Size of avalanches	degrees
Δt	Timestep	s
ΔT_H	Hertz time	s
ΔT_R	Rayleigh time	s
$\Delta\theta_{r,ij}$	Incremental relative rotation between two particles	degrees
Δd_p	Particle size variation during ball milling	

ΔH_0	Standard enthalpy of reaction	kJ/mol
ζ	Ratio small events/large events	
θ	Angle of slope of powder free surface from linear regression	degrees
λ	Overlapping distance	m
μ_s	Sliding friction coefficient	
μ_r	Rolling friction coefficient	
ξ	Flowability descriptor	
ρ_b	Loose bulk density	kg·m ⁻³
ρ_t	Tapped bulk density	kg·m ⁻³
σ	Consolidation stress, normal stress	kPa
σ_{sb}	Shear (normal) stress	
τ	Shear stress, tangential stress	kPa
ν	Poisson's ratio	
ψ	Circularity	
φ_e	Effective angle of internal friction	degrees
ψ, ε	General flowability indicator	
ω	Angular velocity, rotational speed	rpm

General Introduction

Although opinions on the availability of fossil resource stocks may vary from 50 to 500 years, it is widely agreed that the reserve is limited and that it is essential to search for new renewable energy sources. This limitation combined with their observed effects on climate change have propelled the interest on biomass as a CO₂-neutral renewable energy source. The use of biomass-based fuels (biofuels) is one of the most promising technological responses that can help reduce CO₂ and greenhouse gas emissions.

After a first generation of biofuels that uses the edible part of plants, a second generation – which uses the entire lignocellulosic material – has not yet been fully developed. Although there are several transformation routes for biomass valorization, the thermochemical conversion through entrained-flow gasification is one of the preferred pathways to produce second-generation biofuels. The use of a biomass feedstock in powder form increases its reactivity during gasification and facilitates its conveying and injection. Beforehand, it is therefore necessary to grind the solid biomass into powder. However, due to the fibrous and resilient nature of the lignocellulose, this step is hugely energy consuming. Torrefaction, besides improving biomass characteristics such as energy content and decreasing hygroscopicity, is an interesting pretreatment stage that can improve biomass grindability, reducing energy consumption.

Problems related to the handling of the biomass feedstock in a milled form are frequent and greatly hinder the industrialization of 2G processes. The design of efficient feeding storage, handling and feeding solutions needs knowledge on the bulk flow properties of the materials under different conditioning states. Currently, this knowledge remains very limited and very few information is available on the effects of torrefaction on particle characteristics and flow behavior. However, it is essential for the design of industrial biomass conversion equipment and processes and the prevention of problems during conveying or storage.

The objective of this doctoral project is to observe, quantify and understand the effect of the pretreatment stages (torrefaction and grinding) on the physical characteristics of the biomass powder obtained. Within this aim, the combination of experimental and numerical approaches can help to understand the behavior of the material, as well as to develop tools that can be used for the design and optimization of the industrial handling systems for biomass.

First, from an experimental perspective, the understanding of the bulk macroscopic behavior of the powder needs the assessment of the torrefaction effects at the particle scale, namely in terms of particle size and shape characteristics. As granular materials can behave very differently depending on their conditioning and consolidation state, characterization under different conditions is also necessary. Second, from a numerical point of view, modeling using the Discrete Element Method can provide insight on the effects of particle scale characteristics (driven by pretreatment conditions) on the bulk behavior. Additionally, the assessment of the predictive nature of simulations, which is always desired and sought, can reinforce their value as a means to improve the overall biomass valorization process.

Concisely, the aim of this work can be condensed as an attempt to provide answer to the following research questions:

- How torrefaction and grinding conditions affect the particle properties of biomass?
- What is the effect of these particle characteristics on the flow behavior under different conditions?
- Can Discrete Element Simulations reproduce the flow behavior of raw and torrefied biomass materials within a predictive aim?

Manuscript outline

The overall objective of this research was achieved in the various phases of this work presented as distinct chapters. The manuscript outline is schematically shown in Figure 1.

Bibliographical elements are presented in **Chapter I**. A first part mainly deals with concepts related to the biomass-to-liquid technologies and the need for biomass characterization in terms of flow properties, the pretreatment stages and the wood characteristics. The overall context of the study is also described. A second part focusses on the flow characterization of granular materials: the commonly used methods and their application to biomass materials. Finally, the modeling of particulate systems is reviewed with emphasis on the Discrete Element Method. Its generalities as well as the challenges faced when simulating biomass particles are presented.

Chapter II covers the description of the experimental facilities that are common to most of the work. The torrefaction unit, the grinding devices as well as the equipment used to characterize particle size and shape are thus presented. This includes two brief experimental studies on (i) the intraparticle homogeneity of heat treatment and (ii) the effects of torrefaction on the grinding energy consumption.

Chapter III corresponds to the experimental study of the influence of the intensity of torrefaction on the flowability of poplar and spruce powders, evaluated using a Schulze Ring Shear tester. The effects of torrefaction on particle size and shape and their subsequent effect on flow properties are discussed. A complementary section of this chapter presents further results using a ball milling technology.

The need for flow characterization under different conditions has been underlined above. Therefore, the flowability characterization using a rotating drum, in which the powders are in a non-consolidated dynamic state, is discussed in **Chapter IV**. First, an investigation is made on the criteria for assessment of flowability using avalanching behavior for non-cohesive and cohesive materials. A detailed description on the conception, configuration, acquisition and analysis of data using the in-house-designed device is also provided. Then, raw and torrefied biomass powders are studied using the rotating drum device and the results compared to shear analysis.

Chapter V concerns the implementation of the Discrete Element Method (DEM) to the study of biomass powder flow. We present the calibration of a material model for biomass particles through comparison between experimental and simulated bulk responses. A preliminary validation of the calibrated parameters is made by simulating a ring shear test and comparing the simulation results to those presented in Chapter IV. This procedure is subsequently applied to wood powders treated under different torrefaction conditions and with different particle sizes. Finally, the potential of DEM simulations to represent realistic flow in a rotating drum is the subject of the last part of this chapter, in which experimental (from Chapter IV) and simulated results are compared.

A general conclusion, as well as suggestions for future work conclude this manuscript. In an **Appendix** section, in addition to some further results, we detail the implemented image processing algorithms, as well as the DEM input scripts and the algorithms developed for processing the results. Finally, a comprehensive French summary is also provided.

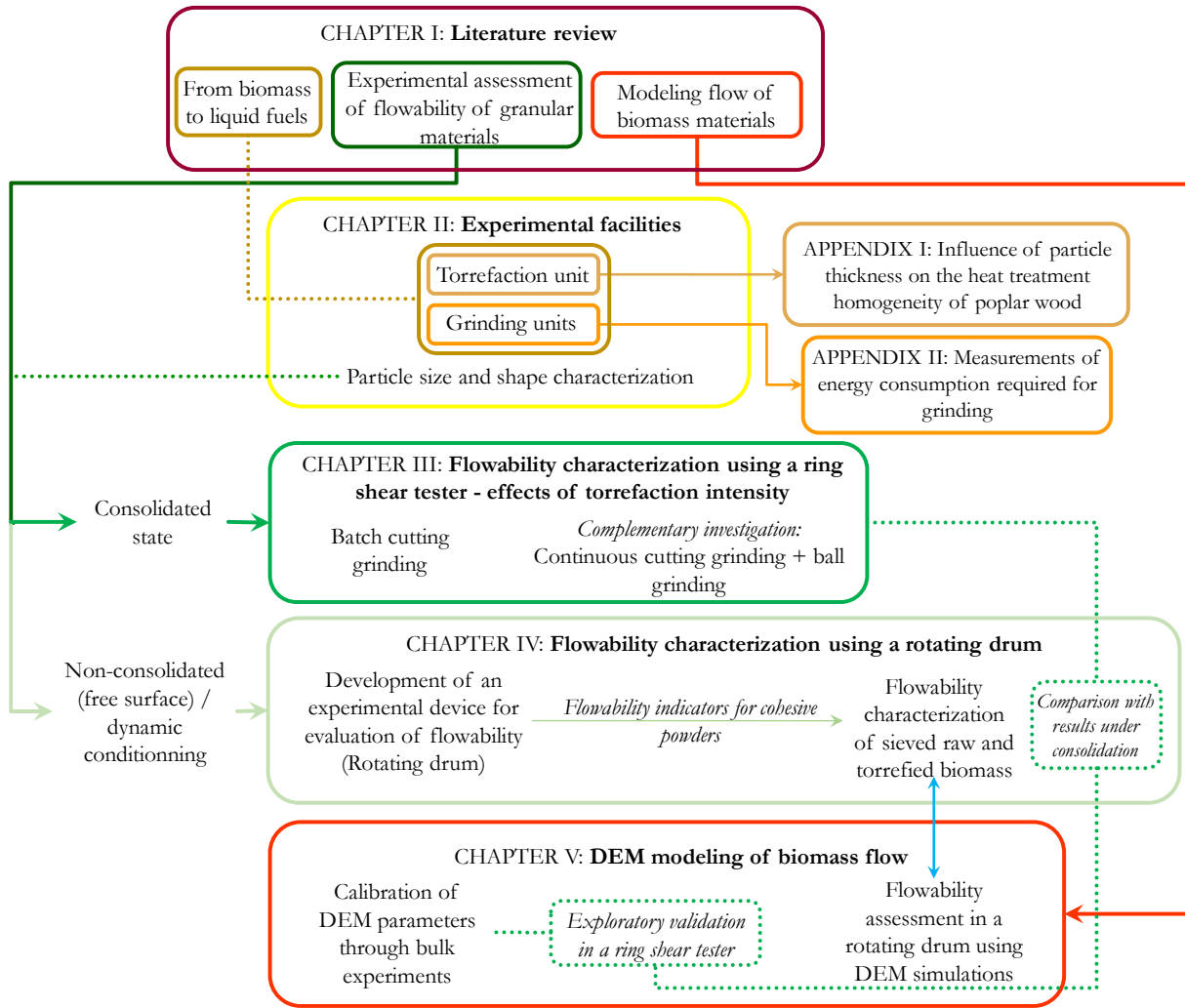


Figure 1. Outline of the main parts of the manuscript.

CHAPTER I

Literature review

A- From biomass to liquid fuels

1. Energetic, environmental and geopolitical context

In the 19th century, the industrial revolution in developed countries enabled them to experience strong economic and demographic growth. During this period and much of the 20th century, the prosperity of a country was assessed in demographic and economic terms and was based mainly on the extensive use of fossil and mineral resources. But the two oil shocks of 1973 and 1979, as well as the industrial disasters of the 1980s made decision-makers aware of the need to combine environmental protection with economic development. Thus, in 1987, the notion of sustainable development appeared at the 42nd session of the United Nations. Since then, several conferences and agreements have been concluded around the world to seek global cooperation around environmental and climate change issues. These agreements involve the establishment of limits and objectives for reduction of greenhouse gas (GHG) emissions and the use and development of alternative energy sources.

With the objective of mitigating climate change, the European targets for renewables and energy efficiency were revised upwards in 2018. The European 2030 climate and energy framework calls thus for the use of biomass in electricity, heat and transport (fuels), in order to reach at least 32 % share of all energy use coming from renewable sources by 2030. As of 2016, renewable energy accounted for an estimated 18.2 % of global total final energy consumption [1]. This implies that the use of biomass should roughly have to double to meet the European targets [2,3].

The main drivers for biomass use include volatility in crude oil market, climate change mitigation and reduction of greenhouse gas emissions, reduced dependence on imported energy resources, increased cost for primary power generation and improved opportunities for agricultural products and rural economies [4]. Beyond the heat and power generation sectors, the transport sector remains the most important sector to which these benefits of biomass utilization could contribute positively.

Indeed, transport has been the sector most resistant to efforts to reduce CO₂ emissions due to its high dependence on fossil fuels and steady growth. On a global scale, the share of renewable energy in transport is low (only 3.1 %) compared to other sectors such as heating (10.3 %) and power generation (26.5 %). Up to 90 % of this share is currently provided by liquid biofuels.

As the technology for converting biomass to energy matures and expands, governments have moved to incentivize biofuel production, particularly bioethanol and biodiesel. In 2015 for example, 34 countries plus the European Union (EU) have renewable fuel usage mandates and stimulus in place. However, currently there is a halt to incentive policies for first generation biofuels (Section 1.1) (except in Asia), due to their mixed environmental record and their impact on food production. Biofuel promotion policies have thus begun to include specific requirements for the use of second-generation cellulosic biofuels. In the EU, for example, the Renewable Energy Directive for 2030 [2,5] proposed by the European Commission in 2017 included a target of 3 % for 2G biofuels and a cap of 7 % on 1G biofuels. Similar requirements for the use of advanced biofuels have already been adopted at the national level in the EU, for example in Italy [1]. In India and China, a medium-term emphasis is been given in development of 2G biofuels over 1G biofuels.

In France, the *Grenelle Acts* (*Grenelle de l'Environnement 1 (2007) and 2 (2010)*) and the Directive 2009/28/CE are the basis for the National Renewable Energy action plan [6]. This plan sets a target of 27 % renewable energy in the electricity sector, 33 % in the heating/cooling sector and 10.5 % in the

transport sector by 2020. The Energy transition Act [7] aims at achieving a total share of renewable energy in the energy mix of 32 % and a 30 % reduction in fossil fuel consumption by 2030 [8]. According to *Grenelle 2*, 50 % of renewable energy targets must be achieved by biomass. Biofuels (mainly 1G) are expected to account for the share of renewable energy (10.5 %) in the transport sector. While the implementation of 2G biofuels is expected by the period 2010-2020, their inclusion in the energy mix is not explicitly mentioned in the renewable energy target.

Biomass valorization through biofuel production is not a new topic, as evidenced by the well-developed technologies for 1G biofuel. Production of 1G biofuels for transport has indeed increased 2.5 % in 2017, with the United States and Brazil remaining the world's largest producers of ethanol and biodiesel [9]. However, even if progress is being made, complementary 2G technologies for biomass valorization, that do not compete with food crops and/or affect arable land, are still to be developed (Section 1.2).

1.1. First-generation biofuels

The first-generation biofuels industry, launched in the late 1970s, was based on the biochemical transformation of sugar or starch crops (mainly sugar cane and maize, respectively) into ethanol fuel and oilseeds into biodiesel. These industries grew rapidly in the first decade of the 21st century, with annual world production rising from 1.7 to $10.6 \times 10^7 \text{ m}^3$ of ethanol from 2000 to 2017 and $31 \times 10^6 \text{ m}^3$ of biodiesel in 2018 [1], the main ethanol-producing countries being USA and Brazil.

It was not until 1992 and the reform of the Common Agricultural Policy (CAP) that biofuels were launched in France and Europe. The objective was then economic and made it possible to offer farmers new opportunities and create jobs in order to revitalize rural areas. More recently, it is mainly environmental objectives that have contributed to the development of the sector, helped by economic incentives.

The development of first generation biofuels was not achieved without controversy, including criticism of crop and biofuel subsidies, concerns about the use of food crops for fuel production and the debate on the environmental impact of biofuel agriculture, including uncertainties about the role of biofuels in reducing greenhouse gas emissions [10]. In France, for instance, a review report on biofuel support policies [11] showed mixed economic results. This study shows that for many years tax exemptions had compensated producers well beyond the extra production costs. In addition, there was little job creation in the agricultural sector. Environmentally, recent Life Cycle Assessments [12] report a reduction in GHG emissions of 30 to 60 % for 1st generation biofuels compared to their fossil fuels, whereas the initial forecasts were for a reduction of 60 to 80 % before 2002. At the geopolitical level, Europe's objective of increasing its energy independence by limiting fossil fuel imports seems difficult to achieve. A significant substitution of this type of energy by first-generation biofuels would require a much larger amount of land than is available [11]. On the other hand, the substitution of food crops for energy crops would imply direct competition between these two possible crop types. The development and expansion of the biofuels sector then contributes to rising food prices in the medium term and increasing food insecurity among the most vulnerable segments of the population in developing countries [13].

Many of these concerns would be mitigated by the development of advanced biofuels that use high-yielding non-food crops that can be grown on marginal or fallow lands. These alternative crops are of two types: lignocellulosic biomass (i.e. second-generation biofuels) and lipids from alternative crops (such as algae, i.e. third-generation biofuels) [14].

It is however important to note that the aforementioned considerations should be taken with prudence. Indeed, they are currently the subject of intense debate [1]. A recent study [15] reveals that first-generation biofuels can still be considered to have very good GHG emission performance compared to second-generation biofuels. Moreover, competition for arable land would be offset by the excellent land efficiency

of first-generation crops and, in the case of wheat, most of the European ethanol production is based on grain of non-food quality and on harvest surpluses, without any competition. A balanced complementarity of use between first- and second-generation biofuels therefore seems to be the way forward.

1.2. Second-generation biofuels

Second-generation (2G) liquid biofuels are produced from agricultural lignocellulosic biomass. The main advantage of producing second-generation biofuels from inedible feedstocks is that it limits direct competition between food and fuel land use associated with first-generation biofuels. Feedstock involved in the process can be grown specifically for energy purposes, increasing production per unit land area, and more of above-ground plant material can be converted and used to produce biofuels. As a result, this will further increase land use efficiency compared to first generation biofuels. Second-generation biofuels are obtained by two different approaches: biochemical or thermochemical processing (Section 2.3). In the current state of development, production processes require sophisticated processing production equipment, high investment per unit of production and large-scale facilities to curtail capital cost via economies of scale. To achieve the potential energy and economic outcome of 2G biofuels, further research, development and application of technologies are required on feedstock production and conversion processes [16].

Despite these limitations, several examples exist of successful implantations of industrial-scale processes for 2G biofuel production. One of them is the Borreggard biorefinery (Norway), established in 1938. It produced about 20 million liters of cellulosic ethanol (by biochemical transformation) from spruce in 2017 [1,17]. Since the early 2010s, five commercial-scale ethanol refineries based on biochemical processes have been opened (in Italy (closed since), Brazil and USA) and two gasification projects (Canada, USA). Thermochemical processes such as gasification are still far from being widely commercialized and, for the most part, only pilot plants are available at the time, most of them located in Europe [18]. The most recent projects for industrial-scale production plants of 2G biofuels include plans by:

- India: plans were announced in 2017 to build at least 12 commercial-scale advanced biofuel plants, mainly to produce cellulosic ethanol from the large volumes of plant residues in the country [1].
- Canada: In 2017, Enerkem adapted its commercial-scale gasification plant to produce lignocellulosic ethanol [1].
- Switzerland: a plant that will produce 50 000 tons of cellulosic ethanol was announced in 2017.
- The Netherlands: initial funding has been granted for developing a lignocellulosic ethanol project in Rotterdam [19] .
- China: Enerkem and Sinobioway Group signed an equity investment to build more than 100 biofuel facilities based on thermochemical processes [20].

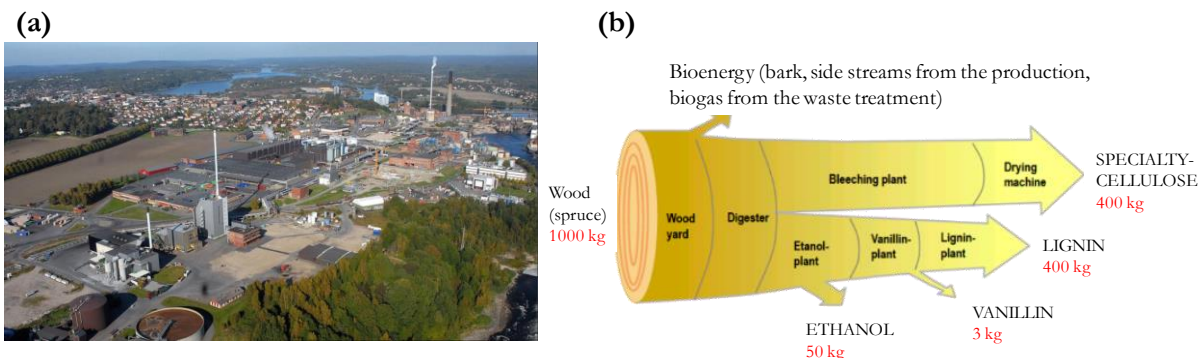


Figure 2. Borreggard biorefinery. (a). Plant in Sarpsborg (Norway), (b) Products and mass balance from 1 ton of woody biomass. Adapted from [17].

1.3. The French scenario: Futurol, BioTfuel and Syndièse projects

The Futurol project was launched in 2008 with the aim of developing a process for the biochemical production of cellulosic ethanol. With a total budget of €76.4 million, this program was carried out by 11 research, industrial and financial partners: ARD, IFPEN, INRA, Lesaffre, Vivescia, ONF, Tereos, Total, Crédit Agricole Nord Est, CGB, and Unigrains. The pilot plant is located on the agro-industrial site of Pomacle-Bazancourt (Marne, France). After 10 years of R&D, the French Futurol 2G ethanol production technology entered its commercialization phase in early 2019 [21,22].

Launched in 2010, the BioTfuel project aims to develop a BtL chain for producing 2G biofuels (diesel and kerosene) by treating the widest possible range of biomass and blends of biomass and fossil resources through a thermal route. It brings together R&D organizations (IFPEN and CEA) and manufacturers (Avril, Axens, Sofiprotéol, Total and Thyssenkrupp). Sited near Dunkirk (gasification-Fischer-Tropsch synthesis) and Venette (pretreatment) in northern France, the objective is to become an established demonstrator of 2G biodiesel and biokerosene production technologies by 2020 [23–25].

The Syndièse project (CEA) is intended to build a demonstrator for the production of 2G biofuels by gasification with a production capacity of 10 tons/hour. The construction of the technological platform for the biomass pretreatment started in October 2013 at the Bure-Saudron site (Meuse, France). In the study phase for several years, its operation is announced over 20 years from 2015 [26].

2. From biomass to liquid fuels

2.1. Biomass, its interest and limitations

Several definitions and categories of ‘biomass’ are available in literature. According to the International Organization for Standardization ISO, biomass is the ‘material of biological origin excluding material embedded in geological formations and/or fossilized’ [27]. This quite comprehensive definition includes animal (obtained from livestock) and vegetal biomass: energy crops, agricultural crops and trees, food, feed and fiber crop residues, aquatic plants, algae, forestry and wood residues, agricultural wastes, processing by-products and other non-fossil organic matters. Vegetal biomass is then classed as:

- Woody biomass: biomass originating from trees, brushes and shrubs
- Herbaceous biomass: biomass from plants that has a non-woody stem, and which dies back at the end of the growing season
- Fruit biomass: correspond to the part of a plant which holds seeds (e.g. oil palm fruit, nuts, olives)
- Aquatic biomass: biomass from so called hydrophytic plants, which are plants that have adapted to living in or aquatic environments.

For its part, the last European Directive on the promotion of the use of energy from renewable sources [28] defines biomass as the ‘biodegradable fraction of products, waste and residues from biological origin from agriculture, including vegetal and animal substances, from forestry and related industries, including fisheries and aquaculture, as well as the biodegradable fraction of waste, including industrial and municipal waste of biological origin’.

Biomass materials are derived from the reaction between CO₂ in the air, water and sunlight, through photosynthesis, to produce carbohydrates that form the building blocks of biomass [29]. The synthesis of biomass takes place within a relatively short timeframe, in contrast to fossil resources that also result from photosynthesis but have been densified, transformed and preserved over geological time scales [30]. In the biomass resource, the energy of sunlight is stored in chemical bonds. When the bonds between adjacent

molecules and atoms are broken by digestion, decomposition or valorization processes, the stored chemical energy is released.

In the context of this work, biomass will rather correspond to the ‘woody’ and ‘herbaceous’ subcategories of the ISO definition that correspond to the commonly named ‘lignocellulosic biomass’. Woody materials (i) contain much more thermal energy than food crops, (ii) the amount of fertilizers and pesticides necessary for wood is much lower and (iii) the production of woody materials is much higher than for food crops which means that the land use becomes smaller.

2.1.1. Drivers for biomass use

Although a subject of debate, the production and application of biomass are considered to have a neutral impact CO₂ carbon cycle [31]. This means that, if biomass is grown sustainably, its production and application does not produce any net amount of CO₂ in the atmosphere: the CO₂ released by the application of biomass is stored in the biomass resource during photosynthesis. Biomass is therefore considered the only natural and renewable carbon resource and large-scale substitute for fossil fuels [32].

Sources of biomass for bioenergy applications are abundant and diverse. These sources include agro-crops (grasses/herbaceous plants, starch and sugar crops and oilseeds), crop residues, and several tree species (woody crops/ lignocellulosic species). These products can be either burnt directly for energy or processed further for conversion to liquid fuels like ethanol and diesel [32]. The diversity of biomass sources and valorization processes means that its use reduces or spreads fuel dependency on a limited number of oil-providing countries, with inherent risks to energy security and sudden price fluctuations.

Despite these advantages for biomass use, there are important drawbacks that hinder its wide utilization at present. A summary of both interest and challenges for utilization of biomass in an energy framework are summarized in Table 1.

2.1.2. Challenges for utilization of biomass

Conversion technologies for biomass still face several challenges that must be overcome for the design of efficient valorization processes. The limitations for the widespread use of biomass feedstock in bioenergy applications are not only related to the characteristics of the raw material itself, but also to societal and economical aspects.

First, technological obstacles are often linked to the intrinsic properties of the raw woody material. Transformation challenges reside in its high oxygen content, its relatively low calorific value, its hydrophilic nature, its high moisture content and its low bulk density [33]. Raw biomass has also a tenacious and fibrous structure which, along with its poor flowability, makes process design and control complicated [34]. These characteristics make biomass transformation expensive compared to fossil fuels use and greatly impact logistics and final energy efficiency.

Additionally, producing bioenergy from biomass needs to overcome logistics challenges in terms of resource availability and supply chain (collection, storage, pre-processing, handling and transportation) [30]. Feedstock production and logistics can contribute more than 35 % of the total costs of 2G biofuels production, with logistics for transporting biomass from source to conversion accounting for 50 to 75 % of these costs [35]. Transport, handling and storage costs of the raw material are high, and challenges arise from competing land use between biomass production for food, material and energy use.

These challenges trigger uncertainties regarding the profitability of the process and partially explain why there are currently no BtL plants operating on a commercial scale. The production costs of BtL are higher than those of fossil diesel, and BtL products are at present not competitive with fossil diesel. However,

competitiveness should increase with the increase in oil prices, possible subsidies and CO₂-environmental taxes, as well as improved transformation technologies [36].

Table 1. Interest and challenges of utilization of lignocellulosic biomass within an energy context.

Interests
Available in a wide range of resources; diversity provides many new structural features to exploit.
Lignocellulosic biomass is less subject to world price fluctuations or supply uncertainties as of fossil fuels
Climate neutral carbon cycle of CO ₂ .
Negligible sulphur content: biomass does not contribute SO ₂ emissions.
Woody materials contain much more energy than food crops.
The amount of fertilizers and pesticides necessary for wood is much lower than for food crops.
Production of woody materials is much higher than for food crops: smaller land use.
Challenges
High oxygen content.
Low calorific value (in comparison to fossil fuels).
Hydrophilic nature.
High moisture content.
Reduced overall energy efficiency.
Tenacious and fibrous structure.
Heterogeneous composition.
Land use conflicts.

2.2. Wood as a model of lignocellulosic biomass: properties and structure

Each dry biomass has specific properties related to the type of raw material, although there are characteristics common to all biomasses. In this research, for the sake of simplicity, we will use wood as biomass model, and we will employ either of these terms indiscriminately.

Wood is a material of biological origin, so there is a high variability in properties between species, within species and even within trees.

2.2.1. Anatomic structure

Wood consists of tissues with lignified walls. In the living tree, this tissue fulfils many functions ranging from sap conduction to mechanical support, storage, restitution, support adaptation and resistance to biological attacks. Wood is formed by the division and differentiation of newly formed cells. The so-called meristematic cells forming tissues (meristem), are found in the tree in two forms. The first are the apical meristems located at the root tips and in the buds of the stem and twigs. They are responsible for the tree height growth and, by differentiation of meristematic cells, they originate the epidermis, the primary xylem and the primary phloem. The second are the lateral meristems forming thin cell sleeves that are found along the entire length of the stem, twigs or roots. This meristem, the cambium (or bifacial cambium) produces the suberophellodermal layer under the bark responsible for the formation of protective tissues (cork and phelloderm) on its external side and the xylem (woody tissues), on the internal side.

In temperate regions, the cambium stops functioning in winter, and it resumes its operation in spring by setting up a new layer of cells distinct from the previous layer. These successive layers are often visible in the form of annual growth rings. During the same year, the seasons influence cambial activity so that it is possible to distinguish clearly in softwoods between wood formed in spring ('early' wood) and that formed in summer ('late' wood). This tissue organization is more complex in hardwoods and depends strongly on

the species. The growth ring width is not constant within the same tree, it varies according to the growing conditions from one year to another, the position in the tree, the social status of the tree in the forest, etc.

Most of the cells formed in the cambium dies after some weeks, after the deposition of the secondary cell wall, a process known as lignification. After a few years of operation, the parenchyma cells, which remained alive, finally die. The wood is transformed to form the heartwood, it is the process of duraminization. This process is responsible for the principal chemical properties (secondary metabolites) which condition wood utilization (durability and color, for example). When the heartwood is colored, it is perfectly distinguishable from the sapwood (active part of the tree regarding the sap flow).

Wood is an orthotropic porous material; that is, it has unique and independent mechanical properties in the directions of three mutually perpendicular axes: longitudinal, radial and tangential. The longitudinal axis L is parallel to the fiber (grain); the radial axis R is normal to the growth rings (perpendicular to the grain in the radial direction); and the tangential axis T is perpendicular to the grain but tangent to the growth rings [37]. These axes are shown in Figure 3.

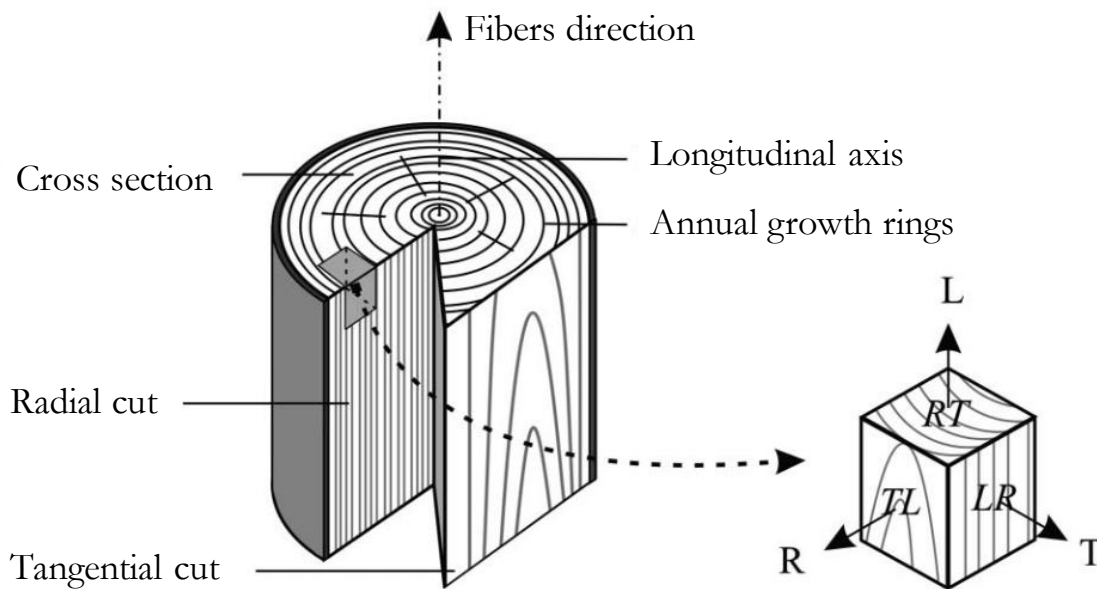


Figure 3. The three principal axes of wood with respect to fibers direction and growth rings [38].

The anatomy of gymnosperms (commonly called conifers or softwood) is different from that of dicotyledonous angiosperms (hardwood). It is more complex for the latter as hardwoods are more evolved botanical species with highly specialized cells (Figure 4).

2.2.1.1. Softwoods

Conifers (gymnosperm trees) have a simple and regular organization. Wood is composed of tracheids and medullary rays. Sometimes transversal tracheids, resin canals and axial parenchyma are also found (Figure 4a). Axial (or longitudinal) tracheids constitute about 90 % of the woody mass and form the conductive tissues for raw sap and support. They are fusiform, long and thin cells of square or rectangular cross-section. They are arranged in rows and connected to each other by their tapered ends. Tracheids communicate with each other by bordered pits and with medullary rays by half-bordered pits. Tracheids formed in the spring have a large cavity (lumen) and thin walls. This geometry favors the flow of sap. At the end of the growing season, the tracheids become more adapted to the supporting role, so the cells then have a smaller section and thicker walls. Softwoods tend therefore to have a clear growth ring boundary.

Medullary rays are composed of radially elongated parenchymal cells over a height of one or more cell layers. They have a role of radial conduction and accumulation of reserves. The resin canals are made up of

secretory cells. Their organization in a circle delimits the channel in which the produced resin flows. Resin canals are not present in all conifers, but their presence is often the first criterion for recognizing coniferous wood. Examples of softwood trees are cedar, Douglas fir, juniper, pine, redwood, spruce and yew.

2.2.1.2. *Hardwoods*

While in softwoods tracheids perform the dual function of support and conduction, in hardwoods (also known as broad-leaved, angiosperm trees), different tissues ensure these two functions: the wood fibers and the vessels. Medullary rays and parenchyma are present as well (Figure 4b). Examples of hardwood trees include alder, balsa, beech, hickory, mahogany, maple, oak, poplar, teak and walnut.

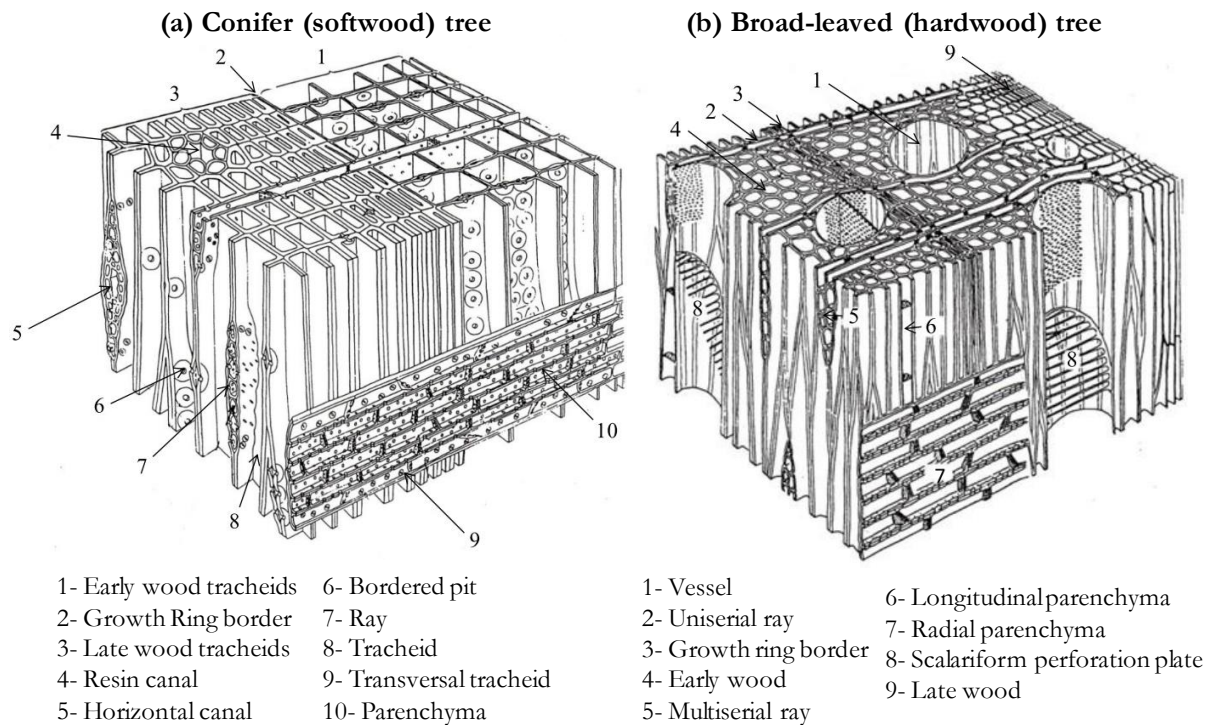


Figure 4. Schematic of cell organization of conifer and broad-leaved trees. Adapted from [39].

Vessels are long rows of cells connected end to end that allow the conduction of raw sap from the roots to the leaves. Sap circulates from one line of cells to another through single or multiple perforations. Pits allow circulation to the parenchyma and neighboring cells *via* bordered or half-bordered pits. In cross-section, the arrangement, grouping and size of vessels are the first important criteria for species recognition.

Fibers are present only in hardwoods. They are long narrow cells that generally resemble latewood tracheids (length from 1 to 2 mm, diameters from 0.01 to 0.05 mm). Fibers have closed ends, mostly pointed and sometimes are equipped with dentations [40]. They mainly play a supporting role and act on the density and mechanical strength of the wood.

2.2.1.3. *The cell walls*

The plant cell wall has a multi-layered structure (Figure 5). The layers and underlayers of this wall differ from each other in their chemical composition and in the organization of their constituents. The secondary wall of wood cells is composed of three layers, S1, S2 and S3, as shown in Figure 5. Each layer within the secondary cell wall can be considered as a natural fiber-reinforced composite where the stiff hydrophobic crystalline cellulose microfibrils are closely packed in a hydrophilic matrix of amorphous cellulose, hemicelluloses and lignin. The central and the thickest layer (named S2, 1-10 μm thick) is the most important structural component of the cell wall, which provides mechanical support for the tissue [41]. The cell walls

are bonded by the compound middle lamella (CML) which is composed of the primary wall and middle lamella.

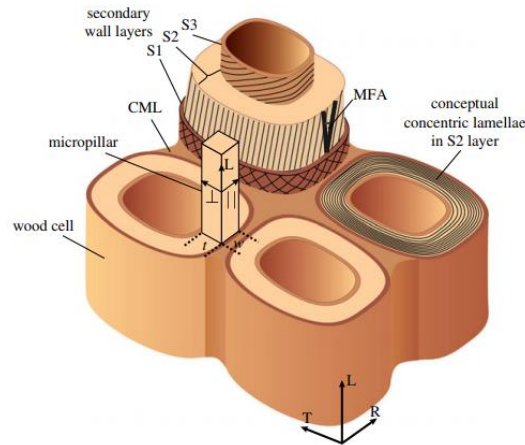


Figure 5. Schematic view of cell wall layers (MFA is the microfibril angle) [41].

2.2.2. Biochemical composition

The moisture content of living trees depends on the wood density and the place in the tree (heartwood or sapwood). The moisture content is close to full saturation in sapwood and in the range of 40 % to 80 % of the total wood mass in heartwood. The moisture content of living tree varies seasonally, and the average values are in the range of 40 % to 50 % of the total wood mass.

The elementary chemical composition is almost the same for all dry wood species (Table 2). This global composition can be represented by the global formula $\text{CH}_{1.5}\text{O}_{0.65}$, neglecting nitrogen and ashes, or $\text{C}_6\text{H}_{8.39}\text{O}_{3.54}\text{N}_{0.1}$, to be more specific [42]. In comparison with other combustibles, wood is relatively poor in carbon content and rich in oxygen content. This is one of the main limitations for widespread use biomass highlighted in section 2.4.

Table 2. Elementary approximated composition of wood [42].

Element	Mass percentage
Carbon	49.5
Hydrogen	6.0
Oxygen	43.0
Nitrogen	0.5
Ashes	1.0

Ashes are variable among species and among the parts of the tree, according to the soil where the tree has grown. Their composition consists essentially of magnesium, lime, silica, potash and phosphoric anhydride.

At the macromolecular level, biomass contains varying amounts of cellulose, hemicelluloses, lignins. Small amounts of low-molecular-mass compounds (extractives), water-soluble organic compounds and inorganic compounds are also present. Table 3 lists the average content of these compounds in wood.

Table 3. Average composition (mass %) of woody biomass [42].

	Conifers (softwoods)	Broad leaved trees (hardwoods)
Cellulose	42 (± 2)	45 (± 2)
Hemicelluloses	27 (± 2)	30 (± 5)
Lignins	28 (± 3)	20 (± 4)
Extractives	3 (± 2)	5 (± 4)

2.2.2.1. Cellulose

Cellulose is a glucose polymer consisting of linear chains of (1,4)-D-glucopyranose units – a six-carbon monosaccharide – linked by a glycosidic link $\beta(1\rightarrow4)$, with a degree of polymerization varying from 5 000 to 14 000 units. It is considered to be the most chemically and thermally stable constituent of wood and plays a fundamental role in the mechanical strength of the cell walls of the anatomical elements of wood. Its chemical representation can be seen in the Figure 6.

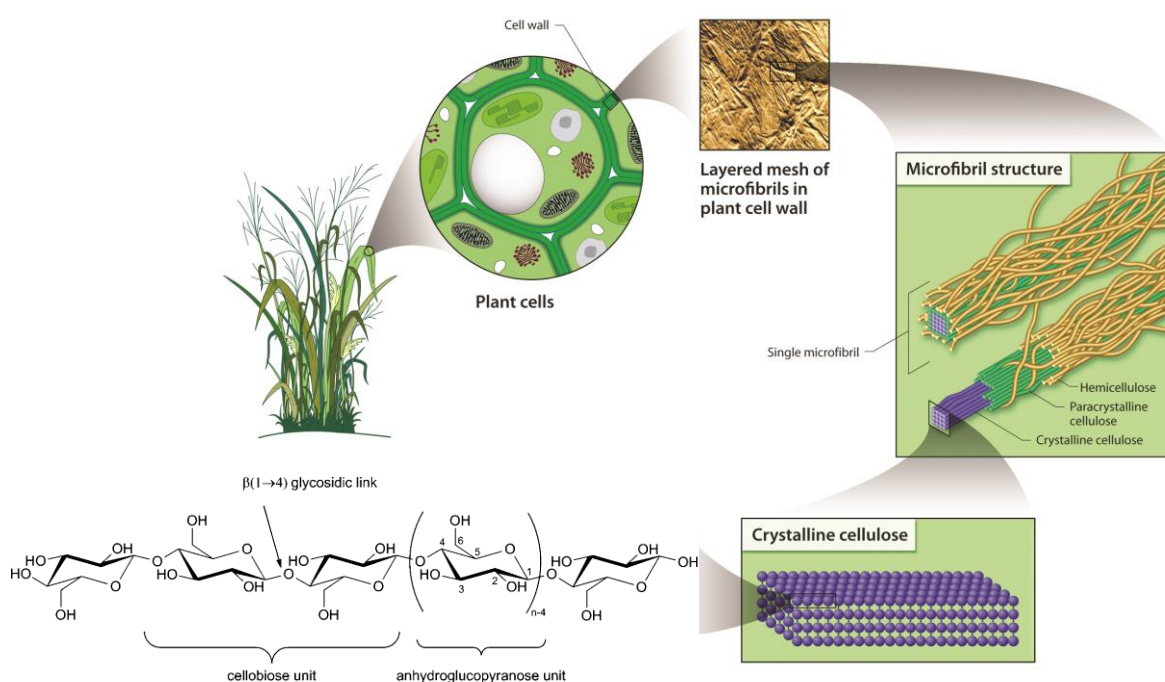


Figure 6. Plant cells, microfibril structure and cellulose chemical representation [43,44].

The tight fiber structure created by hydrogen bonds results in the typical material properties of cellulose: high tensile strength and insolubility in most solvents. The hydroxyl groups present on the chain allow the formation of intermolecular hydrogen bonds at the origin of an organization of cellulose into microfibrils. These links can be random and irregular or perfectly ordered. We then distinguish the so-called amorphous regions (paracrystalline cellulose), consisting of a helical stack of cellulose chains, and rigid and hydrophobic crystalline regions, corresponding to a stack of macromolecular chains oriented preferentially in the axial direction (Figure 6). Due to their poor accessibility, crystalline regions are less reactive to external molecules.

2.2.2.2. Hemicelluloses

Hemicelluloses are a mixture of polysaccharides such as glucose, mannose, xylose and arabinose and methylglucuronic and galaturonic acids with a degree of polymerization of 100-200. Unlike cellulose, hemicelluloses are mostly composed of five-carbon monosaccharides, is highly hydrophilic, has a branched topology and has a short chain length.

The composition and structure of the hemicellulose in softwoods differ from those of hardwoods. In softwoods, mannose is the most important hemicellulosic monomer followed by xylose, glucose, galactose

and arabinose. Most of the mannose is present as O-acetyl-galactoglucomannan (about 20 %) whose structure is shown in Figure 7a. In hardwoods, xylose is the most important hemicellulosic monomer as O-acetyl-4-O-methylglucuronoxylan (Figure 7b).

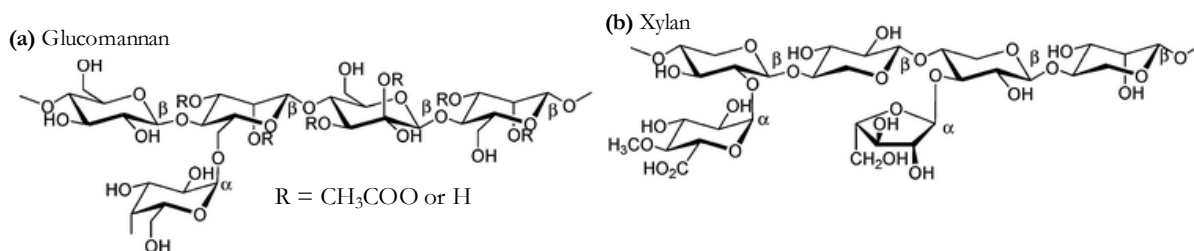


Figure 7. Chemical structure of hemicelluloses (Adapted from [45]).

2.2.2.3. Lignins

Lignins are a group of amorphous, high-molecular-weight, chemically related compounds. The building blocks of lignin are believed to be the phenyl-propanes (Figure 8a), a three-carbon chain attached to rings of six carbon atoms (Figure 8a). The proportions of these precursors in lignins vary with their botanical origin. Lignins present in the wood walls are in part responsible for increasing the mechanical strength and thermal stability of wood and for reducing the hygroscopicity of biomass.

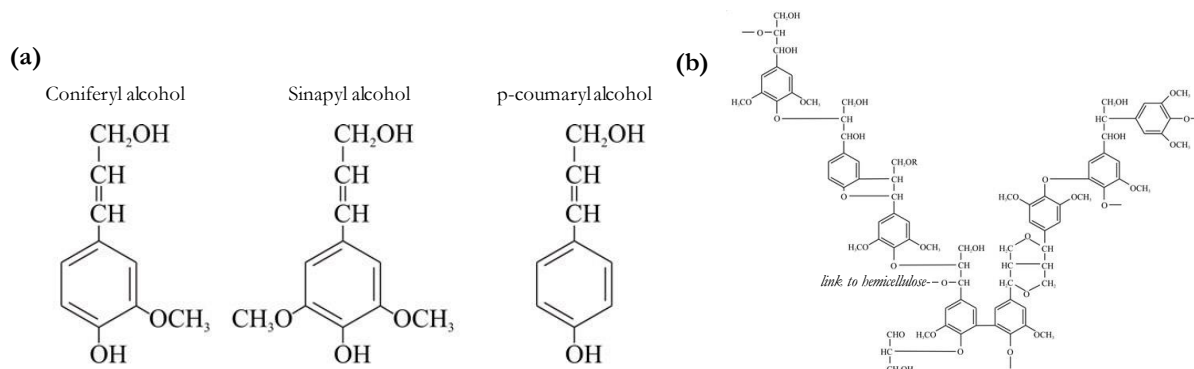


Figure 8. Lignins. (a) Basic units. (b) Schematic formula of the polymer of a hardwood lignin (Adapted from [46]).

2.2.2.4. Extractives

Extractives are non-structural constituents of wood that represent a minor fraction. They contribute to the properties of wood such as color, smell and taste and protect against fungi and insect attacks. Extractives can also be toxic or alter wood hygroscopicity. Wood extractives can be classified into different groups as shown in Table 4.

2.2.3. Poplar and Spruce: potential use as feedstock for BtL processes

Poplar (*Populus spp.*) is one of the most common utility hardwoods in the United States [47] and are popular trees for agriculture and landscape worldwide. Poplars are one of the most desirable feedstocks for 2G biofuels, mainly because of their fast growth (from 3.25 to 21.5 dry tons per hectare and per year [48,49]), which means the ability to produce a significant amount of biomass in a short time. The sequencing of poplar genome has also paved the way for tailoring new clones, optimized for biofuel production [50,51]. Since poplar grows well in poor soils, fertilizer inputs are low compared to other crops. Yield estimates range from 3.25 to 21.52 dry tons per hectare [49].

Table 4. Classification of extractives in wood [46]

Aliphatic and alicyclic compounds	Terpenes and terpenoids (including resin acids and steroids)
	Ester of fatty acids (fats and waxes)
	Fatty acids and alcohols
	Alkanes
Gums (polysaccharides)	Linear-structured gums
	Branched-structured gums
	Branch-on-branch-structured gums
Phenolic compounds	Simple phenols, stilbenes, lignans, isoflavones, condensed tannins, flavonoids, hydrolysable tannins
Inorganic compounds	Cations: Ca^+ , K^+ , Mg^+ , Na^+ , Fe^{2+}
	Anions: NO_3^- , SO_4^{2-} , PO_4^{3-}
Other compounds	Sugars, cyclitols, tropolones, amino acids, alkaloids, coumarins, quinones

France is the leading European producer of poplar and the 2nd largest in the world in terms of planted areas, after China. Poplar plantations in France have a surface of approximately 170 000 ha which means 1,4 % of the total forest surface. The wood volume reaches 30 millions of m^3 , this represents around 158 m^3/ha [52]. The quality of the poplar wood (soft and clear, because its low duraminization) is particularly well suited to the manufacture of plywood, light packaging and furniture [53].

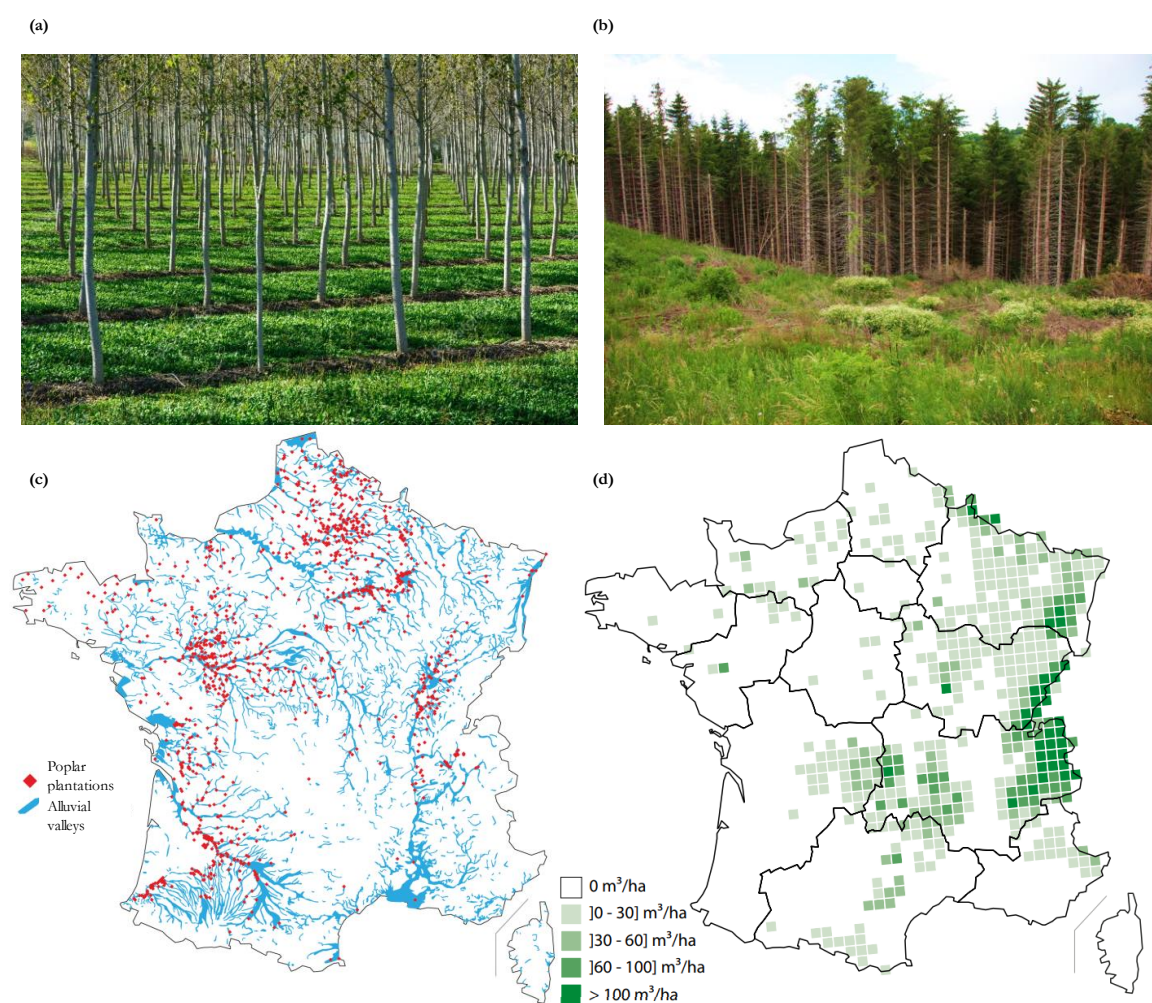


Figure 9. (a) Poplar plantation (b) Spruce plantation in Lanarce (France) (c) Geographic distribution of poplar plantations in France [52]. (d) Spruce average volume per hectare [52].

Although poplar lumber residues represent a relatively minor biomass resource at the national level compared to other sources of woody biomass (0.8 % of the total gross availability of fuelwood), they are easily accessible (Figure 9a-b), and they can be a valuable resource for local actors. In addition, these residues do not currently seem to be systematically recovered; they are sometimes swathed at the end of the plot to be burned on site [54] (this practice has recently been prohibited in France [55]).

Spruce (*Picea abies*) is the dominant species in the Scandinavian forest and it is often used as reference of softwood species for research on bioenergy applications [56–60]. Norway spruce is the feedstock species for the production of biochemicals in the Borregaard's biorefinery [17]. Spruces have an elastic and resistant wood, used as lumber (carpentry, masts, lutherie) or in industry (crates, paper, etc.). In France, spruce represents about 188 million m³ of wood and is the main softwood species on 573 000 ha of forest [52] (Figure 9c-d).

2.3. Processes for biomass valorization into liquid fuels

Processes that have been positively experimented for the conversion of biomass into liquid fuels include (but are not limited to) fast pyrolysis, direct liquefaction, transesterification of vegetable oils to produce diesel fuel, production of bio-ethanol from agricultural crops to blend with gasoline, production of bio-oil from algae, and most recently, the production of higher hydrocarbons by conversion of biomass-derived syngas by a Fischer-Tropsch process. These processes can be divided into two main categories: biochemical/biological and thermochemical transformations. In general, high-moisture content biomass lends itself to a 'wet/aqueous' conversion process, involving biologically mediated reactions such as fermentation, while 'dry' biomass such as wood chips is more economically suited for gasification, pyrolysis or combustion [29]. The choice of conversion processes depends on the type, property and quantity of biomass feedstock, the desired form of the energy, the environmental standards, the economic conditions and the project-specific factors [61,62].

2.3.1. Biochemical conversion of biomass

It involves the use of enzymes and microorganisms to transform plant molecules into fuels, chemicals or electric power. A comprehensive review on the biochemical routes for biomass-based energy has been made by Saxena et al. [61]. In general, biochemical transformation of lignocellulosic biomass follows the same process as the production of ethanol 1G. However, due to the very different nature of the biomass used, additional stages need to be added and others modified. A pretreatment step (mechanical, physico-chemical and/or biological) is necessary to make cellulose molecules accessible. To date, steam explosion is the most mature pretreatment processes. It consists in a high temperature (between 160 and 270 °C) treatment by injection of saturated steam under high pressure (10 to 50 bar) for a short time followed by a sudden expansion until atmospheric pressure. This causes a disintegration of the lignocellulosic structure, a partial hydrolysis of hemicelluloses and the onset of lignin transformation, finally making cellulose molecules much more accessible [63]. The subsequent enzymatic hydrolysis allows the degradation of cellulose into hexoses. Then, the hexose fermentation, which requires special yeasts, takes place. Finally, downstream operations are used to separate and purify the 2G bio-ethanol and other products.

2.3.2. Thermochemical conversion and Biomass to Liquid processes

Biomass to Liquid (BtL) is often used as a synonym of the thermochemical transformation of biomass. Strictly, BtL denotes a subcategory of thermochemical processes that allows the conversion of biomass to liquid synthetic fuels, while thermochemical processing can also produce gaseous products (e.g. via combustion, gasification). Thermochemical processes use heat and catalysts to transform plant polymers into fuels, chemical or electrical power [14]. It occurs at temperatures ranging from at least several hundred degrees Celsius to more than 1000 °C above ambient conditions. Thermochemical routes include

combustion, gasification, fast pyrolysis, hydrothermal processing (or direct liquefaction), catalytic hydrolysis to sugars and supercritical fluid extraction (Figure 10). As shown in Table 5, thermochemical processing presents several advantages relative to biochemical processing such as production of a diversity of oxygenated and hydrocarbon fuels, shorter reaction times, lower cost of catalyst and smaller production plants. A synthetic comparison of the main BtL processes is presented in Table 6.

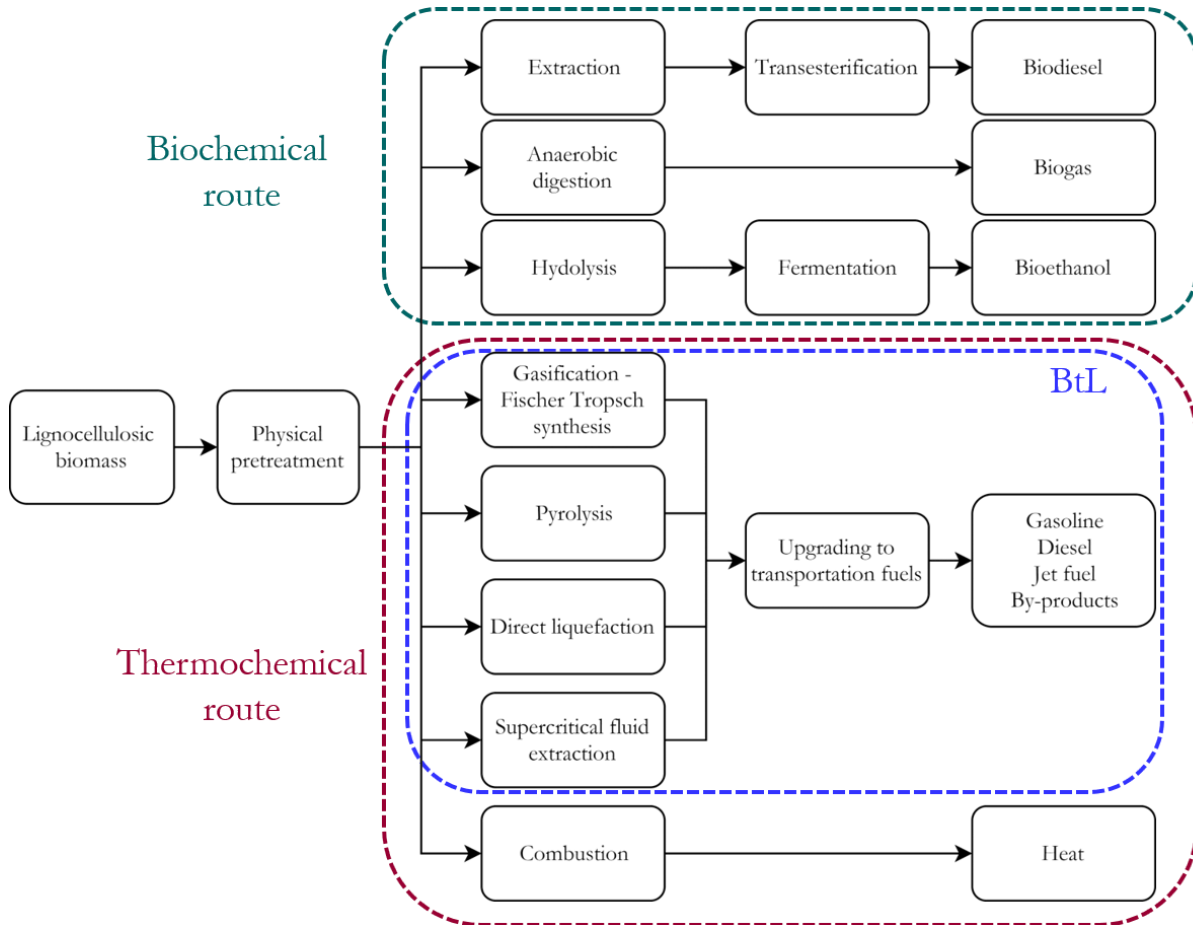


Figure 10. Routes for biomass valorization. Adapted from [18].

Table 5. Comparison of biochemical and thermochemical processing of biomass [14].

	Thermochemical processing	Biochemical processing
Products	Range of fuels	Primarily alcohols
Reaction conditions	100 - 1200 °C, 1 - 250 atm	Less than 70 °C, 1 atm
Residence time	0,2 s - 1 h	2 - 5 days
Selectivity	Depends upon reaction	Can be made very selective
Catalyst/biocatalyst cost	\$0,01/gallon gasoline	\$0,50/gallon ethanol
Sterilization	No sterilization required	Sterilize all feeds
Recyclability	Possible with solid catalyst	Difficult
Size of plants (biomass input)	5-200 ton/day (fast pyrolysis)	2000-8000 tons/ day

Currently, the major BtL production processes are gasification followed by a Fischer-Tropsch synthesis (FTS) and pyrolysis. Within the purpose of this work, only the gasification process will be the examined. A detailed review of the BtL processes and their current state of development has been carried out by Ibarra-Gonzalez et al. [64].

Table 6. Comparison of the main BtL processes (Adapted from [64]).

BtL process	Operation conditions	Reaction mechanisms and process description	Advantages	Disadvantages	References
Gasification followed by FT-synthesis	Temperature: 600-1000 °C; pressure: atmospheric; residence time: 3-4 s; controlled amount of oxidizing agent; drying required.	Syngas containing mainly CO and H ₂ is produced by a sequence of reactions (C-O, Boudouard reaction, C-H ₂ O, hydrogenation reaction). Gas clean-up is followed by a Water-gas shift reaction and a Fischer-Tropsch synthesis.	Mature technology; biomass gasification for generation of heat and power is already commercialized.	Requires high temperatures; produces 20 % wt % oil and 80 wt % gas, therefore it requires FT synthesis to increase liquid product yield.	[14,65–68]
Flash/fast pyrolysis	Temperature: 450-500 °C; pressure: atmospheric; residence time: ca. 1 s; absence of oxygen; drying required.	Lignocellulosic material is converted into a carbon-rich solid and volatile matter by heating in the absence of oxygen. The light small molecules are converted to oily products (bio-oil) through homogeneous reactions in the gas phase and rapid condensation.	High oil yield (up to 80 wt % on dry feed); lower capital cost; Gasification produces heat and combustible gas, while pyrolysis produces bio-oil, gases and heat as principle products.	Poor fuel quality obtained.	[14,69,70]
Hydrothermal liquefaction	Temperature: 300-400 °C; pressure: 5-20 MPa; residence time: 0.2-1.0 h; drying unnecessary.	Occurs in aqueous medium, which involves complex sequences of reactions (dehydration, decarboxylation, and hydrogenation of functional groups, etc.)	Better quality of bio-oil obtained (high heating value, low moisture content).	Relatively low oil yield (20 wt %–60 wt %); need high-pressure equipment, thus, higher capital cost.	[14,69,71,72]

Supercritical fluid extraction	Temperature: 250-400 °C; pressure: 4-5 MPa; residence time: 0.3-4.0 h; requires solvent addition.	Thermal disruption of the lignocellulose or other organic materials for extraction of useful products and for oxidation of the organic materials.	Fast kinetics, higher biomass conversion, ease of continuous operation and elimination of catalysts use.	High temperature and pressure, which increase operation costs. Bio-oil yield of 26 wt %–60 wt %.	[73–76]
--------------------------------	---	---	--	--	---------

2.3.2.1. Gasification

Gasification is the partial oxidation of carbonaceous feedstock in the range of 600 °C to 1000 °C to produce a gas of low calorific value (about 4 to 6 MJ/Nm³ compared with natural gas at 36 MJ/Nm³) that can be used either directly in applications such as gas turbines, engines and fuel cells, or transformed into hydrocarbons and chemicals by a Fischer-Tropsch synthesis. The gas produced is therefore more versatile to use than the original biomass. Due to its higher chemical efficiency (≈ 70 -80 %), expressed as the ratio between the chemical energy in the gas produced and the chemical energy in the feedstock, it is desirable that gasification be increasingly used in the future rather than the direct combustion of biomass [34]. Gasification has been the subject of several reviews, including those by Sikarwar, McKendry, Higman, Probst, et al.[68,77–80].

A schematic representation of a biomass gasification plant is shown in Figure 11. Four main stages are highlighted: the biomass pretreatment, the gasification itself, the conditioning of the syngas and the Fischer-Tropsch synthesis.

2.3.2.1.1. Biomass pretreatment

Biomass is a resource with variable properties, dispersed and low energy concentration (section 2.1.2). It therefore seems necessary to transform it into an intermediate, more homogeneous product better adapted to its transformation into biofuels. The product of the pretreatment steps is a more energy-dense material and well adapted to the transport and supply under pressure of gasifiers. Pretreatment processes are further detailed in section 2.3.3.

1.1.1.1.1. Gasification reaction and equipment

In the gasifier, the biomass is treated under reducing conditions with oxygen added in sub-stoichiometric amounts compared with the amount needed for complete combustion. Gasification can be achieved by direct addition of O₂, using exothermic oxidation reactions to provide the energy necessary for gasification, or by pyrolysis through the addition of sensible heat under anoxic conditions. In both cases, steam may be added to promote additional production of H₂ via the water-gas shift reaction [14].

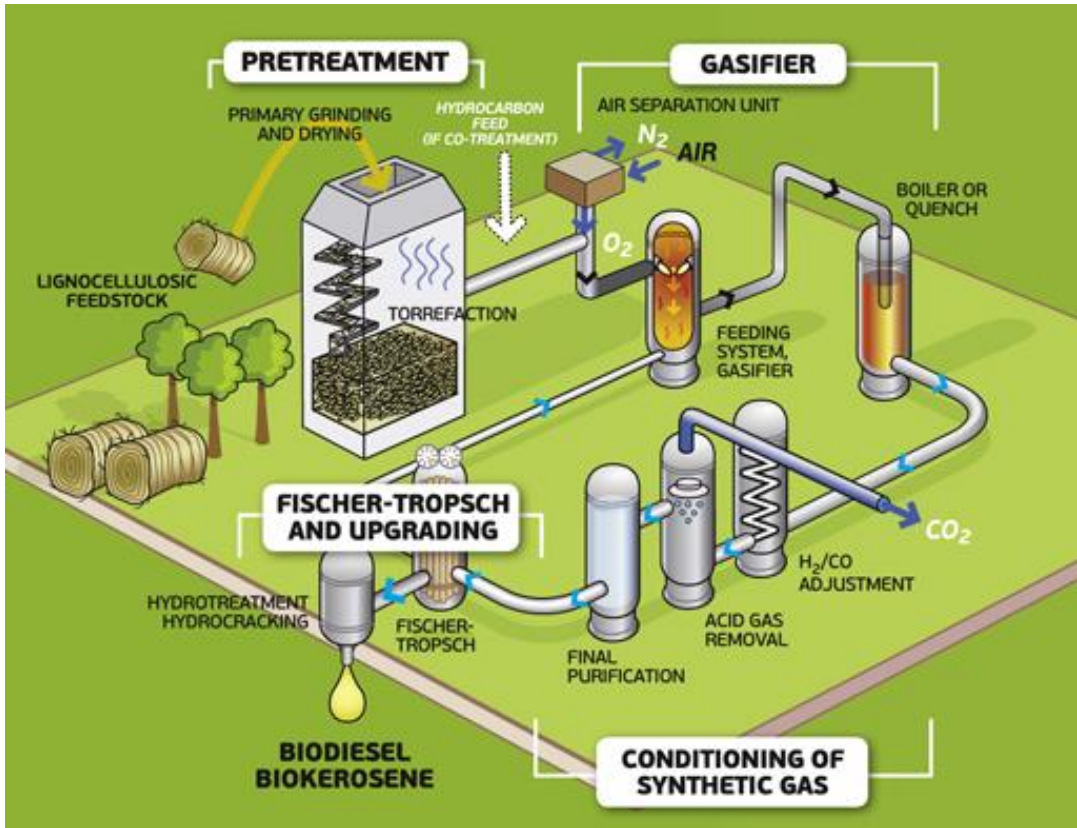


Figure 11. Main stages of a biomass gasification process (BioTfuel project [23,24]).

Gasification reactions at the particle scale are schematically shown in Figure 12. From these reactions, it follows that the gas generated (‘producer gas’) is a mixture CO, CO₂, H₂, CH₄, N₂, H₂O and a rich spectrum of hydrocarbons. The mixture of predominantly CO and CH₄ produced after a separation to remove CO₂ from producer gas is commonly known as ‘syngas’. Its formation can be simplified by the following global reaction:

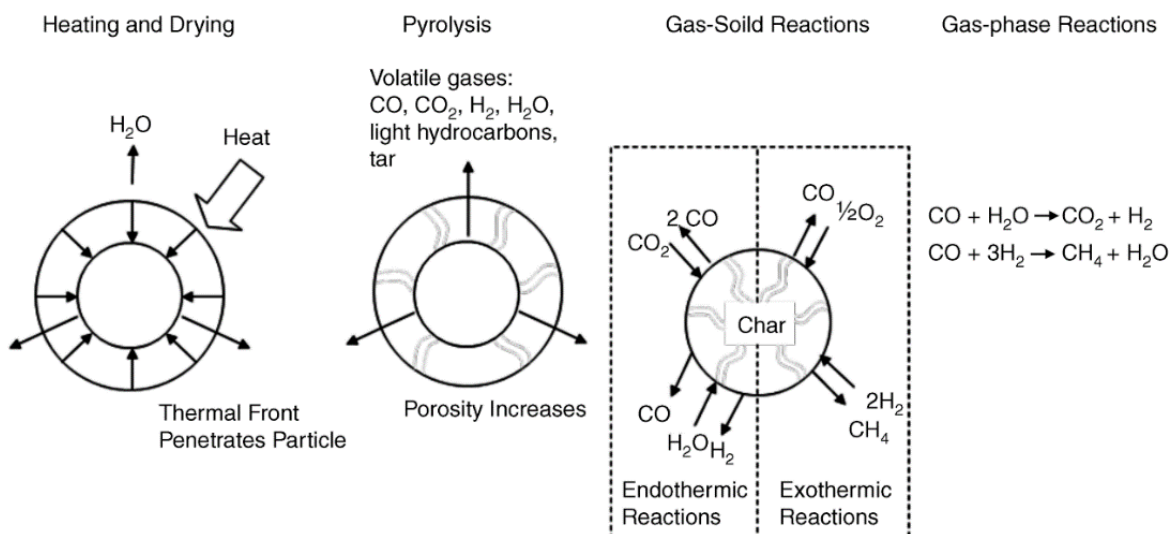
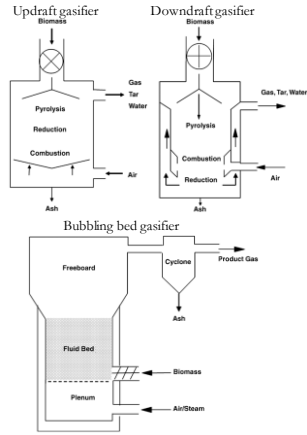
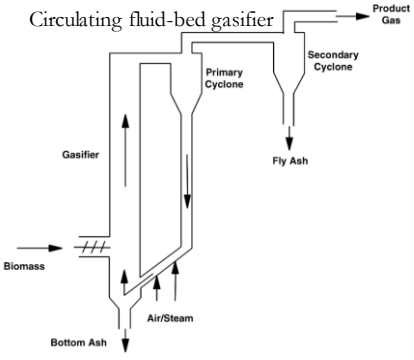
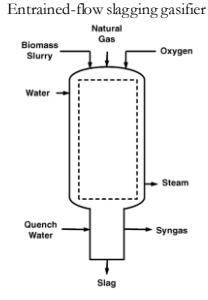


Figure 12. Gasification reactions at the particle scale. Adapted from [14].

To handle different kinds of available biomass feedstocks, a variety of gasification reactors and processes have been developed. They can primarily be classified into three main categories: fixed bed, entrained flow

and fluidized bed reactors (Table 7). Large-scale (industrial) applications usually employ entrained flow or fluidized bed gasifiers, while fixed bed gasifiers are preferred for small-scale gasification.

Table 7. Main reactor designs for gasification [14,18,77].

Gasifier technology	Characteristics	Schematic example [14]
Fixed bed/bubbling bed	Can handle large and coarse particles Release lower temperature gas product High gasification agent consumption Ash is removed as slag or dry High particulate content in gas product stream Simplest and robust design Economical at small scale Tolerant for large range of biomasses Non-uniformity in temperature High tar and char yields	 <p>The diagram shows three types of fixed bed gasifiers. The Updraft gasifier has biomass entering from the top, with gas moving upwards through pyrolysis, reduction, and combustion zones, exiting as gas, tar, and water. The Downdraft gasifier has biomass entering from the top, with gas moving downwards through similar zones, exiting as gas, tar, and water. The Bubbling bed gasifier shows a fluid bed where biomass enters from the bottom, and air/steam is introduced, with product gas exiting from the top and ash from the bottom.</p>
Fluidized bed	Uniform temperature distribution Low tar and char yields Better gas–solid contact Shorter residence time High operating temperature (1000–1200 °C) Suitable for feedstocks with low ash fusion temperature Ash is removed as slag or dry Low particulate content in the gas stream	 <p>The diagram illustrates a circulating fluid-bed gasifier. Biomass enters from the bottom, and air/steam is introduced. The gasifier is connected to a primary cyclone, which separates product gas from fly ash. The fly ash is then sent to a secondary cyclone before being removed as bottom ash. The gasifier itself has a freeboard at the top.</p>
Entrained flow	Need finely milled feed material (ca. 100–400 μm) Very high operating temperatures (>1200 °C) Yields high quality syngas Not suitable for high ash content feedstocks Very high oxygen demand Ash is removed as slag Short residence time Very low tar yield Economical for large scale	 <p>The diagram shows an entrained-flow slagging gasifier. Biomass slurry enters from the top, along with natural gas and oxygen. Water is also added. The gasifier produces steam and syngas, while slag is removed from the bottom. A quench water section is shown at the very bottom.</p>

1.1.1.1.2. Syngas clean-up and conditioning

Syngas clean-up is the removal of undesirable impurities from the gas and depends on its end-use. Gas-phase impurities in syngas include NH_3 , HCN, other nitrogen gases, H_2S , other sulphur gases, HCl, alkali metals, organic hydrocarbons (including tar) and particulates. The concentration of these impurities depends on the feedstock composition and operating conditions. This represents a very technically challenging situation for any syngas cleaning system, which usually are, in consequence, costly processes. Syngas clean-up and conditioning is therefore a key technical barrier to the commercialization of biomass gasification

technologies and has a big impact on the cost of clean syngas. A recent review on syngas clean-up processes can be found in [81]. After cleaning, the hydrogen content is adjusted (steam reforming or water-gas shift) by increasing the H_2/CO ratio to 2, which increases FTS performances.

1.1.1.1.3. Fischer-Tropsch synthesis (FTS)

The Fischer-Tropsch synthesis reaction was formulated in 1923 by two German researchers, Franz Fischer and Hans Tropsch. FTS has long been recognized as a polymerization reaction represented in its simplest form as follows:



The Fischer-Tropsch reaction produces a range of olefins, paraffins and oxygenated compounds such as alcohols, aldehydes, acids and ketones that are mainly linear with a high percentage of olefinic hydrocarbons [14]. The composition of FTS products depends on the FTS catalyst and on the reaction conditions. Catalyst used for FTS are often group VII transition metal oxides (Ru, Fe, Ni, Co, Rh, etc.), and are selected according to the desired products. Nevertheless, iron catalysts are the most common, mainly because of their easy availability and low costs compared to other metals. Figure 13 shows a general flowchart of the FTS process from different fuel sources, including biomass. Depending on the type and quantity of products desired, either a low-temperature (200-240 °C) or a high-temperature (300-350 °C) synthesis is used. The hydrocarbon mixture resulting from FTS is then distilled and purified to obtain the final products, known as the refining stage.

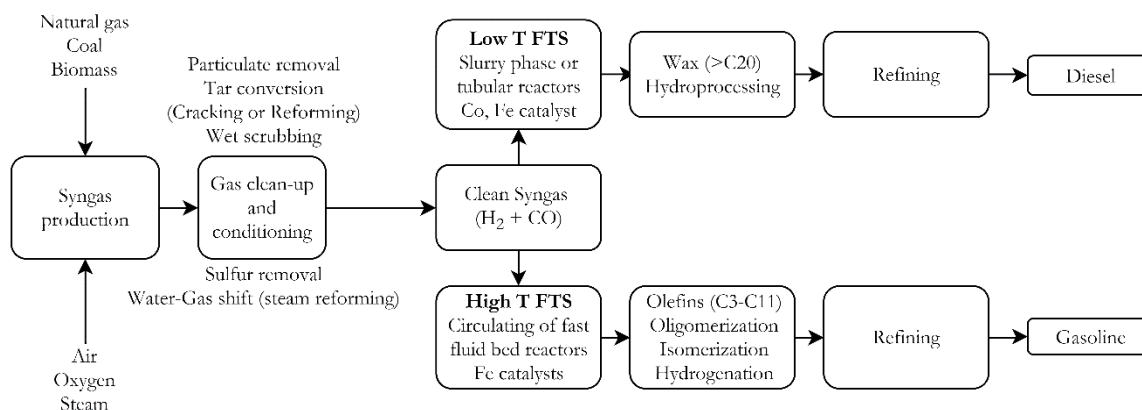


Figure 13. Fischer-Tropsch synthesis process flowchart (adapted from [14]).

2.3.3. Feedstock pretreatment for gasification

To overcome some of challenges for biomass use and make the feedstock suitable for energy applications, pretreatment processes are essential.

The intensity of pretreatment of the biomass feedstock depends on the gasification technology used. Entrained flow reactors are one of the most promising technologies because a rapid high-temperature biomass gasification can be achieved, leading to high-quality syngas [82]. Heat and mass transfers are very efficient in this type of reactor, but the biomass must be dried and ground into particles of several hundred micrometers prior to injection [83]. At least two pretreatment stages are therefore needed:

- **Drying:** moisture content limits gasification efficiency, but also reduces grinding performance. High moisture content leads to inconsistent particle sizes when the particles are less than 2 mm [33]. A drying process should ensure a moisture content of less than 10 to 15 % before gasification.
- **Particle size reduction (grinding):** a fractionation is needed to improve the chemical reactivity by increasing the total surface area, to eliminate mass and heat transfer limitations, to increase bulk

density. It eases the conveying of the raw material along the processing chain and optimizes its injection into the gasifier.

These preliminary steps, particularly the grinding, consume large amounts of energy and represent obstacles to be overcome in order to develop the use of biomass in thermochemical processes [83]. An attractive process that reduces energy consumption for grinding, among other rather beneficial changes in biomass properties, is torrefaction.

2.3.3.1. Grinding

Biomass mechanical size reduction is a treatment process which leads to rupture of plant cell wall and dissociation of tissues (epidermal, parenchymatous and vessel tissue). Barakat et al. [84] has established different process categories according to the size reduction degree: 'powdering' (m to cm), coarse milling (cm to mm), intermediate micronization (cm to 100 μm), fine grinding (<100 μm) and ultra-fine grinding (<30 μm).

The most commonly used grinding equipment is a hammer mill, which has high-speed rotors with metal hammers that beat the biomass apart until it passes through the openings of a metal screen. These type of units are found in most biomass processing systems because of their reliability and flexibility to work with different feedstocks [85].



Figure 14. Hammer mill grinding woody biomass [86].

The type of grinder used to grind wood influences particles shape, size and therefore powder flowability. The poor flowability of wood powder is a drawback for conversion processing (section 2.5). The tendency to present flow obstructions is lower for powders ground in knife mills than for powders ground in hammer mills, due to particles size and shape obtained [87]. To improve particle flow characteristics, new types of mills are being developed. For example, vibration mills decreased grinding energy requirements, and lead to round shaped particles [88].

Power consumption in disintegration of biomass depends on biomass character (soft- and hardwood or herbaceous biomass), moisture content, extent of size reduction and way of disintegration [89], but also on the torrefaction conditions, as described hereafter.

2.3.3.2. Torrefaction

Torrefaction is a thermal treatment operating in the low temperature range of 200 to 300 $^{\circ}\text{C}$. It is carried out under atmospheric pressure in absence of oxygen. The process is characterized by low particle heating rates (<50 $^{\circ}\text{C}\cdot\text{min}^{-1}$) and by a relatively long reactor residence time (typically 1 hour) [90]. The resulting product has intermediate properties between wood and charcoal and exhibits several advantages when

compared to the original material such as decreased hygroscopicity, dimensional stabilization, increased biological resistance to decay, loss of mechanical resilience, etc. [91].

There is documentation on the torrefaction of a wide diversity of biomass resources, including: maritime pine, chestnut, oak eucalyptus, Caribbean pine and Rose gum [92,93], beechwood [82,83], birch, pine, bagasse [94], bamboo [95], wood briquettes residues [96], willow [82], and agricultural residues such as rice straw and rape stalk [97] or oil palm wastes [98,99].

2.3.3.2.1. Chemical transformations during torrefaction

Chemical changes during torrefaction strongly influence the final properties of the torrefied material, therefore a brief review of the main chemical transformations due to thermal treatment is given hereafter.

Chemically, torrefaction reduces the oxygen content in biomass by degradation of the reactive hemicellulose fraction. This generates a final solid product which has a lower O/C ratio compared to the original biomass. The main chemical changes of biomass during torrefaction are listed in Table 8. Exact temperature transitions depend on the type and properties of the biomass [90]. During the initial heating, water due to chemical reactions is removed by a thermocondensation process [33,34]. This occurs at temperatures between 160 and 180 °C and results in the formation of CO₂. At temperatures between 180 and 270 °C, the reaction is more exothermic, and hemicellulose degradation continues. At these temperatures, biomass begins to brown and releases more moisture, CO₂ and large amounts of acetic acid, with some low-energy phenols. In the torrefaction range of temperatures, the main decomposition reactions affect hemicellulose. Xylan-based hemicellulose generally decomposes between 250 to 280 °C. Minor decomposition is to be expected for lignin and cellulose except for chemical changes in their structure, which do not lead to a significant mass loss.

Table 8. Structural and chemical changes in biomass during drying and torrefaction (adapted from [90]).

	Non-reactive drying		Reactive drying	Destructive drying	
Water, organic compounds and gases	Mostly surface moisture removal	Insignificant organic emissions	Initiation of H-C bonds breaking. Emission of lipophylic compounds and unsaturated fatty acids, sterols, terpenes	Breakage of inter- and intramolecular hydrogen, C-O and C-C bonds. Emission of hydrophilic extractives (organic liquid product having oxygenated compounds). Formation of higher molecular mass carboxylic acids (CH ₃ -(CH ₂) _n -COOH), n=10-30), alcohols, aldehydes, ether, CO, CO ₂ and CH ₄	
Cell and tissues	Initial disruption of cell structure	Maximum cell structure disruption and reduced porosity	Structural deformity	Complete destruction of cell structure. Biomass loses its fibrous nature and mechanical resilience.	
Hemicellulose		Drying (A)	Depolymerization and recondensation (C)	Limited devolatilization and carbonization (D)	Extensive devolatilization and carbonization (E)
Lignin		A Glass transition (B)	C	D	E
Cellulose		A		C	D E

50 100 150 200 250 300

Temperature (°C)

At about 280 °C, the reaction is entirely exothermic and gas production increases, leading to the formation of CO, hydrocarbons such as phenols and cresols and other heavier products. Treatment temperatures above 300 °C are not recommended, as they can lead to significant devolatilization of biomass due to the initiation of the pyrolysis process [33].

2.3.3.2.2. Global mass loss

The chemical transformations that occur during torrefaction are accompanied by a mass loss, which can quantitatively be defined as:

$$ML(\%) = \frac{m_0 - m_t}{m_0} \cdot 100 \quad (1)$$

Where, m_0 and m_t are the oven-dried mass before and after torrefaction, respectively. Mass loss is known to be a good indicator of the torrefaction intensity and has been successfully correlated with several properties of the treated biomass such as energy properties [100], dimensional changes [93], particle size after grinding [101,102] and flowability [102]. Mass loss can therefore be considered as a synthetic parameter of the severity of treatment with respect to the process conditions (namely temperature and residence time) [98,103]. Figure 15 indicates the typical mass loss evolution of a poplar sample for three different torrefaction temperatures, showing how the degree of thermal degradation depends on both the treatment duration and the temperature.

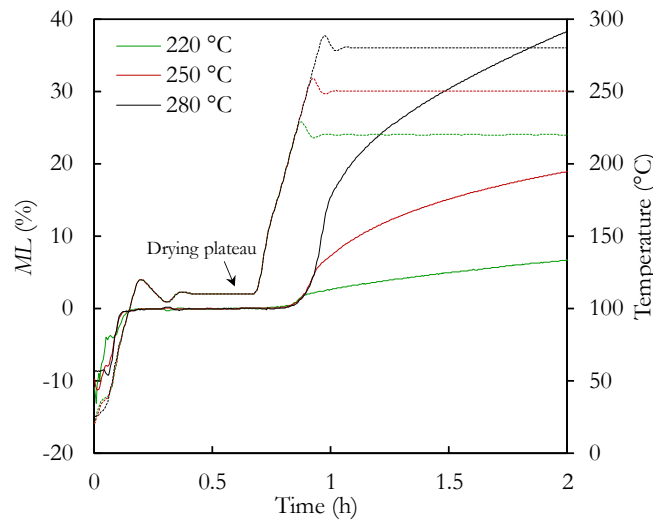


Figure 15. Thermogravimetry of a poplar sample (*Populus euro-americana* 'Koster', obtained in a NETZCH STA 449 F3 Jupiter® thermobalance, temperature ramps at $1\text{ }^{\circ}\text{C}\cdot\text{min}^{-1}$, $m_0 \approx 8.7\text{ mg}$); The dotted line corresponds to the temperature and the solid line to the ML. The zero of ML corresponds to the oven-dried state (Pin, Lu 2016, unpublished results).

The thermal decomposition of xylan-based hemicelluloses occurs at a lower temperature than for other hemicelluloses. Therefore, due to their increased content of xylan-based hemicellulose, the mass loss is expected to be higher for hardwoods than for softwoods at the same treatment conditions [58,93,104].

2.3.3.2.3. Properties of the torrefied biomass solid

Table 9 lists the main modifications in biomass properties triggered by torrefaction, as well as the effect of these changes on the subsequent valorization processes.

2.3.3.2.4. Effect of torrefaction on grindability of biomass resources

In entrained-flow gasification technologies, due to the relatively short residence time of fuel particles in the reactor, a small feedstock particle size is necessary (typically in the order of $100\text{ }\mu\text{m}$ [90]). Biomass resources have a tenacious and fibrous structure which makes it rather difficult to grind. In consequence, large energy consumption is necessary to obtain adequate particle sizes.

As mentioned above, torrefaction has been shown to significantly improve the grindability of biomass by reducing its mechanical resilience. This increase of biomass brittleness has a chemical and anatomical origin. Figure 16a-b shows the damage to the anatomical structure, with several cracks appearing in the most fragile tissues, caused by severe torrefaction in eucalyptus samples [91]. The mechanisms of size reduction are therefore also different between raw and torrefied wood (Figure 16c). When raw biomass is ground, the

stress causes particles to break along the fiber orientation. These leads to the formation of rather needle-shaped particles. In the case of torrefied particles, the stress causes the break of weaker hemicellulosic bonds, forming additional fracture lines depending on the orientation of the microfibrils. Depolymerization of cellulose breaks down or weakens the microfibrils, so the resulting particles are finer and have also decreased length and rounder shape [90].

Several studies have shown the efficiency of torrefaction in facilitating biomass grinding [57,89,105–110]. For instance, a reduction of 80 to 90 % in the power consumption required to grind torrefied biomass compared to untreated biomass has been verified by Bergman and Phanphanich et al. [106,111], which means a power consumption similar to that of coal. Additionally, in their study on pine, spruce and beech chips, Phanphanich and Mani [106] found that specific energy consumption (in kWh·t⁻¹) for grinding decreased linearly with increased torrefaction temperature.

Table 9. Effects of torrefaction on biomass feedstock properties.

Properties	Change during torrefaction	Effects	References
Moisture content	Reduced from 10-50 % to 1-3 % (wet mass basis)	Energy consumption for gasification is reduced. Transportation costs are reduced. Decomposition is prevented.	[90,92]
Bulk and energy density	Significantly reduced bulk density.	Transportation costs per m ³ are reduced.	[90,111,112]
Energy density	Increase in energy density (>60 %). Calorific value is increased.	Gasification efficiency is improved.	[90,111,112]
Grindability	Biomass loses its tenacious nature because of the breakdown of hemicellulose matrix. Fiber length decreases. In some hardwoods (beech and poplar), vessels collapse and deformation of the fibers are observed.	Power consumption for grinding is drastically reduced (up to 70-90 %). Capacity of the mill is increased.	[57,89,105–110]
Particle size distribution Sphericity Particle surface area	Smaller particle sizes and rounder particles are obtained after grinding compared to raw biomass.	Improved chemical reactivity of particles. Flowability is generally improved.	[102,106,113]
Pelletability	Uniform feedstocks are obtained with consistent quality. More lignin-active sites are opened, which eases binding.	The required pressure and energy consumption for palletization is reduced.	[90,92,114]
Chemical composition	Increase in carbon content. Decrease in H/C ratio.	Less smoke and water-vapor formation during combustion and gasification.	[115–117]

Hydrophobicity	Biomass capacity to form OH bonds is reduced; nonpolar unsaturated structures are formed.	Biological degradation is hindered. Stable storage.	[105,114,118]
----------------	---	--	---------------

Several methods are used to assess the ‘grindability’ of biomass resources and the effect of torrefaction on it. These methods can be based on:

- **Particle size distribution (PSD) changes:** Arias et al. [110] studied the particle size distribution (PSD) after milling of torrefied eucalyptus and found that the percentage of particles in the smallest sieve size increased after torrefaction. Similar results were found by other researchers [102,106,108,119,120].
- **Hardgrove Grindability Index (HGI):** Using this grindability test commonly used for coals, Bridgeman et al. [108] evaluated the effect of torrefaction on HGI of willow and Miscanthus samples. The test is described in a standard ISO procedure [121]. It is based in a sieving analysis of ball-milled material and requires a specific device. Torrefaction at high temperatures (290 °C) resulted in biomass with HGI values similar to those of coals. Similar results were obtained by Ibrahim, Williams and Manouchehrinejad et al. [122–124].

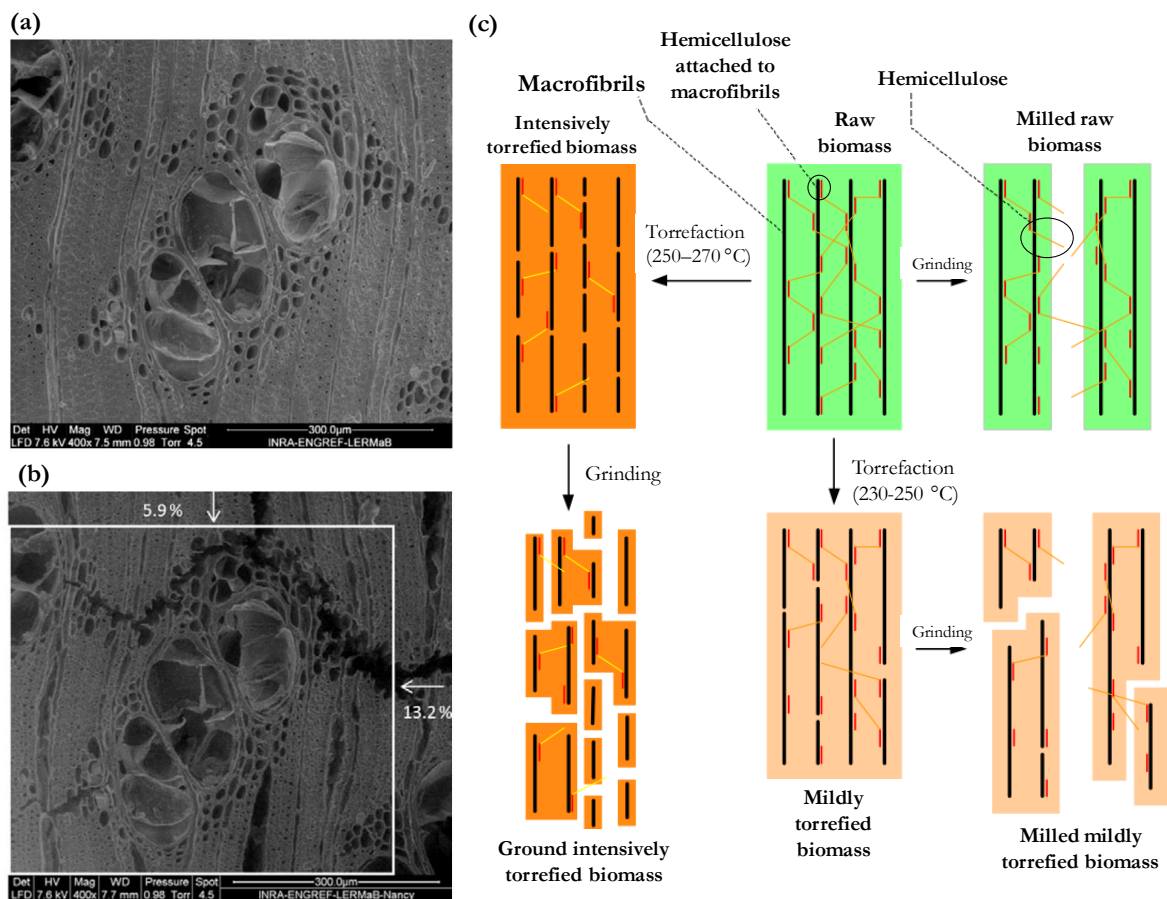


Figure 16. SEM images of a transversal section of *E. Saligna*. (a) Raw sample. (b) Torrefied sample (280 °C, 5 h). White square shows the image dimensions before treatment revealing sample's shrinking [91]. (c) Representation of particle breakdown from raw, mildly treated and intensively treated biomass [90].

- **Energy consumption for grinding:** Several authors have compared the energy consumption for grinding of raw and torrefied biomass [89,90,107,109,125]. For instance, compared to untreated biomass samples, torrefaction at 300 °C reduced grinding energy consumption by ten times for pine

chips and by six times for logging residues [106]. Figure 17 shows the effect of wood moisture content (MC), torrefaction (270 °C, 30 min) and target particle size for willow wood on the grinding energy consumption of a cutting mill [89,90]. While the power consumption for raw biomass increased strongly with a decrease of the resulting particle size, this effect is less pronounced for dried and torrefied wood. In absolute terms, the power consumption was also greatly reduced when the biomass is torrefied.

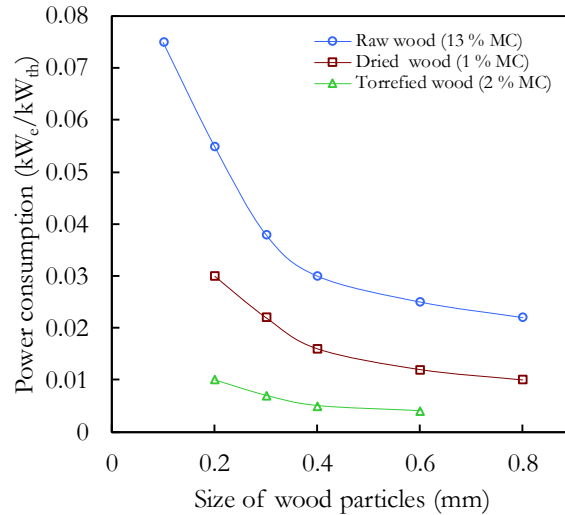


Figure 17. Comparison of power consumptions for milling of raw, dried and torrefied willow wood to final average size between 0.2 and 0.8 mm. The electric power consumption (kW_e) is related to thermal energy of wood flow (in $kJ \cdot s^{-1} = kW_{th}$) (MC: moisture content) [89,90].

2.3.3.2.5. Torrefaction energy requirements compared to reduction of energy consumption for grinding

Since torrefaction requires an energy supply (ca. 0.6 to 1 MJ/kg of feedstock are required [90]), it is therefore reasonable to question the overall energy balance of the coupled torrefaction and grinding processes. While this is a relevant point to be addressed for assessing the interest of torrefaction as pretreatment step, the specific energetic consumptions are strongly determined by the type of technology used for both torrefaction and grinding, the operational conditions and the feedstock. This may explain why few studies have addressed the overall balance of the process so far. We present here some literature elements that could help to clarify the trade-offs encountered when analyzing the efficiency of the two pretreatment operations together.

In their study on spruce and beech torrefaction, Repellin et al. [101] have stated that a mass loss of 8 % was an optimal value to reduce wood grinding energy while maintaining a good energy yield of the material. Over $ML = 8 \%$, grinding energy decreased at a slow rate and any decrease of grinding energy required a significant loss of material. The average particle size decreased almost linearly with the mass loss until $ML = 30 \%$ and was under 200 μm for $ML > 15 \%$ for beech and $ML > 5 \%$ for spruce.

Svoboda et al. [89] suggested that, to minimize the overall energy loss, an optimal process configuration would include torrefaction followed by vibration grinding [88] to particle size below 200 μm . The suitable temperature of torrefaction was between 270 to 280 °C (possible autothermal torrefaction processes could be triggered) and residence time of 0.5 h. The use of feeding methods developed for dry and pulverized coals could then allow a smooth feeding of the entrained-flow gasifier with relatively low energy consumption and high energy density of the biomass fed into the reactor.

Only the torrefaction of the energy intake could already greatly impact the overall efficiency of the system. To achieve high energy efficiency at low cost, innovative torrefaction technologies have been developed, for example, in the Energy Research Center of the Netherlands (ECN) [90] to valorize excess

of heat and volatile energy. The process layout (Figure 18) is based on the direct heating of the biomass during torrefaction using recycled hot gases. The recycled gas consists of the torrefaction gas (combustible organic compounds) which is re-pressurized to compensate for the pressure drop in the recycling loop. It is heated by exchange with the combustion flue gas released. Torrefaction gas produces thus the heat required for torrefaction and pre-drying but utility fuel can also be added. This process configuration showed to be the most promising, achieving autothermal operation.

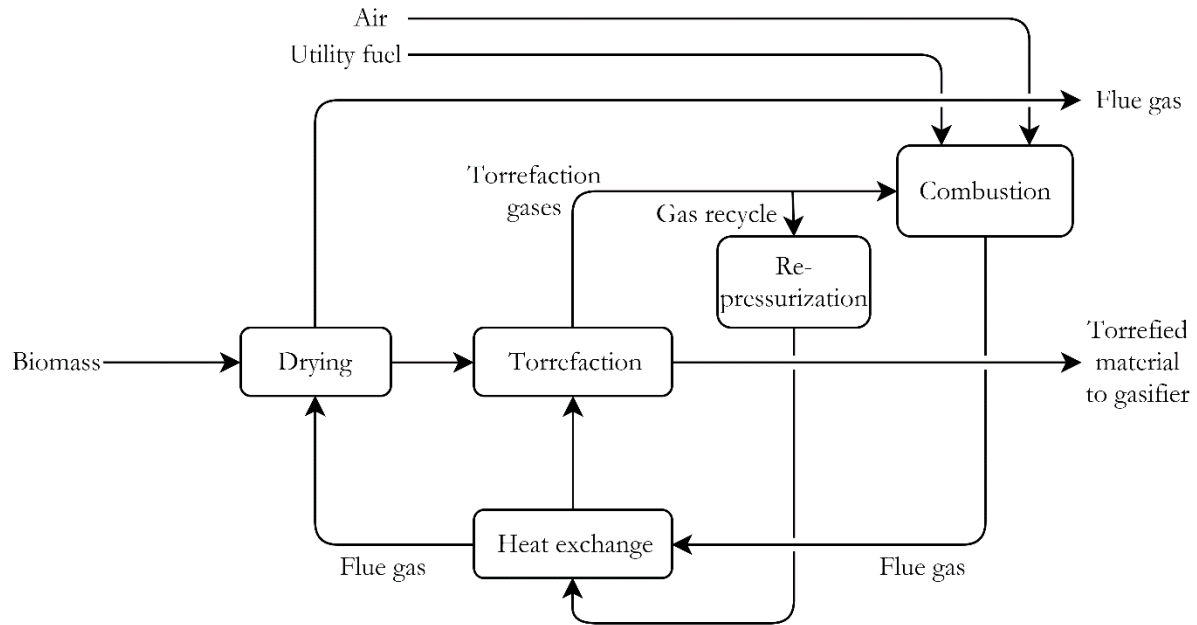


Figure 18. Optimized torrefaction process layout [90].

The considerations presented above clearly show that there is an operational trade-off to be found between the torrefaction intensity, the reduction of grinding energy consumption and the particle characteristics (namely PSD and shape) that would enhance gasification performances. However, the energy balance between energy gain achieved by grinding, the increase in the calorific value of wood and the energy consumption for torrefaction using optimized configurations seems to be globally favorable [82,105], despite the energy required for torrefaction and the energy loss related to the mass loss.

2.4. Obstacles for the industrialization of BtL processes

Although the numerous benefits of using biomass for bioenergy are evident in terms of its potential to provide energy independence and security, rural development and climate change mitigation, the conversion technologies and supply logistics pose serious challenges to their commercialization. A comprehensive review on the barriers for commercial power generation using biomass has been made by Asadullah [126]. Some of the main challenges to be addressed before an economical feasible production of biofuels through BtL processes are:

- Availability of cultivable land areas to produce biomass. They should not be in competition with food production.
- High investment costs.
- Low volumetric energy density of biomass (enhanced by pretreatments steps such as torrefaction)
- The lack of a reliable supply chain that guarantees on-time, cost-effective, all-year-round and continuous delivery of feedstock [127].

- Technological breakthroughs: co-producing electricity and biofuels deserve further research. Synergy with fossil fuels (cofeeding) could also facilitate both scale enlargement and cost reduction [128].

Regarding the pretreatment stages, more research is needed on the effects of process conditions on the fuel characteristics. This will allow to obtain a homogeneous material that will be efficiently transformed in the gasifier. Research on the flow behavior and handling of ground biomass is particularly important to ensure reliable feeding [129].

Regarding gasification, although the related research is mature, development is required of large (about 400 MW input), robust and cost-effective pressurized gasifiers. Feeding systems optimized for biomass particles are also an important technological barrier.

Regarding FTS and downstream processes, research is needed on a gas cleaning section that matches the catalyst's specification as well as on increased catalyst selectivity (for FTS).

2.5. Handling biomass and biomass powders: current issues and problematics

Currently, biomass handling is a key obstacle for the cost-competitive production of 2G biofuels. A common critical challenge is the feeding into the gasification reactor in a smooth continuous rate, but biomass handling problems also arise in the storage or the conveying facilities.

Biomass handling problems are the result of many factors. Particle properties such as size, shape, density, moisture and cohesion, as well as poor design of feeders, hoppers and conveying systems are at the origin of the issues. Raw ground wood particles have needle shapes that confer a low flowability and a poor fluidization behavior to the powder [101]. Large irregularly shaped particles tend to cause bridging in the feeding systems. Due to cohesion effects, fine particles also have strong tendency to bridge and block feeding and storage systems. The elasticity of the particles and their fibrous and sticky behavior make biomass difficult to process.

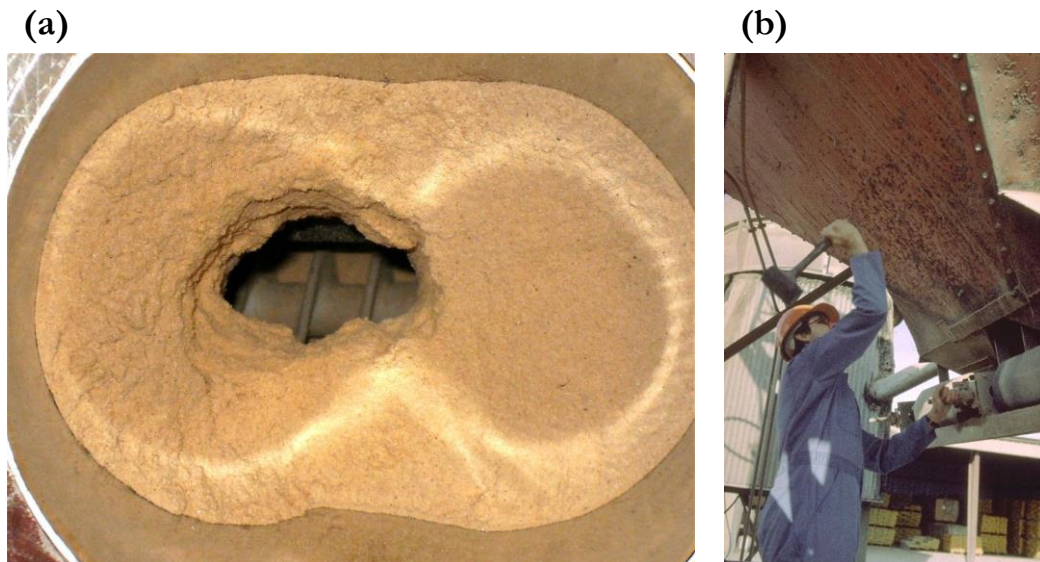


Figure 19. Flow problems in storage units (a) Rathole in biomass (sawdust) hopper (b) Operator hammering on hopper to induce flow [130].

The main types of feeding systems used for biomass are hopper or lock hopper systems, screw feeders, rotary valve feeders, piston feeders, pumps and pneumatic feeding systems. Bridging, ratholes, seal failure, feed rate fluctuations, blockages, reaction in the feed line, mechanical wear and corrosion are some of the issues encountered by many of these systems [129]. Pneumatic transport systems are not suitable for fibrous

and needle-like biomass materials [89]. Fluidization of pulverized wood ($d_p < 0.2$ mm) is also difficult, due to the high cohesion forces between particles and channeling [131,132]. Screw feeding of wood powder suffers from fluctuations of flow rates [133]. These feeding problems can trigger temperature excursions in the gasifiers that cause fluctuations in the producer gas constituents [126].

Pelletizing is a technological alternative that could ease transport and feeding compared to handling of powders. However, pellets are less reactive because of their low specific surface. An alternative consists in pelletizing and then grinding the pellets, which increases costs and reduce overall energy efficiency [134].

It is therefore clear that the emergence of handling issues is closely linked to the characteristics of biomass particles. The study of these properties and the effect of the pretreatment stages on them is therefore important for assessing feeding and reactor performances, downstream operations and equipment for all biomass-related processes. In particular, a better understanding of the effect of particle characteristics on biomass flowability is required for engineers to develop cost-effective processing and handling strategies.

B- Flow behavior of biomass powders

Before describing the methods commonly used to characterize flowability, it is important to consider the general classification of granular materials into two categories: non-cohesive and cohesive. This classification can determine the use of one method or another and it is also crucial to take it into account for simulation purposes (Section C).

1. Non-cohesive and cohesive granular materials

Bulk materials can be divided into two main categories: non-cohesive and cohesive. In non-cohesive bulk materials, the interaction between the particles is mainly determined by the steric repulsion and the friction forces. The macroscopic behavior of the materials is therefore governed by the particle shape and size distributions and the surface interactions between the grains. In the case of cohesive materials, the interparticle cohesive forces (electric charges, liquid bridges, hydrogen bonds or van der Waals interactions and magnetic dipole-dipole interactions) become greater than the weight of the particles. The macroscopic behavior of the powder is therefore mainly governed by the magnitude of the cohesion forces [135].

2. Methods for measuring bulk flow properties

Due to the complexity of granular materials, any single and simple test method cannot characterize completely the flow properties of a powder and flowability can never be expressed as a single value or index [135,136]. Flowability, defined as the ability of a powder to flow, is a multivariate feature of the bulk material and is not an inherent property. It is the combined result of material physical properties and its interactions with the equipment used for handling. There are therefore a variety of test methods that provide different indicators of flow behavior and often different methods can produce different results. A complete review on the methods to measure the flowability of bulk solids has been made by Schwedes [137]. The choice of the method highly depends on the phenomenon the user is trying to capture. Shear tests are typically more relevant for assessment of flow in storage units, while dynamic non-consolidated tests might better reproduce the flow of powders in an open conveyor.

Measurement methods for analyzing the consolidated, non-consolidated, static, quasistatic and dynamic properties of a powder can be strongly different [135]. Some of the methods that are commonly reported to measure the powder flowability are the angle of repose, the Compressibility Index (or Carr Index - Hausner ratio), the avalanching flow in a rotating drum, the flow through an orifice and the shear testing.

In accordance with the objectives of this work, emphasis will be placed on the shear test procedure as well as on the evaluation of dynamic flow in rotating drums. A brief overview of the other methods is finally given.

2.1. Shear tests

Jenike was the first to establish the fundamental methods for determining the flow characteristics of bulk solids [138]. The procedures described by Jenike have become a standard method ASTM D6128 [139]. Jenike used the principles of plastic failure with the Mohr-Coulomb failure criteria [140] to analyze the flow of solids in silos and bins, and to develop a model of flow and no-flow.

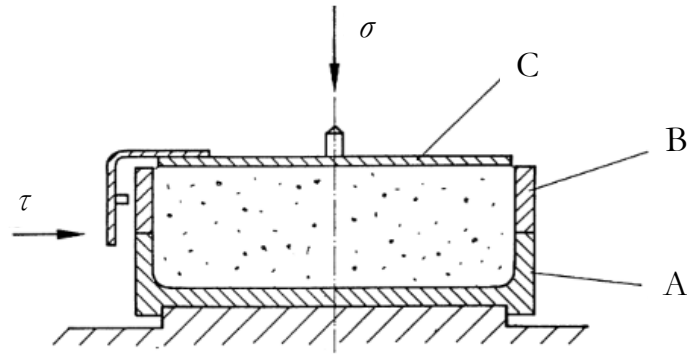


Figure 20. Schematic of a Jenike's shear tester (A: Base, B: ring, C: lid, σ : normal force, τ : shear force). Adapted from [137].

Jenike's direct shear cell tester (Figure 20) and his procedure for designing hoppers have been commonly used in research and industrial applications for characterizing a variety of granular materials. However, the operation of Jenike shear tester requires training, the time required for measurements of a complete yield locus is about one or two hours and often has reproducibility problems [141]. These drawbacks have encouraged the development of devices such as the ring shear tester.

2.1.1. Schulze ring shear tester

Shear testing can be a time-consuming method but it is the most reliable and frequently used for the characterization of powder flowability under consolidation [3].

Ring shear testers (rotary shear testers) have been used in soil mechanics since the 1930s, but it was only until the 1960s that an annular shear tester for bulk solids, where lower stresses than in soil mechanics are required, was developed. In 1992, an automatic and computer-controlled annular shear tester was developed by Schulze. The device automatically measures yield loci, wall yield loci, time consolidation, bulk density, etc. Since 2002, a small computer-controlled ring shear tester (type RST-XS) has been available. This tester allows the use of small sample volumes (9 ml, 30 ml and 70 ml) [142].

Unlike the Jenike shear tester, the Ring Shear tester requires a minimum of skill and uptime. In addition, because of the annular geometry, the shear displacement is not limited. Low variability results can be obtained following a standard ASTM procedure described in [143].

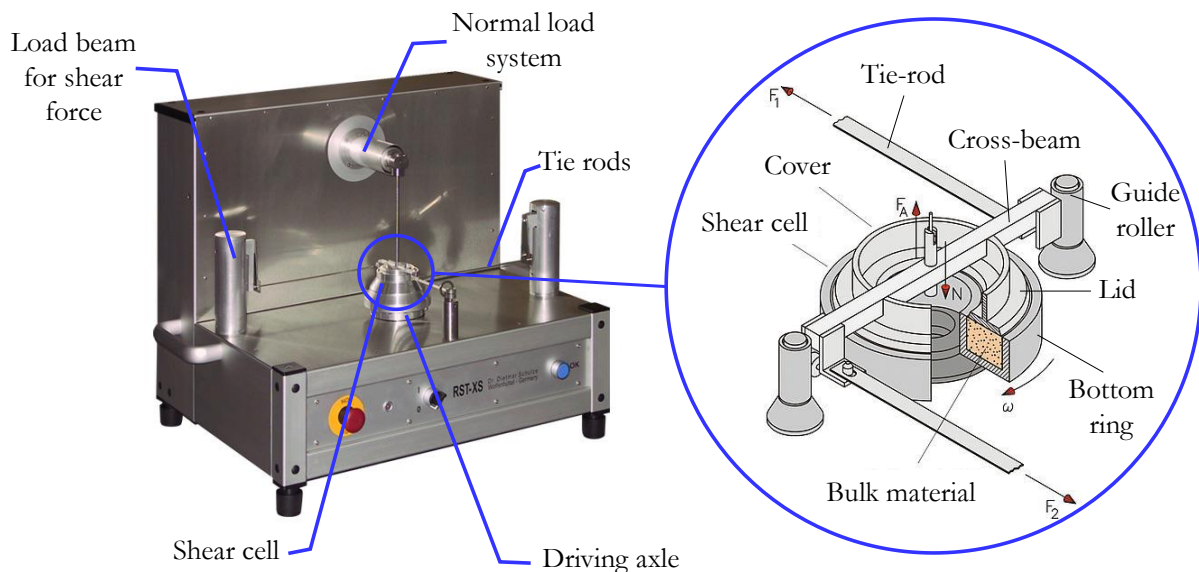


Figure 21. Schulze ring shear tester RST-XS. Adapted from [142].

From the yield locus plot, the application of the Mohr-Coulomb failure theory [140] allows the determination of different properties useful for assessing powder flowability but also for silo design. As shown in Figure 22b, the Mohr circle drawn through the preshear point and tangent to the yield locus locates the major principal consolidation stress (σ_1). The unconfined yield strength (σ_c) is given by the major principal stress established by the Mohr circle passing through the origin and tangent to the yield locus. In Figure 22b, the dashed line passing through the origin and tangent to the larger Mohr circle is the effective yield locus. Its angle of inclination with respect to the σ -axis is the effective angle of internal friction φ_e . The cohesion, C , corresponds to the value of the shear stress where the yield locus intersects with the τ -axis, i.e. at the normal stress $\sigma = 0$. For a complete study of the flow properties of a bulk solid, this procedure should be repeated for a range of initial consolidation loads, resulting in a series of yield loci [146]. The flow function (σ_c vs. σ_1) can thus be drawn (Figure 23).

2.1.1.2. Flow function and flowability

When using shear measurements, the flowability of a bulk solid is characterized mainly by its unconfined yield strength, σ_c , in dependence on the consolidation stress, σ_1 . The ratio FFC is commonly used for quantifying flowability:

$$FFC = \frac{\sigma_1}{\sigma_c} \quad (2)$$

The larger the FFC is, the better a bulk solid flows. A classification of flowability based on FFC can therefore be established (Table 10). Figure 23 shows the graphically the flowability classification zones in a flow function plot. From this diagram, it is clear that FFC of a bulk solid depends on the consolidation stress. For most bulk solids, a better flowability is obtained at greater consolidation stress.

Table 10. Flowability classification according to FFC values.

<i>FFC</i> range	Classification
$FFC < 1$	Not flowing
$1 \leq FFC < 2$	Very cohesive
$2 \leq FFC < 4$	Cohesive
$4 \leq FFC < 10$	Easy flowing
$FFC \geq 10$	Free-flowing

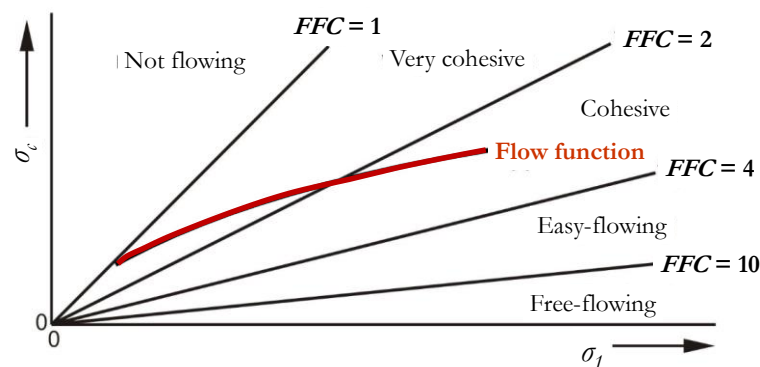


Figure 23. Flow function, lines of constant flowability and flowability classification.

2.1.1.3. Hopper design procedure based on Shear testing results

One of the strengths of shear testing compared to other flowability characterization methods is that the results (yield locus, flow function) can be directly used for the design of storage units, such as hoppers and bins, by following the standard procedure established by Jenike [138]. A brief description of this procedure

is presented below in order to highlight the influence of the flow behavior of the granular material on the equipment design [147].

In general, the design procedure consists of determining the maximum hopper half angle (β , the angle between the vertical vessel and the sloped hopper outlet) to avoid ratholes and funnel flow (Figure 24a), and the minimum hopper outlet size (B , Figure 24b) which prevents arching at the vessel opening. Two values are required: the flow function and a flow factor ff . While the flow function depends solely on the shear strength of the material, ff depends on both, the bulk material properties and the characteristics of the hopper (material of construction, shape, wall friction, etc.). ff describes the ability of a hopper to discharge consolidated solids by gravity. For mass flow to occur (i.e. every particle in the storage vessel moves downward in unison towards the vessel opening), ff must be located above the flow function (i.e. the applied hopper discharge stress must be greater than σ_c).

Besides the flow function, additional material properties required for design are the bulk density as a function of the applied normal stress, the effective angle of internal friction (φ_e) and the wall friction angle (φ_w). The effective angle of internal friction determines the lateral (or outward) stress acting on the vessel wall, while the angle of wall friction, describes the strength of interaction between the bulk solids and the wall material.

Jenike's hopper design protocol can be summarized as follows:

- Obtain the values of φ_e and φ_w and use the Jenike published charts [138] that relate them to both β and ff .
- Determine the critical applied stress (CAS) from the intersection of the measured flow function and the calculated ff line. The ff line is a straight line through the origin with slope equal to $1/ff$.
- Calculate the minimum hopper outlet size (B) using values of CAS , β and bulk density at the consolidated stress at the hopper outlet (ρ_b) as:

$$B = \frac{H(\beta) \cdot CAS}{\rho_b g} \quad (3)$$

$$H(\beta) = 2 + \frac{\beta}{60} \quad (4)$$

where g is the gravitational constant.

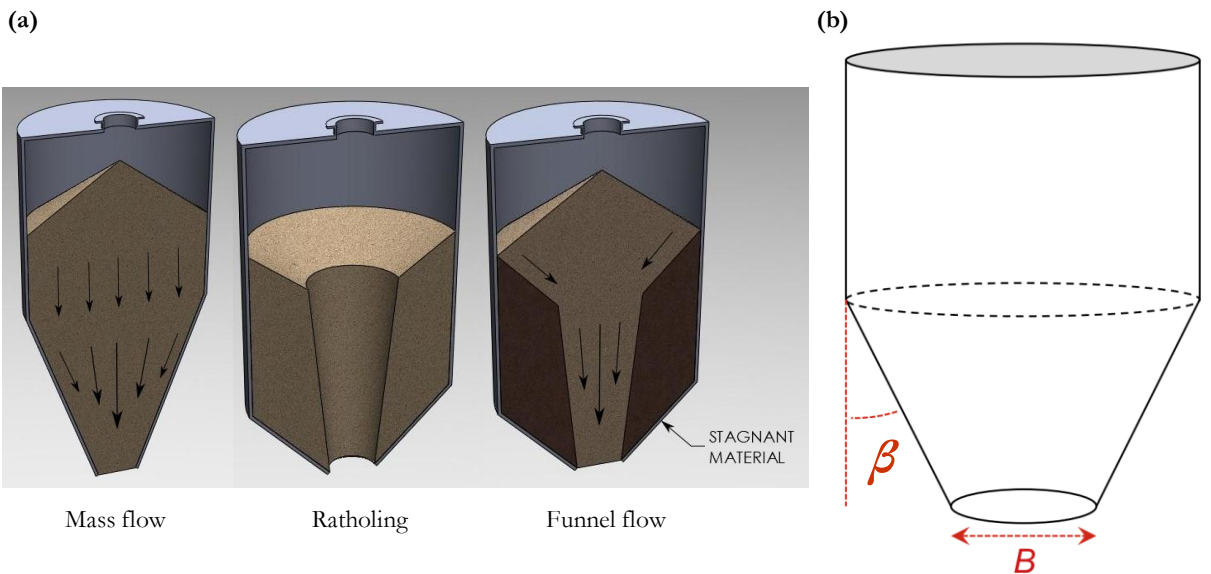


Figure 24. (a). Flow regimes in silos (Adapted from [130]). (b) Scheme of a conical hopper depicting the hopper outlet diameter (B) and the hopper half angle (β) (Adapted from [147]).

2.2. Other measurement methods for determination of flow properties of bulk solids

Examples of further simple test methods relatively widely used are:

- **Hausner ratio (HR) and Carr's compressibility index (CI):** simple and relatively fast to determine. They are based on the unsettled apparent volume ('loose' = V_L) and the final tapped volume ('tapped' = V_T) of the powder after tapping the material until no further volume changes occur (Figure 25a). They are calculated as follows:

$$HR = V_L / V_T \quad (5)$$

$$CI = (1 - V_T / V_L) \cdot 100 \quad (6)$$

Equivalent definitions using the loose bulk density and tapped bulk density can also be used. *CI* and *HR* are not intrinsic properties of the bulk material, i.e. their values might depend on the methodology used (diameter of the cylinder used, number of times the powder is tapped, mass of material used, etc.). A call for harmonization of the procedure for measuring *CI* and *HR* has been made by the United States Pharmacopeia [148].

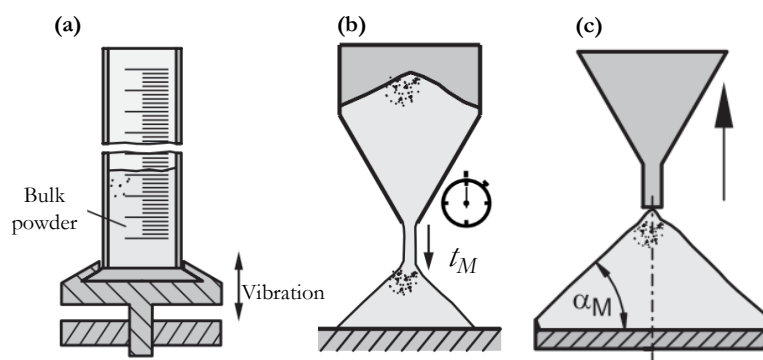


Figure 25. (a). Compressibility test in a tap volumeter. (b). Funnel for measuring time of discharge (t_M). (c). Measurement of poured angle-of-repose (α_M). Adapted from [141].

This method is based on the influence of interparticle adhesive forces on bulk density: in loose solids of poor flowability, large voids are formed due to the effect of adhesive interparticle forces. This is not the case with free-flowing bulk materials. Poorly flowing powders are thus more compressible [141].

- **Flow through an orifice:** Flow through an orifice is generally measured as the mass per time flowing from a number of container types (bottles, funnels, hoppers). The flow rate can be measured in discrete or continuous increments. This method only gives reliable results with free-flowing materials (Figure 25b).
- **Angle-of-Repore:** Angle of repose (AoR) is one of the most used parameters for characterizing the flow behavior of granular materials. AoR is the result of the balance among interparticle forces and gravity forces [149]. One definition of the Angle-of-repose is the constant three-dimensional angle (with respect to the horizontal base) assumed by a conical pile of material formed by different methods [148] (Figure 25c). Although the values of AoR are found to be very dependent on the method used, it continues to be extensively used, especially in the pharmaceutical industry [149–153]. A comprehensive review on the AoR of granular materials, its definitions, its measurement methods and its influencing factors has recently been made by Beakawi et al. [154].

A generally accepted scale of flowability for the Angle-of-Repore, the Compressibility Index (CI) and the Hausner Ratio is given in Table 11. In Figure 26, the different flowability characterization methods reported here are classified relatively to each other according to the stress state of the powder (compacted or loose) and the predominant measurement conditions (static or dynamic).

Table 11. Flowability scale according to several indicators [148].

Flowability	CI (%)	HR	AoR (degrees)
Excellent	≤ 10	1.00 – 1.11	25 – 30
Good	11 – 15	1.12 – 1.18	31 – 35
Fair	16 – 20	1.19 – 1.25	36 – 40
Passable	21 – 25	1.26 – 1.34	41 – 45
Poor	26 – 31	1.35 – 1.45	46 – 55
Very poor	32 – 37	1.46 – 1.59	56 – 65
Very, very poor	> 38	> 1.6	> 66

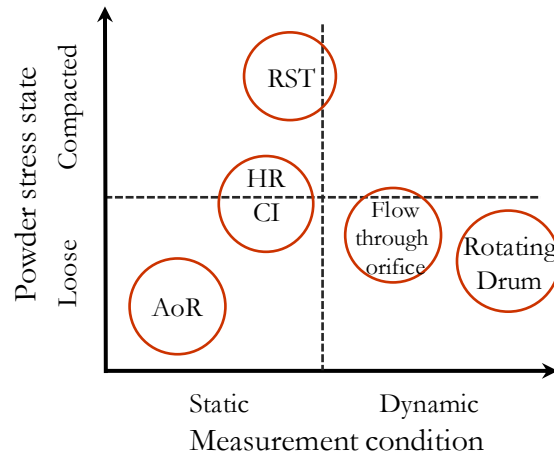


Figure 26. Flowability characterization methods. CI: compressibility index; RST: Ring shear tester; AoR: angle-of-repose.

2.3. Rotating drum systems for measurements of flow properties

Particular interest has been given to granular materials in rotating drums as its usage is present in a wide range of industrial sectors from agricultural to mineral mining. They are used in size reduction, granulators, dryers and reactors for processing granular materials. Rotating cylinders are also used to determine bulk solid flow properties such as the dynamic angle of repose and the avalanching behavior [155]. Laboratory tests in rotating drums have been used for decades to understand the dynamic and shear behavior of particulate materials [156,157] at low stresses and close to the surface of the bulk material. Compared to powder rheometers based on shear measurement, the only stress applied on the powder sample in the rotating system is induced by gravity. Therefore, the rotating drum evaluates powder dynamic properties in a free-surface non-consolidated conditioning [158]. The study of bulk behavior using a rotating drum could therefore better represent the actual stress conditions of powders flowing in a non-consolidated regime through a pipeline (compared to shear tests).

In a rotating drum, flow events during rotation are easily reproducible because the system is continuously self-feeding. The experiments can therefore be replicated a large number of times without operator intervention in a short period of time [159]. These advantages have made rotating drums one of the most practical geometries for studying the flow of granular materials.

Particle flow in a partially filled rotating drum may exhibit a range of complex phenomena, such as avalanche, mixing and segregation. These phenomena are also highly dependent on whether the material is cohesive or non-cohesive.

For non-cohesive materials, extensive research has been conducted to understand the dynamics of granular flow, both from a macroscopic bulk perspective and at the particle scale. A grounding work has been made by Mellmann [160], who identified different flow regimes existing in a drum for non-cohesive

materials: sliding, surging, slumping, rolling (continuous), cascading, cataracting and centrifuging. These regimes depend on the rotational speed, the filling ratio, the wall friction and the dimensions of the drum (Figure 27).

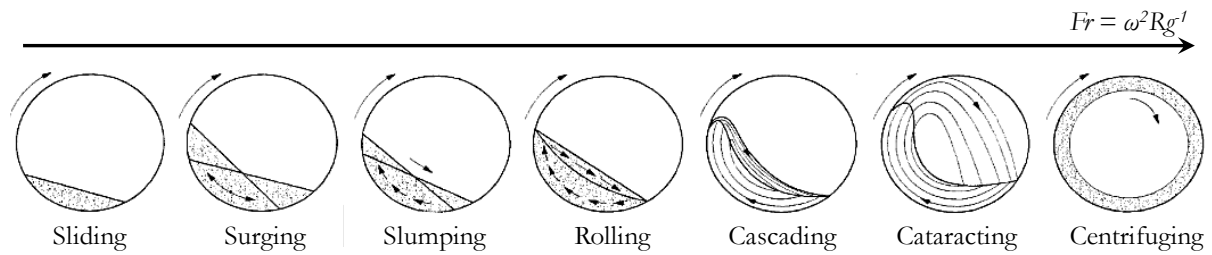


Figure 27. Flow regimes in a rotating drum for non-cohesive powders. Adapted from [160]. Fr is the Froude number i.e. the ratio of centrifugal force to gravity (g). ω is the rotational speed and R is the drum radius.

Although most of the research so far has focused on the study of the description of flow regimes and dynamics [155,159,169–172,161–168], the assessment of flowability through rotating drums has also been a topic of great concern [156,157,173–179]. The main criteria used to characterize flowability of non-cohesive materials using a rotating drum are the dynamic angle of repose (in a continuous regime) and the time elapsed between events (in a slumping regime).

Experimental research to understand the dynamic behavior of various non-cohesive samples has been successful. However, many challenges remain for sticky and cohesive materials like biomass powders. For this type of materials, the behavior of the granular assembly is more complex, and the classification of flow regimes established by Mellmann does not apply. Interparticle cohesion induces intermittencies in the whole range of rotating speed [180–184]. Figure 28 shows the typical flow in a rotating drum for non-cohesive and cohesive granular materials. While in the case of a non-cohesive material, a constant, uniform and smooth slope develops (continuous regime), very irregular free-surface profiles and the formation of agglomerates of particles are characteristic of a cohesive behavior.

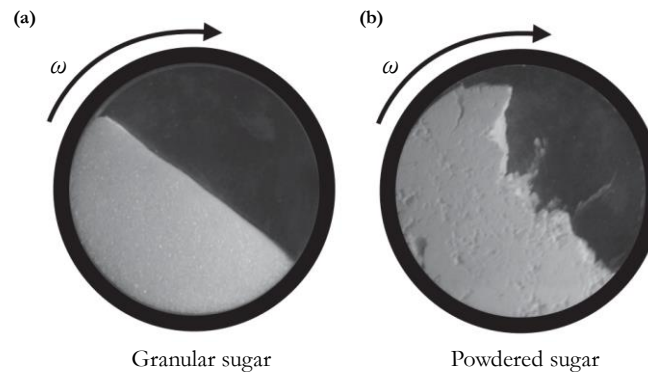


Figure 28. Flow in a rotating drum. (a). Non-cohesive material in a continuous regime. (b). Irregular flow of a cohesive powder. Adapted from [135].

Research on the flow of cohesive powders in rotating drums include the work by Castellanos et al. [181] who have established different flow regimes for fine cohesive materials ($d_p < 30 \mu\text{m}$): as the rotational speed increases, cohesive powders move from a plastic regime to a fluidized regime followed by a entrained or suspended regime. Similarly, Alexander et al [180]. showed a correlation between increase in bed volume (dilation) and cohesion of different samples: as dry cohesion increased the material dilated further.

Iaccoca and German [185] have first used avalanche behavior to characterize powder flowability of cohesive lubricants. They have used strange attractor diagrams, which are plots of time of the n^{th} cascade versus the time of the ' $n + 1$ ' cascade, to evaluate flowability. However, this type of representation, typically used in chaos theory and analysis, was not the best format for analysis of flow behavior and quantitative

comparison between different powders. The cumulative distribution of the time elapsed between events better described the flow dynamics and allowed detection of changes in flow caused by powder additives. Since this work by Iacocca, there has been increased interest in establishing new criteria for assessing flowability of cohesive powders using rotating drum experiments. Lavoie et al. [186] and Soh et al. [187], for example, have proposed ‘fluidity’ and ‘cohesion’ indices based on the avalanche periods, while Alexander et al. [180,188], Davies et al. [189] and Yang et al. [190] have used the variation of the mass center of the powder over time. Because of the irregular surface of avalanches of cohesive materials, adapted measurements of the dynamic angle of repose have also been applied to materials such as wet glass beads [191,192], xerographic developers [193], moist pharmaceutical powders [194], silicon carbide abrasives [135], cocoa powders [183,184] and lactose powders [158,195,196].

2.3.1. Commercial systems for flowability assessment using rotating drum principles

The possibility of assessing flowability of bulk solids using the dynamic avalanching behavior has encouraged the development of commercial devices such as the *Revolution powder analyzer* (Mercury Scientific Inc. SC, USA) [197].

At the heart of the equipment is a rotating cylinder into which bulk powder samples are placed (Figure 29). The drum has two borosilicate glass sides. The standard version of the cylinder is 100 mm diameter, 35 mm wide. The mechanical drive is made through a motor connected to two high precision silicone rollers. A digital camera with the assistance of a cold cathode back lighting takes images of the powder during rotation. The images are processed by a software that measures several aspects of the powder, including the potential energy, angle, surface fractal, time between events and volume.

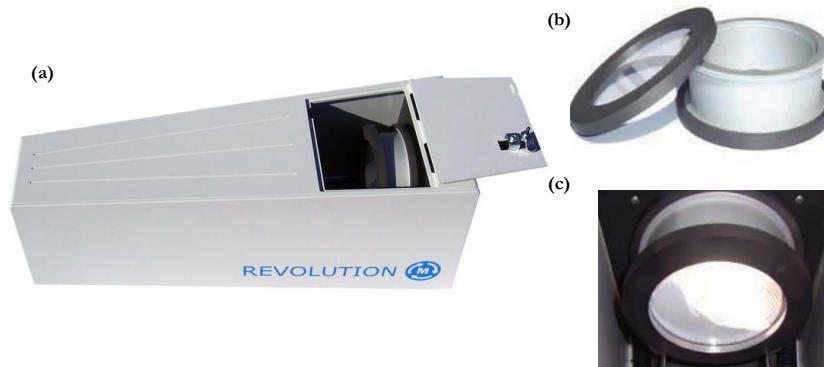


Figure 29. Revolution powder analyzer [197] (a) Top view. (b) Sample drum. (c) Sample inside the drum.

The instrument is easy to use and operator-independent, but problems have been reported regarding powder adhesion to the glass walls which distorts the measurements [198]. Additionally, a warning has been raised as cohesive powders may display short times between avalanches due to aggregate formation, and thereby wrongly be assessed as having good flow.

3. Linking flow properties and granulometry of granular materials

Unfortunately, the relationship between grain properties and the powder bulk behavior of granular materials is far from obvious [199], and therefore both types of measurements have to be performed. Although extensive research has been undertaken on experimental and numerical studies about these relationships, there are currently no general statements applicable to all types of granular materials under all flow conditions.

Flow properties are not always correlated with a single size or shape descriptor and the width of the particle size and shape distributions have also to be considered. Prediction of flowability on the basis of a

particle size distribution is therefore difficult. Nevertheless, the following qualitative rules often apply for materials of uniform particle shape [141]:

- Flowability of granular materials with a similar width and type of PSD increases with increasing median size.
- Flowability of granular materials having the same median size tends to increase with a decrease of particle size polydispersity.
- When considering coarse particles ($d_p > 500 \mu\text{m}$), spherical, smooth particles tend to flow better than non-spherical, rough, sharp-edged particles. For fine powders, interparticle cohesive forces could play a major role. A pronounced roughness could thus hinder the ability of particles to approach each other, thus promoting flow.

Examples of work on the effects of particle size and shape on flowability include the research of Lumay et. al and Boschini et al. [135,158]. In their work with cohesive and non-cohesive granular materials and using different methods for flow characterization, they have found that cohesion between grains becomes important when the grain diameter is inferior to $50 \mu\text{m}$. The repose and flowing angles were thus increased by the cohesion. Therefore, for small grains, the macroscopic properties of a pile were mainly related to the cohesive forces between the grains. For larger grains, the particle shape becomes an important parameter. In particular, the elongation of the grain influences the macroscopic properties of the assembly.

Walton and Braun [200] have investigated the effect of particle shape on the dynamic angle of repose and on the bulk flow behavior in rotating cylinders using Discrete Element Method (DEM) simulations with single spheres and cluster of spheres in a tetrahedral configuration. They have concluded that the angles increase greatly between the spheres and a tetrahedral configuration, as the particle interlocking is much larger.

More recently, Mallick et al. [201] have experimentally addressed the question of the influence of particle size on the cohesion and unconfined yield strength of fly ash of coal fired thermal power stations ($d_p < 150 \mu\text{m}$). They found that increasing in fines content increased the cohesion of fly ash. They have developed correlations for cohesion and unconfined yield strength dependent on the particle size, the span and the compressibility index of the powders. It was the dependence on the compressibility index that was most pronounced.

4. Flowability of biomass materials: state-of-the-art

Several researchers have addressed the question of estimating biomass flowability. Nevertheless, despite the frequent occurrence of handling problems, there is still a relatively poor knowledge of the flow properties of biomass materials and few data on biomass flow properties are available for designing efficient transportation, storage, feeding and handling systems [202].

Recently, the suitability of conventional tests of flow properties such as shear testing applied to biomass materials, has been questioned [202]. The elongated and irregular shapes of biomass particles promote high compressibility and long strain before the attainment of failure and steady state-stress [203,204]. Irregular, fibrous and flaky particles can show a pronounced expansion due to elastic recovery when being unloaded after consolidation. Thus, the properties of the sample change during unloading, leading to erroneous strength measurements [141]. Miccio et al. [202,205] found that shear measurements could however be used for the characterization of flow properties of biomass when the particle size is below 2 mm.

Although new methods based on the tendency of biomass bulk solids to arch over bins and hoppers have been proposed [87,202,206–209], it is still widely accepted that the principles of commonly used methods can be used as fundamental knowledge for obtaining the flow properties of biomass particles [113].

Moreover, these new alternative methods are limited as they do not give results that can be directly used for design.

Research on biomass flow characterization using standard shear tester or other established apparatus includes the works by:

Barletta et al. [208], who have identified some mechanical properties (such as unconfined yield strength) of granular biomass (wood chips, wood powder and straw chops) and indicated some critical requirements for biomass characterization procedures (namely particle sizes below 2 mm). Gil et al. [206] have measured the flowability of woody and herbaceous biomass (poplar and corn stover, $d_p < 5$ mm and 2 mm) under various moisture contents in a shear tester following standard procedures. They have assessed the effects of physical characteristics (particle size, shape and moisture) on flowability, finding that smaller and rounder particles improved flow behavior while long and hooked particles favored bridging and particle interlocking. Crawford et al. [147,210] have studied the effect of physical and chemical pre-processing on the flowability of different kinds of biomass using a FT4 Powder Rheometer [211] and a Jenike shear tester. Zulfikar et al. [212] have determined the flow properties of biomass and coal blends using shear testing. The flow properties are dependent on the form of the biomass (sawdust or woodchips). Coal/sawdust blends were not likely to cause flow problems while coal/woodchip blends were.

Adapa et al. [204] have conducted shear experiments on ground raw and pretreated agricultural biomass ($d_p < 6$ mm), showing that steam-exploded grinds had higher internal friction compared to raw grinds. Stasiak et al. [213] have characterized flowability of sawdust and woodchips against popular construction materials using a direct shear tester. Woodchips had the worst flowability, having the highest angles of internal friction. Larsson [214] have used a Schulze Ring Shear Tester (RST) to measure the friction properties of reed canary grass under a range of normal pressures. The Ring Shear tester was also used by Miccio et al. [202] to determine the flow functions of gypsum powder, sawdust and olive husk. Flow functions are located in the very cohesive region for gypsum powder, in the cohesive zone for sawdust and in the easy-free flowing region for olive husk. Using RST measurements, Barletta and Poletto [215] have determined the flow properties of 'dry' and 'wet' sawdust (moisture content of 16 and 49 %, respectively). The flow function for the wet material was near the very cohesive region while the flow function for the dry powder located in the cohesive zone. Wu et al. [216] have measured the mechanical properties of wood pellets, torrefied pellets, and woodchips with a large-scale annular shear tester and have concluded that wood pellets had the best flowability, followed by torrefied wood pellets and chips.

More recently, Falk et al. [217] have noted that, based on their flow functions, milled torrefied Norway spruce and reed canary grass ($d_p < 1$ mm) could be classified as easy-flowing, while milled raw Norway spruce ($d_p < 1$ mm) was rather cohesive. Stasiak et al. [218] have used a vane shear tester to study the flow behavior of 'forest woodchips' (centimetric size) and have found that the method, easier to implement and less time-consuming, is in good agreement with results based on Jenike method. Shear tests have allowed Craven et al. [59] to conclude that fine milled wood pellets and pulverized coal ($d_p < 1$ mm) require a higher shear stress to flow than coarser materials (wood pellets, torrefied pellets, ground anthracite and torrefied wood chips, $d_p > 1$ cm). Coarse materials could be classified as easy-flowing while milled materials are cohesive.

The use of alternative methods (not based in classical shear measurement) for assessment of biomass flowability has been reported, among others, by Ileleji and Zhou [219], who measured the angle-of-repose of bulk corn stover with different particle sizes (< 6.4 mm) and two moisture contents (dry, < 10 % wet basis and wet, > 20 % w.b.). In general, decreasing moisture content and particle size decreases the AoR, but, in any case, stover particles of the particle size ranges tested have a poor flow behavior. Wu et al. [216] have also used AoR measurements for characterization of wood pellets, torrefied pellets, and woodchips. AoR has also been used by Guo et al. [220] to assess flowability of biomass-coal blends. Xu et al. [113] have used AoR tests, Hausner ratio and Compressibility index to evaluate flowability of raw and torrefied (300 °C,

45 min) agricultural biomass materials (soybean straw, corn straw, rice, straw and rice husk, $d_p < 1$ mm). The same flowability indicators have been used by Tannous et al. [221] for studying Douglas fir powders ($d_p < 1$ mm). Biomass flow assessment based on arch formation in silos has been also widely conducted, especially by the research team of Miccio et al. [202,205,208,215,222,223].

Although these studies have investigated the effects of particle characteristics on the flow properties of various biomass feedstocks, no study has specifically examined how pretreatment stages, including torrefaction and grinding, affect the flowability of biomass.

The need for further understanding and characterization of the flow properties for biomass materials is incontestable. Studies on the relevance and reliability of traditional methods for assessing flow behavior applied to biomass are also required. This information would contribute to the development of currently non-existent standards for the characterization of the flowability of biomass materials [3].

4.1. Size and shape of biomass particles and effects on flowability

Characterization of particle size and shape is part of the flowability assessment, as the flow behavior of bulk materials is closely related to these properties. Biomass feedstock rarely consists of particles of uniform size and shape and it is important to consider this variability in the design and operation of handling systems. Moreover, regarding gasification systems, particle size distribution has been reported as one of the main parameters affecting the composition, quality and final application of the producer gas [224].

Bridgeman et al. [225] have studied the analytical and chemical properties of ball milled switchgrass and reed canary grass as a function of their particle size. Their results highlight the chemical heterogeneity of the biomass materials since smaller particles have a significantly higher concentration of inorganic matter, moisture and nitrogen content but lower carbon content and calorific value than larger particles. This is due to a preferential distribution of the plant sections (with different composition) on the different granulometric ranges. A more homogeneous trend has been reported by Guo et al. [226], who used a cutting mill to produce biomass particles (pine, beanstalk, rice straw, reed) in the range of 83 to 425 μm . By sieving, they obtained linear cumulative particle size distributions that coincided for the different biomass materials.

The effects of particle size on gasification performance have been studied by Tinaut et al. and Hernandez et al. [224,227] who found that the maximum efficiency, fuel conversion and quality of producer gas (in terms of CO and H₂ concentrations) are obtained with the smaller particle sizes. Few studies have addressed the influence of biomass particle size on flow behavior. Chevanan et al. [228], for instance, have realized that the change in particle size greatly affected the friction coefficient of chopped switchgrass, wheat straw and corn stover. In their study on milled poplar and corn stover, Gil et al. [206] have reported that lower particle sizes improved flow behavior as measured by shear tests, mainly due to the lower presence of overlong and hooked particles. In the case of black soybean powders, Lee et al. [229] have concluded that the particle smallest in size require the largest hopper angles and opening dimensions.

Although some standardized framework for determination of biomass PSD by sieving has been recently published [230], there is still a call for consensus on standards using different methods. Indeed, Hartmann et al. [231] have found serious incompatibility when PSD for wood chips is determined by various measuring methods. The measured particle dimension varies as a function of the methods for size classification: images analysis and horizontal or rotating sieving. In their study on milled poplar and corn stover ($d_p < 5$ mm), Gil et al. [232] have established that the size classification obtained by standard sieving corresponds to the particle width (shorter dimension). However, because of the elongated particle shape and agglomeration, ca. 30 % of the particles were ‘wrongly’ classified. From these works it is therefore clear that particle shape must be specified in order to clarify which dimension is taken into account when particle size is evaluated.

Often, for materials such as minerals, plastics and pharmaceuticals, particle shape is simplified by the assumption of sphericity. However, biomass particles at a millimetric scale are far from sphericity and previous research suggests that assuming spherical shape for biomass particles could lead to large errors in terms of modeling of thermal treatment processes [233]. Biomass particle shape is not simple to characterize, in part because of the lack of a homogenized framework for defining particle shape. Biomass cross sections differ from regular geometric forms (square, rectangle, circle, etc.), which makes their classification challenging. In the literature, it is possible to find studies that propose several factors and descriptors for shape classification: aspect ratio, rectangularity, solidity, curl, and others such as circularity ratio, convexity, and so on [206]. However, more studies are still needed in order to establish correlations with typical behaviors observed during biomass handling operations [3].

Concerning biomass handling issues, the influence of particle shape on tendency to bridge has been reported by Mattson et al. [234] for various chipped biomass and Paulrud et al. [87] for ground pine. A high proportion of hooked particles or thin, long particles increases the bridging tendency. More recently, Lee et al. [229] have stated that the internal friction angle of black soybean powders is influenced by both particle size and shape (circularity). It has been found that biomass shape make shear measurements more difficult due to the high compressibility and long strain of the material [202,204]. The need for alternative flowability characterization techniques for elongated fibrous materials has thus been identified [235].

4.2. Effects of torrefaction on flow properties of biomass materials

While research on the effects of torrefaction on the energy properties of biomass has been extensive, there has been little quantitative analysis on the flow properties of the torrefied biomass feedstock.

Xiao et al. [236] have studied the effect of pyrolysis (in the range of 300 to 700 °C) on the angle-of-repose, the bulk density and the internal friction of rice straw. They found that the three measured characteristics were improved through pyrolysis, which could favor the feeding of biomass. The particle shape was nearly spherical after pyrolysis and the adhesion between particles weakened.

Xu et al. [113] have performed flowability tests (angle-of-repose, Hausner ratio and Compressibility index) in milled raw and torrefied soybean straw, corn straw, rice straw and rice husk. They have concluded that flowability, as measured by the selected criteria, was improved by torrefaction. They have argued that the main reason for this improvement was the reduced moisture content of torrefied powders, which hinders the formation of liquid bridges. A second reason was the destruction of the fiber structure that led to more uniform biomass particles.

Almendros et al. [237–239] have studied the effects of combined torrefaction and grinding processes on grindability, particle size and shape distributions, bulk density and compressibility of spruce and beech powders ($d < 500 \mu\text{m}$). They have highlighted that the torrefaction intensity significantly influences the particle size distribution (the particle diameter is reduced when increasing torrefaction temperature) but does not affect the particle morphology in terms of circularity, elongation and roughness. More intensively torrefied powders are also less cohesive and require a lower minimum fluidization velocity.

C - Modeling flow of biomass materials

Over the last decades, interest in simulations has increased for the numerical study of granular media. Although the two approaches are complementary, three major advantages of simulations over experiments can be pointed highlighted [240]:

- Simulation allows any physical quantity to be ‘measured’ without disrupting the system. Experimentally, given the opacity of the grains, it is hard to study individual trajectories or measure local properties. Some techniques have been recently developed (MRI, X-ray tomography) but they require long exposure times and heavy equipment
- All parameters can be varied independently of each other: size distributions, friction properties, coefficient of elasticity, stiffness, etc.
- Simulations are free of undesirable effects such as humidity, static electricity or misalignment.

The appeal of numerical simulations is therefore obvious, and several approaches have been proposed to study particles flow behavior, interactions with handling equipment and process optimization. An overview of the different approaches to simulating granular materials is made in Table 12. In the following sections, emphasis will be placed in the Discrete Element Method (DEM), which has proven to be a reliable, powerful and relevant tool for simulating granular materials.

Table 12. Simulation approaches for granular materials.

Method	Characteristics	Ref.
Numerical methods (FEM/DEM)	Use numerical solutions of partial differential equations for stresses and flows. Relatively inexpensive and amenable to extensive parametric studies with few particles. Challenges remain for simulation of cohesive, fine and polydispersed systems. Parameter calibration is required.	[241]
Particle and continuum mechanics	Granular materials are represented as a solid continuum. They can be computing efficient but often unrealistic regarding the variability of grain characteristics at the particle scale. Assumptions of small or continuous deformation are not valid for granular materials.	[242–245]
Lattice models	Their implementation seems simple and there is the possibility of treating “large” systems. Cellular automata have been used for flow problems and the modeling of avalanches in sand piles, but experiments have shown significant deviations from predictive simulations.	[246–249]
Monte Carlo method	It is statistical method based on the use of random numbers. A drawback is its lack of physicality, as the deterministic mechanical behavior must be mimicked by statistical laws. Usually, Newton’s laws cannot be satisfied with stochastic approaches, and are inherently deterministic. There is no exact framework which could allow the coupling of probabilities and forces.	[250,251]

1. The Discrete Element Method (DEM)

DEM is an increasingly popular numerical technique for computing the behavior of granular materials. This method was originally applied by Cundall in 1979 [241] to problems in rock mechanics. The method is based on the use of an explicit numerical scheme in which interactions between a finite number of shape-invariant particles are monitored contact by contact and the motion of the particles is modeled individually. Two types of DEM approaches are most common: soft-particle and hard particle approaches. They are succinctly compared in Table 13. Because of its numerous assets, the soft-particle DEM method will be developed further and used in this work and referred as ‘DEM’.

Table 13. *Soft-particle and hard-particle approaches of DEM* [252]

‘Soft-particle’ DEM method	Hard-particle DEM method
Particles are allowed to suffer minute deformations which are used to calculate elastic, plastic and frictional forces between particles.	A sequence of collisions is processed, one collision at a time and being instantaneous.
Motion of particles is described by Newton’s laws of motion. A constant time-stepping is performed (time-driven DEM).	The forces between particles are often not explicitly considered.
Capable of handle multiple particle contacts and equilibrium states.	Variable time-step (event driven DEM). Not able to manage static packings of particles.
Extensively used, it represents the best accuracy-effort trade-off for most cases.	Useful in modeling of rapid granular flows.

DEM simulations can provide dynamic information, such as the trajectories of and transient forces acting on individual particles, which is extremely difficult, if not impossible, to obtain by physical experimentation at the current stage of development [252]. To illustrate DEM capabilities, it is noteworthy to mention the work by Bharadwaj et al. [253] who simulated the effect of particle properties such as size, shape, size distribution and friction parameters on the flowability of glass beads in a powder rheometer. They noticed that DEM simulations are well suited for such a study since they isolate the impact of each particle property on the bulk powder behavior. The experiments with millimetric glass beads validated simulation results. The value of DEM is demonstrated by the broad wide of applications reported in the literature going from flow through hoppers [254,255] and conveyors to die filling for tableting [256], fracture of agglomerates and comminution [257].

1.1. Governing equations

A particle in a granular flow can have two types of motion: translational and rotational. In DEM approach, it is generally assumed that, at all times, the resultant forces on a particle can be determined exclusively for its interaction with the contacting particles and vicinal fluid for a coarse particle system (i.e. propagation of disturbance waves from particles and fluid far away are not considered). Newton’s second law can thus be used to describe the motion of individual particles. At any time t , the equations for the translational and rotational motion of a particle i with mass m_i and moment of inertia I_i can be written as:

Translational motion:

$$m_i \frac{d^2 \mathbf{x}_i}{dt^2} = m_i \frac{d\mathbf{v}_i}{dt} = \sum_j \mathbf{F}_{ij}^c + \sum_k \mathbf{F}_{ik}^{ac} + \mathbf{F}_i^f + \mathbf{F}_i^g \quad (7)$$

Rotational motion:

$$I_i \frac{d\omega_i}{dt} = \sum_j \mathbf{M}_{ij}^c \quad (8)$$

where \mathbf{x}_i is the position of the particle i , and \mathbf{v}_i and ω_i are the translational and rotational velocities, respectively, \mathbf{M}_{ij}^c is the torque acting on the particle i by particle j or walls, \mathbf{F}_{ik}^{nc} is the non-contact force acting on particle i by particle k or other sources, \mathbf{F}_i^f is the particle-fluid interaction force on particle i , and \mathbf{F}_i^g is the gravitational force. Figure 30 shows a schematic representation of the 2D interaction between three particles, where particles i and j are in contact, while particle i and k interact through a capillary force.

Once the forces and torques are known, equations (7) and (8) can be solved numerically. The positions, velocities and forces of all particles can be thus determined. The general steps of the DEM implementation are depicted in Figure 31.

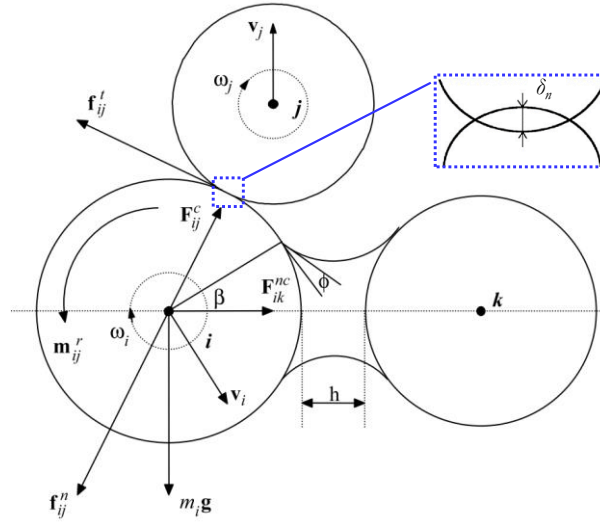


Figure 30. Schematic representation of forces acting on particle i from contacting particle j and non-contacting particle k (capillary interaction). A detail is made on the contact point to show the normal overlap (δ_n) definition (adapted from [252]).

1.2. Interparticle force models

1.2.1. Contact models

The contact between two particles is not at a single point but on a finite area due to the deformation of the particles. In DEM, this is equivalent to the contact of two rigid bodies allowed to overlap slightly (i.e. $<0.5\%$ of the particle diameter). This overlap (δ_n) is not a real phenomenon but rather aims to indirectly represent the deformation of the interacting bodies at the contact point. The distribution of forces over this area can be decomposed into a component in a tangential plane and one normal to the plane, so a contact force has a tangential $\mathbf{f}_{ij}^{c,t}$ and a normal $\mathbf{f}_{ij}^{c,n}$ component:

$$\mathbf{F}_{ij}^c = \begin{cases} \mathbf{f}_{ij}^{c,t} + \mathbf{f}_{ij}^{c,n} & \text{if } \delta_n > 0 \\ 0 & \text{otherwise} \end{cases} \quad (9)$$

The tangential overlap (Figure 30) is defined by the difference between the distance of the particle centers and their radii:

$$\delta_n = \|\mathbf{x}_i - \mathbf{x}_j\| - R_i - R_j \quad (10)$$

where \mathbf{x}_i and \mathbf{x}_j are the position vectors of the center of the particles i and j , and R_i , R_j their respective radii.

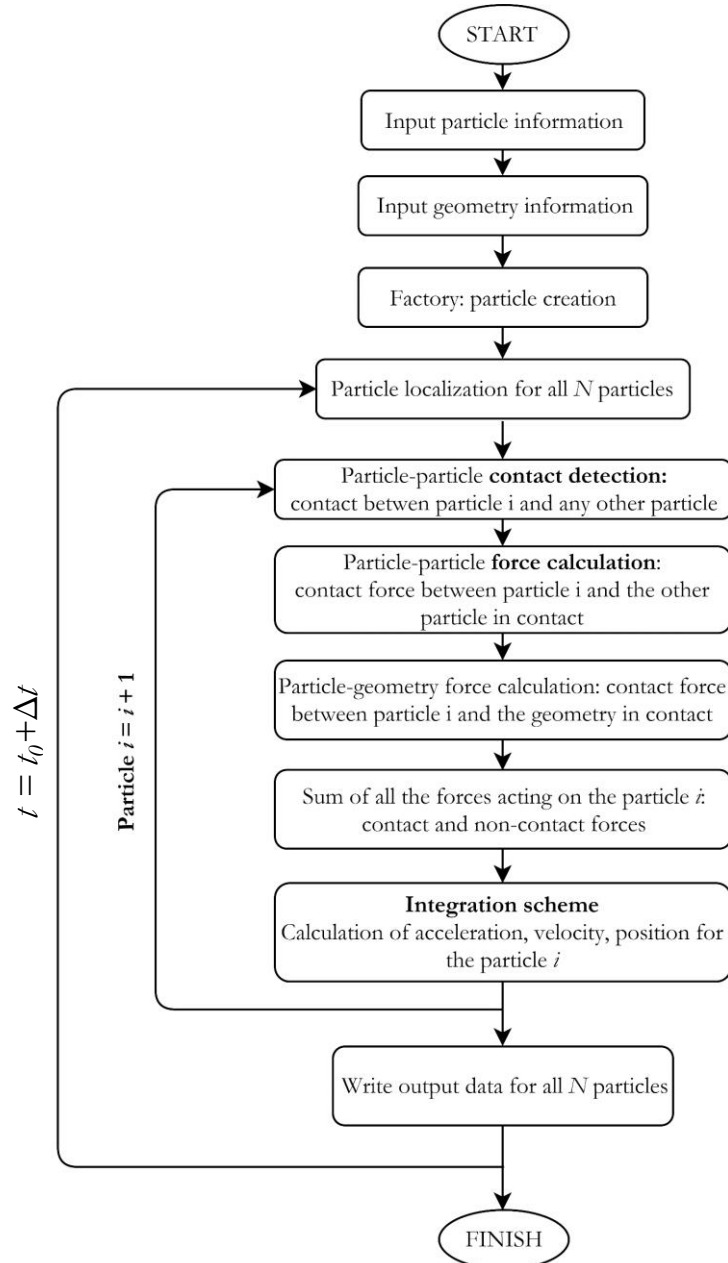


Figure 31. General DEM algorithm.

The normal and tangential components of the contact force are generally calculated according to different procedures, depending on kinematic quantities (positions and velocities of the two grains) or multi-physical parameters. DEM generally adopts simplified force models, often neglecting many geometrical and physical factors that would make the resolution computationally inefficient. In this literature review, a concise description of the force models widely used and available in LIGGGHTS® (commonly used DEM software, used in this work) will be provided. A comprehensive review of the different force models proposed in literature has been carried out by Zhu et al. [252].

1.2.1.1. Hertz-Mindlin contact model

Due to the efficiency and accuracy of its force calculations, the most commonly used contact model is the Hertz-Mindlin non-slip contact model [258,259]. This model offers a compromise between a relatively low computational effort and good agreement with experiments for simulation of static behavior.

A commonly used representation of the Hertz-Mindlin contact model is shown in Figure 32.

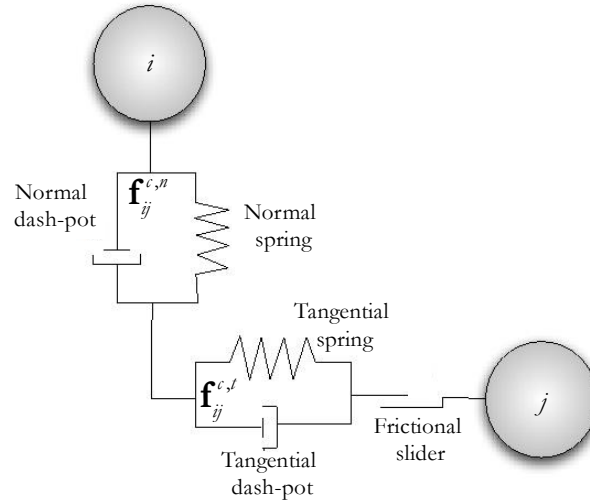


Figure 32. Schematic representation of the Hertz-Mindlin spring dash-pot contact force model.

In Figure 32, particles i and j are in contact. The normal component of the contact force tending to repulse the particles includes an elastic deformation (spring) conservative force ($\mathbf{f}_{ij}^{c,n}|_n$) and a viscous dissipation (damping or dash-pot force) ($\mathbf{f}_{ij}^{c,n}|_n$):

$$\mathbf{f}_{ij}^{c,n} = \mathbf{f}_{ij}^{c,n}|_n + \mathbf{f}_{ij}^{c,n}|_t = -k_n \delta_n - \gamma_n \frac{d\delta_n}{dt} \quad (11)$$

where k_n is the elastic constant for normal contact and γ_n is the viscoelastic damping constant for normal contact. The term $\frac{d\delta_n}{dt}$ corresponds to the relative velocity of the grains in the normal direction \mathbf{n} , which can be expressed as follows:

$$\frac{d\delta_n}{dt} = (\mathbf{v}_i - \mathbf{v}_j) \cdot \mathbf{n} \quad (12)$$

where \mathbf{v}_i and \mathbf{v}_j are the velocity vectors of the center of mass of particles i and j .

The elastic constant for normal spherical contact is defined as [260]:

$$k_n = \frac{4}{3} Y_{eff} \sqrt{R_{eff} \delta_n} \quad (13)$$

The effective radius R_{eff} is calculated from:

$$\frac{1}{R_{eff}} = \frac{1}{R_i} + \frac{1}{R_j} \quad (14)$$

And the effective Young's modulus (Y_{eff}):

$$\frac{1}{Y_{eff}} = \frac{(1-\nu_i^2)}{Y_i} + \frac{(1-\nu_j^2)}{Y_j} \quad (15)$$

where ν is the Poisson's coefficient.

Strictly speaking, it is clear from Eq. (13) that k_n is not a constant term, as it depends on the normal overlap. This makes the Hertz-Mindlin model a non-linear contact model, with a global order for the normal force of $\delta_n^{3/2}$.

The normal viscoelastic damping constant is given by:

$$\gamma_n = \frac{2\sqrt{5/6} \ln(e)}{\sqrt{\ln^2(e) + \pi^2}} \sqrt{2Y_{eff} (R_{eff} \delta_n)^{1/2} m_{eff}} \geq 0 \quad (16)$$

where e is the coefficient of restitution and m_{eff} the effective mass, given by:

$$\frac{1}{m_{eff}} = \frac{1}{m_i} + \frac{1}{m_j} \quad (17)$$

The formulation of Eq. (11) has the disadvantage of applying a generally attractive force during a certain phase of contact: at the very end of unloading (when the two grains are about to separate) the overlap become too small compared to the separation velocity. The repulsive effect therefore becomes negligible compared to the attractive effort that restricts separation. In the absence of cohesion, this situation is not physically realistic. To solve this difficulty, it is possible, for example, to limit the normal contact force to be either \mathbf{f}_{ij}^{cn} for $\mathbf{f}_{ij}^{cn} > 0$, or be replaced by zero if a pre-calculated value of \mathbf{f}_{ij}^{cn} gives an overall attractive force ($\mathbf{f}_{ij}^{cn} < 0$) [261].

The tangential component of the contact force is similarly given by a spring that stores energy from the relative tangential motion, representing the elastic tangential deformation of the particle surface, and a tangential damping force:

$$\mathbf{f}_{ij}^{ct} = -k_t \delta_t - \gamma_t \frac{d\delta_t}{dt} \quad (18)$$

where k_t is the elastic constant for tangential contact, given by:

$$k_t = -8G_{eff} \sqrt{R_{eff} \delta_n} \quad (19)$$

with, G_{eff} the effective Shear modulus:

$$\frac{1}{G_{eff}} = \frac{2(2-\nu_i)(1+\nu_i)}{Y_i} + \frac{2(2-\nu_j)(1+\nu_j)}{Y_j} \quad (20)$$

The tangential damping constant corresponds to:

$$\gamma_t = \frac{2\sqrt{5/6} \ln(e)}{\sqrt{\ln^2(e) + \pi^2}} \sqrt{8G_{eff} (R_{eff} \delta_n)^{1/2} m_{eff}} \geq 0 \quad (21)$$

The tangential displacement cannot be explicitly determined from the particle positions but can be calculated through time integration of relative tangential velocity at the contact point. The tangential contact force can thus be seen as a 'history' effect that accounts for the tangential overlap, δ_t between the particles for the duration of the contact. The relative tangential displacement can therefore be written as:

$$\delta_t = \int_{t_{c,0}}^t v_t(\tau) d\tau \quad (22)$$

where v_t is the tangential relative velocity and $t_{c,0}$ the time when the contact between the particles started.

The magnitude of the tangential force is truncated by the Coulomb frictional limit, where the particles start to slide over each other (frictional slider in Figure 32). The expression of this limit corresponds to:

$$\max(|\mathbf{f}_{ij}^{ct}|) = \mu |\mathbf{f}_{ij}^{cn}| \quad (23)$$

where μ is the sliding friction coefficient.

1.2.1.2. *Non-contact force models: the Johnson-Kendall-Roberts model*

For cohesive solids, cohesive forces are surface interactions that can have various physico-chemical origins (hydrogen bond or van der Waals force, the capillary force and the electrostatic force) that may act concurrently or successively to different extents. Although force models have been proposed for each one of these force contributions [252], it is customary to use a simplified formulation that includes a macroscopic quantity called ‘energy density’. This term represents the energy required to separate two particles in contact [262,263].

The JKR model [264] is a commonly used cohesive model based on the Hertz contact theory. If two particles are in contact, it adds an additional normal force contribution tending to maintain the contact, which writes in its simplified formulation:

$$\mathbf{f}_{ij}^{\text{nc,n}} = CED \cdot \mathcal{A} \quad (24)$$

where CED is the Cohesive Energy Density in J/m^3 and \mathcal{A} is the contact area between particles, calculated as:

$$\mathcal{A} = \frac{\pi}{4} \frac{(d_{ij} - R_i - R_j)(d_{ij} + R_i - R_j)(d_{ij} - R_i + R_j)(d_{ij} + R_i + R_j)}{d_{ij}^2} \quad (25)$$

where d_{ij} is the distance between the center of the particles and R_i , R_j are the radii of the spheres i and j in contact. For a particle (i)-wall (j) contact, the contact area becomes:

$$\mathcal{A} = \pi(R_i^2 - d_{ij}^2) \quad (26)$$

In cohesive systems, the normal contribution triggered by cohesion must be included in the truncation limit of friction (Eq. (23)).

1.3. Numerical resolution and simulation aspects

1.3.1. Integration scheme

There is a variety of methods for the numerical integration of systems of coupled differential equations (e.g. Euler, Leapfrog, Verlet, Gear schemes, etc.). In DEM, the integration of Newton’s equation of motion for granular particle systems (Eqs. (7) and (8)) is numerically difficult due to the short-range interaction with extremely steep gradients.

It has been shown that the actual numerical integration of the equations of motion consumes only small part of the total computational costs [265]. The main part of the computer time is spent on the evaluation of the forces which act on the particles in each time step. Consequently, using a less complicated integration algorithm cannot save much computer time. On the contrary, computer time is wasted by using a less stable numerical integrator since to achieve a comparable accuracy, a smaller time step is needed which increases the number of force evaluations. A stable widely-used integration scheme for DEM is the Velocity-Verlet integration scheme.

1.3.2. Velocity-Verlet Integration scheme

Since velocities of particles are of interest, but not explicitly tracked with the classical Verlet algorithm [266], the Velocity-Verlet integration scheme is more often used. As the accelerations (\mathbf{a}) are position-independent, the algorithm is explicit. Some advantages of the Velocity-Verlet scheme are related to its easy implementation and memory efficiency.

The integration scheme consists, from an initial state $t = 0$, in defining a timestep Δt and calculating the kinematic variables by linearization of the equations of motion. A Taylor expansion is therefore used for both positions and velocities as follows:

$$\mathbf{x}_{i+\Delta t} = \mathbf{x}_i + \mathbf{v}_i \Delta t + 1/2 \mathbf{a}_i (\Delta t)^2 \quad (27)$$

$$\mathbf{v}_{i+\Delta t} = \mathbf{v}_i + 1/2 (\mathbf{a}_i + \mathbf{a}_{i+\Delta t}) \Delta t \quad (28)$$

Integrators of Velocity-Verlet type compute alternately the new positions and velocities in sub-steps. For the second-order Velocity-Verlet method, the sub-steps are:

$$1. \text{ Calculate } \mathbf{v}_{i+1/2\Delta t} = \mathbf{v}_i + 1/2 \mathbf{a}_i \Delta t \quad (29)$$

$$2. \text{ Calculate } \mathbf{x}_{i+\Delta t} = \mathbf{x}_i + \mathbf{v}_{i+1/2\Delta t} \Delta t \quad (30)$$

$$3. \text{ Derive } \mathbf{a}_{i+\Delta t} \text{ from the interaction forces} \quad (31)$$

$$4. \text{ Calculate } \mathbf{v}_{i+\Delta t} = \mathbf{v}_{i+1/2\Delta t} + 1/2 \mathbf{a}_{i+\Delta t} \Delta t \quad (32)$$

1.3.3. Timestep

The timestep (i.e. the duration between two consecutive iterations) must be chosen carefully. Although the explicit integration scheme used in DEM is more computationally efficient than an implicit numerical scheme, it is only conditionally stable, so a small timestep must be used.

Several main aspects have therefore to be considered when selecting the value of the timestep:

- The timestep must be chosen sufficiently small to capture the phenomenon of energy transmission by wave propagation: Within a group of particles, the force transmission between individual particles is supposed to happen essentially through Rayleigh waves that travel through the surface of the bodies. The timestep should therefore be smaller than the time it takes for the wave to transverse the minimum particle size within the group of particles.
- If the calculation time step is too large, the system may not be able to react to all the occurring dynamics: for example, two particles may cross each other if their relative speed is high and the timestep is large.
- The overlap may not exceed a certain limit (typically 0.5 % of the particle diameter), because the overlap represents energy stored in the ‘deformation’ of the particle. Thus, choosing a timestep too large leads to unphysical energy ‘generation’ in the system.
- If the timestep is too small, it unnecessarily consumes time for the calculations.

The selection of an adequate value for the timestep can be made based on criteria from the Rayleigh time and the Hertz contact time [245]. The Rayleigh time (T_R) is the time taken by the wave to propagate through a solid particle. It can be approximated as (in SI units):

$$T_R = \frac{\pi R \left(\frac{\rho}{G} \right)^{0.5}}{0.1631\nu + 0.8766} \quad (33)$$

where R is the radius of the smallest particle in the simulation domain, G the shear modulus and ν is the Poisson’s ratio.

The contact time established by the Hertz’s theory (T_H) depends on the relative particle velocity, the effective mass, the effective radius and the effective Young’s modulus:

$$T_H = 2.87 \left(\frac{\left(m_{eff} \right)^2}{R_{eff} \left(Y_{eff} \right)^2 \mathbf{v}} \right)^{\frac{1}{5}} \quad (34)$$

In practice, it is recommended to use 10 to 30 % of T_R or 5 to 15 % of T_H as an adequate simulation timestep. This ensures that the contact is resolved in an appropriate way without excess overlap energy.

The stability limit for LIGGGHTS® is between ca. 15 % and 25 % of both T_R and T_H , depending on the system.

1.3.4. Contact detection

Contact detection is one of the most important aspects in DEM. The contact search can take up to 90 % of the computation time. It is completely inefficient to check each pair of particles for possible contacts which leads to a computing time of order N^2 where N is the number of particles. Since the forces between particles are of short range, the force computation can be restricted, using a grid-based structure, to pairs of particles which are close neighbors. Therefore, several methods for contact detection and neighborhood algorithms have been proposed in literature [250,267]. This allows us to exclude pairs of particles that are too far away from each other. In general, a pair of spherical particles is included in the neighbor list if:

$$\|\mathbf{x}_i - \mathbf{x}_j\| < R_i + R_j + s \quad (35)$$

where s is the so-called skin parameter that should be optimized during the stages of setup of simulations [268].

1.4. Particle shape in DEM: rolling friction model and multisphere representation

Three-dimensional DEM simulations have often used spherical particles as they have the advantage of computational simplicity. Nevertheless, several authors have shown the importance of particle shape in handling behavior using DEM [255,269,270]. A variety of approaches have been developed to reproduce non-spherical particles in a DEM framework in an efficient way. Shape is an expensive feature to model in DEM, so a first strategy consists in emulating the effect of non-spherical shapes by adding a ‘rolling friction’ contribution to the rotational motion of the spherical particles [271]. Eq. (8) thus becomes:

$$I_i \frac{d\omega_i}{dt} = \sum_j (\mathbf{T}_{ij}^t + \mathbf{T}_{ij}^r) \quad (36)$$

where \mathbf{T}_{ij}^t is the torque generated by the tangential force and causes particle i to rotate, and \mathbf{T}_{ij}^r is the rolling friction torque generated by the asymmetric distribution of normal contact forces that slows down the relative rotation between particles in contact [272]. A variety of contact models are available for calculating the rolling friction torque. For instance, in the EPSD2 (Elasto-plastic spring-dashpot) model [273] the additional torque contribution is given by:

$$\mathbf{T}_{ij}^r = \mathbf{T}_{ij}^{r,k} = -k_r \Delta \boldsymbol{\theta}_{r,ij} \quad (37)$$

where $\mathbf{T}_{ij}^{r,k}$ is a torque component modeled as a mechanical spring, k_r is the rolling stiffness and $\Delta \boldsymbol{\theta}_{r,ij}$ is the incremental relative rotation between two particles. The torque contribution is truncated so:

$$\mathbf{T}_{ij}^{r,k} \leq \mathbf{T}_{ij}^{r,\max} = \mu_r R_{eff} \mathbf{F}_n \quad (38)$$

where μ_r is the rolling friction coefficient, R_{eff} the effective radius and $\mathbf{T}_{ij}^{r,\max}$ being the limiting spring torque which is achieved at a full mobilization rolling angle θ_r^m . In the EPSD2 model, the rolling stiffness k_r is defined as:

$$k_r = k_t R_{eff}^2 \quad (39)$$

where k_t corresponds to the tangential (i.e. shear) stiffness.

Within the aim of simulate more realistic particle shapes, the most commonly used approach is to create simplified representations using spheres connected in a rigid way (multisphere approach) [274]. Using

multisphere representations, it is possible to create clusters with spheres of varying sizes, positions and overlapping degrees to create desired shape and roughness (Figure 33). One motivation for use clusters of spheres is to save computation time compared with using mathematically more complex shapes, due to the reduced number of operations required in the overlap computation; however, this advantage will be lost if many spheres are used. A trade-off between shape representation accuracy and computing efficiency has to be found.

Using simplified representations of the actual shape in DEM is common practice, however the realistic material behavior must be ensured by changing, for example, rolling and sliding friction coefficients. Calibration is therefore required to ensure that the material model represents realistic behavior [275].

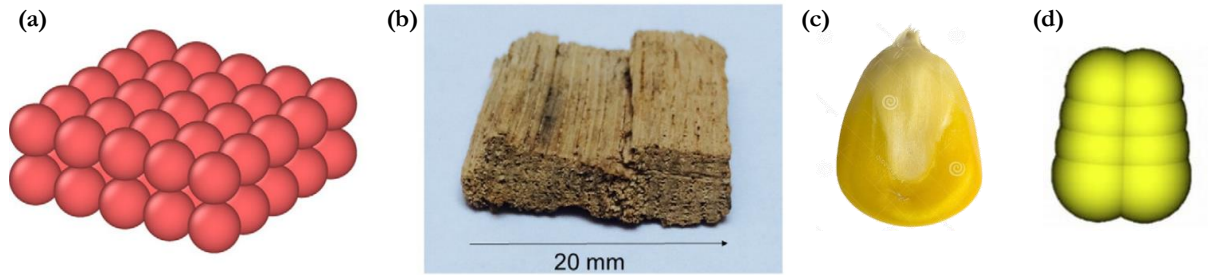


Figure 33. (a) Woodchip approximation using the multisphere approach and (b) actual woodchip particle. (c) Maize grain (d) DEM multisphere model. Adapted from [276,277].

1.4.1. Computational challenges of DEM

With the power of nowadays available computers, DEM can be easily implemented and simulated. Nevertheless, DEM simulations have currently inherent flaws. The main computational challenges for a large-scale implementation of DEM can be summarized in the following points:

- DEM can be a time-consuming method. As a result, the number of particles used in numerical simulations often remains low compared to real systems. Generally, using a standard computer, it seems difficult to simulate more than 10^6 particles over a long period of time whereas, for instance, a liter of fine sand usually contains 10^7 or 10^8 grains. Wide particle size distributions are often avoided in DEM simulations, since the numerical simulation time step is, in addition to material parameters, limited by the size of the smallest particle in the model Eq. (33) [278].
- Reliable results require realistic but computationally-efficient particle shape representations. A trade-off between accuracy of particle shape models and calculation time must be found for irregular-shaped materials.
- It is necessary to determine (or calibrate) the input parameters for simulations. In addition to the requirement for generally large batches of simulations, this can lead to uncertain accuracy of the DEM modeling. Thus, the results DEM can often only be considered qualitative, indicative rather than predictive [279].

Extensive research has been conducted to try to overcome these challenges. Promising approaches that have been successfully applied to a wide range of materials are the scaling of particle size and the implementation of systematic calibration procedures.

1.5. Scaling approaches

Besides the calibration of DEM parameters, the large number of particles present in industrial applications greatly hinders the use of DEM large-scale industrial systems [279]. Particle scaling is one of the existing techniques for reducing the computational cost of DEM simulations.

Different approaches to scale up particle size have been developed and summarized by Roessler and Katterfeld [280]. In *exact scaling* (Figure 34a) the particle size and the domain/geometry are both scaled by the same factor and has no advantage in reducing the number of particles. Another approach (Figure 34b) is to simply ignore particles with a size below a certain value and to assimilate them to particles of bigger size. This approach is called *scalping* [281,282]. *Coarse graining* (Figure 34c) is defined as the increase in particle size while maintaining the domain size, thus reducing the total number of particles in the system [283–285]. Domain or geometry variables such as gravitational acceleration and the velocity of moving boundaries would remain unchanged. Particles are no longer a one-to-one representation of the actual particles and might be referred to as pseudo-particles or representative discrete volume elements.

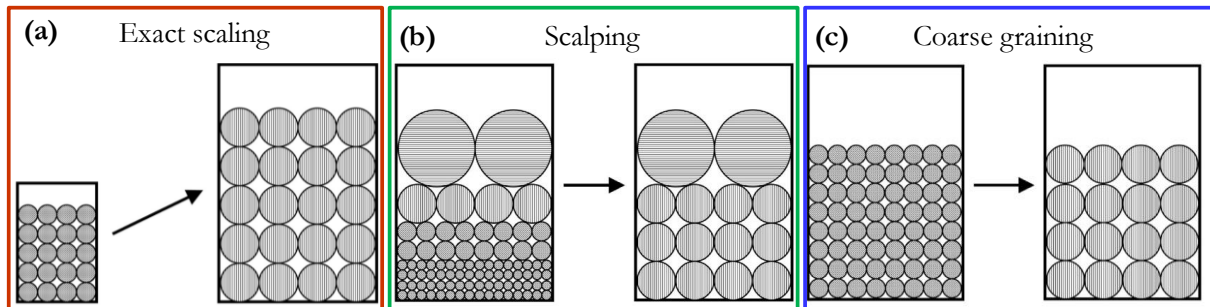


Figure 34. Schematic representation of particle size scaling approaches (adapted from [280]).

1.6. Calibration approaches

In order to obtain reliable results from DEM simulations, the parameter values must be carefully chosen, measured or calibrated. In some cases, parameters calibration may be the more critical component of a DEM simulation project [286].

Two approaches to obtain the input parameters required DEM simulations can be found in literature [287]. In the *Direct measuring approach* parameters such as the coefficient of restitution, the interparticle friction or the particle density are directly measured at particle or contact level. In the *Bulk calibration approach* a simple experiment (or a set of experiments) is conducted and one or more of the material bulk properties is measured. The ‘experiment’ is numerically reproduced and the values of the parameter are adjusted until the predicted bulk behavior matches the measurements. A brief overview of the strengths and weaknesses of each one of the calibration approaches is made in Table 14.

Table 14. Approaches for DEM parameter calibration.

Approach	Advantages	Disadvantages	References
Direct measuring	Parameters are independent of the DEM code used There is a physical interpretation of each parameter.	It is generally difficult to measure particle-scale properties for fine materials. No guarantee for a reliable bulk representation from accurately measured ‘micro-properties’.	[279,288–290]
Bulk calibration	Widely used, mainly because the simplifications usually made to particle size and shape reduce the value of a direct approach. The analysis of bulk responses rather than particle-scale properties better reproduces the granular material behavior.	The physical meaning of the parameters may be lost. The problem is often ill-conditioned: the bulk responses are influenced by more than one parameter, which complicates the obtention of unique solutions.	[279,291–295]

A combination of the two approaches is often used: some parameters are based on values reported in the literature (measured directly in experiments) and other highly influential parameters are adjusted (namely the coefficients of friction) by comparison with experimental bulk responses [296].

1.7. DEM Software

1.7.1. Overview

Different software packages for DEM simulations have been introduced. Some of them, such as EDEM® (version 2018, DEM Solutions Ltd., Edinburgh, UK), ROCKY® (version 4.1, ESSS, Florianópolis, Brazil), and PFCTM (version 6.0, Itasca Consulting Group, Inc., Minneapolis, MN, USA), are commercially distributed, but other ones, like LIGGGHTS® (version LIGGGHTS-PUBLIC 3.3.1, DCS Computing GmbH, Linz, Austria), YADE (The Yade Project, Grenoble, France) or LMGC90 (LMGC, Montpellier University, Montpellier, France) are open-source packages. All these software programs provide several contact models, so it is possible to choose the most appropriate program for simulating different processes or systems. Although some comparative studies have been conducted to evaluate the comparative performances between different codes [297], very little is known about the existence of differences when comparing to each other [277].

The advantage of being a widely used open source code, as well as other valuable features described hereafter guided our decision to use LIGGGHTS® code in this work.

1.7.2. LIGGGHTS®

LIGGGHTS® is an open source Discrete Element Method particle simulation software developed by Sandia National Labs and distributed by DCS Computing GmbH, Linz, Austria [268,298]. LIGGGHTS® stands for LAMMPS Improved General Granular and Granular-heat transfer simulations. LAMMPS is a molecular dynamics software simulator (Large-scale Atomic/Molecular Massively Parallel Simulator) that preceded the creation of LIGGGHTS, an improved version that made the move from Molecular Dynamics to DEM simulations by adding features like contact force formulations involving Hertz/Hooke pair styles, cohesion and rolling friction forces and heat conduction between particles. LIGGGHTS® is currently used by a variety of research institutions world-wide.

Besides approaching the DEM in a reliable and complete way, another goal of LIGGGHTS® is to be used in industrial applications, that is the reason why it also includes the possibility of importing and handling complex CAD geometries, moving meshes to account for moving geometries and other particle insertion options [299].


The LIGGGHTS® code is written in C++ and can be run either in a single processor or in parallel. Several versions of LIGGGHTS® are available, namely a ‘public’ version and a ‘premium’ version. The premium version includes additional features for large-scale industrial applications, available for industrial partner companies.

```
#LIGGGHTS® input script example

atom_style      granular
atom_modify     map array
boundary        m m m
newton          off
communicate     single vel yes
units          si
region          reg block -0.05 0.05 -0.05 0.05 0. 0.15 units box
create_box      1 reg
neighbor        0.002 bin
neigh_modify    delay 0
```

Initialization

- Particle type
- Parallelization settings
- Geometry boundaries
- Neighbor specifications



```
#Material properties required for pair style
fix            m1 all property/global youngsModulus peratomtype 5.e6
fix            m2 all property/global poissonsRatio peratomtype 0.45
fix            m3 all property/global coefficientRestitution peratomtypepair 1 0.95
fix            m4 all property/global coefficientFriction peratomtypepair 1 0.05
pair_style     gran model hertz tangential history
pair_coeff     * *
timestep       0.00001
fix            gravi all gravity 9.81 vector 0.0 0.0 -1.0
fix            zwalls1 all wall/gran model hertz type 1 zplane 0.0
fix            zwalls2 all wall/gran model hertz type 1 zplane 0.15
fix            cylwalls all wall/gran model hertz type 1 zcylinder 0.05 0. 0.
#region of insertion
region         bc cylinder z 0. 0. 0.045 0.00 0.15 units box
#particle distributions
fix            pts1 all particletemplate/sphere 12345787 1 density constant 2500 radius constant 0.25
fix            pddl all particledistribution/discrete 17903 1 pts1 1.0
fix            ins all insert/pack seed 123457 distributiontemplate pddl vel constant 0. 0. -0.5 &
               insert_every once overlapcheck yes all_in yes particles_in_region 1800 region bc
```

Setup

- Material properties
- Geometry settings
- Contact models
- Particle generation

```
#apply nve integration to all particles
fix            integr all nve/sphere
#output settings, include total thermal energy
compute        rke all erotate/sphere
thermo_style   custom step atoms ke c_rke vol
thermo         1000
thermo_modify  lost ignore norm no
compute_modify thermo_temp dynamic yes
dump           dmp all custom 800 post/dump*.newModels id &
               type x y z ix iy iz vx vy vz fx fy fz omegax omegay omegaz radius
```

Detailed settings

- Speed and memory utilization
- Output and saving options

```
#insert particles and run
run            5000
```

Execution

Figure 35. Example of LIGGGHTS® input file with its main sections highlighted.

Some of the features of the public version of LIGGGHTS® are:

- distributed-memory message-passing parallelism (MPI)
- spatial-decomposition of simulation domain for parallelism
- relatively easy to extend
- it runs from an input script
- syntax for defining and using variables and formulas

- syntax for looping over runs and breaking out of loops
- it runs one or multiple simulations simultaneously (in parallel) from one script
- it outputs to the widely used and open source vtk data format
- can be coupled with other codes such as CDFEM® or Open FOAM for coupled CFD-DEM simulations
- import and handling of complex moving geometries using stl walls and vtk meshes
- force and wear analysis on meshes as well as stress-controlled walls
- a variety of particle-particle contact implementations, including models for tangential history, non-sphericity and cohesion
- possibility of implementing heat conduction between particles
- flexible definition of particle distributions for polydispersed systems

Although a graphical user interface (under development) has recently been released, LIGGGHTS® is typically executed by reading commands from a text input script (Figure 35) in a Linux environment one line at a time.

2. The Discrete Element Method applied to biomass systems

To date, no research has been found regarding DEM simulations on millimeter-scale biomass systems. The implementation of DEM for cohesive, elongated and fine systems is far to be complete. So far, discrete element modeling of biomass systems has focused mainly on centimeter-scale studies of wood briquettes or wood chips, with few particles.

Maione et al. [276], for example, developed a model capable to represent the main dynamic phenomena in a rotating pyrolysis reactor for wood chips using a multisphere particle representation (Figure 33). Höhner et al. [300] investigated the effect of particle aspect ratio of wood cylinders (with length between 6 and 30 mm) on the discharge behavior of hoppers. It was shown that the hopper discharge rate decreased with an increase in particle aspect ratio and DEM could correctly predict this behavior. Assessment of the durability and effectiveness of a standard tumbling test has also been investigated for wood pellets through DEM [301]. Heat generated on chute surfaces during handling of biomass pellets has also been investigated by extracting numerical impact/shear density data from DEM simulations [302].

Calibration of DEM parameters for biomass feedstock is complicated because of the elastic, cohesive, fibrous and stringy bulk behavior related to the individual particle characteristics, which makes the experiments poorly reproducible and requires adaptation of existing contact models [235]. One of the first studies on the systematic calibration of cohesive materials has very recently been undertaken by Roessler and Katterfeld [294], who conducted experiments and simulations in wet sand systems. Although rare, research in the field of biomass particle calibration and modeling includes the determination of physical properties of non-cohesive briquettes to be used in DEM models by Ramirez-Gomez et al. [303] and the study through DEM of feeding systems for wood-chips by Rackl et al. [275].

Knowledge gap

This literature review indicates that there is currently insufficient knowledge on the following issues:

- Overall, while much of the literature has focused on the chemical and mechanical changes of biomass during torrefaction, few studies have addressed the issue of its effects on biomass flowability. No quantitative studies on biomass powders have thus been carried out relative to the coupled effect of torrefaction and grinding on both the particle characteristics and the subsequent flow behavior. Even though some researchers have undertaken the study of the flowability of biomass powders, most of the available literature deals only with raw materials. There is an explicit need for more research to improve the understanding on behavior of torrefied biomass.
- At a more fundamental level, further research is needed on the adequacy of different size and shape descriptors for biomass particles, that allow correlations with flow behavior to be established. This is particularly critical for biomass powders where highly polydispersed populations of elongated particles can be obtained after grinding. Computer modeling also requires the definition of simplified material models that should be based on reliable size and shape descriptors.
- Although research on the flow properties of raw biomass using shear test devices has been conducted, the potential of the assessment of dynamic non-consolidated flow behavior using rotating drum setups have not yet been explored for biomass. This is mainly due to the lack of a well-established and reliable framework for the characterization of cohesive materials using avalanching behavior in rotating drums. Some correlations between the flow properties obtained from rotating drum experiments and the behavior in handling industrial systems have been proposed, but additional work is still needed on this subject. The possibility of extracting parameters useful for equipment design, as is the case for shear experiments, also deserves in-depth research.
- Far too little attention has been paid to the combination of experimental and numerical approaches to study biomass powder flow. Until recently, most research using the Discrete Element Method has focused on the study of particle-equipment interactions for wood briquettes, pellets or woodchips. Challenges need to be addressed in the development of DEM material models adapted to biomass materials whose particles are far from the typically-modeled spherical, coarse and non-cohesive systems. The establishment of such models, which must remain computationally efficient, may include new methods for particle shape representation, scaling approaches as well as novel contact force models. Finally, further research is needed on bulk setups for calibration of DEM parameters that are suitable for cohesive materials.

CHAPTER II

Experimental facilities

1. Preamble

In this section, we present the experimental facilities that are common to most of this research. First, the design and main characteristics of the torrefaction unit are introduced. Then, the grinding devices are presented along with a brief study on the energy consumption for grinding and the effects of torrefaction on it. Finally, the system for characterization of particle size and shape is described, as well as the definition of the main size and shape descriptors used throughout this work. Two investigations, one of the intra-particle homogeneity of the heat treatment and another on the energy consumption during grinding; which are presented in Appendices I and II complete this chapter.

2. Torrefaction unit description

The torrefaction reactor consists of a batch temperature-controlled oven supplied with nitrogen. The inert nature of the furnace atmosphere is monitored using an oxygen analyzer (Figure 36).

2.1. The furnace

The torrefaction furnace is a *Memmert UFP 400* oven with a volume of 53 L. Heating elements (1.4 kW), distributed evenly over the base, ceiling and side walls of the box, are used to heat and maintain the chamber at a set temperature of up to 300 °C. The convection in the oven atmosphere is ensured by a vertical fan located on the rear wall of the oven (Figure 36). The oven is equipped with two temperature sensors indicating the temperature of the chamber. The side and rear walls are equipped with wall passages allowing the instrumentation of the wood samples (measurement of pressure and temperature within the samples) and the analysis of the chamber atmosphere (temperature and oxygen level). The tightness of the oven is ensured by using a heat-resistant silicone sealant to close the gaps between the various sheets of the box and Teflon parts to ensure a tight passage of the measuring instruments.

2.2. Oxygen content control

The nitrogen inlet (99.5 % purity, delivered by a *Domnick Hunter LC/MS 15* generator [304]) is located below the oven. The gas stream is heated in the preconditioning chamber before entering the oven through the slots in the vertical walls. A needle screw valve mounted on a flow meter is positioned upstream of the oven to control the nitrogen flow rate (up to 5 L·min⁻¹ at atmospheric pressure) (Figure 36). The oxygen level of the enclosure is controlled by an *Arelco ZOA 100 MDC* analyzer [305] using a zirconium oxide detector. The gases from the torrefaction chamber exit through one of the rear wall passages and are led through a copper tube to the oxygen analyzer sensor. The control of the incoming nitrogen flow rate and the ‘instantaneous’ oxygen content in the oven make it possible to adjust the nitrogen supply according to needs.

2.3. Cooling system

The double wall of the oven provides good thermal insulation. Rapid cooling allows the thermo-activated reactions in the sample to be inhibited once the torrefaction time is over. It was therefore necessary to develop a device allowing fast cooling while guaranteeing the inert nature of the atmosphere. Cooling is thus ensured by an additional supply of nitrogen at room temperature through the double wall of the oven bottom. This results in a cooling of ca. 2 °C·min⁻¹.

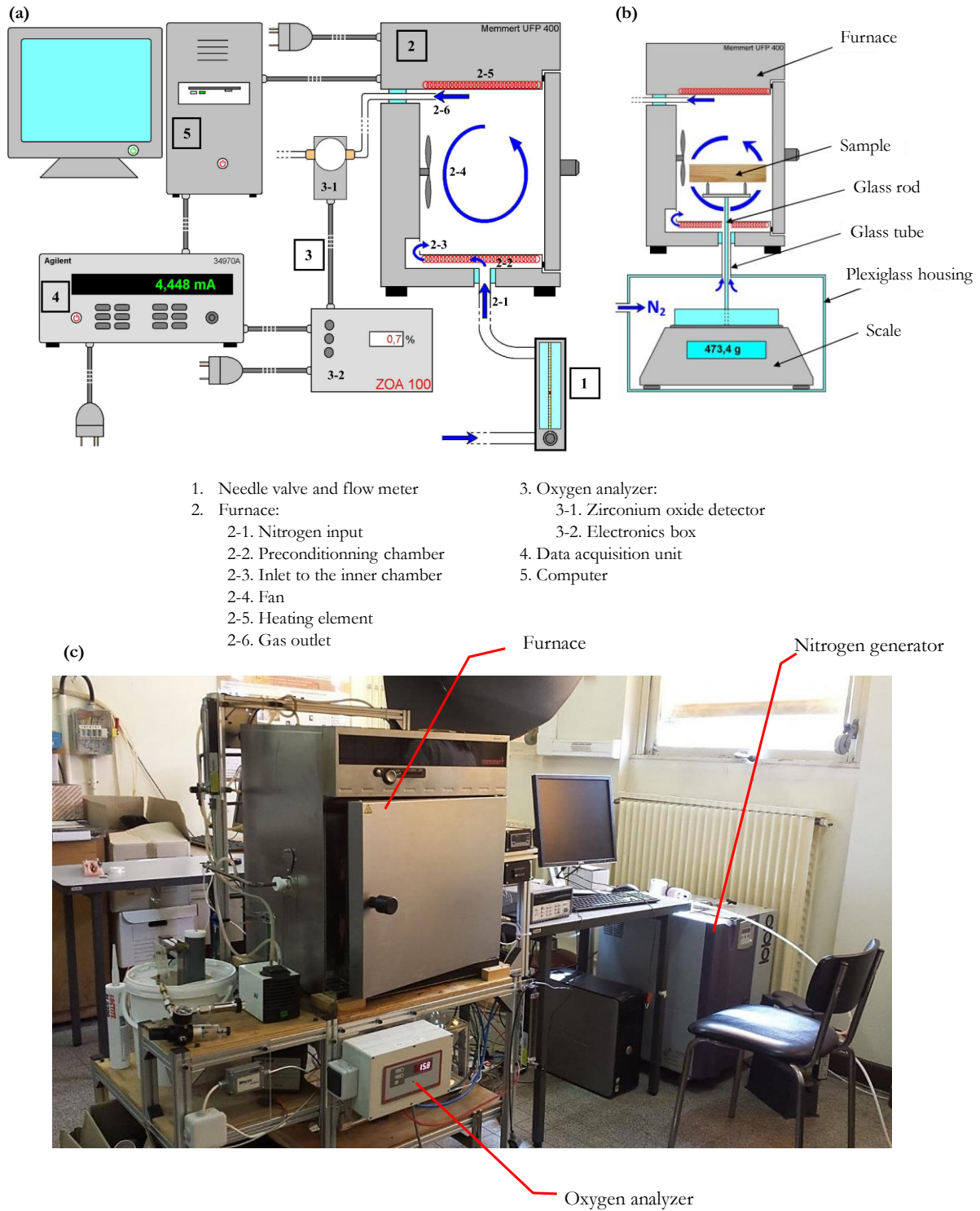


Figure 36. Schematic representation of the torrefaction unit (adapted from [306]) (a) General view of the device. (b) Detail on the mass tracking system (c) Picture of the device.

1.1. Mass loss monitoring

With the designed device, it is possible to continuously track the evolution of the sample mass during torrefaction. This is made using an *Ohaus Explorer Pro* remote scale with a maximum capacity of 6.100 kg and an accuracy of 0.01 g, placed underneath the furnace (Figure 36b). In the chamber, the sample to be torrefied is placed on a tripod support connected via a rigid rod to the balance tray. To ensure the tightness

of the system, the scale is enclosed in a hermetically sealed plexiglass box. This box and the oven are connected by a tube through which the rod of the weighing device passes.

The balance must be maintained at a temperature below 40 °C. To prevent the convection of hot gases from the oven to the balance, the nitrogen stream is supplied to the furnace via the Plexiglas box. The nitrogen then passes through the tube and into the preconditioning chamber of the oven. Thus, at the tube level, the gas flow is always upwards. In addition, the use of glass elements (tube and rod) limits the effect of heat diffusion from the oven to the box along these two elements. To avoid weight disruptions, the nitrogen flow (up to the rod) is automatically interrupted by means of a solenoid valve before each mass measurement. Similarly, the fan is stopped because, in operation, it causes oscillations of the sample, which alters the accuracy of the measurement.

1.2. Temperature profiles

The torrefaction process consists of a 24-hour drying phase at 110 °C followed by a 1-hour treatment phase at the chosen temperature (Figure 37). The relatively fast heating ($10\text{ °C}\cdot\text{min}^{-1}$) and cooling rates limit the duration of the transient regime.

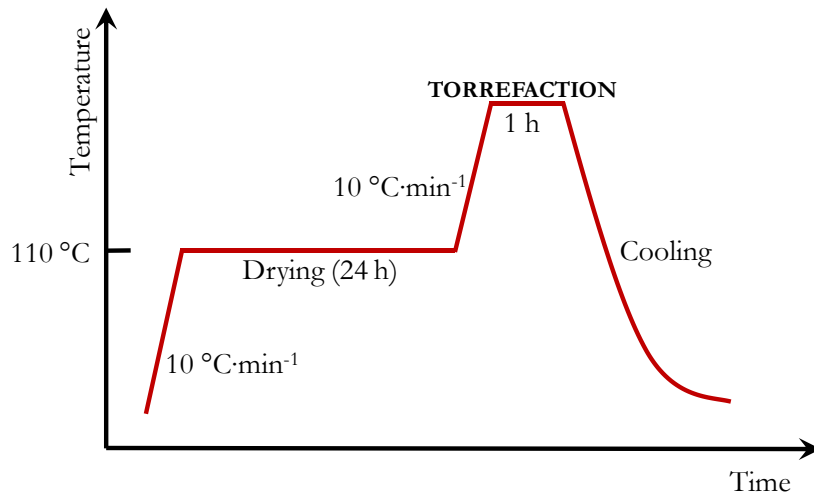


Figure 37. Typical temperature profile during a torrefaction test.

Indeed, as stated by Bergman et al. [90], difficulties in interpreting the torrefaction process may arise from the definition of the torrefaction time. Misunderstanding about the torrefaction time automatically leads to inaccuracies in relating product quality to torrefaction operating conditions. To overcome this problem, in this work, the ‘torrefaction duration’ or ‘torrefaction time’ refers to the duration of the plateau at the treatment temperature (between 200 and 300 °C), independently of the heating and cooling durations. Torrefaction reactions are relatively slow [90], so the heating time between 200 °C (i.e. the temperature at which decomposition reactions are initiated) and the torrefaction temperature is not considered in the torrefaction duration.

2. Influence of particle thickness on the heat treatment homogeneity of poplar wood

During the initial stages of this research, we investigated the effects of the size of wood chips (width) on the torrefaction homogeneity within the particles. The results are presented as a separate article in Appendix I [307]. This study revealed that (i) there are exothermic degradation reactions activated at the core of the samples whose extent depends on the torrefaction intensity and the sample thickness; these

reactions can trigger intra-particle heterogeneity of treatment (ii) the mass loss can also depend on of the sample thickness (ii) there is no significant detected difference in elemental chemical composition along the thickness (in the range of thicknesses tested). This study determined the choice of the sample thickness to be torrefied for the studies in section 3 of chapter III as well as in Chapters IV and V.

3. Grinding units

Several grinding technologies were used throughout this work. First, in the preliminary stages of the study, a batch *IKA M20* cutting mill was used (2nd section of Chapter III). Subsequently, within the purpose of moving closer to an industrial approach in which grinding operations are carried out continuously rather than in batches, a continuous cutting mill was employed (*Retsch SM300*) (Section 3 of Chapter III and Chapters IV and V). This technology also made it possible to obtain powders exhibiting an evenly distributed PSD and to control the output particle size roughly using an output sieve. Finally, a planetary ball mill was employed in a complementary study as a means of obtaining very fine powders of well-controlled granulometry (Section 3 of Chapter III).

3.1. *IKA M20* cutting mill

This device is suitable for dry grinding up to 250 ml (i.e. batch grinding) of hard or brittle materials at a fixed rotational speed of 20 000 rpm. A *M21* stainless steel cutter was used (Figure 38). An automatic system that controlled the grinding and resting cycles was implemented to guarantee the repeatability of the grinding procedure. A circulation of cold water inside the grinder jacket hindered sample heating.



Figure 38. *IKA M20* cutting mill [308].

Table 15. *IKA M20* technical data [308].

Size reduction principle	cutting, impact
Process type	batch
Motor rating input	450 W
Motor rating output	225 W
Circumferential speed max.	72
Feed grain size max.	7 mm
Type of rotors	6-disc rotor
Material cutter	stainless steel 1.4034
Material milling chamber	stainless steel 1.4301
Power-ON time	7 min
W x H x D closed	170 × 350 × 170 mm
Net weight	6.6 kg
Permissible ambient temperature	5 – 40 °C
Permissible relative humidity	80 %
Frequency	50/60 Hz
Power input	550 W

3.2. Retsch SM300 cutting mill

A Retsch SM300 cutting mill (Figure 39) was used to continuously grind raw and torrefied wood chips. The main characteristics of the mill are listed in Table 16.

The general experimental procedure is as follows. The biomass is first introduced through the hopper (sample inlet) and then passes through the chamber where it will be intercepted by the rotor and crushed between it, equipped with knives, and the counter-knives (Figure 39b). Once the biomass has been sufficiently ground (particle size < sieve opening), it passes through a sieve with variable mesh openings (between 1 mm and 10 mm). The outflow particle size can therefore be controlled by changing the outlet sieve. The powder can either be collected directly by gravity in a container or aspirated by a cyclone connected to the outlet.

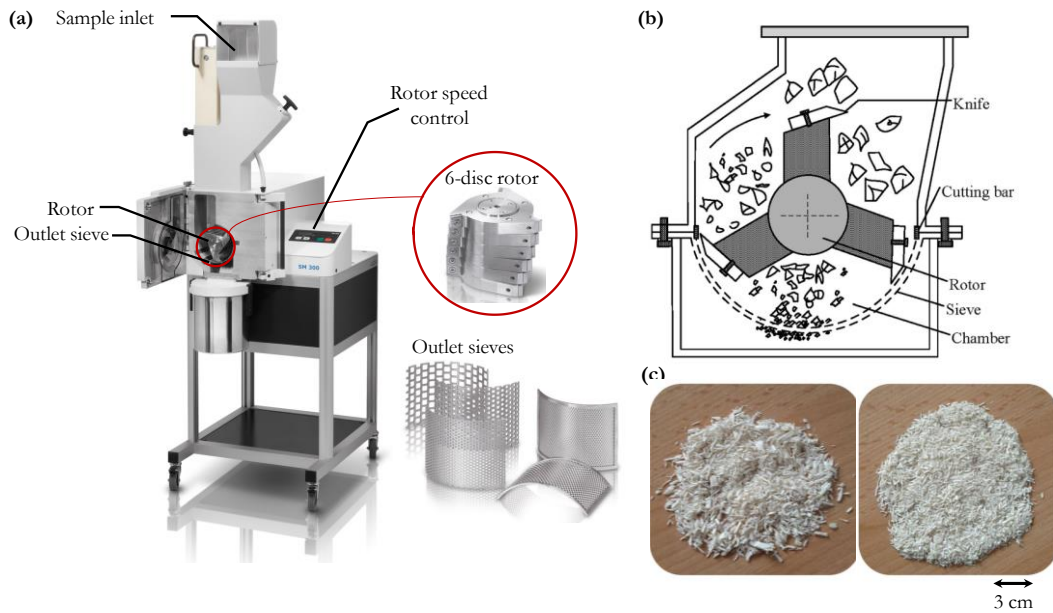


Figure 39. Retsch SM300 cutting mill. (a) Experimental device [309]. (b) Illustration of the grinding chamber (Adapted from [310]). (c) Poplar milled using a 4 mm hole sieve (left) and a 1 mm hole sieve (right).

Table 16. Mean features of the SM300 cutting mill [309].

Size reduction principle	shearing, cutting
Process type	continuous
Material feed size*	< 60 x 80 mm
Final fineness*	0.25 - 20 mm
Speed at 50 Hz (60 Hz)	100 - 3000 min ⁻¹
Rotor peripheral speed	4.7 - 20.3 m/s
Rotor diameter	129.5 mm
Type of rotors	6-disc rotor
Types of hoppers	universal, long stock
Material of grinding tools	tungsten carbide
Sieve sizes	trapezoid holes 1.00 mm
Drive	3-phase asynchronous motor with frequency converter
Drive power	3 kW with flywheel mass ~ 28.5 kg
Power connection	1-phase
Engine brake	yes
Protection code	IP 20
W x H x D closed	576 (1080 opened) x 1677 x 750 mm (with base frame and universal hopper)
Net weight	~ 160 kg
Standards	CE

*depending on feed material and instrument configuration/settings

3.3. Planetary ball mill

A *PM100 Retsch* planetary ball mill can be used secondarily (after grinding with the *SM300* mill) for finer grinding. Planetary ball mills are indeed often used when the highest degree of fineness is required [311]. In this device (Figure 40), the grinding jar is arranged eccentrically on the ‘solar wheel’ of the planetary ball mill. The direction of movement of the solar wheel is opposite to that of the grinding jars in the ratio 1 : -2. The difference in speeds between the balls and the grinding jar produces an interaction between frictional and impact forces, which releases high dynamic energies. The interplay between these forces produces the high degree of size reduction of the planetary ball mill. The main characteristics of the device used in this work are listed in Table 17.



Figure 40. Retsch PM100 planetary ball mill. Adapted from [311].

Table 17. Main features of the PM100 ball mill [311].

Size reduction principle	impact, friction
Material feed size*	< 10 mm
Process type	batch
Final fineness*	< 1 μm , for colloidal grinding < 0.1 μm
Batch size / feed quantity*	max. 1 x 220 ml, max. 2 x 20 ml with stacked grinding jars
No. of grinding stations	1
Speed ratio	1 : -2
Sun wheel speed	100 - 650 min^{-1}
Effective sun wheel diameter	141 mm
G-force	33.3 g
Material of grinding tools	stainless steel, tungsten carbide
Grinding jar volume	250 ml
Setting of grinding time	digital, 00:00:01 to 99:59:59
Interval operation	yes, with direction reversal
Interval time	00:00:01 to 99:59:59
Pause time	00:00:01 to 99:59:59
Measurement of input energy possible	yes
Interface	RS 232 / RS 485
Drive	3-phase asynchronous motor with frequency converter
Drive power	750 W
Electrical supply data	different voltages
Power connection	1-phase
Protection code	IP 30
Power consumption	~ 1250 W (VA)
W x H x D closed	640 x 480 (780) x 420 mm
Net weight	~ 86 kg
Standards	CE

*depending on feed material and instrument configuration/settings

3.4. Measurements of energy consumption required for grinding

In an attempt for illustrating the interest of torrefaction in reducing grinding energy consumption, measurements of the grinding energy of poplar chips were conducted in both the cutting *SM300* and the ball mill. The results of these investigations are presented in Appendix II.

4. Particle size and shape characterization

Particle size and shape highly influence the flow behavior of granular materials, so that their characterization is essential for the purposes of this work. A range of methods and equipment can be used for determination of particle size distributions. Mechanical sieving is the most traditional technique, but other methods based on image analysis or laser diffraction are also available. Throughout the entirety of this research particle size and shape characterization was performed using a *Sympatec QICPIC* unit.

The *QICPIC* imaging system was developed by *Sympatec GmbH* [312] for use on particles sized between 1 μm and 30 mm. This device is based in a dynamic image analysis of the powder. Image analysis uses a digital camera with special optics that captures the particles within the frame. Physical information about particle properties is transmitted to a computer which, using an evaluation software, determines the size and shape descriptors for each particle in the image. An overview of the system is given in Figure 41.

Initially, using the gravity disperser (*GRADIS*), the sample is placed in a hopper. At the start of the test, the hopper is raised by a user-defined height and a controlled vibration of the feeding unit generates a relatively steady flow of particles and adds kinetic energy to the particle before they fall into the vertical shaft. As illustrated in Figure 41b, the particles pass between a light source and a pair of imaging lenses configured to minimize focusing problems. The light source exposure time is less than 1 ns. The camera records a sequence of binary frames of the particles. The camera detector operates at up to 450 frames per second, and therefore a statistically representative number of particles can be analyzed in a short span of time.

As the particles fall through the shaft, particle-to-wall collisions and particle-to-particle collisions create a smooth dispersion with minimal overlap in the images generated. A vacuum-extraction unit placed at the bottom of the system generates a downward flow of air through the shaft (Figure 41c). An outlet slit placed at the end of the shaft aligns the particle flow for imaging beneath its opening [313]. The combination of vibration, free movement, collisions, and use of a vacuum minimizes the tendency for preferential alignment of the particles and makes it possible to assume a random orientation of the particles.

Though dynamic image analysis remains a 2D measurement, the image acquisition system theoretically overcomes the restriction of conventional optical analysis where the plane of the particle image is orthogonal to the shortest axis of the particle and therefore a more realistic measurement of real 3D shapes can be obtained. Statistically representative analyses can therefore be carried out quickly. However, repetitions of the measurements were performed to ensure the repeatability of the measurements.

For materials with particle size under 100 μm a wet dispersion system (*LIXELL* [314]) is recommended. In such a system, a solution containing the powdered material is fed into a cuvette using a pump (Figure 41d).

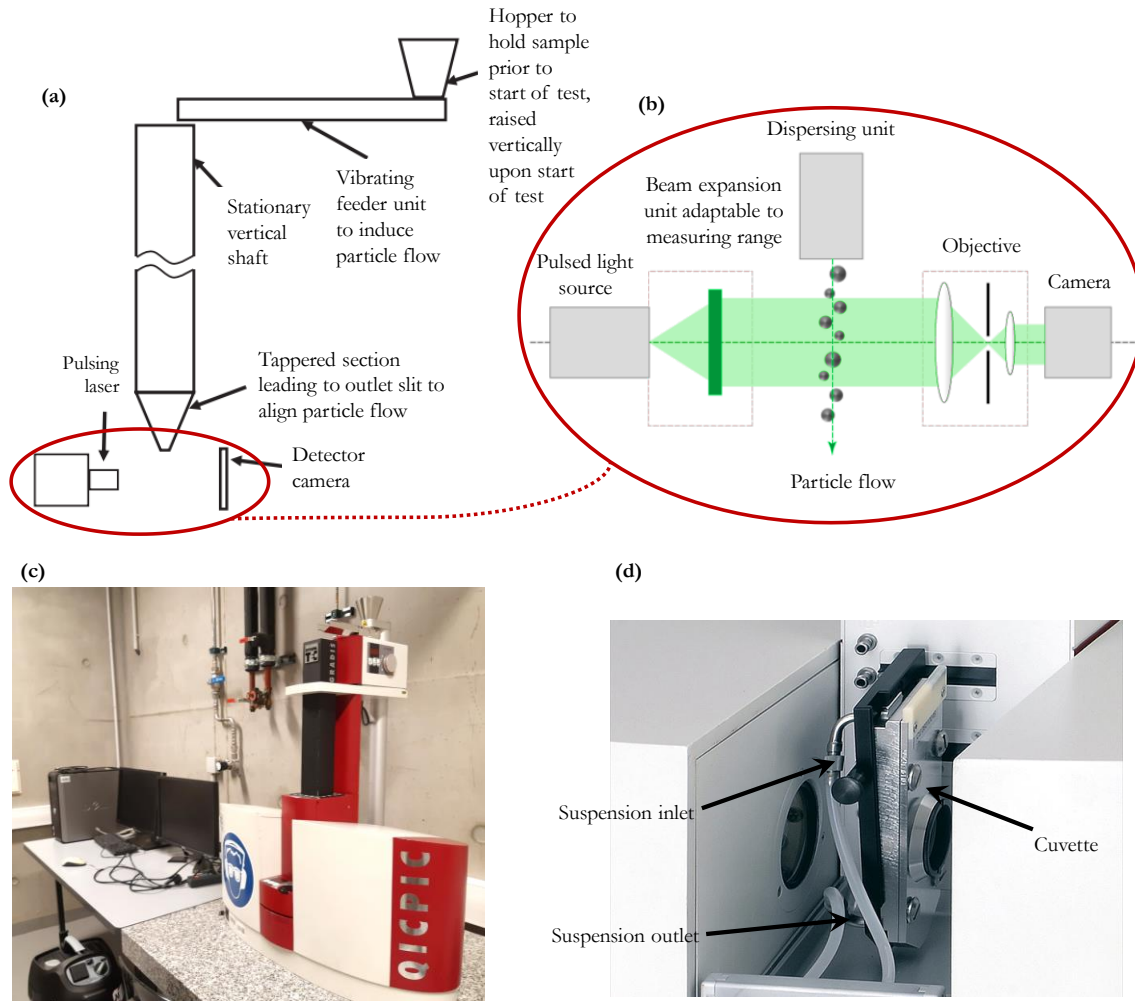


Figure 41. QICPIC apparatus. (a) General overview (Adapted from [313]). (b) Detail on the image acquisition system (Adapted from [315]). (c) Image of the actual device used in this work (dry dispersion unit). (d). View into the LIXELL wet dispersion system (Adapted from [314]).

4.1. Size and shape descriptors

Several particle size measures are directly available within the QICPIC system. Feret diameters are one of the most used descriptors of particle size. They correspond to a group of diameters derived from the distance of two tangents to the contour of the particle in a well-defined orientation. The measurement is therefore equivalent to a slide gauge method. In practice, the Minimum Feret Diameter (d_{Fmin}) and Maximum Feret Diameter (d_{Fmax}) and the Mean Feret Diameter (d_{Fmean}) are used. The minimum Feret diameter is often used as the diameter equivalent to a sieve analysis [313,316,317].

The d_{Fmax} and d_{Fmin} correspond, respectively, to the maximum or minimum Feret diameter after consideration of all possible orientations (0° to 180°). The Feret diameters for a sufficient number of angles are calculated, and their maximum or minimum is selected (Figure 42a). The d_{Fmean} is the mean value of the Feret diameters over all orientations according to the principle described before [317]. Feret diameters vary much more with irregular-shaped particles than with regular shapes, and consequently the maximum and minimum can be considerably different. As an example, the particle size distributions shown in Figure 42b correspond to the same sample of milled raw biomass. The elongated shape of the particles makes the distributions based on d_{Fmin} and d_{Fmax} significantly different. Throughout this work, special precautions were taken to explicitly mention the particle size descriptors used to draw distributions.

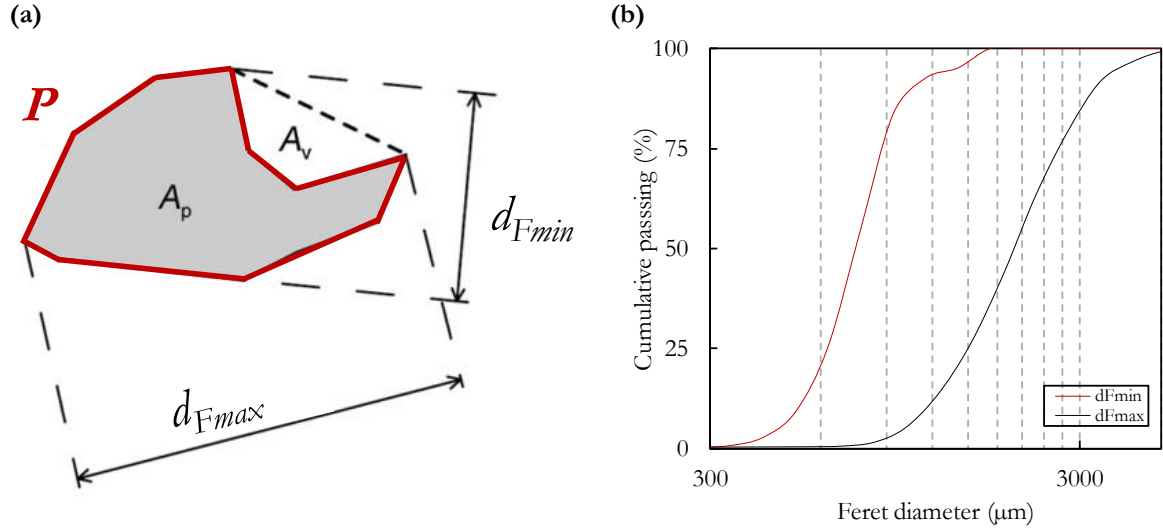


Figure 42. Particle size and shape descriptors. (a). Feret diameters and particle characteristics. (b) PSD of a milled biomass sample using d_{Fmax} and d_{Fmin} .

The in-built shape measurement used in the *QICPIC* system are the aspect ratio (a), the circularity (ψ) and the convexity (Cx).

The aspect ratio ($0 \leq a \leq 1$) gives an indication for the elongation of the particle and is defined as:

$$a = \frac{d_{Fmin}}{d_{Fmax}} \quad (40)$$

The circularity is the ratio of the perimeter of the equivalent circle (i.e. that has the same area as the projected area of the particle A_p) to the real perimeter, P (Figure 42a). The result is a value between 0 and 1:

$$\psi = \frac{2(\pi A_p)^{0.5}}{P} \quad (41)$$

The smaller the value, the more irregular is the shape of the particle. This results from the fact that an irregular shape causes an increase of the perimeter. This ratio is always based on the perimeter of the equivalent circle because this is the smallest possible perimeter with a given projection area.

The convexity is an important shape parameter describing the compactness of a particle. In Figure 42a, the convexity is the ratio of the projection area itself (A_p) and the area of the convex hull ($A_p + A_v$):

$$Cx = \frac{A_p}{A_p + A_v} \quad (42)$$

The maximum theoretical convexity is 1, if there are no concave regions [317].

CHAPTER III

Flowability characterization of powdered biomass under consolidation: effects of torrefaction intensity

1. Preamble

As stated in the literature review, despite the frequent occurrence of handling problems, there is a lack of knowledge on the flow properties of milled biomass. The effects of pretreatment processes such as torrefaction on the energy properties of the treated biomass are relatively well documented, but its impact on the flow behavior of the powdered material has not yet been studied.

The purpose of this chapter is to experimentally investigate the flow behavior of raw and torrefied milled biomass using a shear test procedure. The powders are therefore in a consolidated state, and the properties obtained are intended to be directly used to design storage units in which this type of conditioning is encountered. Understanding the effect of torrefaction intensity on the flow properties measured requires the assessment of the relations between torrefaction and the particle characteristics of the powders obtained after grinding.

A first study on this subject was carried out and published as part of the Proceedings of *Powders and Grains 2017* – 8th International Conference on Micromechanics on Granular Media [318]. This study, which focused on a single softwood species (spruce) was completed by considering a hardwood species (poplar), along with a more complete characterization of the powders, both quantitatively (particle size and shape measurements for fine powders below 100 μm) and qualitatively (Scanning electronic microscope images). These results have led to the publication of a scientific article and are the subject of the second part of this chapter.

The main characteristics of the selected wood species are provided in the materials and methods section. The different stages in the preparation of the biomass powder are also detailed. Torrefaction is carried out using the experimental device described in Chapter II. The torrefaction conditions are chosen in order to obtain a range of mass loss values. The same knife-grinding procedure is then applied to all the torrefied chips. Particle size and shape analysis and the flowability tests are at the heart of the second part of this chapter, from which the main conclusions are drawn.

We observed a gradual shift in the distributions of particle size and shape towards finer and rounder particles as torrefaction intensity increased. Simultaneously, a significant improvement in flowability, as measured by a ring shear tester, with the intensity of torrefaction has also been clearly observed. Powders shifted from a cohesive nature for raw samples to an almost free-flow behavior for the most intensively treated samples. Through the results presented in this chapter, we show that the concomitant changes in particle size, distribution width and flowability parameters are not consistent with the general trends reported in literature for granular materials, smaller particles being expected to have lower flowability. Here, the increase in flowability is mainly due to the presence of rounder particles of treated biomass compared to the long, irregular and needle-shaped particles obtained for native biomass. From these results, the loss of resilience of the woody materials triggered by torrefaction and its subsequent effects on particle properties and bulk behavior is highlighted. Various expressions between the torrefaction operating conditions (as synthesized by the mass loss) and particle properties and flowability are given. In particular, we propose a unique linear expression between torrefaction intensity and the flowability for both species studied here. These expressions are intended as a valuable tool to optimize the BtL upstream processing chain and to quantitatively evaluate the interest of torrefaction to limit handling problems.

A complementary investigation is presented in the last part of this chapter (section 3). Finer powder samples (which are more suitable for measurements in a 30 ml-cell Schulze ring shear tester) are used. This was made possible by using a ball mill after a cutting mill. The study of the impact of the shape and size distributions independently of torrefaction (i.e. a study for a given torrefaction intensity) is described. This last (unpublished) part provides further evidence to the conclusions drawn previously regarding the effects of torrefaction on powdered biomass flow. First, the loss of mechanical resilience of biomass due to torrefaction led to smaller and rounder particles as well as wider distributions when the torrefaction intensity (as measured by the mass loss) is increased. These particle-scale changes are expressed at the bulk scale by an improvement in the flow behavior that gradually shifts from a rather cohesive to a free-flowing nature. Secondly, the analysis of the particle size and shape changes triggered not by different torrefaction intensities, but rather by different grinding intensities (grinding times) showed that long grinding times led to rounder, more uniform and smaller particles. Consistently, this resulted in an improved flowability - despite the decrease in particle size - with the increase of the grinding time.

2. Effect of torrefaction intensity on the flow properties of lignocellulosic biomass powders

John Pachón-Morales ^a, Julien Colin ^a, Florian Pierre ^a, François Puel ^a and Patrick Perré ^a

^aLGPM, Laboratoire de Génie des Procédés et Matériaux, CentraleSupélec, Université Paris-Saclay, 3 rue Joliot Curie, 91192 Gif-sur-Yvette, France

Biomass and Bioenergy 120 (2019) 301- 312

Abstract

Flowability characterization of milled lignocellulosic biomass is essential for developing viable conveying, storing and handling solutions for gasification processes. This study investigated the effect of torrefaction on particles size and shape obtained after grinding and on flow properties of pulverized wood. Spruce and poplar samples with six torrefaction intensities were knife-milled to obtain biomass powders. Particles size and shape distribution were assessed using a morphological particle size analyzer and flowability parameters were determined with a ring shear tester. A more intense treatment produces finer, rounder and more regular particles. Simultaneously, a gradual shifting was observed from a cohesive behavior for native biomass to a nearly free flowing behavior for the most intensively treated samples. The trends in flowability cannot be explained by the size reduction nor the increase of distribution width. Instead, the explanation lies in the reduction of shape factor and the sharpness of particle surfaces for treated samples. However, all observations are consistent with the loss of resilience of treated wood. From our results, it is clear that torrefaction, in addition to its interest on reduction of energy consumption of grinding, should also be considered as a pretreatment step allowing to modify the flow behavior of biomass powders.

Keywords: BtL, torrefaction, particles size and shape, lignocellulosic biomass, flowability

2.1. Introduction

Effective use of biomass gains worldwide attention as a feedstock for production of biofuels likely to reduce greenhouse gas emissions and dependence from petroleum-based energy resources. After the first generation of biofuels, that consumes edible products, a second generation using the lignocellulosic part of plants – such as wood – started to be developed at the industrial scale for lignocellulosic ethanol, but still needs development to produce biomass-to-liquid (BtL) fuels. One thermo-chemical BtL route includes a gasification process followed by a Fischer-Tropsch synthesis [68]. This thermochemical process requires a supply of ground biomass in the form of powder for three main reasons: i) to ease the conveying of the raw material along the processing chain, ii) to optimize its injection into the gasifier and iii) to increase the chemical reactivity of the biomass [119]. Grinding is then essential to obtain biomass powders meeting optimal conditions for gasification. However, due to its fibrous and resilient structure, grinding of native lignocellulosic biomass is an energy-intensive process. Therefore, a pretreatment step, such as torrefaction, is needed to improve the process.

Torrefaction is a thermochemical treatment operating at temperatures in the range 200 to 300 °C under atmospheric pressure and in absence of oxygen. The process is traditionally characterized by low heating rates (<50 °C.min⁻¹) and by a relatively long reactor residence time (typically higher than 30 minutes) [111]. The resulting product is intermediate between wood and charcoal and exhibits several advantages when compared to the original material such as an increased energy density [91], a decreased hygroscopicity, a dimensional stabilization [91], an increased resistance to biological decay [319], a loss of mechanical resilience [93], etc. Several studies have shown the efficiency of heat treatment on easing biomass grinding. A reduction of 80-90 % of the power consumption needed for grinding torrefied biomass can be attained in comparison with raw biomass [111]. This means a power consumption similar to that of coal. Previous research found a linear inverse correlation between the average particle diameter after grinding and the torrefaction temperature for wood chips and logging residues [106]. Pierre et al. developed an original impact device to evaluate the grindability of torrefied biomass [100]. The authors showed an energy consumption reduction of 86 % for oak torrefied to 38 % of mass loss and a reduction of 99 % for pine torrefied to 45 % of mass loss.

Currently, transport and handling of biomass powders are a key obstacle for the cost-competitive production of second-generation biofuels. Indeed, creating a steady flow of the biomass particles out of the storage equipment is a significant issue for biomass processing and conversion. From industrial experience, the most common cause of failure in continuous biomass valorization facilities is feeding problems into the reactors [129].

Notwithstanding the frequent occurrence of handling problems, there is still a relatively poor knowledge of the flow properties of biomass materials [202]. More research is therefore needed in this field to ensure the sustainability of the supply chain [3]. This includes a better understanding of the combined effect of torrefaction and grinding parameters and the effects of particles shape and size distributions on powder flow properties. Flowability is often characterized through the unconfined yield strength (σ_c) which indicates the tendency of a bulk solid to form a cohesive arch in a hopper and to create ratholes in process equipment [320]. Following the procedure described in Section 2.5, unconfined yield strength is obtained from the Mohr analysis of the yield locus (failure strength against load stress) of a granular material.

Regarding particle size, studies for coal-biomass systems have shown that bigger particles tend to reduce the bulk solids yield strength compared to finer particles [212]. Several models have been proposed to relate the particle size properties to the bulk unconfined yield strength. So far, only inverse relationships between the particle size and the unconfined yield strength, whichever the mechanism considered, are proposed (van der Waals Forces, capillary forces, elastic fracture, plastic-elastic fracture) [321–323]. These models have typically the following general expression [320]:

$$\sigma_c = \frac{K}{d_p^n} \quad (43)$$

where σ_c represents the unconfined yield strength, K and n stand for constants dependent on the material properties and d_p is a particle size descriptor. Experiments conducted on flame retardant powders [324] showed that samples cohesion decrease with increase of particle size. Similar conclusions for black soybean powders, where fine fractions were reported as cohesive, were made by Lee et al. [229]. Rohilla [325] concluded that there exists a particular particle size after which intermolecular forces become larger than weight forces, which triggered a decrease on flowability of fly ash samples.

The lack of suitable standard methods for measuring and classifying particle shapes, the heterogeneity of shapes and the fibrous nature of biomass particles makes it difficult to characterize the

effects of these parameters on the flow properties [129]. Yet, several studies assessed the effects of shape on unconfined yield strength and found that irregular shapes tend to increase the cohesive strength between particles. According to [320], two key parameters influence the strength of a bulk powder system: the number of contacts per adjacent particles and the direction of these contacts relative to the centroid axis between adjacent particles. In the case of irregular particles, more effective contacts exist between particles and this situation can therefore increase yield locus values, resulting in a more cohesive behavior. Several studies have shown that bridging properties of chipped solid biofuels are mainly controlled by the shape and the size of the particles [207]. A high proportion of hooked or long and thin particles increased the bridging tendency. Similar results were obtained by Paulrud et al. [87] for ground pine and spruce. Hann [326] found that powders with narrow particle size distributions had better flowability and that bulk solids with rounded edges resulted in a greater unconfined yield strength. Particle shape is also essential when studying the specific surface area that governs mass and heat transfer phenomena during gasification [233,327,328].

Even though particle size and shape are likely to have the greatest impact on powder flow properties, few studies have evaluated powder flow in relation to both, particle size and shape, especially regarding biomass powders, and even less knowledge is available about the effect of heat treatment on particles properties.

Previous works have reported the effect of torrefaction intensity as measured by the global mass loss (*ML*) on the flowability of biomass powders [329]: a direct relationship between the *ML* and the flowability factor was observed. The current work investigates the effect of different torrefaction intensities on the flow properties of knife-milled biomass (spruce and poplar), and assesses the relations between:

- The torrefaction mass loss and the particle size and shape obtained after grinding
- The particle size and shape and the granular material flow behavior.

The results of this research are summarized as expressions between torrefaction operating conditions and physical properties and flowability of biomass particles. They are very useful in optimizing the BtL chain as they allow the compromise between energy loss due to torrefaction, grinding energy and flowability to be clearly assessed.

2.2. Materials and methods

2.2.1. Biomass preparation

A hardwood and a softwood species have been considered for this study. Poplar was chosen as hardwood (*Populus euro-americana* Koster) as it is a promising forest energy crop, namely due to its fast growth in temperate climates. The development of poplar genotypes with improved yield, higher pest resistance, increased site adaptability and easy vegetative propagation has made poplar a commercially valuable energy crop [330,331]. The poplar tree selected for the present study came from a forest located in *La Snippe* valley in Auménancourt-le-Petit (France). Spruce (*Picea abies*), a softwood species, is another potential candidate to be used in BtL chains, mainly because of its intensive current use in the forestry industry. A spruce tree coming from a plantation in the *Le Châtaignier* forest in Riotord (France) was selected. Both trees were chopped and cut in boards that were subsequently dried.

The sample size was chosen to fulfil several constraints such as the amount required for flowability tests (30 cm³ of powder needed), the grinding capacity of the grinder (maximum length) and the

homogeneity of the heat treatment (small thickness). The size of each individual wood chip was thus fixed to $20 \times 20 \times 3 \text{ mm}^3$. Each sample of Table 1 consists of 32 chips of this size. The basic densities (oven-dry mass over saturated volume) are $311 \pm 9 \text{ kg/m}^3$ and $330 \pm 10 \text{ kg/m}^3$, for untreated poplar and spruce respectively. The respective growth ring widths are 14 mm and 2.85 mm. As it is well-known that wood properties present little changes in the longitudinal direction, all samples were collected along a single board to reduce the intra-tree variability. To further average the remaining variability and obtain twin samples, the 32 wood chips of each sample were selected following a recurrent stepped scheme along the board [329].

Table 18. Torrefaction conditions and global mass loss for the 14 samples studied.

Torrefaction temperature (°C)	Duration of torrefaction (h)	Global mass loss, ML (%)	
		Poplar	Spruce
Untreated		0	0
220	1	2.8	2.0
220	5	8.0	4.7
250	1	12.0	7.1
250	5	21.3	14.4
280	1	25.2	18.7
280	5	47.3	38.1

In agreement with previous findings of [93,104,332], the mass loss values confirm the lower thermal resilience of poplar compared to spruce (Table 18). This is mainly explained by the lower resistance of hardwood hemicelluloses and lignins to heat treatment [333,334].

2.2.2. Torrefaction

A batch torrefaction furnace specifically developed in the laboratory was used to treat the samples [335]. The atmosphere of a hermetically closed *Memmert UFP400* chamber is controlled by sweeping a nitrogen flow ($5 \text{ L} \cdot \text{min}^{-1}$) to reduce the oxygen content, thereby avoiding oxidation and ignition. In all cases, the oxygen level, as measured at the gas outlet, remained below 1.5 %. A powerful fan inside the chamber ensures an efficient heat transfer either to heat-up the sample or to limit thermal overshoot due to exothermic reactions. The gas temperature was measured nearby the samples using a K-thermocouple.

A total of six treatments were performed at 220, 250 and 280 °C for 1 or 5 hours with the following protocol: (i) heating from room temperature at a rate of 5 °C min^{-1} up to 100 °C (ii) plateau at 100 °C for 30 minutes to remove the residual bound water (iii) heating at a rate of 5 °C min^{-1} until the treatment temperature. (iv) plateau at the treatment temperature for the desired duration and (v) cooling down thanks to thermal losses and an increased nitrogen flow entering the reactor. Preliminary simulations were performed using a comprehensive computational code to ensure that the treatment duration together with the sample thickness ensures the treatment to be quasi-uniform within the sample [336].

After treatment, samples were weighed to determine the mass loss (ML) due to heat treatment as follows:

$$ML \text{ (%) } = \frac{m_0 - m_t}{m_0} \cdot 100 \quad (44)$$

where, m_0 and m_t are the oven-dry mass before and after torrefaction, respectively. Mass loss is known to be a good indicator of the treatment intensity [91] and has been successfully correlated to several properties of the treated biomass such as energy properties [100] or dimensional changes [93].

2.2.3. Grinding procedure

Heat-treated samples were ground in a *M20 IK4* laboratory 550W knife miller. An automatic control system was implemented to guarantee the repeatability of the grinding procedure. The rotational speed of the knives (stainless steel cutter M21) was 20 000 rpm. To avoid any additive heat treatment due to thermal dissipation, several grinding and resting cycles were carried out, up to a total grinding time of 95 seconds. A circulation of cold water inside the grinder jacket further reduced sample heating.

2.2.4. Particle size and shape analysis

A *Sympatec-QICPIC* morphological particle size analyzer with a M7 lens (measurement ranges from 10 to 10240 μm) with a *GRADIS* dispersion and *VIBRI* feeding units was used in this work [312]. To conduct the test, about 5 g of wood powder was loaded onto the hopper of the instrument. The size and shape of powders were recorded and analyzed using the manufacturer software.

The mean value of the Feret diameters over all orientations of the particle) is used as the magnitude characterizing particles size. The 50th centile of the cumulative volume distributions (x_{50}) was taken as a mean size descriptor of each size distribution. The particle shape was characterized through the circularity, ψ (from 0 to 1), which is defined as the ratio of the perimeter of a circle having the same area as the projected area of a particle to its actual perimeter. A perfect sphere would give $\psi = 1$ and the smaller the value of ψ , the more irregular is the shape of the particle. Mean values of circularity ψ_{50} were calculated as the 50th centile of the cumulative circularity distributions.

The flow of a polydispersed bulk solid primarily depends on flow properties of the fines fraction [212], the size analysis of particles having a size under 100 μm was made for all samples. Hence the sieve fraction of the samples with a size below 100 μm was analyzed. This fraction was obtained by using a vibratory sieve shaker *Retsch AS 200* at an amplitude of 60 % (1.8 mm) for 20 minutes. Particle size and shape were analyzed using a *M4* lens allowing a better resolution for finer particles in the range from < 1 μm to 1700 μm . The use of this lens needs samples to be fed as a liquid dispersion. Biomass powders were first colored by means of a 24-hour soaking in a Safranin-O – 10 % ethanol solution to avoid agglomeration, then diluted in 500 mL of water. This solution was pumped into the *LIXELL* wet dispersion system. Results presented are the combination of three repeatable tests.

2.2.5. Flowability tests

A *RST-XS* Schulze ring shear tester was used to assess the flow properties of biomass powders. The ring shear tester is a widely-used device to measure flow properties of powders, including angle of internal friction, wall friction and bulk density. The standard procedure leads to results with low variability [143]. According to this procedure, once the shear cell with the powder sample has been prepared, the *maximum normal preshear stress*, σ_{pre} , is applied on the cell lid. A typical evolution of the shear stress obtained from torque measurements is represented in Figure 43a. The preshearing step is carried out up to the attainment of a steady state value of shear stress in which the frictional forces between particles are maximum with respect to the applied normal load. At this point the powder attains a well-defined and reproducible state of consolidation corresponding to the top point of the yield locus represented in Figure 43b. This steady state often occurs when the sample volume and thus its bulk density, ρ_b , reaches a steady state value at the end of compaction [337]. After the preshearing, the direction of shear is reversed, i. e. the shear stress is reduced to zero. Then, the normal stress is reduced to a value $\sigma_{sb,1} < \sigma_{pre}$ and the sample is sheared until a peak value of shear stress, τ_{sb} is reached (incipient flow or failure) [202]. The sequence of two steps is repeated with the same σ_{pre} and increasing σ_{sb} . Finally,

a verification point at $\sigma_{sh,1}$ is made. The (σ, τ) couples obtained at failure are drawn to represent the *yield locus* corresponding to the consolidation applied as shown in Figure 43b).

A set of three pre-consolidation stresses (σ_{pre}), considered as representative of the stress range for industrial applications, were tested: 2, 5 and 10 kPa [141]. Three shear points at 25, 50 and 75 % of σ_{pre} for each pre-consolidation stress were used to determine the yield locus of each sample. The yield locus curves were regressed from experimental points by a linear regression.

As represented in Figure 43 b), the Mohr circle drawn through steady state point and tangent to the yield locus locates the *major principal stress* σ_1 , corresponding to the consolidation applied. The *unconfined yield strength* is given by the major principal stress passing through the origin and tangent to the yield locus. In Figure 43b), the dashed line passing the origin and tangent to the larger Mohr circle is the *effective yield locus*. Its angle of inclination with respect to the σ axis is the *effective angle of internal friction* ϕ_e . Yield locus for a non-cohesive granular material passes through the origin, so *cohesion*, C , corresponds to the value of the shear stress where the yield locus intersects with the τ axis, i.e., at the normal stress $\sigma = 0$. By measuring yield loci for different pre-consolidation stresses a flow function (σ_e vs. σ_1) can be drawn.

Unconfined yield strength governs the stress holding the material together on a free surface. It is the major principle stress that acts in a direction parallel to the free surface which supports the external forces tending to tear the surface apart [138]. The bigger its value, the higher the stress required to fail or fracture the granular material to initialize the flow. The unconfined yield strength indicates the tendency of a bulk solid to form a cohesive arch in a hopper and form ratholes in process equipment [320].

The ratio *FFC* (*flow function coefficient*) of consolidation stress to unconfined stress (σ_1/σ_e) is used to quantify the flowability. The larger *FFC*, the better a bulk solid flows. All properties obtained from the Schulze ring shear tester are usually reported as a function of the major principal stress of consolidation.

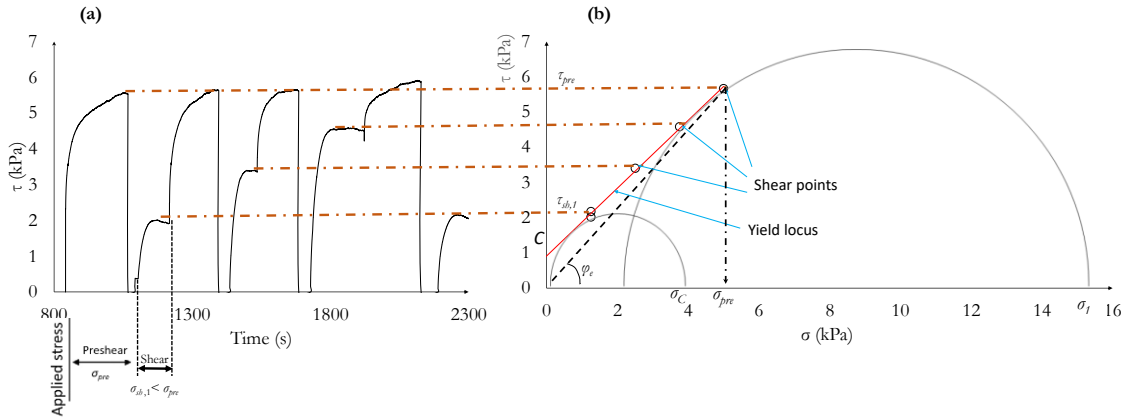


Figure 43. Flow properties determination (Untreated poplar sample, $\sigma_{pre} = 5$ kPa). (a). Experimental course of shear stress; (b) yield locus construction and Mohr stress circles defining unconfined yield strength and consolidation stress.

2.3. Results

2.3.1. Effect of torrefaction intensity on particle size and shape distributions

A surface representation (Figure 44) was chosen to represent both the shape factor and the particle size distributions for three degrees of torrefaction: untreated, mildly treated (250 °C, 1 hour) and intensively treated (280 °C, 5 hours). A gradual shifting from large particles with relatively low circularity

towards finer particles and higher values of circularity becomes evident when increasing the torrefaction intensity. This reduction of particle size is a direct effect of the loss of resilience [107]. This is also the primarily reason of using torrefaction as pretreatment on the BtL chain: to obtain small and reactive particles at a lower grinding energy cost.

These 2D graphs deserve a deeper analysis of the concomitant changes of size, circularity and peak intensity. For poplar powders, the peak value for circularity changed from $\psi = 0.6$ to $\psi = 0.75$ (increase of 25 %) from untreated to the most treated samples. For spruce, circularity peak values increased from $\psi = 0.55$ to $\psi = 0.77$ (increase of 40 %). This increase of circularity with torrefaction was already observed for pine [106].

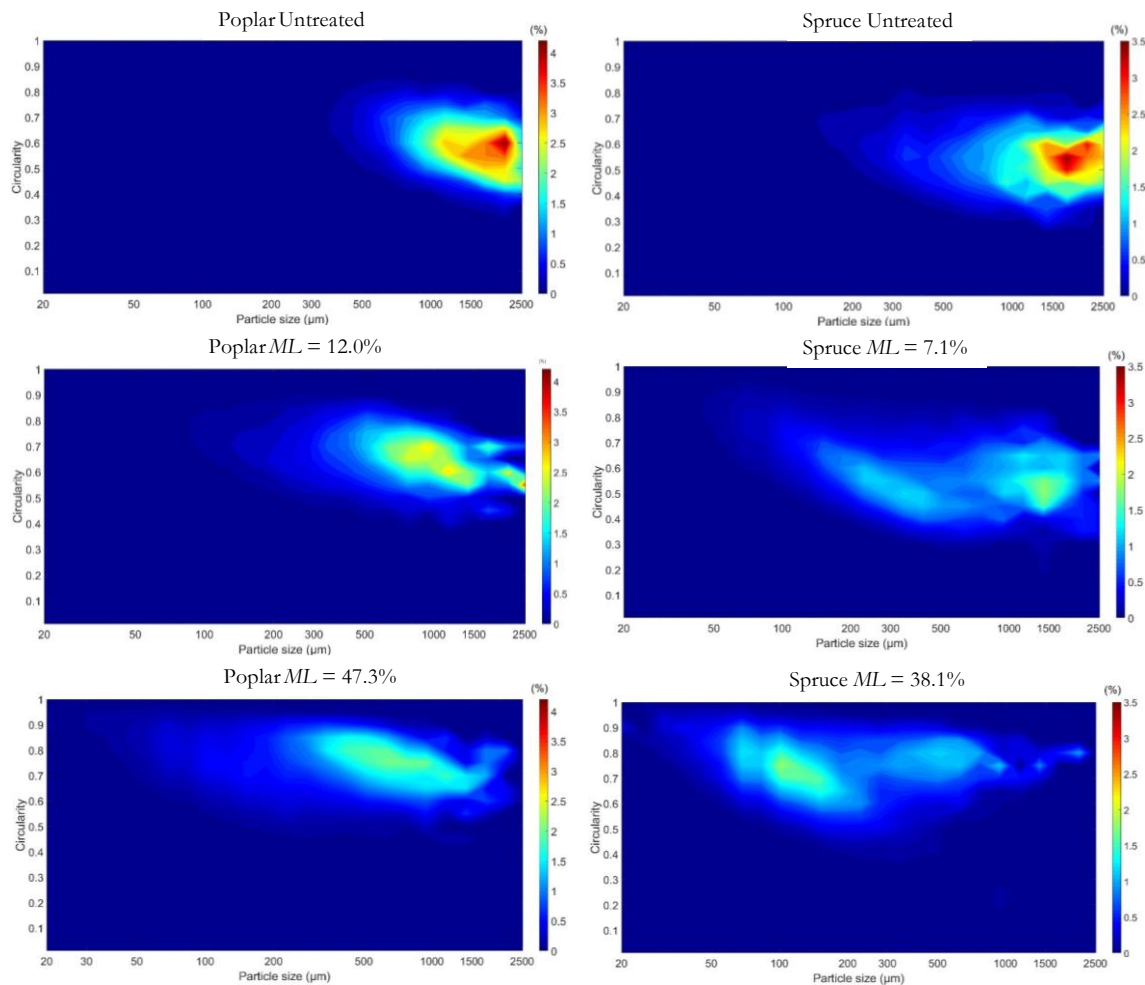


Figure 44. Influence of torrefaction intensity on circularity and size distributions for spruce and poplar powders. The color scale indicates the volume fraction of each size and shape range and varies between the same values regardless of the torrefaction intensity for each species.

From the color scale, it is also noticeable that, for both species, a spreading of the distributions occurs at increased heat treatment intensity. For poplar, the initial, sharp, peak at 2 mm evolved progressively towards a wider peak spreading towards smaller and more spherical particles. Spruce presents a different behavior as two populations gradually appear. The initial peak is slightly shifted towards smaller particles (1800 μm , 1500 μm and 600 μm , from untreated to 7 % and 38 % of ML) and progressively disappears. Another peak is already visible at $ML = 7.1\%$ at a mean particle size of ca. 300 μm . For the most severe treatment ($ML = 38.1\%$) the initial peak almost disappeared and the second

peak represents a large part of the power volume, with smaller (ca. 100 μm) and round particles ($\psi = 0.77$).

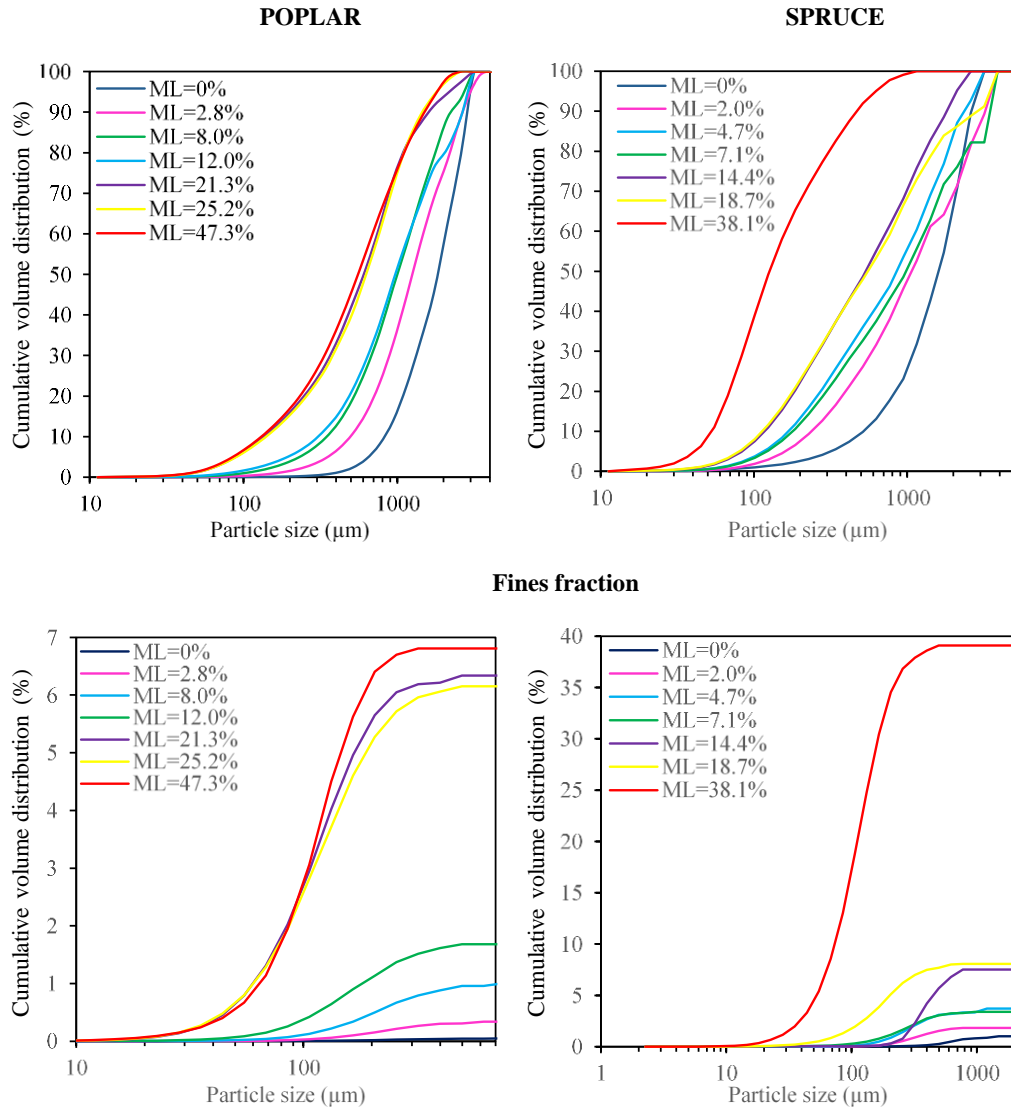


Figure 45. Influence of torrefaction intensity (Mass Loss ML) on PSD: whole sample (top) and fines fraction (bottom).

Figure 45 (top) presents the cumulative volume particle size distribution (PSD) for poplar and spruce. This synthetic representation allows the size reduction at increasing heat treatment intensities to be quantified. The trends reported in this figure confirm literature data [106,119,120]. In the case of poplar, for the highest values of mass loss, the cumulative distributions tend to overlap. This indicates that a plateau in particle size seems to be reached after a certain treatment intensity. Again, spruce presents a different behavior, as a significant shifting of the particle size distribution towards finer particles is still observed for the most severe treatments.

These trends are confirmed by the analysis of the fines fraction (Figure 45, bottom). For poplar, the fines fraction presents a plateau at ca. 7 % of the total particle volume and the three most severe treatments (21 % to 47 % of mass loss) are very close. On the contrary, a large increase of the fines fraction is observed for $ML = 38\%$: almost 40 % of the particle volume. It is also obvious that the particle size distribution continues to shift towards small particles.

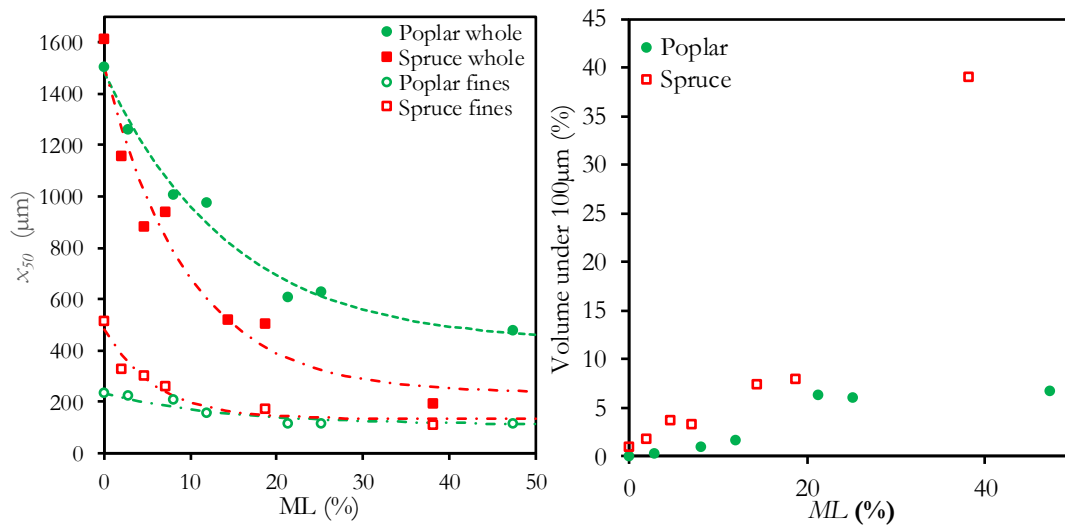


Figure 46. Effect of torrefaction intensity on the mean particle size (left) and volume of fines (right) of poplar and spruce powders.

As synthetic indicator of the particle size reduction, the 50th centile (x_{50}) of the particles size distribution was plotted as a function of ML in Figure 46. For the entire particle samples and for the fines fractions as well. Exponential expressions of the form $x_{50} = a \cdot (b + e^{-c \cdot ML})$ were also fitted from these experimental data. The fitted parameters are presented in Table 19. These models imply an asymptotic behavior whose limit at "infinite torrefaction intensity" equals 427 μm for poplar and 226 μm for spruce.

Table 19. Parameters of the exponential regressions of the form $x_{50} = a \cdot [b + \exp(-c \cdot ML)]$ for the mean particle size after grinding as a function of ML .

Sample	a	b	c
Poplar whole samples	1067	0.40	0.069
Poplar fines	347.4	0.38	0.170
Spruce whole samples	1258	0.18	0.104
Spruce fines	120.7	0.91	0.069

The general trend clearly confirms the loss of resilience at increasing treatment intensity. A similar behavior is observed for the two species. Yet, larger particles are obtained for poplar compared to spruce at similar torrefaction intensity. For spruce, the particles size is reduced by 88 % for untreated to severely treated wood ($ML = 38 \%$). The reduction is only by 68 % for poplar. A higher effect of thermal treatment on the particle size reduction is therefore evident for spruce, even though the ML presents an opposite trend (lower values for spruce than for poplar for given torrefaction conditions).

This result is quite surprising as the alteration of lignins and hemicelluloses by heat treatment explains the increase of cell wall brittleness. The native lignins of conifers are essentially constituted of guaiacyl (G) units together with a low proportion of *p*-hydroxyphenyl (H) units (except in compression wood rich in H units). Along with the G units and traces of H units, the lignins of deciduous trees are constituted of syringyl (S) units. The proportion of resistant bonds in native lignins increases with the frequency of G and H units whereas S units are mostly involved in weaker β -O-4 linkages. From this molecular point of view, poplar resilience should therefore be more deeply altered by heat treatment than spruce.

As the observation regarding PSD depicts an opposite trend, the explanation is likely to rely on the difference in anatomical structure. Poplar is a pore-diffuse hardwood species which presents two levels

of porosity: vessels and cell lumen (fibers and parenchyma cells). This heterogeneity creates various possible fracture pathways of the tissue that permits large particles to be formed. On the contrary, spruce is made of tracheids for 95 % of its volume. Consequently, the formation of particles necessarily required fractures at this unique pore scale. This produces smaller particles, namely single tracheids or fractions of tracheids and a significant proportion of fines particle even at low treatment intensity. Obviously, this trend is stronger at higher *ML* levels, due to its effect in weakening the cell wall. The consequence on the proportion of fines (particle < 100 μm) is impressive: whereas both species depict a linear increase with mass loss, the proportion of fines increases up to 40 % for spruce, against 8 % for poplar.

Finally, two synthetic indicators, in addition to the 50th centile values, are proposed to quantify the spreading of the distributions, the span criteria: S_x for size and S_ψ for circularity, calculated from the respective 90th and 10th centiles of cumulative distributions as follows:

$$S_x = \frac{x_{90} - x_{10}}{x_{90} + x_{10}} \quad (45)$$

$$S_\psi = \frac{\psi_{90} - \psi_{10}}{\psi_{90} + \psi_{10}} \quad (46)$$

where x_{90} and x_{10} stand for the 90th and 10th centiles of the PSD and ψ_{90} and ψ_{10} represent the 90th and 10th centiles of circularity distributions.

These criteria are reported in Table 3. The span of the particle size distribution tends to increase with the increase of torrefaction intensity. This trend is clearer for poplar than for spruce. However, for both species, an important increase from untreated to torrefied samples is observed (+50 % for spruce and +19 % for poplar). Powders of torrefied wood exhibit a more polydispersed population with smaller sizes than powders of native wood. The span of circularity distributions did not depict any clear tendency.

Table 20. Ground samples properties: Global mass loss, mean particle size, mean circularity and span values.

Torrefaction temperature (°C)	Torrefaction duration (h)	Poplar						Spruce					
		<i>ML</i> (%)	x_{50} (μm)	S_x	ψ_{50}	S_ψ		<i>ML</i> (%)	x_{50} (μm)	S_x	ψ_{50}	S_ψ	
Untreated		0	1504	0.56	0.57	0.24		0	1611	0.67	0.52	0.26	
220	1	2.8	1261	0.69	0.60	0.22		2.0	1153	0.86	0.53	0.29	
220	5	8.0	1006	0.73	0.62	0.20		4.7	881	0.87	0.55	0.28	
250	1	12.0	975	0.79	0.63	0.21		7.1	940	0.90	0.54	0.29	
250	5	21.3	606	0.84	0.70	0.19		14.4	520	0.86	0.59	0.28	
280	1	25.2	628	0.82	0.68	0.20		18.7	504	0.88	0.58	0.30	
280	5	47.3	475	0.84	0.72	0.21		38.1	192	0.80	0.72	0.21	

2.3.2. Effect of torrefaction intensity on flow properties of biomass powders

Flow functions presented in Figure 47 give information about the different flowability regimes by considering the ratio between the unconfined yield strength and the major consolidation stress [138]. A *FFC* value below 1 indicates a not flowing behavior, while a value of 4 represents the transition from cohesive to easy-flowing. Above 10, the powder is considered as free-flowing. The graphs obtained for our samples depict a clear effect of the heat treatment intensity on the evolution of these flow functions, either for spruce or for poplar.

For poplar, the curve obtained for the powder of native biomass is close to the line $FFC = 4$. It is therefore at the transition between cohesive and easy-flowing behavior. Starting from this value, a gradual and regular shift of the curves towards higher values of FFC is evident. The most intense treatment lies close to $FFC = 10$, which is the transition between easy-flowing and free-flowing.

Spruce samples depict the same trend, but over a larger amplitude. Untreated biomass is at the middle of the cohesive zone, whereas the curve obtained for the most intense treatment ($ML = 38\%$) the $FFC = 10$ boundary. One has also to notice that the progression observed for spruce is not as regular as for poplar.

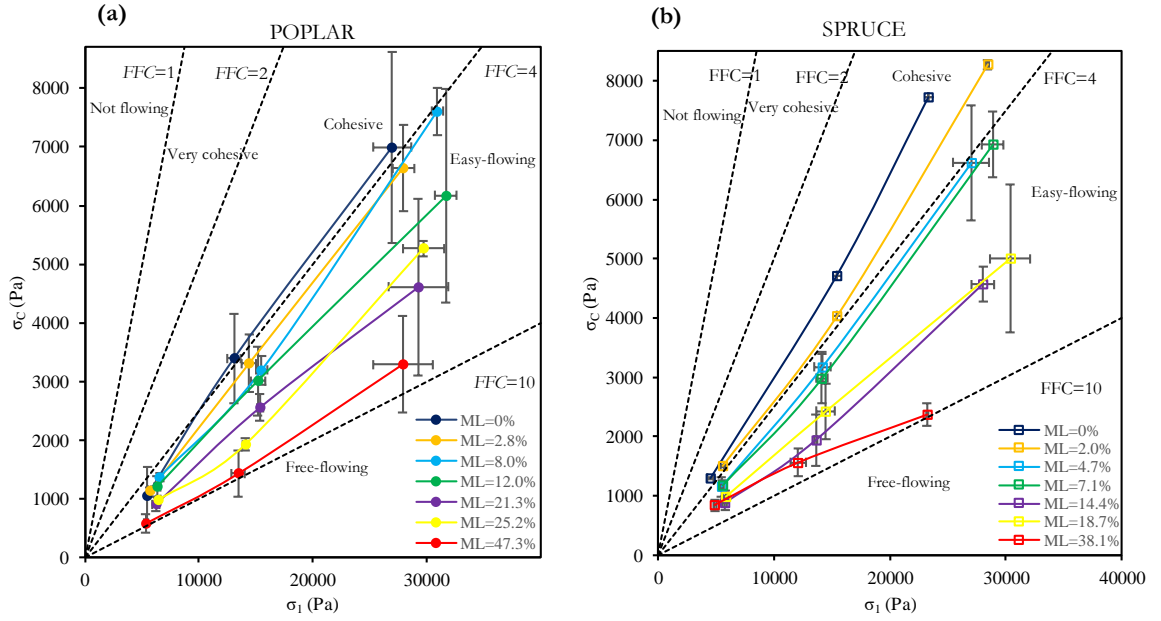


Figure 47. Effect of torrefaction intensity (ML) on flow properties for (a) poplar and b. spruce powders ($\sigma_{pre} = 5$ kPa).

These trends encouraged us to use the mass loss due to heat treatment (ML) as indicator of the flowability of biomass powder. As stated in this introduction, this parameter already proved to be an excellent synthetic indicator [91] for other biomass energy and mechanic properties. To that purpose, the value of FFC obtained with a pre-consolidation stress of 5 kPa was plotted as a function of ML for both species (Figure 48). Except one point for spruce, the quasi-perfect linear relationship obtained is remarkable. Similar trends were found for the other consolidation stresses studied (see the Appendix at the end of this section). Both species showed a quantitatively similar trend. Flowability factor increased by 105 % and 118 % for poplar and spruce, respectively, from the untreated to the most intensively treated samples. Mass loss could then be used in industry for practically assessing the powder flowability of biomass powder under consolidation, since its ease of obtaining. In addition, both species are on the same line. By removing the singular point found for spruce at $ML = 14.4\%$, a unique, linear, expression can be proposed to predict the effect of mass loss on flowability, valid for all the consolidation stresses studied ($r^2 = 0.80$):

$$\frac{FFC}{FFC_{untreated}} = 1 + 2.81ML \quad (47)$$

In this expression, that should be considered has one of the major outcomes of the present work, $FFC_{untreated}$ represents the flowability factor (dimensionless) of powder from native biomass and ML is the mass loss due to heat-treatment (kg/kg). As a conclusion from this trend it can be seen that, in

contrast with raw biomass, torrefied wood particles have higher flowability, which will ease the injection of pulverized biomass into boilers in gasification units.

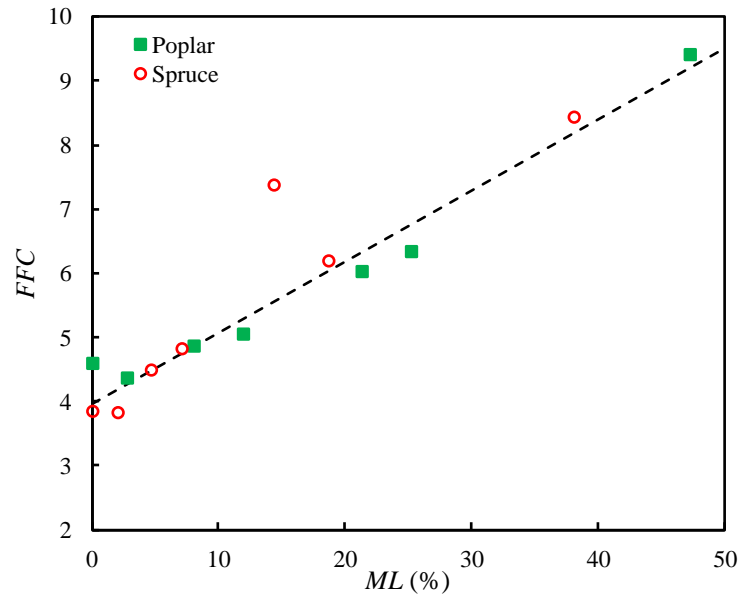


Figure 48. Effect of the torrefaction intensity on the flowability factor of poplar and spruce powders (for clarity purposes only values at $\sigma_{pre} = 5$ kPa are presented).

2.4. Discussion on the combined effects of particle size/shape and treatment intensity

The previous results told us that:

- The treatment intensity allows smaller and more spherical particles to be produced by grinding,
- The flowability of particles obtained from heat-treated wood increases significantly and linearly with mass loss.

It is therefore worthwhile to go further in the explanation and to investigate if the evolution of the flowability can be explained by the particle size and shape. To that purpose, Figure 49 represents some of the flow properties as a function of particle size and circularity. Either for poplar or for spruce, the unconfined yield strength increases with particle size and decreases with circularity. Similar trends were found for the other consolidation stresses studied and presented in Appendix at the end of this section. The third plot (Figure 49c) represents the value of FFC obtained with a pre-consolidation stress of 5 kPa in a 3D plot, which depicts the concomitant change of size and circularity. This last plot summarizes the effect of heat-treatment on flowability:

- Heat-treatment reduces the mean particle size and increases the circularity,
- The cumulated effect of these two trends increases the powder flowability.

As stated in previous works [316,337–339], for a given shape, flow properties tend to improve with mean particle size. As particles become finer, the van der Waals forces of attraction between them increase relatively because of their larger specific surface area (m^2/g). During shear cell testing, there is a larger number of particle-particle contacts on the shear failure plane for a powder comprised of smaller

particles (Hou & Calvin, 2008). Consequently, the total area of contact is larger for smaller particles. At the same time, particles with less mass are subject to lower gravitational forces.

The net result of these effects is the shifting of the yield locus towards higher stresses and thus, a larger value unconfined yield strength and smaller flowability, which is opposite to the clear trends observed in the present work. Other effects are therefore likely to counterbalance the sole effect of particle size. In addition to the mean size, the width of size distribution might be involved. As reported in [141], qualitatively speaking, flowability of bulk solids having the same median, x_{50} , increases with decreasing width of the particle distribution. Again, this observation would produce an effect opposite to our observations: Table 2 tells us that the intensity of heat-treatment increases the width of the particle distribution, yet the flowability increases. Polydispersity effects were also studied by Schulze [337] for a mixture of coarse and fine lactose particles. The larger the percentage of the finer component, the more the yield locus was shifted towards higher stresses and the smaller the flowability. Interestingly, this trend was not observed for torrefied biomass powders.

Additional explanations have therefore to be found. The flowability improvement could then be triggered by the change in the shape factor of the particles. Generally, when considering coarse particles, smooth, spherical particles flow better than rough, sharp-edged, non-spherical particles. This has been demonstrated for different kinds of granular materials: Lewandowski et al. [340] found that the higher the mean circularity the lower the cohesion for glass beads samples. Deviation of particle shape from sphericity led to higher angles of repose for microcrystalline cellulose [341] and higher compressibility in lactose powders [339]. Danjo et al. [151] also concluded that there is an increase in the flowability of bulk solids when there is an increase in the shape factor of the particles.

For untreated biomass powders, the steric repulsion and frictional forces that are a consequence of the particle geometry lead to a greater extent of inter-particulate friction and locking. Hence, yield loci are shifted to bigger values when compared with torrefied samples, resulting in a decreased flowability. Similar findings have been reported previously by Goh et al. [342] for pharmaceutical powders, where some flowability properties such as the internal angle of friction were primarily influenced by particle shape and relatively independent of particle size.

Another effect to take into consideration, regarding polydisperse systems such as biomass powders, is the lubricant effect of fine particles on coarser ones. Flow agents prevent particle surface from direct contact, reducing inter-particle adhesion forces and improving flowability. In the case of intensively torrefied powders, where very fine-grained powders were obtained, the adhesive force between the biggest particles would be reduced due to the increased inter-particle distance caused by very small covering particles acting as lubricant. However, flow agent particles must be sufficiently small in order to limit the adhesive forces of the flow agent particles themselves. The bigger shifting of flow functions from cohesive to free-flowing behavior shown in Figure 47 for spruce powders could be seen as a result of the higher amount of very fine particles compared to poplar samples. Since flow agents are often based on nanosized particles, a granulometric analysis at nanometric resolution would be useful for further validation of this hypothesis.

Besides size and shape modifications, torrefaction is likely to alter the surface properties of biomass powders as well. The hydrophobic nature of torrefied samples could affect flow properties through the electrostatic forces in two ways. Firstly, as the presence of bound water lowers the electrical resistivity, raw samples (which tend to capture moisture more easily) will tend to dissipate the electrostatic charges better. Secondly, as indicated in previous research [343], the electrostatic properties of the particles are directly related to the surface functional group chemistry: hydrophobic groups accumulate greater

quantities of charge than hydrophilic groups. All of this would mean that, all other parameters being the same, torrefied samples are more likely to present flow problems linked to charge build-up. However, flow problems induced by accumulation of electrostatic charges are mainly to be expected in free surface flows of fine powders or when the powder is in contact with non-conductive surfaces. In closed systems, as the ring shear tester, the effect of electric charges could thus be mainly neglected. As the samples were oven-dried prior to the flowability measurements, the formation of liquid bridges at the particle scale (which could increase cohesion) was also neglected.

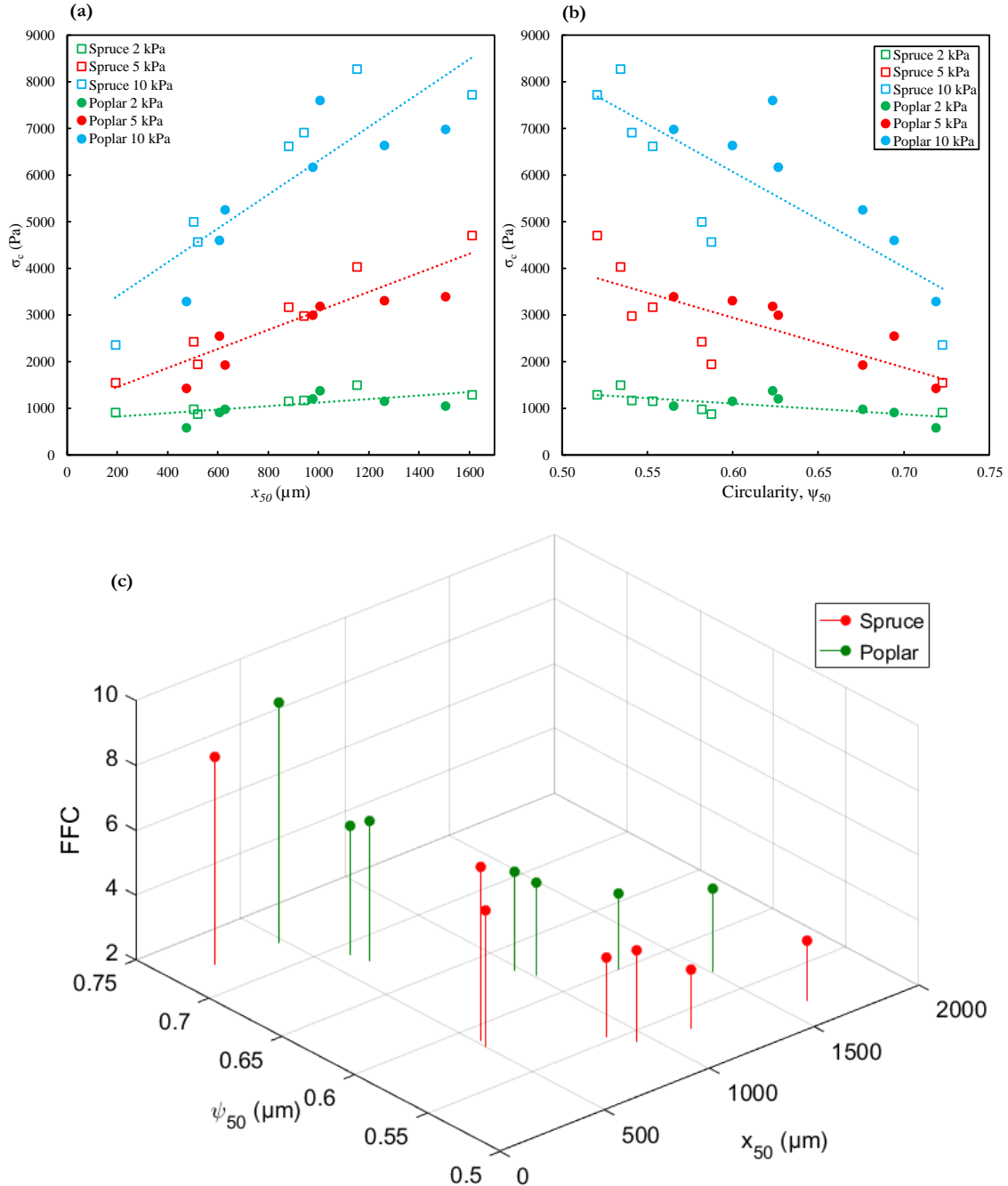


Figure 49. Effect of particle size and shape on flow properties for poplar and spruce powders: a. b. Unconfined yield strength, c. flowability factor ($\sigma_{pre} = 5 \text{ kPa}$).

SEM images of particles were grabbed for spruce and poplar for different treatment intensities using a FEI *Quanta* electron microscope (Figure 50). When the treatment intensity increases, a decrease of

particles length for a relatively similar width can be observed. This means a reduction of particles elongation which generally goes hand-in-hand with a circularity increase, as measured by the granulometric analysis made. The changes of circularity are very gradual, especially at low treatment intensities (Table 20). They become significant for intense treatments (for poplar, average circularity increased by +26 % compared to the raw biomass). SEM images are rather intended to show tearing, pulling-out and breaking profiles, that are affected by torrefaction, in addition to the shape changes (that are better evaluated statistically by the granulometric analysis). For untreated samples, the fibrous and resilient behavior of wood produces irregular needle-like particles, with tearing and pull-out profiles. Pulled-out fibers together with rather elongated particles certainly promote particle agglomeration, which is likely to reduce powder flowability. On the contrary, sharp breaking surfaces are observed for torrefied samples. These observations confirm the conclusions of both shape and size analysis and are in good agreement with those done by Almeida et al. and Arias et al. [110,344]. The effects of loss of resilience on the particle shape becomes thus evident, from native to severely treated biomass.

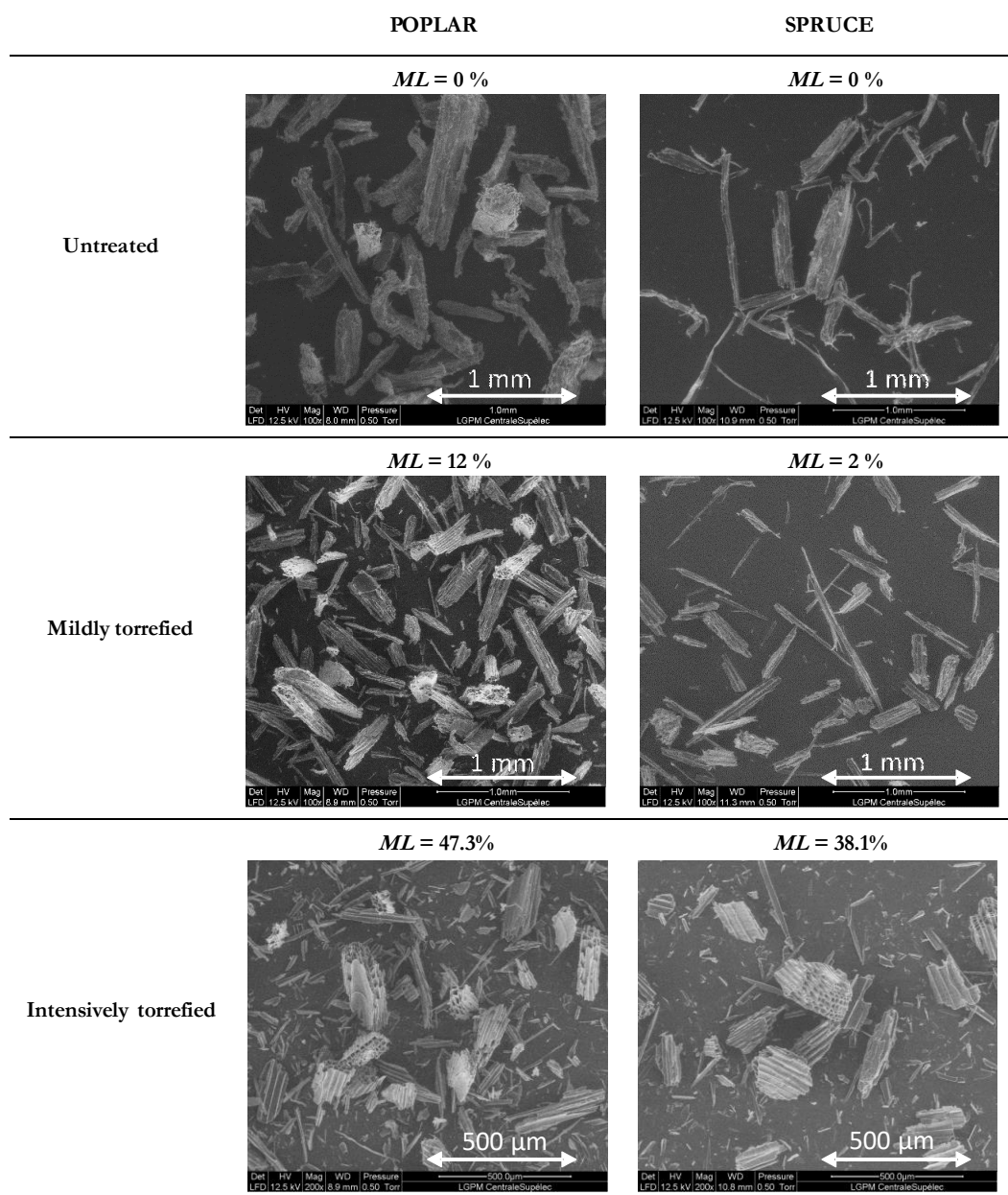


Figure 50. Scanning Electronic Microscopic images for untreated and torrefied spruce and poplar powders.

As a conclusion of this discussion, we proved that the increase in flowability of wood powder with heat-treatment intensity is in complete opposition with the reduction of mean particle size or the increase in distribution width. Therefore, different effects should be involved to counterbalance the effect of particle size and to explain the clear improvement of flowability with heat treatment. Two major effects were pointed out. Both are tied to the loss of resilience of the fibrous behavior of native biomass: i) the reduction of the shape factor (higher particle circularity) and ii) the much higher regular and convex shape of particles.

2.5. Conclusions

The study, focused on two wood species, poplar and spruce, investigated the effect of torrefaction on the particles size and shape obtained after grinding and on the flow properties of milled wood. Overall, a gradual shifting of the particle size and shape distributions towards finer and rounder particles was observed when increasing treatment intensity. At the same time, a significant improvement of the flowability with torrefaction intensity was also clearly exhibited. Milled biomass gradually shifted from a cohesive character for the native samples to a nearly free flowing behavior for the most intensively treated samples. Considering these observations, a unique linear expression between torrefaction intensity and flowability factor was proposed for the two-species studied here.

Finally, we proved that the concomitant evolution of particle sizes and distribution width and flowability parameters are not consistent as smaller particles should exhibit lower flowability. Indeed, the increase of flowability is mostly due to rounder particles with sharp surfaces of treated biomass compared to long and irregular needle-like particles obtained for native biomass. Both consequences, flowability improvement and size/shape factor reduction, are therefore explained by the same effect: the loss of resilience of the fibrous structure of raw wood by heat-treatment.

2.6. Acknowledgements

The support of the Ministère de l'Enseignement Supérieur et de la Recherche (France) is gratefully acknowledged.

APPENDIX: Additional flow properties: angles of friction, cohesion and bulk density

The friction angles are parameters related to the inter-particle friction of bulk solids and are one of the most used parameters to characterize their handling behavior. The angle of internal friction ϕ_{in} is obtained from the slope of the linearized yield locus and the slope of the effective yield locus represents the effective angle of friction ϕ_e [141].

Cohesion characterizes the shear stress at yield under zero normal stress, *i.e.* the intersection of the yield locus with the ordinate. Bulk density is defined as the ratio of the mass of an amount of bulk solid to its volume. It is usually function of the consolidation stress. In the Schulze ring shear tester, the bulk density is calculated from the total charged mass of sample and the volume considering the lid displacement for a given consolidation stress [141].

Table 21 presents the values of the linearized internal angle of friction and the effective angle of internal friction resulting from the Schulze shear cell tests. There is not much difference between the

angles for poplar and spruce showing that there is a similar interparticle friction when the two species are compared. Variations of angles between the different degrees of torrefaction intensity are not very clear and are often below the standard variation of the set of measurements (around 1°). These results are comparable with those obtained by Wu et al. [216] for poplar chips ($\varphi_{lin} \approx 46^\circ$).

Regarding cohesion, it follows the same trend than the unconfined yield strength: a more cohesive behavior is observed for the untreated powders then a gradual decrease follows until the minimal value for the most intensively torrefied samples. Like the other flow properties, cohesion is strongly dependent on the consolidation stress: with increasing consolidation stresses the yield locus skewed towards greater shear stresses because of the greater shear stress necessary to initiate flow. When the two-wood species are compared, relatively more cohesive behavior was found for the spruce samples than for poplar powders.

Table 21. Flow properties for milled poplar and spruce at different torrefaction intensities.

	σ_{pc} (kPa)	Poplar							Spruce						
		ML (%)							ML (%)						
		0.0	2.8	8.0	12.0	21.3	25.2	47.3	0.0	11.4	14.7	17.4	25.4	30.9	46.5
Unconfined yield strength (kPa)	2	1.1	1.1	1.4	1.2	0.9	1.0	0.5	1.3	1.5	1.1	1.2	0.8	1.0	0.9
	5	3.4	3.3	3.2	3.0	2.5	1.9	1.4	4.7	4.0	3.2	3.0	1.9	2.4	1.6
	10	7.0	6.6	7.6	6.2	4.6	5.3	3.3	7.7	8.3	6.6	6.9	4.6	5.0	2.4
Flowability factor FFC	2	5.2	5.0	4.8	5.3	6.9	6.6	9.2	3.5	3.7	4.9	4.7	6.5	6.0	5.8
	5	4.6	4.4	4.9	5.0	6.0	6.3	9.4	3.9	3.8	4.5	4.8	7.4	6.2	8.4
	10	3.9	4.2	4.1	5.1	6.3	5.7	8.5	3.0	3.4	4.1	4.2	6.2	6.3	11.0
Major consolidation stress (kPa)	2	5.5	5.7	6.6	6.4	62.3	6.4	5.3	4.5	5.5	5.5	5.5	5.8	5.8	5.3
	5	13.9	14.4	15.5	15.2	15.3	14.1	13.4	1.5	1.5	14.2	14.1	13.6	14.5	12.9
	10	27.0	28.0	30.9	31.7	29.2	29.7	27.9	2.3	2.8	27.0	28.9	28.0	30.4	25.9
Angle of internal friction, φ_{int} ($^\circ$)	2	43.8	47.4	47.2	48.0	47.7	47.4	45.3	39.0	41.8	43.5	45.1	46.5	46.9	44.7
	5	42.2	44.5	48.0	47.4	46.5	47.3	44.2	40.0	46.2	44.4	44.5	46.5	46.0	44.3
	10	43.4	44.9	46.2	45.2	45.2	45.9	46.2	39.6	44.3	43.5	45.2	45.4	47.2	44.0
Effective angle of friction, φ_e ($^\circ$)	2	48.1	51.6	51.6	51.8	50.7	50.5	47.6	46.2	48.2	47.8	49.2	49.7	50.5	48.4
	5	48.2	49.6	52.3	51.5	50.0	50.4	46.5	47.6	51.9	49.4	49.1	49.5	49.5	46.8
	10	49.3	50.1	51.5	50.3	48.5	49.6	48.6	47.9	51.0	49.1	50.4	48.9	50.6	46.0
Cohesion (kPa)	2	0.2	0.2	0.3	0.2	0.2	0.2	0.1	0.3	0.3	0.2	0.2	0.2	0.2	0.2
	5	0.7	0.7	0.6	0.5	0.5	0.4	0.3	1.1	0.6	0.6	0.6	0.4	0.5	0.3
	10	1.5	1.4	1.5	1.5	0.9	1.1	0.6	1.8	1.7	1.4	1.4	0.9	1.0	0.5
Bulk density (kg/m ³)	2	152	164	180	180	221	211	221	153	153	174	174	217	221	243
	5	152	176	189	187	231	218	224	146	162	188	187	222	232	255
	10	165	181	196	195	238	228	227	188	177	198	198	233	237	266

Bulk density was found to be directly dependent on the torrefaction intensity of the samples and the consolidation stress applied. Most intensively treated samples trigger denser powders after grinding than untreated ones. This is due to the reduction of both inter- and intra-particle voids generated after grinding with the reduction of particle size. This behavior agrees with the observations by Mani et al [119]. The increase of bulk density with torrefaction intensity is important: an average of 43 % is gained for the most intensively torrefied poplar sample with respect to the untreated sample. For spruce an average increase in bulk density of 58 % was observed.

3. Complementary investigation on the biomass flowability under consolidation

3.1. Introduction

The suitability of shear tests for the acquisition of flow properties for elongated biomass particles has been questioned by Miccio et al. [202] when particle size was above 2 mm (passing through a 2 mm sieve). Although the particle size distributions using the mean Feret diameter presented in the second part of this chapter were mostly located at values below 2 mm, the elongated particle shape means that at least one grain dimension could be generally greater than 2 mm. The relaxation after consolidation of the material due to the flexible nature of the elongated particles can lead to results that depend on the orientation of the particle during consolidation. This might explain the relatively high standard deviations of the values of unconfined yield strength obtained.

Additionally, the manufacturer specifications for the ring shear tester [345] state that the dimensions of the shear cells limit the maximum size of the particles that can be tested. Although it is impossible to advise an accurate value for the maximum particle size because of the influence of particle shape and the particle size distribution, a maximum recommended size for the shear cell model used in this work (XS-Mr) is 1.0 mm.

With the aim of joining a particle size range that ensures reliable shear testing results, a ball mill was thus used to further reduce the particle size of the outflow of a *Retsch SM300* cutting mill. The flow properties of the ball-milled powders are subsequently measured using a Schulze RST. The same line of reasoning as that followed in section 2 of this chapter is used for the analysis of the flowability results. Thus, the effect of torrefaction intensity on particle characteristics (size, shape and span of the distributions) is first evaluated, and then the effect of these particle-scale properties on flow behavior is discussed.

A first part of this complementary work is a study of the torrefaction intensity effects on the flowability following the experimental approach of section 2. For this purpose, samples torrefied under different intensities are ground using the same grinding protocol (section 3.2). The differences in the obtained particle and shape characteristics are therefore exclusively the result of the different levels of torrefaction intensity. A second part consisted in taking advantage of the possibility of easily ‘controlling’ the particle size in a ball mill by modifying the grinding time, to study the effects of particle size and shape on flowability independently from torrefaction (section 3.3). A torrefied sample was therefore ground using different grinding times, leading to a range of particle sizes and shapes that could then be correlated to the measured flow properties.

3.2. Effects of torrefaction intensity on flowability of ball-milled poplar powders

3.2.1. Torrefaction conditions

Poplar chips (60×80×15 mm) were cut from dried boards and then thermally treated at four different torrefaction temperatures for 1 hour. Each torrefaction batch consisted in ca. 15 chips. The mass loss values reported in Table 22 are the average of the results for 8 chips.

Table 22. Torrefaction temperature and global mass loss of the samples for a 1-hour treatment.

Sample ID	Torrefaction temperature (°C)	Mass loss, <i>ML</i> (%) [SD*]
Raw	----	0.0
<i>ML</i> = 12.2 %	240	12.2 [2.4]
<i>ML</i> = 24.1 %	260	24.1 [4.1]
<i>ML</i> = 32.0 %	280	32.0 [5.1]
<i>ML</i> = 49.0 %	300	49.0 [7.6]

*Standard deviation

3.2.2. Cutting milling: particle size and shape measurement

The raw and torrefied chips were ground using a *Retsch SM300* cutting mill with a bottom sieve of 1 mm trapezoid holes at the outlet. Particle size distributions depicted in Figure 51 were obtained using the *Sympatec-QICPIC* morphological particle size analyzer. The mean Feret diameter (d_{Fmean}) is used as descriptor of the particle size.

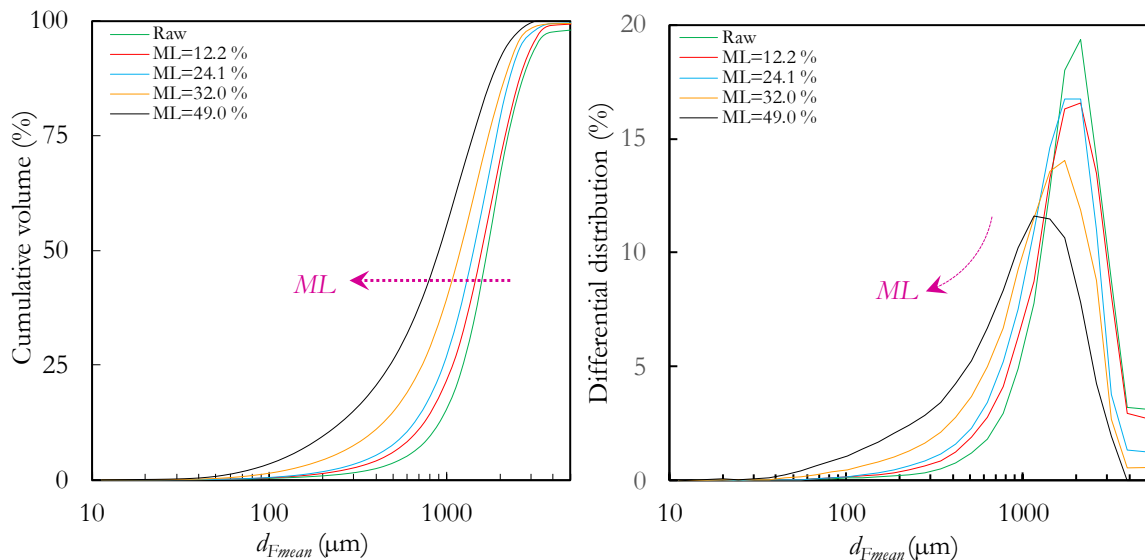


Figure 51. Cumulative (left) and differential (right) size distributions in volume for the SM300 grinder outflow with a 1 mm hole bottom sieve.

Figure 51 reveals that the size measurements of the *Retsch SM300* cutting mill outflow follow the same qualitative trends reported in section 2 for powders obtained using an *M20 IK4* knife mill. The gradual decrease of the particle size when torrefaction intensity is increased is very clear, and from the differential distributions, the increase in the PSD width is also evident. Indeed, using the 50th centiles of the cumulative distributions, Figure 52a shows the relationships between *ML* and the PSD descriptors: an inverse relationship is depicted in the case of the mean particle size while a direct relationship can be observed for the span. As discussed in detail in section 2, these results are the consequence of the loss of mechanical resilience of biomass due to heat treatment.

Due to the use of an average Feret diameter (over all the orientations of the particle) as descriptor of particle size and as consequence of the elongated shape of the particles, the distributions shown in Figure 51 are located at values that exceed the size of the output grid. In Figure 52b, the distributions using the minimum and maximum Feret diameters instead of the mean Feret diameter are drawn.

The distributions using the minimum Feret diameter are located at values under 1 mm. This means that the particles are more likely to pass through the outlet sieve of the grinder through their smallest dimension (width). This is consistent with previous results by Guo et al. [226] who stated that the average widths of biomass particles corresponded with the sieve sizes, while the average lengths exceeded the sieve size.

Similar conclusions to those for Figure 51 regarding the effect of torrefaction intensity can be drawn using both minimum and maximum Feret diameters (except for the $ML = 32.0\%$ sample using d_{Fmin}): a reduction of particle size with the increase of torrefaction intensity is observed. However, interestingly, Figure 52b indicates that the effect of the torrefaction intensity seems to be more important on the minimum dimension (d_{Fmin}) of the particles while the length (d_{Fmax}) is less affected for $ML < 32\%$ and then abruptly reduced for the most intensively torrefied sample ($ML = 49.0\%$). This provides evidence for the breakage mechanism described in section 2.3.3.2.4 of Chapter I. Raw samples are preferably divided following the wood fiber orientation. Then, due to the hemicellulose decomposition that breaks down macrofibrils when torrefaction intensity is increased, the particles after grinding are thus preferentially thinner. By intense torrefaction, the fracture lines can be triggered transversely to the direction of the fibers, resulting in a shorter length.

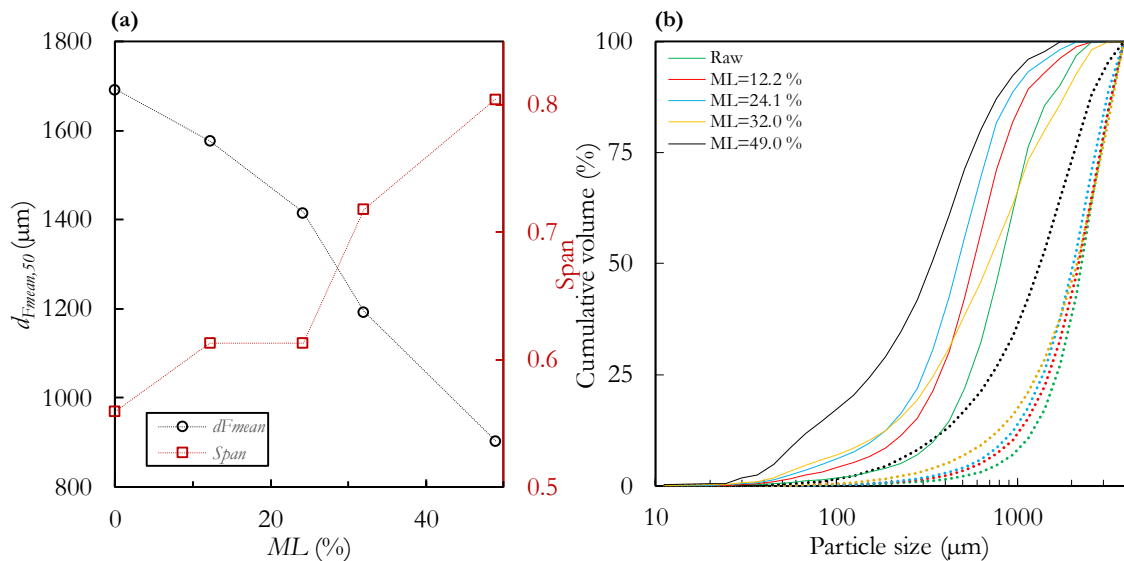


Figure 52. (a) Median descriptors of particle size and PSD span for the five samples. (b) Cumulative size distributions in maximum (dotted curves) and minimum (solid curves) Feret diameters.

3.2.3. Ball milling: particle size and shape measurement

The outflow of the cutting mill was ground using a *Retsch PM100* ball mill. One third of the volume of the grinding jar (90 cm^3) was filled with the biomass sample and another third with 15 stainless steel balls. The rotational speed (grinding jar) was set to 400 rpm. A grinding time of one minute after reaching the set speed was used for all the samples.

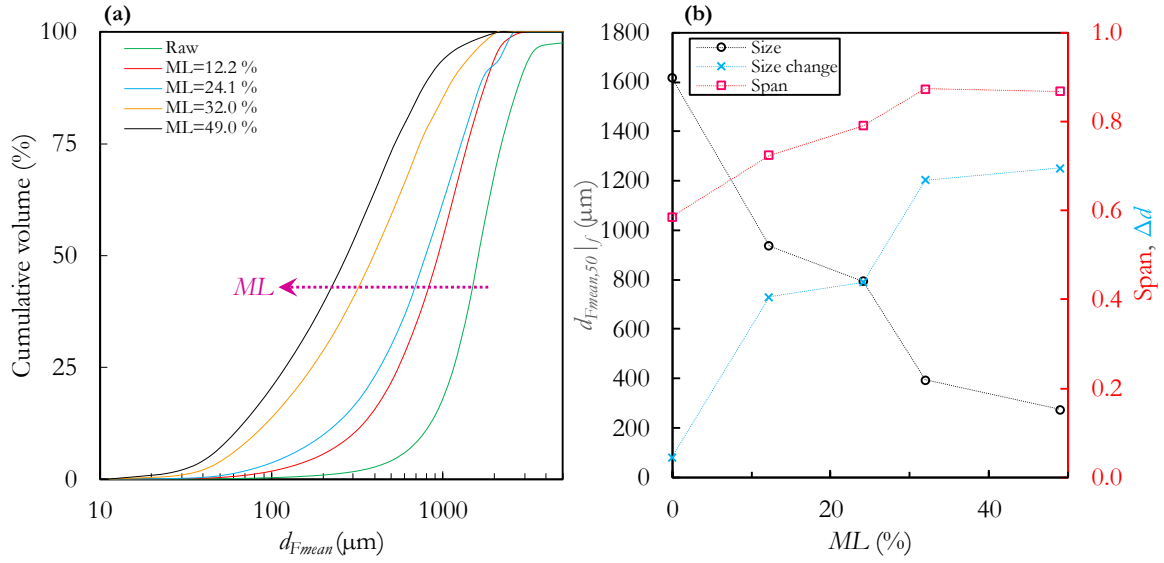


Figure 53. Particle size characteristics after ball milling. (a) Cumulative volume distributions for different torrefaction intensities. (b) Size and shape descriptors as function of the global mass loss.

The cumulative size distributions depicted in Figure 53a show that finer powders are obtained for the most intensively torrefied samples. However, since the input samples for ball milling already do not have the same particle size, a reasoning in terms of the size variation between before and after the grinding seems more appropriate. This size variation Δd , ($0 \leq \Delta d \leq 1$) can be calculated as:

$$\Delta d = 1 - \frac{d_{Fmean,50} |_f}{d_{Fmean,50} |_i} \quad (48)$$

where $d_{Fmean,50} |_i$ and $d_{Fmean,50} |_f$ are the 50th centiles of the volume distribution before and after grinding, respectively.

The size variation as well as the median ($d_{Fmean,50} |_f$) and the span of the particle size distributions are shown in Figure 53b as a function of the global mass loss. While the particle size decreases and the span increases with the increase in torrefaction intensity, there is also a sharp increase of Δd when ML increases. A reduction of only 4.5 % of the median particle size is achieved after one minute of grinding for the raw sample, while the reduction is 70 % for the $ML = 49.0$ % sample. This means that, in absolute terms, as with the cutting mill product, a greater reduction in particle size when the torrefaction intensity increases is verified during ball milling. It is noteworthy that torrefaction until a mass loss of only 12.2 % already significantly increases the grindability compared to the raw sample as the size reduction with the ball mill is nearly 9 times greater than that of the raw biomass.

Regarding the changes in particle shape triggered by torrefaction, Figure 54 shows that, overall, the most intensively torrefied samples tend to generate less elongated particles (higher aspect ratio). Although the differences are not as pronounced as in the case of particle size and the progression depicted in Figure 54b is not entirely monotonous, an increase of the aspect ratio of 26 % is obtained when comparing the raw and the most intensively torrefied sample. SEM images presented in Figure 55 provide a clear and direct visualization of the particle shape. Although similar elongated shapes are visible for both the raw and the slightly torrefied samples, smaller and less elongated particles are obtained for the sample torrefied until a mass loss of 49.0 %.

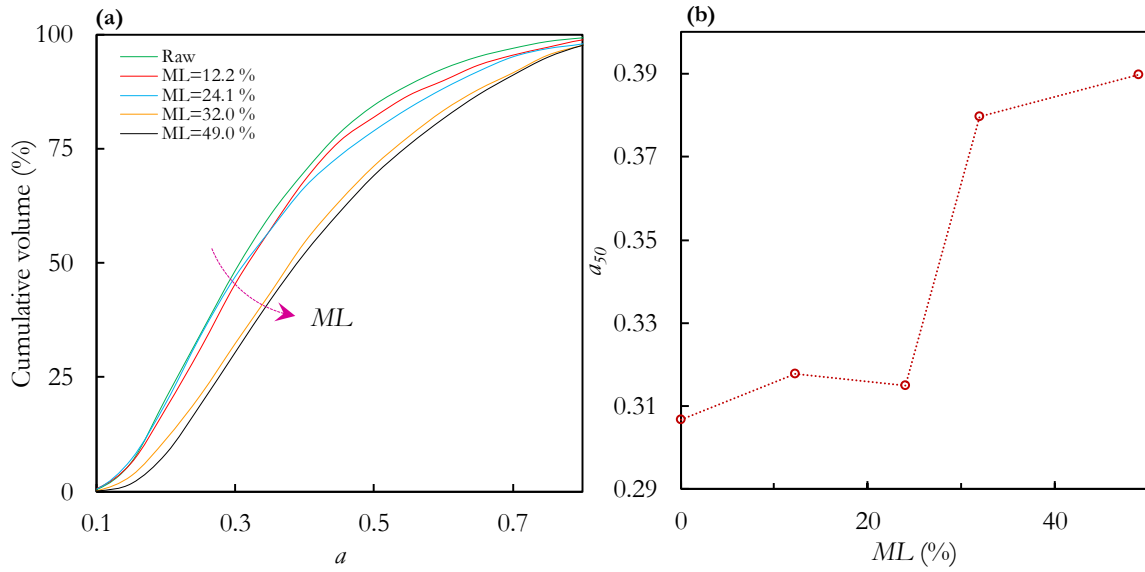


Figure 54. Shape characteristics of the raw and torrefied samples. (a) Cumulative aspect ratio distributions. (b) 50th centile of the aspect ratio distributions as function of the global mass loss.

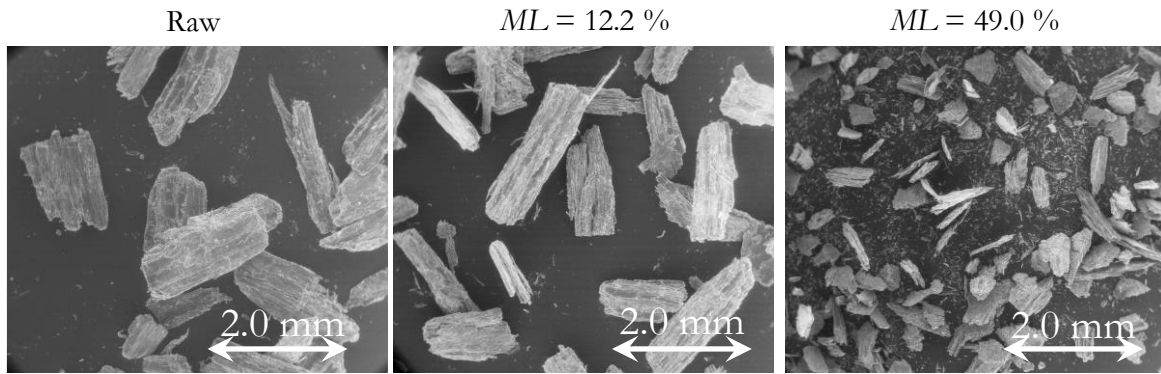


Figure 55. Scanning Electronic Microscopy images for raw, slightly and intensively torrefied poplar powders.

3.2.4. Flowability measurements

The flow properties of the powders obtained after grinding were evaluated using a Schulze Ring shear tester. Three preshear stresses (σ_{pre}) were used at 2 kPa, 5 kPa and 10 kPa with three shear points at 25, 50 and 75 % of each σ_{pre} . The results presented are the average of three measurements repeated using different samples of oven-dried powder. The flow functions presented in Figure 56a were derived by Mohr analysis of the linearly-regressed yield loci.

Although all the flow functions are located in the easy-flowing region, an effect of the torrefaction intensity on the flow behavior is clearly noticeable. There is a gradual shifting of the flow functions from a nearly cohesive behavior for the $ML = 12.2\%$ sample to an almost free-flowing behavior for the $ML = 49.0\%$ sample. Therefore, with the exception of the raw sample, the increase in torrefaction intensity leads to a better flow behavior.

The positive effect of torrefaction intensity on the flowability factor at $\sigma_{pre} = 5$ kPa is shown in Figure 56b. For torrefied samples, the effects of having less elongated and more spherical shapes when increasing torrefaction intensity would be dominant over the size reduction, as discussed in section 2 of this chapter, leading to an improvement of the flowability for the most treated powders.

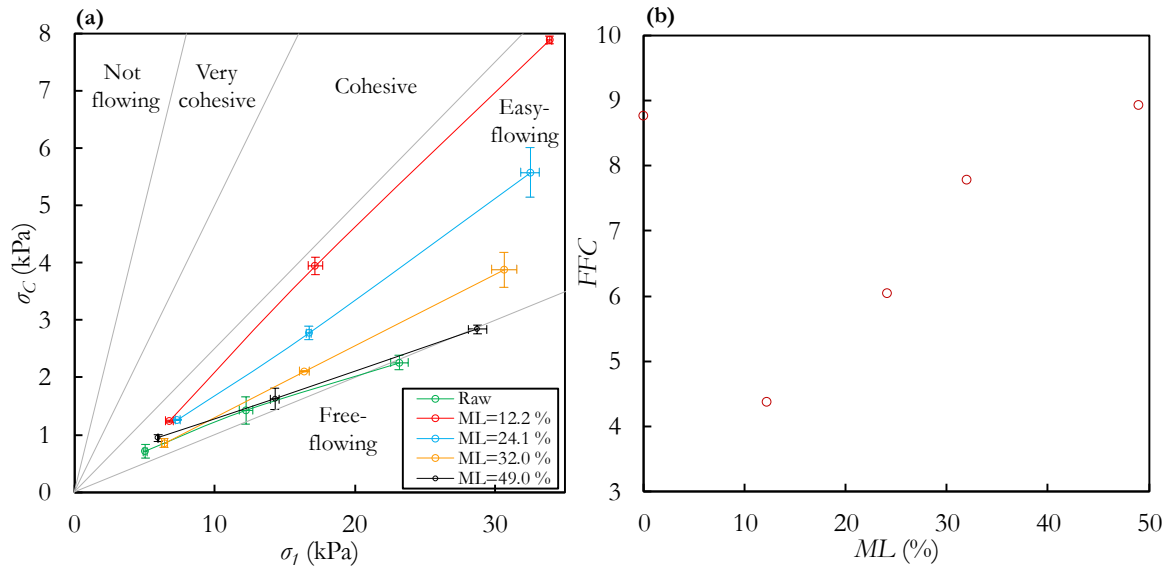


Figure 56. Flowability of raw and torrefied ball-milled biomass samples (a) Flow functions (b) Flowability factor ($\sigma_{pre}=5$ kPa).

The fact that the raw powder has such good flow behavior is somewhat surprising and an explanation it is difficult to be given considering only size and shape characteristics. A probable reason might be the large size of the raw particles compared to the torrefied samples. Size effects would predominate and their flowability is therefore improved as generally larger particle sizes lead to better flow behavior (see Chapter I - section B 3). Moreover, ball milling can also produce a surface erosion phenomenon that is not found in cutting milling, which has the effect of reducing the surface roughness of the particles and thus making it easier for them to slide relative to one another (see images in Figure 50 compared to images in Figure 55). Flowability could also be improved due to the reduced distribution span of the raw powders since monodispersed populations tend to have a better flow behavior [141]. An additional explanation could include the effects of torrefaction on surface interactions at the particle scale that are not assessed on this work, which would enhance cohesion between torrefied particles compared to untreated biomass. Further studies on this topic are therefore required.

It is important to note that, as shown by the error bars in the flow functions (Figure 56a) which represent the standard deviation of the results, the repeatability of the measurements was significantly increased compared to the flowability measurements reported in section 2 for the knife-milled powders. Except for the raw sample, the qualitative trends were similar to those presented in section 2. and the results of the present complementary section therefore support the findings previously reported.

The additional powder properties listed in Table 23 follow the same trend as the flowability factor. A minimum of cohesion and effective angle of friction is observed for the raw samples, while an inverse relationship with the ML increase is observed for the torrefied samples. In the case of the bulk density, raw powders are exceptionally dense and then, as in section 2, an increase of ρ_b with ML is verified.

Table 23. Additional flow properties of ball-milled poplar for different torrefaction intensities ($\sigma_{pre} = 5$ kPa).

	ML (%)				
	Raw	12.2	24.1	32.0	49.0
Cohesion, C (kPa)	0.32	0.63	0.51	0.41	0.33
Effective angle of friction, φ_e (°)	44.3	53.4	52.6	49.8	47.5
Bulk density, ρ_b (kg/m ³)	240.6	172.6	173.1	202.1	228.2

3.3. Particle size and shape effects on flow properties for the same torrefaction intensity

3.3.1. Sample preparation

The outflow of the *SM300* cutting mill corresponding to the poplar wood chips torrefied at 240 °C ($ML = 12.2\%$) was ground using the ball mill with the same grinding parameters described in section 3.2.3 (except for the grinding time). Six samples at grinding times of 1, 2, 3, 4, 5 and 8 minutes were produced.

3.3.2. Particle size and shape

Figure 57 shows surface representations of the aspect ratio and the particle size distributions in volume for three grinding times (1, 4 and 8 min.). As expected, as the grinding time increases, there is a clear shifting of the distributions both towards finer and less elongated particles. Additionally, the color scale, which indicates the volume fraction of particles, highlights the spreading of the distributions with the increase of the grinding duration. While a rather low-dispersed population of particles was obtained at low grinding times, a highly polydispersed powder is therefore produced after 8 minutes of grinding. The distributions at intermediate times, not shown in Figure 57, follow the same general trend.

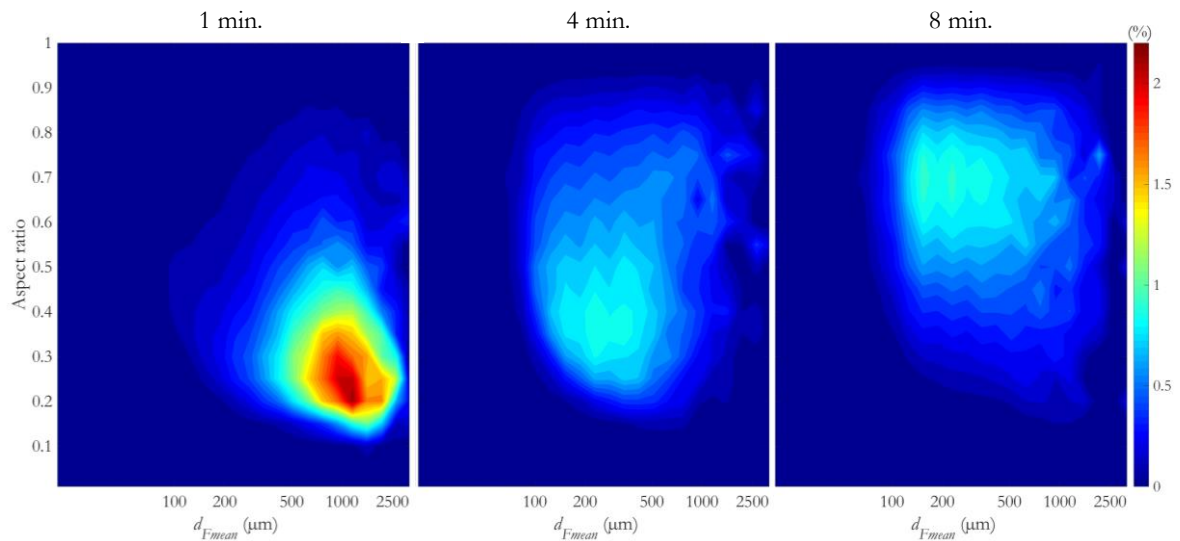


Figure 57. Effect of grinding time on the aspect ratio and size distributions of the powder obtained after ball milling ($ML = 12.2\%$).

The results shown in Figure 58a – b are projections (differential distributions) of the surface plots that ease (but simplify) the visualization of the grinding time effects on particle size and shape. In the case of particle size, a gradual shifting of the distributions towards finer values is clearly noticeable. The shape of the size distribution passes from rather a peak to a flat bell, indicating the spreading of the distributions over a progressively wider range of sizes. Regarding particle shape, the differential distributions shown in Figure 58b progressively shift to the right, so that particles become less and less elongated as result of the ball impacts. Interestingly, unlike the size distributions, the shape distributions seem to flatten when the grinding time is increased from 1 to 4 minutes and then sharpen again from grinding times of 5 minutes with a new peak emerging at 8 minutes. This indicates that, for long grinding times, particles tend to have round uniform shapes over a rather large range of particle sizes. The plots

in Figure 58c summarize these trends by means of average descriptors (50th centile of the cumulative distributions) of the distributions and size spreading (span).

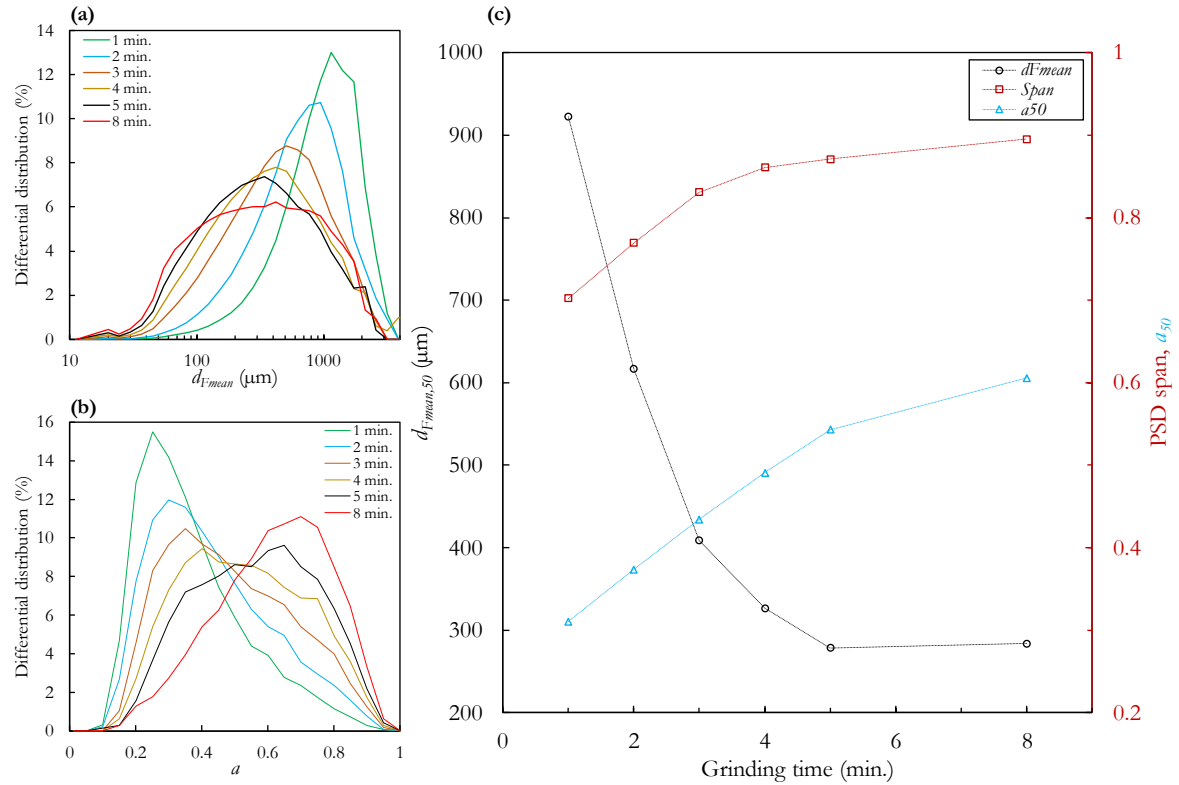


Figure 58. (a) Differential particle size distributions at different grinding times. (b) Differential aspect ratio distributions. (c) Average descriptors of particle size, shape (50th centiles of the cumulative distributions) and span of the PSD as function of the grinding time.

The SEM images shown in Figure 59 illustrate the changes in particle size and shape as the grinding time evolves and qualitatively reinforce the conclusions drawn from the granulometric analysis presented above. The powders were sieved prior to image acquisition in order to better visualize the different size ranges of the particles. Two representative sieving cuts are therefore presented in Figure 59, the qualitative behavior being similar for the other sieving cuts prepared. From large needled-shaped particles at short grinding times, the grains gradually become very round and uniform for the long grindings.

3.3.3. Flowability measurements

Shear testing of the ball-milled powders using a Schulze Ring shear tester led to the flowability results shown in Figure 60. Four preshear stresses (σ_{pre}) were used at 2 kPa, 5 kPa, 10 kPa and 15 kPa with three shear points at 25, 50 and 75 % of each σ_{pre} . Except for the sample ground for 4 minutes, there is gradual improvement of the flow behavior from a nearly cohesive flow for the less ground powders to a nearly free-flowing behavior for the powders obtained after 8 minutes of grinding. The flowability factor therefore shows a strong direct relationship with the grinding time.

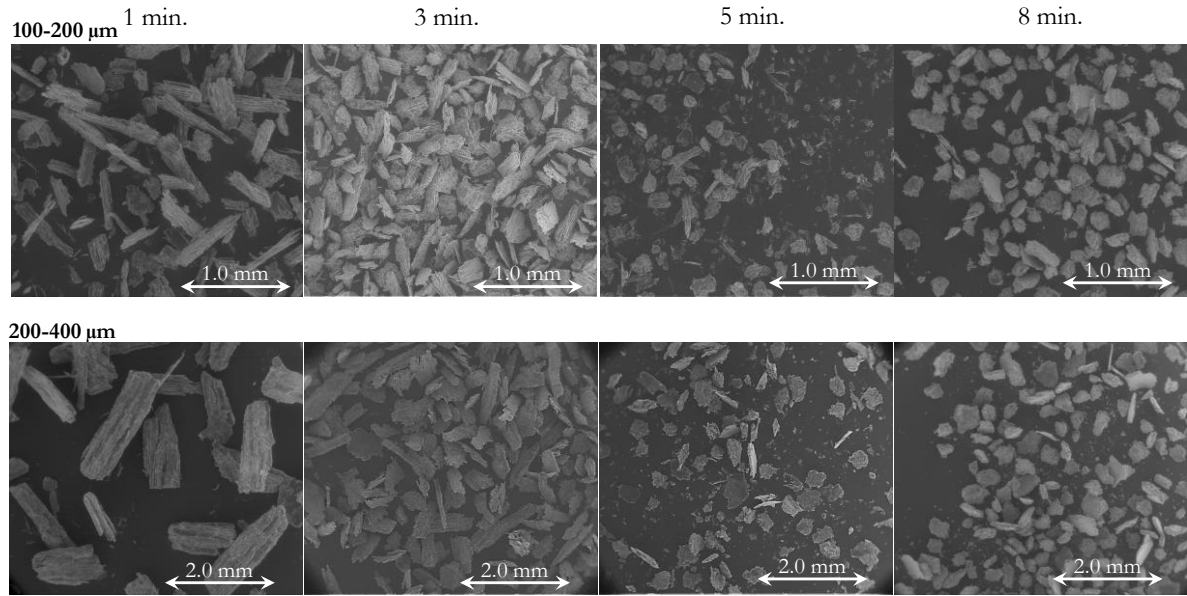


Figure 59. SEM images of the powders obtained after different grinding times. Two representative sieving cuts are shown.

The elongated particle shapes obtained at short grinding times is likely to promote spatial interlocking, which results in a greater cohesiveness of the bulk solid. On the contrary, biomass powders composed of round uniform particles would thus flow better under consolidation than elongated needle-shaped particles, even if the latter are on average larger.

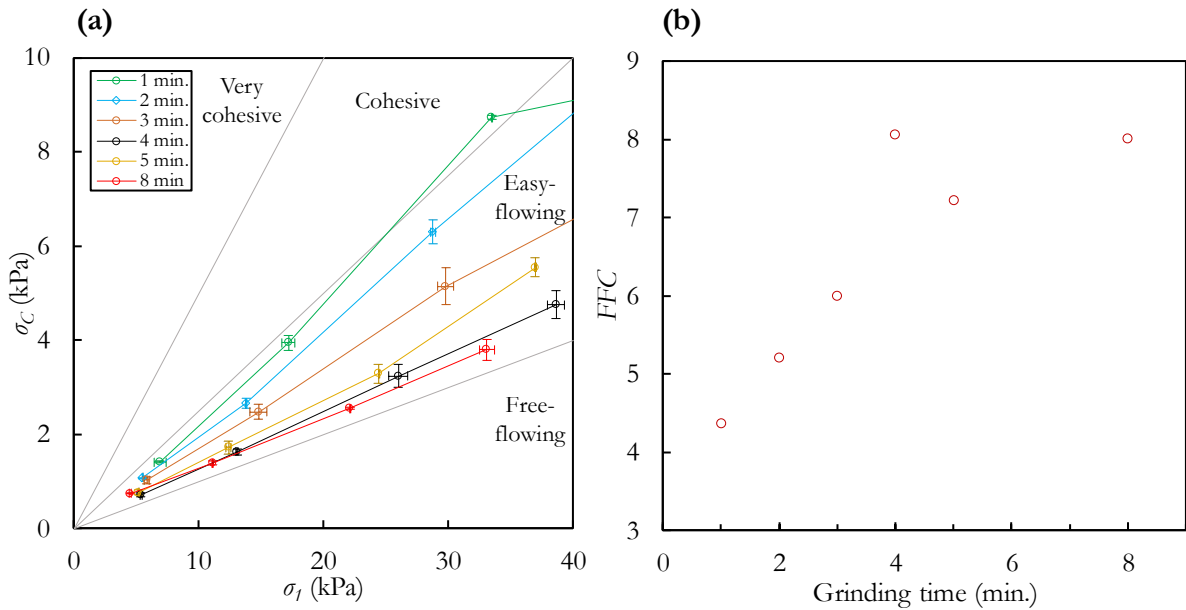


Figure 60. Flowability of torrefied biomass powder (ML = 12.2 %) at different grinding times (a) Flow functions. (b) Flowability factor at $\sigma = 5$ kPa.

Consistently, the additional flow properties reported in Table 24 follow similar trends than the flowability factor. A decrease in the cohesion and the effective angle of friction is observed with the increase of the grinding time, while a better particle stacking leads to an increase of the loose bulk density.

Table 24. Additional flow properties ($\sigma_{pre} = 5 \text{ kPa}$)

	Grinding time (min.)					
	1	2	3	4	5	8
Cohesion, C (kPa)	0.76	0.57	0.52	0.35	0.39	0.33
Effective angle of friction, φ_e (°)	52.5	47.9	47.8	45.3	44.9	42.0
Loose bulk density, ρ_b (kg/m ³)	171.9	206.2	242.8	259.5	276.3	347.0

3.4. Conclusion

This supplementary section was intended to provide additional elements for analysis of the effects of torrefaction on the flow behavior of milled biomass. Particular care was taken to produce powders having a size that guaranteed reliable and repeatable flowability measurements. For this purpose, two experimental investigations were carried out using ball-milled poplar powders. The effects of torrefaction and grinding on particle characteristics (size and shape distributions) were thoroughly discussed and used to understand flowability trends.

First, the loss of mechanical resilience of biomass due to torrefaction led to smaller and rounder particles as well as wider distributions when the torrefaction intensity (as measured by the mass loss) is increased. These particle-scale changes are expressed at the bulk scale by an improvement in the flow behavior that gradually shifts from a rather cohesive to a free-flowing nature.

Secondly, the analysis of the particle size and shape changes triggered not by different torrefaction intensities, but rather by different grinding intensities (grinding times) showed that long grinding times led to rounder, more uniform and smaller particles. Consistently, this resulted in an improved flowability with the increase of the grinding time.

Overall, the results presented in these complementary studies are consistent with those reported in the published part (section 2) of this chapter. They provide further evidence to the hypotheses regarding the concurrent effects of particle size and shape on the flow behavior of biomass materials, according to which the effects on flowability of shape changes would be preponderant over particle size changes.

Since torrefaction followed by grinding produces biomass powders composed of round and uniform particles, with the added benefit of lower energy consumption for grinding, the results presented here suggest that torrefaction should be considered as a valuable process to improve the flow behavior of powdered biomass under consolidation (some reservation remains regarding the raw sample). However, it could be necessary to correctly choose the torrefaction intensity to avoid a degraded flowability of the torrefied biomass compared to that of native biomass.

CHAPTER IV

Flowability characterization of powdered biomass in a non-consolidated – dynamic conditioning using a rotating drum

1. Preamble

In Chapter III, we provided elements to better understanding the flow properties of powdered biomass under consolidation. Using a ring shear tester, the yield loci of the powders were obtained for different degrees of normal stress approaching industrial conditions, for instance, in storage facilities. In a consolidated state, torrefaction seemed thus to have a positive influence on the flow behavior of the milled biomass.

However, in a Biomass-to-liquid industrial plant, the ground biomass can be subjected to a variety of stresses and flow conditions. Thus, for example, when the powder is conveyed, the flow conditioning can be considered as loose and dynamic, whereas in storage units the consolidated flow prevails. As granular materials can behave very differently according to the conditioning state, nothing guarantees that the conclusions drawn under a consolidated state will remain valid in a free-surface flow. Therefore, to predict the powder behavior under either of these conditions, it is necessary to use a wide array of characterization techniques.

To reflect a large range of stress states, we used a second characterization technique for assessment of biomass flowability. Therefore, the objective of this chapter is to describe the characterization of flowability of raw and torrefied biomass powders in a non-consolidated (loose) and dynamic state using a rotating drum setup. Although there is a commercial device on the market that uses avalanching analysis to characterize flowability (as seen in Chapter I), we decided to in-house develop such as device. This work included the development of an image processing procedure for collecting reliable data taking into account the cohesive nature of biomass powders.

The second part of this chapter presents the design and implementation of the rotating drum device. The procedure for image processing and data analysis is also detailed. Although avalanche analysis in rotating drums has been successfully used to characterize flowability of non-cohesive materials, few studies have been conducted on cohesive materials such as biomass. Therefore, we evaluated the relevance of different criteria for assessing flowability using a rotating drum, with a particular focus on cohesive materials. A general framework for the characterization of non-consolidated flowability applicable to both cohesive and non-cohesive materials is therefore proposed and discussed in an article format. This article is to be submitted to the *Advanced powder technology* journal.

In this article we study the flow behavior of three contrasted granular materials (glass beads, fine and coarse biomass). From the temporal evolution of a bulk motion parameter (a ‘centroid angle’), we determine a set of flowability indicators (Upper Angle of Stability, fraction of revolution to trigger events, size of avalanches, etc.). The analysis of these indicators reveals that the use of a bulk descriptor such as the change of the center of mass, instead of the commonly used indicators based on the slope of the free surface of the powder, is relevant for cohesive material study. An approach using a low rotational speed allowed us to obtain distributions of flowability descriptors that discriminate the cohesive extend of the materials tested.

In the third section of this chapter, the developed framework is used to study the flow behavior of two sieving cuts of raw and torrefied biomass presented. A comparison with the results in a consolidated state (using a ring shear tester) is carried out. We analyze the effects of particle size, shape and width of the distributions on the bulk behavior of powders and establish several correlations between particle characteristics and flow descriptors. This study is part of a work on Discrete Element Modeling of flow of biomass particles in a rotating drum described in Chapter V. Wide particle size distributions can

significantly increase computing time for DEM simulations, so a first step in this work was to reduce the polydispersity of milled powders by sieving a grinder outflow. At the same time, this makes possible to evaluate, both experimentally and numerically, the effects of two well-differentiated size distributions on the flow behavior of biomass powders. This section is presented in the form of an article submitted to *Biomass and Bioenergy* journal in early 2019.

From the results presented in this article, we verified that the fine sieved materials had always a greater cohesiveness, either in ring shear tests or in a rotating drum setup. The flowability indicators used allowed us to rank the six samples of biomass. Overall, the fine mildly torrefied powders exhibited the worst flow behavior whilst the intensively torrefied coarse sample had the best flowability. The power laws presented correlated well the particle characteristics such as shape, mean size and PSD span to the flowability indicators. These results highlight the highly interdependent influential factors that should be considered when assessing flowability of biomass materials.

2. Investigation on criteria for assessment of flowability of cohesive and non-cohesive powders using a rotating drum

John Pachón-Morales ^a, Julien Colin ^{a,b}, Joel Casalinho ^a, François Puel ^a, Patrick Perré ^{a,b}

^a LGPM, CentraleSupélec, Université Paris-Saclay, 3 rue Joliot-Curie, 91192 Gif-sur-Yvette, France

^b LGPM, CentraleSupélec, Université Paris-Saclay, SFR Condorcet FR CNRS 3417, Centre Européen de Biotechnologie et de Bioéconomie (CEBB), 3 rue des Rouges Terres, 51110 Pomacle, France

To be submitted to Advanced powder technology journal

Abstract

The assessment of flow properties of granular materials is essential for design and optimization of storage, handling and transport solutions. Rotating drum setups allow reliable characterization of powder flowability in a loose and dynamic state by analyzing avalanching behavior. A key issue is the lack of consensus on the flowability descriptors that can be obtained from this setup, particularly with respect to cohesive materials. Using an in-house rotating drum and materials representative of non-cohesive (glass-beads) and cohesive (two particle size populations of woody biomass) powders, this paper studies the relevance of different criteria to assess flowability. Rather than the slope of powder profile, a motion indicator based on the centroid of the bulk solid is found more pertinent for calculating a variety of flowability descriptors over a range of rotational speeds. While these descriptors successfully distinguish the levels of cohesion of the samples, a single speed analysis is more time-efficient as it allows distributions instead of average values to be obtained. Four relevant and complementary flowability indicators were thus selected to discriminate non-cohesive and cohesive avalanching behavior. The results presented in this work provide a general framework for flowability characterization using rotating drums, with emphasis on cohesive materials.

Keywords: Flow properties, avalanching, centroid of bulk solid, cohesion, woody biomass powder, powder characterization

2.1. Introduction

Powders and bulk solids have to be stored, conveyed or handled in nearly all industries from pharmaceuticals to agriculture. Therefore, characterization of powders in terms of their flow properties is essential to design handling strategies and equipment that will prevent flow problems.

Flowability is a difficult parameter to measure for granular materials. This is partly due to the complexity of particulate materials flow, as they can behave very differently depending on their stress and static/dynamic conditioning. Therefore, a wide variety of flow characterization methods and criteria are available in literature [137]. The most common method is the shear tester in which the force required to shear a powder under well-defined conditions is measured. Shear testers have successfully served as an engineering tool for the design of storage facilities, and work well for determining incipient failure conditions of granular materials. However, determination of flow functions can be time-consuming, and it can be difficult to achieve reproducibility for cohesive powders [137,188].

The conclusions drawn from shear tester measurements are valid for consolidated conditions, in which the powder is in a defined compacted state, which is not always the case in industrial applications. Another category of flowability characterization methods includes the analysis of powders in a loose dilated state. Some of these methods are the static and dynamic angle of repose (using rotating drum setups), the discharge time under standard conditions, the degree of fluidization and the powder aeration rates.

Rotating drum setups allow the dynamic behavior of granular materials to be investigated under low stress conditions. The potential of powder avalanching assessment to determine the effect of an added ingredient on the rheology of a powdered mixture was first investigated by Kaye et al. [156] more than one decade ago. Since then, the interest in rotating drums for flowability characterization has grown steadily. The test does not need an expensive sample preconditioning, is performed quickly and can be repeated many times without operator intervention. Moreover, rotating drums can detect changes in powder flowability brought by powder additives more accurately and with greater reproducibility than other typically-used tests such as angle-of-repose tests and bulk density measurements [185]. These advantages have propelled the use of rotating systems for analysis of powder flowability. A drawback of the method, however, is its relative dependence on the test procedure, so that the characteristics obtained are not intrinsic properties of the material. The main sources of variability in the results from rotating drum tests are the occurrence of segregation and agglomeration phenomena, the air entrainment which can lead to a state of fluidization, or the ratio of particle size to cylinder diameter [177].

While experimental research to understand the dynamic behavior of various non-cohesive materials has been successful [160,177,190,346], many challenges remain for cohesive powders, which are quite common in the agricultural and food industry. Additional research on flowability characterization of cohesive materials using rotating drums is therefore needed, especially since recent works [180,184,190,193,195,347] have highlighted the usefulness of avalanches study to evaluate the flowability of cohesive powders such as moist pharmaceutical [194] and cocoa [183] powders.

2.1.1. Criteria for assessing flowability inside a rotating drum

When using rotating drums to study powders flowability, the establishment of an appropriate set of characterization parameters, usable for both cohesive and non-cohesive materials, remains a major concern. Suitable flowability criteria should fulfill several criteria: i) to be able to distinguish between different degrees of cohesion, ii) to be relatively independent of the experiment conditions and iii) to remain simple to acquire. This last point is especially true if the criteria are intended to be used to validate Discrete Element Method (DEM) simulations, which is commonly the case in recent research on analysis of powder flow using rotating drums [348,349].

Various criteria for flowability characterization through the assessment of powder avalanche flow have been proposed in previous research. Consensus is needed to ensure that measurements made by different research teams are comparable. The most commonly used criterion is the angle formed between the linear free surface and the horizontal in a continuous regime of flow, usually called the dynamic angle of repose [350]. A lower dynamic angle of repose usually indicates an enhanced flowability. A wide range of non-cohesive free flowing materials has been studied using this criterion [165,169,177,178,350–352]. However, with cohesive materials, it can be observed that the bulk solid does not flow continuously downwards over the surface, but rather in clusters of particles, forming a very irregular surface, difficult to describe by a linear approximation.

In the study of cohesive materials, three different approaches have been identified in the literature. A first approach consists in using *average angles* of the surface to describe cohesive profiles [135,158,193,194,353] regardless of the surface irregularities. A second approach is to define *new flowability descriptors*, such as temporal or frequency indicators [179,185–187,190,196,347,354]. Finally, another method consists in defining new *bulk motion indicators* such as the powder volume, surface or centroid to follow powder dynamics [180,183,188].

When using the first approach, in which the powder surface is approximated by a linear profile, allowing an average angle to be defined, usually the Upper Angle of Stability (*UAS*) is used as flowability indicator. It corresponds to the surface's angle at the maximum position before an avalanche, and it is generally directly related to the cohesive nature of the powder. In their work on cohesive materials Quintanilla et al. [193] used the avalanche size, defined as the difference between *UAS* and *LAS* (Lower Angle of Stability) to characterize cohesiveness: the larger the average size of avalanches, the larger the material cohesion.

Within the second approach, previous studies have mostly used either strange attractor diagrams or the mean time needed to trigger an avalanche (*T* or avalanching period in seconds) as flowability indicators [179,185–187,196,347,354]. Strange attractor diagrams are plots of time of the *n*th avalanche versus the time of the *n*+1 avalanche. Although they allow a visual and simple representation of powder dynamics, they have proved to be a quite complex format for quantitative analysis [185]. The avalanching period can be a convenient and relatively reliable method of flowability assessment, usable for both cohesive and non-cohesive materials, as long as avalanches are correctly identified. Generally, a greater value of *T* at a given rotational speed indicates a higher powder cohesion since the events are less frequent. Powder having small values of avalanching period should flow freely. However, as highlighted by Soh et al. [187] *T* may not be discerning enough to differentiate between closely related materials with small differences in flow properties.

Avalanches trigger changes in the degree of aeration, densification and cohesiveness, which in turn affect the subsequent bulk avalanche behavior. As the magnitude of these changes may not be constant and reproducible, variations in *T* arise. Lavoie et al. [186] thus proposed a flowability index based on the mean standard deviation of *T* over a range of rotational speed while Soh et al. [187] introduced two flow indices calculated from the gradient of *T* and its scatter against rotational speed.

Recent research has suggested new indicators for tracking powder motion inside rotating drums. In their work with pharmaceutical powders Faqih et al. [180,188] analyzed the variance in center of mass using a load cell connected to a rotating cylinder. The variance of the signal was thus used as indicator of cohesive interparticle forces. Wojtowski et al. [183] defined a 'surface angle' based on the position of the center of mass of the bulk powder relative to the center of the drum. The *UAS* could then be extracted from the temporal evolution of the surface angle and used as flowability criterion. In the same way, Tay et al. [196] and Nalluri et al. [347] used the potential energy of the powder to follow bulk motion and defined a maximum level of potential energy before avalanche as indicator of cohesion.

Besides numerical descriptors, visual observation of the type of motion in the powder bed is also crucial to derive conclusions about powders flow [179]. In this way, some efforts to quantify the surface shape or roughness and relate it to flow behavior have recently been made [196].

The aim of this work is to study the relevance of different criteria to assess flowability using a rotating drum setup. Particular emphasis is placed on cohesive materials and, therefore, a centroid-based bulk descriptor for tracking the motion of powders is used. This work is intended to propose a set of flow

criteria that allow an accurate, simple and comprehensive description of flowability of both non-cohesive and cohesive powders when using a rotating drum system.

This paper is organized as follows: in section 2, a presentation is given of the in-house experimental device, designed to meet several constraints. In addition, an exhaustive list of the flowability criteria commonly mentioned in the literature is carried out and they are determined for three samples of non-cohesive and cohesive materials. Woody biomass powders are known to have a cohesive behavior and their characterization is especially needed nowadays within a context of energy production from renewable resources [59,235]. This is what motivated its use as representative of cohesive materials in this work. The strengths and weaknesses of the different criteria evaluated over a range of rotation speeds are discussed. A more detailed study of certain criteria at a single rotation speed is carried out using statistical distributions. Finally, by way of conclusion, some recommendations are made to accurately distinguish different levels of cohesion using avalanche assessment.

2.2. Materials and methods

2.2.1. Granular materials

Glass beads (GB) of 1 mm in diameter were used as representative of a non-cohesive material. A *Sympatec-QICPIC* morphological particle size analyzer [312] was used to obtain particle size distributions of the samples. The values of the descriptors of particles size (PSD) and shape distributions are listed in Table 25.

Biomass powders were obtained by grinding poplar chips samples using a *Retsch SM300* cutting mill with a bottom sieve of 1 mm trapezoid holes at the outlet.

In most cases, the flowability of bulk solids decreases with the reduction of particles size. For example, a correlation between a fineness parameter and flowability was found when using similar products with a particle size distribution of similar shape [141]. Therefore, two well differentiated particle size populations were studied to obtain two differentiated cohesive strengths. These samples were obtained by sieving the grinding outflow using sieve fractions between 500 μm and 710 μm for the coarse cut and between 200 μm and 315 μm for the fine cut.

Table 25. Size and shape properties of the samples.

Sample ID	Description	Sieving cut (μm)	x_{50} (μm)*	x_{90} (μm)	x_{10} (μm)	S_x	a_{50}
GB	Glass beads	-----	1 212	1 373	1 051	0.13	0.99
BC	Coarse cut of milled biomass	500-710	746	1 092	519	0.36	0.38
BF	Fine cut of milled biomass	200-315	352	513	243	0.36	0.42

*(x_{50} , x_{90} , x_{10} : 50th, 90th and 10th centiles of cumulative volume PSD distributions, respectively, S_x : distributions span= $(x_{90}-x_{10})/(x_{90}+x_{10})$, a_{50} : 50th centile of the aspect ratio distributions (a =Feret diameter min./Feret diameter max.)

2.2.2. Rotating drum and avalanching tests

Rotating drums testers are among the most practical geometries to study the flow of granular materials. Compared to powder rheometers based on shear measurements, the only stress applied on powder samples in a rotating system is induced by gravity acting on their own mass. Therefore, the rotating drum evaluates powder dynamic and free-surface flow properties [158]. The results of avalanching measurements thus represent more accurately the actual stress conditions of powders flowing on a pipe or conveying line, for example.

When studying avalanching behavior in rotating drums, it is crucial to ensure the absence of external perturbations that would alter the regular motion of powders or modify their dynamic stability. Such a problem has already been encountered in previous research [192]. Keeping this constraint in mind, an in-house experimental device was developed to characterize the dynamics of avalanches over a relatively wide range of rotational speeds. Our device was designed to fulfill several constraints:

- Smooth and regular rotation avoiding any perturbation of the intrinsic powder behavior,
- Quality of lighting allowing a rigorous and easy post-processing of images,
- Drainage of electrical charges to reduce electrostatic force effects,
- Suitable range of rotational speeds

The core piece of this device is a stainless-steel cylinder (10 cm inner diameter, 2 cm width, roughness $R_a \approx 0.4 \mu\text{m}$) clamped inside a roller bearing (*IKO NAG 4924UU*) as shown in Figure 62a-b. This design is the key-feature of our in-house device: it ensures a regular and smooth rotation, without vibrations and permits the uniform lighting required to grab high quality images. Two transparent conductive ITO (Indium-Tin oxide)-coated glass discs are used to ensure the drainage of static electricity. The drive mechanism, built between a motor (*maxon RE040G/PM52*) and the cylinder housing, deserves also attention. The transmission is made through two pulleys (one changeable) connected by a toothed belt. This configuration ensures a steady and stable rotational speed that can range between 0.01 rpm and 73 rpm for the chosen pulley-belt set.

In order to observe and record powder motion, an optical montage ensuring axial alignment between the camera and the drum was built. Images were acquired using a *Photron FASTCAM* high-speed camera (*Mini AX100*, max. resolution 1 024 x 1 024 pixels, max. framerate 4 000 fps) along with a 105 mm f2.8 *EX DG Macro OS SIGMA* lens. A framerate of 50 fps during 355 s with a resolution of 896×720 pixels was used. This configuration allows a relatively high exposure time while taking clear images even during the avalanche motion. The camera was positioned horizontally facing the frontal side of the drum, with the center of view being aligned with the drum axis. A LED lighting panel (*HSC PHLOX 24 V*) was fixed behind the drum to obtain high-contrast shadow images of the powder.

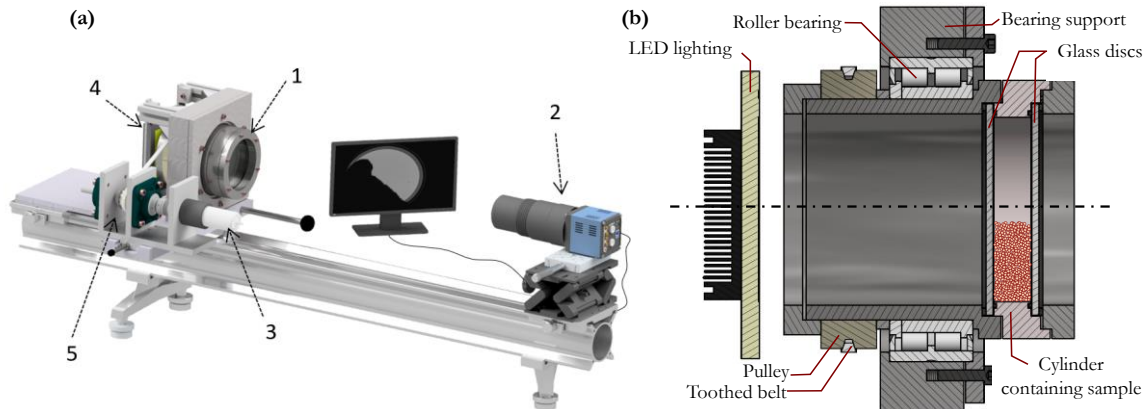


Figure 61. Rotating drum system. a. Experimental setup: 1: rotating cylinder, 2: high-speed camera, 3: motor, 4: lighting panel, 5: drive system. b. detail of the main assembly.

A filling ratio of 40 % (63 cm^3) of the cylinder volume was used. Samples were oven-dried for over 24 hours before each run. All tests were performed at ambient relative humidity (measurements ranged from 46 % to 55 %). Rotational speeds ranged between 0.05 rpm and 20 rpm.

Image post-processing was performed to obtain profiles of avalanche over time. In order to automatically process the large set of images of each test (typically over 18 000 images per test), the whole procedure was implemented using the Image Processing Toolbox™ of MATLAB platform. The condensed sequence of image processing and data analysis is presented as a flowchart in Figure 62a-b.

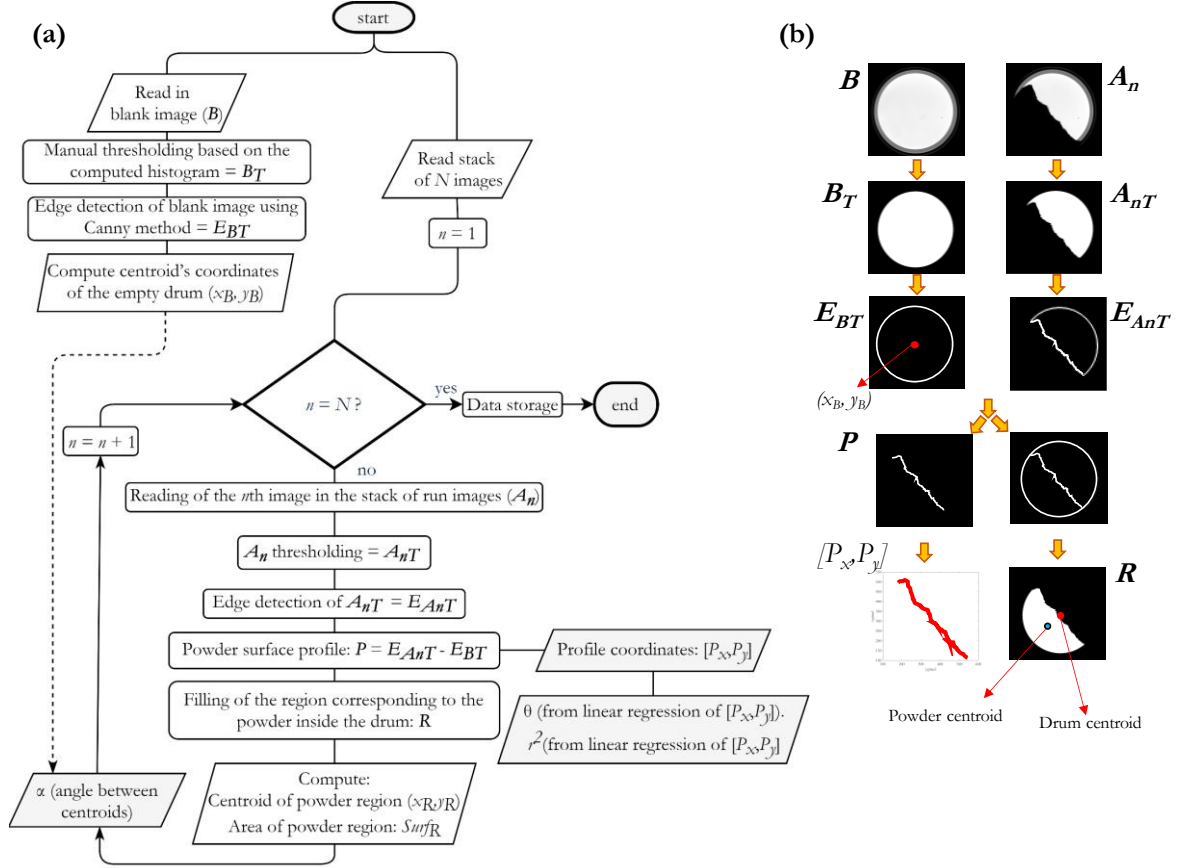


Figure 62. (a) Image processing flowchart. (b) Main stages of image processing.

The length of the surface profile in pixels was typically at least 1.5 times the magnitude of the drum diameter in pixels for a cohesive sample. The typical pixel size was ca. 0.18 mm (100 mm/542). From the coordinates of the powder surface over time, different features could be extracted. First, the average angle of surface (θ) was obtained by linear regression of the P_x versus P_y coordinates. The determination coefficient (r^2) of the linear regression was also evaluated. From the centers of mass of the core cylinder and the bulk powder at a given moment, the relative angle between them, referred as 'centroid angle' (α) was calculated. The area occupied by the powder in pixels was also determined and followed over time. Figure 63 graphically shows the definitions of θ and α angles for an example of both non-cohesive and cohesive powders.

2.2.3. Bulk motion indicator and flowability criteria

Figure 64a depicts typical sequences of the centroid angles α for the three samples studied as well as the average angle of the slope θ for the BC powder (right-side scale). For the non-cohesive glass beads, there is a succession of very regular and periodic events. These events are relatively uniform in size and time spacing. In contrast, in the case of the cohesive samples, quasi-periodic large events take place as well as small random events. Using α as motion indicator allows to easily detect the avalanching

movements, characterized by a rapid drop in the value of α . Visual observation of the images taken during the tests made it possible to verify the correspondence between events occurrence and the α variations.

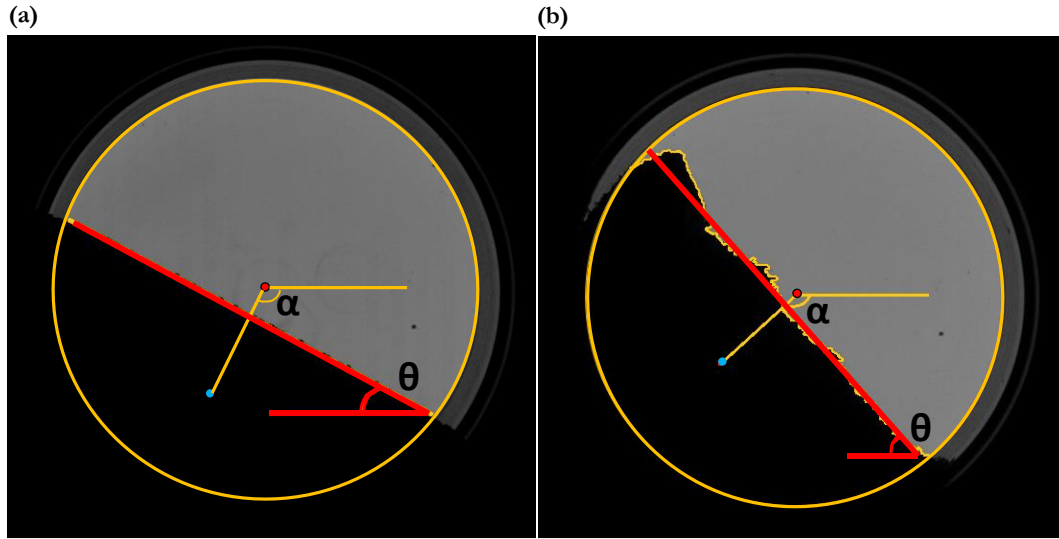


Figure 63. Definitions the average angle of surface (θ) and the centroid angle (α). (a) Non-cohesive sample (b) cohesive sample.

Values of θ presented in Figure 64a for the sample of coarse biomass (BC) show that, obviously, this representation is a poor indicator of the powder motion and flowability. Variations of θ failed to adequately show and quantify slumping events observed during rotation. This is due to the highly irregular profile developed during avalanching for cohesive materials. Indeed, the angle of the linear slope is not sensitive enough to rightly detect changes in the position of the powder or changes in the shape of the surface, which usually occurs during avalanches. The average slope is therefore misleading.

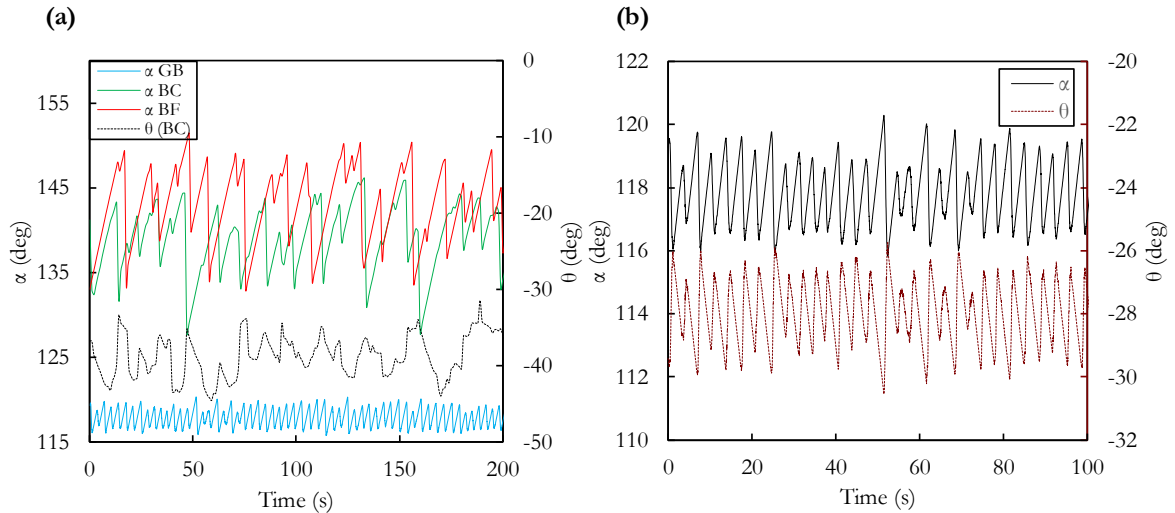


Figure 64. (a) Typical evolution of α for a non-cohesive and two cohesive samples at $\omega = 0.2$ rpm. (b) Equivalence between θ and α motion descriptors for glass-beads.

Consistently, Figure 64b proves the equivalence between α and θ motion descriptors for the non-cohesive glass beads. Thanks to the linear shape obtained for non-cohesive materials, any flow criterion determined from the α evolution in terms of maximum angles of stability, avalanches sizes and time

spacing is thus equivalent to an equivalent criterion obtained from the evolution of absolute values of θ , the latter being the most frequently reported in the literature.

As a conclusion of this section, the centroid angle α is a relevant motion indicator: equivalent to the slope angle θ in the case of non-cohesive powders, it better describes the avalanche movement in the case of cohesive powders. Consistently, in the following, a wide range of flowability descriptors is defined and used to assess the flow behavior using the centroid angle α as indicator of the bulk motion inside the drum. At first, a wide range of rotational speeds is studied and then a detailed analysis is proposed at one single speed. Indeed, previous research on flowability assessment using rotating drums has focused primarily on analysis at one rotational speed, as it is more time-efficient than evaluation over a range of rotational speeds and it led to the same relative rankings of powders flowability [173,184,196,347]. A big number of events at one single rotational speed are thus studied and then statistical distributions of values for some descriptors can be drawn.

For the analysis over a range of rotational speed the following criteria were studied:

- **Average α angle:**

Corresponds to the mean value of α for the measurement period. In general, higher average angles indicate higher cohesion between particles.

- **Upper Angle of Stability (*UAS*) and Lower Angle of Stability (*LAS*):**

The angle α varied between a maximum and a minimum value during an event. The maximum angle before an event is called *UAS* and the value of α after the event corresponds to *LAS*. A peak identification algorithm was used to find local maximum and minimum values from sequences such as the one shown in Figure 64. Angles of stability are homologous to AoR in a static measurement, so higher *UAS* generally correspond to a decreased flowability. In particular, *UAS* is an indicator of the inter-particle frictional forces that particles have to overcome to slide across over each other or to break away from the main body to create an avalanche.

- **Period between avalanches, *T*:**

It corresponds to the mean time elapsed between events in seconds. A greater avalanching period at a given speed generally indicates a bigger powder cohesion since the events are less frequent. Powder having small values of avalanching period should flow freely. For less cohesive powders, the general trend is shorter avalanche periods due to the lower energy requirement for avalanche. Powders exhibiting sharp and narrow avalanche time distributions normally are easy-flowing, and they will be preferable to work with than those displaying a plateau and broader distributions [347].

- **Duration of avalanches:**

Corresponds to the time elapsed between *UAS* and *LAS* for one event. Avalanche duration was used by Li et al. [346] for studying granular avalanches of glass beads in slumping regime ($0.01 \text{ rpm} < \omega < 0.08 \text{ rpm}$) in a quasi-2D packed drum.

- **Load (before avalanche) rate, $d\alpha / dt_{load}$:**

It corresponds to the rate of increase of the angle α during the pre-avalanche period. It is calculated from the average rate of increase of α between the end of an event (*LAS* state) and the beginning of the

next one (*UAS* state). Without slippage and movement of the powder relatively to its center of mass, it should correspond to the rotational speed.

- **Avalanche rate, $d\alpha / dt_{av}$**

Corresponds to the average decreasing rate of the centroid angle, from the *UAS* to the *LAS* angles.

- **Percentage of revolution needed to trigger an avalanche (*f*)**

Similar to the period of avalanche, it is a geometrical indicator of particles flow dynamics, likely to detect change in flow regime when the rotation speed changes. The periods of avalanche are normalized by considering the effects of the rotational speed:

$$f = \frac{\omega T}{60} 100\% \quad (49)$$

- **Size of avalanches, $\Delta\alpha$**

Corresponds to the difference between the *UAS* and *LAS*. It has previously been used to characterize avalanches of dry grains in rotating drums [162,355]. Quintanilla et al. [193] used distributions of size of avalanches to study flowability of cohesive powders, finding that, in general, the greater the cohesion, the larger the average avalanches size. The statistics of avalanche sizes has proven to provide insight into the internal dynamics of granular materials, due to its possible connection to self-organized criticality [192]. Tegzes et al. [192] showed that the avalanche size was equivalent to the potential energy difference of the sample just before and after an avalanche.

- **Cohesion index**

Defined by Lavoie et al. [186], it corresponds to the average value of the time elapsed between events (*T*) over a range of rotational speeds. It is an expression of the powder ability to absorb stress and reflects the inertia of the powder in relation to movement. The higher this value is, the more likely the powder will be to behave as an agglomerate of particles. More stable packings are then formed for particles with higher cohesion index.

$$\text{Cohesion index} = \frac{1}{n} \sum_{i=1}^n \overline{T_i} \quad (50)$$

where *n* is the total number of rotational speeds tested and $\overline{T_i}$ is the average period of avalanche at a given speed *i*. We should however notice that this index value is strongly dependent on the selected rotational speeds as it will be discussed in section 2.3.1.

- **Determination coefficient r^2**

Lee et al. [179] highlighted the importance of considering both the numerical descriptors of flow (such as the ones described before) and the visual inspection of the type of motion in the powder bed in order to draw accurate conclusions of the ease of flow. We propose to include a parameter that indicates the irregularity of the profile: the coefficient of determination r^2 calculated over the profile coordinates as:

$$r^2 = 1 - \frac{\sum_i (y_i - f_i)^2}{\sum_i (y_i - \bar{y})^2} \text{ with } 0 \leq r^2 \leq 1 \quad (51)$$

where f_i is the vertical position computed from the linear regression, \bar{y} the mean of the data and y_i the individual data point.

Powders which flow well generally pack well, thus forming a smoother surface ($r^2 \approx 1$). On the contrary, cohesive powders tend to form agglomerates when tumbling so their surfaces tend to be rougher ($r^2 < 1$).

2.3. Results and discussion

2.3.1. Analysis under a range of rotational speeds

2.3.1.1. Average α

Figure 65a shows the mean values of the centroid angle for the three samples as function of the rotational speed. Clearly, in average, values of α are always higher for cohesive samples than for the non-cohesive glass beads. This reflects the greater effective internal friction of biomass powders and may be due to both the irregular shape and a greater interparticle friction force. A clear influence of the rotational speed on the average value of α was observed for the glass beads sample. Increasing ω from 0.5 rpm to 20 rpm increased values of α by ca. 8° , which is in agreement with previous research [171]. For the cohesive samples, although the influence of ω is less pronounced, a gradual increase of the average α is also noticeable.

2.3.1.2. UAS and LAS

Regarding the Upper and Lower Angles of Stability (Figure 65b), a clear regime transition is observed for glass beads corresponding to the shifting from a slumping (episodic avalanches at low ω) to a rolling regime (continuous flow at $\omega > 1$ rpm), characteristic of non-cohesive materials [160]. This transition is not abrupt. In the episodic avalanching regime, the mass of glass beads rotates as a solid body with the drum until the pile reaches the UAS value at which a layer of beads begins to flow. The avalanche stops when the angle reaches the value of LAS . For the system studied, the values of UAS and LAS are relatively independent of the rotational speed for values of $\omega < 0.3$ rpm. In the continuous flow regime, there is a continuously flowing layer of glass beads on the surface of the rotating bulk solid and there is no further distinction between UAS and LAS values. The angle of the linear surface of the flowing layer (therefore also the centroid angle) remains relatively constant and the average value of α increases with the rotational speed. Similar results were obtained for glass beads by Wagner et al. [171]. In the case of cohesive powders, no clear flow regime transitions were identified using UAS and LAS criteria over the range of rotational speeds studied. For almost the entire range of ω , fine biomass powders had greater UAS and LAS than the coarse biomass powders, which indicates their higher cohesion. At high rotational speeds, the solid bed is lifted at a speed equivalent to the speed of the particles tumbling down the surface during an avalanche. This leads to the increase of LAS at values of $\omega > 2$ rpm and the convergence between UAS and LAS values.

2.3.1.3. Period between avalanches

Period between avalanches, T , is shown in Figure 65c as a function of the rotational speed. For the GB sample, the general trend was shorter avalanche periods due to the lower energy requirement for avalanches. Events for glass beads were launched quite frequently, which means that it was easier to trigger flow, while for the cohesive powders avalanches were triggered at a lower frequency. At a

rotational speed of 0.5 rpm, for instance, avalanches took place 2.6 and 5 times less often for coarse and fine biomass powders, respectively, than for glass beads. For all the samples, the avalanching period decreased as the inverse of the rotational speed, which is consistent with the definition of this criterion. This trend was then also found by Yang et al. [190] for cohesive lactose powders. Differences between powders behavior are significant only in the low rotational speeds range ($\omega < 2$ rpm).

Lavoie et al. suggested to assess flowability of a variety of powders [186,187] using the slope of a $T-\omega^{-1}$ graph (Figure 65d). In the present work, linear relationships between the avalanche period and the inverse of the speed fitted well the experimental data for the three samples ($r^2 > 0.98$). A different slope for each powder could be distinguished. Each slope represents the combined effect of particle size distribution, morphology, density and chemical nature, a higher slope meaning a lower flowability [186]. According to this criterion, the fine biomass powders exhibited the worse flowability, while, as expected, the glass beads had the best flowing behavior. It should be noted that expressing the avalanche period in time units leads to values that depend trivially on the rotational speed. Therefore, a more suitable analysis using the fraction of revolution to trigger events (f) is proposed hereinafter.

2.3.1.4. Duration of avalanches

Concerning the duration of avalanches (Δt), for all the powders there is a clear decreasing trend when rotational speed is increased (Figure 65e). Again, this observation is consistent with the criterion definition which involves directly the rotation speed. Values of the avalanche duration are relatively close for the three samples, so Δt might not be a discriminating criterion when used for study of materials with intermediate cohesion. In addition, this parameter alone gives a poor description of the flow. It should be analyzed together with, for instance, the avalanche size. Avalanches taking the same time but with a greater angle variation could indicate a higher flowability. In the range of $1 \text{ rpm} < \omega < 10 \text{ rpm}$, avalanches were shorter in time for the fine biomass powders, followed by the coarser powders and finally by the glass beads. A shorter avalanche duration may be the result of a higher cohesive nature because (i) during tumbles, particles tend to stick to each other and hinder flow or (ii) there is a predominance of slumping short events (cracking of particles clumps).

Another drawback of using the duration of avalanches as flowability indicator is the measurement resolution required for its precise estimation. The avalanches were often very fast compared to the time elapsed between consecutive avalanches (for instance, for the coarse biomass powders at 0.5 rpm, avalanches took place in 0.64 s whereas the avalanches period was 4.3 s). Depending on the frame rate of the image acquisition system, accurate detection of the beginning and end of avalanches will be more or less possible. Results for Δt can therefore be very sensitive to the detection of the beginning and the end of the events.

2.3.1.5. Load rate

Regarding the ‘load rate’, the results presented in Figure 65f reveal a very different behavior for the cohesive and the non-cohesive samples. A straight dotted line corresponding to the rotational speed in deg/s units has been drawn in Figure 65f as a reference. For the glass beads, at very low rotational speeds (< 0.3 rpm) the movement of the center of mass follows the rotation of the drum: between two avalanches, the powder behaves like a rigid body. When the rotational speed is increased, the glass beads develop a continuous regime and the rate of increase of the centroid angle is offset by the effect of the beads rolling down the surface slope. In other words, there is an overlap between the tumble of individual particles and the lifting of the main bulk bed. Consequently, the powder centroid does not follow the drum motion at the same rate. Over all the range of rotational speeds, load rates remained at values

under 3.5 deg/s which is considerably small compared to the rotational speed. This is not the case for the cohesive powders. Their centroid motion take place at the same rate than rotation of the drum up to ca. $\omega = 5$ rpm. Because of their cohesive character, powders are tilted as an ensemble that rotates at the same rotational speed than the drum.

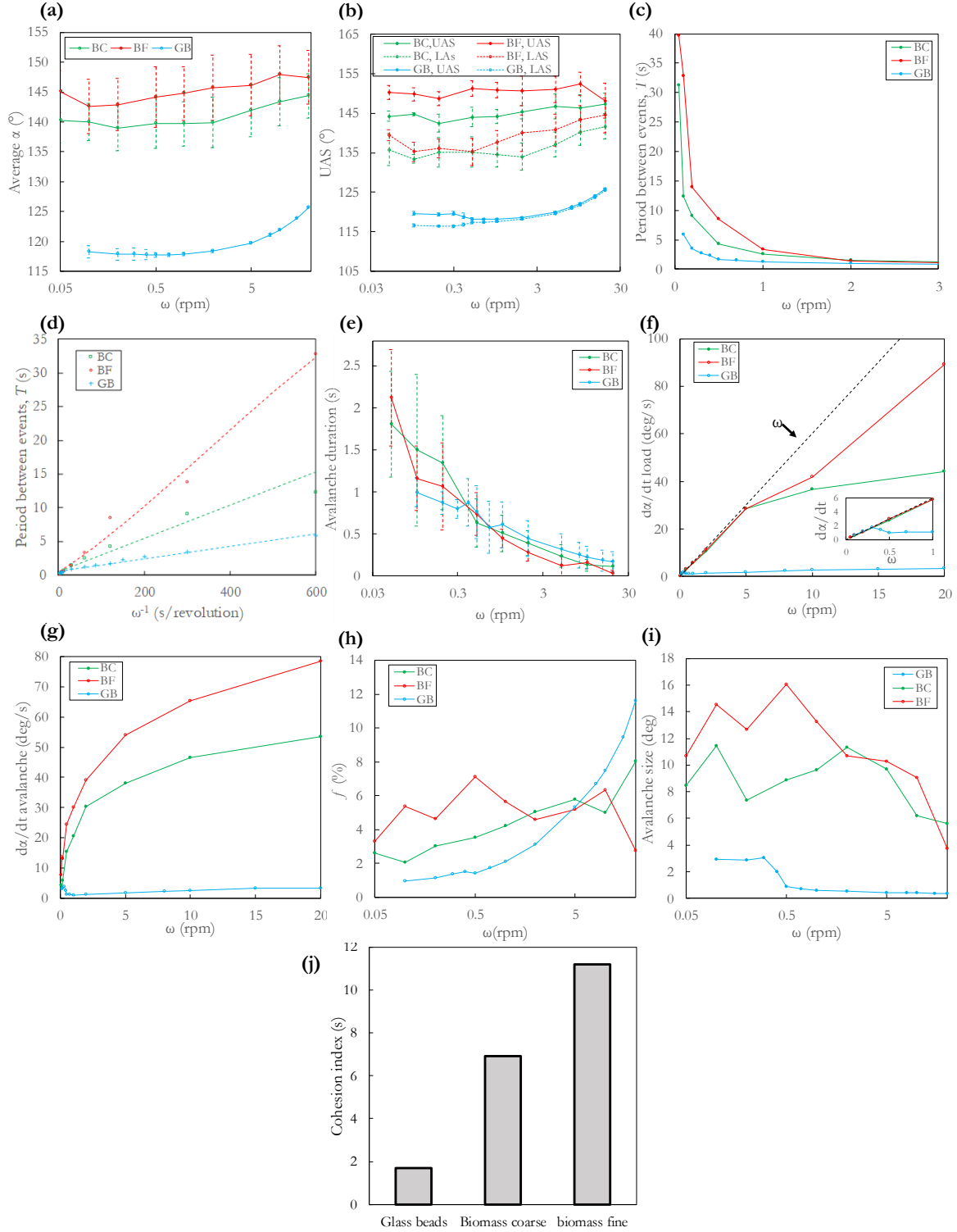


Figure 65. Descriptors used for assessing flowability of non-cohesive and cohesive powders over a range of rotational speeds. (a). Average 'centroid' angle. (b) UAS. (c) Period between events. (d) Period between events against ω^{-1} . (e) Avalanche duration. (f) Load rate. (g) Avalanche rate. (h) Fraction of revolution to trigger events. (i) Avalanche size. (j) Cohesion index.

Under 5 rpm, avalanches frequency is relatively low compared to ω , and events are discrete compared to the powder bed lifting. At rotational speeds over 5 rpm the avalanching events take place continuously during powder rotation, so the motion of the centroid is counterbalanced by the continuous avalanches. The α gradient is therefore smaller than ω . This state could be seen as a ‘continuous’ flow, that consists of an uninterrupted succession of falling clumps events. For the fine biomass, load rates remained closer to the rotational speed than for the coarse ones, indicating a greater differentiation between bed motion and avalanches during rotation. This could also be indicator of a larger cohesion. All together, these results suggest that the load rate criterion is a good candidate to discriminate non-cohesive and cohesive materials at low rotational speeds. Differentiation between different cohesive materials would be possible at relatively high rotational speeds.

2.3.1.6. *Avalanche rate*

The avalanche rate is an indicator of the speed at which particles rearrange during an event. As shown in Figure 65g, the non-cohesive glass beads were characterized by very low avalanche rates ($d\alpha/dt_{av} < 4 \text{ deg/s}$) over the entire range of rotational speed. In the case of the cohesive samples, the avalanche rate is much higher, roughly speaking, by one order of magnitude. The evolution has also a different shape, as the value continues to increase with the rotation speed (a rapid increase for $\omega < 5 \text{ rpm}$ and then a moderate increase for $\omega > 5 \text{ rpm}$). A greater avalanche rate was observed for the fine biomass powders for all values of rotational speed. This is the effect of the faster and greater variations of the centroid position produced by the tumble of particle clumps during avalanches (slumping). This type of event is prevalent in the case of very cohesive materials. For coarse biomass powders, although slumping events are also present, particles also slide over the surface of the main powder bed, resulting in a more gradual variation of the centroid position during avalanches.

2.3.1.7. *f factor: fraction of revolution needed to trigger an avalanche*

The analysis of avalanching dynamics based on fractions of revolution instead of on time interval (or period T) is proposed here (Figure 65h) as it allows the results to be normalized with respect to ω . The effects of the increase in centrifugal force are thus better highlighted. In general, cohesive powders require a larger fraction of revolution to trigger avalanches, for $\omega < 5 \text{ rpm}$. For instance, at 0.5 rpm, in average, more than 7 % of revolution (i. e. 25.2°) are required to trigger events for BF powders, 3.5 % of revolution (12°) were needed for BC samples and only 1.4 % (5°) movements triggered GB events. Figure 65h shows that, for the non-cohesive sample, the fraction of revolution required to trigger events increases uniformly. Increasing rotational speed enhances the centrifugal effect on the bed of powder and therefore the adhesion of particles to the drum wall. Avalanches are thus hindered and flowability reduced. This trend cannot be observed when using the avalanche frequency criteria (Figure 65c). Analysis based on f is therefore preferred because it better reflects powder dynamics than a time based-criterion (such as T) that is intrinsically dependent on ω . For both BC and GB samples, f increased when increasing the rotational speed while no clear trend was observed for BF powders. Although the values of f were generally the highest for BF samples, at $\omega > 5 \text{ rpm}$, events for cohesive samples were triggered at lower revolution fractions than for non-cohesive powders.

2.3.1.8. *Avalanches size UAS-LAS*

As shown in Figure 65i, except for 2 rpm and 20 rpm values, avalanche size is globally greater for the fine biomass samples, followed by BC powders and finally GB (respectively 16° , 8.9° and only 0.9° at 0.5 rpm). The is probably due to the higher tendency of the most cohesive materials to form clumps

of particles that significantly alter the centroid position before and after events when tumbling. Over 0.3 rpm, glass beads flow in a continuous rolling regime so the avalanche size is almost negligible.

Avalanche size tends to decrease with rotational speed for the cohesive powders. This could mainly be due to an overpassing of the particles avalanching rate by the movement of the drum: when particles tumble down and reach the lower stability state the bulk solid has already been lifted a bit by the drum. This reduces differences between UAS and LAS . In addition, since α evolution is highly affected by several types of motion happening simultaneously (tumbling of particles and lifting of the main bulk solid by the rotation movement) at high rotational speeds, distinction of individual avalanches becomes less precise and the differences between powder behaviors are also narrower.

2.3.1.9. Cohesion index

As expected, fine biomass particles have a higher cohesion index, followed by the coarse ones and lastly the glass beads (Figure 65j). Cohesion index values indicate that the cohesive strength of BF powders is 1.6 times greater than BC powders and 6.6 times higher than GB. Despite a classification of the powders flowability in accordance with other flow indicators, the use of cohesion index presents several drawbacks for its wide application. In addition to the fact that the cohesion index is not an absolute criterion since it depends on the range of rotational speeds selected, the limitations previously described concerning time-based indicators obviously also apply to the cohesion index. Experimental conditions should therefore always be mentioned when comparing different data.

Overall, all of the afore-analyzed results confirm the cohesive nature of biomass powders. Fine sieving cuts were almost systematically found to have the worst flow behavior. Indeed, with increasing fineness, the interparticle attractive forces increase in comparison to the force of gravity. This leads to the formation of stable arches that produce a heterogeneous structure characterized by the presence of large internal voids and an increased cohesion. It is important to note that the data acquisition and analysis required to assess flowability over a range of rotational speed and for several samples can be relatively time-consuming, which reduces the practical value of rotating drum tests. A single-speed experimental approach is therefore presented hereafter.

2.3.2. Analysis under a single rotational speed ($\omega = 0.5$ rpm)

Avalanching behavior, particularly in the case of cohesive powders, is the result of a random and chaotic reorganization of particles in the bulk material. A characterization based on a relatively large number of events is therefore necessary to draw statistically sound conclusions about powders flow behavior. Depending on powders flowability, obtaining and analyzing a large number of events may be time consuming. Overall, from the results presented above, the same qualitative ranking of flowability was observed over the entire range of speeds analyzed for most of the flowability descriptors. A single rotational speed analysis could therefore provide a faster overview and flowability classification of several granular materials. With a single speed analysis, the time required for testing is reduced and, therefore, tests can be performed over a longer period of time. This allows the criteria to be analyzed in terms of distributions rather than in terms of average values.

Besides r^2 , three descriptors were studied here as they can convey complementary information about powders flow: UAS , f and $\Delta\alpha$ distributions. The use of these three descriptors together makes it possible to clearly distinguish the behavior of the three materials studied and thus reduces the risk of producing 'false equivalents' for two different powders.

A rotational speed of 0.5 rpm was selected as it was a good trade-off between (i) having enough number of events to represent data in the form of a statistical distribution and (ii) being able to accurately identify each event and to avoid overlapping of particles tumbling and bulk rotation at the same rates (which typically occurs at high speeds). The speed of the drum is therefore slow enough to allow individual avalanches to occur independently of each other.

2.3.2.1. UAS , f and avalanches size distributions

The distributions of the flowability indicators shown in Figure 66 exhibit several interesting features. The right-most curves correspond systematically to the BF sample, the most cohesive material. Due to the similar nature of the cohesive samples BF and BC, their distributions are closer to each other than those of the GB samples. As expected, the width of the distributions is higher for cohesive materials than for glass beads, showing a higher dispersion and irregularity of the descriptors values around a mid-value (already noticeable in Figure 64a).

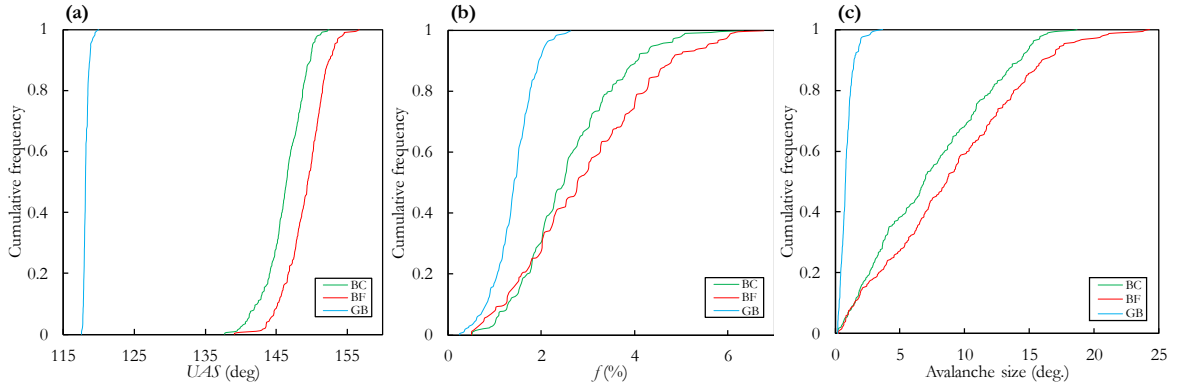


Figure 66. Flowability descriptors distributions for $\omega=0.5\text{rpm}$. (a) Upper Angle of Stability. (b) Fraction of revolution needed to trigger avalanches. (c) Avalanches size.

Quantitatively, the average value of the distributions, as well as their width (as measured by a span ratio) could be used as indicators of flowability. Average values are obtained from the 50th centile of the cumulative distributions and the span ratio, S_p , for the descriptor ϵ is given by:

$$S_\epsilon = \frac{\epsilon_{90} - \epsilon_{10}}{\epsilon_{90} + \epsilon_{10}} \quad (52)$$

where ϵ_{90} and ϵ_{10} are the 90th and 10th centiles of the cumulative ϵ distributions, respectively.

Average and span values of the cumulative distributions for the flowability indicators studied are reported in Table 26.

Regarding UAS distributions, an almost monodisperse distribution is obtained for the non-cohesive glass beads, which reflects the repeatability in terms of the Upper Angle of avalanches for this kind of materials. A dispersion in UAS values for BF and BC powders of 5.6 times and 5.2 times higher than for GB was found, respectively.

Again, in average, the most cohesive samples need a higher fraction of revolution to trigger avalanches. A lower value of f_{50} along with a lower value of S_f are obtained for glass beads, showing their better flowability.

The avalanches are larger in terms of angle variation for cohesive samples. As the cohesion increases, very broad distributions develop. Events for GB occur within a very narrow range of α (error bars in

Figure 64a), triggering variations of α before/after avalanches below 1° . In the case of the cohesive materials, and because of the slump of particles clumps, avalanches generate a high α variation which is greater for the most cohesive material and can reach up to 20 degrees. Distribution span shows that a large avalanches size scatter over a wide range of values for cohesive materials, illustrating the irregularity of the avalanching behavior.

Table 26. Synthetic values from flowability descriptors distributions.

Sample	UAS_{10}	UAS_{90}	UAS_{50}	S_{UAS}	f_{10}	f_{90}	f_{50}	S_f	$\Delta\alpha_{10}$	$\Delta\alpha_{90}$	$\Delta\alpha_{50}$	$S_{\Delta\alpha}$
GB	117.8	118.7	118.1	0.0038	0.80	1.94	1.41	0.42	0.32	1.47	0.8	0.64
BC	144.2	150.0	147.7	0.0197	1.27	4.05	2.48	0.52	1.55	14.4	6.8	0.80
BF	146.4	152.8	149.4	0.0214	1.19	4.78	2.77	0.60	1.48	16.0	8.6	0.83

UAS , f and $\Delta\alpha$ average values and spans allow us to distinguish between a cohesive and a non-cohesive behavior and to establish a flowability ranking. Powders exhibiting the left-most and narrowest UAS , f and $\Delta\alpha$ distributions are likely to have an easy and consistent flow, and they will present less flow problems when flowing in a non-consolidated state.

2.3.2.2. Analysis of regularity of surface profile: Mean r^2 value at $\omega=0.5\text{rpm}$

The analysis of the avalanche size can be seen as a primary indicator of the type of motion during avalanches, as a motion in cohesive clumps generally results in greater angle variations during events. We propose to complete this first insight by the spatial regularity of the avalanche surface, as quantified by the coefficient of determination r^2 . It also gives an idea of the particle rearrangement after an avalanche.

In the case of non-cohesive samples, the grains roll freely during events and the avalanching dynamics is dominated by the propagation of shear fronts over the free surface. These events form nearly flat and smooth surfaces, resulting in values of r^2 very close to 1 (Figure 67a) at 0.5 rpm. On the contrary, for cohesive materials, the grains tend to stick together and form clumps, preventing free rolling of particles. There is a strong interaction between the shape of the surface and the formation of the clusters. Big irregularities over the surface act as trigger points for slumping events. Steep, rugged and usually concave surfaces are thus formed. This leads to values of $r^2 < 1$ that vary greatly during events. The profiles for the BF samples were rougher than for BC powders and higher variations of r^2 during avalanches were also observed (Figure 67a-b). The r^2 criterion allowed not only to discriminate non-cohesive and cohesive materials but also differentiate between different cohesion levels.

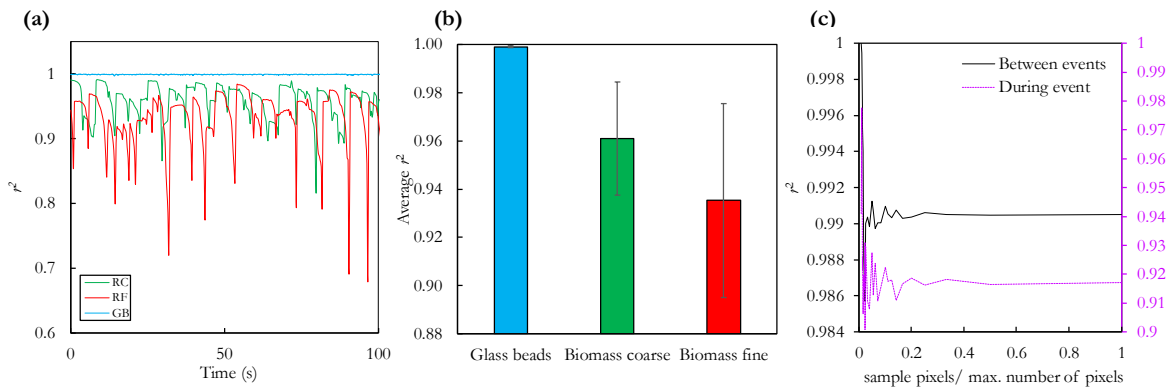


Figure 67. Flow descriptor for the irregularity of surface profile (r^2). (a) r^2 evolution over 100 s of test. (b) average r^2 values for the three samples studied. (c) effect of the number of sampling pixels on r^2 value for the BC sample.

Figure 67c shows the effect of the number of sample points taken over the profile to determine r^2 for two images of tests for sample BC, one taken between two events (solid line) and the other during an event (dotted line). While the values of r^2 obviously depended on the image (i.e. on the powder profile at a given time), the criterion is stable and independent of the number of sampling points as soon as 20 % the resolution used here is used. This correspond to a sampling frequency equal to $D/3.3$, where D is the drum diameter in pixels.

As a conclusion of this section, an analysis at constant low rotational speed was advantageous to quickly and quantitatively assess flowability. Indeed, an analysis at one speed is preferred as it makes possible, for the same experimental time and with lower sample handling, to work in terms of distributions rather than averaged values. The four criteria used here (UAS , f , $\Delta\alpha$ and r^2) clearly distinguished between cohesive and non-cohesive behavior (distributions for cohesive materials were significantly shifted to the right and r^2 evolutions were undoubtedly different). UAS and $\Delta\alpha$ are rather geometrical indicators of the stability of the powder while f is defined from a normalized temporal indicator (period to events). Finally, r^2 characterizes the regularity of the powders profiles and gives an idea of the type of motion during events.

Although the same flowability ranking could be established using any of the four indicators, so one could think that one single criteria may suffice, a complete assessment of flowability requires the use of several criteria. This also reduces the risk of producing false-equivalent samples in terms of flow behavior. Indeed, given the relatively small variety of degrees of cohesion studied in this work, caution should be exercised by using several criteria. Future work will explore materials with intermediate cohesion or nature in order to better assess the discriminating capacity of the flowability criteria from rotating drum tests.

2.4. Conclusion

This paper investigated the flowability assessment of non-cohesive and cohesive samples using a rotating drum setup, a device relevant to analyze powder flowability in a non-consolidated state and dynamic flow. An in-house rotating drum was designed and built to accurately assess the flow behavior of three contrasted powders (glass beads, fine biomass and coarse biomass). Experiments were performed over a range of rotational speeds.

From the temporal evolution of the ‘centroid angle’, several criteria, either proposed in literature or by the authors, were extracted. The analysis of these criteria highlighted the relevance of using a bulk descriptor such as the change of the center of mass, instead of the commonly used surface angle, for characterizing motion of non-cohesive and cohesive materials.

An approach using a single rotational speed was also presented using distributions, instead of average values, for four flowability descriptors: the Upper Angle of Stability (UAS), the fraction of revolution needed for triggering events (f), the size of avalanches ($\Delta\alpha$) and the determination coefficient (r^2). These descriptors were able to clearly discriminate among the cohesive extent of the samples. These flowability descriptors are complementary and should be considered simultaneously to obtain a more accurate conclusion about flow properties.

Acknowledgments

The authors would like to gratefully acknowledge the support of the French Ministry of Higher Education as well as the French Poplar Council (CNP) and the Huberlant sawmill (Cormicy, France) for kindly providing the wood used in this work.

3. Flowability characterization of torrefied biomass powders: static and dynamic testing

John Pachón-Morales ^a, Julien Colin ^{a,b}, Joel Casalinho ^a, Patrick Perré ^{a,b}, François Puel ^a

^a LGPM, CentraleSupélec, Université Paris-Saclay, 3 rue Joliot-Curie, 91192 Gif-sur-Yvette, France

^b LGPM, CentraleSupélec, Université Paris-Saclay, SFR Condorcet FR CNRS 3417, Centre Européen de Biotechnologie et de Bioéconomie (CEBB), 3 rue des Rouges Terres, 51110 Pomacle, France

Submitted to *Biomass and bioenergy*

Abstract

In a context of thermochemical valorization of biomass feedstock, the assessment of biomass powder flowability is essential for designing feeding, storage and handling systems. Biomass valorization processes require powders to be handled under consolidated and static conditions (e. g. storage facilities) or in a free-surface dynamic regime of flow (e. g. feeding systems), which necessitates characterization under different conditions. This paper evaluates the flow properties of two size populations of raw, mildly and intensively torrefied poplar powders using shear tests and avalanching behavior in a rotating drum setup. Size and shape descriptors show that particle size distribution and particle morphology of the six samples are the result of the coupled effects of the torrefaction intensity and the sieving stage. According to shear tests, although flowability trends are stress-dependent, coarse powders have better flow properties. A flowability ranking is established based on the parameters extracted from the dynamics of flow inside a rotating drum (tendency to form clumps of particles, Upper Angle of Stability, irregularity of the avalanche profile, fraction of revolution for avalanche). The fine mildly torrefied powders exhibited the most cohesive dynamic flow behavior. The relationship between the macroscopic flow parameters obtained from both characterization techniques and the powder characteristics (particle mean size, shape and polydispersity) is discussed through adjusted correlations.

Keywords: Ring shear tester, rotating drum, torrefaction, flow properties, cohesion, woody biomass

3.1. Introduction

Thermochemical conversion of lignocellulosic biomass through gasification is a promising alternative for reducing fossil fuels consumption. Recent studies have shown the attractiveness of entrained flow reactors for the gasification of biomass. This technology is commercially available on large scale (for coal and liquid fuels) and yield the maximum efficiency from biomass to syngas [90]. Short residence times involved in entrained flow gasification demand sub-millimeter sized feedstock to optimize fuel injection into the gasifier and to increase chemical reactivity. Optimal performance of gasifiers requires feeding rates to be stable and steady which could be particularly difficult to achieve for biomass feedstocks given their fibrous, flaky and cohesive behavior. Flow fluctuations, bridging and blockage of biomass particles in feeding systems of gasifiers are indeed common industrial problems that can trigger temperature excursions and fluctuations of the fuel gas constituents [126,129].

The key cause of many handling problems is a lack of holistic and meaningful bulk characterization at the earliest stages of equipment design. To facilitate a basis for the design of trouble-free handling, storage and transportation systems for powdered biomass, flowability characterization under different flow conditions is essential. The issues encountered due to poor powder flowability can occur under a

range of flow and stress conditions: static or dynamic, compacted or in a loose packing. For instance, powders storage in silos can be considered as a static and compacted configuration while problems involving fluidization, pneumatic or mechanical transportation would involve rather dynamic, free-surface and loose packing conditions. Due to the complexity of granular materials linked partially to the variety of conditioning states, any simple and single method cannot fully characterize flow behavior. Shear tests and avalanching study in rotating drums are two flowability characterization methods representative of a compacted and quasi-static state and a dynamic free-surface state, respectively.

Although shear testing is often referred as a relatively time-consuming method [137], it is the most frequently used to characterize powder flow under consolidation. This method provides the powder yield loci from which cohesion, yield strength, internal friction, and flow functions can be determined [143]. These properties are useful for design of storage facilities or feeding systems. Though scarce, recent research regarding biomass flowability measurements using shear testers includes the work by Miccio et al. [202], who found that flow properties of particulate biomass (ground olive husk and sawdust) could be reliably measured by shear cells when the particle size is below 2 mm. In their work with comminuted poplar and corn stover ($d_p < 5$ mm), Gil. et al [206] found that lower particle sizes improved flow behavior due to the lower presence of hooked particles, while higher moisture content led to higher tendency to form arches or ratholes. Guo et al. [356] showed that the addition of biomass (rice straw and sawdust) into coal had no effect on cohesion strength but significantly increased internal friction. Additional research using agricultural ground materials includes the works by Littlefield et al. [357] for ground pecan shells and Chevanan et al. [203] and Crawford et al. [147] for pre-treated and wet corn stover.

Rotating drums allows the dynamic behavior of granular materials to be studied under low stress conditions. The test does not need an expensive sample preconditioning, is performed quickly and can be repeated many times without operator intervention. Moreover, rotating drums can detect changes in powder flowability brought by powder additives more accurately and with greater reproducibility than other typically used tests such as angle-of-repose and bulk density measurements [185]. These advantages have propelled the use of rotating drum systems for analysis of powder flowability. Even if an overwhelming majority of work using rotating drums has focused on non-cohesive materials [160,177,190,346], recent research [180,184,190,193,195,347] have highlighted the usefulness of avalanches study for assessing flowability of cohesive powders such as moist pharmaceutical [194] and cocoa [183] powders. In the case of biomass materials, results from avalanching behavior have been found to be correlated to the discharge rates at the outlet of screw feeders for biomass [217]. The avalanche characterization of biomass powder, which has a recognized cohesive character, could thus provide a new insight on the dynamic free-surface flow behavior of this material.

Along with slurry or dissolved wood, torrefied powders are one of the basic forms of wood suitable for feeding of entrained flow gasifiers [89]. Biomass torrefaction is a pretreatment process that improves fuel characteristics in terms of energy density, hydrophobicity and physico-chemical stability [90]. It consists in a mild pyrolysis process carried out at temperatures ranging from 200 °C to 300 °C, under anoxic atmosphere and at relatively low particle heating rate (less than 50 °C/min). Several studies have highlighted the interest of torrefaction for increasing grindability of woody biomass so energy consumption for milling could be reduced down to 10 % of the energy needed for raw biomass [106,108,110]. Previous research suggests that torrefaction might also be of interest for improving biomass flow properties as measured by a shear tester [329] mainly because of the increase of particles circularity with torrefaction intensity.

Indeed, particle size and shape have been confirmed to have a significant influence on flow properties, in particular with regard to biomass materials. Mattson and Kofman [207] found that the most important property to explain bridging tendency of solid biomass was particle shape. Poor flow was directly related to the content of hooked or long and thin particles. Combined effects of particles size and shape on bridging tendency, yield strength and bulk density were observed Paulrud et al. for pine and spruce powders [87] and by Gil et al. for SRF poplar and corn stover [206]. Since biomass materials do not have the same composition or structure, the values of flow properties or their response to particle size or shape may vary with each material or pretreatment processes such as torrefaction.

The main aim of this work is to assess the flow behavior of raw and torrefied biomass powder using two characterization techniques representative of either a compacted or a free-surface stress state. Effects of particle properties, such as particle size and shape, on the bulk behavior of powders are also highlighted. This study is carried out as part of a work on Discrete Element Modeling of flow of biomass particles in a rotating drum conducted by the authors. Broad particle size distributions can significantly increase DEM simulations run time, so a first stage in this work consisted in reducing the polydispersity of milled powders by sieving a grinder outflow. At the same time, this makes possible to evaluate, both experimentally and numerically, the effects of two well-differentiated size distributions on the flow behavior of biomass powders.

3.2. Materials and methods

3.2.1. Biomass powder preparation

Poplar (*Populus euro-americana* 'Koster') was chosen as a representative of lignocellulosic biomass since it is a promising energy crop, namely due to its fast growth in temperate climates. In addition, the development of poplar genotypes with improved yield, higher pest resistance, increased site adaptability and easy vegetative propagation has made poplar a commercially valuable energy crop [330,331]. The poplar tree selected for this study (25 years old, basic density of $311 \pm 9 \text{ kg/m}^3$, growth ring width of 14 mm) came from a forest located in *La Snippe* valley in Auménancourt-le-Petit (France). The tree was chopped and cut in boards that were subsequently dried. Samples of $60 \times 80 \times 15 \text{ mm}^3$ were cut from the boards.

3.2.1.1. Torrefaction

A batch torrefaction furnace specifically developed in the laboratory was used to thermally treat the samples [335]. The atmosphere of a hermetically sealed *Memmert UFP400* chamber was controlled by sweeping a nitrogen stream (5 L min^{-1}) to reduce the oxygen content and thus avoid oxidation and ignition. In all cases, the oxygen level measured at the gas outlet remained below 1.5 %. A powerful fan inside the chamber ensures efficient heat transfer, either to heat-up the sample or to limit thermal overheating due to exothermic reactions. The gas temperature was measured in the vicinity of the samples using a K-thermocouple. Two treatments were carried out at 240 °C and 280 °C for 1 hour with the following protocol: (i) heating from room temperature at a rate of $10 \text{ °C} \cdot \text{min}^{-1}$ up to 100 °C (ii) plateau at 100 °C for 12 hours to remove the residual bound water (iii) heating at a rate of $10 \text{ °C} \cdot \text{min}^{-1}$ until the treatment temperature. (iv) plateau at the treatment temperature for 1 hour and (v) cooling due to thermal losses and an increased nitrogen flow into the reactor. Preliminary experiments [307] and simulations performed using a comprehensive computational code [336] were performed to ensure that the treatment duration together with the sample thickness guarantees the treatment to be quasi-uniform within the sample.

After treatment, samples were weighed to determine the mass loss (ML) due to heat treatment as follows:

$$ML (\%) = \frac{m_0 - m_t}{m_0} \cdot 100 \quad (53)$$

where, m_0 and m_t are the oven-dried mass before and after torrefaction, respectively. Mass loss is known to be a good indicator of the treatment intensity and has been successfully correlated to several properties of the treated biomass such as energy properties [100], dimensional changes [93] and flowability [102]. Mass losses of $9.6 \pm 0.8 \%$ and $24.5 \pm 3 \%$ were obtained for the samples treated at 240°C and 280°C , respectively.

3.2.1.2. Grinding and sieving

Raw and torrefied materials were ground using a *Retsch SM300* cutting mill with a bottom sieve of 1 mm trapezoid holes at the outlet. Powders obtained after grinding were sieved to obtain two well differentiated sieving cuts representative of coarse and fine particles. A vibratory sieve shaker *Retsch AS 200* at an amplitude of 60 % (1.8 mm) for 20 minutes was used along with sieves of opening 500 μm and 710 μm for the coarse cut and 200 μm and 315 μm for the fine cut.

3.2.2. Particle size and shape measurements

A *Sympatec-QICPIC* [312] morphological particle size analyzer was used to obtain biomass particle size distribution (PSD) after sieving. The values of the descriptors of particle size and shape distributions are listed in Table 27. The minimum value of the Feret diameter over all orientations of the particle is used to characterize particles size (d_p). The 50th centile of the cumulative volume distributions (dp_{50}) is the mean size descriptor of each size distribution. PSD span was calculated from values of the 90th and 10th centiles as:

$$S_x = (d_{p_{90}} - d_{p_{10}}) / (d_{p_{90}} + d_{p_{10}}) \quad (54)$$

Particle shape was characterized through two shape descriptors (i) the aspect ratio, a ($0 \leq a \leq 1$), which is defined as the ratio between the minimum and the maximum Feret diameters and (ii) the circularity ϕ ($0 \leq \phi \leq 1$), defined as the ratio of the perimeter of the equivalent circle having the same area to the perimeter of the projected area of the particle. A perfect circular projection would give $\phi = 1$ and the smaller the value of ϕ , the more irregular or rough is the particleshape. Mean values of the aspect ratio and circularity (a_{50} and ϕ_{50} , respectively) were obtained from the 50th centiles of the cumulative shape distributions, and the shape descriptors span is defined by:

$$S_\psi = (\psi_{90} - \psi_{10}) / (\psi_{90} + \psi_{10}) \quad (55)$$

where ψ_{90} and ψ_{10} correspond respectively to the 90th and 10th centiles of the ψ shape descriptor distribution, either aspect ratio or circularity.

Table 27. Powder size and shape descriptors.

Sample ID	Description	Torrefaction temperature	ML (%)	Sieving cut (μm)	x_{50} (μm)	x_{90} (μm)	x_{10} (μm)	S_x	a_{50}	S_a	Φ_{50}	S_Φ
1	Raw coarse	Untreated	0	500-710	746	1092	519	0.36	0.38	0.49	0.63	0.28
2	Raw fine	Untreated	0	200-315	352	513	243	0.36	0.42	0.53	0.59	0.34
3	ML=9.6 % coarse	240 °C	9.6	500-710	667	929	448	0.35	0.31	0.56	0.59	0.31
4	ML=9.6 % fine	240 °C	9.6	200-315	320	440	224	0.33	0.33	0.58	0.57	0.35
5	ML=24.5 % coarse	280 °C	24.5	500-710	526	862	303	0.48	0.41	0.50	0.69	0.23
6	ML=24.5 % fine	280 °C	24.5	200-315	253	370	162	0.39	0.43	0.56	0.68	0.26

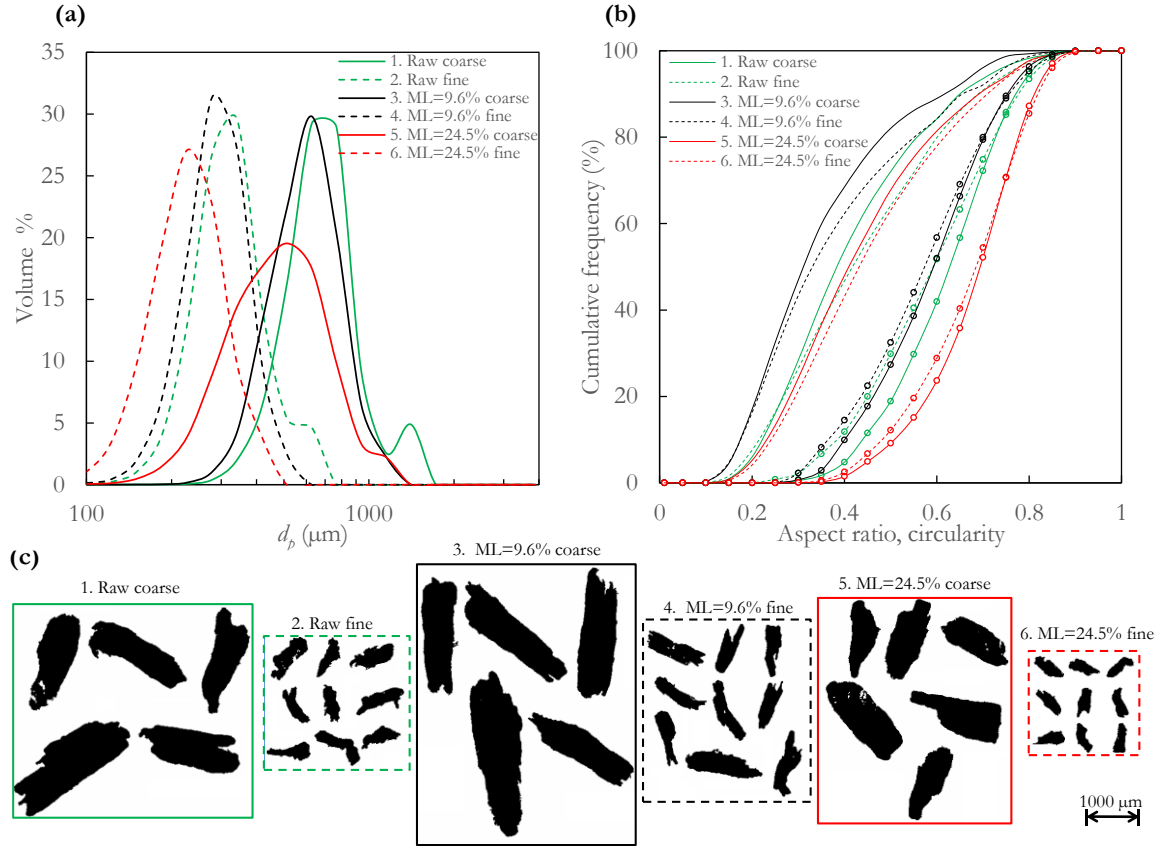


Figure 68. Biomass size and shape characteristics: (a) Particles size distribution, (b) Aspect ratio a (series without marker) and circularity Φ (series with circular marker) distributions, (c) Examples of particle shape for each sample.

Regarding particle size, data reported in Table 27 and Figure 68a show that, even though a sieving stage reduces polydispersity of the grinder outflow and created two well distinguished populations for each torrefaction intensity, the same sieving cuts do not necessarily have the same characteristics. Raw and mildly torrefied samples had relatively similar particle size while the most intensively torrefied samples had smaller particles and broader distributions. The same trend was observed for both the coarse and the fine sieving cuts. This is a consequence of the much higher brittleness of the torrefied samples at $ML = 24.5\%$ which could lead to particle breakage and fines generation during the sieving process. The fact that similar PSD were observed for raw and mildly torrefied samples seems to indicate the presence of an abrupt change of brittleness between $ML = 9.6\%$ and $ML = 24.5\%$.

Particle shape also depended on both the torrefaction intensity and the sieving cuts (Figure 68b, c). Small particles were less elongated (lower aspect ratio) but had a more irregular surface (lower circularity) than the coarse ones. Intensively torrefied powders had rounder and less elongated particles than raw and mildly torrefied samples. Samples torrefied at $ML = 9.6\%$ had the most needle-shaped and rough particles.

All the powders were oven-dried at 103 °C for at least 24 hours before the flowability tests.

3.2.3. Flowability tests

3.2.3.1. *Ring shear tester*

A RST-XS Schulze ring shear tester [143,345] was used to assess the flow properties of the biomass powders under consolidation. The ring shear tester is a widely-used device to measure flowability of powders, including unconfined yield strength (σ_c), the major principal stress of consolidation (σ_1) and the flowability factor (FFC). The standard procedure leads to results with low variability [143]. A brief overview of the theory behind these tests and some specificities related to tests on biomass powders are presented in the appendix of this section. A set of three pre-consolidation stresses (σ_{pre}), considered as representative of the stress range for industrial applications, were tested: 2, 5 and 10 kPa [36]. Three shear points (σ_{sh}) at 25, 50 and 75 % of σ_{pre} for each pre-consolidation stress were used to determine the yield locus of each sample. The yield locus curves were regressed from experimental points by a linear regression.

The unconfined yield strength governs the stress holding the material together on a free surface. It is the major principle stress that acts in a direction parallel to the free surface which supports the external forces tending to tear the surface apart [37]. The bigger its value, the higher the stress required to fail or fracture the granular material to initialize the flow. The unconfined yield strength indicates the tendency of a bulk solid to form a cohesive arch in a hopper and to form ratholes in process equipment [12]. The ratio FFC (flow function coefficient) of consolidation stress to unconfined stress ($FFC = \sigma_1/\sigma_c$) is used to quantify the flowability. In general, the larger FFC , the better the bulk solid flows. All properties obtained from the Schulze ring shear tester are usually reported as a function of the major principal stress of consolidation (σ_1).

2.3.2. *Dynamic free-surface conditioning: rotating drum experiments*

Rotating drums testers are considered one of the most practical geometry to study the flow of granular materials. Compared to powder rheometers based on shear measurements, the only stress applied on powder samples in a rotating system is induced by gravity acting on their own mass. The results of avalanching measurements better represent real stress conditions of powders flowing in a pipe or handled by a conveying screw, for example.

An in-house experimental device was developed to characterize the dynamics of avalanches of the biomass samples. The core piece is a stainless-steel cylinder (10 cm inner diameter, 2 cm width) clamped inside a roller bearing as show in the Figure 69a. This design ensures a regular and smooth rotation, without vibrations and permits the uniform lighting required to grab high quality images. Two transparent conductive ITO (Indium-Tin oxide)-coated glass discs are used to enhance drainage of static electricity. The drive mechanism, built between a motor and the cylinder housing, consists of two pulleys connected by a toothed belt. This configuration ensures a steady and stable rotational speed that can range between 0.01 rpm and 73 rpm for the chosen pulley-belt set.

Images acquisition was made using a *Photron FASTCAM* high-speed camera at a framerate of 50 fps during 355 s with a resolution of 896×720. An image post-processing was performed to obtain the powder surface profile over time. To automatically process the large set of images of each test (typically ca. 18 000 images per test), the whole procedure was implemented using the Image Processing Toolbox™ of MATLAB platform. Details on the setup, definition of the best criteria for assessing

flowability and preliminary tests on non-cohesive and cohesive materials can be found in [358]. A volume of 63 cm³ of oven-dried powder was charged in the drum, corresponding to a filling ratio of 40 %. All tests were performed at ambient humidity between 46 % and 55 %. A rotational speed of 0.5 rpm was selected as it was a good trade-off between (i) having enough number of events to represent data in the form of statistic distributions and (ii) being able to identify each event accurately and to avoid overlapping of particles tumbling and bulk rotation at the same rates (which typically occurs at high rotational speeds). This drum speed was therefore sufficiently slow to allow individual avalanches to occur independently from one another.

When using rotating drum systems to characterize powder flow, a commonly used bulk motion indicator is the angle of the air/powder interface with the horizontal [135,177,351,353]. This indicator is successful for describing motion of non-cohesive materials since a smooth and linear surface is developed at low rotational speeds. On the contrary, due to the marked irregularity of the interface profile for cohesive powders, a ‘centroid angle’ (α) was used in this work. This angle is defined as the angle between the center of gravity of the powder and the center of the drum (Figure 69b). Using α as motion indicator makes it possible to accurately detect the avalanching movements, characterized by a rapid drop in the value of α [358]. From the temporal evolution of α several flow parameters could be estimated using a peak identification algorithm to find local maximum and minimum values of α .

The angle α varied between a maximum and a minimum value during an event. The maximum angle before an event is called Upper Angle of Stability (*UAS*) and the value of α after the event corresponds to the Lower Angle of Stability (*LAS*). *UAS* is an indicator of the inter-particle frictional forces that particles have to overcome to slide across over each other or to break away from the main body to create an avalanche. Angles of stability are homologous to AoR (angle-of-repose) in a static measurement, so higher *UAS* values and wider *UAS* distributions generally correspond to a decreased flowability.

The percentage of revolution needed to trigger events (f) was also determined. It is calculated as:

$$f = \frac{\omega T}{60} 100\% \quad (56)$$

where T is the time (s) needed to trigger events and ω is the rotational speed (rpm).

A greater value of f generally indicates a bigger powder cohesion since the events are less frequent. Powder having small values of f distributions should flow freely and require lower energy to trigger flow. Powders exhibiting sharp and narrow f distributions normally are easy-flowing, and they will be preferable to work with than those displaying a plateau and broader distributions [347].

The duration of events (Δt) was evaluated from the time elapsed between *UAS* and *LAS* states. Duration of events is a good indicator of the type of phenomena taking place during avalanches and was used by Li et al. [346] for studying granular avalanches of glass beads in slumping regime (0.01 rpm < ω < 0.08 rpm) in a quasi-2D packed drum.

The mere use of flow descriptors such as *UAS* or f could lead to similar conclusions in terms of flow behavior for samples having very different surface profiles. Consequently, in order to derive an accurate conclusion of the ease of flow, the visual inspection of the type of motion in the powder bed is also important [179]. In this work, the coefficient of determination r^2 of the linear regression of the powder profile was used as a criterion to quantify of the irregularity of the interface. Powders which flow well generally pack well, thus forming a surface which is smoother. The coefficient r^2 is therefore close to 1. Cohesive powders, instead, will tend to form agglomerates when tumbling so their surfaces are expected to be rougher and more irregular, leading to values of r^2 lower than 1.

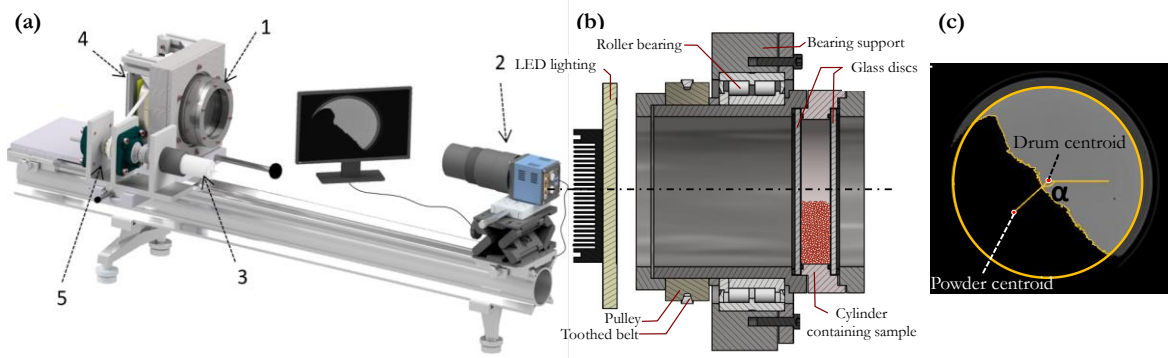


Figure 69. Rotating drum system. (a). Experimental setup: 1: rotating cylinder, 2: high-speed camera, 3: motor, 4: lighting panel, 5: drive system, (b). detail on the cylinder (c) Centroid angle (α) definition.

3.3. Results and discussion

3.3.1. Ring shear tests

The yield loci obtained for all the samples at $\sigma_{pre} = 5$ kPa are represented in Figure 70a-b for the coarse and fine sieving cuts, respectively. Overall, the yield loci of the fine samples are higher than those of the coarse powders i.e. the stress required to failure is greater. In addition, for both size populations, effects of the torrefaction intensity are also observed as the higher yield loci corresponds to the most intense thermal treatments.

Applying Mohr stress analysis to the yield locus plots, the values of the unconfined yield strength (σ_c) and the major principal stress of consolidation (σ_1) were obtained. From these values, the flow functions presented in Figure 71a-b were drawn.

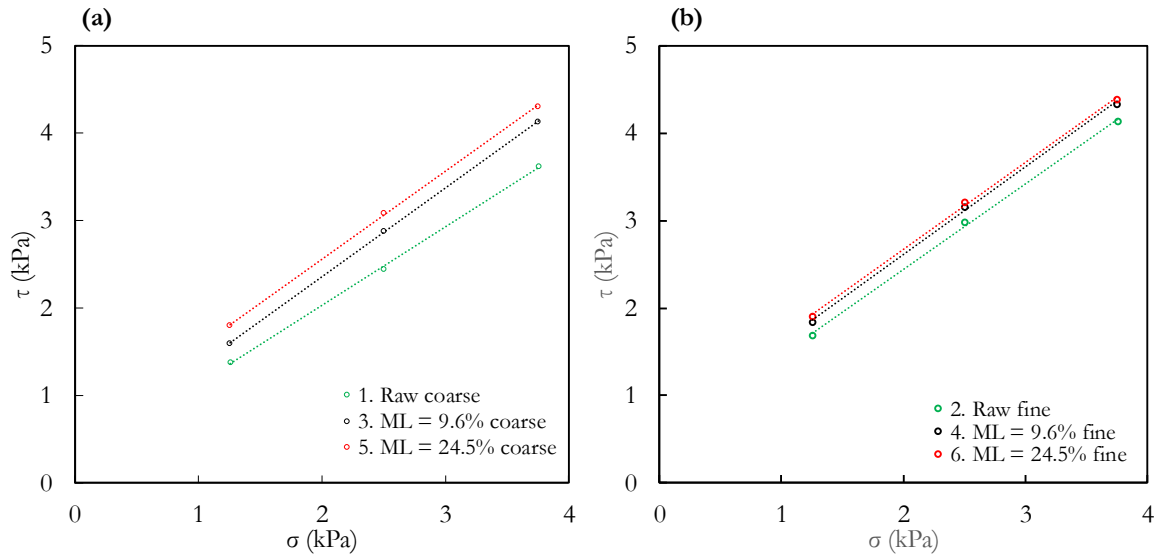


Figure 70. Yield loci at $\sigma_{pre} = 5$ kPa for (a) Coarse sieving cut and (b) Fine sieving cut.

The flow function diagram represents the strength of the material at the free surface and reveal the tendency of a granular material to form a cohesive arch inside a hopper. Flow functions are not necessarily linear, so instead of drawing linear regressions, the 3 points corresponding to the 3 preshear stresses studied were connected with smoothed curves to ease the visualization in Figure 71a-b.

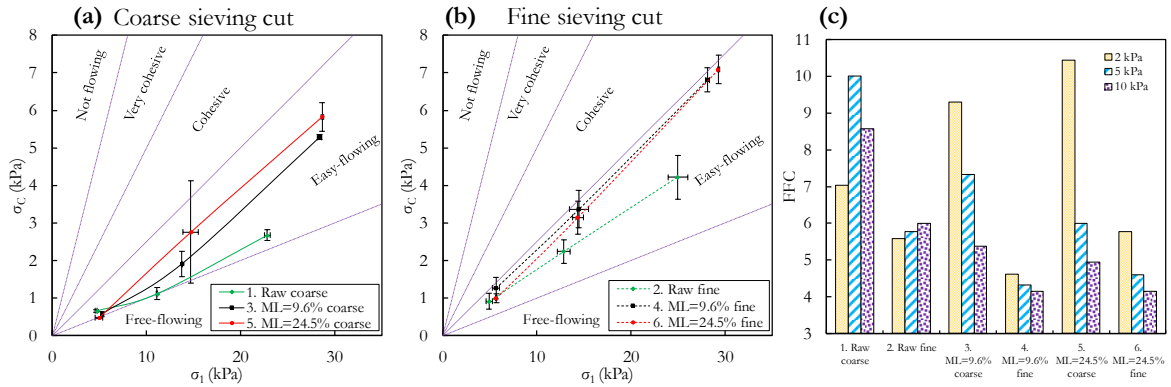


Figure 71. (a) (b). Flow functions and (c) flowability factor FFC for the biomass sieving cuts.

Although the flow functions are all located in the ‘easy-flowing’ region according to the Jenike classification [138], the raw coarse powder was almost ‘free-flowing’ and the fine torrefied samples were nearly in the ‘cohesive’ region. Some trends could therefore be identified. First, for the same torrefaction intensity, the flow functions for finer materials were always higher than those of the coarse cuts, which means that fine sieving cuts had higher cohesive strength. Second, the flow functions for the torrefied powders were located at higher values than for raw samples. In the case of the coarse sieving cut, the cohesiveness was greatest for the sample 5 ($ML = 24.5\%$) while in the case of fine samples, although both functions for the treated powders were very close, the sample 4 ($ML = 9.6\%$) was slightly more cohesive.

The curves of Figure 71a-b intersect and overlap within the range of stresses studied. In addition, since the drawn flow functions are based on a limited number of preshear stresses, it might not be appropriate to draw general conclusions or to rank flowability exclusively on the basis of flow functions diagrams. An analysis of the flowability factor FFC (Figure 71c) may be more relevant.

Indeed, the trends described above were found to be partially stress-dependent. For the same torrefaction intensity and preshear stress, fine powders had always a lower flowability. For coarse samples, at σ_{pre} of 2 kPa, flowability increased with increasing torrefaction intensity. At σ_{pre} of 5 kPa and 10 kPa this trend was reversed so raw samples flowed better. This suggests that in the case of the coarse samples, torrefaction would improve flowability only at small stresses. High stresses should be avoided when storing or discharging torrefied materials. For the fine sieving cuts, the raw powder flowed better for all consolidation stresses and there was always a minimum of flowability for the mildly torrefied sample 4.

Interestingly, results of FFC revealed a decrease in flowability with increase in consolidation for the torrefied powders, regardless of the sieving cut. This decrease was greater for coarse samples. For most common materials, flow functions always show a decreasing slope as the consolidation stress increases, so that the flowability increases with the extent of consolidation (as is the case for sample 2) [337]. The particular behavior of torrefied biomass powders was observed by Schulze [141] for hemp hurds, and it is mainly caused by the flexible nature of the plate-shaped particles. At high consolidation stresses, particles might change their orientation and adjust their shape as they ‘snuggle’ together. This leads to plastic deformations of the total bulk solid and more intensive overlap of the particles, an increase of the transferable friction force and therefore a higher yield strength. The rearrangement of particles to form a failure plan is facilitated by small particles dimensions, which may explain the smaller variation of FFC when increasing consolidation for the finer sieving cuts (samples 4 and 6).

Overall, the fine sieving cut of mildly torrefied powder (sample 4) had the lower flowability. This material will be more susceptible to problems such as bridging, agglomeration and blockage in compacted feeding systems. These results may seem in contrast with previous findings by Pachón-Morales, et al. [102,359] who stated that torrefied powders led to better flowability than raw powders. Since the samples used in this work have been sieved in order to obtain two populations of distinct sizes, the results are not fully comparable to those of previous works. Polydispersity therefore also seems to play a role and should be considered to precisely conclude on the influence of powders properties on flow behavior. Considerations on the effects of particle size, shape and polydispersity are made in section 3.3.3.

3.3.2. Dynamic free-surface conditioning: Rotating drum tests

3.3.2.1. Categorization of events

Figure 72 compares a typical sequence of the centroid angle for a non-cohesive reference material such as glass beads (diameter = 1 mm) and two examples of biomass powders (samples 1 and 5). Overall, very different flow dynamics were observed when cohesive and non-cohesive materials were studied in a rotating drum. For the non-cohesive glass beads at a speed of 0.5 rpm, a continuous flow regime was almost fully developed, so that the particles rolled uniformly over a layer of particles on the surface and only very small variations of the angle occurred [358]. On the other hand, for the cohesive biomass powders, there was a succession of: (i) ‘large’ quasi-periodic events with angles differences of up to 20°, (ii) random events with variations in α from less than one to a few degrees (‘small’ events). Small events were especially visible for the raw powder.

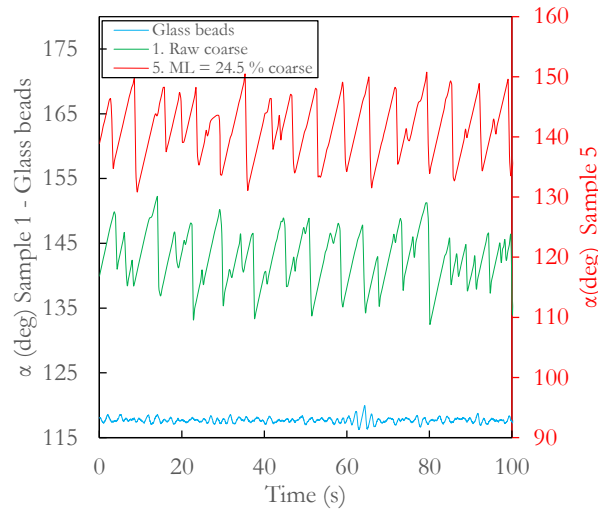


Figure 72. Typical evolution of the centroid angle for two examples of biomass powders and non-cohesive glass beads. Note that values of the sample 5 are on the right y-axis.

An analysis of the event categories that take place during powder rotation is important for assessing flowability descriptors. Indeed, two distinct event categories were detected by visual observation of the avalanches during rotation. These events are illustrated by the image sequence of the sample 1 (raw coarse) and the sample 5 ($ML = 24.5\%$ coarse) shown in Figure 73. In the case of the sample 1, during a large event, particles formed relatively stable clumps that slumped and collapsed together over the powder surface forming a very rough and irregular profile at the end of the event (Figure 73c). The curved irregularities over the surface act then as trigger points for the forthcoming collapses which will occur in a rather local region. These small events correspond more to a material failure or break than to

a uniform shear sliding and are short in time and angle variation. In Figure 72, these events can be identified by a succession of small ‘precursor’ avalanches separated by short time intervals before a large avalanche. These small precursors contribute to gradually smoothen the surface. For the smooth surface, most of its grains meet simultaneously the condition of critical equilibrium and thus a large avalanche usually closes the cycle.

For the sample 5, although slumping was also observed, during small events particles tended to uniformly slide over the entire length of the profile (Figure 73g), resulting in very smooth profiles after events (Figure 73h). During larger events, particles moved due to the shear failure within the sample and slid over the entire profile. Large events were thus predominant, as can be seen in the plot for the sample 5 in Figure 72.

The assessment of flowability descriptors should take into account the categories of events described above. If the *UAS* criterion is used, for example, the analysis should be based on the maximum angles of stability that trigger large events since they correspond to the critical equilibrium state of the whole bulk material. On the contrary, when using time-based indicators such as the period between events, considering both the precursor and the large events could give a better idea of the powder dynamics. Of course, both types of events may occur simultaneously during an avalanche which makes their identification challenging.

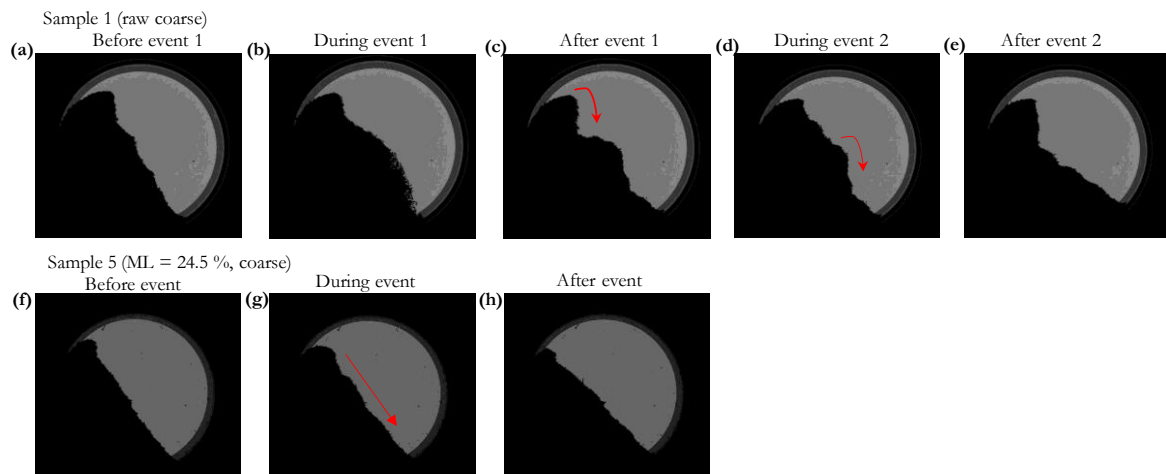


Figure 73. Flow inside the rotating drum for two biomass samples.

The duration of the events is used in this work as an indicator of their category and represented as frequency distributions in the Figure 74. Indeed, fast events are likely to correspond to clumps breaks from irregular profiles, while large sliding events occur generally over a longer period of time. Two well differentiated peaks show the occurrence of small and large events. The third peak especially noticeable for sample 5 at durations around 0.94 s corresponds to some exceptional sequences of large events.

For the coarse samples, the slumping events with durations of ca. 0.3 s are predominant for the raw and the mildly treated samples (samples 1 and 3), while the shear sliding events observed at durations around 0.65 s prevail for the intensively torrefied powder (sample 5). These results corroborate the observations shown in Figure 72. In the case of the fine powders, even though the small slumping events are dominant over the large sliding events for all the samples, the raw fine samples presented slumping events more frequently, followed by the mildly treated and finally by the intensively torrefied sample. Quantitatively, a flowability indicator ξ can be defined by:

$$\xi = \frac{\text{Number of 'long' shear events}}{\text{Number of 'short' clumping events}} \quad (57)$$

The lower the value of ξ , the more the powders tend to form stable clumps of particles that break on the free surface of the bulk material and give irregular profiles typical of cohesive powders. The values of the ξ indicator for the six biomass samples are listed in Table 28. The sample 5 stands out by its high tendency to have sliding homogeneous events, while the sample 4 is the most likely to form cohesive clusters of particles.

Table 28. Values of the flowability descriptors from a rotating drum setup biomass powders. Span values are indicated in round brackets, flowability ranking is reported in square brackets.

Sample	ξ	$UAS_{50} (S_{UAS})$ (deg)	$f_{50} (S)$ (%)	$r^2_{50} (S_{r2})$
1. Raw coarse	1.012 [II]	146.3 (2.8) [II]	5.45 (0.68) [II]	0.966 (0.030) [II]
2. Raw fine	0.712 [V]	149.1 (2.8) [IV]	6.08 (0.74) [V]	0.944 (0.046) [V]
3. $ML = 9.6$ % coarse	0.967 [IV]	148.2 (3.3) [III]	5.72 (0.66) [III]	0.956 (0.040) [III]
4. $ML = 9.6$ % fine	0.571 [VI]	153.3 (3.0) [VI]	6.83 (0.73) [VI]	0.929 (0.051) [VI]
5. $ML = 24.5$ % coarse	3.288 [I]	146.2 (3.2) [I]	5.79 (0.77) [IV]	0.991(0.014) [I]
6. $ML = 24.5$ % fine	0.994 [III]	151.1 (2.5) [V]	4.62 (0.74) [I]	0.947 (0.030) [IV]

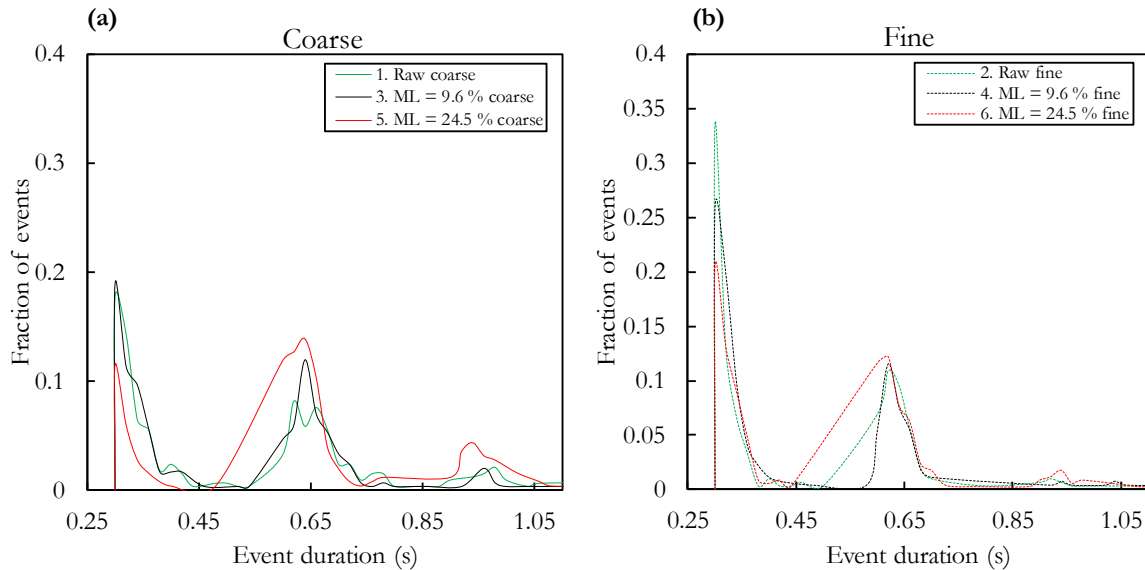


Figure 74. Events duration for coarse (a) and fine (b) biomass powders.

3.3.2.2. UAS distributions

The distributions shown in Figure 75 were calculated using the values of UAS corresponding to the large events. While non-cohesive materials would exhibit unimodal and steep cumulative distributions, an increase in cohesiveness is usually accompanied by a shift of the UAS distribution to the right. The UAS distributions for the fine sieving cuts are systematically located at higher values than for the coarse sieving cuts, indicating a better flowability for biomass powders made of coarse particles. Mildly torrefied samples have the most right-handed distributions, followed by the intensively torrefied powders and the raw samples that have the best flow behavior in terms of UAS .

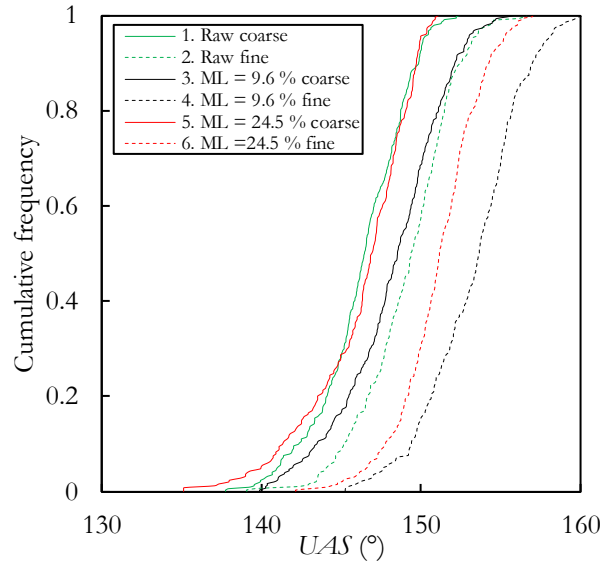


Figure 75. UAS distributions for both sieving fractions of raw, mildly and intensively torrefied samples.

The avalanching behavior of cohesive powders, and particularly the Upper Angle of Stability is highly correlated with the uniformity of flow in screw feeders [217]. Materials have to build up at the end of the screw until collapsing, so fine mildly torrefied powders are likely to have highly varying flow rates, whereas the flow would be more even for coarse materials. Values of the 50th centile (UAS_{50}) and span (S_{UAS} , eq. 52) of the UAS distributions are reported in Table 28.

3.3.2.3. f distributions

The time between events (or period of avalanche) is generally used as a criterion of flowability and is commonly reported without consideration of the type of the events occurring inside the drum [179,185–187,190,196,354]. Like the period of avalanche, the fraction of revolution required to trigger events (f) is an indicator of particles flow dynamics, likely to detect changes in flow regimes when the rotation speed changes. Periods of avalanche are thus normalized by considering the effects of the rotational speed (Eq. 56). Figure 76 compares the fraction of revolution required to trigger events for the six samples when all the events are taken into account (Figure 76a) and when only the ‘large’ events are considered (Figure 76b). Overall, according to Figure 76a, sample 5 required a higher fraction of revolution to trigger events, i.e. events tend to occur less frequently than for the other powders studied, while events for sample 1 were triggered more often. These results alone would lead to the conclusion that the powder 5 has the lowest flowability. However, it is crucial to consider the categories of events described above. Indeed, even if the frequency of events is lower for sample 5, the avalanches correspond rather to large sliding events than to clump breakings, which is an indicator of a better flow behavior. Therefore, although the frequency of events or the time elapsed between events is generally considered a good indicator of flowability in rotating drum setups, the findings presented here highlight the importance of considering the visual observation of the type of motion to derive an accurate conclusion of the ease of flow. Similar conclusions were drawn by Lee et al. [179]. Figure 76b shows the fraction of revolution to trigger events when only large events are considered. Distributions are thus closer and may overlap and intersect in some regions, indicating that a similar dynamic was obtained for the samples and making it more difficult to visually establish a ranking or flowability trend. Values of the 50th centile (f_{50}) of the distributions presented in Figure 76b are reported in Table 28. The fine powders had in average greater f_{50} values for the raw and mildly torrefied samples indicating a more cohesive

behavior. In the case of the highly torrefied samples, f_{50} values indicate that events were more frequently triggered for the fine sieve cut powders.

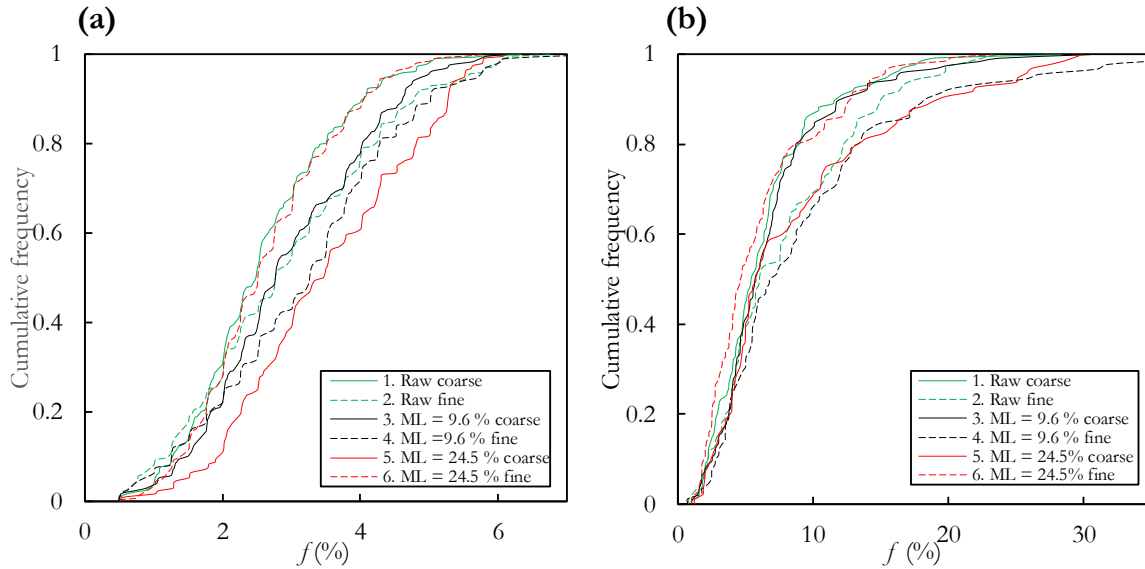


Figure 76. Distributions of the fraction of revolution required to trigger events. (a) all the events. (b) only large events.

3.3.2.4. Irregularity of powder bed profile r^2

Figure 77a shows an example of the temporal evolution of the coefficient of determination r^2 for the sample 4 and 5 which exhibit radically different behaviors. In the case of the sample 5, due to the predominant sliding events, the powder surface was always relatively smooth, so the r^2 values are closer to 1 than in the case of the sample 4. The Figure 77b compares the cumulative distributions of r^2 for the six samples. Coarse samples had always more regular and smooth powder profiles, while fine powders had irregular and rough ones, characteristic of cohesive behavior. According to the r^2 indicator, the sample 5 has the least cohesive behavior and the lowest tendency to form clumps of particles while the sample 4 is likely to form clusters of particles that cause irregular flow. Values of the average r^2 and the span of the distributions are reported in Table 28.

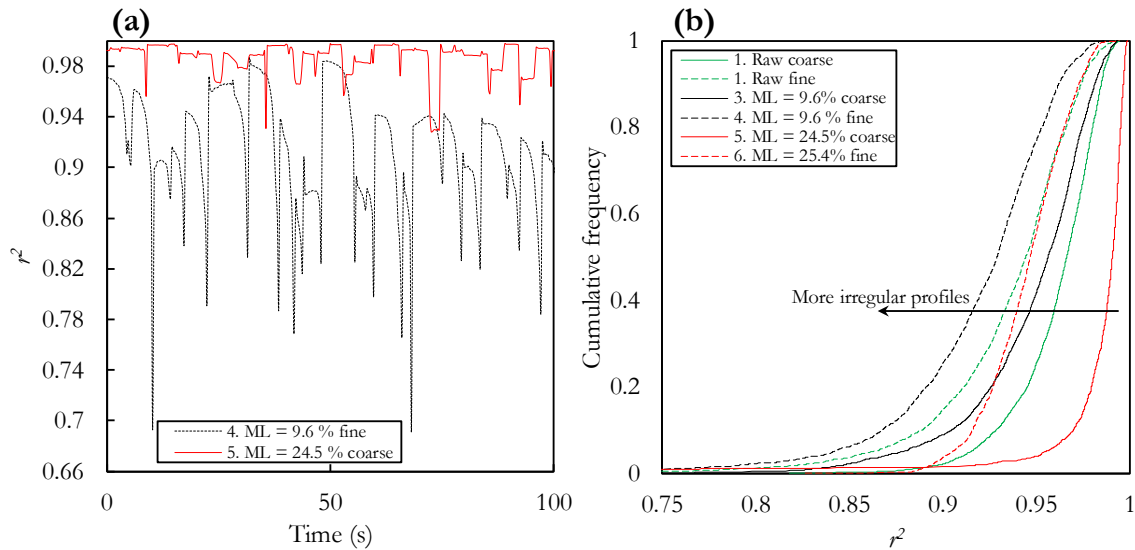


Figure 77. Coefficient of determination r^2 . a. Evolution over time for two examples of powders. b. Cumulative distributions.

A flowability ranking for the six powders was established according to the different criteria obtained from avalanching behavior analysis. This ranking is indicated in square brackets for each parameter in Table 28. Overall, the fine mildly torrefied powders (sample 4) exhibited the worst flow behavior, with a greater tendency to form clumps of particles, greater stability angles, greater f values and the most irregular powder profiles. In contrast, the intensively torrefied coarse sample (sample 5) had the best flowability according to three of the four descriptors used.

It is interesting to compare the flowability ranking that can be established from results at low consolidation stress (2 kPa) from shear tests and the one obtained from avalanching behavior using, for example, r^2 as indicator. From shear tests, from best to worst flow behavior: sample 5, 3, 1, 6, 2, 4. From rotating drum tests: sample 5, 1, 3, 6, 2, 4. Low stress and free-surface conditions led to similar rankings of flowability. Nevertheless, given the valuable insight on dynamic flow behavior that avalanching tests provided above, both static and dynamic characterization techniques should be employed to completely understand the flow properties of biomass powder and predict its behavior under different process conditions [353].

3.3.3. Discussion on the effects of particle characteristics

Experimental results shown above revealed a clearly distinct flow behavior between the samples. These differences are likely to be the result of the combined effect of the particle properties and the state of consolidation during flow. Particle properties are determined by the intensity of the torrefaction treatment but also by the sieving stage. The particle mean size and shape as well as the span of the PSD are considered to be the main particle characteristics affecting the flow properties. In view of the results presented above, several observations can be made:

- Fine materials were always found to have a greater cohesiveness, both in a consolidated and in a loose packing condition. Therefore, flowability seems to be inversely correlated to the particle size of the samples. Indeed, fine particles have a larger specific surface area for the van der Waals forces of attraction to become dominant, thus decreasing the flowability of the powder samples [324].
- Mildly torrefied samples (number 3 and 4) had an especially low flowability. These samples were also among the samples with the lowest circularity and aspect ratio (Table 27). As pointed out in previous research [102], particle shape is likely to significantly affect flow properties of raw and torrefied biomass powders. Samples with irregular shapes are thus expected to have greater cohesiveness, which means lower flowability factors, higher angles of stability and more irregular powder profiles after avalanches. More elongated and less rounded particles shapes are therefore likely to partially explain the poor flow behavior of the mildly torrefied samples.
- The span of the PSD is susceptible to play an important role on powder behavior. An attempt was made to limit its effect in this work due to the sieving stage, but the intensively torrefied samples still had relatively broad particle size distributions.

Based on these observations, the power laws of Eqs. (58) to (60) were developed to correlate particle characteristics (mean particle size, span of the size distribution and mean aspect ratio) with the average values of three flowability criteria: FFC , UAS_{50} and r_{50}^2 . Using Microsoft Excel Solver functionality, the four parameters of each flowability descriptor i (m_i , a_i , b_i , c_i) were fitted by considering the set of experimental data. Their values are listed in Table 29.

$$FFC_{10kPa} = m_{FFC} x_{50}^{a_{FFC}} \left(S_x^{b_{FFC}} \right)^{-1} a_{50}^{c_{FFC}} \quad (58)$$

$$UAS_{50} = m_{UAS} \left(x_{50}^{a_{UAS}} S_x^{b_{UAS}} a_{50}^{c_{UAS}} \right)^{-1} \quad (59)$$

$$r_{50}^2 = m_r x_{50}^{a_r} S_x^{b_r} a_{50}^{c_r} \quad (60)$$

Figure 78 shows that Eqs. (58) to (60) correctly described the relationships between powder characteristics and the flowability descriptors.

In Eq. (58) values of FFC at $\sigma_{pre} = 10$ kPa were chosen as representative of a highly consolidated state. Eq. (58) indicates that the flowability, as measured by the ring shear tester, is directly related to the mean particle size and aspect ratio, an inversely related to the PSD span. This is in agreement with the physical observations made above. As for the PSD span, Zulficar et al. [212] in their study on flow properties of biomass and coal blends established that the flow of a polydispersed bulk solids primarily depends on the strength of the fines fraction. Therefore, among powder samples having similar mean size, the one having large PSD range is likely to have stronger particle to particle cohesion, i.e. lower FFC [141]. This could explain the relatively low FFC obtained for sample 5 and 6 at high consolidation despite their rounder and less elongated shape. This is in good agreement with earlier findings on other powdered materials [201,338].

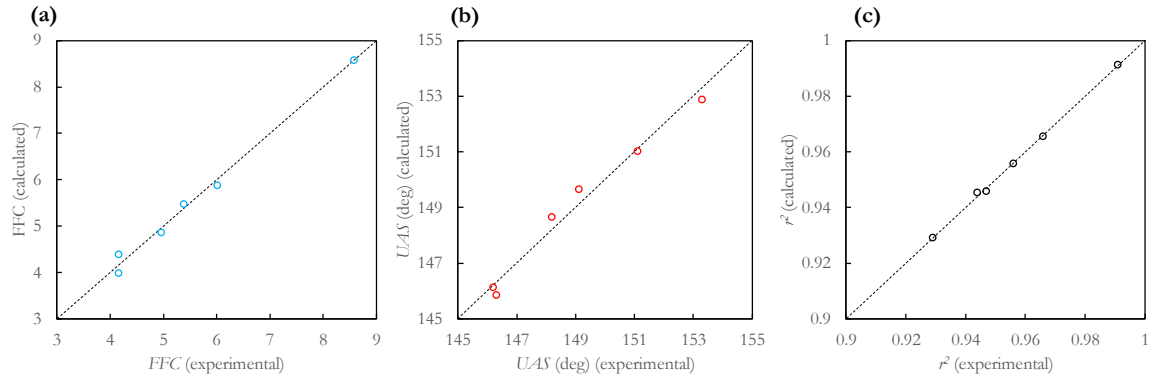


Figure 78. Experimental and calculated values of three flowability descriptors. The dotted line corresponds to the diagonal $x = y$.

Table 29. Parameters of the power law relationships (Eqs. (58) to (60)) for three flowability descriptors.

i	m_i	a_i	b_i	c_i
FFC	0.10	0.72	1.55	1.99
UAS_{50}	174.96	0.04	0.03	0.07
r_{50}^2	0.91	0.03	0.12	0.02

Regarding the flowability descriptors obtained from avalanche assessment, Eq. (59) and (60) indicate that fine, rough and needle-shaped particles, as well as powders with narrow PSD would lead to a more cohesive behavior. Interestingly, increasing the powder polydispersity seems to improve flow properties in a non-consolidated free-surface regime. The relatively good flow behavior of the intensively torrefied samples (sample 5 and 6) could therefore be the combined result of the more rounded particle shape, as well as of the higher PSD span. In a free-surface dynamic flow, fine particles in a polydispersed population might act to some extent as flow agents that will reduce the tendency of large particles to entangle and interlock.

Although the relationships of Eqs. (58) to (60) are well consistent with the experimental data, caution should be exercised with respect to the influence of other particles properties or process conditions not assessed here. Indeed, besides size and shape modifications, torrefaction is likely to alter the surface

properties of biomass powders as well. The hydrophobic nature of torrefied samples could affect flow properties through the electrostatic forces in two ways. Firstly, as the presence of bound water lowers the electrical resistivity, raw samples (which tend to capture moisture more easily) will tend to drain electrostatic charges better. Secondly, as indicated in previous research [169], the electrostatic properties of the particles are directly related to the surface functional group chemistry: hydrophobic groups accumulate greater quantities of charge than hydrophilic groups. All of this would mean that, all other parameters being the same, torrefied samples are more likely to present flow problems linked to charge build-up. Flow problems induced by accumulation of electrostatic charges are mainly to be expected in free surface flows or when the powder is in contact with non-conductive surfaces. Although a particular care was taken in the design of the rotating drum setup to limit the effect of electrostatic charges, a lower electrical drainage for torrefied powders might also be the reason for the reduced flowability of samples 3 and 4 (besides their more elongated and rough shape). For the highly torrefied samples, the positive effect on flowability of both a large PSD span and a more rounded shape might surpass the negative effect of the charge build-up.

3.4. Conclusion

This paper investigates the flow behavior of raw and torrefied biomass powders using a ring shear tester and a rotating drum setup, corresponding respectively to either a flow under consolidation or a free-surface dynamic flow. Six samples were studied: two sieving cuts (200 to 315 μm and 500 to 700 μm) for 3 torrefaction intensities (mass loss $ML = 0\%$, $ML = 9.6\%$ and $ML = 24.5\%$).

Fine materials had always a greater cohesiveness, either in ring shear tests or in a rotating drum setup. If the material is to be handled or stored at higher consolidation stresses, results from shear tests suggested that raw coarse powders are less likely to present flow problems. However, *FFC* results were found to be stress-dependent, and at low stresses intensively torrefied coarse powders flowed better.

The analysis of avalanche behavior allowed the identification of two main categories of motion. The most cohesive powders had a greater tendency to form clumps of particles that flowed badly, while shear sliding events were characteristic of good flow behavior. Four flowability criteria were determined (ξ , UAS , f and r^2) and made it possible to rank the six samples. Overall, fine mildly torrefied powders (sample 4) exhibited the worst flow behavior and the intensively torrefied coarse sample (sample 5) had the best flowability.

This work provided relationships between several flowability indicators under the two regimes of flow and particle characteristics such as shape, mean size and the PSD span. The power laws given fitted well the experimental data and corresponded to the expected physical behavior and observations of previous research. These results highlighted the multivariate and highly interdependent effects that should be considered when assessing flowability of biomass materials.

Acknowledgments

The authors would like to gratefully acknowledge the support of the French Ministry of Higher Education as well as the French Poplar Council (CNP) and the Huberlant sawmill (Cormicy, France) for kindly providing the wood used in this work.

Appendix A. Flow properties measurements using shear testers

The theory involved in the use of shear testing to evaluate the flow properties of powdered materials has been described in detail in [141], but will be briefly summarized here for better understanding of the subject.

According to the standard procedure, once the shear cell with the powder sample has been prepared, the maximum normal preshear stress, σ_{pre} , is applied on the cell lid. The preshearing step is carried out up to the attainment of a steady state value of shear stress in which the frictional forces between particles are maximum with respect to the applied normal load. At this point the powder attains a well-defined and reproducible state of consolidation corresponding to the top point shown in Figure 22. This steady state often occurs when the sample volume and thus its bulk density, ρ_b , reaches a steady state value at the end of compaction [141]. After the preshearing, the direction of shear is reversed, i. e. the shear stress is reduced to zero. Then, the normal stress is reduced to a value $\sigma_{sh,1} < \sigma_{pre}$ and the sample is sheared until a peak value of shear stress, τ_{sh} is reached (incipient flow or failure) [10]. The sequence of two steps is repeated with the same σ_{pre} and increasing σ_{sh} . Finally, a verification point at $\sigma_{sh,1}$ is made. The (σ, τ) couples obtained at failure are drawn to represent the yield locus corresponding to the consolidation applied.

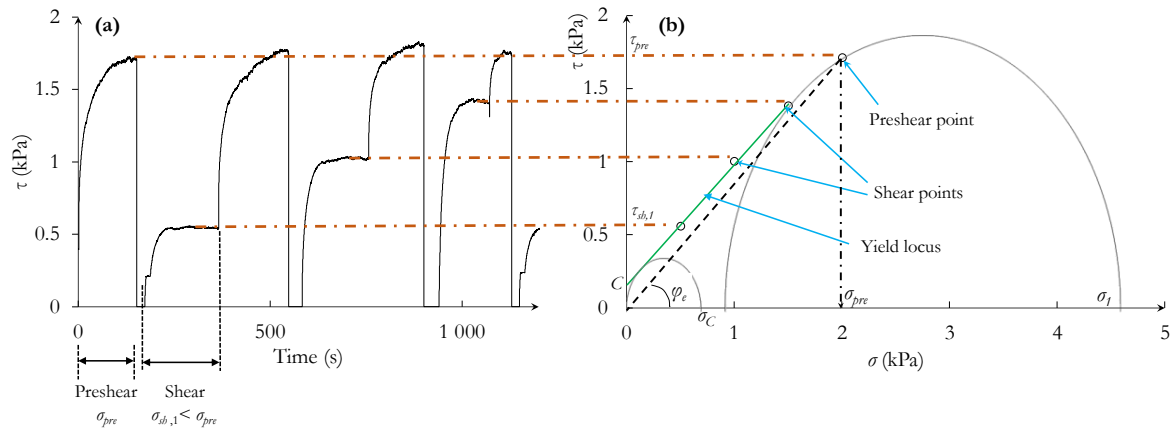


Figure 79. Shear stress testing for sample 1 at $\sigma_{pre} = 2$ kPa. a. Evolution of the shear stress over time. b. Yield locus construction and Mohr circles defining unconfined yield strength (σ_c) and consolidation stress (σ_l).

As represented in Figure 22, the Mohr circle drawn through the steady state point and tangent to the yield locus locates the major principal stress σ_l , corresponding to the consolidation applied. The unconfined yield strength (σ_c) is given by the major principal stress passing through the origin and tangent to the yield locus. In Figure 22, the dashed line passing the origin and tangent to the larger Mohr circle is the effective yield locus. Its angle of inclination with respect to the σ -axis is the effective angle of internal friction φ_e . Yield locus for a non-cohesive granular material passes through the origin, so cohesion, C , corresponds to the value of the shear stress where the yield locus intersects with the τ axis, i.e., at the normal stress $\sigma = 0$. For a full investigation of the flow properties of a bulk solid, plots such as Figure 22 should be prepared for a range of initial consolidation loads, resulting in a series of yield loci [146]. Flow function (σ_c vs. σ_l) can thus be drawn.

Appendix B. Considerations on shear testing of biomass powders

To produce accurate and reproducible yield loci using an annular shear tester, the material should reach a steady-state flow defined as plastic deformation of the bulk solid at constant shear stress and

bulk density. Fibrous, flaky materials such as biomass powders may not achieve a steady state flow during preshear. The material may also relax when the stress is relieved before the shear stage. This can be seen in Figure 80a as an increase in the lid displacement (equivalent to an increase of the bed height and decrease of the bulk density), as the shear stress is removed between the preshear and the shear stages. As a result, the material is not over-consolidated while it is sheared to failure which results in a lower yield locus and underestimation of the unconfined yield strength. Instead of a sharp maximum of τ when shearing, the curve reaches a plateau and looks like another preshear at lower consolidation stress. Miccio et al. [202] stated that the absence of peak values for the shear stress might also be due to a slight expansion of the biomass sample at the end of preshear (slight decrease of the lid displacement). However, in this study, this expansion was also present for samples that exhibited τ peaks at shear (Figure 80b). This observations are in agreement with previous research by Miccio, Falk and Barletta et al. [202,208,217] who highlighted the particular behavior during shear tests of biomass powders with respect to conventional elasto-plastic solids.

This behavior was rather observed for the tests at low σ_{pre} (i. e. 2 kPa) for the coarse sieving cuts like sample 1 shown in Figure 80a. Yield loci were therefore calculated taking steady-state values for shear stress during the shear stages when peak values were not detectable. Despite the above-mentioned peculiarities, (σ, τ) points show good repeatability and the corresponding yield loci can be linearized. Fine samples showed shear stress curves similar to those of common granular materials. An example is shown in Figure 80b (sample 6) where τ peak values during the shear stage can be clearly seen.

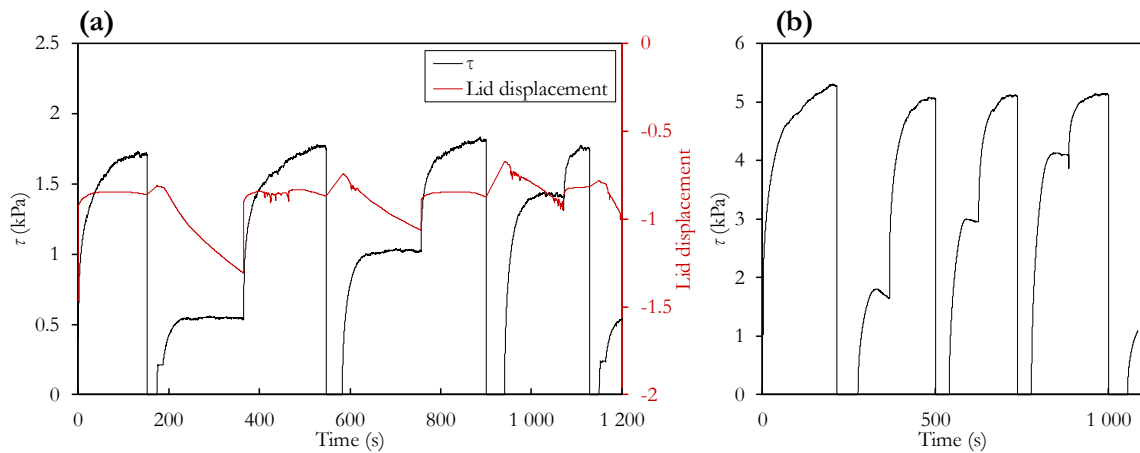


Figure 80. (a) Shear stress and lid displacement during shear test of Sample 1 at $\sigma_{pre} = 2$ kPa. (b) Shear stress evolution of Sample 6 at $\sigma_{pre} = 5$ kPa (note the presence of peak values when shearing to failure).

CHAPTER V

Towards a Discrete Element Model for
raw and torrefied milled biomass particles

1. Preamble

In addition to experimental approaches, simulations can provide valuable insight into the flow behavior of granular materials and, in particular, can be used to predict the performances of handling and transport facilities. The Discrete Element Method has recently attracted considerable interest for simulation of bulk solids, compared to traditionally-used continuum approaches which, as their name suggests, require often unrealistic assumption of a continuum system. In order to benefit from the interest and potential of DEM simulations, we opted to implement this method, which is still however under-development, to model the flow of biomass particles.

A first step towards a realistic modeling of milled biomass is to establish a particulate model that approximates the main characteristics of the biomass grains. Since simplifying approaches are required to produce a computer-efficient representation of particles, adjusting the contact force parameters by comparison with experiments is essential. This adjustment, commonly referred to as ‘DEM calibration’, can be done by trial and error tests, but this becomes unviable when several parameters are calibrated over a wide range of values. We therefore aimed at using an automated calibration procedure. Although several automated calibration frameworks have been investigated in the literature, few have dealt with materials with the characteristics of biomass powders, that is, elongated, submillimetric and cohesive. In the first article presented in this chapter (section 2), we present the application of an automatic calibration framework which uses a genetic algorithm of optimization to obtain a population of optimal DEM parameters (friction and cohesion coefficients) that match experimental bulk responses. This is carried out for the two sieving cuts of raw samples characterized in Chapter IV. This article has recently been published in *Advanced Powder Technology* journal [360].

We develop a DEM material model for biomass powders by using a coarse-grained multisphere representation of shape and size distributions of particles along with a Hertz-Mindlin-EPDS2-SJKR cohesive force model. The application of a calibration procedure that uses a NSGA-II optimization algorithm is successful in determining the coefficients of sliding friction, rolling friction and a cohesive energy density term for two biomass powder populations: a coarse sieving cut between 500 μm and 710 μm , and a fine cut between 200 and 315 μm . The results in the Section 2 of this chapter show that the calibrated contact-law parameters fit the physical responses accurately, and a validation using a ring shear tester gives promising results.

The same calibration procedure is repeated for the other four samples (two sieving cuts of two different torrefaction intensities) and the results are compared in the following part (section 3) of this chapter. Since the bulk measurements required for calibration can also provide knowledge on the flow behavior of the samples, comparative comments on the values of these bulk responses for the six samples are also given and related to the particle characteristics. This section is composed of unpublished results.

In the last part (section 4), we evaluate the capability of DEM simulations to capture the flow behavior of biomass powders in a non-consolidated dynamic condition, i.e. in a rotating drum. For this purpose, we used the calibrated particle models developed using the bulk setups described in section 2 as they are relatively simple to implement within a calibration framework (compared to the time-consuming simulations of a rotating drum setup). Due to computational time limitations, this assessment is restricted to the coarse sieving cuts of the samples studied in Chapter IV. We transpose the flowability

characterization framework set in Chapter IV for cohesive materials in rotating drums to simulations using similar image processing and data analysis strategies. The DEM simulation outputs are compared to the experimental results presented in Chapter IV and used to establish qualitative flowability rankings. These investigations are the subject of a recently submitted article to *Advanced Powder Technology* journal.

Overall, the DEM results reproduced well the experimental behavior and distinguished between the different cohesive extent of the samples. Similar distributions of several flowability indicators (Upper Angle of Stability, fraction of revolution to trigger events and size of avalanches) are thus obtained from DEM simulations and experimental results. Realistic results are thus obtained with upscaled simplified representations of particle shape that are efficient in terms of computing time. The simulation outcome shows that DEM is a relevant technique to assess flowability of biomass powders in a non-consolidated dynamic flow. This paves the way for the study of the effects of particle characteristics on bulk flow, which are briefly discussed.

2. DEM modeling for flow of cohesive lignocellulosic biomass powders: Model calibration using bulk tests

John Pachón-Morales ^a, Huy Do ^b, Julien Colin ^{b,c}, François Puel ^a, Patrick Perré ^{b,c}, Dingena Schott^b

^aLGPM, CentraleSupélec, Université Paris-Saclay, 3 rue Joliot-Curie, 91192 Gif-sur-Yvette, France

^bSection Transport Engineering and Logistics, Department Maritime & Transport Technology, Faculty of Mechanical, Maritime and Materials Engineering, Delft University of Technology, Mekelweg 2, 2628CD Delft, The Netherlands

^cLGPM, CentraleSupélec, Université Paris-Saclay, SFR Condorcet FR CNRS 3417, Centre Européen de Biotechnologie et de Bioéconomie (CEBB), 3 rue des Rouges Terres, 51110 Pomacle, France

Published in Advanced Powder Technology 30 (4) (2019) 732-750

Abstract

Biomass feeding problems greatly hinder the industrialization of entrained-flow gasification systems for production of 2nd generation biofuels. Appropriate DEM modeling could allow engineers to design solutions that overcome these flow problems. This work shows the application of a DEM calibration framework to produce a realistic, calibrated and efficient material model for lignocellulosic biomass. A coarse (500-710 μm) and a fine (200-315 μm) sieving cuts of milled poplar were used in this study. The elongated shape and the cohesive behavior were respectively simulated using a coarse-grained multisphere approach and a cohesive SJKR contact model. Measurements of three physical responses (angle-of-repose, bulk density, a retainment ratio) allowed calibration of the sliding (μ_s) and rolling friction (μ_r) coefficients and the cohesion energy density (CED). Using a statistical analysis, the most influential calibration parameters for each bulk response were identified. A Non-Dominated Sorting Genetic Algorithm was used to solve the calibration multi-objective optimization problem. Several sets of optimal solutions reproduced accurately the three physical responses and the experimental shear responses were closely reproduced by simulations for the population of coarse particles. The DEM calibration framework studied here aims to produce material models useful for assessing flow behavior and equipment interaction for biomass particles.

Keywords: Woody biomass powder, Discrete Element Method, Parameter calibration, Multi-objective optimization, Cohesion

2.1. Introduction

Entrained-flow biomass gasification appears one of the most suitable technology for production of second-generation biodiesel, mainly because of its great flexibility for treating a variety of biomass feedstock and because it generates the purest syngas [131,361]. This process requires lignocellulosic biomass to be fed in sub-millimetric powder form. However, a major technical obstacle for a cost-effective industrialization of this technology is related to the feeding, handling and transport of biomass particles. Unsteady flow and equipment blockages are linked to the fibrous and cohesive characteristics of biomass powders, as well as to their relatively low weight per unit volume. Despite the importance of

achieving trouble-free flow and the frequency of feeding problems, much more attention has been devoted typically to reactor design and operation than to biomass feeding and flow characterization [129].

Evaluation and design of biomass feeding systems need a full comprehension of the effects of biomass intrinsic properties such as particle size and shape on the flow characteristics. For this purpose, the use of numerical simulations constitutes a powerful alternative to experimental approaches, which are often limited regarding the exploration domain of influential variables, the presence of intrinsic sample variability, or as for the experimental difficulty of isolating individual parameter effects.

The discrete element method (DEM) is the most frequently implemented method when designing and modeling particulate bulk solid handling systems. The particulate system is modeled as an assembly of singular discrete and interacting particles. Particle positions, velocity and forces acting on each particle are calculated at small intervals based on a force-displacement contact law and Newton's second law of motion [241]. Whilst DEM simulations are being used more and more extensively in a wide range of applications, the question of whether DEM is capable of producing quantitative predictions, rather than only qualitative representations of a granular solid remains largely unanswered. Therefore, one of the main constraints for application of DEM in an industrial context is the determination of the input parameters needed to adequately simulate the behavior of particulate systems.

Due to the disparity between physical properties obtained via traditional tests and the simulation parameters such as stiffness, sliding and rolling friction, calibrations tests are essential. Though scarce, research in the area of calibrating and modeling biomass particles includes the determination of physical properties of briquettes to be used in DEM models by Ramirez-Gomez et al. [303] and the study through DEM of feeding systems for wood-chips by Rackl et al. [275]. More research remains to be done regarding measurements or calibrations of biomass particles at a sub-millimetric and powder scale.

Calibration of biomass feedstocks can be complicated by the elastic, fibrous or stringy bulk behavior related to individual particle characteristics and requires adaptation of existing contact models [235]. Integration of realistic shape models remains also of major concern. Indeed, previous DEM investigations have primarily focused on spherical particles. However, non-spherical powders such as biomass powders are more often encountered in industrial applications. Recent advances in computing speed and power have opened the way to more complex approaches for non-spherical particles representation. Possible shape descriptors in two and three dimensions are multi-sphere approaches, ellipses or ellipsoids, super-quadric bodies, discrete functions, shape combinations, composite particles and flexible fibers models. An overview of possible methods for DEM particles representation is given in [362–365].

Another major challenge for DEM simulations is the limitation regarding the number of particles that can be modeled in a reasonable time period. Most of DEM simulations considers a restricted number of particles (in the order of hundreds of thousands) with diameters in the order of some millimeters to achieve a reasonable computing time [366]. In industrial practice, however, it is often necessary to deal with billions of particles within a wide range of particle sizes. For this reason, it is unavoidable to upscale the particle size to reduce the total number of particles and thus the computational time. Several approaches of particles scale-up have been developed and can be generally sorted as: “exact scaling” [282,367,368], “coarse-graining” [280,369–371] and “cutting-off” [280,372]. Exact scaling has no advantage regarding the reduction of the number of particles, so the computation time can be reduced, as scaling factors are applied to both the equipment geometries and the particles size. Coarse-graining is defined as the reduction of computational cost by replacing actual particles by scaled representative

models [370]. The scaling factor in the coarse-graining approach is only applied to the radius or volume of the particle, while the geometries of the equipment are not scaled. Coarse-graining approaches has been widely applied to spherical cohesionless materials [293,369,370,373] but, besides works by Thakur et al. [283], little research about its relevance on simulation of elongated and cohesive particles has been made.

The main aim of this paper is to describe the application of a calibration framework proven successful for spherical materials [295,374,375] to biomass powders which are constituted of sub-millimetric elongated particles and have cohesive characteristics. In addition, other subjacent goals are: (i) to explore the usefulness of a coarse-graining approach for simulation of a large number of elongated biomass particles (ii) to assess the influence of DEM calibration parameters on the bulk properties of the material (iii) to illustrate the trade-offs encountered when dealing with multiobjective calibration and the multiplicity of valid solutions. In a broader perspective, this work intends to establish calibrated, realistic and efficient material models allowing the assessment of the effects of biomass particle properties on bulk behavior. This will allow the study of efficient design strategies of handling equipment for powdered lignocellulosic biomass.

2.2. Materials and methods

2.2.1. Sample preparation and particle size and shape characterization

Poplar was chosen as a representative for lignocellulosic biomass as it is a promising energy crop, namely due to its fast growth in temperate climates. Additionally, the development of poplar genotypes with improved yield, higher pest resistance, increased site adaptability and easy vegetative propagation has made poplar a commercially valuable energy crop [330,331]. The poplar tree selected for the present study came from a forest located in *La Snippe* valley in Auménancourt-le-Petit (France). The tree was shopped and cut in boards that were subsequently dried.

Samples of $60 \times 80 \times 15$ mm³ were cut from the boards and ground using a Retsch SM300 cutting mill with a bottom sieve of 1 mm trapezoid holes at the outlet. The powders obtained after grinding were sieved to obtain two well differentiated sieving cuts representative of coarse and fine particles. A vibratory sieve shaker Retsch AS 200 at a frequency of 60 Hz for 20 minutes was used along with sieves of opening 500 μ m and 710 μ m for the coarse cut and 200 μ m and 315 μ m for the fine cut.

A *Sympatec-QICPIC* morphological particle size analyzer was used to obtain biomass particles size distribution (PSD) after sieving [312]. The values of the descriptors of particles size distribution and shape distribution are listed in Table 30. The minimum value of the Feret diameters over all orientations of the particle is used as the magnitude characterizing particles size. The 50th centile of the cumulative volume distributions (x_{50}) was taken as a mean size descriptor of each size distribution. PSD span (S_x) was calculated from values of the 90th and 10th centiles as:

$$S_x = (x_{90} - x_{10}) / (x_{90} + x_{10}) \quad (61)$$

Particle shape was characterized through the aspect ratio, a , which is defined as the ratio between the minimum and the maximum Feret diameters for a given particle. Mean values of the aspect ratio, a_{50} were calculated as the 50th centile of the cumulative aspect ratio distributions, and the aspect ratio span S_a is defined by:

$$S_a = (a_{90} - a_{10}) / (a_{90} + a_{10}) \quad (62)$$

where a_{90} and a_{10} correspond to the 90th and 10th centiles of the aspect ratio distribution, respectively.

Table 30. Sample nomenclature and size/shape characteristics.

Sample	Sieving cut (μm)	x_{50} (μm)	x_{90} (μm)	x_{10} (μm)	S_x	a_{50}	S_a
1 (Coarse sieving cut)	500-710	746	1092	519	0.36	0.38	0.49
2 (Fine sieving cut)	200-315	352	513	243	0.36	0.42	0.53

2.2.2. Bulk behavior tests

The first stage in the DEM calibration procedure consists of choosing an adequate number of bulk experiments that characterize particles bulk behavior. Suitable calibration measurements should: (i) be easy to implement in laboratory tests and time-efficient, (ii) produce sufficiently discriminating values from variations in material properties and (iii) be highly reproducible and repeatable. From this point of view, the bulk setups described hereafter have been proven suitable for cohesive materials such as biomass powders, according to preliminary tests made as part of this work.

2.2.2.1. Angle-of-Repose from bulk solid heaps

Angle-of-repose measurements have been extensively used in previous research for calibration of DEM models for bulk materials [291–293,376], with special focus on non-cohesive materials.

Conventional methods for measuring the AoR such as the lifting cylinder test [280] were tested in the preliminary stages of this work. Due to the cohesive strength and interlocking effects within biomass samples, stable structures were formed regardless of the filling method or the cylinder size. As a result, this method was unsuccessful to obtain a heap from which the AoR could be calculated.

A poured AoR method adapted from [152,153] was used in this work. Repeatable measurements of the AoR were attained by pouring 40 g of the powders manually over a stainless steel inclined surface, and then measuring the slope of the heap formed over a flat paper surface by the particles flowing out of the ramp (Figure 81). The inclination of the surface was fixed to be $\theta = 40^\circ$ for the coarse samples and $\theta = 50^\circ$ for the finer. The inclination was measured using a calibrated angle-meter fixed to the inclined surface. Flow rate was controlled manually to avoid accumulation of the particles on the surface and set to be around 0.5 g/s. A camera taking images from a side view of the heap was placed always at the same position during the experiments. Each measurement was repeated seven times.

Image analysis using ImageJ [377] allowed heap profile extraction and AoR determination by linear regression. Shape and symmetry of the heap were occasionally influenced by flow intermittencies, so values of AoR were calculated from the left side of the heap as it was the region less sensitive to abrupt perturbations.

For calculation of the AoR, a direct linear regression procedure using the heap surface line instead of an indirect measurement from the heap diameter and height [378] was preferred. Indeed, several authors have shown that there could be significant differences in AoR measurements depending on the chosen method of calculation, especially for asymmetric heaps [379–381]. Indirect methods can be very sensitive to the choice of the extreme points of the heap, while a calculation including the entire profile line represents better the pile shape. In all cases, relatively symmetric heaps were obtained and determination coefficients (r^2) of linear regressions were always over 0.95.

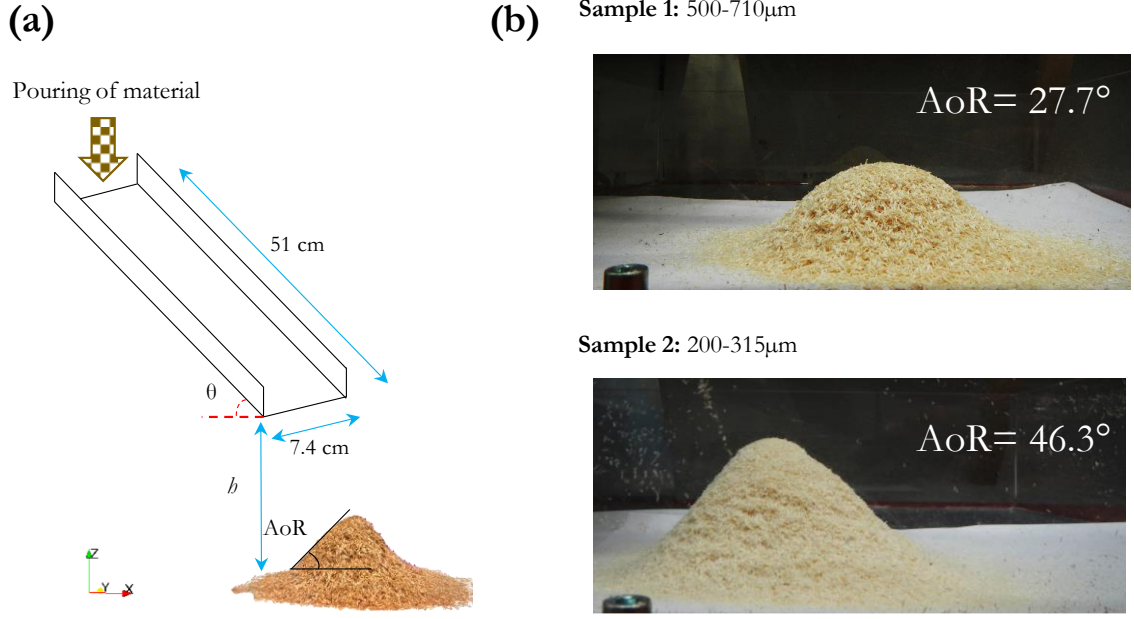


Figure 81. AoR setup: (a). Heap formation and main setup dimensions; (b). Examples of biomass powders heaps.

2.2.2.2. Bulk density

Loose bulk density, ρ_b in kg/m^3 , refers to the ratio of the mass of bulk sample m_l over its aerated volume V_l ($\rho_b = m_l / V_l$). It represents the most loosely packed density of the material. Around 50 ml of oven-dried samples were smoothly poured into a graduated plastic vessel, and the mass of solid was then recorded. Each measurement was repeated for six refills using different oven-dried powder of the same sample.

2.2.2.3. Rectangular container test

Preliminary studies showed that calibrated parameters for biomass powders using only information from AoR and bulk density measurements did not represent a realistic cohesive flow behavior when particles settled inside a container. Rectangular containers, also called “shear box” or “ledge test”, have been used in previous research for DEM calibration tests [280,291,382]. Therefore, a rectangular container with adjustable walls was used in this work for complementary calibration (Figure 82). Walls were adjusted to adapt to the available volume of sample, so that the final dimensions of the container were 25 cm (height) x 6 cm (length) x 5.7 cm (width). The bulk material was poured in the volume and the powder surface was carefully kept flat at the end of the pouring. The final height of the stack was 7 cm. The cabin lid of the container was then lifted, and particles were allowed to flow out of the volume.

For simulation purposes, the retainment ratio p is defined by:

$$p = \frac{m_r}{m_0} \quad (63)$$

where m_r is the mass remaining in the volume after the cabin lid is lifted, and m_0 corresponds to the mass initially poured inside the container.

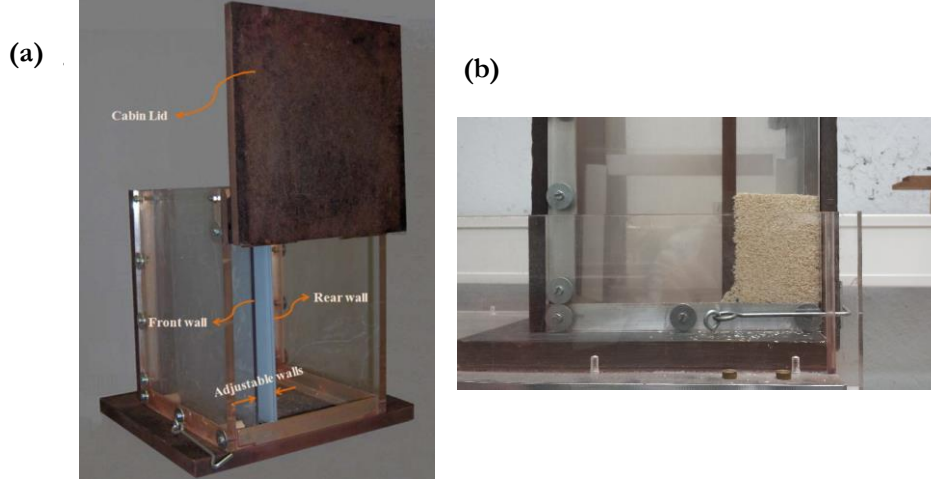


Figure 82. Rectangular container device. (a) Container. (b) Example of a sample inside a volume reduced by the adjustable walls.

2.2.2.4. Ring shear tester

A RST-XS Schulze ring shear tester [143,345] was used to assess the flow properties of the biomass powders. The ring shear tester is a widely-used device to measure flow properties of powders, including unconfined yield strength, angle of internal friction and wall friction. The standard procedure leads to results with low variability [143]. A consolidation stress $\sigma_{pre} = 5$ kPa, considered as representative of the stress range for industrial applications, was tested [141]. Three shear points at 25 %, 50 % and 75 % of σ_{pre} were used to determine the yield locus of each sample. The yield locus curves were regressed from experimental points by a linear regression.

2.2.3. DEM simulations setup

This section contains an overview of the DEM contact model used in this work as well as the procedure for representing particles characteristics through a multisphere and coarse-graining approach. Then the simulation setup for each bulk test is presented.

2.2.3.1. DEM contact model

In this study, simulations were run using the public version of LIGGGHTS® 3.8.0 DEM code [268], on a E5-2620 v4 2.10 GHz Intel® Xeon® machine with 125.8 GB of RAM, and with parallelization on 8 cores. A Hertz-Mindlin contact model along with an elastic-plastic spring-dashpot (EPSD2) rolling friction model and a simplified Johnson-Kendall-Roberts (SJKR) cohesion model were used. The Hertz-Mindlin model stands as the most commonly used contact model due to its efficient and accurate force calculations. A representation of the contact model, accounting for a spring elastic force, a viscous damping and a frictional slider in the tangential direction, is shown in Figure 83 [260]. At any time t , the equations governing the translational and rotational motion of particle i of mass m_i and radius R_i can be written as:

$$m_i \frac{d\mathbf{v}_i}{dt} = \sum_j (\mathbf{F}_{ij}^e + \mathbf{F}_{ij}^d + \mathbf{F}_{ij}^{coh}) + m_i \mathbf{g} \quad (64)$$

and

$$I_i \frac{d\boldsymbol{\omega}_i}{dt} = \sum_j (\mathbf{T}_{ij}^t + \mathbf{T}_{ij}^r) \quad (65)$$

where \mathbf{v}_i and $\boldsymbol{\omega}_i$ are the translational and rotational velocities of particle i , and I_i is the moment of inertia of the particle. The forces involved are: the gravitational force $m_i \mathbf{g}$ and the forces between particles (and between particles and walls) which include the an elastic force \mathbf{F}_{ij}^e , a viscous damping component \mathbf{F}_{ij}^d and cohesive contributions through the \mathbf{F}_{ij}^{coh} term. The torque acting on particle i due to particle j includes two components: \mathbf{T}_{ij}^t which is generated by the tangential force and causes particle i to rotate, and \mathbf{T}_{ij}^r , the rolling friction torque generated by asymmetric distribution of normal contact force and slows down the relative rotation between particles in contact [272]. If particle i undergoes multiple interactions, the individual interaction forces and torques sum up for all particles interacting with particle i . The equations for calculation of the particle-particle interaction forces within the Hertz-Mindlin contact model are listed in Table 31.

Table 31. Equations for calculations of forces and torques on particle i according to the Hertz-Mindlin model.

Force or torque contribution	Equation
Normal elastic force, $\mathbf{F}_{ij,n}^e$	$k_n \delta_{ij,n} = -\frac{4}{3} Y_{eff} \sqrt{R_{eff}} \delta_{ij,n}^{3/2}$
Normal damping force, $\mathbf{F}_{ij,n}^d$	$\gamma_n \mathbf{v}_{ij,n} = -\frac{2\sqrt{5/6} \ln(e)}{\sqrt{\ln^2(e) + \pi^2}} \sqrt{2Y_{eff} (R_{eff} \delta_{ij,n})^{1/2}} m_{eff} \mathbf{v}_{ij,n}$
Tangential elastic force, $\mathbf{F}_{ij,t}^e$	$k_t \delta_{ij,t} = -8G_{eff} \sqrt{R_{eff} \delta_{ij,n}} \delta_{ij,t}$
Tangential damping force, $\mathbf{F}_{ij,t}^d$	$\gamma_t \mathbf{v}_{ij,t} = -\frac{2\sqrt{5/6} \ln(e)}{\sqrt{\ln^2(e) + \pi^2}} \sqrt{8G_{eff} (R_{eff} \delta_{ij,n})^{1/2}} m_{eff} \mathbf{v}_{ij,t}$
Coulomb friction limit	$\delta_{ij,t}$ truncated to satisfy $\mathbf{F}_{ij,t}^e \leq \mu_s \mathbf{F}_{ij,n}^e + \mathbf{F}_{ij,n}^d + \mathbf{F}_{ij,n}^{coh} $
Torque by tangential forces, \mathbf{T}_{ij}^t	$\mathbf{R}_{ij} \times (\mathbf{F}_{ij,t}^e + \mathbf{F}_{ij,t}^d)$
Torque by rolling friction, \mathbf{T}_{ij}^r	EPSD2 model

Where $1/m_{eff} = 1/m_i + 1/m_j$, $1/R_{eff} = 1/R_i + 1/R_j$, $1/Y_{eff} = (1-\nu_i^2)/Y_i + (1-\nu_j^2)/Y_j$, $1/G_{eff} = 2(2-\nu_i)(1+\nu_i)/Y_i + 2(2-\nu_j)(1+\nu_j)/Y_j$, $\mathbf{R}_{ij} = \mathbf{r}_j - \mathbf{r}_i$, $\mathbf{r}_i, \mathbf{r}_j$: position vectors of particles i and j , \mathbf{e} : coefficient of restitution, Y : Young's modulus, G : shear modulus, ν : Poisson's ratio.

Regarding rolling friction modeling, the alternative elastic-plastic spring-dashpot model EPSD2 [273] adds an additional torque contribution to the particles motion given by:

$$\mathbf{T}_{ij}^r = \mathbf{T}_{ij}^{r,k} = -k_r \Delta \boldsymbol{\theta}_{r,ij} \quad (66)$$

where $\mathbf{T}_{ij}^{r,k}$ is a torque component modeled as a mechanical spring, k_r is the rolling stiffness and $\Delta \boldsymbol{\theta}_{r,ij}$ is the incremental relative rotation between two particles. The torque contribution is truncated so:

$$\mathbf{T}_{ij}^{r,k} \leq \mathbf{T}_{ij}^{r,max} = \mu_r R_{eff} \mathbf{F}_n \quad (67)$$

where μ_r is the rolling friction coefficient, R_{eff} the effective radius and $\mathbf{T}_{ij}^{r,max}$ being the limiting spring torque which is achieved at a full mobilization rolling angle θ_r^m . In the EPSD2 model, the rolling stiffness k_r is defined as:

$$k_r = k_t R_{eff}^2 \quad (68)$$

where k_t corresponds to the tangential (i.e. shear) stiffness. Figure 83b shows the mechanism of rolling resistance and the physical meaning of the coefficient of rolling friction μ_r , which is a scalar value that represents the eccentricity of the resulting normal force exerted by a surface on a rolling particle. In the

EPSD2 model μ_r does not appear explicitly in the expression for the rolling stiffness (as for CDT or EPSD models) but instead is used for restricting the maximum spring torque.

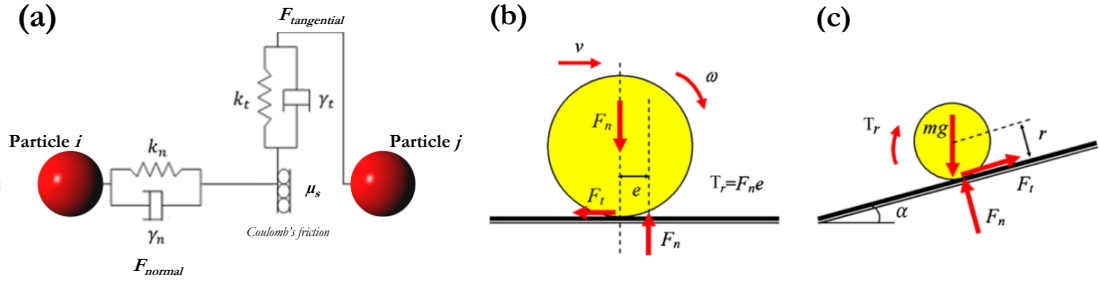


Figure 83. Schematic representation of the contact model used in this study: (a) Hertz-Mindlin contact model. (b) Mechanism of rolling resistance. (c) rolling resistance angle [383].

The simplified Johnson-Kendall-Roberts model (SJKR) [384], used to simulate cohesion between particles, adds an additional normal force $\mathbf{F}_{ij,n}^{coh}$ tending to maintain the contact between two particles, given by:

$$\mathbf{F}_{ij,n}^{coh} = CED \cdot A \quad (69)$$

where CED is the Cohesive Energy Density in J/m^3 and A is the particle contact area.

2.2.3.2. Particle representation

The biomass powders were modeled as monodispersed populations of clumps of spheres (multi-sphere method). Spheres comprising a multi-sphere particle are fixed in position relative to each other and may overlap to approximate more closely to the actual particle shape [274]. The multi-sphere method stands as one of the most general and most efficient method for representing shape within DEM. By using a multi-sphere approach it is possible to ensure computational efficiency for contact detection and force calculation and it is widely implemented in many DEM codes [385,386]. Multi-sphere representations have previously been used for describing flow in silos of agricultural resources such as maize and rice grains [277,387]. When using a multisphere approach, finding a trade-off between particles representation accuracy and DEM run time is essential. For instance, in their study with maize grains, Markauskas et al. [277] found that models with 6 sub-spheres successfully reproduced discharging time in silos, but similar results could be obtained with 4 sub-spheres using another set of calibration parameters.

In order to reduce the number of spheres needed to represent one single particle, in this study individual spheres were oriented over one single longitudinal axis, so the particles were needle-shaped (Figure 84). To approximate the true morphology obtained by PSD measurements, a simplified model for particle representation was proposed. In this model, the number of spheres in a clump, n_{sph} , is function of the particles mean size (x_{50}), the mean aspect ratio (a_{50}) and an overlapping factor ϵ .

The overlapping factor can be expressed as $\epsilon = \lambda / x_{50}$, where λ is the overlapping distance between adjacent spheres in μm (Figure 84). A value of $\epsilon = 0$ means two spheres touching each other at one single point and $\epsilon = 1$ represents a total overlap between two contiguous spheres. As ϵ increases the effective roughness of the particle decreases. Previous work [386] suggested that reducing surface roughness by increasing the number of spheres per clump did not necessarily lead to a better approximation of particles behavior. A value of ϵ of 20 % was chosen as it is considered a good trade-off between the accuracy of particles representation and the number of spheres needed.

The diameter of each sphere is set to be equal to the mean minimum Feret diameter of the population, x_{50} . Therefore, the length of the clump (l_{clump}), which corresponds to the mean maximum Feret diameter, can be calculated as follows:

$$l_{clump} = x_{50} / a_{50} = n_{sph} \cdot (x_{50} - \lambda) + \lambda \quad (70)$$

So, from the definitions of a_{50} and c , the number of spheres needed per clump is:

$$n_{sph} = \frac{\frac{1}{a_{50}} - c}{1 - c} \quad (71)$$

The calculated values were rounded to the closest integer and the length of the clump recalculated accordingly.

Calculation of bulk density from simulations needs the value of the mass of each clump, which is computed from the clump volume, given by:

$$V_{clump} = n_{sph} \pi r^3 \left(\frac{4}{3} - \frac{n_{sph} - 1}{12 n_{sph}} (6 - 2c)(4c^2) \right) \quad (72)$$

where r is the spheres radius $r = x_{50} / 2$. Table 32 shows the model parameters used for particles representation. For the sake of comparison with spherical models for particle representation, the equivalent radius of a sphere having the same volume as one individual clump (R_{eq}) is also reported.

Table 32. Parameters of multisphere model for particle representation.

	Sample 1	Sample 2
n_{sph}	3	3
r (μm)	373	176
l_{clump} (μm)	1940	915
V_{clump} (mm^3)	0.6282	0.0658
R_{eq} (μm)	531	251

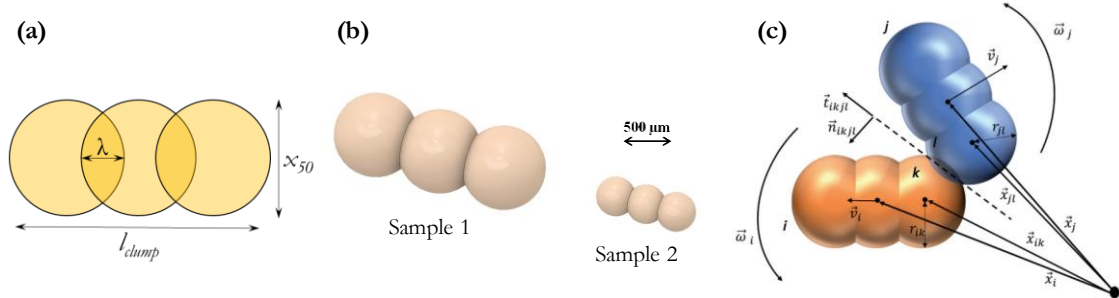


Figure 84. Particle representation for biomass samples. (a) Nomenclature of main dimensions in a clump. (b) Samples multispheres models (true relative size). (c) Representation of a collision between spheres k and i within two multi-sphere particles (\vec{t}_{ijk} : tangential unit vector, \vec{n}_{ijk} : normal unit vector of contact zone) [296].

2.2.3.2.1. Scaling particle size up

Since parameters calibration commonly involves running an extensive amount of simulations, the representation of the actual number of particles used during the bulk tests would not be possible within a realistic frame time. A scaling factor, SF , can be defined as the ratio between the simulated particle radius and the actual value from PSD. As shown in Figure 85a, the computational time required to simulate one real-time second of heap formation for sample 1 significantly decreases by increasing the scaling factor, as the number of particles ($n_{particles}$) decreases. A series of test runs were performed to assess

the effect of scaling particle size up on the AoR of the heap formed using non-calibrated parameters ($\mu_s = 0.9$, $\mu_r = 0.5$ and $CED = 0 \text{ J/m}^3$). Testing values of SF over 7 leads to high uncertainty on the value of AoR as the number of particles is not enough to form a proper heap. The linear downward trend showed in Figure 85b clearly indicates that scaling effects on the AoR are not negligible. This is in contrast with results by Roessler and Katterfeld [280] who found AoR to be scale-independent. However, their conclusions referred to the case of quasi-static formation of a heap using lifting cylinder setups, which is hardly the flow condition of particles forming the heap in this work.

In the aim of reducing computing time, a coarse-graining approach was followed and a trade-off between the actual representation accuracy and the calculation effort was made by scaling particles size up by a factor of 4. Since the effect of the scaling factor on the bulk responses could vary depending on the values of the calibrated parameters, calibration was made using the actual values from experiments (instead of, for example a value corrected by the SF using the trend of Figure 85b). This allowed us to run a typical heap formation simulation in a computing time of approximately 1 hour for coarse particles and in 8 hours for fine particles, while several weeks would be needed to run a single simulation of fine particles at their actual size.

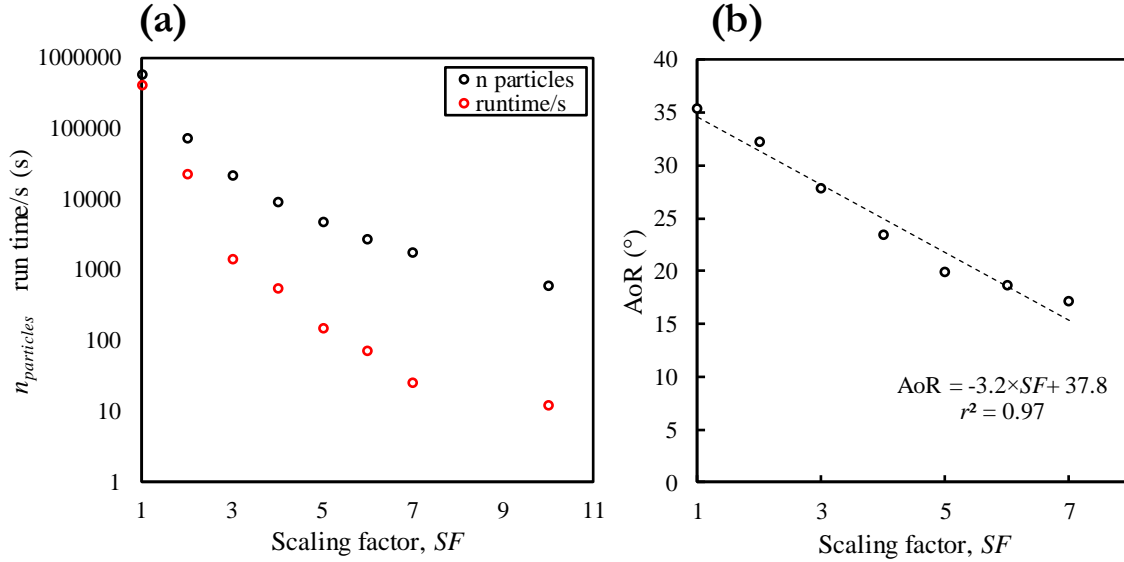


Figure 85. Influence of scaling particles size up for sample 1: (a). Number of particles and simulation time. (b). Angle-of-repose value.

2.2.3.3. Time-step

Because of the explicit numerical scheme used for DEM integration, only relatively small time-step values (Δt) guarantee stable simulations. A common strategy to fix a value for Δt is based on the Rayleigh (ΔT_R) and Hertz (ΔT_H) critical time-steps, calculated as [388]:

$$\Delta T_R = \frac{\pi r \sqrt{\rho / G}}{0.1631\nu + 0.8766} \quad (73)$$

$$\Delta T_H = 2.87 \left(\frac{m_{eff}^2}{r_{eff} Y_{eff}^2 V_{max}} \right)^{0.2} \quad (74)$$

Where r is the minimum particle radius in the system and V_{max} is the maximum relative velocity. The other parameters correspond to those defined previously in Section 2.2.3. In this work, both critical time-

steps were calculated during DEM integration and the simulation time-steps were fixed to be lower than 10 % of ΔT_R and ΔT_H . Values for both samples are reported in Table 33.

2.2.3.4. Angle-of-Repouse and bulk density determination from simulations

The experimental test shown in Figure 81 was numerically replicated using LIGGGHTS®. To reduce the simulation time, the simulated conveyor length is reduced to a half of the experimental length. The angle-of-repose and bulk density were calculated using the positions of the particles in the heap at the end of the simulation when all the particles are in a stable state. To avoid underestimation of those two bulk values, the particles non-connected to the heap were not considered in the calculation.

As for the experiments, the angle of repose in the xz -plane was calculated for the left side of the heap. At first, the positions of the particle at the top and the particle at the leftmost of the heap were identified to determine the domain of the angle-of-repose slope. The particles in this domain were then binned into 20 equally-spaced horizontal layers. For each layer, the x and z coordinates of the top particle on the slope were identified. The angle of repose was then determined using linear regression of these 20 x - z coordinates on the slope. The number of layers = 20 was chosen as it is high enough to produce stable values of AoR and high correlation coefficient values for all calculations.

The bulk density of the heap was calculated from its bulk mass divided by its aerated volume. The bulk mass is equal to the mass of one clump multiplied by the number of clumps in the heap. The concept of numerical integration in volume calculation was implemented in a C++ algorithm to estimate the aerated volume of the heap (analytically as the left-hand side of Eq. (75), and numerically “discretized”, as the right-hand side of the Eq. (75):

$$\iint_{x_{min}, y_{min}}^{x_{max}, y_{max}} h(x, y) dx dy \approx \sum_{i=1}^{n_x} \sum_{j=1}^{n_y} h(x_i, y_j) \Delta x \Delta y \quad (75)$$

where x_{min} , x_{max} , y_{min} , y_{max} are the minimum and maximum of the x and y coordinates of particles inside the heap, respectively, n_x and n_y are the number of discretization intervals in the x and y directions, Δx and Δy are the distances between two adjacent sample points corresponding to x and y directions and $h(x_i, y_j)$ is the height of the heap at the coordinate x_i, y_j . The choice of n_x and n_y is a trade-off between the numerical accuracy and the computational time. It should be high enough to mitigate the estimation error and at the same time it should be as low as possible for quick calculations and less consuming use of computer memory. In the present work, n_x and n_y were set to 10000. This number of sample points guarantees that each calculation takes only few seconds on a normal desktop computer and the results of bulk volume converge.

2.2.3.5. Ring shear tester simulations

The simulated geometry of a ring shear tester cell (Figure 86) is analogous to the experimental device described in Section 2.2.2.4. Previous research [389] has shown that the yield stress was independent of the shear cell size in simulations. However, a high particle-to-cell size ratio inside the shear cell could lead to erroneous values of the shear measurements [144], so the geometry was also scaled up by a $SF = 4$. A servo-control functionality of LIGGGHTS® was applied to the top lid so the vertical component of the applied stress was continuously updated and maintained constant during the simulation. As in experiments, a preshear stage at $\sigma_{pre} = 5$ kPa followed by a shear at $\sigma = 2.5$ kPa was simulated. Shear stress is calculated from the z -component of the torque exerted over the top lid surface as follows [143]:

$$\tau = \frac{M_D}{r_m A_D} \quad (76)$$

where M_D is the torque acting during shear on the top of the lid, $r_m = \left(\frac{2}{3}\right)(r_{out}^3 - r_{in}^3)/(r_{out}^2 - r_{in}^2)$ is the moment arm and $A_D = \pi(r_{out}^2 - r_{in}^2)$ is the area of the lid, with and the outer r_{out} and inner r_{in} radii of the top lid, respectively. Other input parameters needed for the ring shear tester simulations are listed in Table 33.

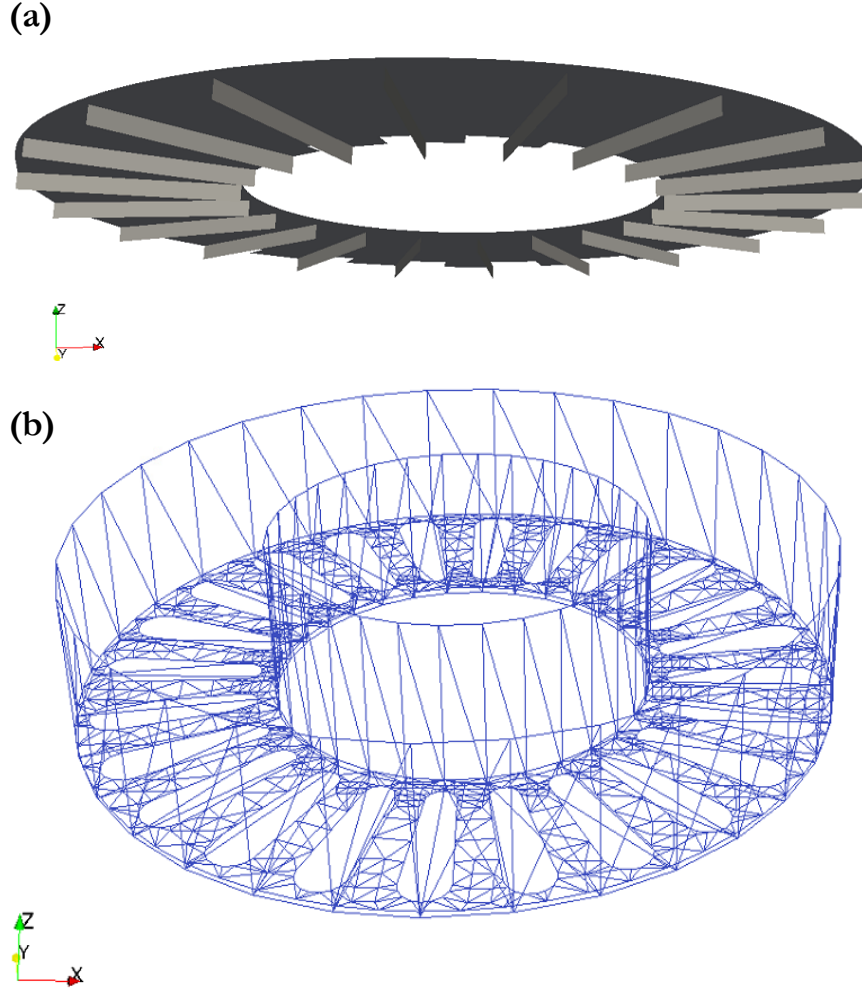


Figure 86. Geometry of the simulated ring shear tester. (a). Top lid. (b). Bottom cell.

2.2.4. Calibration approach

The flowchart of the calibration approach is presented in Figure 87. Regarding the choice of the parameters to be calibrated, a minimization of their number is desired since each additional parameter increases the complexity of the calibration. The previous research highlighted the high influence of the sliding and rolling friction coefficients on the angle-of-repose obtained in DEM simulations [280,293,390]. As the particle to wall interactions are very specific to each industrial or scientific problem, in this research only interparticle interaction parameters are calibrated: the sliding friction coefficient μ_s , the rolling friction coefficient μ_r and the cohesion energy density CED . All the other input values needed for the DEM model are shown in Table 33 and were set based on literature values for woody materials

[275]. Preliminary simulations did not show significant effects of the particle density on the AoR nor the void fraction inside the heap, so the value is set to 1000 kg/m^3 for the fine samples in order to increase the time-step allowing stable simulations.

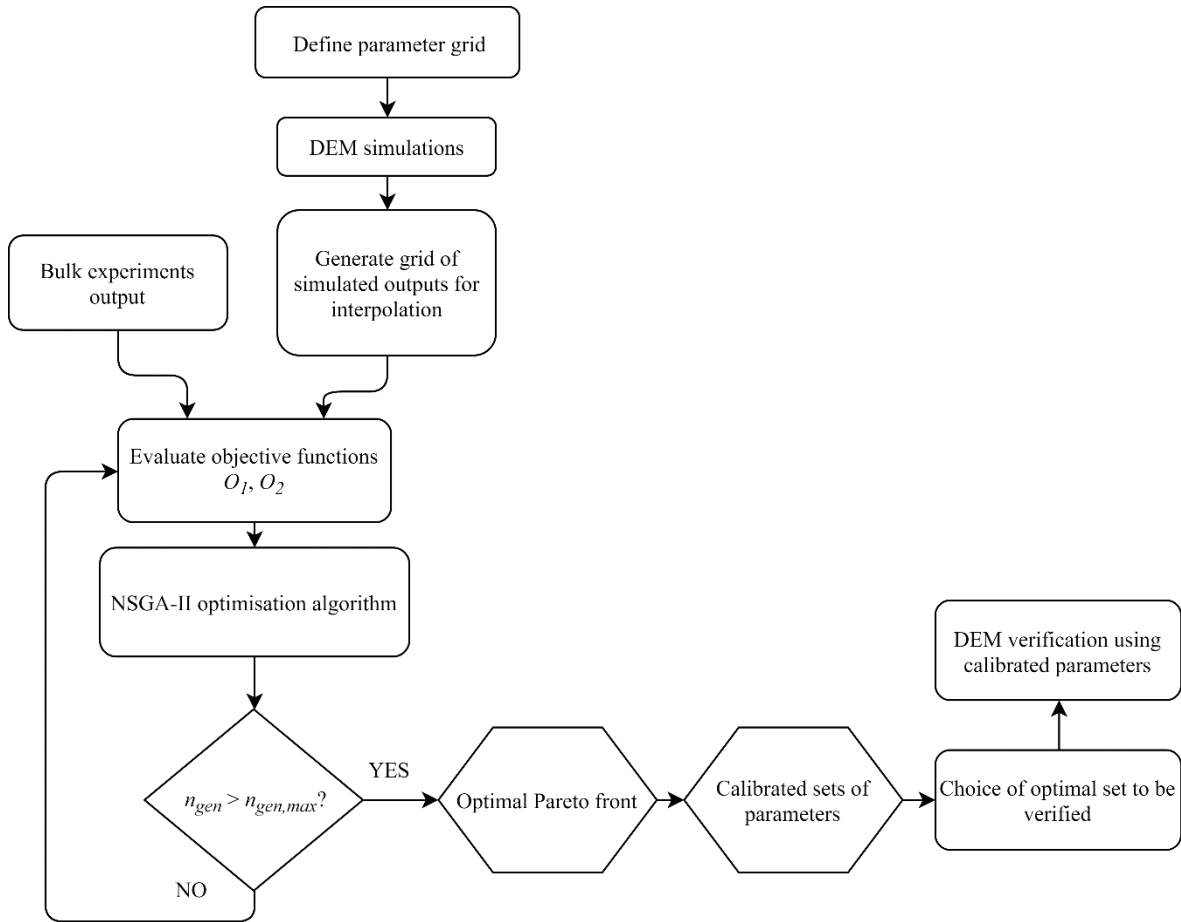


Figure 87. Flowchart of the calibration procedure.

2.2.4.1. Selection and range of values of parameters to be calibrated

The tested values of each calibration parameter are shown in Table 34. If 5 values for each variable were to be tested, $5^3 = 125$ simulations would be needed using a full factorial combination of variables. This is feasible in a practical time-frame for coarse samples (Sample 1) but for fine powders (Sample 2), even if using a coarse-graining approach, the high computation time required imposed a reduction of the number of values of the calibrated parameters from 5 to 3 (27 simulations). These values are the maximum, minimum and mean values written in bold type in Table 34. The full experimental plan of this work is presented in Appendix A.

Table 33. DEM simulation parameters for particles and walls.

Parameter	Sample 1	Sample 2
Poisson's ratio (particle-particle)		0.3
Poisson's ratio (particle-walls)		0.3
Particles density, kg/m ³	350	1000
Young's modulus (particle-particle), Pa		5×10 ⁶
Young's modulus (particle-wall), Pa		5×10 ⁶
Coefficient of restitution (particle-particle)		0.1
Coefficient of restitution (particle-walls)		0.1
Coefficient of sliding friction (particle-steel)		0.4
Coefficient of sliding friction (particle-paper surface)		0.5
Coefficient of rolling friction (particle-walls)		0.5
Cohesion Energy Density (particle-walls), J/m ³		0
Time-step (s)	1×10 ⁻⁵	7×10 ⁻⁶
Total number of particles (3 particles/clump)	10638	81309
Factory mass flow, heap AoR test, kg/s		5×10 ⁻⁴
Ring shear tester simulations		
External radius, top lid, mm		127
Internal radius, top lid, mm		65
Depth, bottom cell, mm		52
Total number of particles (3 particles/clump)	15000	150000
Rotational speed, top lid, deg/s		18

Table 34. Set of calibration parameters tested.

Parameter	Variable values				
Coefficient of sliding friction (μ_s)	0.1	0.3	0.5	0.7	0.9
Coefficient of rolling friction (μ_r)	0.1	0.3	0.5	0.7	0.9
Cohesion Energy Density, CED (J/m ³)	0	10000	20000	50000	80000

2.2.4.2. Optimization problem setup (genetic algorithm)

The optimization was carried out using a multiobjective evolutionary algorithm (Non-dominated Sorting Genetic Algorithm II, NSGA-II) [391] proven successful for DEM calibration [295,374]. Input parameters for the genetic algorithm are listed in Table 35. By using 10 bits for encoding each calibration parameter, the number of possible values for each parameter is $2^{10} = 1024$. Since 3 parameters are being optimized, each “individual” in the population is encoded by a binary string of length 30 bits. This leads to the numerical precision listed in Table 6 for each parameter.

Table 35. Input parameters of NSGA-II.

Population size	2000
Chromosome length (bit)	30
Maximum number of generations	100
Crossover probability	0.9
Mutation probability	0.01

Two specific objective functions were defined for the minimization of the discrepancy between numerical and experimental results. The first objective function O_1 is defined as the total relative error between the simulation results and the experimental measurements of AoR and bulk density:

$$O_1 = \frac{|AoR_{ex} - AoR_{sim}|}{AoR_{ex}} + \frac{|\rho_{ex} - \rho_{sim}|}{\rho_{ex}} \quad (77)$$

In this optimization function, the weights of the two error components are equally contributing to the total simulation error.

The second objective function O_2 is based on the rectangular container output and aims to reduce the difference between the simulated and the experimental p factor:

$$O_2 = \frac{|p_{ex} - p_{sim}|}{p_{ex}} \quad (78)$$

Table 36. Numerical precision of binary encoded factors.

Parameter	Interval	Numerical precision
μ_s	[0.1, 0.9]	7.81×10^{-4}
μ_r	[0.1, 0.9]	7.81×10^{-4}
CED	[0, 80000]	78.125

2.3. Results and discussion

2.3.1. Bulk behavior tests

2.3.1.1. Bulk density

The experimental results in Table 37 show an effect of particle characteristics on bulk density of the samples. Interestingly, regarding the particle size, smaller values of bulk density were systematically found for powders with the lowest granulometry. Finer samples had a bulk density 10 % lower than coarse samples. When dealing with non-cohesive materials, a better spatial arrangement of particles is obtained for finer particles so, generally, a decrease of particle size is accompanied by an increase in bulk density. The opposite trend observed for biomass samples would be due to cohesion effects: the presence of fine cohesive particles creates bigger void spaces which reduces bulk density. Similar results were observed by Mani et al. [119] for wheat and barley straws, corn stover and switchgrass samples.

2.3.1.2. Angle of Repose tests

The mean values of the angles of repose are reported in Table 37. The values of the standard deviation are also reported and show that error was always below 4 %, meaning a relatively good reproducibility.

There is an obvious effect of the sample characteristics on the AoR of the heaps formed. The finer sieving cut (sample 2) formed steeper heaps with values of AoR 67 % greater than the coarse cut (sample 1).

Table 37. Bulk behavior experiments results (standard deviation is reported in parentheses).

Sample	1 (Coarse sieving cut)	2 (Fine sieve cut)
ρ_b (kg/m ³)	184.2 (5.7)	165.6 (5.1)
AoR (°)	27.7 (0.7)	46.3 (1.6)

Following the classification criteria based on the AoR established by Ileji et al. [219] for lignocellulosic plant biomass, coarse poplar powders could be classified as free flowing, while fine powders are rather poor flowing.

2.3.1.3. Rectangular container test

No biomass particles were observed to flow when the lid of the rectangular container was lifted. Indeed, very stable stacks of particles were formed for all the samples. This is the result of the combined effect of particles shape and size that trigger interlocking and interparticle cohesive forces. As result of this, the retainment ratio p (Eq. 3) was found to be 1 for both samples.

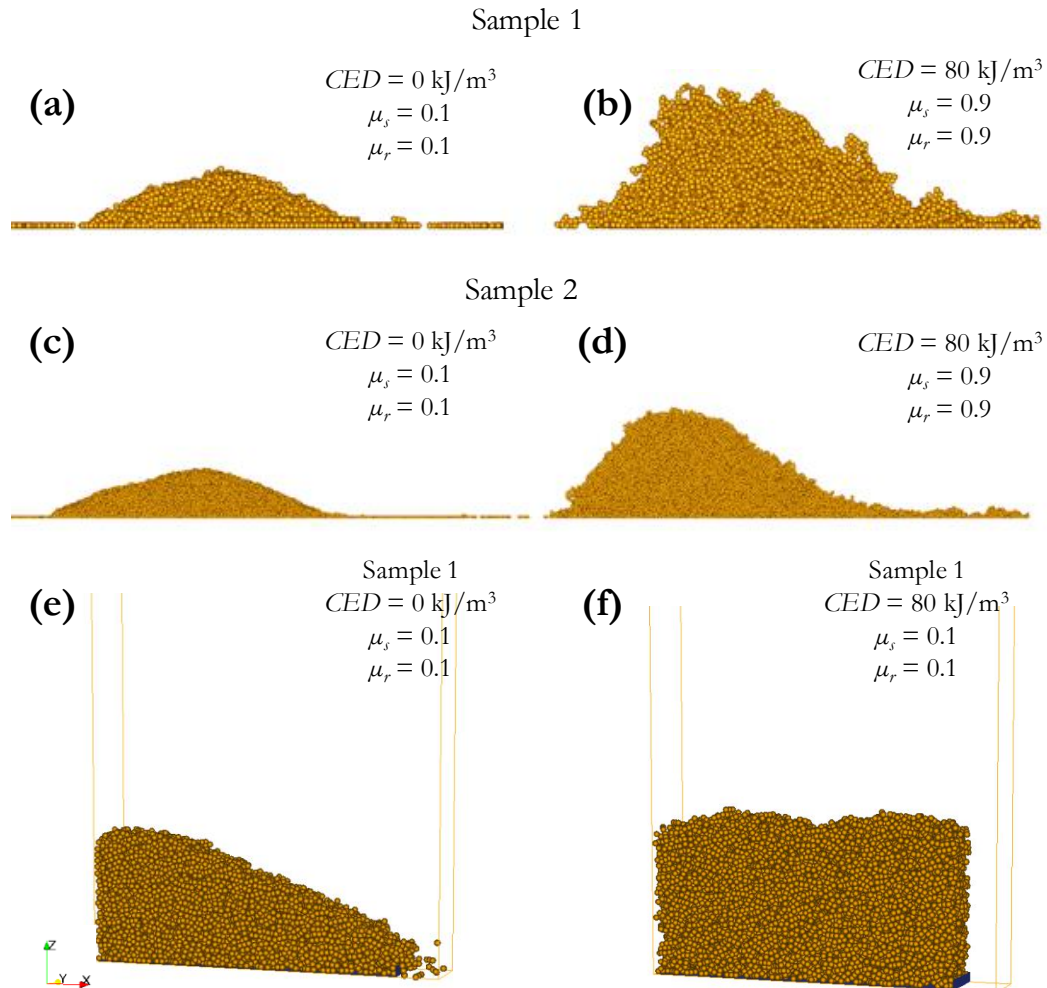


Figure 88. Examples of heaps obtained and rectangular container test from DEM simulations.

2.3.2. DEM simulations

Figure 88 shows some typical heaps and rectangular containers obtained by DEM modeling for both samples, along with the values of the calibration parameters used. Visually, the effect of modifying contact model parameters is evident. The situations represented on the left side of the Figure 88 show a material with a rather free flowing behavior, while images on the right side of Figure 88 represent rather a very cohesive behavior, with greater angles of repose and the formation of a stable stack of particles inside a container.

2.3.2.1. Pareto chart analysis

Determining if variation of DEM parameters produce discriminative effects in bulk responses is important to reduce the number of calibration inputs. For this purpose, a statistical analysis using Pareto charts was used in this work. A Pareto chart allows to compare the relative magnitude and the statistical significance of effects of tested variables on the measured responses. Details on the elaboration and interpretation of the Pareto charts can be found in [392].

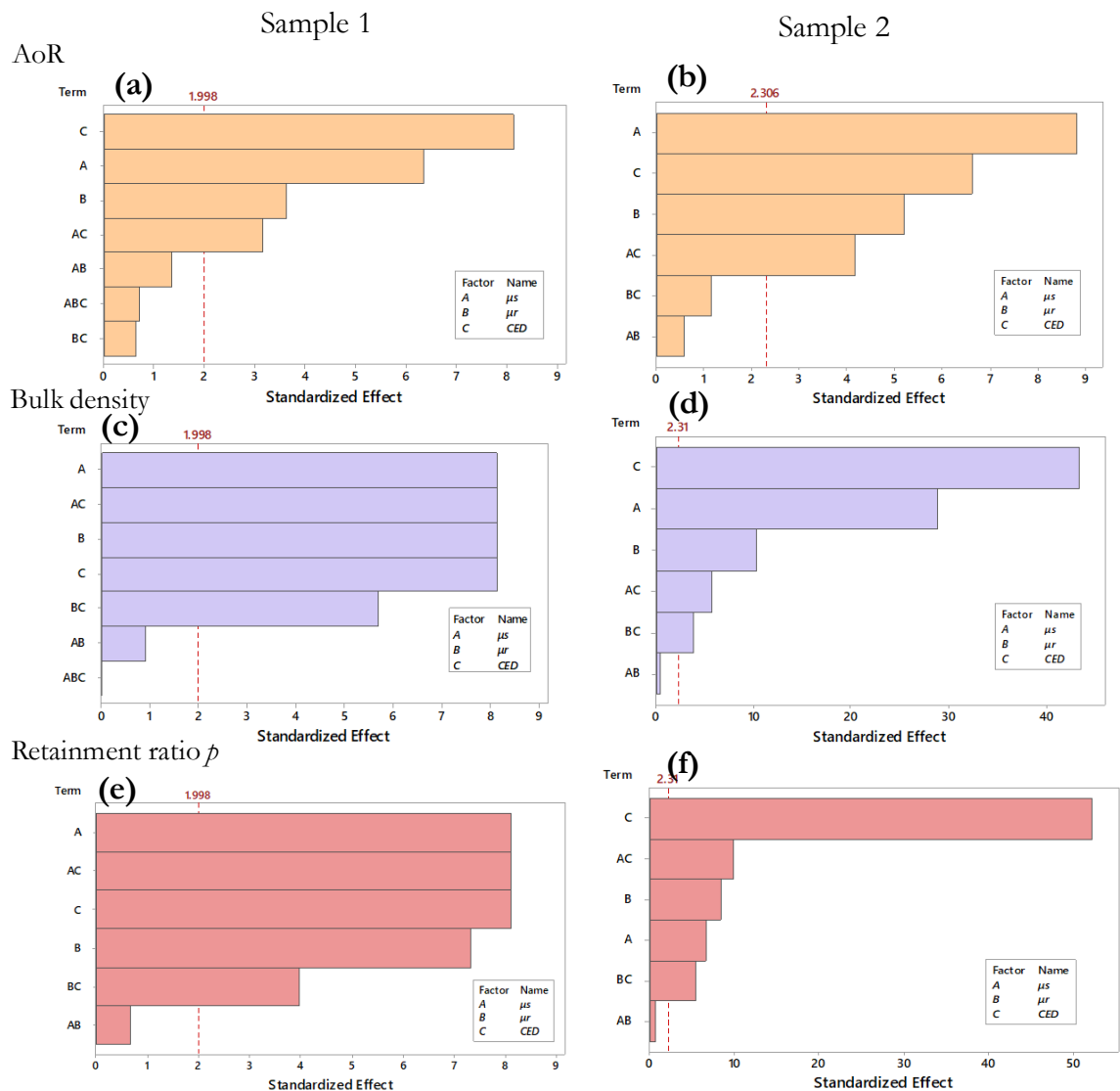


Figure 89. Pareto charts of the standardized effects.

For the coarse samples, the CED has the biggest effect on the values of AoR (Figure 89a). In a lower degree, sliding friction, rolling friction and the combined effect of sliding friction and CED also influenced the AoR. In the case of the bulk density (Figure 89c), all the 3 factors seem to have the same level of influence on the response, as well as the combined effects of μ_s - CED . Regarding the retainment ratio, although CED and μ_s and their interactions had the greater effect, rolling friction also played a role in controlling the number of particles remaining in the container after the lid is opened (Figure 89c).

For the fines sample, CED was the predominant influential factor for both bulk density and p ratio responses (Figure 89b,d), while in the case of AoR, μ_s had a greater effect (Figure 89f).

These results suggest that the three chosen calibration parameters were important in controlling the measured responses and determined the main effects that influence the system. In addition, the relative effects were different depending on the analyzed response. Therefore, their calibration is required.

2.3.2.2. Heap angle of repose and bulk density

Figure 90 and Figure 91 show 2D contour surface representations of the effects of the calibration parameters on the AoR, the bulk density and the retainment ratio p . For clarity reasons, only surfaces for $CED = 0, 20$ and 80 kJ/m^3 are presented. Contour surfaces of the p ratio for $CED = 80 \text{ kJ/m}^3$ are not shown as all simulations led to $p \approx 1$, regardless of μ_s and μ_r values. These representations clearly show the coupled effects that sliding and rolling friction coefficients as well as cohesion have on the three responses analyzed.

From the contours of Figure 90 it is noticeable that a single value of the bulk responses can be achieved from a wide range of parameters (each contour line spans over a wide range of both sliding and rolling friction coefficients and the same colors in the color scale can be found in two or more different graphs). This highlights the importance of choosing enough bulk setups and responses for a robust DEM calibration.

In the case of the AoR response, changing cohesion level affects the trends of the surfaces, showing that effects of μ_s and μ_r are dependent on each other but also on CED magnitude. This is especially noticeable for the highest values of CED . For non-cohesive simulations (Figure 90a), rolling friction effects are more important when sliding friction is increased, and maximum values of AoR are attained for the highest values of μ_s and μ_r . This is in agreement with previous results by Wensrich and Katterfeld [271] who stated that the only way in which a large angle of repose could be achieved was if both of these mechanisms (rolling and sliding) worked together. However, interestingly, when cohesion is included, even if AoR tends to increase with increase in μ_s and μ_r values, maximum AoR values do not necessarily correspond to the highest values of μ_s and μ_r ; instead, they are located at intermedium values of μ_s and μ_r . Figure 90c shows that effects of rolling and sliding friction follow a less monotonous trend when CED is 80 kJ/m^3 . A reason for this is that, for values of CED over 50 kJ/m^3 , particles flowing over the conveyor tend to form relatively stable agglomerates that are spread over the heap surface, forming heaps with a rougher and more irregular surface (Figure 88b). Therefore, AoR determination for very cohesive simulations could lead to values with higher uncertainty as heap profiles are less well-described by linear regressions. This can be quantified through the calculation of the average coefficient of determination (r^2) as function of the CED values (Figure 92). Indeed, a downward trend which is more marked for the sample 1 (coarse particles) than for sample 2 (fine particles) was observed.

As for the AoR, effects of calibration parameters on bulk density go hand-in-hand. Bulk density decreases when friction and cohesion are increased or when the rolling is more restricted (so a less “spherical behavior”). This is the result of a higher void created between particles when normal forces

are allowed to dissipate to a bigger extent through bigger μ_s values. Increasing the rolling resistance and cohesion also prevent particulates from finding a more compact spatial arrangement, so void fraction could be reduced. Bulk density seems to be sliding dominated for the values on top left of the contour figures ($\mu_s < 0.3$) and rolling dominated for the values at the bottom right corner on those representations. This accentuates when cohesion is increased.

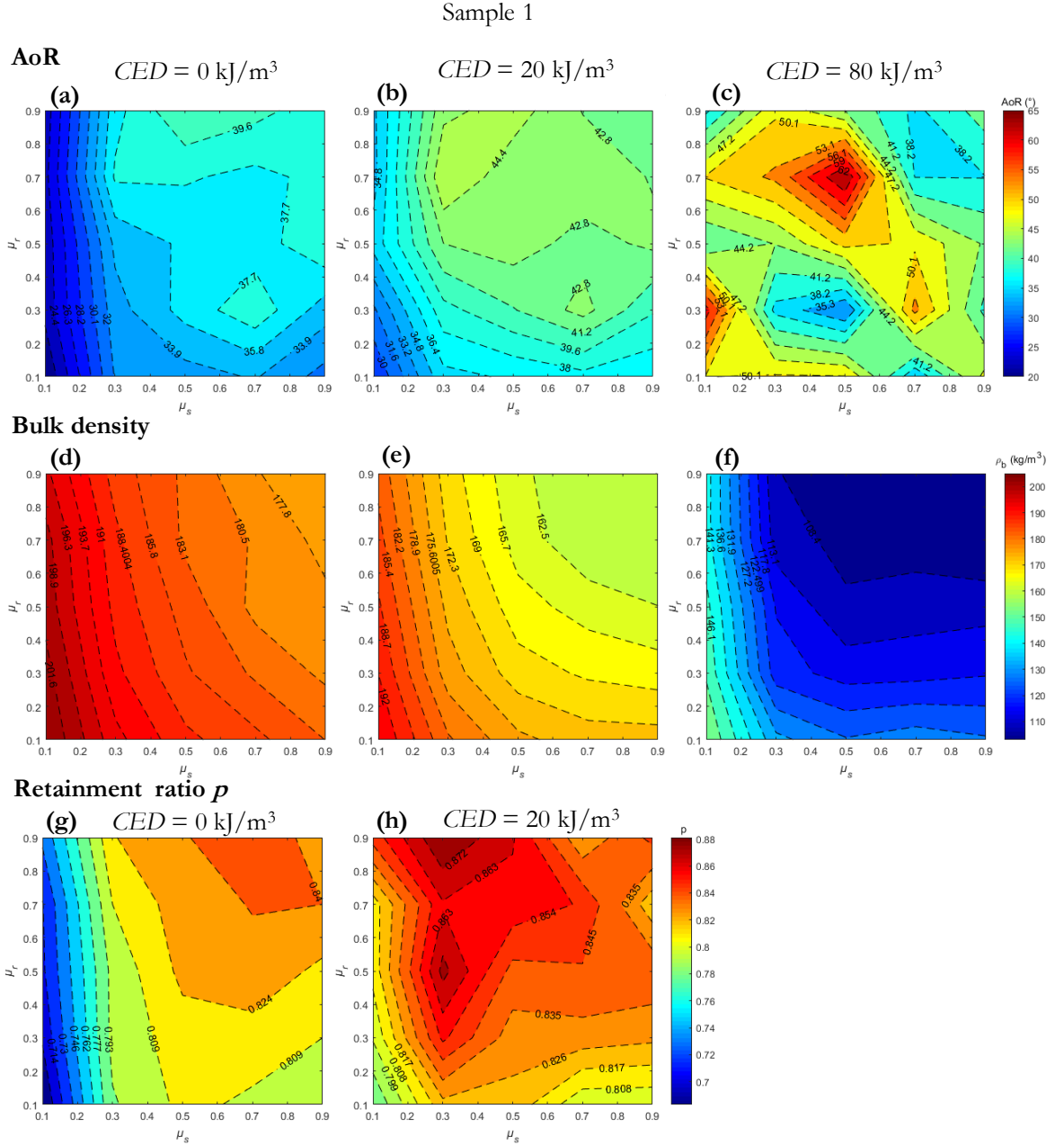


Figure 90. Contour surface responses for sample 1.

For sample 1, experimental values of AoR and bulk density ($AoR = 27.7^\circ$, $\rho_b = 184.2 \text{ kg/m}^3$) can only be found for the lower values of cohesion, but a high p ratio needs a high value of CED . Thus, a trade-off through optimization has to be found.

Regarding sample 2, small effects of cohesion on the AoR were found within the range 0 to 20 kJ/m^3 . Unlike sample 1, a more gradual increase of AoR with rolling resistance increase was found for

$CED = 80 \text{ kJ/m}^3$. Regarding bulk density, similar trends were found between both samples. Target values ($AoR = 46.3^\circ$, $\rho_b = 165.6 \text{ kg/m}^3$) can be found on Figure 91c and e, but as for sample 1, a p value of 1 is only possible for the most cohesive sets of simulations.

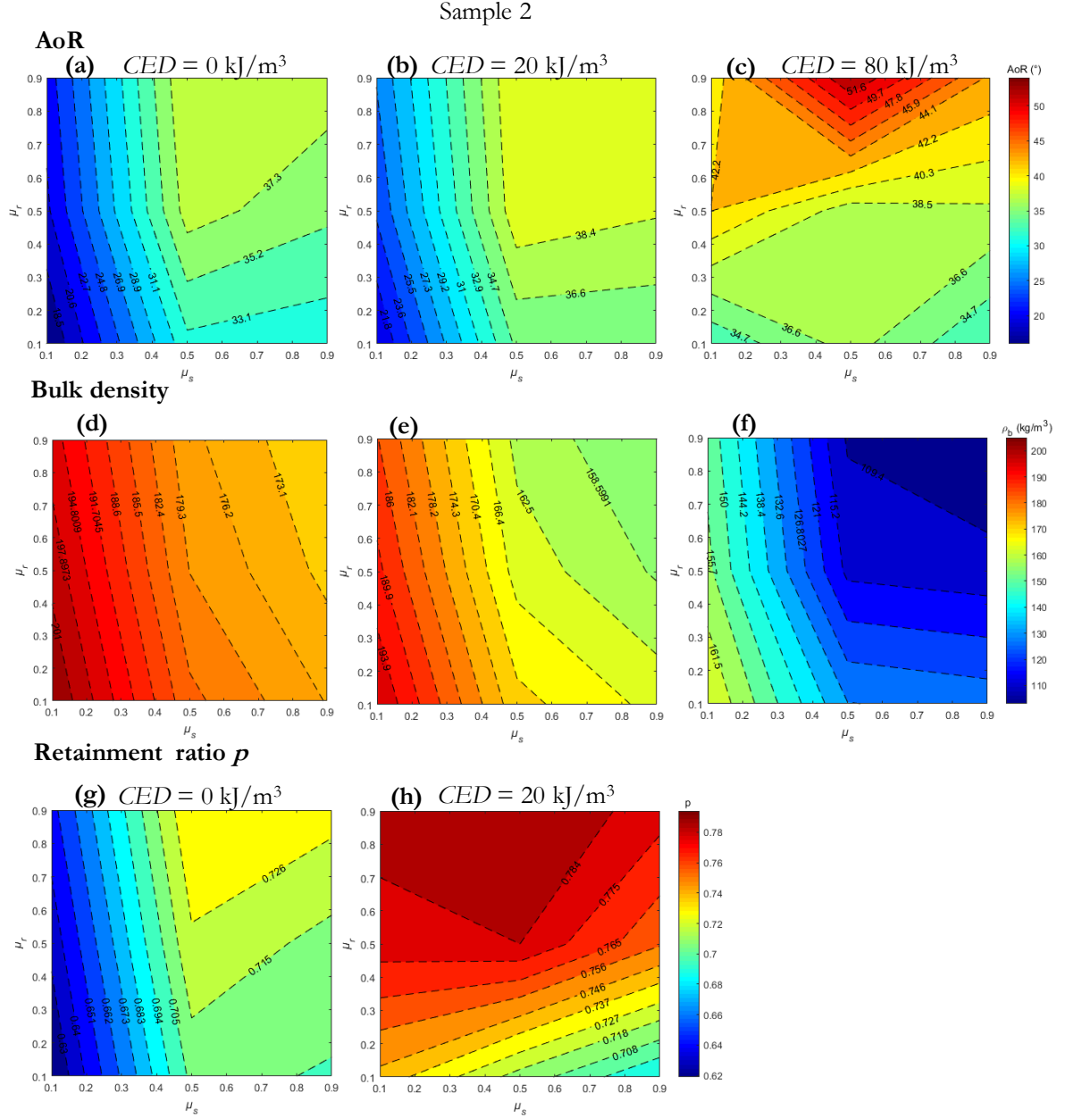


Figure 91. Contour surface responses for sample 2.

In order to reach values of p ratio close to 1, a particle shape representation that strengthens particles spatial interlocking could reduce the need for high CED values (e.g. through non-axial or hooked shapes). Nevertheless, this would typically require a particle model including more spheres per clump, as well as a highly polydisperse system, which would reduce simulation performances beyond a practical interest.

Globally, when comparing simulations for samples 1 and 2 with low-mid cohesion, relatively similar values of AoR and bulk density were found for the two samples when calibration parameters were the same. On the contrary, the experimental results for samples 1 and 2 were significantly different.

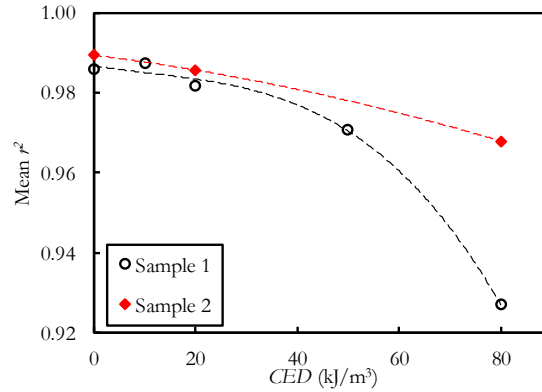


Figure 92. Average coefficients of determination of heaps profiles.

2.3.2.3. Main effects of calibrated parameters

Using MINITAB tool for analysis of factorial designs [393], the main effects plots presented in Figure 93 were obtained. These plots are useful for quantitatively assessing the influence of each level of μ_s , μ_r and CED on the mean responses of AoR, bulk density and p ratio.

Globally, similar trends were found for both samples, both qualitatively and quantitatively, with a greater resolution for sample 1 than that for sample 2 as more parameters values could be tested. In the case of the coarse sample 1, a sharp increase (21 %) of AoR was observed as μ_s increased from 0.1 to 0.3. In average, higher values of AoR were obtained for $\mu_s = 0.5$. Sliding friction governs the translational motion of the particles by defining the magnitude of normal force that it is dissipated as a tangential component. This means that a large sliding friction coefficient can tolerate a large magnitude of the elastic deformation in the tangential direction and enhance the stability of the individual contacts amongst particles. However, sliding friction defines only a truncation parameter of the tangential force and not its absolute value when the truncation criteria is not met. This could explain the important gap of AoR observed when μ_s is increased from 0.1 to 0.3 and the low AoR variation when μ_s is increased above 0.3. For very low values of μ_s the tangential displacement is highly constrained and corresponds to the value defined by the product of μ_s and the normal force on particles (Coulomb's friction limit). For higher values of μ_s the probability of normal forces exceeding the truncation criteria is reduced and therefore further increase of μ_s would have a lower effect on the variation of the tangential dissipation and therefore on the angle of repose.

Increasing rolling friction from $\mu_r = 0.1$ to $\mu_r = 0.7$ gradually increased the mean AoR by +15 % as shown in Figure 93a. A large rolling friction coefficient means a large resistance force to the rotational movement of the spheres clump, which provides an effective mechanism to consume the kinetic energy and reduce the rotational motion, leading to the formation of heaps with higher potentials and AoR [394].

The greatest variation of AoR was observed when the CED effect is analyzed: AoR below 35° were obtained for non-cohesive simulations while the highest values of CED led to AoR over 46° (+36 %).

Regarding bulk density, the downward trends of Figure 93c-d summarize the observations made for the contour surfaces presented in section 2.3.2.2. The increase of sliding and rolling friction coefficients triggered a less compacted settlement of particles inside the heap, thus creating more void spaces and reducing bulk density. For values of $\mu_s, \mu_r > 0.7$ bulk density seems to reach a low plateau. As for CED effect, an important decrease of ρ_b by 36 % and 30 % for sample 1 and sample 2 respectively was observed when non-cohesive and highly cohesive simulations ($CED = 80 \text{ kJ/m}^3$) are compared.

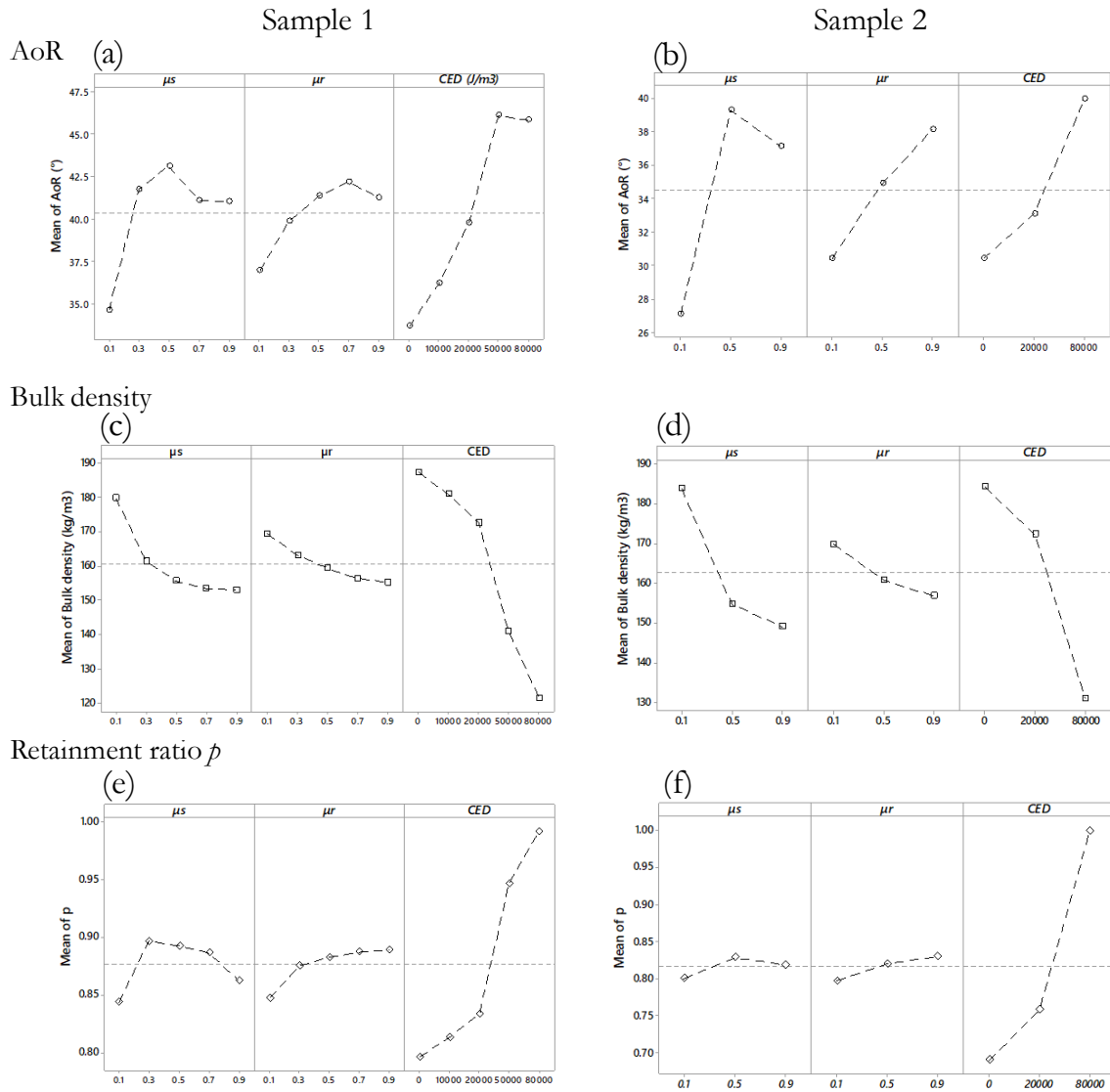


Figure 93. Main effects plots. The dotted horizontal line represents the overall mean.

For both samples, there is a peak of p ratio when varying μ_s values from 0.1 to 0.9. Interestingly, in the case of the coarse sample, increasing sliding friction coefficient to 0.9 lead to much more particles flowing out of the container. This is probably because when increasing friction, particles at the border of the stack are more likely to be dragged by particles flowing out the silo, which, together with the effects of cohesion, will lead to smaller values of the retainment ratio. For $CED = 80 \text{ kJ/m}^3$, however, cohesion is strong enough to hold particles together and conceal the effects of μ_s or μ_r .

For both samples, limiting particles rotation tended to generate more stable stacks as can be seen from the slight increase of the p ratio with increase of μ_r . Finally, increasing values of the CED was directly related with the number of particles staying in the container after the lid was opened. Among the variables studied, CED increase is therefore the best approach to simulate particle interlocking and to numerically reproduce the particles cohesion observed in experiments.

2.3.3. Calibration and selection of optimal values

2.3.3.1. Pareto fronts, 3D representation of optimal values

The evolution of the two objective functions for sample 1 over 100 generations are shown in the Figure 94. The 2000 individuals constituting the initial population are spread over a relatively wide range of the objective function values that gradually narrows with successive iterations. The number of individuals stay constant, so the Pareto fronts shrink around the optimal values with the evolution of the population. Through the iteration process, the fronts converged to an optimum where no further improvement was observed in succeeding generations. For both samples, a convergent front was obtained from the 50th generation.

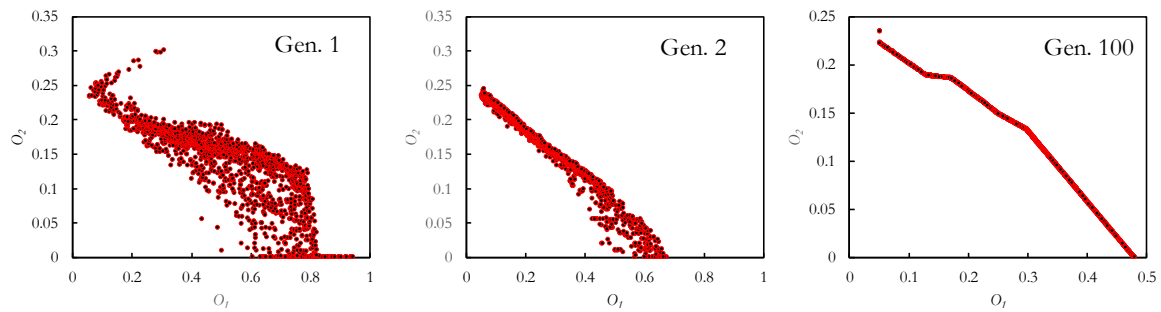


Figure 94. Pareto front evolution over 100 generations of NSGA-II optimization.

As observed through the Pareto fronts, multiobjective optimizations lead to results in which trade-offs between the objective functions were encountered. The optimal solutions that allowed to obtain values of AoR and bulk density closer to the experimental measurements yielded low P values and vice versa. In order to have a comprehensive view of the sets of calibrated parameters that better adjust the bulk experimental properties of each sample, the optimal values for the last generation of NSGA-II optimizations are presented in Figure 95. A color and size scale were used to highlight the values of the total error, calculated as the sum of the values of the objective functions $O_1 + O_2$. For sample 1, sets of optimal calibration parameters with a relatively broad range of solutions were obtained, especially for CED values which could vary between 10 and 50 kJ/m³. For sample 2, a narrower range of optimal sets is shown in Figure 95. The solutions giving the lowest value of $O_1 + O_2$ were input in the LIGGGHTS® program and the simulation results are presented and compared against the experimental values in Table 38.

The calibrations based exclusively on the angle of repose and the bulk density would not lead to a material having enough interparticle cohesion to hold particles together inside a container. Therefore, including the rectangular container test as a bulk response for calibration was decisive to expose the cohesive character of biomass particles. Incorporating the retainment ratio response adds a cohesive feature to the material that could more realistically simulate blocking problems on feed systems for biomass particles. Additionally, calibration using the p ratio sensibly reduced the diversity of the optimal values of μ_s , μ_r and CED . Thus, it is clear that separate calibration test from different macroscopic responses can yield different results and that calibration based on a large number of parameters and bulk responses is preferable.

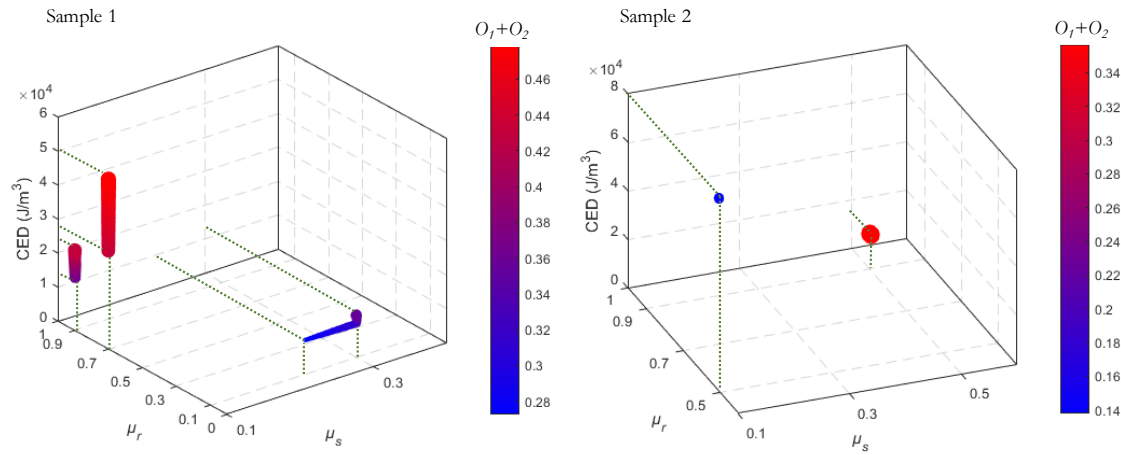


Figure 95. Sets of optimal calibrated parameters for sample 1 and 2. Size and color scale indicate the sum of $O_1 + O_2$ values corresponding to each set of μ_s , μ_r and CED .

Table 38. Optimized values of μ_s , μ_r and CED and comparison of simulated responses (Sim.) against experimental measurements (Exp.). e : relative error between experimental and DEM responses.

Sample	μ_s	μ_r	CED (kJ/m ³)	$O_1 + O_2$	AoR (°)			ρ_b (kg/m ³)			p		
					Sim.	Exp.	e (%)	Sim.	Exp.	e (%)	Sim.	Exp.	e (%)
1	0.2298	0.1000	10.01	0.27	30.0	27.7	8.3	192.2	184.2	4.3	0.80	1	20.0
2	0.1000	0.5004	80.00	0.17	42.3	46.3	8.7	157.1	165.6	5.1	1.00	1	0.0

From Table 38 it can be seen that there was little discrepancy between the simulated and the experimental AoR, bulk density and p ratio for both samples. In the case of sample 1, even if the AoR and bulk density values were better adjusted than those of sample 2, optimization led to particles without enough cohesive strength to form a stable stack in the rectangular container simulations. The optimized values of CED reflect a much more cohesive behavior for finer samples, which corresponds to the experimental observations.

2.3.3.2. Ring shear tester simulations

Values presented in Table 38 were used to simulate a shear sequence in a ring shear tester. Figure 96 compares the simulation results against the experimental evolution of shear stress. Two shear cycles are represented, starting by a preshear step at $\sigma_{pre} = 5$ kPa and followed by a shear at $\sigma_{sh} = 2.5$ kPa. This preshear-shear sequence is repeated for $\sigma_{sh} = 3.75$ kPa. Stresses are plotted against rotation angle defined as the product of time and shear velocity. Although simulation results are relatively noisy (due to the scaled particles and the oscillation of the servo-controlled normal force), it is encouraging that simulation results for sample 1 were very close to experimental shear stress profiles in terms of evolution of the curve shape and the average yield stresses.

Yield stresses of preshear and shear for both samples are listed in Table 39. Values of shear stress were slightly underestimated in DEM simulations for sample 1. A greater gap between the experimental and simulations results was yet observed for sample 2. This can be related to the fact that responses shown in Section 2.3.3.1 for sample 2 were less well predicted using the calibrated parameters than those of coarse powders.

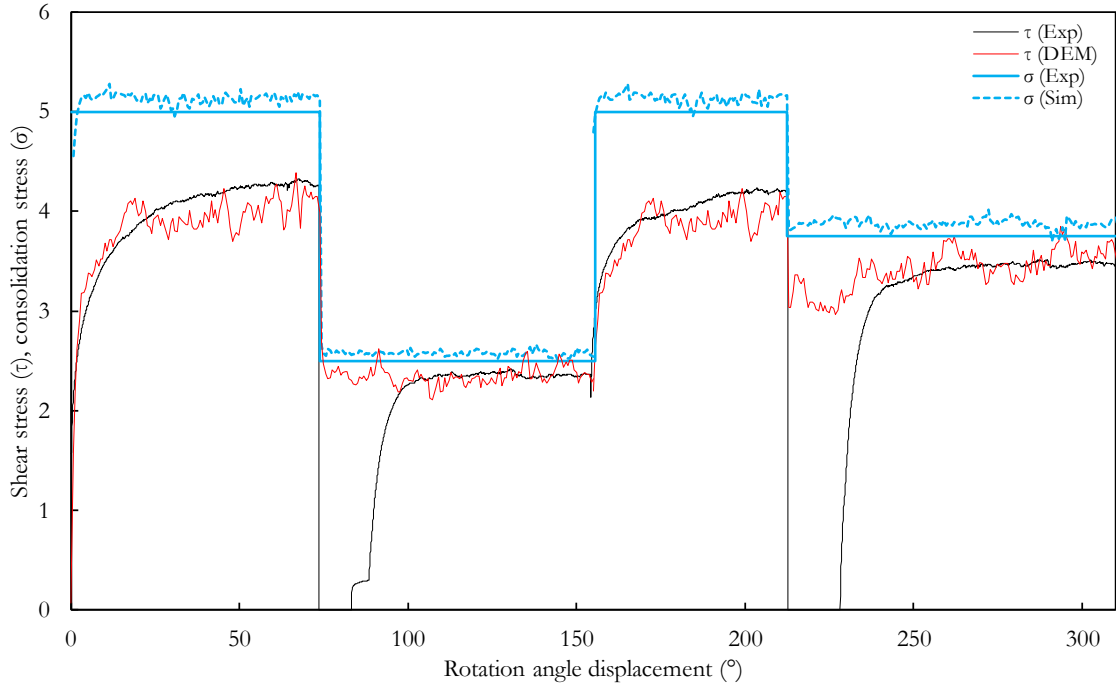


Figure 96. Simulated (DEM) and experimental (Exp) evolution of shear (τ) and consolidation stresses (σ) for sample 1.

Table 39. Simulation (Sim.) and experimental (Exp.) results for ring shear tester tests.

	Preshear stress at $\sigma_{presb} = 5$ kPa			Shear stress at $\sigma_{sb} = 2.5$ kPa		
	Exp.	Sim.	e (%)	Exp.	Sim.	e (%)
Sample 1	4.31	3.94	8.6	2.45	2.32	5.3
Sample 2	4.81	3.49	27.4	2.87	2.51	12.5

The under-estimation of the experimental results from simulations for sample 2 shows that these results should be treated with caution. Indeed, as highlighted by Roessler et al. [395], calibration should take into account the nature of the actual simulated process. Calibration using angle of repose, bulk density and shear box tests might therefore not be sufficient for simulation of materials under a consolidated state, as is the case in shear testers. Furthermore, the use of JKR cohesion models has recently been shown not to adequately capture the stress behavior of some cohesive powders, particularly at relatively high consolidation stresses [396]. This has led to the development of new cohesion contact models that consider contact plasticity. Additional work will therefore evaluate the relevance of JKR models compared to cohesive elasto-plastic models for biomass particles.

2.4. Conclusion

Biomass powder characteristics – such as small particles size, cohesive behavior, low particle density and elongated shape – make bulk simulations highly challenging considering the current DEM state of development. This work aimed at producing a realistic, calibrated and efficient material model for lignocellulosic biomass powders to be eventually used in feeding systems for entrained-flow gasification. We successfully developed a DEM material model for biomass powders by using a coarse-grained multisphere representation of shape and size distributions of particles along with a Hertz-Mindlin-EPDS2-SJKR cohesive force model.

The application of a calibration procedure that uses a NSGA-II optimization algorithm was successful in determining the coefficients of sliding friction, rolling friction and a cohesive energy density term for two biomass powder populations: a coarse sieving cut between 500 μm and 710 μm , and a fine cut between 200 and 315 μm . The results presented here showed that the calibrated contact-law parameters fitted the physical responses accurately, and a validation using a ring shear tester showed promising results. The application of a typically used trial-and-error approach for calibration would have been highly time-consuming compared to the systematic approach used in this work.

This work highlighted the importance of adequately selecting bulk experiments for calibration: only taking results from angle-of-repose and bulk density measurements would not replicate the cohesive behavior of biomass particles to their actual extent. The inclusion of additional bulk responses such as a rectangular container test (shear box) reduced the diversity of optimal calibrated parameters and has resulted in a material model that represents better blocking problems in feeding systems.

With the aim of improving the predictive capability of the DEM model for biomass powders, future research could include additional bulk setups that discriminate between different cohesive strengths of biomass powders, as well as validation under a variety of stress and flow conditions.

The findings presented here showed a scale-dependency of the simulations for the AoR test. The prospect of being able to apply at an industrial scale the calibrated parameters found using the framework described here serves as a stimulus for future research on the scalability of the calibration setups. This remains an important issue to be addressed in future studies, especially regarding cohesive and elongated materials such as biomass particles. Future work should also address the relevance of using flexible particle models that might be more suitable for biomass particles.

Acknowledgements

The authors would like to acknowledge the Ministry of Higher Education and Research of France as well as the French-Dutch Network (Eole Scholarship) for their financial support. John Pachón-Morales is also grateful to the section Transport Engineering and Logistics of Delft University of Technology, where a part of the presented work was conducted. We are especially thankful to the French Council for Poplar (CNP) and the sawmill Huberlant (Cormicy, France) for kindly providing the wood used in this work.

Appendix A. Experimental plan

The Table 40 contains the experimental plan used in this work.

Table 40. *Experimental plan of this work.*

Sample 1								Sample 2			
Run N°	μ_s	μ_r	CED (kJ/m³)	Run N°	μ_s	μ_r	CED (kJ/m³)	Run N°	μ_s	μ_r	CED (kJ/m³)
1	0.1	0.1	0	43	0.5	0.7	10	85	0.9	0.3	50
2	0.3	0.1	0	44	0.7	0.7	10	86	0.1	0.5	50
3	0.5	0.1	0	45	0.9	0.7	10	87	0.3	0.5	50
4	0.7	0.1	0	46	0.1	0.9	10	88	0.5	0.5	50
5	0.9	0.1	0	47	0.3	0.9	10	89	0.7	0.5	50
6	0.1	0.3	0	48	0.5	0.9	10	90	0.9	0.5	50
7	0.3	0.3	0	49	0.7	0.9	10	91	0.1	0.7	50
8	0.5	0.3	0	50	0.9	0.9	10	92	0.3	0.7	50
9	0.7	0.3	0	51	0.1	0.1	20	93	0.5	0.7	50
10	0.9	0.3	0	52	0.3	0.1	20	94	0.7	0.7	50
11	0.1	0.5	0	53	0.5	0.1	20	95	0.9	0.7	50
12	0.3	0.5	0	54	0.7	0.1	20	96	0.1	0.9	50
13	0.5	0.5	0	55	0.9	0.1	20	97	0.3	0.9	50
14	0.7	0.5	0	56	0.1	0.3	20	98	0.5	0.9	50
15	0.9	0.5	0	57	0.3	0.3	20	99	0.7	0.9	50
16	0.1	0.7	0	58	0.5	0.3	20	100	0.9	0.9	50
17	0.3	0.7	0	59	0.7	0.3	20	101	0.1	0.1	80
18	0.5	0.7	0	60	0.9	0.3	20	102	0.3	0.1	80
19	0.7	0.7	0	61	0.1	0.5	20	103	0.5	0.1	80
20	0.9	0.7	0	62	0.3	0.5	20	104	0.7	0.1	80
21	0.1	0.9	0	63	0.5	0.5	20	105	0.9	0.1	80
22	0.3	0.9	0	64	0.7	0.5	20	106	0.1	0.3	80
23	0.5	0.9	0	65	0.9	0.5	20	107	0.3	0.3	80
24	0.7	0.9	0	66	0.1	0.7	20	108	0.5	0.3	80
25	0.9	0.9	0	67	0.3	0.7	20	109	0.7	0.3	80
26	0.1	0.1	10	68	0.5	0.7	20	110	0.9	0.3	80
27	0.3	0.1	10	69	0.7	0.7	20	111	0.1	0.5	80
28	0.5	0.1	10	70	0.9	0.7	20	112	0.3	0.5	80
29	0.7	0.1	10	71	0.1	0.9	20	113	0.5	0.5	80
30	0.9	0.1	10	72	0.3	0.9	20	114	0.7	0.5	80
31	0.1	0.3	10	73	0.5	0.9	20	115	0.9	0.5	80
32	0.3	0.3	10	74	0.7	0.9	20	116	0.1	0.7	80
33	0.5	0.3	10	75	0.9	0.9	20	117	0.3	0.7	80
34	0.7	0.3	10	76	0.1	0.1	50	118	0.5	0.7	80
35	0.9	0.3	10	77	0.3	0.1	50	119	0.7	0.7	80
36	0.1	0.5	10	78	0.5	0.1	50	120	0.9	0.7	80
37	0.3	0.5	10	79	0.7	0.1	50	121	0.1	0.9	80
38	0.5	0.5	10	80	0.9	0.1	50	122	0.3	0.9	80
39	0.7	0.5	10	81	0.1	0.3	50	123	0.5	0.9	80
40	0.9	0.5	10	82	0.3	0.3	50	124	0.7	0.9	80
41	0.1	0.7	10	83	0.5	0.3	50	125	0.9	0.9	80
42	0.3	0.7	10	84	0.7	0.3	50				

Appendix B. Individual simulation results

Figure 97 shows the totality of results from simulations. Each run number corresponds to a set of μ_s , μ_r and CED values listed in Table 40.

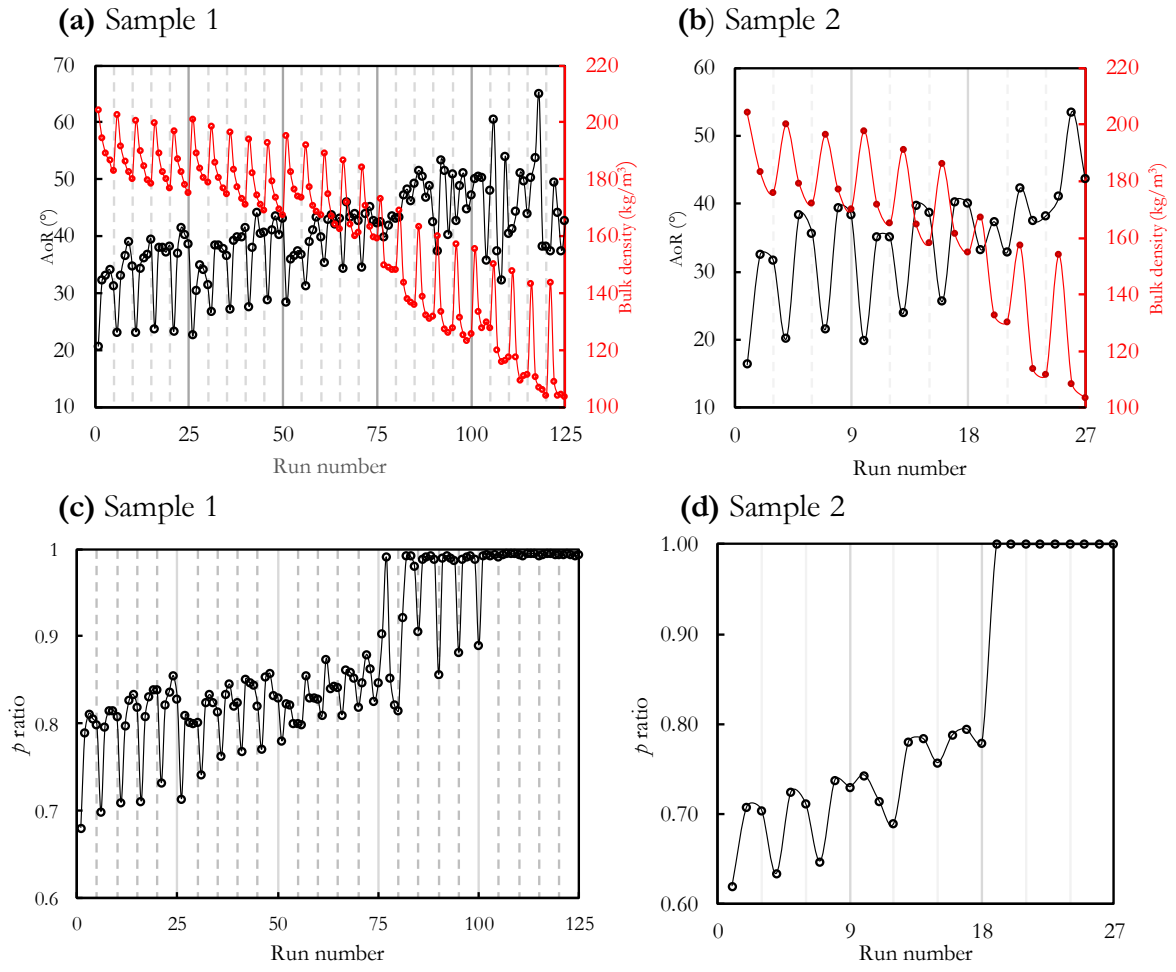


Figure 97. Simulation results of AoR, bulk density and p ratio for Sample 1 and 2.

3. Implementation of the calibration procedure of DEM parameters for torrefied biomass powders

This section provides details on the implementation of the calibration framework described previously in the section 2 of this chapter to the full set of biomass samples studied in Chapter IV (two sieving cuts of raw and torrefied powders). The implementation of an additional optimization procedure for DEM parameters without interpolation is also discussed at the end of this section.

In addition to their utility as calibration responses, the bulk measurements (angle of repose, bulk density and retainment ratio) provide knowledge on the flow behavior of the biomass materials. In particular, the Angle-of-Repose and the Compressibility Index (derived from bulk density measurements) are generally used as methods for flowability characterization (Chapter I, section B-2.2). Therefore, comparative observations on the values of the bulk measurements for the six samples are also provided in this section and related to their particle characteristics.

3.1. Sample preparation and particle size and shape characteristics

The procedure for producing the powder samples has been detailed in Chapter IV. The same nomenclature of the six samples is used in this section. The granulometric characteristics of the samples relevant to this section are recalled in Table 41.

Table 41. Nomenclature of the samples, size and shape characteristics.

Sample ID	Description	Torrefaction temperature (°C)	ML (%)	Sieving cut (μm)	x_{50} (μm)	S_x	a_{50}
1	Raw coarse	----	0	500-710	746	0.36	0.38
2	Raw fine	----	0	200-315	352	0.36	0.42
3	ML = 9.6 % coarse	240	9.6	500-710	667	0.35	0.31
4	ML = 9.6 % fine	240	9.6	200-315	320	0.33	0.33
5	ML = 24.5 % coarse	280	24.5	500-710	526	0.48	0.41
6	ML = 24.5 % fine	280	24.5	200-315	253	0.39	0.43

3.2. Bulk behavior tests

3.2.1. Angle-of-repose from bulk solid heaps, bulk density and compressibility index

As stated in the section 2 of this chapter, conventional methods for measuring the angle-of-repose were tested in the preliminary stages of this work. One of these methods uses a lifting cylinder or funnel to produce a heap from which the angle-of-repose can be measured (Figure 98a). Figure 98b shows examples of the cylindrical structures formed with raw and torrefied biomass samples after the cylinder

was removed. Stable structures were formed regardless of the filling method or the cylinder size, making quantitative measurements impossible.



Figure 98. Lifting cylinder preliminary tests. (a) Schematic of the experiment (adapted from [380]). (b) Examples of the stable stacks of biomass formed.



Figure 99. Angle-of-repose experiments. (a) Schematic representation of the main setup and dimensions. (b) Examples of the heaps formed for the biomass powders.

The poured AoR method described in the second section of this chapter was applied to the six samples of biomass. A schematic view of the experimental setup for AoR measurements as well as examples of the heaps formed for the biomass powders are shown in Figure 99. Each measurement was repeated seven times.

Measurements of the loose bulk density (ρ_b) were also replicated for the torrefied set of powders. Each measurement was repeated for six refills using different dried samplings of the same batch. Taking advantage of the similar experimental protocol required, measurements of the tapped bulk density (ρ_t) were also conducted. The tapped bulk density is obtained by tapping the container holding the aerated sample until no further volume variation is observed. Comparing the loose and tapped bulk densities gives a quick estimation of bulk compressibility and flowability [397]. For this purpose, the compressibility index (CI) can be defined as:

$$CI = \left(1 - \frac{\rho_t}{\rho_b} \right) \cdot 100\% \quad (79)$$

As seen in the section B-2.2 of Chapter I, the compressibility index test is based on the influence of interparticle adhesive forces on bulk density: in loose bulk solids of poor flowability relatively large voids

are formed under the influence of adhesive forces, making them more compressible. This is not the case of free-flowing powders where the structure will collapse and the arrangement has little opportunity for further consolidation. Therefore, higher values of CI mean poorer flowability [141,324].

Table 37 lists the average values of the angle-of-repose, bulk and tapped densities as well as the compressibility index. A relatively low standard deviation was observed for these bulk measurements (mostly below 10 % of the measured value), meaning a good experimental repeatability.

Table 42. Results of bulk measurements for the biomass powders (the values in parentheses correspond to the standard deviation).

Sample	1. Raw coarse	2. Raw fine	3. ML = 9.6 % coarse	4. ML = 9.6 % fine	5. ML = 24.5 % coarse	6. ML = 24.5 % fine
AoR (°)	27.7 (0.7)	46.3 (1.6)	39.1 (3.3)	51.3 (2.9)	35.8 (2.9)	47.1 (2.6)
ρ_b (kg/m ³)	184.2 (5.7)	165.6 (5.1)	116.2 (9.1)	90.6 (1.0)	120.6 (1.1)	102.3 (1.2)
ρ_t (kg/m ³)	233.7 (5.7)	240.2 (3.8)	159.8 (4.7)	145.0 (2.6)	173.6 (0.9)	157.5 (3.0)
CI	21.2 (3.8)	31.1 (1.3)	28.6 (3.9)	37.6 (1.0)	30.6 (0.5)	35.0 (1.5)

The differences of the values of ρ_b , AoR and CI between the different samples indicate that there is a significant effect of the sample characteristics on the measured bulk behavior that is worth discussing.

Regarding the loose bulk density, previous research has shown that in the case of non-cohesive materials, a better spatial arrangement is achieved for finer particles so a decrease of particle size is generally accompanied by an increase in bulk density [203,397]. Interestingly, in the case of the biomass powders, the opposite trend was observed: lower loose bulk densities were systematically obtained for the fine sieving cuts. For raw biomass, the finer samples had a bulk density 10 % lower than the coarse samples. This difference was 22 % and 15 % for mildly and intensively torrefied samples, respectively. This trend is likely to be caused by cohesion effects: the presence of fine cohesive particles creates more voids which reduces bulk density. For coarse powders the interparticle cohesive forces weaken with respect to the weight of the particles, so the powder packs in a denser condition. Similar observations were made by Mani et al. [119] for wheat straw and corn stover when particle size was below 0.4 mm.

These observations seem to be in conflict with results presented in section 3 of Chapter III, where a direct relationship between the bulk density and grinding time (i.e. particle size reduction) was found. These differences in behavior are likely to be related to the differences in particle shape and span of the distributions between the samples used in both parts of this research. Indeed, in the case of the samples studied in section 3 of Chapter III, the shape of the particles became considerably rounder when particle size decreased. Wide distributions were also obtained with intensive ball milling, which implies that there are fine particles available to occupy the voids between larger particles. This better spatial arrangement triggers an increase of the bulk density of with size decrease. In the case of the samples studied in this chapter, the elongated shape is still very present for the finer particles and distributions are relatively narrow because of the sieving stage. There are probably not enough particles to fill the voids between the larger particles. These effects, combined to an increased interparticle cohesion due to the small particle size, would result in loose lower bulk densities.

Regarding the treated samples, the mildly torrefied powders have, on average, lower loose bulk densities than the raw and the intensively treated samples. The raw samples had the highest loose bulk density (+41 % and +36 % when compared to mildly and intensively torrefied samples, respectively). A first possible reason for this behavior could be a lower particle density for the torrefied powders. However, it has been reported in the literature that there were no significant differences of particle densities between raw and torrefied samples due to the combined effects of mass loss and volumetric

shrinkage during torrefaction [109]. Therefore, more likely, the reduction of particle bulk density with torrefaction could be the result of a looser particle arrangement triggered by the combined effect of irregular shapes and an increased particle cohesion. Indeed, several experimental and computational studies [255,270,398] have shown that irregular and elongated shapes lead to more points of contact between particles. This makes the relative motion more difficult leading to greater volume voids and lower bulk density. Again, these trends seem to be contrary to the behavior presented in Chapter III where the bulk density was directly related to the intensity of torrefaction. As mentioned above, these differences are likely due to the sieving stage and its effects on the shape and polydispersity characteristics of the samples.

As for the loose bulk density, the tapped bulk density was highest for the raw samples followed by the highly torrefied and the mildly torrefied powder. In the case of the torrefied samples, reducing particle size led to a lower tapped density, whereas there was not significant difference between the tapped density of the both sieving cuts for the raw samples.

Globally, the AoR and *CI* followed the same qualitative trends (Figure 100). Regarding the AoR, the finer sieving cuts formed steeper heaps with values of AoR up to 67 % greater than the coarse cuts (in the case of the raw samples). Regarding the torrefaction intensity, by taking the average value of both particle sizes, the following general AoR ranking can be established: Mildly torrefied > intensively torrefied > untreated samples. According to the classification criteria based on the AoR established by Ileleji et al. [219] for lignocellulosic biomass, the sample 1 can be classified as free flowing ($\text{AoR} < 30^\circ$), the samples 5 and 3 are fairly flowing ($35^\circ < \text{AoR} < 40^\circ$), the samples 2 and 6 are poor flowing ($40^\circ < \text{AoR} < 50^\circ$) and the sample 4 has a very poor flow behavior ($\text{AoR} > 50^\circ$).

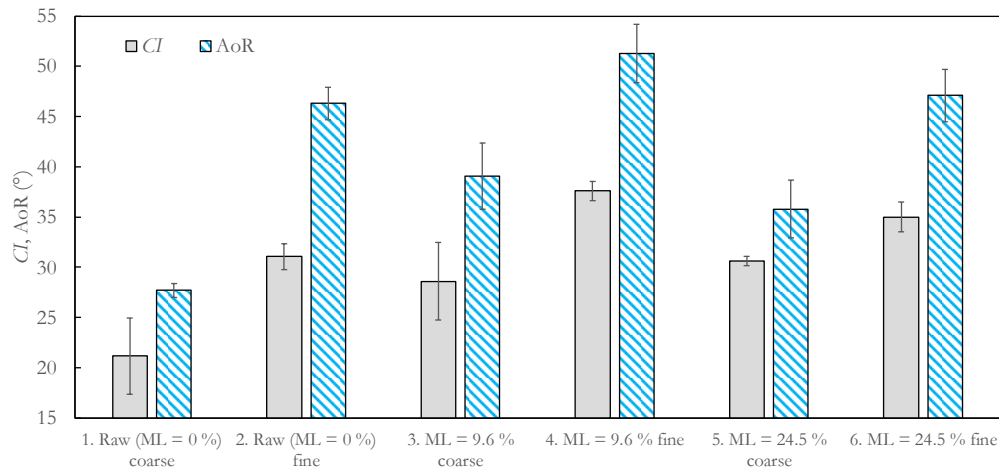


Figure 100. Compressibility index and angle-of-repose for the six biomass samples.

Coherently, the fine sieving cuts had always a higher *CI* than the coarse powders, meaning a higher cohesive behavior. As with the AoR results, the greatest difference between fine and coarse sieving cuts was observed for the untreated samples, for which a 47 % higher *CI* was obtained for the fine powder. The differences between sieving cuts are less pronounced for the torrefied samples. The raw coarse powders had the lowest compressible behavior and thus the best flowability according to the *CI* criterion. The most compressible powder being the fines of the mildly torrefied sample (sample 4), it is expected that it will have a very poor-flowing behavior under non-consolidated conditions. Following the classification based on *CI* established by Carr [399], the sample 1 (raw coarse) has a 'passable flow' behavior ($21 < CI < 25$), the samples 2, 3 and 5 (raw fine and torrefied coarse) are 'poor flowing' ($26 < CI < 31$), the sample 6 ($ML = 24.5\%$ fine) has a very poor flow behavior ($32 < CI < 37$) and

sample 4 ($ML = 9.6\%$ fine) has extremely poor flow characteristics ($CI > 37$). These observations are in agreement with the results presented in Chapter IV where mildly torrefied samples had poor flow in a non-consolidated conditioning. The compressibility index and angle-of-repose measurements seem therefore to capture this flow behavior well.

3.2.2. Rectangular container test

As for the hollow cylinder tests, stable stacks of particles were formed for all the samples when the lid of the rectangular container was lifted. The retainment ratio p is therefore 1.0 for the six samples.

3.3. DEM simulations

The elongated shape of the biomass particles was represented in DEM simulations using a multisphere approach. For all the samples, monodispersed populations were simulated using the average size and shape descriptors presented in Table 41. Table 43 lists the model parameters used for particle representation using an overlapping factor (ϕ) of 20 %. The 3D representations for the six samples are shown in Figure 101.

Table 43. Parameters for multisphere model representation of biomass samples.

Sample	1	2	3	4	5	6
n_{sph}	3	3	4	4	3	3
d (μm)	746	352	668	320	526	252
l (μm)	1940	915	2273	1089	1367	657
V_{clump} (mm^3)	0.6282	0.0658	0.5997	0.0659	0.2199	0.0244
R_{eq} (μm)	531	251	523	251	374	180

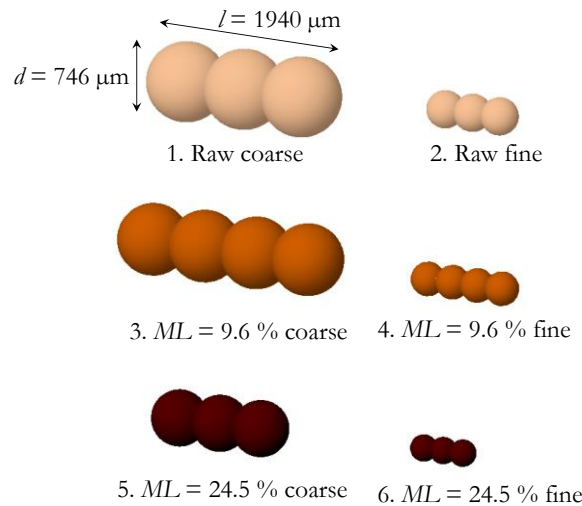


Figure 101. DEM particle representation of biomass samples (true relative size) using a multisphere approach.

A coarse-graining approach to reduce computing time was used for all the samples, so the particle size was scaled up by a factor of 4. The particle-wall interaction parameters for the simulations of the heap formation setup were reported in section 2 of this chapter and were kept the same for the simulations of the torrefied powders. Table 44 shows additional DEM parameters of simulations of the torrefied samples. The calibration simulations (heap formation) were partially conducted using the

‘Reynolds’ cluster of the Maritime and Transport Technology department of TU Delft [400]. This cluster consists of 14 compute nodes with 28 cores each (2× Xeon® E5-2680 v4 64 GB machine).

Table 44. DEM features for simulations of heap formation.

Parameter	Sample 3	Sample 4	Sample 5	Sample 6
Particle density (kg/m ³)	350	1,000	350	1,000
Timestep (heap) (s)	1×10^{-5}	7×10^{-6}	8×10^{-6}	7×10^{-6}
Total number of spheres (heap)	14,868	108,268	30,444	219,195
Number of processors	8	8	8	8
Computation time (hours)	11.2	9.58	7.11	22.6

3.4. Calibration results using NSGA-II optimization

By applying the same factorial design (5^3) described in section 2, the values of μ_s , μ_r and CED were varied within a range from 0.1 to 0.9 for the friction coefficients and from 0 to 80 kJ/m³ for the Cohesion Energy Density. The same qualitative trends as described in section 2, regarding the effects of the friction coefficients and CED on the bulk responses were observed for the simulated torrefied particles. An example of the values of the bulk density, AoR and the retainment ratio obtained from simulations for sample 5 ($ML = 24.5\%$) is shown in Figure 102.

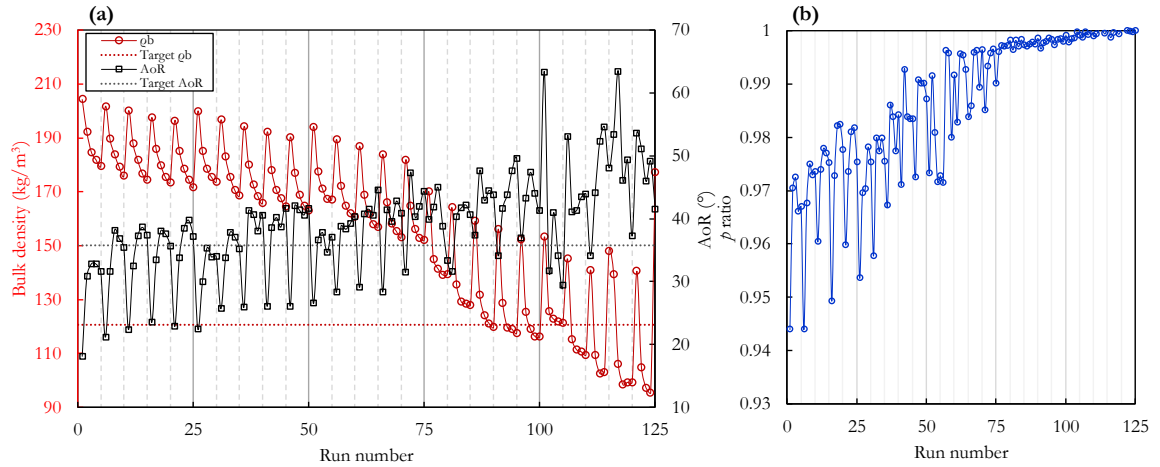


Figure 102. Simulation results for the sample $ML = 24.5\%$. (a) Bulk density and AoR. (b) retainment ratio (p). The run number corresponds to an individual set of parameter combinations of the $5 \times 5 \times 5$ design (reported in section 2 of this chapter).

Figure 103 illustrates the final (i.e. after 100 generations) Pareto fronts obtained using the NSGA-II optimization algorithm. The compromise between the two objective functions is therefore evident. While relative low errors could be achieved for the objective function O_2 (related to the retainment ratio p), the deviations for O_1 (related to both the bulk density and the AoR) were generally larger.

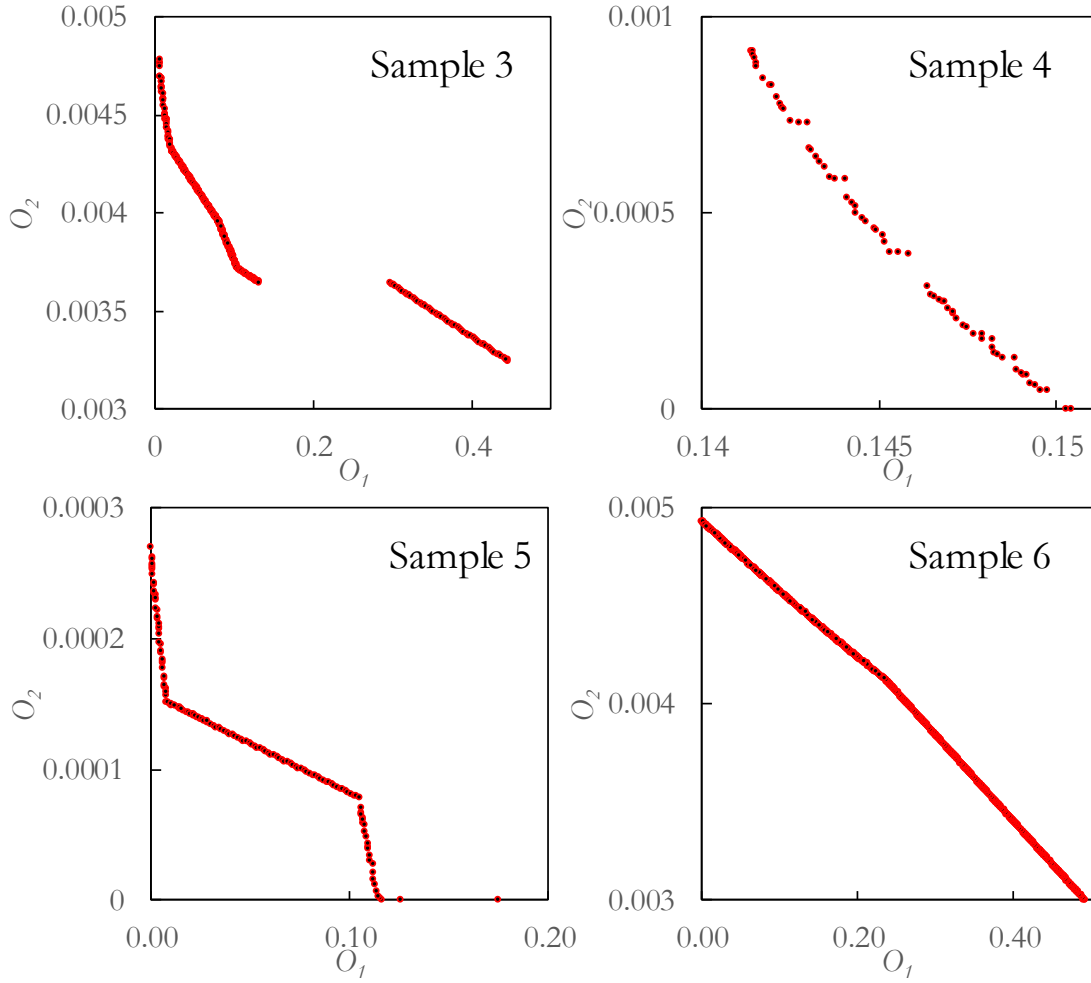


Figure 103. Pareto fronts after 100 generations of NSGA-II optimization.

The optimal values for the latest generation of the NSGA-II optimizations are presented in Figure 104, using a color and size scale for the data points that represents the sum of the objective functions. The sets of parameters giving the lowest value of $O_1 + O_2$ for each sample were entered in the LIGGGHTS[®] input script and the simulation results are compared against the experimental values in Table 45.

While the differences between the simulated and the experimental results for the retainment ratio were almost neglectable, and acceptable for the bulk density, the error was quite significant for the AoR (except for sample 4). The differences between the ‘expected’ AoR (using the optimized parameters) and the one effectively obtained from simulations are the result of the deviation of the AoR from linear profiles at high values of CED which affects the accuracy of the interpolation (the optimization algorithm uses an interpolation of the responses based on the simulation grid of μ_s , μ_r and CED values). This is the case, for example, in Figure 102a for the last 25 sets of parameter combinations (100 to 125) corresponding to $CED = 80 \text{ kJ/m}^3$, where the AoR values fluctuate without a clear monotonous trend. Since the values of $p = 1$ are only obtained for high values of CED (Figure 102b), the optimization algorithm forces the solutions towards the sets of parameters for which the AoR values are the most uncertain.

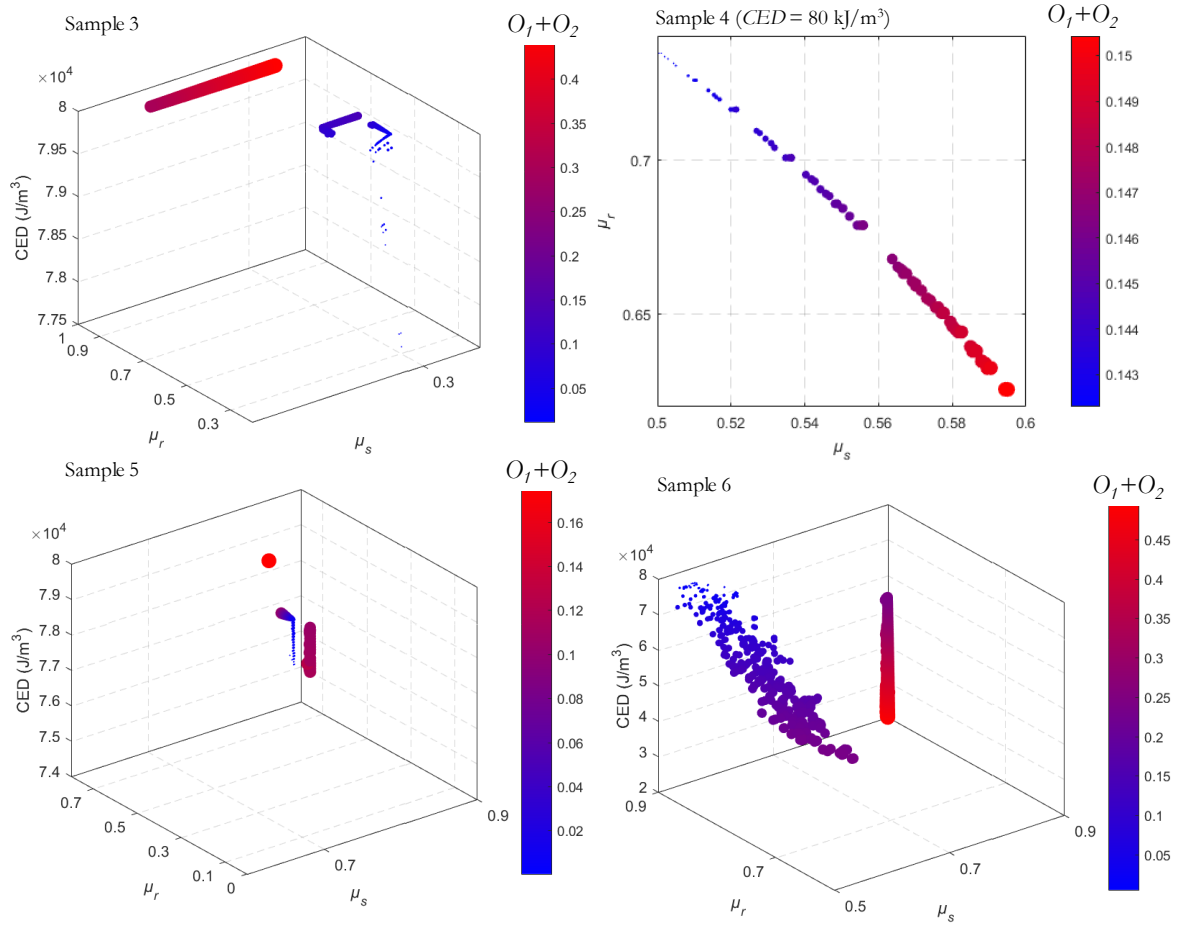


Figure 104. Sets of optimal parameters for torrefied samples. The size and color scale of the data points indicate the value of the sum O_1+O_2 for each set of μ_s , μ_r and CED.

Table 45. Optimized values of μ_s , μ_r and CED and comparison of simulated responses (Sim.) against experimental measurements (Exp.). e: relative error between the experimental and DEM responses.

Sample ID	μ_s	μ_r	CED (J/m ³)	O_1+O_2 (%)	AoR (°)			ρ_b (kg/m ³)			p		
					Sim.	Exp.	e (%)	Sim.	Exp.	e (%)	Sim.	Exp.	e (%)
3	0.3002	0.3002	77576	1.16	45.9	39.1	17.5	114.5	116.2	1.5	1	1	0.0
4	0.5004	0.7342	80000	14.2	50.5	51.3	1.5	104.3	90.6	15.1	1	1	0.1
5	0.6935	0.1313	79062	0.031	45.9	35.8	28.4	119.2	120.6	1.1	1	1	0.4
6	0.5481	0.8844	77967	0.5	38.7	47.2	17.9	104.0	102.3	1.7	1	1	0.5

3.5. Optimization without interpolation using Minitab®

A Response Optimizer tool in Minitab® is used to identify the combination of input variables that fits the set of experimental responses. The particularity of the Minitab® optimizer, compared to the NSGA-II procedure, is that in its Factorial Design Response Optimizer, only the values of variables belonging to the parameter grid are possible candidates for optimization, so no interpolation is made. Figure 105 shows an example of the optimization plot obtained for samples 1 and 2, with the identified optimal parameters in red ('Cur').

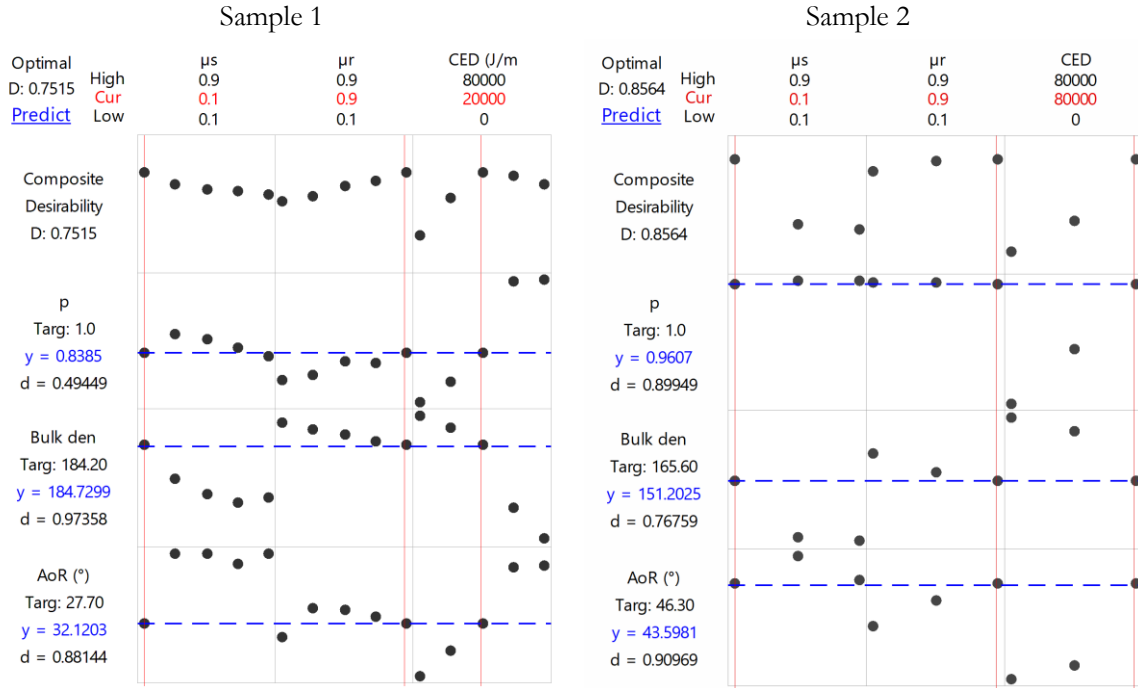


Figure 105. Examples of optimization results from MINITAB for samples 1 and 2.

Individual and composite desirability assess how well a combination of variables satisfies the goals defined for the responses. The individual desirability (d) evaluates how the settings optimize a single response; composite desirability (D) evaluates how the settings optimize a set of responses overall. Desirability (both individual and composite) has a range of zero to one. One represents the ideal case in which the responses exactly match the targets set; zero indicates that one or more responses are outside their acceptable limits. The Response Optimizer calculates individual desirability using a desirability function d_i , defined as:

$$d_i(Y_i) = \begin{cases} 0 & \text{if } Y_i(x) < L_i \\ \left(\frac{Y_i(x) - L_i}{T_i - L_i} \right)^s & \text{if } L_i \leq Y_i(x) \leq T_i \\ \left(\frac{Y_i(x) - U_i}{T_i - U_i} \right)^t & \text{if } T_i \leq Y_i(x) \leq U_i \\ 0 & \text{if } Y_i(x) > U_i \end{cases} \quad (80)$$

where Y_i is the particular response to be optimized, which is function of x , the set of optimal individuals; L_i and U_i stand for the low and upper limits of possible values for Y_i . The exponents s and t determine how important it is to hit the target value Y_i . For $s = t = 1$, the desirability function increases linearly towards T_i ; for $s < 1$, $t < 1$, the function is convex, and for $s > 1$, $t > 1$, the function is concave.

In this work, all targets were set to be equally important [401]. The desirability function approach is one of the most widely used methods in industry for the optimization of multiple response processes. The composite desirability, D , is the weighted geometric mean of the individual desirabilities for the responses:

$$D = (d_1(Y_1)d_2(Y_2)\cdots d_k(Y_k))^{1/k} \quad (81)$$

with k denoting the number of responses. Minitab® determines a global optimal set of variables by maximizing the composite desirability [402]. The calibrated DEM parameters obtained using this procedure, along with the corresponding values of the bulk responses from simulations are listed in Table 46.

Table 46. Calibrated DEM parameters using Minitab® optimizer.

Sample ID	μ_s	μ_r	CED (kJ/m ³)	$Composite$ desirability	AoR (°)			ρ_b (kg/m ³)			P		
					Sim.	Exp.	ϵ (%)	Sim.	Exp.	ϵ (%)	Sim.	Exp.	ϵ (%)
1	0.1	0.9	20	0.75	32.1	27.7	15.9	184.7	184.2	0.3	0.83	1	17
2	0.1	0.9	80	0.86	43.6	46.3	5.8	151.2	165.6	8.7	0.96	1	4
3	0.9	0.7	50	0.88	44.2	39.1	13.0	120.8	116.2	3.9	0.97	1	3
4	0.5	0.9	80	0.94	49.4	51.3	3.7	101.9	90.6	12.5	1.0	1	0
5	0.9	0.3	50	0.93	40.3	35.8	12.6	123.2	120.6	2.1	1.0	1	0
6	0.5	0.9	80	0.93	44.0	47.2	6.8	105.7	102.3	3.3	0.99	1	1

As no interpolation is made during optimization, values presented in Table 46 correspond to actual tested values of the parameter factorial design, so no verification was needed. The error for the AoR was reduced compared to the NSGA-II optimization results. Additionally, it is interesting to note that significantly lower CED values were obtained for the coarse samples (samples 1, 3, 5), which is consistent with their lower macroscopic cohesive nature compared to the fine sieving cuts (samples 2, 4, 6). An optimization using only values within the parameter grid seems therefore more reliable than an algorithm using interpolation. As discussed in the section 2 of this chapter, however, the accuracy of the results can be improved by increasing the resolution of the parameter grid.

4. Potential of DEM for investigation of non-consolidated flow of cohesive and elongated biomass particles

John Pachón-Morales ^a, Patrick Perré ^{a,c}, Joel Casalinho ^a, Huy Do ^b, Dingena Schott ^b, François Puel ^a, Julien Colin ^{a,c}

^aLGPM, CentraleSupélec, Université Paris-Saclay, 3 rue Joliot-Curie, 91192 Gif-sur-Yvette, France

^bSection Transport Engineering and Logistics, Department Maritime & Transport Technology, Faculty of Mechanical, Maritime and Materials Engineering, Delft University of Technology, Mekelweg 2, 2628CD Delft, The Netherlands

^cLGPM, CentraleSupélec, Université Paris-Saclay, SFR Condorcet FR CNRS 3417, Centre Européen de Biotechnologie et de Bioéconomie (CEBB), 3 rue des Rouges Terres, 51110 Pomacle, France

Submitted to Advanced powder technology journal

Abstract

The evaluation of the flow properties of biomass powders is essential for the design of efficient storage, handling, and transportation systems within a thermochemical valorization context. Although Discrete Element Method (DEM) is a useful tool for simulation of the bulk behavior of granular materials, it has been rarely used for studying biomass feedstocks. This study is focused on the numerical investigation of the flow of raw and torrefied biomass particles in a loose and dynamic conditioning using a rotating drum setup. The relevance of DEM parameters calibrated using bulk experiments (angle-of-repose, bulk density, retainment ratio) was tested by comparison with experimental data obtained using a rotating drum system. The calibrated DEM material model considers the elongated, submillimetric and cohesive nature of the biomass powder. Several relevant flowability descriptors, such as the Upper Angle of Stability, the size of the avalanches, the fraction of revolution to trigger events and the irregularity of the free surface, are evaluated using both experimental data and DEM simulations. DEM results reproduced well the experimental trends and distinguished between the different cohesive extent of the samples. Realistic results could thus be obtained with upscaled simplified representations of particle shape that are efficient in terms of computing time. The simulation outcome shows that DEM is a relevant technique to assess flowability of biomass powders in a non-consolidated dynamic flow. This paves the way for the study of the effects of particle characteristics on bulk flow, which are briefly discussed.

Keywords: Woody biomass powder; DEM parameter calibration; Flowability; Avalanching; Multisphere approach; Coarse-graining; Particle shape; Rotating drum

4.1. Introduction

Interest in lignocellulosic biomass has sharply increased recently due to its potential as a renewable energy source to produce chemicals and gaseous or liquid biofuels. In biomass gasification processes for 2nd generation biofuel production, the granular flowability of the biomass feedstock influences the continuous, stable and controllable operation of the gasifier, which affects the design of reactors and

composition of the product gas [126,129,220]. Flow fluctuations, bridging and blockage of biomass particles in feeding systems of gasifiers are common industrial problems that hinder the cost-effective industrialization of biomass valorization facilities.

Before being fed into the gasifier, the biomass can be pre-treated, namely by torrefaction. Torrefaction is a mild pyrolysis at temperatures ranging between 200 °C and 300 °C in an inert environment. Details on the effects of torrefaction on biomass properties and its interest as pretreatment step for biomass valorization can be found in [33,403]. In addition to improving the energy density and grindability of the material, torrefaction also influences the size and shape of the particles obtained after grinding [113,404] which has an impact on flow properties.

Flow issues can be correctly addressed through knowledge of the flow behavior of bulk solids. Despite the relatively frequent occurrence of flow problems, little is known about the flow properties of biomass materials, which may differ significantly from those of conventional granular materials used in industry [216]. Research on the flow properties of milled biomass has primarily focused on measurements using shear testers [102,202,208,212,217,222] in which powders are in a consolidated and quasi-static state.

Rotating drums are widely used devices for characterizing flowability of powders in a loose and dynamic state. They stand as a very practical geometry to study the flow of granular materials through, for instance, the evaluation of their avalanching behavior. The test does not require an extensive sample preconditioning, is performed quickly and can be repeated many times without operator intervention. In addition, rotating drums can detect changes in powder flowability brought by powder additives with greater precision and reproducibility than other commonly used loose-state tests such as angle-of-repose tests and bulk density measurements [185]. Although an overwhelming majority of work using rotating drums has focused on cohesionless materials [160,177,190,346], recent research [180,184,190,193,195,347] has highlighted the pertinence of the study of avalanches to assess flowability of cohesive materials such as moist pharmaceutical [194] and cocoa [183] powders. The avalanche characterization of biomass powder -which has a recognized cohesive character- could provide a new insight on the dynamic free-surface flow behavior of this material. For instance, values of the Upper Angle of Stability obtained from rotating drum experiments have been correlated to the discharge rates at the outlet of screw feeders for biomass [217].

With the rapid development of high-performance computing technology, the discrete element method (DEM) [405] is becoming a powerful simulation tool to understand granular dynamics, particularly in rotating drum flows [349]. Experimental evaluation of the isolated effects of shape, size or surface interactions on the flow behavior of bulk solids can be difficult to achieve since these properties are often correlated. Access to the individual particle dynamics of fine materials is also a major difficulty in experimental work. The ability to run a large number of simulations with full control of the physical properties of the system under study makes DEM simulations a cost-effective way to help overcome experimental limitations. It also gives an insight on the particle-scale phenomena taking place during flow.

Two approaches are commonly used in literature to study the flow of granular materials in rotating drums using DEM. First, a large number of investigations focuses on the microdynamics of particles flow within the drum, namely through the assessment of coordination numbers, collision frequencies of individual particles and velocity profiles [348,406–409]. A second approach includes the evaluation of global bulk characteristics such as dynamic angles of repose or the study of mixing and segregation of polydisperse populations [163,191,414,269,348,349,408,410–413]. The latter approach was used in this

work, since flowability was assessed using bulk flow descriptors based on the motion of the mass center of the powder bed.

Due to limited computing power, implementation of DEM has limitations for simulating full-scale industrial applications, where large quantities of particles are involved [367]. Non-spherical particle shapes as well as cohesive behavior are also expensive features to model in DEM, mainly due to the need for more complex contact detection algorithms and force models. In consequence, so far, most numerical studies on granular flow in rotating drums are restricted to either spherical, non-cohesive or coarse ($d_p > 1$ cm) materials. However, challenging aspects of modeling biomass particles are precisely the inclusion of a realistic shape model, along with a cohesive behavior for low-particle-density and submillimetric particles.

The effects of particle shape on the flow behavior of non-cohesive granular materials inside rotating drum setups, using both DEM and experimental approaches, have been the subject of recent research [155,269,416,348,385,410–415]. For instance, Norouzi et al. [410] numerically studied the flow behavior of both spherical and non-spherical cohesionless polystyrene particles. They found that, at the same operating conditions (namely, rotational speed and filling ratio), the dynamic angle of repose -defined as the angle between the flat surface of particles and the horizontal axis- was greater for non-spherical than for spherical particles. Similar conclusions were drawn by Santos et al. [348] for rice grains compared to spherical glass beads. Mead et al. [412] comprehensively studied the influence of the aspect ratio, angularity, particle size distribution and inter-particle contact friction on the angle of repose obtained using a rotating cylinder in an avalanching regime. Wachs et al. [416] and Höhner et al. [269] have conducted DEM simulations of spheres and three different polyhedral particles in a rotating drum. They have found that the dynamic angle of repose increased with decreasing particle sphericity. Additionally, angular particles led to a less flat free surface of the particle bed and an intermittent flow behavior.

Unlike non-cohesive free-flowing materials, cohesive flow in rotating drums has been investigated far less. Granular cohesive systems may exhibit very different flow patterns and physical behavior (e. g. avalanching) than systems where cohesion is not significant [180,417]. Prior studies on DEM simulation of cohesive bulk materials in rotating drums include the study of velocity profiles [418], avalanching and surface angles [180,191,418], segregation and axial dispersion [417,419]. Brewster et al. [418] have reported that the magnitude of interparticle cohesion has a significant effect on the shape of the powder free surface. At low rotation rates and high enough interparticle cohesion, the powder free surface is convex. Decreasing the cohesion or increasing the rotation rate causes the free surface to flatten. Using DEM simulations Faqih et al. [188] have shown that the cohesion of the material is directly proportional to the standard deviation of the center of mass of a powder inside a rotating drum.

To obtain results that accurately reproduce experimental behavior, DEM parameters must be carefully chosen, measured or adjusted through calibration. Prior studies have used results from rotating drum experiments, predominantly the dynamic angle of repose, for DEM calibration of non-cohesive materials [150,348,376]. However, reaching a steady state may need several rotations of the drum, which requires long computation times, especially for a large number of submillimetric particles. Since calibration procedures generally involve running several batches of simulations with combined DEM parameters, the entire process would result in impractical timeframes. A first attempt for accelerating DEM calibration using rotating drum results was made by Hu et al. [349], by using the critical upper and lower angles of the first avalanche. This approach has yielded satisfactory results for spherical and non-cohesive materials. However, in the case of elongated and cohesive powders, the highly chaotic and history-dependent nature of the avalanches requires an assessment of dynamics over a long period of time.

As previously commented, in addition to the calibration of DEM parameters, the large number of particles of typical industrial processes is another factor that limits the use of DEM in industry [279]. Scaling up particle size is one technique that allows simulations to be run in a reasonable period. Coetzee [414] studied the effect of using upscaled particles on the dynamic angle of repose of corn grains in a rotating drum and identified a single set of calibrated parameters for all particles with scaling factors ranging from 1.0 to 4.0. Several particle scaling approaches have been proposed in literature, including exact scaling [367,368], coarse graining [370,371] and cutting-off approach [255]. A coarse-graining approach reduces computational effort by replacing individual (real) particles by representative upscaled ‘meso’-particles [280,370,420]. This approach has shown promising results for simulation of submillimetric biomass particles [360].

This paper presents a numerical study on the macroscopic flow behavior of raw and torrefied biomass powders in a rotating drum setup using DEM. Comparison with experimental data makes it possible to assess the relevance of DEM parameters calibration from bulk experiments, applied to a rotating drum system. The results are intended to be useful in understanding the effect of particle size, shape and interparticle forces on the flowability of biomass powders in a non-consolidated and dynamic regime.

First, the material characteristics and the experimental setup are presented in the materials and method section. Thereafter, the DEM simulation methodology is detailed. Several relevant flowability descriptors such as the Upper Angle of Stability, the avalanche size, the fraction of revolution to trigger events and the irregularity of the free surface are evaluated from experimental data and DEM simulations. A comparison is made and comments on the effects of particle characteristics on flow behavior are finally provided.

4.2. Granular materials and experimental setup

4.2.1. Granular material preparation

Poplar (*Populus euro-americana* ‘Koster’) was used in this study as representative of a fast-growing lignocellulosic crop. A poplar tree was cut into boards that were then dried. Samples of 60×80×15 mm³ were cut from a selected board.

The coupled effect of torrefaction and sieving on particle characteristics was considered in this work. Torrefaction was made in a batch furnace especially developed to assure homogeneous inter-particle treatment [335]. A controlled inert atmosphere, swept by a nitrogen flow, guaranteed an oxygen level below 1.5 %. Two treatments were performed at 240 °C and 280 °C for 1 hour according to the following protocol: (i) heating from room temperature to 100 °C at a rate of 10 °C·min⁻¹ (ii) plateau at 100 °C for 12 hours to remove bound residual water (iii) heating at a rate of 10 °C·min⁻¹ to the treatment temperature (iv) plateau at the treatment temperature for 1 hour and (v) cooling ensured by thermal losses and increased nitrogen flow into the reactor.

The oven-dried mass of the samples before (m_0) and after (m_t) torrefaction was measured to calculate the mass loss (ML) due to heat treatment:

$$ML \text{ (\%)} = \frac{m_0 - m_t}{m_0} \cdot 100 \quad (82)$$

The mass loss is known to be a good indicator of the torrefaction intensity and has been successfully correlated to several properties of the treated biomass such as dimensional changes [93], energy

properties [100], and flowability [102,329]. Mass losses of $9.6 \pm 0.8 \%$ and $24.5 \pm 3 \%$ were obtained for the samples torrefied at 240 °C and 280 °C, respectively.

The biomass samples (raw and treated) were ground using a *Retsch SM300* knife mill with a 1-mm trapezoidal hole bottom sieve at the outlet. Although an outlet sieve was used during grinding, the powders obtained were still quite polydisperse and had many fine particles. The timestep for DEM simulations of strongly polydispersed systems should be reduced according to the smallest particle present, which, in the case of biomass samples, would lead to impractical simulation times [421]. Therefore, the powders obtained after grinding were sieved to reduce polydispersity in particle size and shape. A *Retsch AS 200* vibratory sieve shaker at an amplitude of 60 % (1.8 mm) for 20 minutes was used along with sieves of opening 500 μm and 710 μm . Particle size and shape distributions were obtained using a *Sympatec-QICPIC* morphological particle size analyzer [312]. The main descriptors of the distributions are listed in Table 47.

For comparative purposes, 1-mm diameter glass beads were used as representative of materials with spherical and non-cohesive particles. The SEM images presented in Figure 106 depict the elongated shape of biomass particles compared to glass beads. It is noteworthy that, despite the sieving stage, the average particle size (minimum Feret diameter) decreased with the intensity of torrefaction. The aspect ratio values reveal that intensively torrefied samples were also less elongated than the raw and the mildly torrefied ones, which is likely to influence their flow properties as discussed in Chapter IV.

Table 47. Sample size and shape characteristics.

Sample	Torrefaction temperature	ML (%)	Sieving cut (μm)	d_{50}^* (μm)	d_{90} (μm)	d_{10} (μm)	S_d	a_{50}
Glass beads	----	----	----	1212	1373	1051	0.13	0.99
Raw biomass	Untreated	0	500-710	746	1092	519	0.36	0.38
Mildly torrefied biomass	240 °C	9.6	500-710	667	929	448	0.35	0.31
Intensively torrefied biomass	280 °C	24.5	500-710	526	862	303	0.48	0.41

*(d_{50} , d_{90} , d_{10} : 50th, 90th and 10th centiles of the cumulative volume PSD, respectively, S_d : distributions span= $(d_{90}-d_{10})/(d_{90}+d_{10})$, a_{50} : 50th centile of the aspect ratio distributions (a =minimum Feret diameter/maximum Feret diameter)

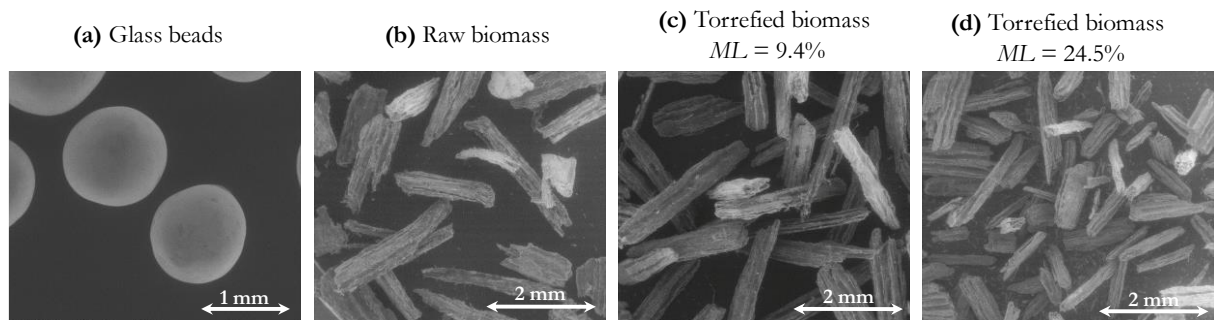


Figure 106. Typical SEM images of the granular materials used in this work.

4.2.2. Rotating drum and avalanching tests

An in-house-designed device was used to evaluate the dynamic flow behavior of the granular materials (Figure 69b). The core piece is a stainless-steel cylinder (10 cm inner diameter, 2 cm width)

clamped inside a large roller bearing as show in the Figure 69a. Two transparent conductive ITO (Indium-Tin oxide)-coated glass discs are used to enhance drainage of static electricity. The drive mechanism, built between a gear motor and the cylinder housing, consists of two pulleys connected by a toothed belt. This design ensures a regular and smooth rotation, without vibrations and provides the uniform lighting required to grab high quality images.

A volume of 63 cm³ of oven-dried materials was charged into the drum, corresponding to a filling ratio of 40 %. All the tests were performed at ambient relative humidity between 46 % and 55 % and at a rotational speed of 0.5 rpm. Image acquisition was made using a Photron FASTCAM high-speed camera at a framerate of 50 fps, exposure time of 1/30 000 s during 1 065 s with a resolution of 896×720.

Details on the setup, definition of the best criteria for assessing flowability and preliminary tests on non-cohesive and cohesive materials can be found in [358]. To automatically process the large set of images of each test (typically ca. 18.000 images per test), a post-processing procedure was implemented using the Image Processing Toolbox™ of MATLAB platform. Powder motion inside the drum was followed using the ‘centroid angle’ (α) defined as the angle between the horizontal and the line from center of the drum to the center of mass of the powder bed (Figure 69c). This indicator has been found relevant for the experimental evaluation of the flowability of cohesive materials using a rotating drum [358].

Three flow parameters were extracted from the temporal evolution of α . The first one is the Upper Angle of Stability (*UAS*), which is defined as the maximum value of α before an event (or ‘avalanche’). *UAS* is an indicator of the inter-particle frictional forces that particles must overcome to slide across over each other or to detach from the main bed to create an avalanche. Higher *UAS* values and wider *UAS* distributions generally correspond to a decreased flowability. The second one is the size of avalanches, that corresponds to the α variation during an event. Large avalanches in cohesive materials are generally an indicator of poor flowability, as particles tend to form large clumps that break off and collapse over the powder surface. Finally, the third parameter is the fraction of revolution needed to trigger events (f), defined as $f = \omega T / 60 \cdot 100 \%$, where T is the time (s) between events and ω is the rotational speed (rpm). A greater value of f normally indicates a greater powder cohesion since the events are less frequent. On the contrary, powders having small values of f -distributions should flow freely and require lower energy to trigger flow [347]. The determination coefficient (r^2) was also calculated as an indicator of the smoothness of the free-surface profile of the powders. This coefficient evaluates the goodness of fit of a linear regression to the surface profile. Cohesive materials tend to form agglomerates when tumbling, so their surfaces are expected to be rough and irregular, resulting in values of r^2 much less than the unit.

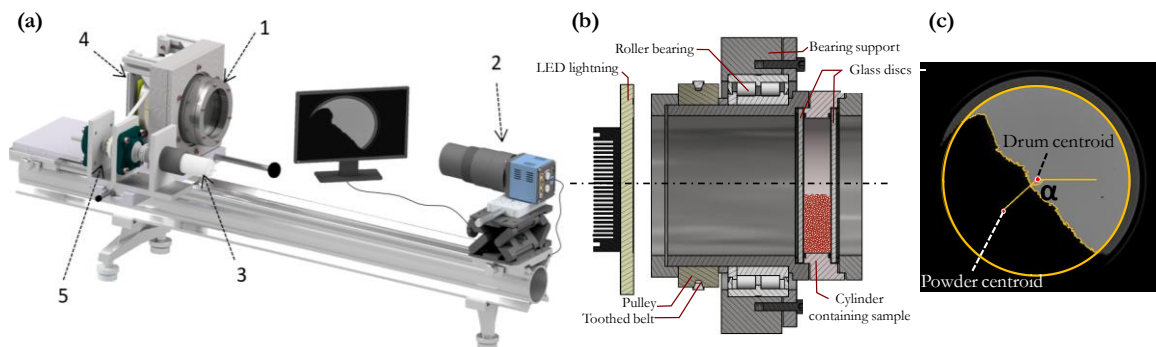


Figure 107. Rotating drum system. a. Experimental setup: 1: rotating cylinder, 2: high-speed camera, 3: motor, 4: lighting panel, 5: drive system, b. detail on the cylinder c. Centroid angle (α) definition.

4.3. DEM modeling

This section starts with an overview of the DEM contact model used in this work and the procedure for representing particle size and shape using a coarse-grained multisphere approach. Then, the methodology for calibrating the DEM parameters is briefly explained and finally the geometry of the simulated rotating drum is presented.

4.3.1. Contact model

Simulations were conducted using the public version of LIGGGHTS 3.8.0 DEM code [268], parallelized on a E5-2620 v4 2.10 GHz Intel® Xeon® machine with 125.8 GB of RAM. A classic non-linear spring-dashpot model of Hertz-Mindlin was used as the basic contact model for all samples. For biomass samples, an elastic-plastic spring-dashpot (EPSD2) rolling friction model and a simplified Johnson-Kendall-Roberts (SJKR) cohesion model were also included.

The Hertz-Mindlin model stands as the most commonly used contact model due to its efficient and accurate force calculations. At any time t , the equations governing the translational and rotational motion of particle i of mass m_i and radius R_i can be written as:

$$m_i \frac{d\mathbf{v}_i}{dt} = \sum_j \left(\mathbf{F}_{ij}^e + \mathbf{F}_{ij}^d + \mathbf{F}_{ij}^{coh} \right) + m_i \mathbf{g} \quad (83)$$

and

$$I_i \frac{d\boldsymbol{\omega}_i}{dt} = \sum_j \left(\mathbf{T}_{ij}^t + \mathbf{T}_{ij}^r \right) \quad (84)$$

where \mathbf{v}_i and $\boldsymbol{\omega}_i$ are the translational and rotational velocities of particle i . m_i and I_i are the mass and the moment of inertia of the particle. The indices i and j can also represent particle-wall interactions. The forces involved are: the gravitational force $m_i \mathbf{g}$ and the forces between particles which include an elastic force \mathbf{F}_{ij}^e , a viscous damping component \mathbf{F}_{ij}^d and cohesive contributions (for biomass samples) through the \mathbf{F}_{ij}^{coh} term. The torque acting on particle i due to particle j includes two components: \mathbf{T}_{ij}^t which is generated by the tangential force and causes particle i to rotate, and \mathbf{T}_{ij}^r , the rolling friction torque generated by asymmetric distribution of the normal contact force and slows down the relative rotation between particles in contact [272,422]. If particle i undergoes multiple interactions, the individual interaction forces and torques sum up for all particles interacting with particle i . The equations for calculation of each force contribution are reported in Table 48. A complete description of the elasto-plastic spring-dashpot rolling friction model EPSD2 is given in [273].

Cohesive force models in DEM include the Johnson, Kendall and Roberts (JKR) model [264], the recently developed Parallel Bond Contact Model [423] and Adhesive Elasto-Plastic Contact Models [396]. The simplified formulation of the widely-used Johnson-Kendall-Roberts model (sJKR) [384] was used in this work, for several reasons: (i) because of its availability in LIGGGHTS, (ii) the need for a single calibration parameter and (iii) the successful description of low-stress cohesive material flows that has been observed in previous research [360,417]. This model adds an additional normal force $\mathbf{F}_{ij,n}^{coh}$ tending to maintain the contact between two particles, given by:

$$\mathbf{F}_{ij,n}^{coh} = CED \cdot A \quad (85)$$

where CED is the Cohesive Energy Density in J/m^3 and \mathcal{A} is the contact area between particles, calculated as:

$$\mathcal{A} = \frac{\pi}{4} \frac{(d_{ij} - R_i - R_j)(d_{ij} + R_i - R_j)(d_{ij} - R_i + R_j)(d_{ij} + R_i + R_j)}{d_{ij}^2} \quad (86)$$

where d_{ij} is the distance between the center of the particles and R_i, R_j are the radii of the spheres i and j in contact. For a particle (i)-wall (j) contact, the contact area becomes:

$$\mathcal{A} = \pi(R_i^2 - d_{ij}^2) \quad (87)$$

Table 48. Equations for calculations of forces and torques on particle i according to the Hertz-Mindlin model.

Force or torque contribution	Equation
Normal elastic force, $\mathbf{F}_{ij,n}^e$	$\kappa_n \delta_{ij,n} = -\frac{4}{3} Y_{eff} \sqrt{R_{eff}} \delta_{ij,n}^{3/2}$
Normal damping force, $\mathbf{F}_{ij,n}^d$	$\gamma_n \mathbf{v}_{ij,n} = -\frac{2\sqrt{5/6} \ln(e)}{\sqrt{\ln^2(e) + \pi^2}} \sqrt{2Y_{eff} (R_{eff} \delta_{ij,n})^{1/2}} m_{eff} \mathbf{v}_{ij,n}$
Tangential elastic force, $\mathbf{F}_{ij,t}^e$	$\kappa_t \delta_{ij,t} = -8G_{eff} \sqrt{R_{eff} \delta_{ij,n}} \delta_{ij,t}$
Tangential damping force, $\mathbf{F}_{ij,t}^d$	$\gamma_t \mathbf{v}_{ij,t} = -\frac{2\sqrt{5/6} \ln(e)}{\sqrt{\ln^2(e) + \pi^2}} \sqrt{8G_{eff} (R_{eff} \delta_{ij,n})^{1/2}} m_{eff} \mathbf{v}_{ij,t}$
Coulomb friction limit	$\delta_{ij,t}$ truncated to satisfy $\mathbf{F}_{ij,t}^e \leq \mu_s \mathbf{F}_{ij,n}^e + \mathbf{F}_{ij,n}^d + \mathbf{F}_{ij,n}^{rob} $
Torque by tangential forces, \mathbf{T}_{ij}^r	$\mathbf{R}_{ij} \times (\mathbf{F}_{ij,t}^e + \mathbf{F}_{ij,t}^d)$
Torque by rolling friction, \mathbf{T}_{ij}^r	EPSD2 model

where $1/m_{eff} = 1/m_i + 1/m_j$, $1/R_{eff} = 1/R_i + 1/R_j$, $1/Y_{eff} = (1 - \nu_i^2)/Y_i + (1 - \nu_j^2)/Y_j$, $1/G_{eff} = 2(2 - \nu_i)(1 + \nu_i)/Y_i + 2(2 - \nu_j)(1 + \nu_j)/Y_j$, $\mathbf{R}_{ij} = R_i(\mathbf{r}_j - \mathbf{r}_i)/(R_i + R_j)$, e : coefficient of restitution, Y : Young's modulus, G : shear modulus, ν : Poisson's ratio.

4.3.2. Particle shape approximation

To simulate the elongated shape of the biomass particles, a multi-sphere approach was used [424]. Indeed, since spherical shapes facilitate computationally-efficient contact detection, the multi-sphere method is one of the most widely used approach for representing particle shape in DEM [385,386]. Spheres within a multi-sphere cluster are fixed in position relative to each other and may overlap to approximate more closely to the actual particle shape [274]. Multi-sphere representations have previously been used for describing flow of submillimetric biomass particles [360], wood chips [276] and agricultural resources such as maize and rice grains [277,387].

Each sample was simulated as a monodisperse population of multi-sphere clusters. High-quality approximations of particle shape using a multisphere approach may require a large number of spheres, making simulations very demanding in memory and computation time. To reduce the number of spheres required to represent a single particle, the individual spheres were oriented on a single longitudinal axis, so that the particles were needle-shaped (Figure 108). To approximate the actual morphology obtained by the PSD measurements, a simplified model of particle representation was proposed. In this model, the number of spheres in a clump, n_{sph} , is function of the particle mean size (d_{50}), the average aspect ratio (a_{50}) (Table 47) and an overlapping factor ϵ .

The overlapping factor is defined as $\epsilon = \lambda / d_{50}$, where λ is the overlapping distance between adjacent spheres in μm (Figure 108a). A value of $\epsilon = 0$ means that two spheres touch at one single point and $\epsilon = 1$

represents a total overlap between two contiguous spheres. As ϵ increases, the effective roughness of the particle decreases. Previous work [386] has suggested that reducing surface roughness by increasing the number of spheres per cluster does not necessarily lead to a better approximation of particle behavior. A value of ϵ of 20 % was chosen as it is considered a good trade-off between the accuracy of particle representation and the number of spheres required.

The diameter of each sphere is set to be equal to the median minimum Feret diameter of the population, d_{50} . Therefore, the length of the clump (l_{clump}), which corresponds to the average maximum Feret diameter, can be calculated as follows:

$$l_{clump} = d_{50} / a_{50} = n_{sph} \times (d_{50} - \lambda) + \lambda \quad (88)$$

So, from the definitions of a_{50} and ϵ , the number of spheres needed per clump is:

$$n_{sph} = \frac{1/a_{50} - \epsilon}{1 - \epsilon} \quad (89)$$

The calculated values were rounded to the closest integer and the length of the clump was recalculated accordingly.

The volume of each clump is given by:

$$V_{clump} = n_{sph} \pi \left(\frac{d_{50}}{2} \right)^3 \left(\frac{4}{3} - \frac{n_{sph} - 1}{12n_{sph}} (6 - 2\epsilon)(4\epsilon^2) \right) \quad (90)$$

Table 49 shows the multisphere model parameters that define each sample. For the sake of comparison with spherical models for particle representation, the equivalent diameter of a sphere having the same volume as one individual clump (d_{eq}) is also reported. Figure 108b presents the multisphere model of each sample used in this investigation.

Table 49. Characteristics of the multisphere model for representation of biomass particles (non-scaled).

	Raw	ML = 9.6 %	ML = 24.5 %
n_{sph}	3	4	3
l_{clump} (μm)	1940	2273	1367
V_{clump} (mm ³)	0.6282	0.5997	0.2199
d_{eq} (μm)	1062	1046	748

4.3.3. Particle size upscaling and material model calibration

Using simplified shape representations of the actual particle shape is a common practice. However a realistic material behavior has to be ensured through calibration [275].

The material DEM model of biomass powders was calibrated using the procedure described in detail in [360,374]. Calibration of the inter-particle coefficients of sliding (μ_s) and rolling friction (μ_r) and the Cohesion energy density (CED) was performed by comparing experimental bulk measurements against results of DEM simulations. The bulk responses used were: angle-of-repose from a heap, bulk density and a shear box retainment ratio. According to the dimensions of the particle clumps reported in Table 33, to simulate the formation of a full heap, several hundreds of thousands of particles would have to be included in the simulation domain, which would require several weeks of computation. Consequently, a

coarse-graining approach [280,285,371] was followed and a trade-off between the actual representation accuracy and the calculation effort was made by scaling particle size up by a factor of 4. This led to a computation time for a typical heap formation simulation of ca. 1 hour and ca. 1 week for the simulation of three drum rotations.

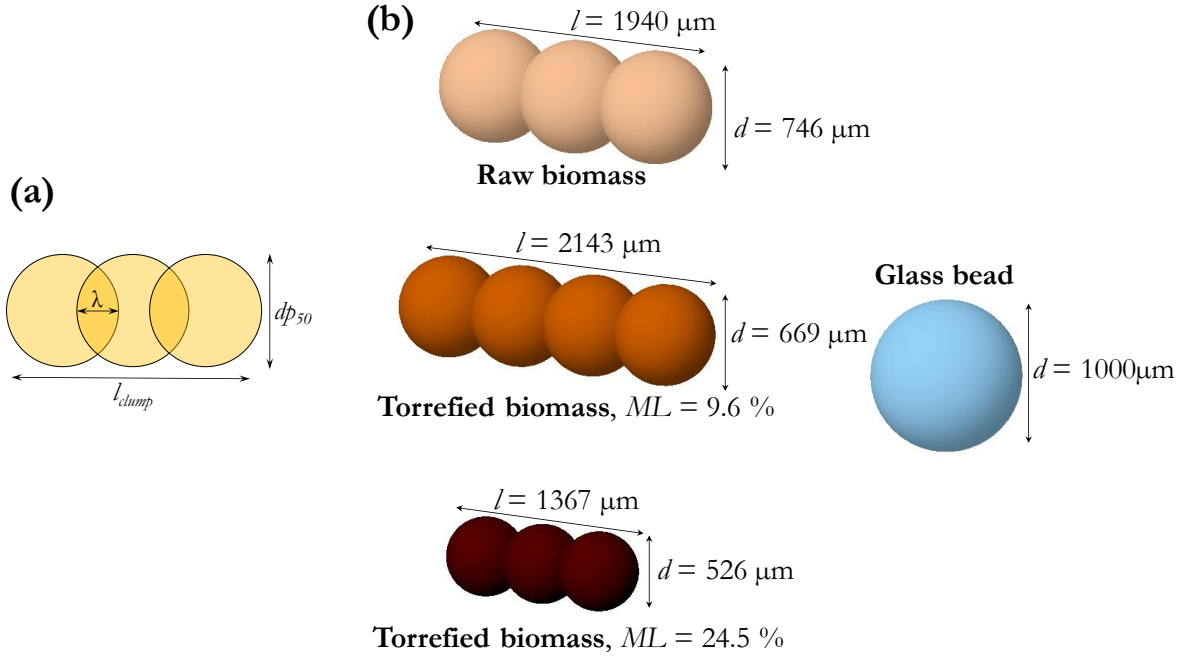


Figure 108. Multisphere particle representation. (a). Nomenclature of main dimensions within a multisphere clump. (b). Models of biomass samples and glass bead used in DEM simulations (non-scaled, true relative size).

Figure 109 shows the experimental setup used for the determination of the angle of repose as well as some examples of the experimental and DEM-simulated heaps for the three biomass samples.

Following the procedure described in [360] led to a population of optimal possible combinations of parameters that adjusted well the physical responses obtained from bulk setups. Preliminary simulations showed that low values of CED (e.g. 10 kJ/m^3) did not yield a qualitative cohesive behavior in the rotating drum simulations (revealed in the experiment by an irregular powder surface or the generation of particle agglomerates) for the raw biomass sample. Similar observations have been made by Nasato et al. [370] where too low cohesive forces in simulations of a shear test led to an identical flow behavior of a non-cohesive Hertz contact model. Therefore, the values of μ_s , μ_r and CED used for rotating drum simulations (Table 33) were selected among the optimal parameter sets with the highest values of CED [360]. Values for glass beads reported in Table 33 were taken from [270]. Except for CED , particle-walls interaction parameters were set based on literature values for woody materials [275,303]. In line with previous research [425,426], particle-steel CED was set at half the value of the interparticle CED .

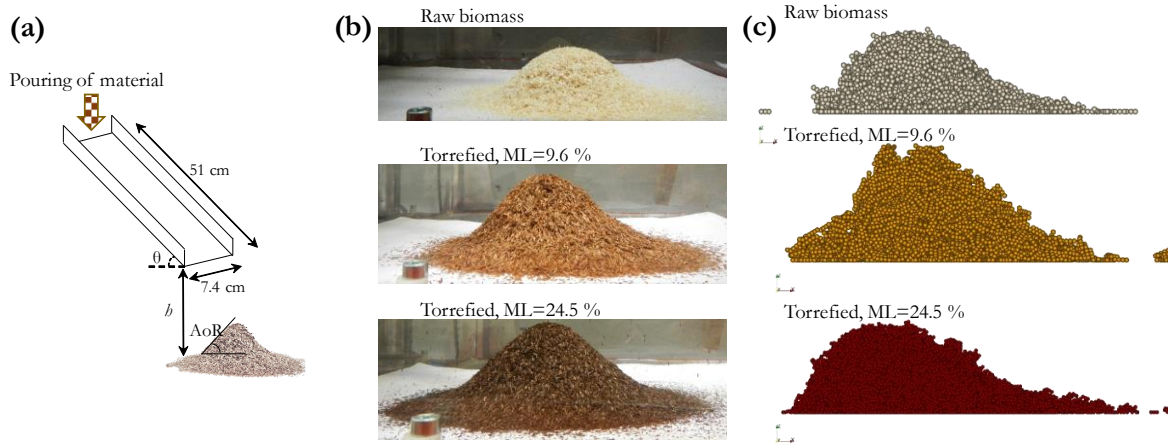


Figure 109. Calibration bulk experiment (Heap formation). (a) Main setup dimensions. (b) Examples of formed heaps for the biomass samples. (c) Corresponding DEM simulations.

4.3.4. Simulated system description

The upscaled calibrated particle models were first used in simulations of the rotating drum at its actual dimensions. However, due to the upscaled particle size, very few grains were included in the domain when the real cylinder dimensions were used in simulations. This, combined with the resulting very high wall effects, prompted us to scale the cylinder dimensions up by a factor of 4 (i.e. to use an ‘exact scaling’ approach [282,367,368]). However, as this significantly increased the number of particles to be simulated, the application of a periodic boundary conditions (PBC) approach was explored on a preliminary basis. Indeed, besides particle size scaling, another approach commonly used to increase computational efficiency in symmetric axial geometries such as cylinders, is to apply periodic boundary conditions in the axial direction [427]. This approach considers the bed of particles as an infinite array of identical translated layers of itself. Particles exiting one end of an axial boundary re-enter at the opposite boundary. Therefore, the effects of the endplates are not considered and only a thinner slice representing the center of the drum needs to be simulated, which could drastically reduce the computing time compared to the full system.

A cylindrical slice of the drum of 20 mm wide and 400 mm in diameter was used for PBC simulations. This width (axial dimension) of the disc corresponded to $\frac{1}{4}$ of the scaled width. Figure 110 shows a comparison between experimental images for a biomass sample and glass beads (Figure 110a and d), snapshots of the corresponding simulations using PBC (Figure 110b and e) and images using a closed geometry with the same width and endplates (Figure 110c and f).

The behavior obtained from DEM simulations with PBC did not correspond to the experimental observations: in the case of the glass bead samples, a slumping rather than a continuous regime developed [160], while for biomass samples, the powder collapsed on itself at very low α angles. Simulations using glass endplates reproduced better the experimental behavior displaying correct qualitative features: a continuous flow regime with a constant slope developed for glass beads and high-potential avalanches took place for biomass. This shows that the inclusion of wall friction effects is required to simulate a realistic flow. Therefore, the final simulated drum configuration included these endplates.

Table 50. DEM simulation parameters for particles and walls.

Parameter	Glass beads	Raw biomass	Torrefied $ML = 9.6 \%$	Torrefied $ML = 24.5 \%$
Poisson's ratio (particle-particle)	0.22	0.3	0.3	0.3
Poisson's ratio (particle-walls)	0.22	0.3	0.3	0.3
Particles density, kg/m^3	2550	350	350	350
Young's modulus (particle-particle), Pa	5×10^6	5×10^6	5×10^6	5×10^6
Young's modulus (particle-walls), Pa	5×10^6	5×10^6	5×10^6	5×10^6
Coefficient of restitution (particle- particle)	0.87	0.1	0.1	0.1
Coefficient of restitution (particle- walls)	0.87	0.1	0.1	0.1
Sliding friction coefficient (particle- particle)	0.2	0.1	0.3	0.693
Sliding friction coefficient (particle- steel)	0.6	0.4	0.4	0.4
Sliding friction coefficient (particle- glass)	0.2	0.5	0.5	0.5
Rolling friction coefficient (particle- particle)	----	0.7	0.3	0.131
Rolling friction coefficient (particle- walls)	----	0.5	0.5	0.5
Cohesion Energy Density (particle- particle), J/m^3	----	50 049	77 576	79 062
Cohesion Energy Density (particle- steel), J/m^3	----	25 024	38 788	39 531
Time-step (s)	1.5×10^{-5}	1×10^{-5}	1.5×10^{-5}	1×10^{-5}
Total number of spheres	19 791	39 366	34 288	72 816
Number of clumps	----	13 122	8 572	24 272
Number of processors	8	2	4	8

The main drum dimensions used for simulations are presented in Table 51. It should be noted that to reduce computing time, the cylinder width used for PBC simulations was kept in the finally simulated system. The number of particles between endplates for the elongated biomass samples (n) is calculated based on the equivalent diameter of the clumps $n = n' / (d_{eq} \times 4)$ (Table 49). The values of n were in all cases above 4. Johnstone [155] reported that four particles between the endplates were a good compromise between computational time requirement and the accuracy of the dynamic angle determination. For each sample, the number of particles to achieve a 40 % fill volume is also reported in Table 51. The values for biomass samples correspond to the number of elongated clumps, so the total number of simulated individual spheres correspond to the value reported in Table 51 multiplied by the number of spheres per clump.

Torrefied biomass, $ML = 24.5 \%$

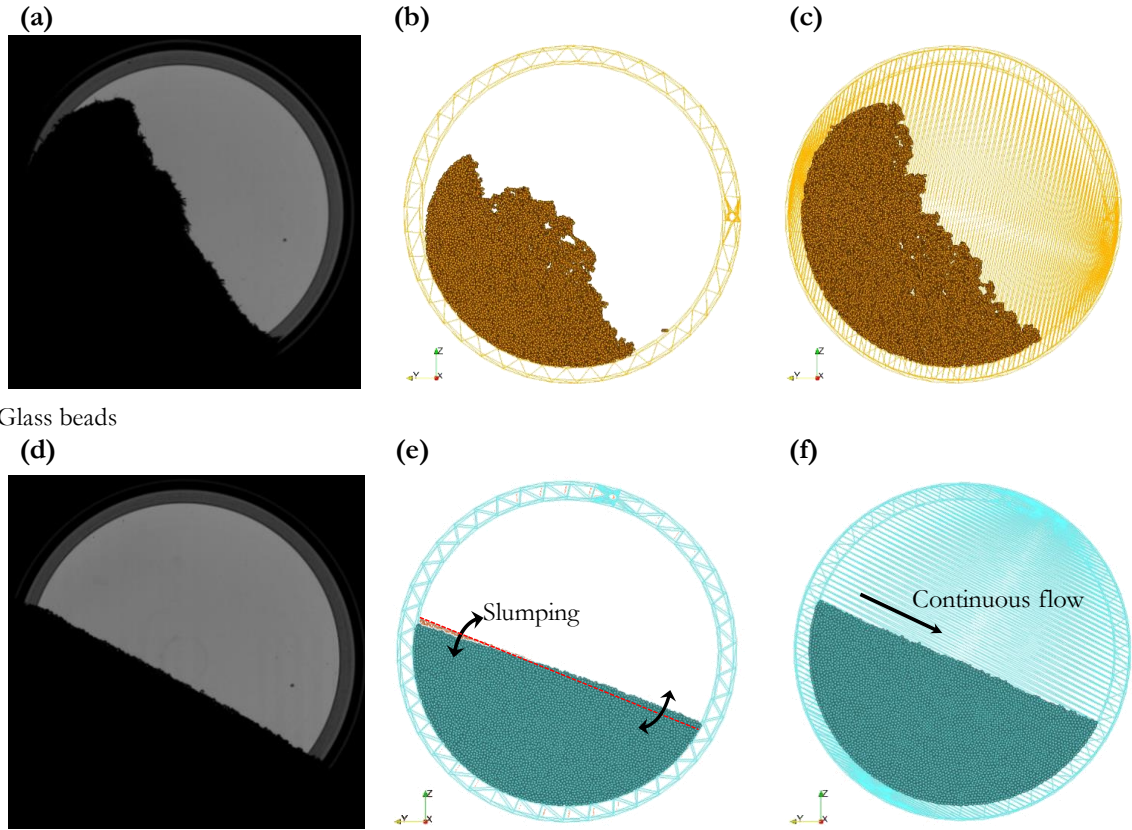


Figure 110. Experimental and DEM-simulated motion inside the rotating drum for torrefied biomass and glass beads samples. (a,d). Experimental images. (b,e). DEM simulation snapshots using PBC. (c,f). DEM simulations with endplates.

As in experiments, the rotational speed of the drum was 0.5 rpm. The randomly-oriented particles were inserted into the cylinder volume and allowed to settle for 10 000 timesteps. Previous research by Marigo [279] on cohesionless alumina cylindrical pellets has shown that a steady-state could be achieved after one rotation while DEM simulations of plastic balls by Liu et al. [428] needed at least two rotations to reach steady state. Mishra et al. [417] reported the attainment of a steady-state for agglomeration of cohesive particles inside a rotating drum after 1.5 revolutions of the drum. In this work, simulations were conducted for a duration equivalent to 3 drum rotations (360 s).

Table 51. Characteristics of the simulated rotating drum system.

Drum diameter	Glass beads	100 mm
	Biomass samples	400 mm
Drum width (w)	Glass beads	5 mm
	Biomass samples	20 mm
Number of particles between endplates (n/d_{eq})	Glass beads	5
	Raw biomass	4.7
	Torrefied, $ML=9.6 \%$	4.8
	Torrefied, $ML=24.5 \%$	6.7
Number of elongated clumps in domain	Glass beads	19 791
	Raw biomass	19 376
	Torrefied, $ML=9.6 \%$	8 572
	Torrefied, $ML=24.5 \%$	24 272

4.4. Results and discussion

In this section, comparisons between the experimental behavior and DEM simulations are made, firstly, based on the visual observations of the material motion and then from quantitative flowability indicators. The experimental results presented here have been thoroughly discussed in Chapter IV, so that the analysis hereafter focuses on the description of the numerical results and their comparison with the observed experimental behavior.

Figure 111 shows a qualitative comparison between representative experimental and simulation captions after avalanches. Visually, the similarities between the simulation and the experimental results are encouraging. Overall, the differences in behavior between the different samples studied here are well captured by the DEM simulations.

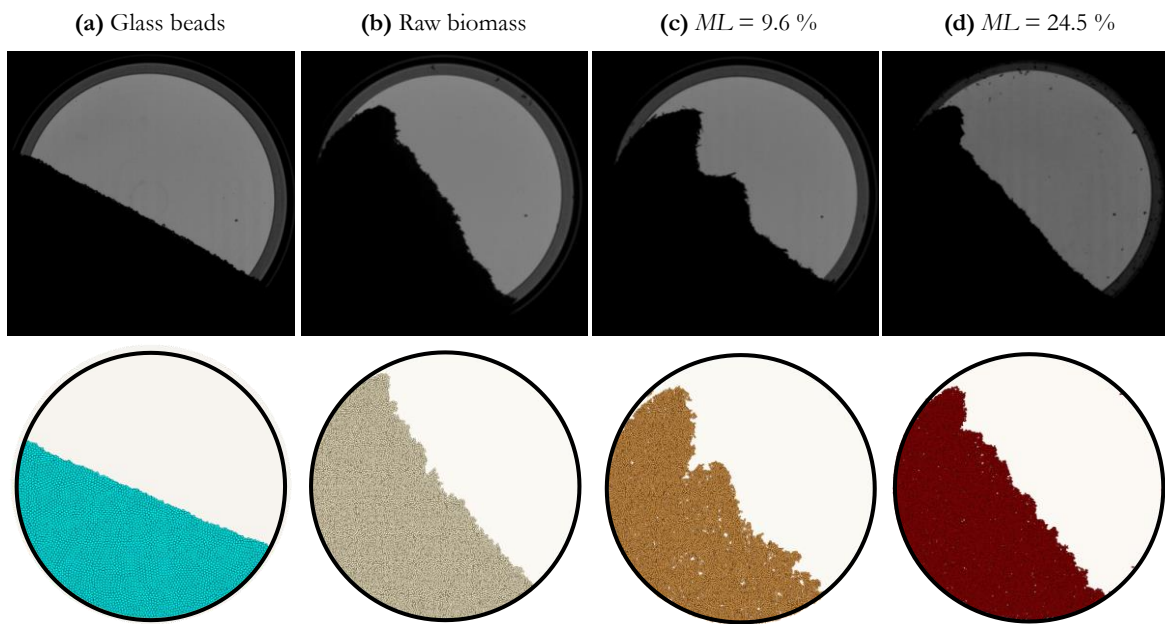


Figure 111. Typical experimental and simulated post-avalanche profiles after one rotation.

Both experimentally and numerically, a continuous regime of flow develops for glass beads with little variations of the flat free-surface slope. For biomass samples, qualitatively, the motion of the powder bed occurs in the form of intermittent collapses of particle clusters, which is a characteristic behavior of cohesive materials [193] (Chapter IV). This led to irregular free-surface profiles after avalanches that are well reproduced by simulations. This behavior is more pronounced for the mildly torrefied sample (Figure 111c), for which very rugged and irregular profiles are observed. In all cases, simulations led to a higher roughness of the free-surface than that observed in experiments. A higher apparent porosity of the powder bed compared to experiments is also visible in the simulations, which is likely to be mainly a visualization effect, since the width of the simulated drum (i.e. the number of axially superposed particles) was reduced compared to the real setup.

The temporal evolution of the centroid angle α during one drum rotation is shown Figure 112. Numerically, for glass beads, it took 8 % of rotation to trigger the first avalanche, while for biomass powders around 20 % of a rotation was needed. After the first avalanche, both numerically and experimentally, there is no clear evolution towards a steady-state in terms of the centroid angle, so the segments showed in Figure 112 can be considered as qualitatively representative of the entire simulated period (3 drum rotations).

The qualitative behavior of the four samples in terms of α evolution was well reproduced by simulations. Both numerically and experimentally, for glass beads, there are very rapid and very short variations of α of up to 2° while, for biomass, there is a succession of large quasiperiodic events consisting in decreases of α of up to 20° . Small random events are also common for the simulations of both raw and mildly torrefied biomass (Figure 112b and c) while a more regular pattern of large events (nearly uniform in size and time spacing) is visible for the intensively torrefied sample (Figure 112c). Quantitatively, it is however apparent from Figure 112 that there is an evident minor quantitative gap between experimental results and simulations.

The flowability parameters explained in Section 4.2.2 were evaluated from the experimental and simulation results and used to quantitatively differentiate the cohesiveness of the different powders.

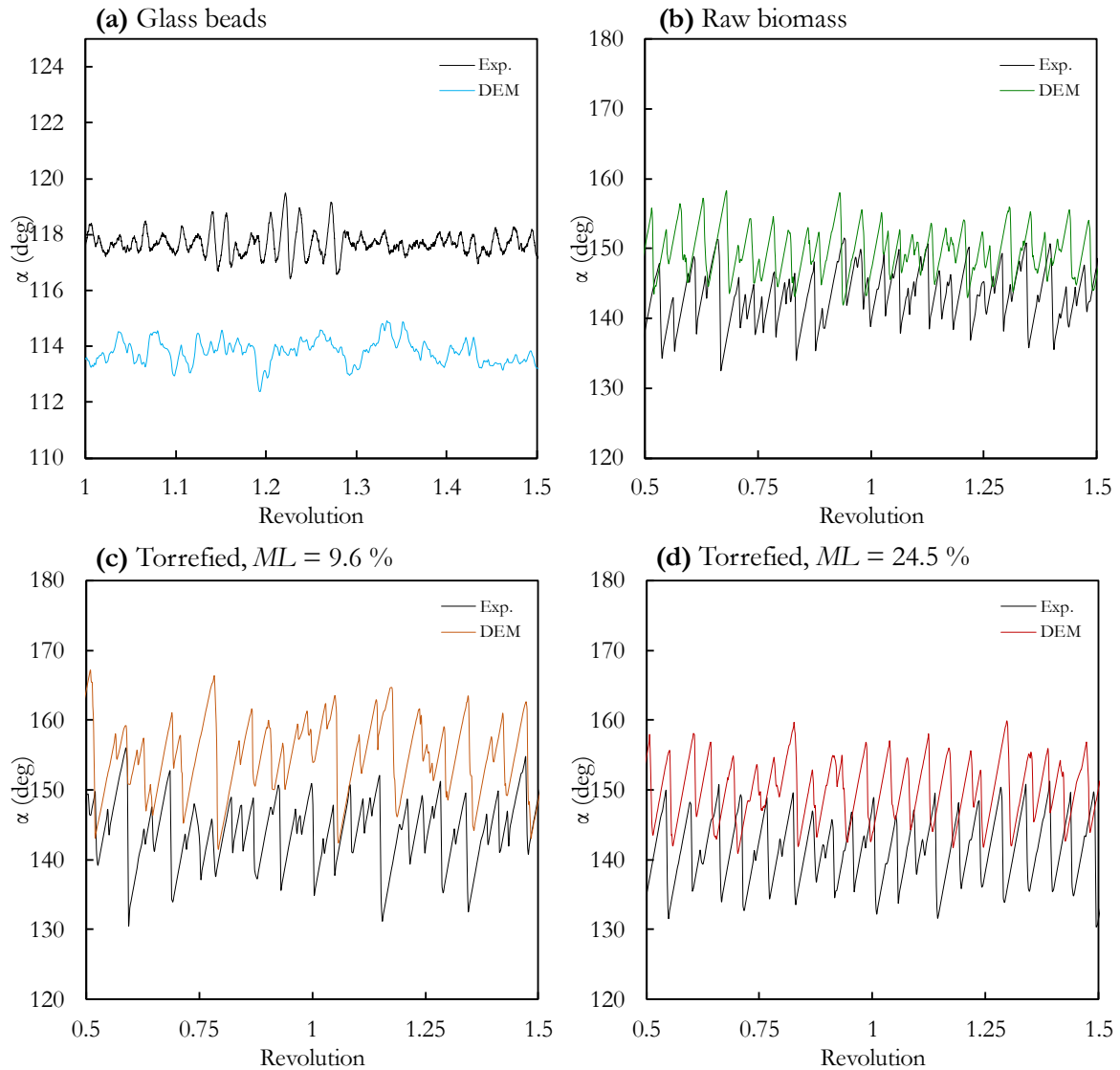


Figure 112. Experimental and DEM-modeled evolution of the 'centroid angle'. The x -axis ('Revolution') is the fraction of rotation (i.e. the product between the rotational speed and the elapsed time in homogeneous units).

Because of the highly variable profiles shown in Figure 112, the flowability parameters are presented in Figures 8 to 11 in terms of occurrence distributions rather than simply as average values. The median values of the distributions (50th centile) are reported in Table 52 and used to establish flowability

rankings. Quantitatively, the width of the distributions for a given flowability parameter ‘ ε ’ is quantified by the span S_ε , calculated as follows:

$$S_\varepsilon = \frac{\varepsilon_{90} - \varepsilon_{10}}{\varepsilon_{90} + \varepsilon_{10}} \quad (91)$$

where ε_{90} and ε_{10} are the 90th and 10th centiles of the cumulative ε -distributions, respectively.

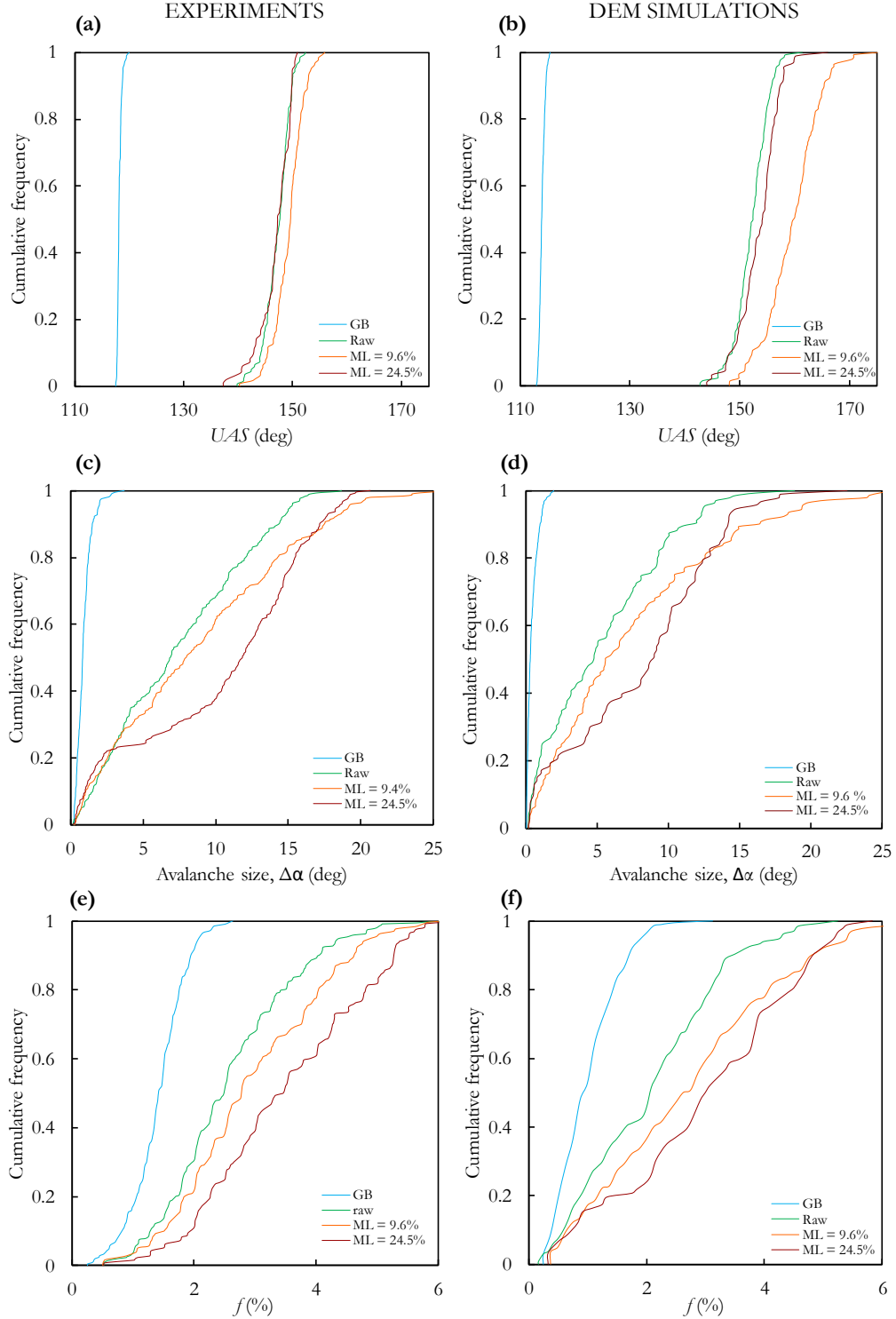


Figure 113. Distributions of flowability descriptors. Left-side plots correspond to the experimental results, right-side are the results obtained from DEM simulations. (a,b) UAS. (c,d) Avalanche size. (e,f) Fraction of revolution needed to trigger events.

Figure 113 shows the cumulative distributions for the Upper Angle of Stability obtained from the experimental results (Figure 113a) and the DEM simulations (Figure 113b). Overall, the behavior for simulations and experiments in terms of UAS is similar: a very steep unimodal distribution is obtained for the glass beads, around a value a few tens of degrees lower than that of biomass powders, which is indicator of a free-flowing behavior. In the case of the biomass powders, the distributions spread over a wider range of values, as can be expected from the plots in Figure 112. The raw and the intensively torrefied samples exhibit very close UAS distributions, while the mildly torrefied samples have greater UAS values, indicating a higher cohesive nature.

In addition to interparticle interactions, the moment at which particles detach from the drum walls is likely to be strongly influenced by the wall-particle particle-wall interactions, namely the coefficients of friction and the cohesion energy. These parameters were not considered in the calibration framework (Section 4.3.3). This might explain the quantitative offset of the DEM distributions compared to the experimental results. Nevertheless, results of Table 52 for UAS show that DEM simulations predicted within a low margin of error (below 7 %) the experimental values.

Figure 113c-d compares the experimental and simulated avalanche size ($\Delta\alpha$) distributions. While very short avalanches were observed for glass beads, which is characteristic of a non-cohesive material, large angle variations during events were observed for the biomass powders. These large variations of α are produced by the tumbling of clusters of particles, measured experimentally and nicely reproduced numerically, which rapidly modify the center of mass of the powder bed. While the qualitative similarity between the plots in Figure 113 is encouraging, the average avalanche size (Table 52) was always underestimated by the DEM simulations. However, the same experimental and numerical ranking of flowability could be established.

Table 52. Experimental and simulated results for several flowability indicators. Span values (Eq. 10) are indicated in round brackets, flowability ranking is reported in square brackets from I being the worst flowing material to IV the material with the best flowability. The relative error is referred to as e .

	UAS_{50} (S_{UAS}) (deg)			f_{50} (S_f) (%)			Avalanche size $\Delta\alpha$ (deg)			r^2_{50} (S_r^2)		
Sample	Exp.	DEM	e (%)	Exp.	DEM	e (%)	Exp.	DEM	e (%)	Exp.	DEM	e (%)
Glass beads	118.1 (0.004) [IV]	114.0 (0.006) [IV]	3.5	1.41 (0.42) [IV]	0.93 (0.63) [IV]	34.0	0.81 (0.64) [IV]	0.32 (0.85) [IV]	60.5	0.999 (0.00) [IV]	1.00 (0.00) [IV]	0.1
Raw biomass	147.7 (0.02) [II]	152.4 (0.024) [III]	3.2	2.48 (0.52) [III]	2.06 (0.71) [III]	16.9	6.84 (0.80) [III]	4.79 (0.92) [III]	30.0	0.966 (0.030) [II]	0.98 (0.02) [III]	1.5
Torrefied, ML = 9.6 %	149.6 (0.02) [I]	159.8 (0.041) [I]	6.8	2.77 (0.51) [II]	2.62 (0.76) [II]	5.5	7.98 (0.88) [II]	5.61 (0.90) [II]	29.7	0.956 (0.040) [I]	0.68 (0.36) [I]	28.9
Torrefied ML = 24.5 %	147.2 (0.02) [III]	154.1 (0.03) [II]	4.7	3.44 (0.46) [I]	3.00 (0.74) [I]	12.8	11.8 (0.89) [I]	8.88 (0.93) [I]	24.7	0.991 (0.014) [III]	0.96 (0.11) [II]	3.13

Similar observations can be made from Figure 113e-f regarding the fraction of revolution f needed to trigger events. Again, lower fractions were obtained for glass beads, indicating a greater ease of flow. For the biomass samples, events required a larger fraction of revolution to occur, i.e. they were triggered less frequently, which is an indicator of a reduced flowability. Qualitatively, the shape and locations of

the simulated f -distributions were consistent with the experimental results. Lower discrepancies between the average simulated and the experimental values of f were obtained for the biomass materials than for the glass beads (Table 52), and the same flowability ranking as in the experiments could be established. Intensively torrefied samples were less prone to flow in terms of event frequency, followed by the mildly torrefied sample, the raw sample and finally the non-cohesive glass beads. A comprehensive critical analysis on the use of the f parameter as indicator of flowability has been made in previous research (Chapter IV). The identification of the type of events is also important to conclude on flowability when using this indicator. For the intensively torrefied samples, even if the events are more spaced over time, the representations in Figure 112d show that there are fewer ‘small’ events for these materials than for the mildly torrefied or the raw samples. These small events were associated to small clumps breakings over the powder bed, which are typical of a cohesive flow. Experimentally, the flow of the intensively torrefied samples was dominated by ‘large’ shear-flow events rather than ‘small’ clumps breaks. This behavior was also verified by visual observation of the simulation output. This highlights the importance of considering the type of motion taking place during avalanches, and not only isolated numerical indicators of the event frequency or size.

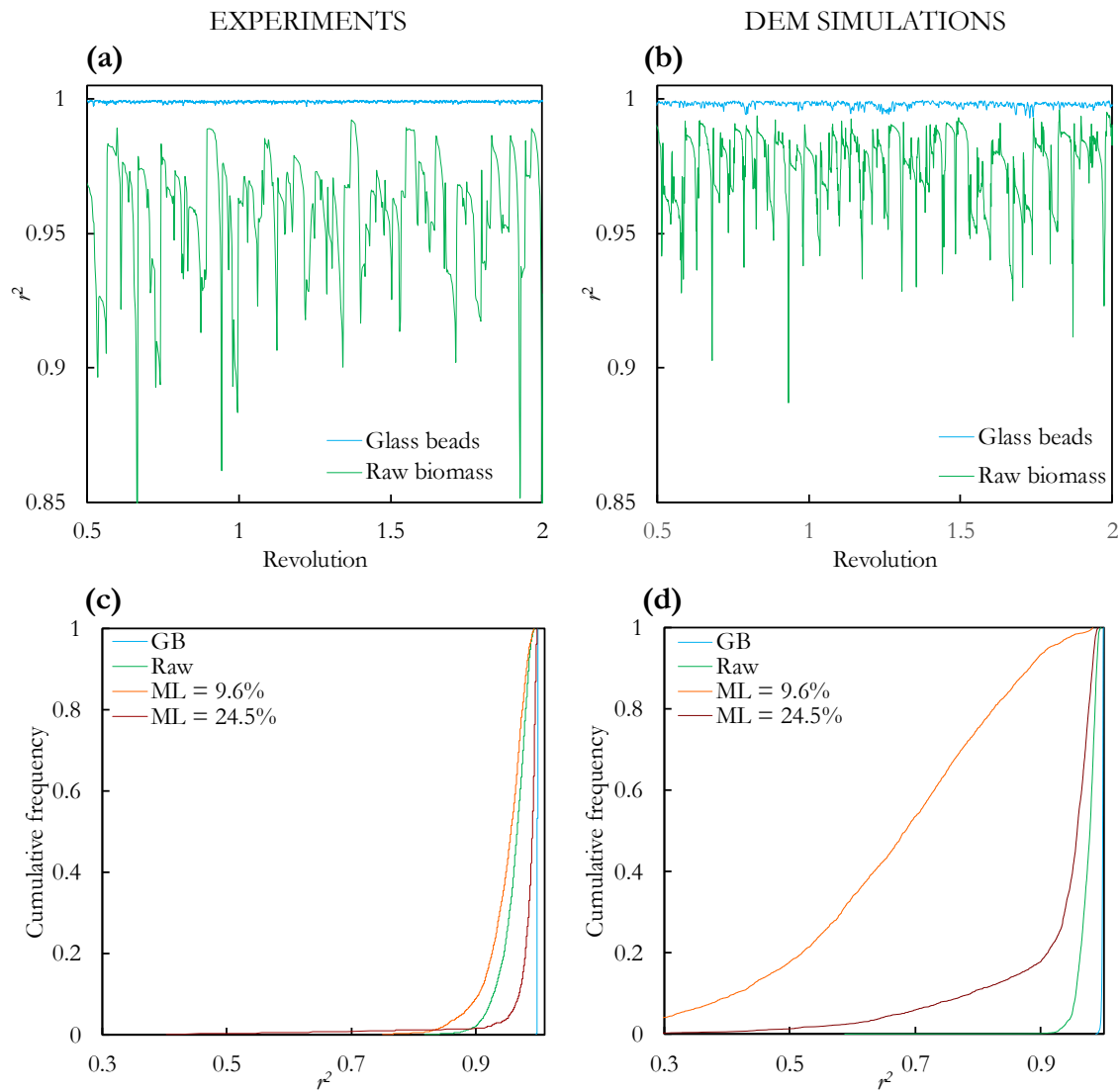


Figure 114. Irregularity of the free-surface profile as measured by the coefficient of determination (r^2). (a) Experimental evolution for raw biomass and glass beads. (b) Simulated evolution for raw biomass and glass beads. (c) Experimental r^2 -distributions. (d) r^2 -distributions from simulation results.

The evaluation of the coefficient of determination (r^2) completes the analysis of flowability by examining the irregularity of the free-surface profile of the powder. Figure 114a-b correspond to the evolution of r^2 obtained from experiments and simulations for the glass beads and the raw biomass sample. While for the glass beads the values of r^2 are nearly constant at ca. 1, for the biomass powder great deviations from a linear profile develop, especially during avalanches. The very distinct behavior between the non-cohesive and the cohesive materials was well reproduced by simulations as can be seen in Figure 114: a high irregularity was observed for the biomass sample compared to the glass beads.

The cumulative distributions in Figure 114c-d were derived from the evolution of r^2 over time. The comparison of experimental and simulated distributions reveals rather significant differences. Most striking are the significantly low values of r^2 obtained for the mildly torrefied samples from simulations. This is the combined result of the high *CED* value for this sample and its higher elongation that led to very rough and irregular profiles. However, except for mildly torrefied samples, the average values of r^2 were similar in simulations and in experiments (Table 52) and were used to establish a flowability ranking, with the mildly torrefied sample exhibiting the most cohesive behavior and the glass beads being non-cohesive.

For all criteria, differences in the behavior showed between simulations and experiments are also likely to be the effect of the reduced number of events considered to draw the distributions from simulations. Indeed, in the experiments, distributions are calculated on the basis of about 3 times the number of events recorded for simulations (e.g. 145 events for raw biomass). While longer simulations would likely reduce experimental-DEM gaps, the good agreement shown in Figure 113 in terms of UAS , $\Delta\alpha$ and f indicates that the number of events analyzed in simulations is globally representative of the powder behavior.

One avenue left unexplored in this work is the relative cohesive strength of interaction of particles with the drum walls, which may have a strong influence on the powder motion (in particular the moment when particles detach from the walls). Further investigation and experimentation might evaluate calibration of particle-wall interaction parameters and their effects on the bulk flow.

The results presented here suggest that calibrated DEM parameters obtained from relatively easy-to-implement bulk setups (angle-of-repose, bulk density and a retainment ratio) could be used to reproduce a realistic dynamic non-consolidated flow of biomass particles. One might consider directly applying a calibration framework such as the one presented in [360] using rotating drum simulations and experiments to better adjust powder dynamic behavior. However, as highlighted by Hu et al. [349] and as noted in this work, the long computation time that would be required for calibration using indicators from a rotating drum makes this strategy impractical at present. Instead, the results obtained from avalanche assessment in rotating drums could be dedicated to narrow the population of optimal sets of parameters obtained from bulk experiments, with fewer/shorter simulations required. This leads to a more realistic and robust DEM material model and to a better representation of flow behavior under a wide range of flow conditions.

4.5. Potential of DEM simulations for exploration of shape and cohesion effects on flow

The previous results proved that DEM simulations are capable of representing a realistic bulk flow of biomass particles under dynamic free-surface conditions. One of the greatest strengths of the simulation approach is that it allows the effect of the powder characteristics such as particle size, shape

or interparticle cohesion on bulk flow to be studied independently. An overview of this potential is given hereinafter.

Figure 115 shows simulation snapshots that illustrate the effect of changes in particle properties (shape and cohesion) on the powder profile. Figure 115a corresponds to non-cohesive spherical particles with an equivalent diameter equal to that of the raw biomass scaled clumps ($d_{eq} = 2.12$ mm), all the other DEM parameters being the same than those used for raw biomass simulations. Figure 115b shows the effect of adding a cohesive contribution of $CED = 50.049$ kJ/m³ (i.e. CED for raw biomass particles reported in Table 33.). In Figure 115c the elongated shape of the raw biomass clumps is used but interparticle cohesive forces are neglected and Figure 115d corresponds to the simulated raw biomass sample with the parameters of Table 33.

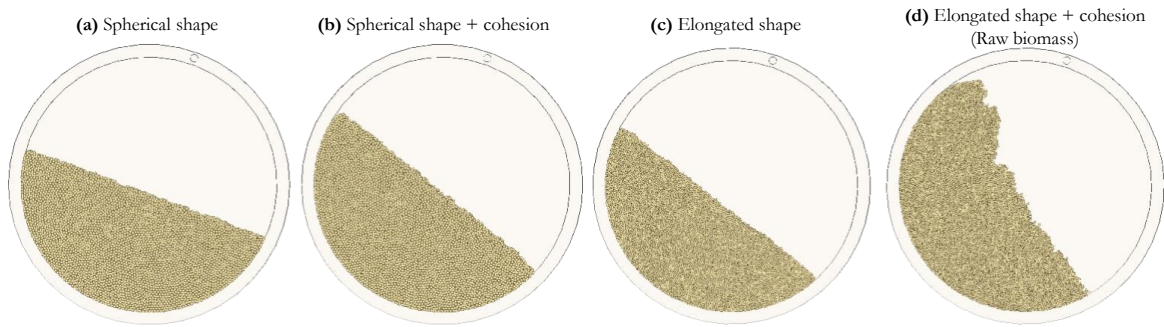


Figure 115. Snapshots of DEM simulations showing the effect of particle shape and interparticle cohesion on flow.

To facilitate the visualization of the dynamic flow behavior, snapshots of the flow with particles colored according to their instantaneous speed are presented in Figure 116 for two successive moments at t_i and t_j . The ease of access to detailed information at the particle-scale highlighted by the representations in Figure 116 shows another interesting feature of DEM simulations. Figure 117 presents the evolution of the centroid angle during one rotation for the four cases presented in Figure 115 and Figure 116.

The lowest values of α were obtained for the non-cohesive spherical particles and, as for the glass beads, a continuous regime of flow developed with a flat and constant slope and a permanent layer of spheres rolling down the free-surface (Figure 116a). Adding a cohesive contribution not only increased the centroid angle (Figure 115b), but also resulted in a slumping regime in which periodic events took place: the solid bed was lifted (Figure 116b, top) and leveled off (Figure 116b, bottom) by successive small discrete avalanches at the surface.

Elongated shape promotes particle interlocking while limiting their free movement, which results in greater centroid angles than for spherical particles (Figure 115c). Equivalent results for the dynamic angle of repose are reported in previous research by Höhner and Wachs et al. [269,416]. Interestingly, without cohesive interactions, a continuous regime of flow develops as in the case of the spherical particles. Elongated particles simply shift the mean angle towards a higher value and the thickness of the shear front of particles continuously flowing over the powder bed decreases (Figure 116c). Figure 117 shows that the increase in the centroid angle triggered by the addition of cohesion (case b) or by an elongated shape (case c) is, in average, comparable (ca. $+20^\circ$ compared to the simulation of spherical particles). The difference between these two cases is the presence of short oscillations when a cohesive contribution is taken into account. Therefore, if only an average value of α had been considered for flowability characterization (as is often the case in literature), similar conclusions about flow would have been

wrongly drawn for both cases. This underlines the importance of considering several flow indicators in addition to average angles.

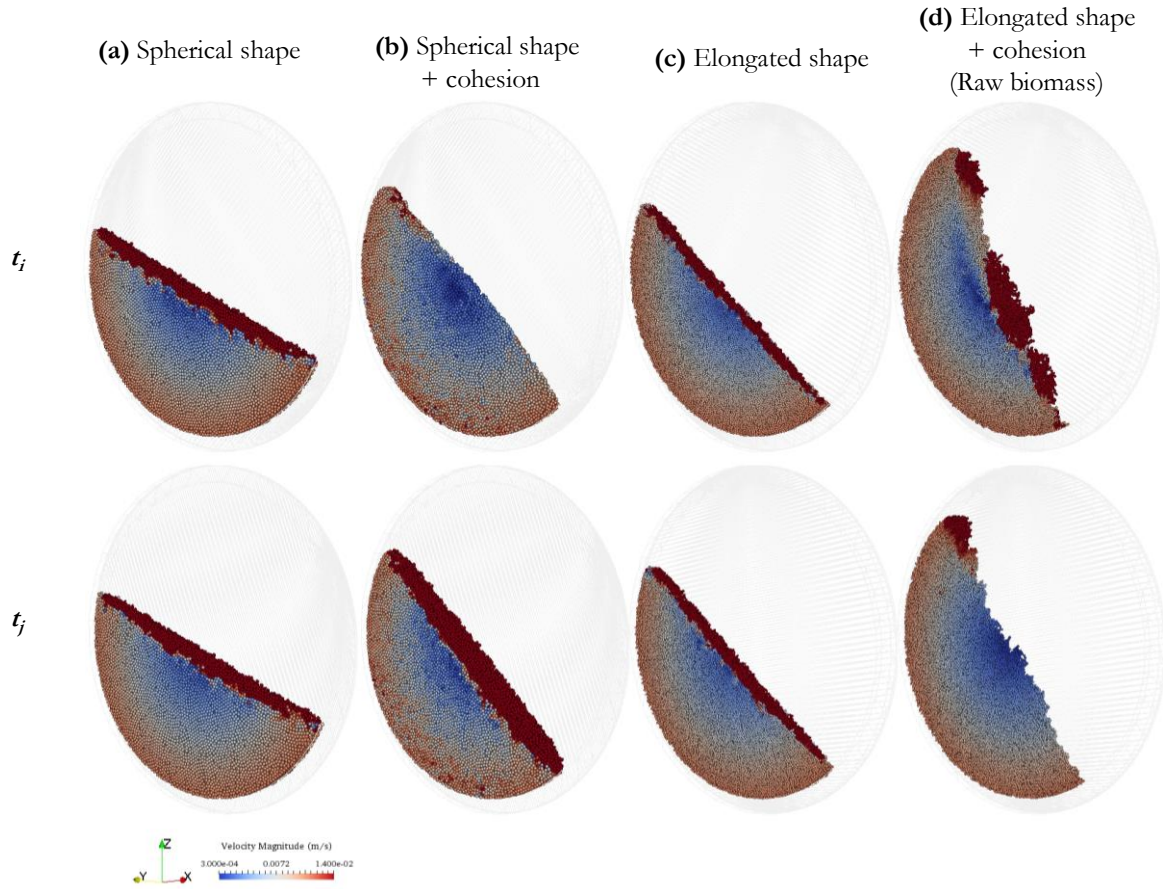


Figure 116. Effect of particle characteristics on the flow behavior at two consecutive moments t_i and t_j .

As seen in Figure 115d, only the coupled effects of the elongated particle shape and the interparticle cohesion were able to reproduce a realistic behavior for the raw biomass samples, with discrete avalanches (Figure 116d top) and the formation of clusters of particles collapsing over the free-surface. This triggered the large α variations depicted in Figure 117 that closely mimic the experimental behavior.

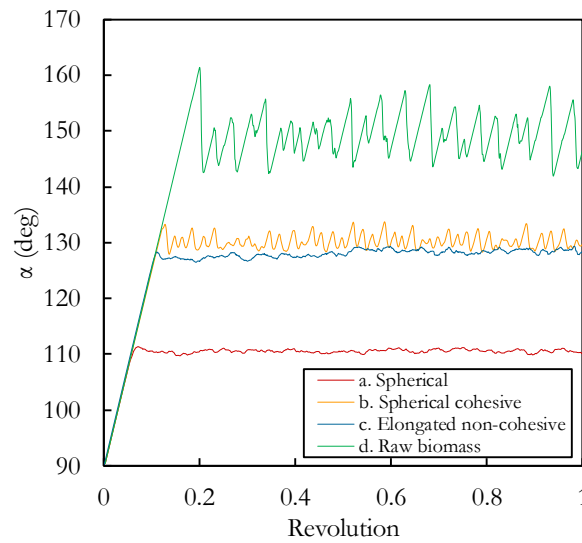


Figure 117. Effect of particle characteristics on the temporal evolution of α during one drum revolution.

In this study, only monodispersed populations of particles were used in the simulations. However, experimentally, although a sieving stage reduced the polydispersity of the biomass powders, there was still a variety of particle sizes, especially for the intensively torrefied samples, which is likely to influence flow behavior. A natural progression of this work is to analyze the effect of polydispersity on flow behavior through simulations. Although this will be the subject of future research, a first effort in this direction is shown here by simulating a polydispersed population with characteristics approximated from the PSD of the raw biomass sample. Thus, three particle sizes at $d_{8.2}$ (500 μm), d_{50} (746 μm) and d_{75} (890 μm) were combined with volume proportions of 25 %, 50 % and 25 %, respectively, maintaining the same average aspect ratio as the monodispersed system. As shown in Figure 118, the inclusion of two additional particle sizes did not significantly change the bulk behavior in terms of the centroid angle evolution. Similar UAS and f distributions were thus obtained compared to those of the monodispersed raw biomass. However, the computing time was greatly increased due to the presence of finer particles which led to a higher number of particles to be simulated to reach the same fill ratio (19 376 for the polydispersed system compared to 13 122 for the monodisperse raw biomass). This suggests that a polydisperse system could be adequately represented by a simplified monodisperse population, thus saving time in terms of calculation. Further work with a higher degree of polydispersity might be required to reinforce these findings.

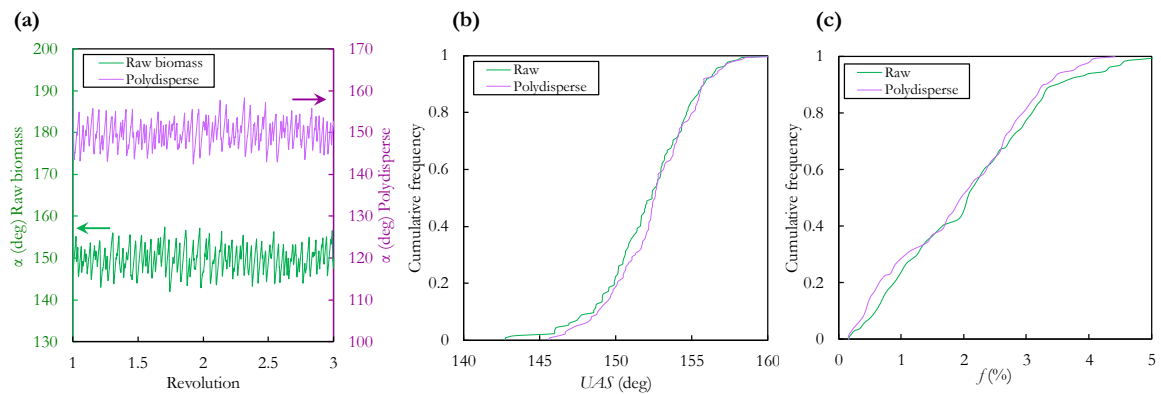


Figure 118. Comparison of DEM results between monodisperse raw biomass and a polydisperse sample. (a) Evolution of the α angle over time (for clarity, the y-axis of the data sets is not the same; e.g. the raw biomass results should be read on the left y-axis). (b) UAS cumulative distributions. (c) f cumulative distributions.

4.6. Conclusions

Rotating drum tests are pertinent for studying bulk flow of granular materials in a non-consolidated and dynamic conditioning. In this study, we evaluated the ability of DEM simulations for assessing flow behavior of raw and torrefied milled biomass in a rotating drum.

The challenging characteristics of biomass particles with respect to simulations (submillimetric size, elongated shape, cohesive nature) were integrated in a DEM model using a coarse-grained multisphere approach for shape representation, along with a cohesive SJKR contact model. Bulk measurements of the angle-of-repose, the bulk density and a retainment ratio were used for calibration of the interparticle coefficients of sliding friction, rolling friction and the Cohesion Energy Density.

Qualitative comparison with the experimental behavior in a rotating drum system made it possible to reduce the number of optimal sets of calibrated DEM parameters. To reproduce the experimental cohesive behavior, it was therefore necessary to select a set of optimum interparticle parameters among those with the highest cohesive energy density values. The selected parameters led to a realistic

representation of the avalanche motion for the biomass materials that could be achieved through the combined effects of an elongated particle shape and interparticle cohesion. The calibrated DEM parameters obtained from relatively easy-to-implement bulk setups can therefore be used to reliably reproduce a dynamic non-consolidated flow of biomass particles, the latter being much more expensive to use as calibration setup.

Overall, the granular flow dynamics was correctly captured by the DEM simulations. Similar distributions of several flowability indicators (Upper Angle of Stability, fraction of revolution to trigger events and size of avalanches) were obtained from DEM simulations and experimental results. Although significant differences were found regarding the irregularity of the free-surface profile, similar numerical and experimental rankings of flowability could be established. This confirms the suitability of the DEM simulations for assessing flow of cohesive biomass particles in a free-surface dynamic system.

While physical sound results were obtained using parameters calibrated using simple-to-implement bulk setups, the robustness of these parameters remains to be further clarified through, for example, the investigation of other flow conditions (including under consolidation). Future studies could also explore the effects of the particle-wall interaction parameters, polydispersity as well as more elaborate particle shape representations that are more favorable to particle interlocking.

Acknowledgments

The authors would like to gratefully acknowledge the support of the French Ministry of Higher Education and Research as well as the French-Dutch Network (Eole Scholarship) for their financial support. We are especially thankful to the French Council for Poplar (CNP) and the Huberlant sawmill (Cormicy, France) for kindly providing the raw wood used in this work.

CONCLUSION AND PERSPECTIVES

General conclusion

This work addressed an explicit need to better control the flowability of powdered biomass in a context Biomass-to-Liquid conversion. In particular, the objective of this research was to provide knowledge to understand the effects of the pretreatment stages (namely torrefaction and grinding) of a BtL processing chain on the flow properties of lignocellulosic biomass powders.

To fulfil this aim, we first explored the effects of torrefaction on the flow properties of biomass powders under consolidation using a ring shear tester. Samples of two wood essences, poplar (hardwood) and spruce (softwood), were thus torrefied and comminuted (knife-ground or ball-milled). Since the bulk flow behavior is highly influenced by particle-scale properties, we measured the impact of the heat treatment on the distributions of particle size and shape in order to understand the evolution of the flowability. The loss of resilience of the fibrous structure of raw wood by torrefaction was verified by the gradual shifting of the particle size and shape distributions towards wider distributions of finer and rounder particles when the samples were more intensively torrefied.

At the same time, a significant improvement in flowability with the intensity of torrefaction has also been clearly demonstrated: milled biomass gradually shifted from a cohesive nature for the raw samples to a nearly free-flowing behavior for the most intensively torrefied powders. This positive trend was not straightforward to anticipate, according to the general trends exhibited by granular materials. Indeed, the intensively torrefied samples were composed of a high proportion of fine particles, which should generally lead to a lower fluidity due to the enhancement of the interparticle cohesive forces compared to the weight of the particles. However, our results suggested that the decrease in particle interlocking (triggered by more rounded particle shapes) has a dominant effect that results in a better bulk flow. It is therefore the evolution of the shape of the particles rather than their size that is a decisive parameter to increase flowability. The improvement in flowability and the changes in size and shape factor were therefore explained by the same effect: the loss of resilience of the fibrous structure of the raw wood by heat treatment.

The mass loss is a synthetic indicator of the intensity of the heat treatment in torrefaction, since it includes temperature level and residence time. This indicator has been successfully correlated in previous research to physicochemical properties of the torrefied biomass. Our results highlighted the possibility to correlate this mass loss to a flowability factor through a linear relationship for the two-species studied here. We therefore propose to consider the mass loss as an indicator of the consolidated flowability as well. In this way a unique indicator, linked to the torrefaction conditions, could be used for process design.

The flow properties determined for raw and torrefied milled biomass represent valuable information that can be used directly, through the Jenike procedure, for the design of industrial storage facilities such as hoppers and bins. Since torrefaction followed by grinding generates biomass powders composed of round and uniform particles, with the added benefit of reducing energy consumption for grinding, our results indicate that torrefaction should also be regarded as a valuable pretreatment process to improve the flow behavior of consolidated powdered biomass. Additional work is however required to determine whether the energy cost of torrefaction offset the reduction of the energy cost of grinding.

In a second stage of our experimental work, we focused on the flow behavior of biomass powders when they are in a free-surface condition, i.e. under no-consolidation beyond the load exerted by the own weight of the material. This is the material conditioning that is usually found in feeding systems such as feeding screws or pipelines. One of the most relevant experimental setups to study the flow of granular materials under these conditions is a rotating drum. We therefore designed and built an in-house experimental device coupled with an efficient image-processing procedure that allowed us to reliably evaluate the dynamic

behavior of biomass powders with minimal operator intervention through avalanche analysis. Due to the absence in the literature of standard flowability descriptors for cohesive materials from rotating drum experiments, we first investigated the relevance of a bulk motion indicator, the ‘centroid angle’ to describe powder flow. It is based on the changes of the mass center of the powder during rotation. This centroid angle was proven effective to capture the bulk powder dynamics and allowed us to evaluate several flowability descriptors such as the Upper Angle of Stability, the fraction of revolution required to trigger events and the size of avalanches. A more reliable assessment of flowability of cohesive materials in a non-consolidated state was therefore possible compared to the use of the average slopes of the powder profile, which is a commonly used indicator, but unreliable for the irregular surfaces developed for cohesive powders.

In addition to the flowability descriptors mentioned above, the irregularity of the free-surface profile in the rotating drum - characterized by the determination coefficient r^2 of the linear regression following the total least squares method - made it possible to distinguish between the cohesive extent of glass beads and biomass samples. The assessment of flowability at a relatively slow rotational speed led to distributions of descriptors from which reliable conclusions about unconfined flow could be drawn. The proposed flowability descriptors appeared to be complementary to each other and should be considered simultaneously to obtain a more accurate conclusion about flow properties.

The general framework established for the flowability assessment using a rotating drum allowed us to investigate the flow behavior of raw and torrefied poplar powders and compare it to measurements in a consolidated state using a ring shear tester. The study of two sieving cuts (‘fine’ and ‘coarse’) of raw and torrefied biomass samples showed that fine powders always had a greater cohesiveness than the coarse sieving cuts. For a given torrefaction intensity, the fine and coarse sieving cuts had similar shape characteristics, so, in accordance with the outcome of the previous studies carried out as part of this work, a net negative effect of particle size reduction was verified. It supports the notion that cohesion of biomass samples constituted of particles with similar shape would be increased by reduction in particle size. Moreover, for a given sieving cut, these results therefore highlight the importance of particle shape effects on bulk behavior.

We established two main categories of motion of biomass powders in a non-consolidated conditioning. The most cohesive powders had a greater tendency to form clumps of particles that flowed poorly, while shear sliding events were characteristic of good flow behavior. Our results suggest that, for instance, in a feeding screw system, the fine sieving cut of mildly torrefied powder would be more likely to have an intermittent mass flow and to trigger blocking problems, than the coarse sieving cut of raw powder. Several empiric correlations allowed us to elucidate these trends based on particle characteristics. The flowability descriptors obtained from shear testing and rotating drum experiments were therefore related to the average particle size and shape and width of the distributions. In a non-consolidated free-surface conditioning, fine, rough and needle-shaped particles, as well as powders with narrow PSD would be more cohesive. The quantitative relationships established indicate that the flowability factor, as measured by the ring shear tester, is directly related to the mean particle size (minimum Feret) and the aspect ratio, an inversely related to the PSD span. Unlike in a non-consolidated state, the increase in powder polydispersity seems therefore to hinder flow behavior in the presence of consolidation.

In a second phase of this work, in an attempt to benefit from the power of the Discrete Element Method for simulation of granular materials, we developed and implemented a DEM model of biomass particles using LIGGGHTS®, an open source particle simulation software. The prospect of realistically reproducing the behavior of biomass materials through a simplified particle representation and contact force models required the adjustment of the DEM parameters. At the time of this research, no calibration framework had yet been documented for materials that are simultaneously submillimetric, elongated and cohesive. Therefore, as a first stage of the DEM implementation, we developed and applied an automatic calibration

framework to obtain optimal sets of interaction parameters (sliding friction coefficient, rolling friction coefficient and Cohesion Energy Density) that reproduced well bulk experimental responses such as the angle-of-repose from a heap, the bulk density and a retainment ratio. This calibration procedure has been carried out for two sieving cuts of raw and torrefied biomass powders. A coarse-grained multisphere approach for particle shape and size representation has allowed us to capture the elongated nature of the biomass particles in a simplified but computationally efficient way. The use of a coarse-grained representation (particle scale up by a factor of 4) was indeed necessary to limit the number of simulated particles and thus reduce the computing time. The simulation of a preshear and a shear sequences in a ring shear tester for a coarse sieving cut of raw biomass resulted in tangential preshear and shear stresses similar to those of experiments. This shows that the calibrated parameters could in principle also be used under consolidated conditions.

The potential of DEM for the simulation of biomass powder flow was further investigated by representing the rotating drum system used for the non-consolidated flowability study. In doing so, we were able to simultaneously test the calibration parameters established previously using bulk measurements for two sieving cuts of raw, mildly torrefied and intensively torrefied samples. The DEM simulations of the avalanching behavior reproduced well the experimental results in terms of several flowability descriptors (Upper Angle of Stability, fraction of revolution required to trigger avalanches and size of the avalanches). This shows that DEM could be used as a reliable tool to analyze and predict unconsolidated flow of biomass powders.

Overall, torrefaction improves biomass flow properties under consolidation. The milled torrefied biomass is therefore less likely to trigger blocking problems in storage units. On the contrary, since only sieved samples were tested under non-consolidated conditions, conclusions about the net effect of torrefaction on non-consolidated flow are not easy to draw from the results presented here. For sieved samples, however, the beneficial effect of torrefaction is attenuated and less clear than under consolidated conditions. Although torrefaction appears to be an efficient treatment to improve shape characteristics and therefore flow behavior, we are aware that, in a gasification process, other constraints than optimizing powder flow (e.g. the energy consumption and the energy density of the product) can drive the general choice of the torrefaction conditions. However, this work highlighted that the choice of the pretreatment parameters was crucial to define the physical properties of the powder and that these effects should be considered in the general design and optimization of the BtL pretreatment processes.

Altogether, this research has provided a framework for characterizing flowability of powdered biomass using experimental and simulation tools. The reported results add to a growing body of literature on characterization of biomass and assessment of handling behavior for BtL applications. The general line of thought was as follows: within a predictive ambition, we initially sought to anticipate the biomass flowability from the torrefaction conditions, and therefore to be able to use these conditions as a lever to optimize biomass flow. However, this required intermediate stages of understanding. First, it includes the assessment of the effects of torrefaction and grinding on the particle properties (namely particle size and shape distributions). Then, the correlations between these particle-scale characteristics and several indicators of flowability under different conditioning states, that allow the prediction of flow behavior once the material has been reliably characterized. Finally, the establishment of simplified DEM models also based in synthetic descriptors of the physical characteristics can be used as a valuable tool to understand further particle-equipment interactions or the effect of particle characteristics (driven by torrefaction and grinding conditions) on bulk flow.

The research questions announced in the General Introduction section were addressed through the entirety of this research. If we succinctly reconsidered them:

How torrefaction and grinding conditions affect the particle properties of biomass? We know now the general trends correlating the torrefaction intensity and particle shape and size distributions obtained after grinding for the lignocellulosic species studied. There is still work to be done on the effect of these pretreatment processes on surface characteristics and electrostatic interactions (see Perspectives section).

What is the effect of these particle characteristics on the flow behavior under different conditions? The work is at a satisfactory state of advancement, whether in a consolidated or non-consolidated state. The interest of flow characterization under different conditions has been highlighted in this work and the differences in the effects of particle characteristics on flowability indicators depending on conditioning have been emphasized.

Can Discrete Element Simulations reproduce the flow behavior of raw and torrefied biomass materials within a predictive aim? Although the Discrete Element method is still under development and several challenges remain, DEM simulations enabled us to work out a particle model that realistically reproduces the bulk behavior of sieved raw and torrefied biomass. This opens the way to the study flow behavior and particle-equipment interactions via a numerical tool, complementary to experimental approaches.

Perspectives and suggestions for future work

A variety of perspectives and opportunities for further research emerge from this work. They can be classified under three different axes, as follows:

- First, the pursuit of experimental investigations would provide further understanding on the relationships between particle properties and flowability in confined and unconfined conditioning. Several perspectives therefore arise:
 - The general improvement in flow behavior under consolidation with the extent of torrefaction could be considered as a combined effect of several factors: the changes in particle size and width of the distributions, the improvement of shape characteristics and the changes in surface interactions. In this work, we primarily focused on the size and shape characteristics that are likely to predominantly influence flow behavior. Although this approach seemed to describe the observed behavior well adequately, the evaluation of the surface interactions (electrostatic forces, roughness) and their effects on biomass flow is an important issue that should be considered for future research.
 - Further insight into the behavior of the bulk biomass can be gained by understanding the mechanisms of interaction that exist between particles. More research is therefore required to clearly understand the origin of the cohesive nature of biomass particles. For instance, the shape of the particles and their relative position can create a kind of ‘apparent cohesion’ within the granular medium without physical or chemical attraction between the particles. This type of cohesion is referred to as ‘apparent’ because there is no real cohesive action between the grains, but there is resistance to relative grain movement, which is similar to cohesion. The geometry of the surfaces in contact can create blockages due to microscopic reliefs and therefore resistance to movement in one direction. This resistance to displacement due to particle shape or surface irregularities contributes to overall cohesion by limiting the movement of particles in contact with each other. Therefore, it is important to assess the relative contribution to the cohesive extent of these mechanical interlocking effects (which are mainly caused by elongated and irregular shapes) and the inter-particulate forces of cohesion.
 - Due to the heterogeneity of characteristics between particles, the practical quantitative analysis of particle features often needed simplification to average values. For characterization of size and shape, the variety of available descriptors complicates the task of finding relevant parameters for description and prediction of flow behavior. While an effort was made in this work to convey our results in terms of distributions, the use of average descriptors of size and shape was unavoidable. Further stages of this work should evaluate the pertinence of these average descriptors to characterize flow behavior and the opportunity to develop and integrate polydispersity descriptors (for both size and shape). In addition, more research is required to confirm the predictive potential of the correlations between flowability descriptors and particle characteristics presented in Chapter IV.

- With regard to the assessment of non-consolidated flowability using a rotating drum, future studies may investigate the extent of segregation phenomena during the test and its effects on the flowability descriptors obtained. This could be achieved, for instance, by examining the evolution of avalanches during a long period of time and repeating this experiment several times after mixing the powder.
- Although the characterization of two well-differentiated populations in terms of particle size (obtained by sieving) allowed us to draw conclusions on the effects of particle characteristics on unconsolidated flow, a natural progression of this work should include the test of unsieved powders.
- Second, this research can be pursued through numerical approaches such as DEM taking into account the following points:
 - The use of a multisphere approach in this work was a first attempt to take into account the needle-like shape biomass particles. However, we are aware of the possibilities in terms of accuracy of particle shape representation that other methods can offer. The use of approaches other than multispheres is therefore encouraged for future work. For instance, the last version of LIGGGHTS® (3.8.0) has implemented a major new feature for particle shape representation: superquadric shape particles [429]. The equation of a the points on the surface of basic superquadric particle is given by:

$$\left|\frac{x}{a}\right|^r + \left|\frac{y}{b}\right|^s + \left|\frac{z}{c}\right|^t = 1 \quad (92)$$

where a , b , c , r , s and t are parameters that allow a wide variety of shapes to be simulated [430]. In particular, the use of superquadrics is likely to closely mimic the flat plate-like shape of biomass particles. The multisphere approach used in this work still required the inclusion of rolling friction to mimic a reduced rotation of the spherical particles. By using flat particles through superquadrics models, the need for rolling friction models (and their calibration) could be reduced. Flexible fiber models for DEM that are starting to emerge [365] are also of great interest for simulation of biomass particles that can bend and relax under consolidation. However, these models are not yet integrated into DEM software nor are yet time-efficient for simulation of large quantities of particles.

- For DEM simulations, particle density was assumed to be independent of the torrefaction intensity. The underlying hypothesis was that the mass loss was balanced by the dimensional shrinkage of the material during treatment. This hypothesis deserves further validation, so measurements of particle density relevant to DEM simulations should be undertaken in future research, especially since the numerical bulk density values used for calibration are highly sensitive to particle density.
- As part of the DEM calibration framework presented, different values of the weighting coefficients of the objective functions (that were set to be the same in the case of the first objective function) could be tested. This would, for instance, result in a better adjustment of the bulk responses that were more repeatable or that better highlight a given feature of the biomass (e.g. the cohesive nature).
- Further work is required to establish calibration tests, in addition to the angle-of-repose used in this work, that could discriminate between different cohesive strengths of biomass materials. In addition, more research on the scalability of the calibration setups and the reliability of a coarse-

grained particle representation would assess the applicability of the calibration framework on an industrial scale.

- Finally, a third axis of further work concerns the integration of the methodologies and results presented in this work to the design and evaluation of biomass pretreatment technologies within BtL applications. We have shown how the outcomes of this work could be used either for equipment design (e.g. silos and conveyor screws), or to adjust the couple of torrefaction intensity/grinding intensity as a pair, in terms of energy balance and to satisfy gasification requirements. However, several avenues for future work can be explored:
 - Validation of the mass loss as flowability indicator would require experiments showing that mass losses obtained by different torrefaction conditions (temperature and residence time) would give the same flow properties, as has been the case for energy properties and dimensional changes [91,93]. This naturally requires establishing whether samples treated at the same mass loss obtained under different conditions will yield similar particle size and shape distributions after grinding.
 - Although the trade-offs between the energy inputs of torrefaction and direct grinding energy consumption were briefly discussed in Chapter I, mainly on the basis of the literature, there is room to advance the knowledge on these compromises. In particular, a process-scale assessment of the energy savings generated by the improved handling characteristics of biomass by torrefaction would be important to confirm the overall positive value of torrefaction as pretreatment step.
 - In order to enhance the applicability of the flow properties provided by this research for equipment design, complementary measurements (by shear testing) of wall friction as well as time consolidation effects are recommended.
 - The evaluation of the adequate extrapolation of the results of rotating drums to the study of the performance of feeding systems such as screw feeders is to be undertaken. This would confirm the interest of the characterization setup, beyond the sole comparative analysis of powders.
 - Throughout this work, we have verified that the study of granular materials in general and of powder flowability in particular is highly multivariate. Flow behavior can depend on the particle characteristics, the degree of consolidation and other external conditions (humidity, interaction with other materials, etc.). It is desirable to isolate the individual effects of each parameter on flowability, but this is hardly achievable through experiments. Although initial progress in this direction has been made in this research, further studies on this topic are recommended, in particular by combining experimental and simulation approaches.

APPENDIXES

Appendix I

Influence of particle thickness on the heat treatment homogeneity of poplar wood

(Originally published (in French) in « Recent Récent Progrès en Génie des Procédés » 2017 ISBN: 978-2-910239-85-5)

Abstract

The BtL processing route for valorization of biomass into 2G biofuels begins with pretreatment operations. Torrefaction is a mild pyrolysis treatment that reduces the fibrous, resilient and hygroscopic nature of biomass. This thermal treatment makes downstream grinding operations less energy-consuming and facilitates storage. Ensuring homogeneity of torrefaction within the particles is essential to guarantee the production of a material with homogeneous characteristics in terms of energy density, chemical composition and mechanical properties. In this work, the cross effects of the thickness of poplar particles and the heat treatment intensity on the torrefaction homogeneity are studied. For this purpose, we examine the temperature profiles at the core of the samples, as well as mass loss measurements and localized elemental analyses. An increase in the temperature overshoot was observed with treatment thickness and torrefaction temperature. Effects of particle thickness on mass loss were also shown. The homogeneity of the heat treatment within the particles is the result of a balance between the convective heat flow from the external source (the torrefaction reactor), and the heat flow released into the particles by the exothermic degradation reactions.

Keywords: BtL, torrefaction, elemental analysis, mass loss, temperature overshoot, poplar

1. Introduction

In a BtL production chain, torrefaction is considered to be one of the most advantageous required pretreatments. This process, which is a thermal treatment of biomass at atmospheric pressure, in the absence of oxygen and at temperatures between 200 °C and 300 °C, produces a solid with intermediate characteristics between native biomass and charcoal. Torrefied biomass has lower hygroscopicity and mechanical resilience than raw biomass, as well as higher energy content and resistance to biological degradation [431]. Thermally treated biomass is also more uniform than untreated biomass: torrefied lignocellulosic biomass of different origin has similar physical and chemical properties [90]. All these effects of torrefaction on lignocellulosic biomass lead to a significant reduction in energy consumption of downstream grinding processes, as well as the facilitation of storage [34,333].

Ensuring the homogeneity of the heat treatment within the biomass particles is necessary to guarantee that the product properties are as expected. This makes possible to reliably model the process for better control and optimization.

Two successive phenomena can be at the origin of the heterogeneity of torrefied biomass at the particle scale. First, the thermal resistance to heat transfer from the surface to the core while the atmosphere is warmer than the particle. Second, the thermal resistance through the material for evacuation from the core to the surface of the energy produced when exothermic biomass degradation

reactions are thermo-activated. The combination of these two phenomena generates temperature profiles over the thickness of the material and therefore a heterogeneous heat treatment.

Indeed, differential thermal analysis (DTA) studies have demonstrated the presence of exothermic degradation reactions during lignocellulosic biomass torrefaction [432,433]. During torrefaction, the oxygen present in hemicelluloses is partially consumed, thus giving rise to exothermic behavior [432].

The purpose of this work is to characterize the effects of biomass particle thickness and heat treatment intensity (duration, temperature) on torrefaction intraparticle homogeneity. As a result, an optimal particle size that ensures good homogeneity of the treatment in the sample could be established.

2. Materials and methods

2.1. Woody biomass

Samples of poplar (*Populus euro-americana* ‘Koster’) were cut from a 25-year-old tree from a plantation in the Suippe Valley, Auménancourt-le-Petit, Grand Est, France. The tree was sawn before drying.

2.2. Sample preparation

The dimensions of the samples are 80×60 mm² in the tangential and longitudinal directions, respectively, and 10, 12, 15, 17 and 20 mm in the radial direction (thickness). These samples were cut in the longitudinal direction of the same board to limit the effects due to biological variability within the tree. This precaution makes it possible to interpret the differences observed as resulting from differences in operating conditions.

2.3. Torrefaction conditions and mass loss (ML) measurements

The samples were heat treated using an in-house developed batch for biomass torrefaction. The torrefaction furnace is a *Memmert UFP400* oven with a volume of 53 L. Heating elements are regularly distributed at the base, ceiling and side walls of the internal chamber. The oven is equipped with a PID temperature control system. The convection of the oven atmosphere is forced by a vertical centrifugal fan located on the bottom wall. The hermetically closed chamber is swept by a continuous flow of nitrogen (5 L.min⁻¹) ensures an oxygen concentration lower than 1.5 % [306]. The O₂ concentration is measured on the sweeping gas at the oven outlet. An acquisition software has been developed to i) take control of the oven's PID to reproduce the desired temperature profile and ii) save on file the temperatures of the various samples and the actual conditions of the furnace.

Three treatment intensities were tested corresponding to three temperatures at 240 °C, 260 °C and 280 °C for 1 hour. The protocol followed is as follows: a. Heating from ambient temperature (about 20 °C) at a rate of 10 °C.min⁻¹ to 100 °C; b. Plateau at 100 °C (drying stage) for 24 hours; c. Heating at 10 °C.min⁻¹ to the treatment temperature; d. Plateau at the torrefaction temperature for 1 hour; e. Cooling by heat loss and nitrogen flow sweeping in the furnace.

For each treatment, ten samples (two of each thickness) were torrefied. The samples were instrumented with type K thermocouples (0.5 mm in diameter) to measure their core temperature, as shown in Figure 119.

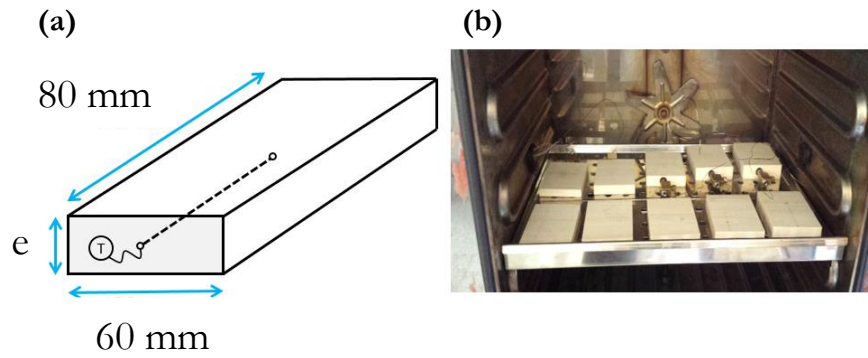


Figure 119. (a) Sample conditioning (the core thermocouple is schematized). (b). Samples inside the torrefaction furnace.

Due to its synthetic nature of temperature and treatment duration [431], the overall anhydrous mass loss (ML) is used to characterize the intensity of the torrefaction. ML does not include water released during the drying phase:

$$ML (\%) = \frac{m_0 - m_t}{m_0} \cdot 100 \quad (93)$$

where m_0 and m_t are the initial and final anhydrous oven-dried masses (after torrefaction), respectively.

2.4. Elemental analysis CHNS/O

Samples of 2 mm thickness were taken from the surface and core of the treated woodchips and ground in a *Retsch MM400* ball mill to obtain a powder suitable for elemental analysis.

A CHNS/O Flash 2000 elemental analyser (*ThermoFischer Scientific*[®]) was used to determine the composition of the heat-treated samples. The analysis of C, H, N and S was performed by dynamic “flash” combustion of the sample at 930 °C using a V_2O_5 catalyst. The oxygen analysis uses pyrolysis of the sample at 1000 °C. The gaseous products of the reactions were then separated by GC chromatography and quantified using a katharometer.

3. Results and discussion

3.1. Temperature profiles

Results in Figure 120 show the evolution of sample core temperature at a torrefaction temperature of 280 °C. Qualitatively, similar profiles were found for the other the temperatures studied. A temperature overshoot is observed for all the thicknesses investigated. This confirms the presence of exothermic reactions caused by degradation of hemicelluloses at the temperatures applied. Consistently, the temperature peak increases with the sample thickness due to the increased resistance to heat transfer towards the surrounding gas. This increases the core temperature and activates further the exothermic reactions. For a thickness of 20 mm at 280 °C, this results in a core temperature 20 °C higher than that of the oven gas (Figure 120 and Figure 121).

In the first moments of temperature rise, heat is transferred from the gas to the sample surface and from the surface to the core. When the core reaches a temperature high enough to activate the exothermic degradation reactions, the direction of the heat flow is reversed towards the surface of the sample.

The thermal diffusivity, expressed in $\text{m}^2\cdot\text{s}^{-1}$, is dimensionally equivalent to the ratio of the square of a characteristic length and a characteristic diffusion time:

$$\alpha = \frac{\lambda}{\rho \cdot C} \propto \frac{l^2}{\tau_c} \quad (94)$$

The characteristic time therefore represents the time required to transfer a quantity of heat over a distance l in a thermally diffusive material [434]. The increase in sample thickness is a barrier to heat dissipation, leading to the formation of a larger exothermal peak. As shown in Figure 121, for a given thickness, this exothermicity increases with the torrefaction temperature. The two phenomena (heat conduction and exothermic reactions) are therefore coupled and the torrefaction homogeneity over the thickness depends on their relative importance.

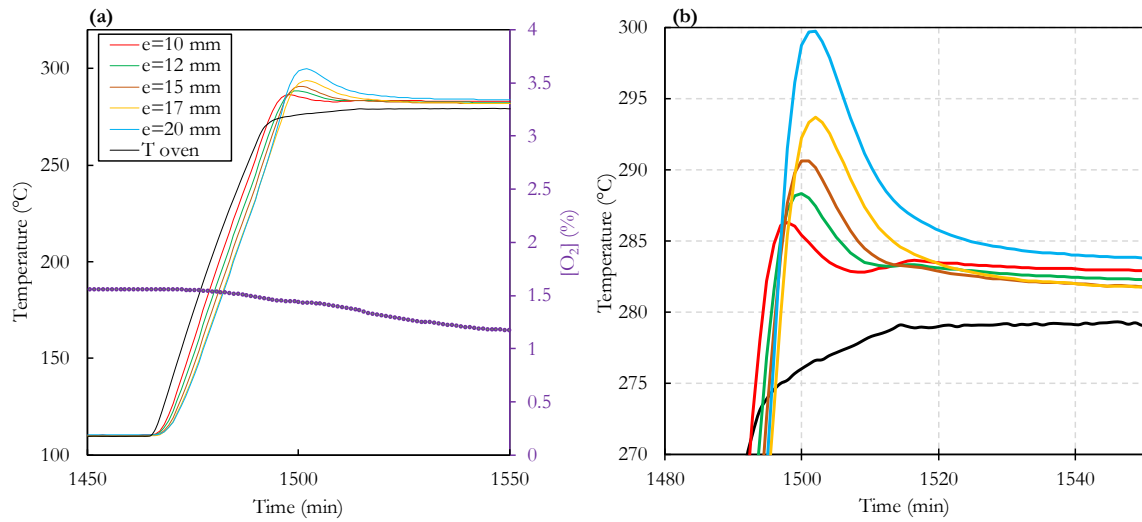


Figure 120. Effect of sample thickness on core temperature at a torrefaction temperature of 280 °C for one-hour treatment (a) Temperature profile evolution (dotted line corresponds to the oxygen content) (b). Zoom on the temperature overshoots at the beginning of the thermal treatment.

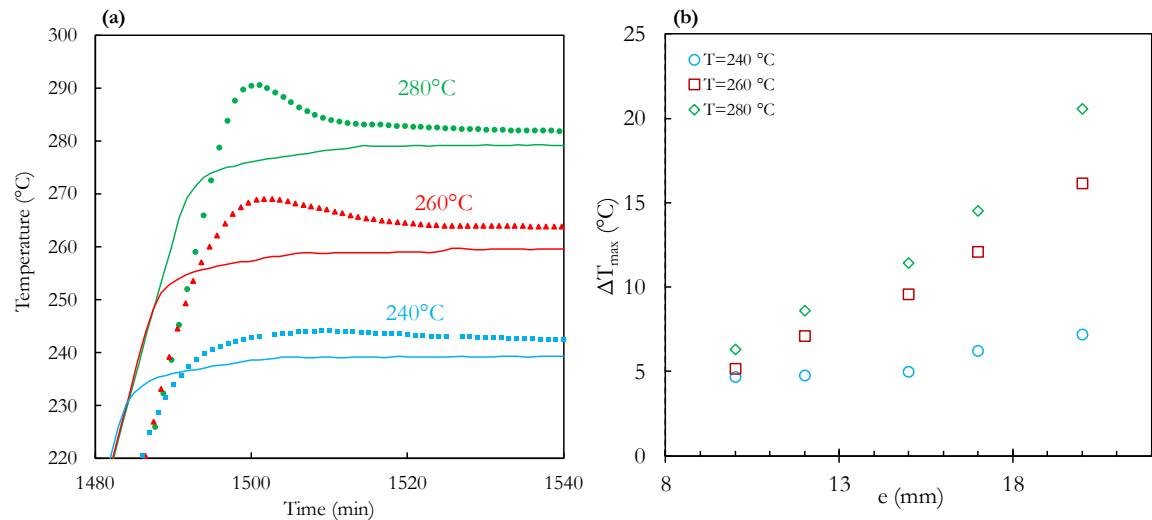


Figure 121. Comparison of temperature overshoot for three treatment intensities. (a) Temperature evolution for 15 mm thick samples (solid lines are the furnace temperatures; dotted lines are the core temperatures). (b) Peak amplitude for all the thicknesses tested.

3.2. Mass loss

The overall mass loss is used as indicator of the torrefaction intensity. Figure 122 shows the influence of the thickness of the treated samples on their mass loss. A similar trend is observed for the three temperatures studied: the mass loss decreases in the range of 10 to 12 mm and then increases for the thickest samples. Overall, the increase in exothermic peak amplitude associated with the increase in sample thickness is accompanied by a higher treatment intensity. From 12 mm thickness onwards, the increase in transfer time due to the increase in the characteristic length of heat transfer from the oven to the center of the sample is balanced and exceeded by the heat source produced by the exothermic reactions. However, for the thinnest samples, heat conduction from the atmosphere to the sample predominates over exothermic reactions at short times, which extends the treatment duration for thin particles and leads to a higher torrefaction intensity.

An overall comparison of the three graphs confirms a direct effect of temperature on treatment intensity, with mass loss increasing from an average of 12 % at 240 °C to an average of 26 % at 280 °C.

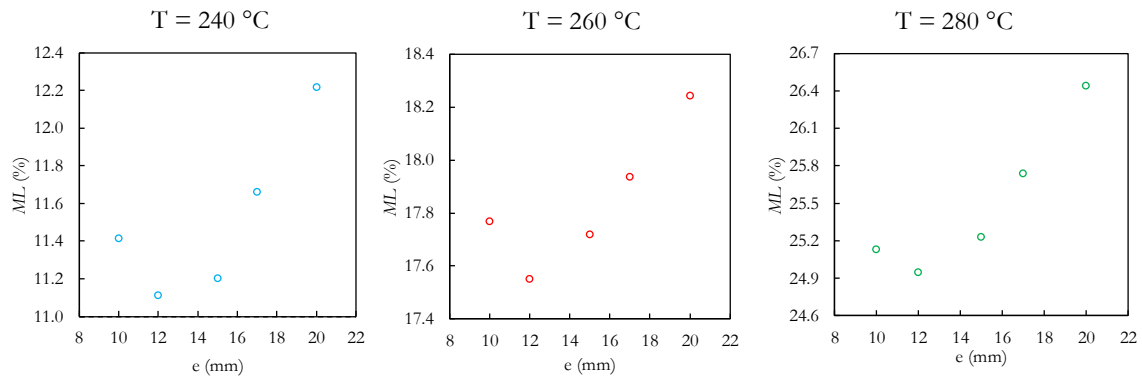


Figure 122. Effect of particle thickness and torrefaction temperature on the overall mass loss (ML).

3.3. Composition CHNS/O

Preliminary results of the elemental analyses show an increase in carbon content as well as a decrease in hydrogen and oxygen contents as the torrefaction intensity increases (Figure 123). These results are entirely consistent with previous research [82]. However, the effect of thickness on the surface and core elemental composition is not clear for the thickness values studied. Further research on greater thicknesses will need to be undertaken to capture such an influence.

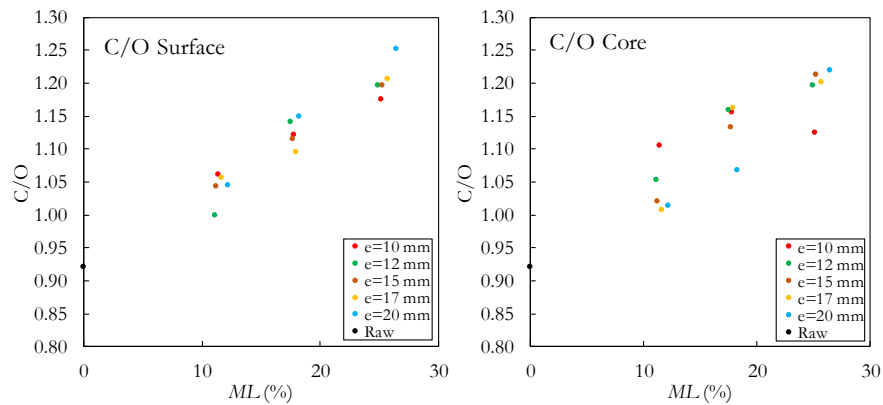


Figure 123. Elementary ratios of carbon and oxygen composition on the sample surface and core as a function of the torrefaction intensity for different thicknesses.

4. Conclusion and perspectives

Due to the influence of the thickness of poplar chips on heat transfer within the samples, the effect of exothermic reactions increases as particle thickness increases for values between 10 mm and 20 mm. The homogeneity and overall intensity of torrefaction therefore depends strongly on the characteristic dimension for heat transfer as well as the on the torrefaction temperature for a given residence time.

In future investigations, the study of differences in core and surface temperatures as a function of thickness, as well as in chemical compositions should provide more understanding on the intraparticle treatment heterogeneity. An optimal particle sample size that guarantees treatment homogeneity could then be established.

Appendix II

Measurements of energy consumption required for grinding

In an attempt for illustrating the interest of torrefaction in reducing grinding energy consumption, measurements of the grinding energy of poplar chips were conducted in both the *SM300* cutting and the *PM100* ball mill.

Effects of torrefaction on grindability as measured by the grinding energy consumption have been relatively well documented in literature (Chapter I), so our analysis will be limited to the comparison of energy consumptions for raw and torrefied samples in a rather qualitative manner. Further quantitative analysis of these trends is considered beyond the scope of this work.

Power consumption measurements were conducted using a wattmeter (*Chauvin Arnoux* C.A 8332B [435]) connected to the mills with by a single-phase electrical connection. The power data were processed using the Power Analyzer Transfer Software [436]. The acquisition frequency was 1 second.

Regarding the cutting mill, poplar samples at three levels of torrefaction intensity were ground: $ML = 0\%$ (raw material), $ML = 9.6\%$ (1-hour treatment at $240\text{ }^{\circ}\text{C}$) and $ML = 24.5\%$ (1-hour treatment at $280\text{ }^{\circ}\text{C}$). Wood chips ($60 \times 80 \times 15\text{ mm}^3$) were individually fed into the grinder once the rotor reached its steady rotational speed (set at 1500 rpm). A 1 mm trapezoidal holes outlet sieve was used.

Figure 124 compares the power consumption profile recorded when the chips were individually fed into the grinder. Five chips were ground in the case of the raw and the mildly torrefied material, while four intensively torrefied chips were ground. The first peak corresponds to the start-up of the grinder to reach the set constant rotational speed. An idle power consumption of ca. 0.5 kW was measured. Each of the subsequent peaks corresponds to the grinding of one chip.

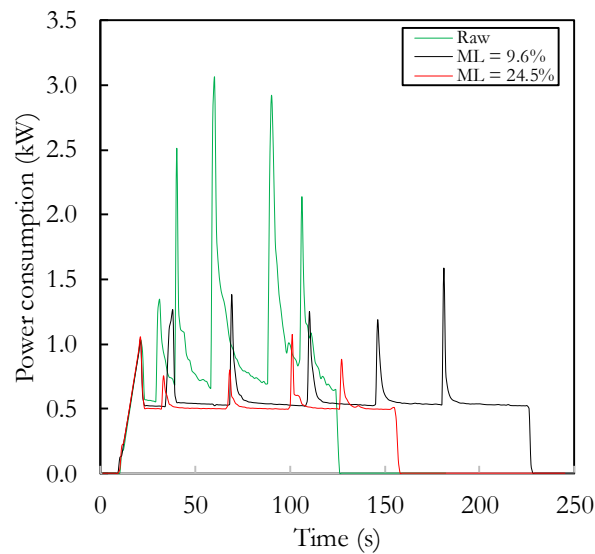


Figure 124. Power consumption profile for raw and torrefied wood chips in a *SM300* grinder.

In the case of the raw samples, when a chip was fed into the grinder there was a great peak power draw. Power consumption peaks reached values over 2 kW. Because of its high mechanical resilience, the material took relatively long to meet the output sieve size, therefore remaining in the grinding chamber. As a result, the power consumption peak spread over a duration of over 20 seconds, which is quite high compared to the torrefied samples.

In the case of the mildly torrefied samples, not only is the peak power draw significantly lower than that of the raw samples, but the power consumption rapidly stabilizes at the idle consumption value. The power peaks were at ca. 1.3 kW and it took around 8 seconds to drop back to the idle value. For the intensively torrefied samples, the peak power consumption is the lowest (on average 0.87 kW) and the grinding draw lasted about 6 seconds.

Additionally, according with the experimental observations, it was noteworthy that torrefied samples passed easily through the bottom sieve, which made it possible to quickly feed the series of chips. Intensively torrefied samples were thus faster to grind. On the contrary, raw samples were more likely to block the rotor if they were continuously fed with no rest time.

From these results, it is therefore clear that torrefaction intensity has a positive influence on the grinding energy consumption and grinding time. Indeed, due to the thermochemical degradation of the wood structure during torrefaction, the heat treatment is well known to increase the material brittleness and in consequence, the biomass grindability.

The order of magnitude of the recording period is similar to the one of the grinding duration for all samples. At present, it is therefore difficult to obtain a precise description of the power peak and to evaluate its amplitude. In future work, the accuracy of the results could be improved by increasing the data recording frequency.

Regarding the planetary ball mill, the outflow of the *SM300* mill was ground using 15 stainless steel balls (20 mm diameter) for 1 minute. In addition to a raw sample, four torrefied samples at different torrefaction intensities were tested ($ML = 12.2, 24.1, 32.0$ and 49.0%). A volume of biomass corresponding to $1/3$ of the jar volume was filled.

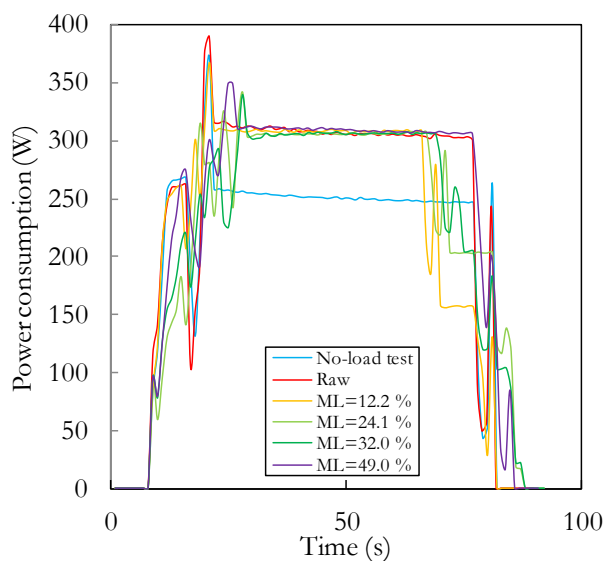


Figure 125. Power consumption in a planetary ball mill for an empty grinding jar ('no-load test') and filled with raw and torrefied biomass.

Power measurements represented in Figure 125 show that, apart from the effect of the load (compared to the empty jar), no significative differences were found regarding the effects of torrefaction intensity on the grinding energy consumption of ball milling. Indeed, the whole powder remains in the jar all along the grinding process. For this type of grinder, the power consumption has to be considered over the time required to obtain a given PSD. In order to highlight the duration effect, the input PSD has to be the same for all torrefaction intensities. This could be the subject of further study.

Appendix III

Automated calculation of avalanche angles in a rotating drum system

In this section, we present the MATLAB source code of the image processing algorithm described in Chapter IV for the analysis of the powder motion in a rotating drum. The input data are the stack of images captured during an experiment and a 'blanc' image of the empty cylinder. The threshold values are set manually and can be changed according to the evaluated histograms. Results (image number, average angle from linear regression, centroid angle, powder surface, r^2 , etc.) are stored in 'evol_angles' matrix.

```
%Automated calculation of avalanche angles in a rotating drum system
%Copyright (©) 2018 John Pachón-Morales <john.pachon@centralesupelec.fr>
<julien.colin@centralesupelec.fr>
clc; % Clear the command window.
close all; % Close all figures (except those of imtool.)
clear; % Erase all existing variables.
workspace; % Make sure the workspace panel is showing.
format long g;
format compact;
fontSize = 20;
%=====
%=====
filefolder=fullfile(pwd);
dirOutput=dir(fullfile(filefolder,'Image_stack_name*.jpg'));
imageNames={dirOutput.name}';
[imageNames,index] = sort_nat(imageNames); %Schwarz 2011
numImages=numel(imageNames);

evol_angles=zeros(numImages,6);
evol_angles(:,1)=1:1:numImages;
img_non_prises=zeros(numImages,1);
w=1;
%=====
%=====
% Blanc image processing
blancrgb=imread('BLANC.jpg');
[rowsb, columnsb, numberOfColorChannelsb] = size(blancrgb);
if numberOfColorChannelsb>1
    BlancGray=rgb2gray(blancrgb);
else
    BlancGray=blancrgb; %It's already gray.
end
Xdblanc=im2double(BlancGray);
thresholdValueb=0.7;
% Binary image
BWb=Xdblanc>thresholdValueb;
BWb=imfill(BWb,'holes');
statsblanc=regionprops('table',BWb,'Centroid');
CentreBlanc=statsblanc.Centroid;
%Edge extraction using Canny method
contblanc=edge(BWb,'Canny');
contblanc_sans_bord=contblanc;
```



```
contblanc(:,1) = true; contblanc(:,end) = true;contblanc(1,:) =
true;contblanc(end,:) = true;
%=====
%=====
% Experiment images (rotating drum + powder)
for za=1:numImages
Xrgb=imread(imageNames{za});
[rows, columns, numberOfColorChannels] = size(Xrgb);
if numberOfColorChannels>1
    % It's not really gray scale like we expected - it's color.
    % Use weighted sum of ALL channels to create a gray scale image.
    Xgray=rgb2gray(Xrgb);
else
    Xgray=Xrgb; %It's already gray.
end
Xd=im2double(Xgray);
thresholdValue=0.6;
% Image binaire
BW=Xd>thresholdValue;
BW=imfill(BW,'holes');
% Edge extraction (Canny method)
cont1=edge(BW,'Canny');
%=====
%=====
%Edge sustraction
cont_avalanche=cont1-contblanc;
cont_avalanche=cont_avalanche>0;
cont2=cont_avalanche;
% % Translate edge to erase misalignment borders
number_trans=7;
for q=1:number_trans
%Left
contblancctr=imtranslate(contblanc,[-q, 0]);
cont2b=cont2-contblancctr;
cont2b=cont2b>0;
%Down
contblancctr2=imtranslate(contblanc,[0, -q]);
cont2c=cont2b-contblancctr2;
cont2c=cont2c>0;
%Right
contblancctr3=imtranslate(contblanc,[q, 0]);
cont2d=cont2c-contblancctr3;
cont2d=cont2d>0;
%Up
contblancctr4=imtranslate(contblanc,[0, q]);
cont2e=cont2d-contblancctr4;
cont_plus_tambour=cont2e.*cont2e;
cont2e=cont2e>0;
cont2=cont2e;
end
%Bridge = complete possible empty pixels
cont2=bwmorph(cont2, 'bridge');
cont2=bwareaopen(cont2,40); %remove remaining clumps of max. 40 pixels
cont2e=cont2;
%=====
%=====
%Powder free surface coordinates
[i,j]=find(cont2e==1); %i=row, j=columns, so i-->(-y), j-->(x)
[i_avalanche,j_avalanche]=find(cont_avalanche==1);
i_cartesian=length(cont2e(:,1))-i;
length_image=length(cont_avalanche(:,1));
i_avalanche=length_image-i_avalanche;
A=[j,i_cartesian];
A_avalanche=[j_avalanche,i_avalanche];
P=zeros(size(A));
```

```

n=1;
minx=min(A(:,1));
maxx=max(A(:,1));
N=length(A(:,1));
for valx=minx:maxx
    for i=1:N
        if A(i,1)==valx
            if P(n,2)<A(i,2)
                P(n,2)=A(i,2);
                P(n,1)=valx;
            else
                P(n,2)=P(n,2);
            end
        else
            i=i+1;
        end
    end
    n=n+1;
end
[d,e]=find(P(:,1));
P=P((1:length(d)),:);
condition=P(:,1)==0;
P(condition,:)=[];
%=====
%=====
%Drawing cylinder circle
r=sqrt((CentreBlanc(1,1)-P(1,1))^2+(length(cont2e(:,1))-CentreBlanc(1,2)-P(1,2))^2);
r_avalanche=sqrt((CentreBlanc(1,1)-A_avalanche(1,1))^2+(length(cont_avalanche(:,1))-CentreBlanc(1,2)-A_avalanche(1,2))^2);
xb=CentreBlanc(1,1);
yb=CentreBlanc(1,2);
mat_rayons=cercle_blanc(xb,yb,contblanc_sans_bord);
rcercle_blanc=mode(round(mat_rayons(:,3)));
[xunit,yunit] = circle(xb,yb,rcercle_blanc);
XData=xunit;
YData=yunit;
%ymax calculation
[i,j]=find(cont2e==1);
y_max=min(i);
y_max=length(cont2e(:,1))-y_max;
evol_angles(za,6)=y_max;

for counter=1:length(XData)
    cont2(round(YData(counter)),round(XData(counter)))=1;
end
%Closing the contour before filling
[i,j]=find(cont2e==1);
Mat_cercle_blanc=[round(XData)',round(YData)'];
y1=find(Mat_cercle_blanc(:,2)==i(1));
xc0=min(unique(Mat_cercle_blanc(y1,1)));
for counter=xc0:j(1)
    cont2(i(1),counter)=1;
end
cont2_before_skel=cont2;
cont2_skel=bwmorph(cont2,'skel',Inf);
arr=cont2_skel;
rMax=30;
%Edge connection if holes
arr = connectDots(arr,rMax); %Keith Coffman,2016 Algorithm
cont2=arr;
%=====
%=====
%Filling powder
    
```

```

powder_filled=imfill(cont2,[700 600]);%Select coordinates of powder
%Erasing circle
for counter2=1:length(XData)
    powder_filled(round(YData(counter2)),round(XData(counter2)))=0;
end
powder_filled=bwareaopen(powder_filled,50); %Remove small points remaining
powder_filled=imfill(powder_filled, 'holes');
stats=regionprops('table',powder_filled,'Centroid');
CentrePoudre=stats.Centroid;
%=====
%Computing area of powder on image
powder_area=bwarea(powder_filled);
area_blanc=bwarea(BWb);
if (powder_area<0.7*area_blanc) && (powder_area>0.1*area_blanc)
    xp=CentrePoudre(1,1);
    yp=CentrePoudre(1,2);
%Computing centroid angle
    beta=atand(-(yp-yb)/(xp-xb)); %-y cause y-counting is made upside-down to
cartesian coordinates
    if yp>yb && xp>xb %quadrant I
        beta=beta;
    elseif yp>yb && xp<xb %quadrant II
        beta=beta+180;
    elseif yp<yb && xp<xb %quadrant III
        beta=beta+180;
    elseif yp<yb && xp>xb %quadrant IV
        beta=beta+360;
    end
    surf_angle=360-beta;
    evol_angles(za,3)=surf_angle;
    evol_angles(za,5)=powder_area;
%=====
%Linear regression angle
partition=10;
s=round(length(P)/partition);
mat_angle=zeros(length(P),2);
for k=1:length(P)-s
    Px=P((k:s+k-1),1);
    Py=P((k:s+k-1),2);
    p=polyfit(Px,Py,1);
    angle=radtodeg(atan(p(1)));
    mat_angle(k,1)=P(k,1);
    mat_angle(k,2)=angle;
end
lin_tous=polyfit(P(:,1),P(:,2),1);
ycalc_tous=polyval(lin_tous,P(:,1));
angle_tous=radtodeg(atan(lin_tous(1)));
% Computing r2
yresid=ycalc_tous-P(:,2);
SSresid=sum(yresid.^2);
SStotal=length(P(:,2))*var(P(:,2));
rsq=1-SSresid/SStotal;
evol_angles(za,4)=rsq;
%=====
%=====
[d,e]=find(mat_angle(:,1));
mat_angle=mat_angle((1:length(d)),:);
angle_moyen=mean(mat_angle(:,2));
evol_angles(za,2)=angle_moyen;
za
else
za
    img_non_prises(w,1)=za;

```

```

w=w+1;
end
end
condition2=evol_angles(:,2)==0;
evol_angles(condition2,:)=[];
condition3=img_non_prises(:,1)==0;
img_non_prises(condition3,:)=[];
removed_percentage=length(img_non_prises)/numImages*100
%=====
%=====
%Plotting and saving results
mkdir Results
figure;
plot(evol_angles(:,1),evol_angles(:,2),'Color',[0 0 0] )
title('Evolution mean angle', 'FontSize', fontSize, 'Interpreter', 'None');
xlabel('Image', 'FontSize', fontSize);
ylabel('Angle(degrees)', 'FontSize', fontSize);
saveas(gcf,[pwd '/Results/angle_moyen.fig']);
figure;
plot(evol_angles(:,1),evol_angles(:,3),'Color',[0 0 1] )
title('Centroid angle', 'FontSize', fontSize, 'Interpreter', 'None');
xlabel('Image', 'FontSize', fontSize);
ylabel('Angle(degrees)', 'FontSize', fontSize);
saveas(gcf,[pwd '/Results/angle_centroids.fig']);
figure;
plot(evol_angles(:,1),evol_angles(:,4),'Color',[0 1 0] )
title('r2 (Goodness of fit)', 'FontSize', fontSize, 'Interpreter', 'None');
xlabel('Image', 'FontSize', fontSize);
ylabel('r2', 'FontSize', fontSize);
saveas(gcf,[pwd '/Results/r2.fig']);
figure;
plot(evol_angles(:,1),evol_angles(:,5),'Color',[1 0 0] )
title('Powder surface', 'FontSize', fontSize, 'Interpreter', 'None');
xlabel('Image', 'FontSize', fontSize);
ylabel('Surface', 'FontSize', fontSize);
saveas(gcf,[pwd '/Results/powder_surface.fig']);
figure;
plot(evol_angles(:,1),evol_angles(:,6),'Color',[1 0 0] )
title('Y_max', 'FontSize', fontSize, 'Interpreter', 'None');
xlabel('Image', 'FontSize', fontSize);
ylabel('Y_max', 'FontSize', fontSize);
saveas(gcf,[pwd '/Results/Y_max.fig']);
close all;

```

Embedded functions

```

function mat_rayons=cercle_blanc(xb,yb,contblanc_sans_bord)
[coord_contblanc_i,coord_contblanc_j]=find(contblanc_sans_bord==1);
mat_rayons=zeros(length(coord_contblanc_j),3);
for i=1:length(coord_contblanc_j)
rb=sqrt((xb-coord_contblanc_j(i))^2+(yb-coord_contblanc_i(i))^2);
mat_rayons(i,1)=coord_contblanc_j(i);
mat_rayons(i,2)=coord_contblanc_i(i);
mat_rayons(i,3)=rb;
end

```

```

function [xunit,yunit] = circle(xb,yb,rcercle_blanc)
th = 0:pi/50000:2*pi;
xunit = rcercle_blanc * cos(th) + xb;
yunit = rcercle_blanc * sin(th) + yb;

```

```

function arr = connectDots(arr,rMax)
% Checks each pixel of a logical array to see if it is connected to other pixels.
% If not connected, it attempts to draw connections to pixels within a region of

```

```
% length s = 2*r+1 up to a maximum distance rMax (not circular).
%load edgeVecs % pre-calculated list of perimeter coordinates to save processing
time
for r = 1:rMax
    s = 2*r+1;
    edgeVecs{1,r} = [1:s repmat(s,[1 s-1]) s-1:-1:1 ones([1 s-2])];
    edgeVecs{2,r} = [ones([1 s-1]) 1:s repmat(s,[1 s-1]) s-1:-1:2];
end
d = size(arr);
for x = 1:d(2)
    for y = 1:d(1)
        if arr(y,x)
            connected = 0; r=0;
            while connected < 2 && r <= rMax-1
                r=r+1;
                xVec = edgeVecs{1,r}+x-r-1; yVec = edgeVecs{2,r}+y-r-1; % Indices
of pixels r-away from (y,x)
                xVec(xVec<1)=1; yVec(yVec<1)=1; % Avoid
index violations
                xVec(xVec>d(2))=d(2); yVec(yVec>d(1))=d(1);
                for ndx = 1:numel(xVec)
                    cX = xVec(ndx); cY = yVec(ndx);
                    if arr(cY,cX) % A kindred pixel has been found
                        sX = 1; if x-cX<0 sX=-1;end %Step direction for indexing
                        sY = 1; if y-cY<0 sY=-1;end
                        if sum(sum(arr(cY:sY:y,cX:sX:x))) == 2 % No intermediate
pixels
                            connected = connected+1;
                            if r>1
                                [xPts,yPts] = bresenham(cX,cY,x,y); % Draw line to
connect them
                                    arr(sub2ind(d,yPts,xPts)) = true;
                                    end
                                end
                            end
                        end
                    end
                end
            end
        end
    end
end
end
function [x,y]=bresenham(x1,y1,x2,y2)
% Line to pixel approximation algorithm (Bresenham's line algorithm)
% Credit: Aaron WetzlerAll (2010)
dx=abs(x2-x1);dy=abs(y2-y1);
steep=abs(dy)>abs(dx);
if steep t=dx;dx=dy;dy=t; end
if dy==0
    q=zeros([dx+1,1]);
else
    q=[0;diff(mod((floor(dx/2):-dy:-dy*dx+floor(dx/2))',dx))>=0];
end

if steep
    if y1<=y2 y=(y1:y2)'; else y=(y1:-1:y2)'; end
    if x1<=x2 x=x1+cumsum(q);else x=x1-cumsum(q); end
else
    if x1<=x2 x=(x1:x2)'; else x=(x1:-1:x2)'; end
    if y1<=y2 y=y1+cumsum(q);else y=y1-cumsum(q); end
end
end

function [cs,index] = sort_nat(c,mode)
%sort_nat: Natural order sort of cell array of strings.
% usage: [S,INDEX] = sort_nat(C)
```

```
%
% where,
%   C is a cell array (vector) of strings to be sorted.
%   S is C, sorted in natural order.
%   INDEX is the sort order such that S = C(INDEX);
%
% Natural order sorting sorts strings containing digits in a way such that
% the numerical value of the digits is taken into account. It is
% especially useful for sorting file names containing index numbers with
% different numbers of digits. Often, people will use leading zeros to get
% the right sort order, but with this function you don't have to do that.
% For example, if C = {'file1.txt','file2.txt','file10.txt'}, a normal sort
% will give you
%
%       {'file1.txt' 'file10.txt' 'file2.txt'}
%
% whereas, sort_nat will give you
%
%       {'file1.txt' 'file2.txt' 'file10.txt'}
%
% See also: sort
% Version: 1.4, 22 January 2011
% Author: Douglas M. Schwarz
% Email: dmschwarz=ieee*org, dmschwarz=urgrad*rochester*edu
% Real_email = regexprep(Email,{'=','*'},{'@','.'})
% Set default value for mode if necessary.
if nargin < 2
    mode = 'ascend';
end
% Make sure mode is either 'ascend' or 'descend'.
modes = strcmpi(mode,{'ascend','descend'});
is_descend = modes(2);
if ~any(modes)
    error('sort_nat:sortDirection',...
        'sorting direction must be ''ascend'' or ''descend''.')
end
% Replace runs of digits with '0'.
c2 = regexprep(c,'\d+','0');
% Compute char version of c2 and locations of zeros.
s1 = char(c2);
z = s1 == '0';
% Extract the runs of digits and their start and end indices.
[digruns,first,last] = regexp(c,'\d+','match','start','end');
% Create matrix of numerical values of runs of digits and a matrix of the
% number of digits in each run.
num_str = length(c);
max_len = size(s1,2);
num_val = NaN(num_str,max_len);
num_dig = NaN(num_str,max_len);
for i = 1:num_str
    num_val(i,z(i,:)) = sscanf(sprintf('%s ',digruns{i}{:}),'%f');
    num_dig(i,z(i,:)) = last{i} - first{i} + 1;
end
% Find columns that have at least one non-NaN. Make sure activecols is a
% 1-by-n vector even if n = 0.
activecols = reshape(find(~all(isnan(num_val))),1,[]);
n = length(activecols);
% Compute which columns in the composite matrix get the numbers.
numcols = activecols + (1:2:2*n);
% Compute which columns in the composite matrix get the number of digits.
ndigcols = numcols + 1;
% Compute which columns in the composite matrix get chars.
charcols = true(1,max_len + 2*n);
charcols(numcols) = false;
charcols(ndigcols) = false;
```

```
% Create and fill composite matrix, comp.
comp = zeros(num_str,max_len + 2*n);
comp(:,charcols) = double(s1);
comp(:,numcols) = num_val(:,activecols);
comp(:,ndigcols) = num_dig(:,activecols);

% Sort rows of composite matrix and use index to sort c in ascending or
% descending order, depending on mode.
[unused,index] = sortrows(comp);
if is_descend
    index = index(end:-1:1);
end
index = reshape(index,size(c));
cs = c(index);
```

Evaluating flowability characteristics from the evolution of the ‘centroid angle’

The following MATLAB code evaluates the flow characteristics analyzed in Chapter IV from the temporal evolution of the centroid angle (UAS , f , size of avalanches, duration distributions, etc.). The code operation is mainly based on the identification of the peaks of centroid angle.

```
close all;
clear all;
load('evol_angles.mat');
evol_angles_1=evol_angles;
img_max_1=max(evol_angles(:,1));
load('evol_angles_restarted.mat')
evol_angles_2=evol_angles;
evol_angles_2(:,1)=evol_angles_2(:,1)+img_max_1;
evol_angles=[evol_angles_1
              evol_angles_2];
%              evol_angles_3];
evol_angles=evol_angles(220:end,:);
f=1;
centroids=[evol_angles(1:f:end,1),evol_angles(1:f:end,3)];
figure;
plot(centroids(:,1),centroids(:,2),'Color',[0 0 1] )
title(sprintf('1-Glass beads -- f=%g img',f), 'FontSize', 15, 'Interpreter',
'None');
xlabel('Image', 'FontSize', 15);
ylabel('Angle(degrés)', 'FontSize', 15);
saveas(gcf,[pwd '/centroids.fig']);

fps=10; %to be modified according to image acquisition parameters

centroid=evol_angles(1:f:end,:);
save('centroid.mat','centroid');
time=centroid(:,1)/fps;

MPP_All_events=0.2;
[pks,locs,w,p]=findpeaks(centroids(:,2),'MinPeakProminence',MPP_All_events);
figure; plot(centroids(:,1)/fps,centroids(:,2),centroids((locs),1)/fps,pks,'or')
xlabel('Time (s)')
ylabel('Angle')
axis tight
title(sprintf('PEAKS MAX MinPeakProminence=%f',MPP_All_events))
figure; histogram(w/fps,'BinWidth',1); title('Width en s');
```

```

figure; h=histogram(p,'BinWidth',1); title('Prominence en °');
figure; cum=cdfplot(p);
x=cum.XData(2:end-1).';
y=cum.YData(2:end-1).';
f=polyfit(y,x,4);plot(y,x,y,polyval(f,y));
threshold=ceil(polyval(f,0.01));

[pks_min,locs_min]=findpeaks(centroids(:,2)*-
1,'MinPeakProminence',MPP_All_events);
pks_min=-pks_min;
figure; plot(centroids(:,1)/fps,centroids(:,2),centroids((locs_min),1)/fps,-
pks_min,'or')
xlabel('Img Number')
ylabel('Angle')
axis tight
plot(centroids(:,1)/fps,centroids(:,2),centroids((locs_min),1)/fps,pks_min,'or')
xlabel('Time (s)')
ylabel('Angle')
axis tight
title(sprintf('PEAKS MIN MinPeakProminence=%f',MPP_All_events))

repos=pks_min;
avalanche=pks;

BinWidth=1;

figure; h1=histogram(repos,'Normalization','probability');
h1.BinWidth=BinWidth;
hold on;
h2=histogram(avalanche,'Normalization','probability');
h2.BinWidth=BinWidth;
mu1=mean(repos);
mu2=mean(avalanche);
sigma1=std(repos);
sigma2=std(avalanche);
y1=h1.BinLimits(1):0.1:h1.BinLimits(2);
f1 = exp(-(y1-mu1).^2./(2*sigma1^2))./(sigma1*sqrt(2*pi))*h1.BinWidth;
hold on;
plot(y1,f1,'LineWidth',1.5,'Color',[0 0 1]);
h1.FaceColor=[0 1 1];

y2=h2.BinLimits(1):0.1:h2.BinLimits(2);
f2 = exp(-(y2-mu2).^2./(2*sigma2^2))./(sigma2*sqrt(2*pi))*h2.BinWidth;
hold on;
plot(y2,f2,'LineWidth',1.5,'Color',[0 0 0]);
h2.FaceColor=[1 0 0];
% Create xlabel
xlabel('Angle (°)');
% Create ylabel
ylabel('Frequency');
legend('Min','Max','Location','northwest')

MPP_Big_events=threshold;
[pks_big,locs_big,w_big,p_big]=findpeaks(centroids(:,2),'MinPeakProminence',MPP_B
ig_events);
figure;
plot(centroids(:,1)/fps,centroids(:,2),centroids((locs_big),1)/fps,pks_big,'or')
xlabel('Time (s)')
ylabel('Angle')
axis tight
title(sprintf('PEAKS MAX MinPeakProminence=%f',MPP_Big_events))

[pks_big_min,locs_big_min]=findpeaks(centroids(:,2)*-
1,'MinPeakProminence',MPP_Big_events);
pks_big_min=-pks_big_min;
    
```



```
hold on;
plot(centroids(:,1)/fps,centroids(:,2),centroids((locs_big_min),1)/fps,pks_big_min, 'or')
xlabel('Img Number')
ylabel('Angle')
axis tight
plot(centroids(:,1)/fps,centroids(:,2),centroids((locs_big_min),1)/fps,pks_big_min, 'or')
xlabel('Time (s)')
ylabel('Angle')
axis tight
title(sprintf('PEAKS MIN MinPeakProminence=%f',MPP_Big_events))

%Duration of avalanches

close all;
if numel(locs_big)==numel(locs_big_min)
    if locs_big(1)<locs_big_min(1)
        duration=(centroids(locs_big_min,1)-centroids(locs_big,1))/fps; %
        NORMAL1=start by MAX and finish by MIN
        disp('MAX-MIN')
    else
        duration=(centroids(locs_big_min(2:end),1)-centroids(locs_big(1:end-1),1))/fps; %NORMAL2-starts by MIN finish by MAX
        disp('MIN-MAX')
    end
elseif numel(locs_big)>numel(locs_big_min)
    duration=(centroids(locs_big_min,1)-centroids(locs_big(1:end-1),1))/fps; %MAX-MAX
    disp('MAX-MAX')
elseif numel(locs_big)<numel(locs_big_min)
    duration=(centroids(locs_big_min(2:end),1)-centroids(locs_big,1))/fps;
    %starts AND finish by a MIN
    disp('MIN-MIN')
end
figure;plot(centroids(:,1)/fps,centroids(:,2),centroids((locs_big),1)/fps,pks_big, 'or');

hold on;
plot(centroids(:,1)/fps,centroids(:,2),centroids((locs_big_min),1)/fps,pks_big_min, 'or');
title('peaks big');

duration=round(duration,2);
figure; histogram(duration,40); title('Duration in s');
tolerance=15000; %to be modified if more or less peaks are to be counted
vrais=find(duration>mode(duration)-
tolerance*mode(duration)&duration<mode(duration)+tolerance*mode(duration));
duration_vrais=duration(vrais);

pks_big_2=pks_big(vrais);
locs_big_2=locs_big(vrais);
pks_big_min_2=pks_big_min(vrais);
locs_big_min_2=locs_big_min(vrais);

period_max=mean(diff(centroids((locs_big_2),1)))/fps
period_min=mean(diff(centroids((locs_big_min_2),1)))/fps

figure;figure1=plot(centroids(:,1)/fps,centroids(:,2),centroids((locs_big_2),1)/fps,pks_big_2, 'or');

hold on;
plot(centroids(:,1)/fps,centroids(:,2),centroids((locs_big_min_2),1)/fps,pks_big_min_2, 'or');
title('peaks big_2');
```

```

%//// RATE LOAD
if numel(locs_big_2)==numel(locs_big_min_2)
    if locs_big_2(1)<locs_big_min_2(1)
        rate_load2=(pks_big_2(2:end)-pks_big_min_2(1:end-1))./((centroids(locs_big_2(2:end),1)-centroids(locs_big_min_2(1:end-1),1))/fps);
%MAX-MIN
    else
        rate_load2=(pks_big_2-pks_big_min_2)./((centroids(locs_big_2,1)-centroids(locs_big_min_2,1))/fps); %MIN-MAX
    end
elseif numel(locs_big_2)>numel(locs_big_min_2)
    rate_load2=(pks_big_2(2:end)-pks_big_min_2(1:end))./((centroids(locs_big_2(2:end),1)-centroids(locs_big_min_2(1:end),1))/fps); %MAX-MAX
elseif numel(locs_big_2)<numel(locs_big_min_2)
    rate_load2=(pks_big_2-pks_big_min_2(1:end-1))./((centroids(locs_big_2,1)-centroids(locs_big_min_2(1:end-1),1))/fps); %MIN-MIN
end

hold on; plot(rate_load2);
%////RATE AVALANCHE

if numel(locs_big_2)==numel(locs_big_min_2)
    if locs_big_2(1)<locs_big_min_2(1)
        rate_avalanche=(pks_big_min_2-pks_big_2)./((centroids((locs_big_min_2),1)-centroids((locs_big_2),1))/fps); %NORMAL=start by MAX, finish by MIN
    else
        rate_avalanche=(pks_big_min_2(2:end)-pks_big_2(1:end-1))./((centroids((locs_big_min_2(2:end)),1)-centroids((locs_big_2(1:end-1)),1))/fps); %MIN-MAX
    end
elseif numel(locs_big_2)>numel(locs_big_min_2)
    rate_avalanche=(pks_big_min_2-pks_big_2(1:end-1))./((centroids((locs_big_min_2),1)-centroids((locs_big_2(1:end-1)),1))/fps);
%MAX - MAX
elseif numel(locs_big_2)<numel(locs_big_min_2)
    rate_avalanche=(pks_big_min_2-pks_big_2(1:end-1))./((locs_big_min_2-locs_big_2(1:end-1))/fps); %MIN-MIN
end

hold on; yyaxis right; plot(rate_avalanche);
legend('rate-load-big','rate-avalanche');
rate_avalanche_rounded=round(rate_avalanche,0);
figure; histogram(rate_avalanche_rounded,50); title('Rate avalanche');
rate_avalanche_mean=mean(rate_avalanche)
rate_load_mean2=mean(rate_load2)
periode_deriv=round((0.5*(period_min+period_max)*fps/1),0);
der=round((diff(centroids(1:periode_deriv:end,2))./(diff(centroids(1:periode_deriv:end,1))/fps))),2);
figure;der_h=histogram(der(der>0),20); title('Rate load');
mode_frequency_position=find(der_h.Values==max(der_h.Values));

figure;histogram(der(der<0),50); title('derivative<0');
figure;plot((1:1:size(der))/fps*periode_deriv,der); title('derivative');
rate_load_mode=0.5*(der_h.BinEdges(mode_frequency_position)+der_h.BinEdges(mode_frequency_position+1))

%RESULTS

ABS_Upper_Lower=[max(pks) min(pks_min)]
MEAN_Upper_Lower=[mean(pks) mean(pks_min)]
STD_Upper_Lower=[std(pks) std(pks_min)]
T_max=period_max
T_min=period_min

```

```

MEAN_Duration=mean(duration)
STD_Duration=std(duration)
MEAN_Load_rate=rate_load_mean2
MEAN_Avalanche_rate=rate_avalanche_mean
Approx_rate_load=(mean(pks)-mean(pks_min))/(period_max-mean(duration))
Approx_rate_avalanche=-(mean(pks)-mean(pks_min))/(mean(duration))

%DURATION DISTRIBUTION
figure;[cummul_duration,stats_duration]=cdfplot(duration);
[f_duration,x_duration]=ecdf(duration);
hold on;scatter(x_duration,f_duration,'r'); title('Duration distribution')
Duration_distribution=[x_duration,f_duration];

%PERIOD-FREQUENCY DISTRIBUTIONS
periods=diff(centroids((locs),1))/fps;
periods_min=diff(centroids((locs_min),1))/fps;
figure;[cummul_period,stats]=cdfplot(periods);
[f_period,x_period]=ecdf(periods);
hold on;scatter(x_period,f_period,'r'); title('T distribution');
T_distribution=[x_period,f_period];

frequency=1./periods;
figure;[cummul_frequency,stats_frequency]=cdfplot(frequency);
[f_frequency,x_frequency]=ecdf(frequency);
hold on;scatter(x_frequency,f_frequency,'b'); title('Frequency distribution')
Frequency_distribution=[x_frequency,f_frequency];

%SIZE DISTRIBUTION
figure;
plot(centroids(:,1)/fps,centroids(:,2),centroids((locs),1)/fps,pks,'or')
hold on;
plot(centroids(:,1)/fps,centroids(:,2),centroids((locs_min),1)/fps,pks_min,'or')

if numel(locs)==numel(locs_min)
    if locs(1)<locs_min(1)
        amplitude=pks-pks_min; %NORMAL=starts by MAX and finish by MIN
    else
        amplitude=pks(1:end-1)-pks_min(2:end); %starts by MIN finish by MAX
    end
elseif numel(locs)>numel(locs_min)
    amplitude=pks(1:end-1)-pks_min; %starts by MAX and finish by MAX
elseif numel(locs)<numel(locs_min)
    amplitude=-(pks_min(2:end)-pks(1:end)); %start and finish by a min
end

figure;[cummul_size,statssize]=cdfplot(amplitude);
[f_amp,x_amp]=ecdf(amplitude);
hold on; scatter(x_amp,f_amp,'r'); title('d\theta (size) distribution');
Size_distribution=[x_amp,f_amp];

%UPPER AND LOWER ANGLES DISTRIBUTIONS
figure;[cummul_pks,stats_peaks]=cdfplot(pks);
[f_pks,x_pks]=ecdf(pks);
hold on;scatter(x_pks,f_pks,'g');
Upper_angle_distribution=[x_pks,f_pks];
[cummul_pks_min,stats_pks_min]=cdfplot(pks_min);
[f_pks_min,x_pks_min]=ecdf(pks_min);
hold on;scatter(x_pks_min,f_pks_min,'b'); title(' Upper and lower angle
distribution')
Lower_angle_distribution=[x_pks_min,f_pks_min];

%DISTRIBUTION r2
figure;[cummul_r2,stats_r2]=cdfplot(centroid(:,4));
[f_r2,x_r2]=ecdf(centroid(:,4));

```

```
hold on;scatter(x_r2,f_r2,'b');  
r2_distribution=[x_r2,f_r2];
```

Appendix IV

Examples of LIGGGHTS® input scripts

1. Heap formation

```

#in.multisphere input file
#AoR of heap formed from flow on an inclined surface
#MULTISPHERE representation x4
#Parameters variation, 3 variables, 6 values
atom_style      sphere
atom_modify     map array sort 0 0
boundary        f f f
newton          off
communicate     single vel yes
processors      2 2 2
units           si
region          reg block -2.0 2.0 -2.0 2.0 -0.168 0.45 units box
create_box      3 reg
neighbor        0.003 bin
neighbor_modify  delay 0
variable a universe 1 2 3 4 5 6 7 8 9 10 11 12 13 14 15 16 17 18 19 20 21 22
23 24 25 26 27 28 29 30 31 32 33 34 35 36 37 38 39 40 41 42 43 44 45 46 47 48 49
50 51 52 53 54 55 56 57 58 59 60 61 62 63 64 65 66 67 68 69 70 71 72 73 74 75 76
77 78 79 80 81 82 83 84 85 86 87 88 89 90 91 92 93 94 95 96 97 98 99 100 101 102
103 104 105 106 107 108 109 110 111 112 113 114 115 116 117 118 119 120 121 122
123 124 125
variable sf universe 0.1 0.3 0.5 0.7 0.9 0.1 0.3 0.5 0.7 0.9 0.1 0.3 0.5 0.7
0.9 0.1 0.3 0.5 0.7 0.9 0.1 0.3 0.5 0.7 0.9 0.1 0.3 0.5 0.7 0.9 0.1 0.3 0.5 0.7
0.9 0.1 0.3 0.5 0.7 0.9 0.1 0.3 0.5 0.7 0.9 0.1 0.3 0.5 0.7 0.9 0.1 0.3 0.5 0.7
0.9 0.1 0.3 0.5 0.7 0.9 0.1 0.3 0.5 0.7 0.9 0.1 0.3 0.5 0.7 0.9 0.1 0.3 0.5 0.7
0.9 0.1 0.3 0.5 0.7 0.9 0.1 0.3 0.5 0.7 0.9 0.1 0.3 0.5 0.7 0.9 0.1 0.3 0.5 0.7
0.9 0.1 0.3 0.5 0.7 0.9 0.1 0.3 0.5 0.7 0.9
variable rf universe 0.1 0.1 0.1 0.1 0.1 0.1 0.3 0.3 0.3 0.3 0.3 0.5 0.5 0.5 0.5
0.5 0.7 0.7 0.7 0.7 0.7 0.9 0.9 0.9 0.9 0.9 0.1 0.1 0.1 0.1 0.1 0.3 0.3 0.3 0.3
0.3 0.5 0.5 0.5 0.5 0.5 0.7 0.7 0.7 0.7 0.7 0.9 0.9 0.9 0.9 0.9 0.1 0.1 0.1 0.1
0.1 0.3 0.3 0.3 0.3 0.3 0.5 0.5 0.5 0.5 0.5 0.7 0.7 0.7 0.7 0.7 0.9 0.9 0.9 0.9
0.9 0.1 0.1 0.1 0.1 0.1 0.3 0.3 0.3 0.3 0.3 0.5 0.5 0.5 0.5 0.5 0.7 0.7 0.7 0.7
0.7 0.9 0.9 0.9 0.9 0.9 0.1 0.1 0.1 0.1 0.1 0.3 0.3 0.3 0.3 0.3 0.5 0.5 0.5 0.5
0.5 0.7 0.7 0.7 0.7 0.7 0.9 0.9 0.9 0.9
variable CED universe 0.0 0.0 0.0 0.0 0.0 0.0 0.0 0.0 0.0 0.0 0.0 0.0 0.0 0.0 0.0
0.0 0.0 0.0 0.0 0.0 0.0 0.0 0.0 0.0 0.0 0.0 0.0 0.0 0.0 0.0 0.0 0.0 0.0 0.0 0.0
10000 10000 10000 10000 10000 10000 10000 10000 10000 10000 10000 10000 10000
10000 10000 10000 10000 10000 10000 20000 20000 20000 20000 20000 20000 20000
20000 20000 20000 20000 20000 20000 20000 20000 20000 20000 20000 20000 20000
20000 20000 20000 20000 20000 50000 50000 50000 50000 50000 50000 50000 50000
50000 50000 50000 50000 50000 50000 50000 50000 50000 50000 50000 50000 50000
50000 50000 50000 80000 80000 80000 80000 80000 80000 80000 80000 80000 80000
80000 80000 80000 80000 80000 80000 80000 80000 80000 80000 80000 80000 80000
80000 80000 80000
log log.$a
print "A=$a"
#Material properties
fix      m1 all property/global youngsModulus peratomtype 5.e6 5e6 5e6
fix      m2 all property/global poissonsRatio peratomtype 0.3 0.3 0.3
fix      m3 all property/global coefficientRestitution peratomtypepair 3 0.1
0.1 0.1 0.1 0.1 0.1 0.1 0.1 0.1 0.1

```

```

fix          m4 all property/global coefficientFriction peratomtypepair 3 ${sf}
0.4 0.5 0.4 0.5 0.5 0.5 0.5 0.5
fix          m5 all property/global coefficientRollingFriction peratomtypepair 3
${rf} 0.5 0.5 0.5 0.5 0.5 0.5 0.5 0.5
fix          m6 all property/global cohesionEnergyDensity peratomtypepair 3 ${CED}
0 0 0 0 0 0 0
    print "SF=${sf}"
    print "RF=${rf}"
    print "CED=${CED}"
#pair style
pair_style gran model hertz tangential history cohesion sjkr rolling_friction
epsd2
    pair_coeff      * *
    timestep 0.00001
    fix          integrate all nve/sphere
    fix          gravity all gravity 9.81 vector 0.0 0.0 -1.0
#box walls
fix boxwalls_z1 all wall/gran model hertz tangential history primitive type 3
zplane -0.168
#import mesh from cad:
fix          cad1 all mesh/surface file feeder40.stl type 2      scale 0.001
fix foot_wall all wall/gran model hertz tangential history mesh n_mesher 1
meshes cad1
#region of insertion
region      factory block -0.195 -0.17 -0.036 0.036 0.165 0.223 units
box
#particle distributions
fix          pts1 all particletemplate/multisphere 15485863 atom_type 1 density
constant 300 nspheres 3 ntry 1000000 spheres file data/1_untreated.multisphere &
scale 0.000004 type 1
fix          pdd1 all particledistribution/discrete 15485867 1 pts1 1.0 0
fix          ins all insert/rate/region seed 86028121 distributiontemplate pdd1
verbose yes mass 0.05 vel constant 0. 0. -1. &
massrate 0.05 insert_every 50000 overlapcheck yes all_in yes region factory
fix          integr all multisphere
fix          ts all check/timestep/gran 1000 0.1 0.1
thermo_style custom step atoms ke f_ts[1] f_ts[2] vol
thermo      1000
thermo_modify lost ignore norm no
#make a dump of particles and the stl file
shell mkdir post_${a}
dump          dump all custom 5000 post_${a}/dump*.multi_${a}_sph300 id type type x y
z ix iy iz vx vy vz fx fy fz omegax omegay omegaz radius
dump          vtk all custom/vtk 5000 post_${a}/dump*.multi_${a}_sph.vtk id type type
x y z ix iy iz vx vy vz fx fy fz omegax omegay omegaz radius
dump          dmpstl1 all mesh/stl 5000 post_${a}/geo300_${a}*.stl cad1
#run with particle insertion
run          1000 upto
#unfix      ins
run          450000 upto
next a sf rf CED #iterate over variables
clear #delete old simulations results
jump in.multisphere #jump to top

```

2. Rectangular container simulations

```

# Rectangular container input file
#MULTISPHERE-SAMPLE 1
#ps,ur,CED variables, 5 values/variable
atom_style      sphere
atom_modify      map array sort 0 0
boundary         f p f
newton           off
communicate      single vel yes

```

```

units                si
region               reg block -0.08 0.1 -0.016 0.016 -0.2 0.2 units box
create_box           3 reg
neighbor             0.003 bin
neigh_modify         delay 0

variable a universe 28 29 30 31 32 33 34 35 36 37 38 39 40 41 42 43 44 45 46
47 48 49 50 51 52 53 54 55 56 57 58 59 60 61 62 63 64 65 66 67 68 69 70 71 72 73
74 75 76 77 78 79 80 81 82 83 84 85 86 87 88 89 90 91 92 93 94 95 96 97 98 99 100
101 102 103 104 105 106 107 108 109 110 111 112 113 114 115 116 117 118 119 120
121 122 123 124 125
variable sf universe 0.5 0.7 0.9 0.1 0.3 0.5 0.7 0.9 0.1 0.3 0.5 0.7 0.9 0.1
0.3 0.5 0.7 0.9 0.1 0.3 0.5 0.7 0.9 0.1 0.3 0.5 0.7 0.9 0.1 0.3 0.5 0.7 0.9 0.1
0.3 0.5 0.7 0.9 0.1 0.3 0.5 0.7 0.9 0.1 0.3 0.5 0.7 0.9 0.1 0.3 0.5 0.7 0.9 0.1
0.3 0.5 0.7 0.9 0.1 0.3 0.5 0.7 0.9 0.1 0.3 0.5 0.7 0.9 0.1 0.3 0.5 0.7 0.9 0.1
0.3 0.5 0.7 0.9 0.1 0.3 0.5 0.7 0.9 0.1 0.3 0.5 0.7 0.9 0.1 0.3 0.5 0.7 0.9 0.1
0.3 0.5 0.7 0.9
variable rf universe 0.1 0.1 0.1 0.3 0.3 0.3 0.3 0.3 0.3 0.5 0.5 0.5 0.5 0.5 0.7
0.7 0.7 0.7 0.7 0.9 0.9 0.9 0.9 0.9 0.1 0.1 0.1 0.1 0.1 0.3 0.3 0.3 0.3 0.3 0.5
0.5 0.5 0.5 0.5 0.7 0.7 0.7 0.7 0.7 0.9 0.9 0.9 0.9 0.9 0.1 0.1 0.1 0.1 0.1 0.3
0.3 0.3 0.3 0.3 0.5 0.5 0.5 0.5 0.5 0.5 0.7 0.7 0.7 0.7 0.7 0.9 0.9 0.9 0.9 0.9 0.1
0.1 0.1 0.1 0.1 0.3 0.3 0.3 0.3 0.3 0.3 0.5 0.5 0.5 0.5 0.5 0.7 0.7 0.7 0.7 0.7 0.9
0.9 0.9 0.9 0.9
variable CED universe 10000 10000 10000 10000 10000 10000 10000 10000 10000 10000
10000 10000 10000 10000 10000 10000 10000 10000 10000 10000 10000 10000 10000
10000 20000 20000 20000 20000 20000 20000 20000 20000 20000 20000 20000 20000
20000 20000 20000 20000 20000 20000 20000 20000 20000 20000 20000 20000 20000
50000 50000 50000 50000 50000 50000 50000 50000 50000 50000 50000 50000 50000
50000 50000 50000 50000 50000 50000 50000 50000 50000 50000 50000 50000 80000
80000 80000 80000 80000 80000 80000 80000 80000 80000 80000 80000 80000 80000
80000 80000 80000 80000 80000 80000 80000 80000 80000 80000 80000 80000

log log.$a
print "A=$a"
#Material properties
fix m1 all property/global youngsModulus peratomtype 5.e6 5e6 5e6
fix m2 all property/global poissonsRatio peratomtype 0.3 0.3 0.3
fix m3 all property/global coefficientRestitution peratomtypepair 3 0.1 0.1
0.1 0.1 0.1 0.1 0.1 0.1 0.1
fix m4 all property/global coefficientFriction peratomtypepair 3 ${sf} 0.4 0.5
0.4 0.5 0.5 0.5 0.5 0.5
fix m5 all property/global coefficientRollingFriction peratomtypepair 3 ${rf}
0.5 0.5 0.5 0.5 0.5 0.5 0.5 0.5
fix m6 all property/global cohesionEnergyDensity peratomtypepair 3 ${CED} 0 0
0 0 0 0 0
print "SF=${sf}"
print "RF=${rf}"
print "CED=${CED}"
#pair style
pair_style gran model hertz tangential history cohesion sjkr rolling_friction
epsd2
pair_coeff * *
timestep 0.00001
fix integrate all nve/sphere
fix gravity all gravity 9.81 vector 0.0 0.0 -1.0
#box walls
fix boxwalls_x1 all wall/gran model hertz tangential history primitive type 1
xplane -0.08
fix boxwalls_x2 all wall/gran model hertz tangential history primitive type 1
xplane +0.08
#import mesh from cad:
fix cad2 all mesh/surface file base.stl type 2 scale 0.01
fix cad1 all mesh/surface file edge.stl type 2 scale 0.01
fix foot_wall all wall/gran model hertz tangential history mesh n_meshes
2 meshes cad1 cad2
#region of insertion

```

```

factory block -0.0075 0.0075 -0.0012 0.0012 -0.02 0.01 units box
region          factory block -0.08 0.08 -0.016 0.016 -0.2 0.18 units box
#particle distributions
fix            pts1 all particletemplate/multisphere 15485863 atom_type 1 density
constant 350 nspheres 3 ntry 1000000 spheres file data/1_untreated.multisphere &
              scale 0.000004 type 1
fix            pdd1 all particledistribution/discrete 15485867 1 pts1 1.0
fix            ins all insert/pack seed 86028121 distributiontemplate pdd1 vel constant
0. 0. 0. orientation random vel constant 0. 0. -1. &
insert_every 100 overlapcheck yes all_in yes particles_in_region 5000 region
factory
fix            integr all multisphere
#make a dump of particles and the stl file
shell mkdir post_${a}
dump           dmp all custom 4000 post_${a}/dump*.recContdump_${a}_msph id type
type x y z ix iy iz vx vy vz fx fy fz omegax omegay omegaz radius
dump           dmpvtk all custom/vtk 4000 post_${a}/dump*.recCont_${a}_msph.vtk id type
type x y z ix iy iz vx vy vz fx fy fz omegax omegay omegaz radius
dump           dumpstl all mesh/stl 4000 post_${a}/dump_${a}_*.stl
#run with particle insertion
run            10000 upto
unfix          ins
#run to let particle settle
run            50000
unfix          boxwalls_x2
run            200000 upto
next a sf rf CED #iterate over variables
clear #delete old simulations results
jump in.rectangle #jump to top

```

3. Ring shear tester simulations

```

# Shear Cell
#Sample 1 - 2.5kPa
### Initialization
units          si
atom_style      sphere
atom_modify     map array sort 0 0
boundary        f f f
newton          off
communicate      single vel yes
processors      2 2 2
# Declare domain
region          reg block -0.128 0.128 -0.128 0.128 -0.005 0.06 units box
create_box      2 reg
### Setup
neighbor        0.002 bin
neigh_modify    delay 0
variable sf equal 0.2298
variable rf equal 0.1
variable CED equal 10010
# Material and interaction properties
fix m1 all property/global youngsModulus peratomtype 5.0e6 5.0e6
fix m2 all property/global poissonsRatio peratomtype 0.3 0.3
fix m3 all property/global coefficientRestitution peratomtypepair 2 0.1 0.1
0.1 0.1
fix m4 all property/global coefficientFriction peratomtypepair 2 ${sf} 0.9
0.9 0.5
fix m5 all property/global coefficientRollingFriction peratomtypepair 2 ${rf}
0.5 0.5 0.2 #0.01 0.01 0.01 0.1
fix m6 all property/global cohesionEnergyDensity peratomtypepair 2 ${CED}
${CED} ${CED} 0
print "SF=${sf}"

```



```
print "RF=${rf}"
print "CED=${CED}"
# Physics
pair_style gran model hertz tangential history cohesion sjkr
rolling_friction epsd2
pair_coeff * *
# Particle setup insertions to be handled below
fix pts1 all particletemplate/multisphere 15485863 atom_type 1 density
constant 350 nspheres 3 ntry 1000000 spheres file 1_untreated.multisphere & scale
0.000004 type 1
fix pdd1 all particledistribution/discrete 32452843 1 pts1 1.
# Geometry
fix cad2 all mesh/surface/stress file bottom.stl type 2 scale 0.001
stress on
fix ins_mesh all mesh/surface/planar file factory.stl type 1 scale 0.001
fix geometry all wall/gran model hertz tangential history cohesion sjkr
rolling_friction epsd2 mesh n_meshes 1 meshes cad2
### Detailed settings
# Integration
fix integrator all nve/sphere
# Gravity
fix grav all gravity 9.81 vector 0.0 0.0 -1.0
# Timestep
timestep 0.000007
# Thermodynamic output
thermo_style custom step atoms ke cpu
thermo 10000
thermo_modify lost ignore norm no
### Execution and further settings
fix ins all insert/stream seed 32452867 distributiontemplate pdd1
nparticles 10000 & vel constant 0. 0. -2. particlerate 33750 & overlapcheck yes
insertion_face ins_mesh extrude_length 0.015
fix integr all multisphere
run 100000
fix cad3 all mesh/surface/stress/servo file lid.stl type 2 scale 0.001
& stress on com 0 0 0.055 axis 0. 0. 1. ctrlPV force target_val -192.92 vel_max
5.0
unfix geometry
fix geometry all wall/gran model hertz tangential history cohesion sjkr
rolling_friction epsd2 mesh n_meshes 2 meshes cad2 cad3
# Update the thermodynamic output
thermo_style custom step atoms ke cpu f_cad3[1] f_cad3[2] f_cad3[3] f_cad3[4]
f_cad3[5] f_cad3[6] f_cad3[7] f_cad3[8] f_cad3[9]
thermo 5000
# Settle the plate on top of the particles
run 150000
# Set the dumps
dump dmp all custom 5000 post/dump*.ring id type type x y z ix iy iz
vx vy vz fx fy fz omegax omegay omegaz radius
dump vtk all custom/vtk 5000 post/dump*.ring.vtk id type type x y z ix iy
iz vx vy vz fx fy fz omegax omegay omegaz radius
dump dmpstl1 all mesh/stl 5000 post/cell*.stl cad2
dump dmpstl2 all mesh/stl 5000 post/lid*.stl cad3
# Describe shearing action
fix movecad all move/mesh mesh cad2 rotate origin 0. 0. -0.002 axis 0.
0. 1. period -20.0
# Shear
run 750000
fix_modify cad3 target_val -96.46 #2500 kPa
#fix_modify cad3 target_val -144.69 #(3750 kPa)
run 1000000
```

4. Rotating drum simulations

```

#Rotating drum input file
#w=0.5 rpm
#Calibrated particles - HIGH COHESION
#Sample 1- Tambour scaled up + verres (noPBC)
#Mat. 1=wood, 2=steel, 3=glass

atom_style      sphere
atom_modify     map array sort 0 0
boundary        f f f
newton off

communicate     single vel yes

units           si
processors      1 1 2
region reg block -0.025 0.01 -0.25 0.25 -0.25 0.25 units box
create_box      3 reg

neighbor        0.002 bin
neigh_modify    delay 0

#Material properties required for new pair styles

fix            m1 all property/global youngsModulus peratomtype 5.e6 5.e6 5.e6
fix            m2 all property/global poissonsRatio peratomtype 0.3 0.3 0.3
fix            m3 all property/global coefficientRestitution peratomtypepair 3 0.1
0.1 0.1 0.1 0.1 0.1 0.1 0.1 0.1
fix            m4 all property/global coefficientFriction peratomtypepair 3 0.1 0.4
0.5 0.4 0.5 0.5 0.5 0.5 0.5
fix            m5 all property/global coefficientRollingFriction peratomtypepair 3
0.7 0.5 0.5 0.5 0.5 0.5 0.5 0.5
fix            m6 all property/global cohesionEnergyDensity peratomtypepair 3 50049
25024 0 25024 0 0 0 0

#New pair style
pair_style      gran model hertz tangential history cohesion sjkr rolling_friction
epsd2
pair_coeff       * *

timestep        0.00001
fix             1 all nve/sphere
fix             2 all gravity 9.81 vector 0.0 0.0 -1.0

#the cylinder
fix            cad all mesh/surface file meshes/tambourPBC.stl heal
auto_remove_duplicates type 2 scale 4.0 move -0.02 0 0

#fix          cad all mesh/surface file meshes/tambourPBC.stl heal
auto_remove_duplicates type 2 move -0.0125 0 0
fix           verrel all mesh/surface file meshes/verre.stl type 3 scale 4.0 move
-0.024 0 0
fix           verre2 all mesh/surface file meshes/verre.stl type 3 scale 4.0 move
0 0 0
fix granwalls all wall/gran model hertz tangential history cohesion sjkr
rolling_friction epsd2 mesh n_meshes 3 meshes cad verrel verre2

#distributions for insertion
fix           pts1 all particletemplate/multisphere 15485863 atom_type 1 density
constant 350 nspheres 3 ntry 1000000 spheres file data/1_untreated.multisphere &
scale 0.000004 type 1
fix           pdd1 all particledistribution/discrete 32452843 1 pts1 1

```

```

#region and insertion
group          nve_group region reg

region bc cylinder x 0.0 0.0 0.2 -0.02 0 units box

#particle insertion
fix            ins all insert/pack seed 32452867 distributiontemplate pddl &
              maxattempt 100000 vel constant 0 0 -1 insert_every once overlapcheck
              yes all_in yes orientation random verbose yes volumefraction_region 0.21
              region bc

fix            integr all multisphere

#output settings, include total thermal energy
compute        1 all erotate/sphere
fix            ts all check/timestep/gran 1000 0.1 0.1
thermo_style   custom step atoms ke c_1 f_ts[1] f_ts[2] vol
thermo         1000
thermo_modify  lost ignore norm no

#insert the first particles so that dump is not empty
run            1
dump           vtk all custom/vtk 10000 post/dump*.1_SCALE_VERRES_HIGHCoh.vtk id
type type x y z ix iy iz vx vy vz fx fy fz omegax omegay omegaz radius
#dump          dump all custom 10000 post/dump*.1_SCALE_VERRES id type type x y z
ix iy iz vx vy vz fx fy fz omegax omegay omegaz radius
dump           dumpstl all mesh/stl 10000 post/dump*.1_SCALE_VERRES_HIGH_Coh.stl
restart        10000 restart/1_SCALE_VERRES_HIGH_Coh.restart

#run to let particle settle
run            10000

#rotation of the drum and the glass wall
fix            movecad1 all move/mesh mesh cad rotate origin 0. 0. 0. axis 1. 0. 0.
period 120
fix            movecad2 all move/mesh mesh verre1 rotate origin 0. 0. 0. axis 1. 0.
0. period 120
fix            movecad3 all move/mesh mesh verre2 rotate origin 0. 0. 0. axis 1. 0.
0. period 120

#rotation
run            24000000

```

References

- [1] Secrétariat REN21, Renewables 2018 Global Status Report, 2018. www.ren21.net (accessed February 8, 2019).
- [2] European Commission, A policy framework for climate and energy in the period from 2020 to 2030, Brussels, 2014. <https://eur-lex.europa.eu/legal-content/EN/TXT/PDF/?uri=CELEX:52014DC0015&from=EN> (accessed February 26, 2019).
- [3] A. Ramirez-Gómez, Research needs on biomass characterization to prevent handling problems and hazards in industry, Part. Sci. Technol. 34 (2016) 432–441. doi:10.1080/02726351.2016.1138262.
- [4] J.B. Holm-Nielsen, E.A. Ehimen, Biomass Supply Chains for Bioenergy and Biorefining, Elsevier, 2016. doi:10.1016/C2014-0-01700-5.
- [5] European Commission, 2030 Energy Strategy, (n.d.). <https://ec.europa.eu/energy/en/topics/energy-strategy-and-energy-union/2030-energy-strategy> (accessed February 26, 2019).
- [6] Plan d'action national en faveur des énergies renouvelables - Période 2009-2020, 2009. http://www.ebb-eu.org/legis/ActionPlanDirective2009_28/national_renewable_energy_action_plan_france_fr.pdf (accessed February 26, 2019).
- [7] French government, Energy transition | Gouvernement.fr, (n.d.). <https://www.gouvernement.fr/en/energy-transition> (accessed February 27, 2019).
- [8] Alliance Nationale de Coordination de la Recherche pour l'Energie, Organisation des filières biomasse pour l'énergie Synthèse des livrables et conclusions, 2015. <https://www.irstea.fr/sites/default/files/ckfinder/userfiles/files/Synthese GP1A - 310315.pdf> (accessed February 26, 2019).
- [9] IEA Bioenergy, Future Biomass-based Transport Fuels Summary and Conclusions from the IEA Bioenergy ExCo67 Workshop, Helsinki, 2011. www.ieabioenergy.com. (accessed February 26, 2019).
- [10] T. Searchinger, R. Heimlich, R.A. Houghton, F. Dong, A. Elobeid, J. Fabiosa, S. Tokgoz, D. Hayes, T.H. Yu, Use of U.S. croplands for biofuels increases greenhouse gases through emissions from land-use change., Science. 319 (2008) 1238–40. doi:10.1126/science.1151861.
- [11] H. Prévot, V. Hespel, J.Y. Dupré, F. Baratin, D. Gagey, L'optimisation du dispositif de soutien à la filière biocarburants, Direction de l'information légale et administrative, 2005. <https://www.ladocumentationfrancaise.fr/rapports-publics/054000742/index.shtml> (accessed February 8, 2019).
- [12] Agence de l'Environnement et de la Maîtrise de l'Énergie, Analyses de Cycle de Vie appliquées aux biocarburants de première génération – ADEME, 2010. <https://www.ademe.fr/analyses-cycle-vie-appliquees-biocarburants-premiere-generation-consommee-france> (accessed February 8, 2019).
- [13] OCDE, Politiques de soutien des biocarburants : une évaluation économique, OECD, 2009. doi:10.1787/9789264050167-fr.
- [14] R.C. (Robert C. Brown, Thermochemical processing of biomass conversion into fuels, chemicals and power, Wiley, 2011.
- [15] M. Carus, E. Breitmayer, N. De Beus, Sustainable First and Second Generation Bioethanol for Europe, (2017).
- [16] D.P. Ho, H. Hao Ngo, W. Guo, A mini review on renewable sources for biofuel, (2014). doi:10.1016/j.biortech.2014.07.022.
- [17] European Technology and Innovation Platform - Bioenergy, Borregaard-commercial plant in Sarpsborg, Norway, 2016. <http://www.borregaard.com> (accessed February 9, 2019).
- [18] T. Damartzis, A. Zabaniotou, Thermochemical conversion of biomass to second generation biofuels through integrated process design-A review, (n.d.). doi:10.1016/j.rser.2010.08.003.

- [19] Enkern, Rotterdam is proposed location for waste-to-chemicals plant using Enkern's technology - Enkern, (n.d.). <https://enkern.com/nouvelles/rotterdam-is-proposed-location-for-waste-to-chemicals-plant-using-enkerns-technology/> (accessed February 9, 2019).
- [20] Enkern, Newsroom - Enkern, (n.d.). https://enkern.com/newsroom/?communiqué_id=122564 (accessed February 9, 2019).
- [21] IFPEN, [Bioéthanol avancé] - En route vers la commercialisation de la technologie FUTUROL, (n.d.). <http://www.ifpennergiesnouvelles.fr/Actualites/Communiqués-de-presse/Bioethanol-avance-En-route-vers-la-commercialisation-de-la-technologie-FUTUROL> (accessed February 10, 2019).
- [22] Procetol-2G, Le projet Futurol, (n.d.). https://www.projetfuturol.com/Le-Projet_a21.html (accessed February 10, 2019).
- [23] IFPEN, Inauguration of the BioTfuel project demonstrator in Dunkirk: 2nd generation biodiesel and biokerosene production up and running, (n.d.). <http://www.ifpennergiesnouvelles.com/News/Press-releases/Inauguration-of-the-BioTfuel-project-demonstrator-in-Dunkirk-2nd-generation-biodiesel-and-biokerosene-production-up-and-running> (accessed February 9, 2019).
- [24] J.C. Viguié, N. Ullrich, P. Porot, L. Bournay, M. Hecquet, J. Rousseau, BioTfuel Project: Targeting the Development of Second-Generation Biodiesel and Biojet Fuels, *Oil Gas Sci. Technol.* 68 (2013) 935–946. doi:10.2516/ogst/2013162.
- [25] K. Radtke, BioTfuel Biomass+X to Liquid Synfuels Plant and Alternative Syngas Applications at thyssenkrupp, (n.d.). <https://www.globalsyngas.org/uploads/downloads/2016-4-2-ThyssenKrupp-KarstenRadtke.pdf>.
- [26] P. Syndiese, Projet SYNDIESE : inauguration de la plateforme technologique de prétraitement de la biomasse, 33 (2014).
- [27] International Organization for Standardization, ISO 16559:2014 - Solid biofuels -- Terminology, definitions and descriptions, n.d. <https://www.iso.org/standard/57111.html> (accessed February 8, 2019).
- [28] European Parliament, Directive (EU) 2008/2001 of the European Parliament and of the Council, (2018).
- [29] P. McKendry, Energy production from biomass (part 1): Overview of biomass, *Bioresour. Technol.* 83 (2002) 37–46. doi:10.1016/S0960-8524(01)00118-3.
- [30] J.B. Holm-Nielsen, E.A. Ehimen, Biomass supply chains for bioenergy and biorefining, 2016. doi:<https://doi.org/10.1016/C2014-0-01700-5>.
- [31] European Commission, Commission Decision 2007/589/EC of 18 July 2007 establishing guidelines for the monitoring and reporting of greenhouse gas emissions pursuant to Directive 2003/87/EC of the European Parliament and the Council, 229 (2007) 1–85. doi:10.1111/j.1477-8947.2004.00084.x.
- [32] R.S. Dhillon, G. von Wuehlisch, Mitigation of global warming through renewable biomass, *Biomass and Bioenergy.* 48 (2013) 75–89. doi:10.1016/j.biombioe.2012.11.005.
- [33] J.S. Tumuluru, S. Sokhansanj, J.R. Hess, C.T. Wright, R.D. Boardman, A review on biomass torrefaction process and product properties for energy applications, *Ind. Biotechnol.* 7 (2011) 384–401. doi:10.1089/ind.2011.0014.
- [34] M.J.C. van der Stelt, H. Gerhauser, J.H.A. Kiel, K.J. Ptasinski, Biomass upgrading by torrefaction for the production of biofuels: A review, *Biomass and Bioenergy.* 35 (2011) 3748–3762. doi:10.1016/j.biombioe.2011.06.023.
- [35] R. Hess, C. Wright, K. Kenney, Cellulosic biomass feedstocks and logistics for ethanol production, *Biofuels, Bioprod. Biorefining.* (2007) 181–190. doi:10.1002/bbb.
- [36] K. Sunde, A. Brekke, B. Solberg, Environmental impacts and costs of woody Biomass-to-Liquid (BTL) production and use - A review, *For. Policy Econ.* 13 (2011) 591–602. doi:10.1016/j.forpol.2011.05.008.
- [37] R.B. Miller, Structure of Wood, *Wood Handb. Wood as an Eng. Mater.* (1999) 30. doi:10.1159/000144207.
- [38] B. Franke, P. Quenneville, Numerical Modeling of the Failure Behavior of Dowel Connections in Wood, *J. Eng. Mech.* 137 (2011) 186–195. doi:10.1061/(ASCE)EM.1943-7889.0000217.

- [39] D. Grosser, *Die Hölzer Mitteleuropas*, München, 2007. www.forstbuch.de, (accessed February 10, 2019).
- [40] Mendel University, Microscopic structure of wood, (n.d.). https://is.mendelu.cz/eknihovna/opory/zobraz_cast.pl?cast=19204 (accessed February 10, 2019).
- [41] A. Rafsanjani, M. Stiefel, K. Jefimovs, R. Mokso, D. Derome, J. Carmeliet, Hygroscopic swelling and shrinkage of latewood cell wall micropillars reveal ultrastructural anisotropy, *J. R. Soc. Interface*. 11 (2014). doi:10.1098/rsif.2014.0126.
- [42] R. Dumon, M. Gelus, *La valorisation chimique du bois*, Masson, 1982.
- [43] S. Eyley, W. Thielemans, Surface modification of cellulose nanocrystals, *Nanoscale*. 6 (2014) 7764–7779. doi:10.1039/C4NR01756K.
- [44] U.S. Department of Energy Office of Biological and Environmental Research, Gateway to U.S. DOE Biological and Environmental Research Image Galleries, (n.d.). <https://public.ornl.gov/site/gallery/default.cfm?restsection=> (accessed February 10, 2019).
- [45] H. V. Lee, S.B.A. Hamid, S.K. Zain, Conversion of Lignocellulosic Biomass to Nanocellulose: Structure and Chemical Process, *Sci. World J.* 2014 (2014) 1–20. doi:10.1155/2014/631013.
- [46] P. Stenius, Suomen Paperi-insinöörien Yhdistys., Technical Association of the Pulp and Paper Industry., Forest products chemistry, Published in cooperation with the Finnish Paper Engineers' Association and TAPPI, 2000.
- [47] The Wood Database, Poplar, (n.d.). <https://www.wood-database.com/poplar/> (accessed February 10, 2019).
- [48] J.A. Stanturf, C. van Oosten, D.A. Netzer, M.D. Coleman, C.J. Portwood, Ecology and silviculture of poplar plantations, D.I.; Isebrands, J.G.; Eckenwalder, J.E.; Richardson, J., Eds. *Poplar Cult. North Am. Part A*, Chapter 5. Ottawa NRC Res. Press. Natl. Res. Coun. Canada 153–206. (2002). <https://www.srs.fs.usda.gov/pubs/3190> (accessed February 10, 2019).
- [49] P. Townsend, S. Kar, R. Miller, Poplar (*Populus* spp.) Trees for Biofuel Production - eXtension, (n.d.). <https://articles.extension.org/pages/70456/poplar-populus-spp-trees-for-biofuel-production> (accessed February 10, 2019).
- [50] JGI Genome portal, Home - *Populus trichocarpa* v1.1, (n.d.). https://genome.jgi.doe.gov/Poptr1_1/Poptr1_1.home.html (accessed February 10, 2019).
- [51] P. Sannigrahi, A.J. Ragauskas, G.A. Tuskan, Poplar as a feedstock for biofuels: A review of compositional characteristics, *Biofuels, Bioprod. Biorefining*. 4 (2010) 209–226. doi:10.1002/bbb.206.
- [52] IGN Institut National de l'Information géographique et forestière, Inventaire forestier 2016, 2016. www.ign.fr (accessed February 11, 2019).
- [53] CNP - Conseil National du Peuplier, Aujourd'hui, des peupliers, pourquoi ? - Peupliers de France, (n.d.). <https://www.peupliersdefrance.org/n/aujourd-hui-des-peupliers-pourquoi/n:1172> (accessed February 11, 2019).
- [54] ADEME, Biomasse forestière, populicole et bocagère disponible pour l'énergie, n.d. www.ademe.fr (accessed February 11, 2019).
- [55] MEDDTL, Circulaire du 18 novembre 2011 relative à l'interdiction du brûlage à l'air libre des déchets verts, 2011. <http://centre.ademe.fr/sites/default/files/files/DI/Déchets/circulaire-brulage-dechets-verts.pdf> (accessed April 15, 2019).
- [56] T. Khazraie Shoulafar, N. DeMartini, A. Ivaska, P. Fardim, M. Hupa, Measuring the concentration of carboxylic acid groups in torrefied spruce wood, *Bioresour. Technol.* 123 (2012) 338–343. doi:10.1016/j.biortech.2012.07.069.
- [57] A. Govin, V. Repellin, R. Guyonnet, M. Rolland, J.L. Duplan, Effect of torrefaction on grinding energy requirement for thin wood particle production, *Récents Progrès En Génie Des Procédés*. 98 (2009) 1–6.
- [58] V. Repellin, A. Govin, M. Rolland, R. Guyonnet, Modelling anhydrous weight loss of wood chips during torrefaction in a pilot kiln, *Biomass and Bioenergy*. 34 (2010) 602–609. doi:10.1016/j.biombioe.2010.01.002.
- [59] J.M. Craven, J. Swithenbank, V.N. Sharifi, Investigation into the Flow Properties of Coarse Solid Fuels for Use in Industrial Feed Systems, *J. Powder Technol.* 2015 (2015) 1–12.

- doi:10.1155/2015/786063.
- [60] A. Skonhoft, Forestry and the climate problem : Joint timber and bioenergy production, (2014).
- [61] R.C. Saxena, D.K. Adhikari, H.B. Goyal, Biomass-based energy fuel through biochemical routes: A review, *Renew. Sustain. Energy Rev.* 13 (2009) 167–178. doi:10.1016/j.rser.2007.07.011.
- [62] P. McKendry, Energy production from biomass (part 2): Conversion technologies, *Bioresour. Technol.* 83 (2002) 47–54. doi:10.1016/S0960-8524(01)00119-5.
- [63] K. Wang, J. Chen, S.N. Sun, R.C. Sun, Steam Explosion, Pretreat. Biomass. (2015) 75–104. doi:10.1016/B978-0-12-800080-9.00006-2.
- [64] P. Ibarra-Gonzalez, B.G. Rong, A review of the current state of biofuels production from lignocellulosic biomass using thermochemical conversion routes, *Chinese J. Chem. Eng.* (2018). doi:10.1016/j.cjche.2018.09.018.
- [65] K. Rajendran, Effect of Moisture Content on Lignocellulosic Power Generation: Energy, Economic and Environmental Impacts, *Processes*. 5 (2017) 78. doi:10.3390/pr5040078.
- [66] M.J.A. Tijmensen, A.P.C. Faaij, C.N. Hamelinck, M.R.M. van Hardeveld, Exploration of the possibilities for production of Fischer Tropsch liquids and power via biomass gasification, *Biomass and Bioenergy*. 23 (2002) 129–152. doi:10.1016/S0961-9534(02)00037-5.
- [67] A. Kumar, D. Jones, M. Hanna, A. Kumar, D.D. Jones, M.A. Hanna, Thermochemical Biomass Gasification: A Review of the Current Status of the Technology, *Energies*. 2 (2009) 556–581. doi:10.3390/en20300556.
- [68] P. McKendry, Energy production from biomass (part 3): Gasification technologies, *Bioresour. Technol.* 83 (2002) 55–63. doi:10.1016/S0960-8524(01)00120-1.
- [69] S. Xiu, A. Shahbazi, Bio-oil production and upgrading research: A review, (2012). doi:10.1016/j.rser.2012.04.028.
- [70] A. Demirbaş, G. Arin, An Overview of Biomass Pyrolysis, *Energy Sources*. 24 (2002) 471–482. doi:10.1080/00908310252889979.
- [71] A. Demirbaş, Biomass resource facilities and biomass conversion processing for fuels and chemicals, *Energy Convers. Manag.* 42 (2001) 1357–1378. doi:10.1016/S0196-8904(00)00137-0.
- [72] E. Chornet, R.P. Overend, Biomass Liquefaction: An Overview, in: *Fundam. Thermochem. Biomass Convers.*, Springer Netherlands, Dordrecht, 1985: pp. 967–1002. doi:10.1007/978-94-009-4932-4_54.
- [73] D. Wen, H. Jiang, K. Zhang, Supercritical fluids technology for clean biofuel production, *Prog. Nat. Sci.* 19 (2009) 273–284. doi:10.1016/J.PNSC.2008.09.001.
- [74] H. Durak, Bio-oil production from biomass via supercritical fluid extraction, in: *AIP Conf. Proc.*, AIP Publishing LLC, 2016: p. 020099. doi:10.1063/1.4945925.
- [75] M.K. Akalın, K. Tekin, S. Karagöz, Supercritical fluid extraction of biofuels from biomass, *Environ. Chem. Lett.* 15 (2017) 29–41. doi:10.1007/s10311-016-0593-z.
- [76] S. Brand, R.F. Susanti, S.K. Kim, H.S. Lee, J. Kim, B.I. Sang, Supercritical ethanol as an enhanced medium for lignocellulosic biomass liquefaction: Influence of physical process parameters, *Energy*. 59 (2013) 173–182. doi:10.1016/J.ENERGY.2013.06.049.
- [77] V.S. Sikarwar, M. Zhao, P.S. Fennell, N. Shah, E.J. Anthony, Progress in biofuel production from gasification, *Prog. Energy Combust. Sci.* 61 (2017) 189–248. doi:10.1016/j.pecs.2017.04.001.
- [78] C. Higman, M. van der Burgt, *Gasification*, Gulf Professional Pub./Elsevier Science, 2008.
- [79] R.F. Probst, R.E. Hicks, *Synthetic fuels*, Dover Publications, 2006.
- [80] V. Singh Sikarwar, M. Zhao, P. Clough, J. Yao, X. Zhong, M.Z. Memon, N. Shah, E.J. Anthony, P.S. Fennell, An overview of advances in biomass gasification, *Energy Environ. Sci.* 9 (2016) 2939. doi:10.1039/c6ee00935b.
- [81] N. Abdoulmoumine, S. Adhikari, A. Kulkarni, S. Chattanathan, A review on biomass gasification syngas cleanup, (2015). doi:10.1016/j.apenergy.2015.05.095.
- [82] M.J. Prins, K.J. Ptasiński, F.J.J.G. Janssen, More efficient biomass gasification via torrefaction, *Energy*. 31 (2006) 3458–3470. doi:10.1016/j.energy.2006.03.008.
- [83] C. Couhert, S. Salvador, J.M. Commandré, Impact of torrefaction on syngas production from wood, *Fuel*. 88 (2009) 2286–2290. doi:10.1016/j.fuel.2009.05.003.
- [84] A. Barakat, H. de Vries, X. Rouau, Dry fractionation process as an important step in current and future lignocellulose biorefineries: A review, *Bioresour. Technol.* 134 (2013) 362–373.

- doi:10.1016/j.biortech.2013.01.169.
- [85] J. Tallaksen, Biomass Gasification Project Biomass Gasification: A Comprehensive Demonstration of a Community-Scale Biomass Energy System Chapter 8: A Case Study in Biomass Preprocessing Biomass Gasification: A Comprehensive Demonstration of a Community Scale Biomass Energy System USDA Final Report Chapter 8: A Case Study in Biomass Preprocessing, n.d. http://renewables.morris.umn.edu/biomass/documents/USDA_Report/SII_Preprocessing.pdf (accessed February 12, 2019).
 - [86] Power Engineering, The Daily Grind - Power Engineering, (n.d.). <https://www.power-eng.com/articles/print/volume-115/issue-3/features/the-daily-grind.html> (accessed February 12, 2019).
 - [87] S. Paulrud, J.E. Mattsson, C. Nilsson, Particle and handling characteristics of wood fuel powder: Effects of different mills, *Fuel Process. Technol.* 76 (2002) 23–39. doi:10.1016/S0378-3820(02)00008-5.
 - [88] N. Kobayashi, P. Guilin, J. Kobayashi, S. Hatano, Y. Itaya, S. Mori, A new pulverized biomass utilization technology, (2007). doi:10.1016/j.powtec.2007.02.041.
 - [89] K. Svoboda, M. Pohořelý, M. Hartman, J. Martinec, Pretreatment and feeding of biomass for pressurized entrained flow gasification, *Fuel Process. Technol.* 90 (2009) 629–635. doi:10.1016/j.fuproc.2008.12.005.
 - [90] P. Bergman, A. Boersma, J. Kiel, M.J. Prins, K. Ptasiński, F.J. Janssen, Torrefaction for entrained-flow gasification of biomass, 2nd World Conf. Technol. Exhib. Biomass Energy, Ind. Clim. Prot. a (2005) 78–82. <http://www.ecn.nl/publications/PdfFetch.aspx?nr=ECN-RX--04-029#page=78>.
 - [91] G. Almeida, J.O. Brito, P. Perré, Alterations in energy properties of eucalyptus wood and bark subjected to torrefaction: The potential of mass loss as a synthetic indicator, *Bioresour. Technol.* 101 (2010) 9778–9784. doi:10.1016/j.biortech.2010.07.026.
 - [92] E.S. Lipinsky, J.R. Arcate, T.B. Reed, Enhanced Wood Fuels Via Torrefaction, 2002. https://web.anl.gov/PCS/acsfuel/preprint_archive/Files/47_1_Orlando_03-02_0071.pdf (accessed February 11, 2019).
 - [93] G. Almeida, D.V.B. Santos, P. Perré, Mild pyrolysis of fast-growing wood species (Caribbean pine and Rose gum): Dimensional changes predicted by the global mass loss, *Biomass and Bioenergy*. 70 (2014) 407–415. doi:10.1016/j.biombioe.2014.07.028.
 - [94] E.B. M. Pach, R. Zanzi, Torrefied Biomass a Substitute for Wood and Charcoal. In: 6th Asia-Pacific international symposium on combustion and energy utilization, 6th Asia-Pacific Int. Symp. Combust. Energy Util. (2002).
 - [95] G. Sridhar, D.N. Subbukrishna, H. V Sridhar, S. Dasappa, P.J. Paul, H.S. Mukunda, Torrefaction of bamboo, n.d. <http://repository.ias.ac.in/76088/1/11-p.pdf> (accessed February 12, 2019).
 - [96] F.F. Felfli, C.A. Luengo, J.A. Suárez, P.A. Beatón, Wood briquette torrefaction, *Energy Sustain. Dev.* 9 (2005) 19–22. doi:10.1016/S0973-0826(08)60519-0.
 - [97] J. Deng, G. jun Wang, J. hong Kuang, Y. liang Zhang, Y. hao Luo, Pretreatment of agricultural residues for co-gasification via torrefaction, *J. Anal. Appl. Pyrolysis*. 86 (2009) 331–337. doi:10.1016/j.jaap.2009.08.006.
 - [98] K.M. Sabil, M.A. Aziz, B. Lal, Y. Uemura, Synthetic indicator on the severity of torrefaction of oil palm biomass residues through mass loss measurement, (2013). doi:10.1016/j.apenergy.2013.05.067.
 - [99] Y. Uemura, W.N. Omar, T. Tsutsui, S.B. Yusup, Torrefaction of oil palm wastes, *Fuel*. 90 (2011) 2585–2591. doi:10.1016/J.FUEL.2011.03.021.
 - [100] F. Pierre, G. Almeida, F. Huber, P. Jacquin, P. Perré, An original impact device for biomass characterisation: Results obtained for spruce and poplar at different moisture contents, *Wood Sci. Technol.* 47 (2013) 537–555. doi:10.1007/s00226-012-0512-9.
 - [101] V. Repellin, A. Govin, M. Rolland, R. Guyonnet, Energy requirement for fine grinding of torrefied wood, *Biomass and Bioenergy*. 34 (2010) 923–930. doi:10.1016/j.biombioe.2010.01.039.
 - [102] J. Pachón-Morales, J. Colin, F. Pierre, F. Puel, P. Perré, Effect of torrefaction intensity on the

- flow properties of lignocellulosic biomass powders, *Biomass and Bioenergy*. 120 (2019) 301–312. doi:10.1016/j.biombioe.2018.11.017.
- [103] Y.P. Rago, D. Surroop, R. Mohee, Torrefaction of textile waste for production of energy-dense biochar using mass loss as a synthetic indicator, *J. Environ. Chem. Eng.* 6 (2018) 811–822. doi:10.1016/j.jece.2017.12.055.
- [104] F. Avat, Contribution à l'étude des traitements thermiques du bois jusqu'à 300 °C : Transformations chimiques et caractérisations physico-chimiques, Ecole Nationale Supérieure des Mines de Paris; Ecole Nationale Supérieure des Mines de Saint-Etienne, 1993.
- [105] P.C.A. Bergman, J.H.A. Kiel, Torrefaction for biomass upgrading, 2005. www.ecn.nl/biomass (accessed February 11, 2019).
- [106] M. Phanphanich, S. Mani, Impact of torrefaction on the grindability and fuel characteristics of forest biomass, *Bioresour. Technol.* 102 (2011) 1246–1253. doi:10.1016/j.biortech.2010.08.028.
- [107] F. Pierre, G. Almeida, J. Colin, P. Perré, Reduction of biomass resilience by torrefaction: apparent stiffness during failure (ASF) and specific failure energy (SFE) assessed by a custom impact device, *Holzforschung*. 71 (2017) 863–872. doi:10.1515/hf-2016-0191.
- [108] T.G. Bridgeman, J.M. Jones, A. Williams, D.J. Waldron, An investigation of the grindability of two torrefied energy crops, *Fuel*. 89 (2010) 3911–3918. doi:10.1016/j.fuel.2010.06.043.
- [109] B. Colin, J.L. Dirion, P. Arlabosse, S. Salvador, Quantification of the torrefaction effects on the grindability and the hygroscopicity of wood chips, *Fuel*. 197 (2017) 232–239. doi:10.1016/j.fuel.2017.02.028.
- [110] B. Arias, C. Pevida, J. Feroso, M.G. Plaza, F. Rubiera, J.J. Pis, Influence of torrefaction on the grindability and reactivity of woody biomass, *Fuel Process. Technol.* 89 (2008) 169–175. doi:10.1016/j.fuproc.2007.09.002.
- [111] P. Bergman, A. Boersma, R. Zwart, J. Kiel, Torrefaction for biomass co-firing in existing coal-fired power stations, *Energy Res. Cent. Netherlands ECN ECNC05013*. (2005) 71. doi:ECN-C-05-013.
- [112] T.O. Rodrigues, P. Rousset, Effects of torrefaction on energy properties of *Eucalyptus grandis* wood, *Rev. Cern.* 15 (2009). http://publications.cirad.fr/une_notice.php?dk=552787 (accessed February 11, 2019).
- [113] G. Xu, M. Li, P. Lu, Experimental investigation on flow properties of different biomass and torrefied biomass powders, *Biomass and Bioenergy*. 122 (2019) 63–75. doi:10.1016/j.biombioe.2019.01.016.
- [114] P. Bergman, J. Kiel, H. Veringa, Combined torrefaction and pelletisation - The TOP process, 2005. www.senternovem.nl (accessed February 11, 2019).
- [115] S. Sadaka, S. Negi, Improvements of biomass physical and thermochemical characteristics via torrefaction process, *Environ. Prog. Sustain. Energy*. 28 (2009) 427–434. doi:10.1002/ep.10392.
- [116] T.G. Bridgeman, J.M. Jones, I. Shield, P.T. Williams, Torrefaction of reed canary grass, wheat straw and willow to enhance solid fuel qualities and combustion properties, *Fuel*. 87 (2008) 844–856. doi:10.1016/J.FUEL.2007.05.041.
- [117] J. Bourgois, M.C. Bartholin, R. Guyonnet, Thermal treatment of wood: analysis of the obtained product, *Wood Sci. Technol.* 23 (1989) 303–310. doi:10.1007/BF00353246.
- [118] I. Pastorova, P.W. Arisz, J.J. Boon, Preservation of d-glucose-oligosaccharides in cellulose chars, *Carbohydr. Res.* 248 (1993) 151–165. doi:10.1016/0008-6215(93)84123-N.
- [119] S. Mani, L.G. Tabil, S. Sokhansanj, Grinding performance and physical properties of wheat and barley straws, corn stover and switchgrass, *Biomass and Bioenergy*. 27 (2004) 339–352. doi:10.1016/j.biombioe.2004.03.007.
- [120] M. Himmel, M. Tucker, J. Baker, C. Rivard, K. Oh, K. Grohmann, Comminution of biomass: hammer and knife mills., *Proc. 7th Symp. Biotechnol. Fuels Chem. Gatlinburg, Tennessee*, 14–17 May, 1985. (1986) 39–58. <https://www.cabdirect.org/cabdirect/abstract/19862429390> (accessed July 11, 2018).
- [121] ISO, ISO 5074:2015 - Hard coal -- Determination of Hardgrove grindability index, (n.d.). <https://www.iso.org/standard/63236.html> (accessed February 12, 2019).
- [122] R.H.H. Ibrahim, L.I. Darvell, J.M. Jones, A. Williams, Physicochemical characterisation of torrefied biomass, *J. Anal. Appl. Pyrolysis*. 103 (2013) 21–30. doi:10.1016/j.jaap.2012.10.004.

-
- [123] O. Williams, C. Eastwick, S. Kingman, D. Giddings, S. Lormor, E. Lester, Investigation into the applicability of Bond Work Index (BWI) and Hardgrove Grindability Index (HGI) tests for several biomasses compared to Colombian La Loma coal, *Fuel*. 158 (2015) 379–387. doi:10.1016/j.fuel.2015.05.027.
 - [124] M. Manouchehrinejad, I. van Giesen, S. Mani, Grindability of torrefied wood chips and wood pellets, *Fuel Process. Technol.* 182 (2018) 45–55. doi:10.1016/j.fuproc.2018.10.015.
 - [125] M. Temmerman, Énergie nécessaire au broyage de la biomasse et des produits densifiés Michaël, 15 (2011) 349–360.
 - [126] M. Asadullah, Barriers of commercial power generation using biomass gasification gas: A review, *Renew. Sustain. Energy Rev.* 29 (2014) 201–215. doi:10.1016/j.rser.2013.08.074.
 - [127] B. Sharma, R.G. Ingalls, C.L. Jones, A. Khanchi, Biomass supply chain design and analysis: Basis, overview, modeling, challenges, and future, *Renew. Sustain. Energy Rev.* 24 (2013) 608–627. doi:10.1016/j.rser.2013.03.049.
 - [128] C.N. Hamelinck, A.P.C. Faaij, Outlook for advanced biofuels, *Energy Policy*. 34 (2006) 3268–3283. doi:10.1016/j.enpol.2005.06.012.
 - [129] J. Dai, H. Cui, J.R. Grace, Biomass feeding for thermochemical reactors, *Prog. Energy Combust. Sci.* 38 (2012) 716–736. doi:10.1016/j.pecs.2012.04.002.
 - [130] Jenike & Johanson, Solve Poor Flow Problems | Jenike & Johanson Bulk Material Engineering, (n.d.). <http://jenike.com/your-need/poor-flow/> (accessed February 13, 2019).
 - [131] A. Van der Drift, H. Boerrigter, B. Coda, Entrained flow gasification of biomass., *ECN - Energy Cent. Netherlands*. (2004) 58. doi:10.1016/j.fuel.2011.10.063.
 - [132] H. Cui, J.R. Grace, Fluidization of biomass particles: A review of experimental multiphase flow aspects, *Chem. Eng. Sci.* 62 (2007) 45–55. doi:10.1016/j.ces.2006.08.006.
 - [133] A. Joppich, H. Salman, Wood powder feeding, difficulties and solutions, *Biomass and Bioenergy*. 16 (1999) 191–198. [https://doi.org/10.1016/S0961-9534\(98\)00082-8](https://doi.org/10.1016/S0961-9534(98)00082-8).
 - [134] J. Dai, Biomass granular feeding for gasification and combustion, The University of British Columbia, 2007.
 - [135] G. Lumay, F. Boschini, K. Traina, S. Bontempi, J.C. Remy, R. Cloots, N. Vandewalle, Measuring the flowing properties of powders and grains, *Powder Technol.* 224 (2012) 19–27. doi:10.1016/j.powtec.2012.02.015.
 - [136] J.K. Prescott, R.A. Barnum, On Powder Flowability, (2000).
 - [137] J. Schwedes, Review on testers for measuring flow properties of bulk solids, *Granul. Matter.* 5 (2003) 1–43. doi:10.1007/s10035-002-0124-4.
 - [138] A.W. Jenike, Gravity flow of bulk solids, (1961). <https://collections.lib.utah.edu/details?id=709033> (accessed January 2, 2019).
 - [139] American Standard Testing Material International, Standard Shear Testing Test Method for Shear Testing of Bulk Solids Using the Jenike Shear Cell, (2001) 1–24. doi:10.1520/D6128-06.2.
 - [140] J.F. Labuz, A. Zang, Mohr–Coulomb Failure Criterion, *Rock Mech. Rock Eng.* 45 (2012) 975–979. doi:10.1007/s00603-012-0281-7.
 - [141] D. Schulze, *Powders and Bulk Solids*, Springer Berlin Heidelberg, Berlin, Heidelberg, 2007. doi:10.1007/978-3-540-73768-1.
 - [142] D. Schulze, Flow properties testing with Ring Shear Testers RST-XS, (2011).
 - [143] ASTM International, D6773-02: Standard Test Method for Bulk Solids Using Schulze Ring Shear Tester 1, *Annu. B. ASTM Stand.* (2002) 1–26. doi:10.1520/D6682-08.
 - [144] R.S.T. Rst-xs, D. Schulze, Rst-control 95 xs, (2014).
 - [145] C.J. (Chris J.. Brown, J. (Jørgen) Nielsen, *Silos : fundamentals of theory, behaviour, and design*, E & FN Spon, 1998. <https://www.crcpress.com/Silos-Fundamentals-of-Theory-Behaviour-and-Design/Brown-Nielsen/p/book/9780419215806> (accessed February 14, 2019).
 - [146] C.R. Woodcock, J.S. Mason, *Bulk Solids Handling: an Introduction to the Practice and Technology*, Springer Netherlands, 1988.
 - [147] N.C. Crawford, N. Nagle, D.A. Sievers, J.J. Stickel, The effects of physical and chemical preprocessing on the flowability of corn stover, *Biomass and Bioenergy*. 85 (2016) 126–134. doi:10.1016/j.biombioe.2015.12.015.
 - [148] USP United States Pharmacopeia, Powder flow, n.d.

- <http://www.usppf.com/pf/pub/index.html2/7> (accessed February 15, 2019).
- [149] W. Wang, J. Zhang, S. Yang, H. Zhang, H. Yang, G. Yue, Experimental study on the angle of repose of pulverized coal, *Particuology*. 8 (2010) 482–486. doi:10.1016/j.partic.2010.07.008.
- [150] S. Just, G. Toschkoff, A. Funke, D. Djuric, G. Scharrer, J. Khinast, K. Knop, P. Kleinebudde, Experimental Analysis of Tablet Properties for Discrete Element Modeling of an Active Coating Process, *AAPS PharmSciTech*. 14 (2013) 402–411. doi:10.1208/s12249-013-9925-5.
- [151] K. Danjo, K. Kinoshita, K. Kitagawa, K. Iida, H. Sunada, A. Otsuka, Effect of particle shape on the compaction and flow properties of powders., *Chem. Pharm. Bull. (Tokyo)*. 37 (1989) 3070–3073. doi:10.1248/cpb.37.3070.
- [152] I.M.F. Wouters, D. Geldart, Characterising semi-cohesive powders using angle of repose, *Part. Part. Syst. Charact.* 13 (1996) 254–259. doi:10.1002/ppsc.19960130408.
- [153] D. Geldart, E.C. Abdullah, A. Hassanpour, L.C. Nwoke, I. Wouters, Characterization of powder flowability using measurement of angle of repose, *China Particuology*. 4 (2006) 104–107. doi:10.1016/S1672-2515(07)60247-4.
- [154] H.M. Beakawi Al-Hashemi, O.S. Baghabra Al-Amoudi, A review on the angle of repose of granular materials, *Powder Technol.* 330 (2018) 397–417. doi:10.1016/j.powtec.2018.02.003.
- [155] M.W. Johnstone, Calibration of DEM models for granular materials using bulk physical tests, (2010). <http://hdl.handle.net/1842/4655>.
- [156] B.H. Kaye, J. Gratton-Liimatainen, N. Faddis, Studying the Avalanching Behaviour of a Powder in a Rotating Disc, *Part. Part. Syst. Charact.* 12 (1995) 232–236. doi:10.1002/ppsc.19950120505.
- [157] B.H. Kaye, Characterizing the flowability of a powder using the concepts of fractal geometry and chaos theory, *Part. Part. Syst. Charact.* 14 (1997) 53–66. doi:10.1002/ppsc.199700013.
- [158] F. Boschini, V. Delaval, K. Traina, N. Vandewalle, G. Lumay, Linking flowability and granulometry of lactose powders, *Int. J. Pharm.* 494 (2015) 312–320. doi:10.1016/j.ijpharm.2015.08.030.
- [159] G. Félix, Ecoulements de milieux granulaires en tambour tournant Étude de quelques transitions de régime., Institut National Polytechnique de Lorraine - INPL, 2002.
- [160] J. Mellmann, The transverse motion of solids in rotating cylinders-forms of motion and transition behavior, *Powder Technol.* 118 (2001) 251–270. doi:10.1016/S0032-5910(00)00402-2.
- [161] P. Dutta, P.M. Horn, Low-frequency fluctuations in solids: 1f noise, *Rev. Mod. Phys.* 53 (1981) 497–516. doi:10.1103/RevModPhys.53.497.
- [162] J. Rajchenbach, Flow in powders: From discrete avalanches to continuous regime, *Phys. Rev. Lett.* 65 (1990) 2221–2224. doi:10.1103/PhysRevLett.65.2221.
- [163] C.M. Dury, G.H. Ristow, J.L. Moss, M. Nakagawa, Boundary effects on the angle of repose in rotating cylinders, *Phys. Rev. E - Stat. Physics, Plasmas, Fluids, Relat. Interdiscip. Top.* 57 (1998) 4491–4497. doi:10.1103/PhysRevE.57.4491.
- [164] G.H. Ristow, Dynamics of granular material in a rotating drum, *Eur. Lett.* 34 (1996) 263–268.
- [165] R. Fischer, P. Gondret, B. Perrin, M. Rabaud, Dynamics of dry granular avalanches, *Phys. Rev. E - Stat. Nonlinear, Soft Matter Phys.* 78 (2008) 1–4. doi:10.1103/PhysRevE.78.021302.
- [166] M.W. Johnstone, J.Y. Ooi, Experiment and DEM modelling of rotating drum with spherical and non-spherical particle, (2004) 8.
- [167] X.Y. Liu, X. Xu, Y.Y. Zhang, Experimental Study on Time Features of Particle Motion in Rotating Drums, *Chem. Eng. Technol.* 34 (2011) 997–1002. doi:10.1002/ceat.201000483.
- [168] H. Yang, R. Li, P. Kong, Q.C. Sun, M.J. Biggs, V. Zivkovic, Avalanche dynamics of granular materials under the slumping regime in a rotating drum as revealed by speckle visibility spectroscopy, *Phys. Rev. E - Stat. Nonlinear, Soft Matter Phys.* 91 (2015) 1–8. doi:10.1103/PhysRevE.91.042206.
- [169] H. Yang, B.F. Zhang, R. Li, G. Zheng, V. Zivkovic, Particle dynamics in avalanche flow of irregular sand particles in the slumping regime of a rotating drum, *Powder Technol.* 311 (2017) 439–448. doi:10.1016/j.powtec.2017.01.064.
- [170] H. Maghsoodi, E. Luijten, Chaotic dynamics in a slowly rotating drum, *Rev. Cuba. Fis.* 33 (2016) 50–54.
- [171] G.L. Wagner, Granular flow in a Rotating Drum, (2013) 1–29.
- [172] S. Courrech, D. Pont, Avalanches granulaires en milieu fluide Thèse de Doctorat Avalanches

- granulaires en milieu fluide, (2004).
- [173] R.P. Hegde, J.L. Rheingold, S. Welch, C.T. Rhodes, Studies of powder flow using a recording powder flowmeter and measurement of the dynamic angle of repose, *J. Pharm. Sci.* 74 (1985) 11–15. doi:10.1002/jps.2600740104.
 - [174] S. Rastogi, G.E. Klingzing, Characterizing the Rheology of Powders by studying dynamic avalanching of the powder, *Part. Part. Syst. Charact.* 11 (1994) 453–456. doi:10.1002/ppsc.19940110608.
 - [175] F. Cantelaube, Y. Limon-Duparcmeur, D. Bideau, G.H. Ristow, Geometrical Analysis of Avalanches in a 2D Drum, *J. Phys. I* 5 (1995) 581–596. doi:10.1051/jp1:1995107.
 - [176] T. Poole, United States Patent (19) 11 Patent Number :, 1998.
 - [177] Y.L. Xiao, E. Specht, J. Mellmann, Experimental study of the lower and upper angles of repose of granular materials in rotating drums, *Powder Technol.* 154 (2005) 125–131. doi:10.1016/j.powtec.2005.04.040.
 - [178] D.L. Amon, T. Niculescu, B.C. Utter, Granular avalanches in a two-dimensional rotating drum with imposed vertical vibration, *Phys. Rev. E - Stat. Nonlinear, Soft Matter Phys.* 88 (2013) 1–8. doi:10.1103/PhysRevE.88.012203.
 - [179] Y.S. Lee, R. Poynter, F. Podczeczek, J.M. Newton, Development of a dual approach to assess powder flow from avalanching behavior., *AAPS PharmSciTech.* 1 (2000) E21. doi:10.1208/pt010321.
 - [180] A.W. Alexander, B. Chaudhuri, A. Faqih, F.J. Muzzio, C. Davies, M.S. Tomassone, Avalanching flow of cohesive powders, *Powder Technol.* 164 (2006) 13–21. doi:10.1016/j.powtec.2006.01.017.
 - [181] A. Castellanos, J.M. Valverde, A.T. Pérez, A. Ramos, P.K. Watson, Flow regimes in fine cohesive powders, *Phys. Rev. Lett.* 82 (1999) 1156–1159. doi:10.1103/PhysRevLett.82.1156.
 - [182] A. Castellanos, M. Sánchez, J. Valverde, The Onset of Fluidization of Fine Powders in Rotating Drums, *Mater. Phys. Mech.* 3 (2001) 57–62.
 - [183] M. Wojtkowski, O.I. Imole, M. Ramaioli, E. Chaóvez Montes, S. Luding, Behavior of cohesive powder in rotating drums, *AIP Conf. Proc.* 1542 (2013) 983–986. doi:10.1063/1.4812098.
 - [184] S.C. Thakur, J.Y. Ooi, M.B. Wojtkowski, O.I. Imole, V. Magnanimo, H. Ahmadian, E.C. Montes, M. Ramaioli, Characterisation of cohesive powders for bulk handling and dem modelling, 3rd Int. Conf. Part. Methods Fundam. Appl. Part. 2013. (2013) 310–321. doi:10.1063/1.4812098.
 - [185] R.G. Iacocca, R.M. German, The experimental evaluation of die compaction lubricants using deterministic chaos theory, *Powder Technol.* 102 (1999) 253–265. doi:10.1016/S0032-5910(98)00217-4.
 - [186] F. Lavoie, L. Cartilier, R. Thibert, New methods characterizing avalanche behavior to determine powder flow, *Pharm. Res.* 19 (2002) 887–893. doi:10.1023/A:1016125420577.
 - [187] J.L.P. Soh, C. V. Liew, P.W.S. Heng, New indices to characterize powder flow based on their avalanching behavior, *Pharm. Dev. Technol.* 11 (2006) 93–102. doi:10.1080/10837450500464123.
 - [188] A.M. Faqih, B. Chaudhuri, A.W. Alexander, C. Davies, F.J. Muzzio, M. Silvina Tomassone, An experimental/computational approach for examining unconfined cohesive powder flow, *Int. J. Pharm.* 324 (2006) 116–127. doi:10.1016/j.ijpharm.2006.05.067.
 - [189] C.E. Davies, A. Williams, S.J. Tallon, K. Fenton, N. Brown, A New Approach to Monitoring the Movement of Particulate Material in Rotating Drums, *Dev. Chem. Eng. Miner. Process.* 12 (2008) 263–275. doi:10.1002/apj.5500120404.
 - [190] H. Yang, G.L. Jiang, H.Y. Saw, C. Davies, M.J. Biggs, V. Zivkovic, Granular dynamics of cohesive powders in a rotating drum as revealed by speckle visibility spectroscopy and synchronous measurement of forces due to avalanching, *Chem. Eng. Sci.* 146 (2016) 1–9. doi:10.1016/j.ces.2016.02.023.
 - [191] S.T. Nase, W.L. Vargas, A.A. Abatan, J.J. McCarthy, Discrete characterization tools for cohesive granular material, *Powder Technol.* 116 (2001) 214–223. doi:10.1016/S0032-5910(00)00398-3.
 - [192] P. Tegzes, T. Vicsek, P. Schiffer, Development of correlations in the dynamics of wet granular avalanches, *Phys. Rev. E - Stat. Physics, Plasmas, Fluids, Relat. Interdiscip. Top.* 67 (2003) 17. doi:10.1103/PhysRevE.67.051303.

- [193] M.A.S. Quintanilla, J.M. Valverde, A. Castellanos, The transitional behaviour of avalanches in cohesive granular materials, *J. Stat. Mech. Theory Exp.* (2006). doi:10.1088/1742-5468/2006/07/P07015.
- [194] E. Emery, J. Oliver, T. Pugsley, J. Sharma, J. Zhou, Flowability of moist pharmaceutical powders, *Powder Technol.* 189 (2009) 409–415. doi:10.1016/j.powtec.2008.06.017.
- [195] V. Jaggi, M.C. Leaper, A. Ingham, Measuring the flow properties of small powder samples using an avalanche tester, *Dry. Technol.* 34 (2016) 723–728. doi:10.1080/07373937.2015.1072093.
- [196] J.Y.S. Tay, C.V. Liew, P.W.S. Heng, Powder Flow Testing: Judicious Choice of Test Methods, *AAPS PharmSciTech.* 18 (2017) 1843–1854. doi:10.1208/s12249-016-0655-3.
- [197] Mercury Scientific, Revolution powder analyzer, n.d. <http://www.meteo-tech.co.il/ImagesDownloadFiles/RPA.PDF> (accessed February 15, 2019).
- [198] K. Thalberg, D. Lindholm, A. Axelsson, Comparison of different flowability tests for powders for inhalation, (n.d.). doi:10.1016/j.powtec.2004.08.003.
- [199] P.G. De Gennes, Granular matter: a tentative view, *Rev. Mod. Phys.* 71 (1999). <https://journals.aps.org/rmp/pdf/10.1103/RevModPhys.71.S374> (accessed March 1, 2019).
- [200] O. Walton, R. Braun, Simulation of rotary-drum and repose tests for frictional spheres and rigid sphere clusters, in: *Flow Part. Fluids*, Ithaca, NY, 1993.
- [201] S.S. Mallick, L. Rohilla, V. Garg, G. Setia, Modeling flow properties of fine dry powders using particle morphological properties and its effects on geometry of fly ash evacuation hoppers, *Part. Sci. Technol.* 36 (2018) 464–472. doi:10.1080/02726351.2017.1367746.
- [202] F. Miccio, D. Barletta, M. Poletto, Flow properties and arching behavior of biomass particulate solids, *Powder Technol.* 235 (2013) 312–321. doi:10.1016/j.powtec.2012.10.047.
- [203] N. Chevanan, A.R. Womac, V.S.P. Bitra, C. Igathinathane, Y.T. Yang, P.I. Miu, S. Sokhansanj, Bulk density and compaction behavior of knife mill chopped switchgrass, wheat straw, and corn stover, *Bioresour. Technol.* 101 (2010) 207–214. doi:10.1016/j.biortech.2009.07.083.
- [204] P. Adapa, L. Tabil, G. Schoenau, Physical and frictional properties of non-treated and steam exploded barley, canola, oat and wheat straw grinds, *Powder Technol.* 201 (2010) 230–241. doi:10.1016/j.powtec.2010.03.038.
- [205] F. Miccio, A. Landi, D. Barletta, M. Poletto, Preliminary assessment of a simple method for evaluating the flow properties of solid recovered fuels, *Part. Sci. Technol.* 27 (2009) 139–151. doi:10.1080/02726350902775988.
- [206] M. Gil, D. Schott, I. Arauzo, E. Teruel, Handling behavior of two milled biomass: SRF poplar and corn stover, *Fuel Process. Technol.* 112 (2013) 76–85. doi:10.1016/j.fuproc.2013.02.024.
- [207] J.E. Mattsson, P.D. Kofman, Method and apparatus for measuring the tendency of solid biofuels to bridge over openings, *Biomass and Bioenergy.* 22 (2002) 179–185. doi:10.1016/S0961-9534(01)00067-8.
- [208] D. Barletta, R.J. Berry, S.H. Larsson, T.A. Lestander, M. Poletto, Á. Ramírez-Gómez, Assessment on bulk solids best practice techniques for flow characterization and storage/handling equipment design for biomass materials of different classes, *Fuel Process. Technol.* 138 (2015) 540–554. doi:10.1016/j.fuproc.2015.06.034.
- [209] P.D. Jensen, J.E. Mattsson, P.D. Kofman, A. Klausner, Tendency of wood fuels from whole trees, logging residues and roundwood to bridge over openings, *Biomass and Bioenergy.* 26 (2004) 107–113. doi:10.1016/S0961-9534(03)00101-6.
- [210] N.C. Crawford, A.E. Ray, N.A. Yancey, N. Nagle, Evaluating the pelletization of “pure” and blended lignocellulosic biomass feedstocks, *Fuel Process. Technol.* 140 (2015) 46–56. doi:10.1016/j.fuproc.2015.08.023.
- [211] Freeman Technology, Powder Flow Tester | Powder Rheology | FT4 Powder Rheometer, (n.d.). https://www.freemantech.co.uk/_powders/ft4-powder-rheometer-universal-powder-tester (accessed February 13, 2019).
- [212] M. Zulfikar, B. Moghtaderi, T.F. Wall, Flow properties of biomass and coal blends, *Fuel Process. Technol.* 87 (2006) 281–288. doi:10.1016/j.fuproc.2004.10.007.
- [213] M. Stasiak, M. Molenda, M. Bańda, E. Gondek, Mechanical properties of sawdust and woodchips, *Fuel.* 159 (2015) 900–908. doi:10.1016/j.fuel.2015.07.044.
- [214] S.H. Larsson, Kinematic wall friction properties of reed canary grass powder at high and low

- normal stresses, *Powder Technol.* 198 (2010) 108–113. doi:10.1016/j.powtec.2009.10.022.
- [215] D. Barletta, M. Poletto, An assessment on silo design procedures for granular woody biomass, *Chem. Eng. Trans.* 32 (2013) 2209–2214. doi:10.3303/CET1332369.
- [216] M.R. Wu, D.L. Schott, G. Lodewijks, Physical properties of solid biomass, *Biomass and Bioenergy*. 35 (2011) 2093–2105. doi:10.1016/j.biombioe.2011.02.020.
- [217] J. Falk, R.J. Berry, M. Broström, S.H. Larsson, Mass flow and variability in screw feeding of biomass powders — Relations to particle and bulk properties, *Powder Technol.* 276 (2015) 80–88. doi:10.1016/j.powtec.2015.02.023.
- [218] M. Stasiak, M. Molenda, M. Gancarz, J. Wiącek, P. Parafiniuk, A. Lisowski, Characterization of shear behaviour in consolidated granular biomass, *Powder Technol.* 327 (2018) 120–127. doi:10.1016/j.powtec.2017.12.037.
- [219] K.E. Ileleji, B. Zhou, The angle of repose of bulk corn stover particles, *Powder Technol.* 187 (2008) 110–118. doi:10.1016/j.powtec.2008.01.029.
- [220] Z. Guo, X. Chen, H. Liu, Q. Guo, X. Guo, H. Lu, Theoretical and experimental investigation on angle of repose of biomass-coal blends, *Fuel*. 116 (2014) 131–139. doi:10.1016/j.fuel.2013.07.098.
- [221] K. Tannous, P.S. Lam, S. Sokhansanj, J.R. Grace, Physical properties for flow characterization of ground biomass from douglas fir wood, *Part. Sci. Technol.* 31 (2013) 291–300. doi:10.1080/02726351.2012.732676.
- [222] F. Miccio, N. Silvestri, D. Barletta, M. Poletto, Characterization of woody biomass flowability, *Chem. Eng. Trans.* 24 (2011) 643–648. doi:10.3303/CET1124108.
- [223] D. Barletta, S.H. Larsson, R.J. Berry, M. Poletto, Can bulk solids best practice techniques for flow characterization and handling equipment design be used reliably for biomass materials?, (2012).
- [224] J.J. Hernández, G. Aranda-Almansa, A. Bula, Gasification of biomass wastes in an entrained flow gasifier: Effect of the particle size and the residence time, *Fuel Process. Technol.* 91 (2010) 681–692. doi:10.1016/j.fuproc.2010.01.018.
- [225] T.G. Bridgeman, L.I. Darvell, J.M. Jones, P.T. Williams, R. Fahmi, A. V. Bridgwater, T. Barraclough, I. Shield, N. Yates, S.C. Thain, I.S. Donnison, Influence of particle size on the analytical and chemical properties of two energy crops, *Fuel*. 86 (2007) 60–72. doi:10.1016/j.fuel.2006.06.022.
- [226] Q. Guo, X. Chen, H. Liu, Experimental research on shape and size distribution of biomass particle, *Fuel*. 94 (2012) 551–555. doi:10.1016/j.fuel.2011.11.041.
- [227] F. V Tinaut, A. Melgar, J.F. Pérez, A. Horrillo, Effect of biomass particle size and air superficial velocity on the gasification process in a downdraft fixed bed gasifier. An experimental and modelling study, *Fuel Process. Technol.* 89 (2008) 1076–1089. doi:10.1016/j.fuproc.2008.04.010.
- [228] N. Chevanan, A.R. Womac, V.S. Bitra, D.C. Yoder, Flowability parameters for chopped switchgrass, wheat straw and corn stover., 0300 (2008).
- [229] Y.J. Lee, W.B. Yoon, Flow behavior and hopper design for black soybean powders by particle size, *J. Food Eng.* 144 (2015) 10–19. doi:10.1016/j.jfoodeng.2014.07.005.
- [230] D.S. En, Dansk standard Fast biobrændsel – Bestemmelse af partikelstørrelsesfordeling – Del 2 : Sigtemetode med vibrerende sigter på 3 , 15 mm og derunder Solid biofuels – Determination of particle size distribution – Part 2 : Vibrating screen method using, (2015).
- [231] H. Hartmann, T. Böhm, P. Daugbjerg Jensen, M. Temmerman, F. Rabier, M. Golser, Methods for size classification of wood chips, *Biomass and Bioenergy*. 30 (2006) 944–953. doi:10.1016/j.biombioe.2006.06.010.
- [232] M. Gil, E. Teruel, I. Arauzo, Analysis of standard sieving method for milled biomass through image processing. Effects of particle shape and size for poplar and corn stover, *Fuel*. 116 (2014) 328–340. doi:10.1016/j.fuel.2013.08.011.
- [233] H. Lu, E. Ip, J. Scott, P. Foster, M. Vickers, L.L. Baxter, Effects of particle shape and size on devolatilization of biomass particle, *Fuel*. 89 (2010) 1156–1168. doi:10.1016/j.fuel.2008.10.023.
- [234] J.E. Mattsson, P.D. Kofman, Method and apparatus for measuring the tendency of solid biofuels to bridge over openings., *Biomass and Bioenergy*. 22 (2002) 179–185. doi:10.1016/S0961-9534(01)00067-8.

- [235] D. Ilic, K. Williams, R. Farnish, E. Webb, G. Liu, On the challenges facing the handling of solid biomass feedstocks, *Biofuels, Bioprod. Biorefining*. 12 (2018) 187–202. doi:10.1002/bbb.1851.
- [236] R. Xiao, X. Chen, F. Wang, G. Yu, Pyrolysis pretreatment of biomass for entrained-flow gasification, *Appl. Energy*. 87 (2010) 149–155. doi:10.1016/j.apenergy.2009.06.025.
- [237] M. Almendros, Rheological and morphological characterization of torrefied wood biomass Rheological analysis, (2012).
- [238] M. Almendros, O. Bonnefoy, Changes on wood powder morphology and flowability due to thermal pretreatment, in: *Proc. Du XIII Congrès La SFGP 2011*, 2011: pp. 1–6. <http://hal.archives-ouvertes.fr/docs/00/65/82/52/PDF/MA-SFGP-207.pdf%5Cnhttp://hal-emse.ccsd.cnrs.fr/hal-00658252/>.
- [239] M. Almendros, O. Bonnefoy, A. Govin, W. Nastoll, E. Sanz, R. Andreux, R. Guyonnet, Influence of torrefaction treatment on wood powder properties, 19th Eur. Biomass Conf. Exhib. (2011) 1902–1904.
- [240] P. Richard, N. Taberlet, Recent advances in DEM simulations of grains in a rotating drum, *Soft Matter*. 4 (2008) 1345–1348. doi:10.1039/b717129c.
- [241] P.A. Cundall, O.D.L. Strack, A discrete numerical model for granular assemblies, *Géotechnique*. 29 (1979) 47–65. doi:10.1680/geot.1979.29.1.47.
- [242] J. Tomas, Assessment of mechanical properties of cohesive particulate solids. Part 2: Powder flow criteria, *Part. Sci. Technol.* 19 (2001) 111–129. doi:10.1080/02726350152772065.
- [243] J. Tomas, Product design of cohesive powders - Mechanical properties, compression and flow behavior, *Chem. Eng. Technol.* 27 (2004) 605–618. doi:10.1002/ceat.200406134.
- [244] J. Tomas, Adhesion of ultrafine particles-A micromechanical approach, *Chem. Eng. Sci.* 62 (2007) 1997–2010. doi:10.1016/j.ces.2006.12.055.
- [245] R. Tykhoniuk, J. Tomas, S. Luding, M. Kappl, L. Heim, H.J. Butt, Ultrafine cohesive powders: From interparticle contacts to continuum behaviour, *Chem. Eng. Sci.* 62 (2007) 2843–2864. doi:10.1016/j.ces.2007.02.027.
- [246] G.W. Baxter, R.P. Behringer, Cellular automata models for the flow of granular materials, *Phys. D Nonlinear Phenom.* 51 (1991) 465–471. doi:10.1016/0167-2789(91)90252-5.
- [247] P. Bak, C. Tang, K. Wiesenfeld, Self-Organized Criticality: An Explanation of $1/f$ Noise, n.d. <http://cqb.pku.edu.cn/tanglab/pdf/1987-8.pdf> (accessed February 18, 2019).
- [248] H.M. Jaeger, C.H. Liu, S.R. Nagel, Relaxation at the Angle of Repose, 1989. <https://journals.aps.org/prl/pdf/10.1103/PhysRevLett.62.40> (accessed February 18, 2019).
- [249] N. Yoshioka, A sandpile experiment and its implications for self-organized criticality and characteristic earthquake, *Earth, Planets Sp.* 55 (2003) 283–289. doi:10.1186/BF03351762.
- [250] H.-G. Matuttis, J. Chen, Understanding the Discrete Element Method: Simulation of Non-Spherical Particles for Granular and Multi-body Systems, 2 (2014) 448 p. doi:10.1002/9781118567210.
- [251] T.A.J. Duke, G.C. Barker, A. Mehta, A Monte Carlo Study of Granular Relaxation, *Europhys. Lett.* 13 (1990) 19–24. doi:10.1209/0295-5075/13/1/004.
- [252] H.P. Zhu, Z.Y. Zhou, R.Y. Yang, A.B. Yu, Discrete particle simulation of particulate systems: Theoretical developments, *Chem. Eng. Sci.* 62 (2007) 3378–3396. doi:10.1016/j.ces.2006.12.089.
- [253] R. Bharadwaj, W.R. Ketterhagen, B.C. Hancock, Discrete element simulation study of a Freeman powder rheometer, *Chem. Eng. Sci.* 65 (2010) 5747–5756. doi:10.1016/j.ces.2010.04.002.
- [254] Á. Ramírez-Gómez, The discrete element method in silo/bin research. Recent advances and future trends, *Part. Sci. Technol.* 0 (2018) 1–18. doi:10.1080/02726351.2018.1536093.
- [255] P.W. Cleary, M.L. Sawley, DEM modelling of industrial granular flows: 3D case studies and the effect of particle shape on hopper discharge, *Appl. Math. Model.* 26 (2002) 89–111. doi:10.1016/S0307-904X(01)00050-6.
- [256] C.Y. Wu, DEM simulations of die filling during pharmaceutical tableting, *Particuology*. 6 (2008) 412–418. doi:10.1016/J.PARTIC.2008.07.008.
- [257] N.S. Weerasekara, M.S. Powell, P.W. Cleary, L.M. Tavares, M. Evertsson, R.D. Morrison, J. Quist, R.M. Carvalho, The contribution of DEM to the science of comminution, *Powder Technol.* 248 (2013) 3–24. doi:10.1016/J.POWTEC.2013.05.032.
- [258] D.R. Mindlin, Elastic Spheres in Contact Under Varying Oblique Forces, *J. Appl. Mech.* 20

- (1953) 327–344. <https://ci.nii.ac.jp/naid/10014584853/> (accessed February 19, 2019).
- [259] H. Hertz, Ueber die Berührung fester elastischer Körper, *J. Für Die Reine Und Angew. Math.* 92 (1881) 156–171. <https://home.uni-leipzig.de/pwm/web/download/Hertz1881.pdf> (accessed February 19, 2019).
- [260] C.G. DCS, gran model hertz model — LIGGGHTS v3.X documentation, Gran Hertz Model. (n.d.). https://www.cfdem.com/media/DEM/docu/gran_model_hertz.html (accessed September 7, 2018).
- [261] G. Mollon, I. De Lyon, *Mécanique des matériaux granulaires*, (2015) 2014–2015.
- [262] J. Subero, Z. Ning, M. Ghadiri, C. Thornton, Effect of interface energy on the impact strength of agglomerates, 1999. www.elsevier.com/locate/powtec (accessed February 19, 2019).
- [263] S.J. Antony, Evolution of force distribution in three-dimensional granular media, *Phys. Rev. E.* 63 (2000) 011302. doi:10.1103/PhysRevE.63.011302.
- [264] K.L. Johnson, K. Kendall, A.D. Roberts, Surface Energy and the Contact of Elastic Solids, *Proc. R. Soc. A Math. Phys. Eng. Sci.* 324 (1971) 301–313. doi:10.1098/rspa.1971.0141.
- [265] T. Pöschel, T. Schwager, *Computational granular dynamics*, Springer, Berlin, Germany, 2005.
- [266] H. Grubmüller, H. Heller, A. Windemuth, K. Schulten, Generalized Verlet Algorithm for Efficient Molecular Dynamics Simulations with Long-range Interactions, *Mol. Simul.* 6 (1991) 121–142. doi:10.1080/08927029108022142.
- [267] F. Radjai, F. Dubois, *Discrete-element modeling of granular materials*, ISTE, 2011. <https://hal.archives-ouvertes.fr/hal-00691805> (accessed February 19, 2019).
- [268] C. Kloss, C. Goniva, A. Hager, S. Amberger, S. Pirker, Models, algorithms and validation for opensource DEM and CFD-DEM, *Prog. Comput. Fluid Dyn. An Int. J.* 12 (2012) 140. doi:10.1504/PCFD.2012.047457.
- [269] D. Höhner, S. Wirtz, V. Scherer, A study on the influence of particle shape and shape approximation on particle mechanics in a rotating drum using the discrete element method, *Powder Technol.* 253 (2014) 256–265. doi:10.1016/j.powtec.2013.11.023.
- [270] J. Härtl, J.Y. Ooi, Numerical investigation of particle shape and particle friction on limiting bulk friction in direct shear tests and comparison with experiments, *Powder Technol.* 212 (2011) 231–239. doi:10.1016/j.powtec.2011.05.022.
- [271] C.M. Wensrich, A. Katterfeld, Rolling friction as a technique for modelling particle shape in DEM, *Powder Technol.* 217 (2012) 409–417. doi:10.1016/j.powtec.2011.10.057.
- [272] Q.J. Zheng, H.P. Zhu, A.B. Yu, Finite element analysis of the rolling friction of a viscous particle on a rigid plane, *Powder Technol.* 207 (2011) 401–406. doi:10.1016/j.powtec.2010.11.026.
- [273] K. Iwashita, M. Oda, Rolling Resistance at Contacts in Simulation of Shear Band Development by DEM, *J. Eng. Mech.* 124 (1998) 285–292. doi:10.1061/(ASCE)0733-9399(1998)124:3(285).
- [274] J.F. Favier, Modeling nonspherical particles using Discrete Element Methods, (2001) 971–977.
- [275] M. Rackl, F. Top, C.P. Molhoek, D.L. Schott, Biomass and Bioenergy Feeding system for wood chips : A DEM study to improve equipment performance, *Biomass and Bioenergy.* 98 (2017) 43–52. doi:10.1016/j.biombioe.2017.01.003.
- [276] R. Maione, S. Kiesgen De Richter, G. Mauviel, G. Wild, DEM investigation of granular flow and binary mixture segregation in a rotating tumbler: Influence of particle shape and internal baffles, *Powder Technol.* 286 (2015) 732–739. doi:10.1016/j.powtec.2015.09.011.
- [277] D. Markauskas, Á. Ramírez-Gómez, R. Kačianauskas, E. Zdancevičius, Maize grain shape approaches for DEM modelling, *Comput. Electron. Agric.* 118 (2015) 247–258. doi:10.1016/j.compag.2015.09.004.
- [278] C. Thornton, *Granular Dynamics, contact mechanics and particle system simulations: a DEM study.*, Springer International Publishing, 2016.
- [279] M. Marigo, E.H. Stitt, Discrete element method (DEM) for industrial applications: Comments on calibration and validation for the modelling of cylindrical pellets, *KONA Powder Part. J.* 32 (2015) 236–252. doi:10.14356/kona.2015016.
- [280] T. Roessler, A. Katterfeld, Scaling of the angle of repose test and its influence on the calibration of DEM parameters using upscaled particles, *Powder Technol.* 330 (2018) 58–66. doi:10.1016/j.powtec.2018.01.044.
- [281] T. Roessler, A. Katterfeld, Scalability of Angle of Repose Tests for the Calibration of DEM

- Parameters, ICBMH2016 Conf. (2016) 201–211.
- [282] Y.T. Feng, K. Han, D.R.J. Owen, J. Loughran, On upscaling of discrete element models: Similarity principles, *Eng. Comput.* (Swansea, Wales). 26 (2009) 599–609. doi:10.1108/02644400910975405.
- [283] S.C. Thakur, J.Y. Ooi, H. Ahmadian, Scaling of discrete element model parameters for cohesionless and cohesive solid, *Powder Technol.* 293 (2016) 130–137. doi:10.1016/j.powtec.2015.05.051.
- [284] T. Weinhart, C. Labra, S. Luding, J.Y. Ooi, Influence of coarse-graining parameters on the analysis of DEM simulations of silo flow, *Powder Technol.* 293 (2015) 138–148. doi:10.1016/j.powtec.2015.11.052.
- [285] D.S. Nasato, C. Goniva, S. Pirker, C. Kloss, Coarse graining for large-scale DEM simulations of particle flow - An investigation on contact and cohesion models, *Procedia Eng.* 102 (2015) 1484–1490. doi:10.1016/j.proeng.2015.01.282.
- [286] T. Gröger, A. Katterfeld, On the numerical calibration of discrete element models for the simulation of bulk solids, *Comput. Aided Chem. Eng.* 21 (2006) 533–538. doi:10.1016/S1570-7946(06)80100-8.
- [287] C.J. Coetzee, Review: Calibration of the discrete element method, *Powder Technol.* 310 (2017) 104–142. doi:10.1016/j.powtec.2017.01.015.
- [288] C. González-Montellano, Á. Ramírez, E. Gallego, F. Ayuga, Validation and experimental calibration of 3D discrete element models for the simulation of the discharge flow in silos, *Chem. Eng. Sci.* 66 (2011) 5116–5126. doi:10.1016/j.ces.2011.07.009.
- [289] J. Quist, M. Evertsson, Framework for DEM Model Calibration and Validation, n.d. <https://core.ac.uk/download/pdf/70613655.pdf> (accessed February 20, 2019).
- [290] T.A.H. Simons, R. Weiler, S. Strege, S. Bensmann, M. Schilling, A. Kwade, A ring shear tester as calibration experiment for DEM simulations in agitated mixers - A sensitivity study, *Procedia Eng.* 102 (2015) 741–748. doi:10.1016/j.proeng.2015.01.178.
- [291] S.M. Derakhshani, D.L. Schott, G. Lodewijks, Micro-macro properties of quartz sand: Experimental investigation and DEM simulation, *Powder Technol.* 269 (2015) 127–138. doi:10.1016/j.powtec.2014.08.072.
- [292] P. Frankowski, M. Morgeneyer, Calibration and validation of DEM rolling and sliding friction coefficients in angle of repose and shear measurements, *AIP Conf. Proc.* 1542 (2013) 851–854. doi:10.1063/1.4812065.
- [293] M. Rackl, K.J. Hanley, A methodical calibration procedure for discrete element models, *Powder Technol.* 307 (2017) 73–83. doi:10.1016/j.powtec.2016.11.048.
- [294] T. Roessler, A. Katterfeld, DEM parameter calibration of cohesive bulk materials using a simple angle of repose test, *Particuology*. (2019). doi:10.1016/j.partic.2018.08.005.
- [295] H.Q. Do, A.M. Aragón, D.L. Schott, Automated discrete element method calibration using genetic and optimization algorithms, *EPJ Web Conf.* 140 (2017) 15011. doi:10.1051/epjconf/201714015011.
- [296] F. Elskamp, H. Ruggel-Emden, M. Hennig, U. Teipel, A strategy to determine DEM parameters for spherical and non-spherical particles, *Granul. Matter.* 19 (2017) 1–13. doi:10.1007/s10035-017-0710-0.
- [297] C. Ramírez-Aragón, J. Ordieres-Meré, F. Alba-Elías, A. González-Marcos, Comparison of Cohesive Models in EDEM and LIGGGHTS for Simulating Powder Compaction, *Materials (Basel)*. 11 (2018) 2341. doi:10.3390/ma11112341.
- [298] DCS Computing, LIGGGHTS(R)-PUBLIC Documentation, Version 3.X — LIGGGHTS v3.X documentation, (n.d.). <https://www.cfdem.com/media/DEM/docu/Manual.html> (accessed February 19, 2019).
- [299] C. Bosch Padrós, Discrete element simulations with LIGGGHTS, Zienkiewicz Centre for Computational Engineering, 2014.
- [300] D. Höhner, S. Wirtz, V. Scherer, A study on the influence of particle shape on the mechanical interactions of granular media in a hopper using the Discrete Element Method, *Powder Technol.* 278 (2015) 286–305. doi:10.1016/j.powtec.2015.02.046.
- [301] D.L. Schott, R. Tans, V. Hancock, G. Lodewijks, Assessing a Durability Test for Wood Pellets

- by Discrete Element Simulation, *FME Trans.* 44 (2016) 279–284. doi:10.5937/fmet1603279S.
- [302] D. Ilic, T. Donohue, On the design and analysis of transfer chute systems, in: XXVI Encontro Nac. Trat. Minérios e Metal. Extrativa, Poços de Caldas, Brazil, 2015. <https://search.proquest.com/docview/1717074611?accountid=188395>.
- [303] Á. Ramírez-Gómez, E. Gallego, J.M. Fuentes, C. González-Montellano, F. Ayuga, Values for particle-scale properties of biomass briquettes made from agroforestry residues, *Particuology*. 12 (2014) 100–106. doi:10.1016/j.partic.2013.05.007.
- [304] fisherscientific, Parker domnick hunter™ LC/MS Nitrogen Gas Generators, (n.d.). <https://www.fishersci.ca/shop/products/parker-domnick-hunter-lc-ms-nitrogen-gas-generators-2/p-3050815> (accessed February 21, 2019).
- [305] Tecora, ZOA 100 - Fiche technique, (n.d.) 4.
- [306] J. Colin, Etude de la pyrolyse ménagée du bois : mise au point d'un four de traitement thermique, essais expérimentaux et utilisation d'un code numérique de simulation, LERMAB, AgroParisTech ENGREF, Nancy Université, 2007.
- [307] J. Pachón-Morales, J. Colin, F. Pierre, F. Puel, P. Perré, Influence de l'épaisseur de particule sur l'homogénéité de traitement thermique d'un bois de peuplier, *Récents Progrès En Génie Des Procédés - SFGP*. 110 (2017) 1–7.
- [308] IKA, Technical Data - M 20 Universal mill, (n.d.). <https://www.ika.com/en/Products-Lab-Eq/Mills-Lab-mills-Grinding-mill-csp-194/M-20-Universal-mill-Technical-Data-cptd-1603600/> (accessed February 25, 2019).
- [309] Retsch, Cutting Mill SM 300, (n.d.). <https://www.retsch.com/products/milling/cutting-mills/sm-300/function-features/> (accessed February 21, 2019).
- [310] P. Zhang, Z.J. Pei, X. Song, M. Zhang, T.W. Deines, D. Wang, Size Reduction of Cellulosic Biomass in Biofuel Manufacturing: A Study on Confounding Effects of Particle Size and Biomass Crystallinity, *J. Manuf. Sci. Eng.* 134 (2012) 011009. doi:10.1115/1.4005433.
- [311] Retsch, Planetary Ball Mill PM 100, (n.d.). <https://www.retsch.com/products/milling/ball-mills/planetary-ball-mill-pm-100/function-features/> (accessed February 21, 2019).
- [312] Sympatec, QICPIC GmbH, (2018). <https://www.sympatec.com/en/particle-measurement/sensors/dynamic-image-analysis/qicpic/> (accessed July 11, 2018).
- [313] F. Altuhafi, ; C O'sullivan, I. Cavarretta, Analysis of an Image-Based Method to Quantify the Size and Shape of Sand Particles, (2013). doi:10.1061/(ASCE)GT.1943-5606.0000855.
- [314] Sympatec, LIXELL, (n.d.). <https://www.sympatec.com/en/particle-measurement/dispersing-units/lixell/> (accessed February 25, 2019).
- [315] Sympatec, Dynamic Image Analysis, (n.d.). <https://www.sympatec.com/en/particle-measurement/sensors/dynamic-image-analysis/> (accessed February 25, 2019).
- [316] Y. Liu, X. Guo, H. Lu, X. Gong, An investigation of the effect of particle size on the flow behavior of pulverized coal, *Procedia Eng.* 102 (2015) 698–713. doi:10.1016/j.proeng.2015.01.170.
- [317] Sympatec, Particle Shape, (n.d.). <https://www.sympatec.com/en/particle-measurement/glossary/particle-shape/> (accessed February 25, 2019).
- [318] J. Pachón-Morales, J. Colin, F. Pierre, T. Champavert, F. Puel, P. Perré, Flowability of lignocellulosic biomass powders: Influence of torrefaction intensity, in: EPJ Web Conf., 2017. doi:10.1051/epjconf/201714013017.
- [319] R. Hosseinpourpia, C. Mai, Mode of action of brown rot decay resistance of thermally modified wood: Resistance to Fenton's reagent, *Holzforschung*. 70 (2016) 691–697. doi:10.1515/hf-2015-0141.
- [320] K. Johanson, Effect of particle shape on unconfined yield strength, *Powder Technol.* 194 (2009) 246–251. doi:10.1016/j.powtec.2009.05.004.
- [321] O. Molerus, The role of science in particle technology, *Powder Technol.* 122 (2002) 156–167. doi:10.1016/S0032-5910(01)00412-0.
- [322] H. Rumpf, Particle Technology, Part. Technol. Ser. (1975). doi:10.1007/978-94-011-7944-7.
- [323] D.W. SPECHT, Caking of Granular Materials: an Experimental and Theoretical Study, (2006) 127.
- [324] E. Abdullah, D. Geldart, The use of bulk density measurements as a flowability, *Powder Technol.*

- 102 (1999) 151–165. doi:10.1017/CBO9781107415324.004.
- [325] L. Rohilla, V. Garg, S.S. Mallick, G. Setia, An experimental investigation on the effect of particle size into the flowability of fly ash, *Powder Technol.* 330 (2018) 164–173. doi:10.1016/j.powtec.2018.02.013.
- [326] D. Hann, J. Stražisar, Influence of Particle Size Distribution, Moisture Content, and Particle Shape on the Flow Properties of Bulk Solids, *Instrum. Sci. Technol.* 35 (2007) 571–584. doi:10.1080/10739140701540453.
- [327] H. Thunman, B. Leckner, F. Niklasson, F. Johnsson, Combustion of wood particles - A particle model for Eulerian calculations, *Combust. Flame.* 129 (2002) 30–46. doi:10.1016/S0010-2180(01)00371-6.
- [328] R.K. Jalan, V.K. Srivastava, 99/02102 Studies on pyrolysis of a single biomass cylindrical pellet kinetic and heat transfer effects Jalan, R. K. and Srivastava, V. K. *Energy Convers. Manage.*, 1999, 40, (5), 467–494, *Fuel Energy Abstr.* 40 (1999) 215. doi:10.1016/S0140-6701(99)97872-4.
- [329] J. Pachón-Morales, J. Colin, F. Pierre, T. Champavert, F. Puel, P. Perré, Flowability of lignocellulosic biomass powders: Influence of torrefaction intensity, *EPJ Web Conf.* 140 (2017). doi:10.1051/epjconf/201714013017.
- [330] Y.H. Jung, H.J. Cho, J.S. Lee, E.W. Noh, O.K. Park, K.H. Kim, Evaluation of a transgenic poplar as a potential biomass crop for biofuel production, *Bioresour. Technol.* 129 (2013) 639–641. doi:10.1016/j.biortech.2012.12.074.
- [331] D. Dickmann, *Poplar culture in North America*, NRC Research Press, 2001.
- [332] D.P. Kamdem, A. Pizzi, A. Jermannaud, Durability of heat-treated wood, (n.d.). doi:10.1007/s00107-001-0261-1.
- [333] V. Repellin, A. Govin, M. Rolland, R. Guyonnet, Modelling anhydrous weight loss of wood chips during torrefaction in a pilot kiln, *Biomass and Bioenergy.* 34 (2010) 602–609. doi:10.1016/j.biombioe.2010.01.002.
- [334] M.J. Prins, K.J. Ptasinski, F.J.J.G. Janssen, Torrefaction of wood. Part 2. Analysis of products, *J. Anal. Appl. Pyrolysis.* 77 (2006) 35–40. doi:10.1016/j.jaap.2006.01.001.
- [335] J. Colin, Séchage en continu du bois énergie comme moyen de conditionnement en vue de sa conservation thermochimique : approches expérimentale et numérique, *AgroParisTech*, 2011. <https://pastel.archives-ouvertes.fr/pastel-00861231>.
- [336] P. Perré, R. Rémond, I. Turner, A comprehensive dual-scale wood torrefaction model: Application to the analysis of thermal run-away in industrial heat treatment processes, *Int. J. Heat Mass Transf.* 64 (2013) 838–849. doi:10.1016/j.ijheatmasstransfer.2013.03.066.
- [337] D. Schulze, Flow properties of powders and bulk solids (fundamentals), *Powder Technol.* 65 (2010) 321–333.
- [338] H. Lu, X. Guo, Y. Liu, X. Gong, Effect of particle size on flow mode and flow characteristics of pulverized coal, *KONA Powder Part. J.* (2015). doi:10.14356/kona.2015002.
- [339] X. Fu, D. Huck, L. Makein, B. Armstrong, U. Willen, T. Freeman, Effect of particle shape and size on flow properties of lactose powders, *Particuology.* 10 (2012) 203–208. doi:10.1016/j.partic.2011.11.003.
- [340] C.M. Lewandowski, A Preliminary Investigation Concerning The Effect Of Particle Shape On a Powder's Flow Properties, *Eff. Br. Mindfulness Interv. Acute Pain Exp. An Exam. Individ. Differ.* 1 (2015) 1–10. doi:10.1017/CBO9781107415324.004.
- [341] T. Horio, M. Yasuda, S. Matsusaka, Effect of particle shape on powder flowability of microcrystalline cellulose as determined using the vibration shear tube method, *Int. J. Pharm.* 473 (2014) 572–578. doi:10.1016/j.ijpharm.2014.07.040.
- [342] H.P. Goh, P. Wan, S. Heng, C.V. Liew, Comparative evaluation of powder flow parameters with reference to particle size and shape, *Int. J. Pharm.* 547 (2018) 133–141. doi:10.1016/j.ijpharm.2018.05.059.
- [343] K.W. Biegaj, M.G. Rowland, T.M. Lukas, J.Y.Y. Heng, Surface Chemistry and Humidity in Powder Electrostatics: A Comparative Study between Tribocharging and Corona Discharge, *ACS Omega.* 2 (2017) 1576–1582. doi:10.1021/acsomega.7b00125.
- [344] G. Almeida, F. Pierre, L. Murta, P.M.P. Perré, Caractérisation mécanique du produit traité et mise en relation des taux de dégradations avec les propriétés mécaniques, (2009).

-
- [345] D. Schulze, Ring Shear Tester RST-XS - Operating instructions, 2012.
 - [346] R. Li, H. Yang, G. Zheng, Q.C. Sun, Granular avalanches in slumping regime in a 2D rotating drum, *Powder Technol.* 326 (2018) 322–326. doi:10.1016/j.powtec.2017.12.032.
 - [347] V.R. Nalluri, M. Kuentz, Flowability characterisation of drug-excipient blends using a novel powder avalanching method, *Eur. J. Pharm. Biopharm.* 74 (2010) 388–396. doi:10.1016/j.ejpb.2009.09.010.
 - [348] D.A. Santos, M.A.S. Barrozo, C.R. Duarte, F. Weigler, J. Mellmann, Investigation of particle dynamics in a rotary drum by means of experiments and numerical simulations using DEM, *Adv. Powder Technol.* 27 (2016) 692–703. doi:10.1016/j.appt.2016.02.027.
 - [349] Z. Hu, X. Liu, W. Wu, Study of the critical angles of granular material in rotary drums aimed for fast DEM model calibration, *Powder Technol.* 340 (2018) 563–569. doi:10.1016/j.powtec.2018.09.065.
 - [350] N.S. Cheng, K. Zhao, Difference between static and dynamic angle of repose of uniform sediment grains, *Int. J. Sediment Res.* 32 (2017) 149–154. doi:10.1016/j.ijsrc.2016.09.001.
 - [351] R. Fischer, P. Gondret, M. Rabaud, Transition by intermittency in granular matter: From discontinuous avalanches to continuous flow, *Phys. Rev. Lett.* 103 (2009) 2–5. doi:10.1103/PhysRevLett.103.128002.
 - [352] D.A. Santos, R. Scatena, C.R. Duarte, M.A.S. Barrozo, Transition phenomenon investigation between different flow regimes in a rotary drum, *Brazilian J. Chem. Eng.* 33 (2016) 491–501. doi:10.1590/0104-6632.20160333s20150128.
 - [353] M. Krantz, H. Zhang, J. Zhu, Characterization of powder flow: Static and dynamic testing, *Powder Technol.* 194 (2009) 239–245. doi:10.1016/j.powtec.2009.05.001.
 - [354] A. Crouter, L. Briens, The Effect of Moisture on the Flowability of Pharmaceutical Excipients, *AAPS PharmSciTech.* 15 (2014) 65–74. doi:10.1208/s12249-013-0036-0.
 - [355] P. Evesque, *Eléments de mécanique quasi-statique des milieux granulaires mouillés ou secs*, *Poudres Et Grains.* 60 (2000) 1–156.
 - [356] Z. Guo, X. Chen, Y. Xu, H. Liu, Study of flow characteristics of biomass and biomass-coal blends, *Fuel.* 141 (2015) 207–213. doi:10.1016/j.fuel.2014.10.062.
 - [357] B. Littlefield, O.O. Fasina, J. Shaw, S. Adhikari, B. Via, Physical and flow properties of pecan shells-Particle size and moisture effects, *Powder Technol.* 212 (2011) 173–180. doi:10.1016/j.powtec.2011.05.011.
 - [358] J. Pachón-Morales, J. Colin, J. Casalinho, F. Puel, P. Perré, Investigation on criteria for assessment of flowability of cohesive and non-cohesive powders using a rotating drum, *Submitt. to Chem. Eng. J.* (2019) 1–32.
 - [359] J. Pachón-Morales, J. Colin, F. Pierre, T. Champavert, F. Puel, P. Perré, Flowability of lignocellulosic biomass powders: Influence of torrefaction intensity, *EPJ Web Conf.* 140 (2017) 0–3. doi:10.1051/epjconf/201714013017.
 - [360] J. Pachón-Morales, H. Do, J. Colin, F. Puel, P. Perré, D. Schott, DEM modelling for flow of cohesive lignocellulosic biomass powders: Model calibration using bulk tests, *Adv. Powder Technol.* (2019). doi:10.1016/j.appt.2019.01.003.
 - [361] J.C. Vigié, N. Ullrich, P. Porot, L. Bournay, M. Hecquet, J. Rousseau, BioTfuel Project: Targeting the Development of Second-Generation Biodiesel and Biojet Fuels, *Oil Gas Sci. Technol.* 68 (2013) 935–946. doi:10.2516/ogst/2013162.
 - [362] C. Hogue, Shape representation and contact detection for discrete element simulations of arbitrary geometries, 15 (1996) 374–390. doi:https://doi.org/10.1108/02644409810208525.
 - [363] J.P. Latham, A. Munjiza, The modelling of particle systems with real shapes., *Philos. Trans. A. Math. Phys. Eng. Sci.* 362 (2004) 1953–72. doi:10.1098/rsta.2004.1425.
 - [364] Y. Guo, C. Wassgren, B. Hancock, W. Ketterhagen, J. Curtis, Computational study of granular shear flows of dry flexible fibres using the discrete element method, *J. Fluid Mech.* 775 (2015) 24–52. doi:10.1017/jfm.2015.289.
 - [365] Y. Guo, K. Buettner, V. Lane, C. Wassgren, W. Ketterhagen, B. Hancock, J. Curtis, Computational and Experimental Studies of Flexible Fiber Flows in a Normal-Stress-Fixed Shear Cell, *AIChE J.* (2018). doi:10.1002/aic.16397.
 - [366] P. Pizette, N. Govender, D.N. Wilke, N. Abriak, New advances in large scale industrial DEM

- modeling towards energy efficient processes Résumé : Abstract :, (2017).
- [367] Y.T. Feng, D.R.J. Owen, Discrete element modelling of large scale particle systems—I: exact scaling laws, *Comput. Part. Mech.* 1 (2014) 159–168. doi:10.1007/s40571-014-0010-y.
 - [368] T. Pöschel, C. Saluena, T. Schwager, Can we scale granular systems?, (2001).
 - [369] J.E. Hilton, P.W. Cleary, Comparison of non-cohesive resolved and coarse grain DEM models for gas flow through particle beds, *Appl. Math. Model.* 38 (2014) 4197–4214. doi:10.1016/j.apm.2014.02.013.
 - [370] D.S. Nasato, C. Goniva, S. Pirker, C. Kloss, Coarse graining for large-scale DEM simulations of particle flow - An investigation on contact and cohesion models, *Procedia Eng.* 102 (2015) 1484–1490. doi:10.1016/j.proeng.2015.01.282.
 - [371] M. Sakai, S. Koshizuka, Large-scale discrete element modeling in pneumatic conveying, *Chem. Eng. Sci.* 64 (2009) 533–539. doi:10.1016/j.ces.2008.10.003.
 - [372] A.P. Grima, P.W. Wypych, Development and validation of calibration methods for discrete element modelling, *Granul. Matter.* 13 (2011) 127–132. doi:10.1007/s10035-010-0197-4.
 - [373] M. Stahl, H. Konietzky, Discrete element simulation of ballast and gravel under special consideration of grain-shape, grain-size and relative density, *Granul. Matter.* 13 (2011) 417–428. doi:10.1007/s10035-010-0239-y.
 - [374] H.Q. Do, A.M. Aragón, D.L. Schott, A calibration framework for discrete element model parameters using genetic algorithms, *Adv. Powder Technol.* (2018) 1–11. doi:10.1016/j.apt.2018.03.001.
 - [375] H.Q. Do, M. Mohajeri, D.L. Schott, CHoPS 2018 9 International Conference on Conveying and Handling of Particulate Solids CHoPS 2018 9 International Conference on Conveying and Handling of Particulate Solids, (2018) 1–6.
 - [376] M. Combarros, H.J. Feise, H. Zetzener, A. Kwade, Segregation of particulate solids: Experiments and DEM simulations, *Particuology.* 12 (2014) 25–32. doi:10.1016/j.partic.2013.04.005.
 - [377] ImageJ, (n.d.). <https://imagej.nih.gov/ij/> (accessed July 30, 2018).
 - [378] I. Darstellung, I.N. Kurzform, *Fm* 2 582, (1991).
 - [379] M. Rackl, F.E. Grötsch, M. Rusch, J. Fottner, Qualitative and quantitative assessment of 3D-scanned bulk solid heap data, *Powder Technol.* 321 (2017) 105–118. doi:10.1016/j.powtec.2017.08.009.
 - [380] M. Rackl, K.J. Hanley, A methodical calibration procedure for discrete element models, *Powder Technol.* 307 (2017) 73–83. doi:10.1016/j.powtec.2016.11.048.
 - [381] J. Fraczek, A. Złobecki, J. Zemanek, Assessment of angle of repose of granular plant material using computer image analysis, (2007). doi:10.1016/j.jfoodeng.2006.11.028.
 - [382] S.M. Derakhshani, Modelling Dust Liberation in Bulk Material Handling Systems, PhD thesis, Delft University of Technology, 2016. doi:10.4233/uuid:0d8c6401-fc4e-4b7b-babc-6eb9573d79b3.
 - [383] J. Ai, J. Chen, J.M. Rotter, J.Y. Ooi, Assessment of rolling resistance models in discrete element simulations, *Powder Technol.* 206 (2011) 269–282. doi:10.1016/j.powtec.2010.09.030.
 - [384] GmbH DCS Computing, gran cohesion sjkr model — LIGGGHTS v3.X documentation, (n.d.). https://www.cfdem.com/media/DEM/docu/gran_cohesion_sjkr.html (accessed September 7, 2018).
 - [385] M. Kodam, R. Bharadwaj, J. Curtis, B. Hancock, C. Wassgren, Cylindrical object contact detection for use in discrete element method simulations. Part I – Contact detection algorithms, (2010). doi:10.1016/j.ces.2010.08.006.
 - [386] H. Kruggel-Emden, S. Rickelt, S. Wirtz, V. Scherer, A study on the validity of the multi-sphere Discrete Element Method, *Powder Technol.* 188 (2008) 153–165. doi:10.1016/j.powtec.2008.04.037.
 - [387] D. Markauskas, R. Kačianauskas, Investigation of rice grain flow by multi-sphere particle model with rolling resistance, *Granul. Matter.* 13 (2011) 143–148. doi:10.1007/s10035-010-0196-5.
 - [388] Y. Li, Y. Xu, C. Thornton, A comparison of discrete element simulations and experiments for “sandpiles” composed of spherical particles, *Powder Technol.* 160 (2005) 219–228. doi:10.1016/j.powtec.2005.09.002.
 - [389] O. Baran, A. DeGennaro, E. Ramé, A. Wilkinson, DEM simulation of a schulze ring shear tester,

- AIP Conf. Proc. 1145 (2009) 409–412. doi:10.1063/1.3179948.
- [390] Y.C. Zhou, B.H. Xu, A.B. Yu, P. Zulli, An experimental and numerical study of the angle of repose of coarse spheres, *Powder Technol.* 125 (2002) 45–54. doi:10.1016/S0032-5910(01)00520-4.
- [391] K. Deb, A. Pratap, S. Agarwal, T. Meyarivan, A fast and elitist multiobjective genetic algorithm: NSGA-II, *IEEE Trans. Evol. Comput.* 6 (2002) 182–197. doi:10.1109/4235.996017.
- [392] S.L.C. Ferreira, A.O. Caires, T. da S. Borges, A.M.D.S. Lima, L.O.B. Silva, W.N.L. dos Santos, Robustness evaluation in analytical methods optimized using experimental designs, *Microchem. J.* 131 (2017) 163–169. doi:10.1016/j.microc.2016.12.004.
- [393] © 2017 Minitab Inc., What is a main effects plot?, (n.d.). <http://support.minitab.com/en-us/minitab/17/topic-library/modeling-statistics/anova/basics/what-is-a-main-effects-plot/> (accessed September 17, 2018).
- [394] A.B. Zhou, Y. C.; Wright, B. D.; Yang, R. Y.; Xu, B. H; Yu, Rolling friction in the dynamic simulation of sandpile formation, *Phys. A Stat. Mech. Its Appl.* 269 (1999) 536–553. doi:10.1016/j.physa.2005.01.019.
- [395] T. Roessler, C. Richter, A. Katterfeld, F. Will, Development of a standard calibration procedure for the DEM parameters of cohesionless bulk materials – part I: Solving the problem of ambiguous parameter combinations, *Powder Technol.* (2018) #pagerange#. doi:10.1016/j.powtec.2018.11.034.
- [396] S.C. Thakur, J.P. Morrissey, J. Sun, J.F. Chen, J.Y. Ooi, Micromechanical analysis of cohesive granular materials using the discrete element method with an adhesive elasto-plastic contact model, *Granul. Matter.* 16 (2014) 383–400. doi:10.1007/s10035-014-0506-4.
- [397] P.S. Lam, S. Sokhansanj, X. Bi, L.J. Naimi, M. Hoque, S. Mani, A.R. Womac, X.P. Ye, S. Narayan, Bulk density of wet and dry wheat straw and switchgrass particles, *Appl. Eng. Agric.* 24 (2008) 351–358.
- [398] X. Fu, D. Huck, L. Makein, B. Armstrong, U. Willen, T. Freeman, Effect of particle shape and size on flow properties of lactose powders, *Particuology.* 10 (2012) 203–208. doi:10.1016/j.partic.2011.11.003.
- [399] L. Carr, Evaluating Flow Properties of Solids, *Chem. Eng.* 18 (1965) 163–168.
- [400] I. Akkerman, Reynolds Cluster, (n.d.). <http://homepage.tudelft.nl/4x7d5/computer-facilities.html> (accessed March 9, 2019).
- [401] G. Derringer, R. Suich, Simultaneous Optimization of Several Response Variables, *J. Qual. Technol.* 12 (1980) 214–219. doi:10.1080/00224065.1980.11980968.
- [402] © 2017 Minitab Inc., What are individual desirability and composite desirability?, (n.d.). <https://support.minitab.com/en-us/minitab/18/help-and-how-to/modeling-statistics/using-fitted-models/supporting-topics/response-optimization/what-are-individual-desirability-and-composite-desirability/> (accessed August 29, 2018).
- [403] W.H. Chen, J. Peng, X.T. Bi, A state-of-the-art review of biomass torrefaction, densification and applications, *Renew. Sustain. Energy Rev.* 44 (2015) 847–866. doi:10.1016/j.rser.2014.12.039.
- [404] J. Pachón-Morales, J. Colin, F. Pierre, F. Puel, P. Perré, Effect of torrefaction intensity on the flow properties of lignocellulosic biomass powders, *Biomass and Bioenergy.* 120 301–312. doi:10.1016/j.biombioe.2018.11.017.
- [405] P.A. Cundall, O.D.L. Strack, A discrete numerical model for granular assemblies, *Géotechnique.* 29 (1979) 47–65. doi:10.1680/geot.1979.29.1.47.
- [406] R.Y. Yang, R.P. Zou, A.B. Yu, Microdynamic analysis of particle flow in a horizontal rotating drum, *Powder Technol.* 130 (2003) 138–146. doi:10.1016/S0032-5910(02)00257-7.
- [407] E. Alizadeh, F. Bertrand, J. Chaouki, Comparison of DEM Results and Lagrangian Experimental Data for the Flow and Mixing of Granules in a Rotating Drum, *AIChE J.* 60 (2014) 60–75. doi:10.1002/aic.14259.
- [408] R.Y. Yang, A.B. Yu, L. McElroy, J. Bao, Numerical simulation of particle dynamics in different flow regimes in a rotating drum, *Powder Technol.* 188 (2008) 170–177. doi:10.1016/j.powtec.2008.04.081.
- [409] H. Chen, Y.G. Xiao, Y.L. Liu, Y.S. Shi, Effect of Young’s modulus on DEM results regarding transverse mixing of particles within a rotating drum, *Powder Technol.* (2017).

- doi:10.1016/j.powtec.2017.05.047.
- [410] H.R. Norouzi, R. Zarghami, N. Mostoufi, Insights into the granular flow in rotating drums, *Chem. Eng. Res. Des.* 102 (2015) 12–25. doi:10.1016/j.cherd.2015.06.010.
- [411] R.N. Cunha, K.G. Santos, R.N. Lima, C.R. Duarte, M.A.S. Barrozo, Repose angle of monoparticles and binary mixture: An experimental and simulation study, *Powder Technol.* 303 (2016) 203–211. doi:10.1016/j.powtec.2016.09.023.
- [412] S.R. Mead, P.W. Cleary, G.K. Robinson, Characterising the failure and repose angles of irregularly shaped three-dimensional particles using DEM, *Ninth Int. Conf. CFD Miner. Process Ind.* CSIRO, Melbourne, Aust. (2012) 1–6.
- [413] G.G. Pereira, S. Pucilowski, K. Liffman, P.W. Cleary, Streak patterns in binary granular media in a rotating drum, *Appl. Math. Model.* 35 (2011) 1638–1646. doi:10.1016/j.apm.2010.09.040.
- [414] C.J. Coetzee, Particle upscaling: Calibration and validation of the discrete element method, *Powder Technol.* 344 (2019) 487–503. doi:10.1016/J.POWTEC.2018.12.022.
- [415] M. Marigo, Discrete element method modelling of complex granular motion in mixing vessels: evaluation and validation, (2012) 1–341. <http://core.kmi.open.ac.uk/download/pdf/8821055.pdf>.
- [416] A. Wachs, L. Girolami, G. Vinay, G. Ferrer, Grains3D, a flexible DEM approach for particles of arbitrary convex shape - Part I: Numerical model and validations, *Powder Technol.* 224 (2012) 374–389. doi:10.1016/j.powtec.2012.03.023.
- [417] B.K. Mishra, C. Thornton, D. Bhimji, A preliminary numerical investigation of agglomeration in a rotary drum, *Miner. Eng.* 15 (2002) 27–33. doi:10.1016/S0892-6875(01)00194-7.
- [418] R. Brewster, G.S. Grest, A.J. Levine, Effects of cohesion on the surface angle and velocity profiles of granular material in a rotating drum, *Phys. Rev. E - Stat. Nonlinear, Soft Matter Phys.* 79 (2009) 1–7. doi:10.1103/PhysRevE.79.011305.
- [419] M. Sebastian Escotet-Espinoza, C.J. Foster, M. Ierapetritou, Discrete Element Modeling (DEM) for mixing of cohesive solids in rotating cylinders, *Powder Technol.* 335 (2018) 124–136. doi:10.1016/j.powtec.2018.05.024.
- [420] S. Luding, M.M. Msm, Mesoscale modeling of particles and particles in fluids - Multi-Scale (Models) and - Continuum Theory (Applications) - Jamming and un-jamming, (2013).
- [421] T. Lichtenegger, S. Pirker, CFD-DEM modeling of strongly polydisperse particulate systems, *Powder Technol.* 325 (2018) 698–711. doi:10.1016/j.powtec.2017.11.058.
- [422] M. Obermayr, C. Vrettos, P. Eberhard, T. Däuwel, A discrete element model and its experimental validation for the prediction of draft forces in cohesive soil, *J. Terramechanics.* 53 (2014) 93–104. doi:10.1016/j.jterra.2014.04.003.
- [423] Z. Shen, M. Jiang, C. Thornton, DEM simulation of bonded granular material. Part I: Contact model and application to cemented sand, *Comput. Geotech.* 75 (2016) 192–209. doi:10.1016/j.compgeo.2016.02.007.
- [424] J.F. Favier, M.H. Abbaspour-Fard, M. Kremmer, Modeling nonspherical particles using multispheres, *J. Eng. Mech.* 127 (2001) 971–977.
- [425] D. Mateo-Ortiz, R. Méndez, Microdynamic analysis of particle flow in a confined space using DEM: The feed frame case, *Adv. Powder Technol.* 27 (2016) 1597–1606. doi:10.1016/j.apt.2016.05.023.
- [426] M. Florian-Algarin, R. Mendez, Blend Uniformity and Powder Phenomena Inside the Continuous Tumble Mixer Using DEM Simulations, *AIChE J.* 61 (2015) 792–801. doi:10.1002/aic.14694.
- [427] W. Yang, Z. Zhou, D. Pinson, A. Yu, Periodic boundary conditions for discrete element method simulation of particle flow in cylindrical vessels, *Ind. Eng. Chem. Res.* 53 (2014) 8245–8256. doi:10.1021/ie404158e.
- [428] X. Liu, Z. Hu, W. Wu, J. Zhan, F. Herz, E. Specht, DEM study on the surface mixing and whole mixing of granular materials in rotary drums, *Powder Technol.* 315 (2017) 438–444. doi:10.1016/j.powtec.2017.04.036.
- [429] LIGGGHTS® Version History | CFDEM®project, (n.d.). <https://www.cfdem.com/node/42> (accessed March 23, 2019).
- [430] A. Podlozhnyuk, S. Pirker, C. Kloss, Efficient implementation of superquadric particles in

- Discrete Element Method within an open-source framework, *Comput. Part. Mech.* 4 (2017) 101–118. doi:10.1007/s40571-016-0131-6.
- [431] G. Almeida, J.O. Brito, P. Perré, Changes in wood-water relationship due to heat treatment assessed on micro-samples of three Eucalyptus species, *Holzforschung*. 63 (2009) 80–88. doi:10.1515/HF.2009.026.
- [432] W.H. Chen, P.C. Kuo, Torrefaction and co-torrefaction characterization of hemicellulose, cellulose and lignin as well as torrefaction of some basic constituents in biomass, *Energy*. 36 (2011) 803–811. doi:10.1016/j.energy.2010.12.036.
- [433] S. Cavagnol, E. Sanz, W. Nastoll, J.F. Roesler, V. Zyma, P. Perré, Inverse analysis of wood pyrolysis with long residence times in the temperature range 210–290 C: Selection of multi-step kinetic models based on mass loss residues, *Thermochim. Acta*. 574 (2013) 1–9. doi:10.1016/j.tca.2013.09.009.
- [434] J. Crank, *The Mathematics of Diffusion*, Clarendon Press, Oxford, 1975.
- [435] Chauvin Arnoux, C. A 8332B wattmeter, (n.d.). <http://www.chauvin-arnoux.com/en/produit/CA8332B> (accessed February 21, 2019).
- [436] Chauvin Arnoux Metrix, PAT Power Analyser Transfer, (n.d.). <http://www.chauvin-arnoux.com/fr/pat-power-analyser-transfer> (accessed February 25, 2019).

Titre : Torréfaction et broyage de biomasse lignocellulosique pour sa valorisation thermochimique : influence des conditions de prétraitement sur les propriétés d'écoulement des poudres

Mots clés : Biomasse lignocellulosique, BtL, torréfaction, DEM, test de cisaillement, coulabilité de poudres, distribution de taille et forme de particules

Résumé : Une technologie prometteuse pour répondre à la demande croissante en énergie renouvelable est la gazéification de biomasse lignocellulosique pour la production de biocarburants de deuxième génération. Ce procédé nécessite une alimentation en biomasse sous forme de poudre. Les problèmes de convoyage et de manipulation liés à la faible coulabilité de la biomasse broyée sont un verrou pour l'industrialisation des procédés BtL. La torréfaction comme procédé de prétraitement, en plus d'augmenter la densité énergétique de la biomasse, peut influencer également les propriétés des particules obtenues après broyage, et en conséquence, l'écoulement des poudres. L'évaluation de l'écoulement des poudres de biomasse sous différentes conditions de consolidation est essentielle pour concevoir des technologies de manipulation et de convoyage efficaces. L'objectif de ce travail est d'évaluer l'effet des conditions de torréfaction et de broyage sur l'écoulement de poudres de biomasse. Une première partie consiste en une étude expérimentale dans laquelle la coulabilité d'échantillons torréfiés sous différentes intensités a été évaluée à l'aide d'un appareil de cisaillement annulaire. La coulabilité est corrélée à l'intensité de la torréfaction (mesurée par la perte de masse globale) pour deux essences différentes. La forme des particules semble être le paramètre qui influence de manière prédominante la coulabilité des poudres à l'état consolidé.

La caractérisation de la coulabilité à l'état non consolidé a été effectuée à l'aide d'un tambour rotatif par l'analyse des avalanches des poudres. Des corrélations entre les caractéristiques des particules et la coulabilité sont ainsi établies. La modélisation de l'écoulement de la biomasse à l'aide de la Méthode des Éléments Discrets (DEM) constitue une deuxième partie de ces travaux de recherche. La taille submillimétrique des particules de biomasse, ainsi que leur faible densité, leur forme allongée et leur comportement cohésif sont des défis pour l'implémentation d'un modèle de réaliste d'écoulement particulaire en DEM. Un modèle DEM des particules de biomasse est mis en œuvre à l'aide d'une représentation simplifiée (assemblage de sphères) à gros grains de la forme des particules, ainsi que d'un modèle de force cohésif. Une procédure systématique de calibration des paramètres DEM permet d'obtenir un ensemble de paramètres ajustés. L'évolution expérimentale des contraintes de cisaillement d'une poudre dans un état consolidé peut alors être reproduite de façon réaliste. De même, le comportement d'avalanche des poudres dans un tambour tournant est également bien reproduit par les simulations, de façon qualitative et quantitative. Ces résultats mettent en évidence le potentiel des simulations DEM pour étudier l'effet des caractéristiques des particules, qui sont influencées par la torréfaction et les conditions de broyage, sur le comportement d'écoulement de la biomasse en poudre.

Title: Torrefaction and grinding of lignocellulosic biomass for its thermochemical valorization: influence of pretreatment conditions on powder flow properties

Keywords: Lignocellulosic biomass, BtL, torrefaction, DEM, shear testing, rotating drum, powder flowability, particle size and shape distribution

Abstract: Gasification of lignocellulosic biomass for production of second-generation biofuels is a promising technology to meet renewable energy needs. However, feeding and handling problems related to the poor flowability of milled biomass considerably hinder the industrial implementation of Biomass-to-Liquid processes. Torrefaction as pretreatment step, in addition to improving energy density of biomass, also affects the properties of the milled particles (namely size and shape) that significantly influence flow behavior. The evaluation of biomass flow characteristics under different flow conditions is essential to design efficient and trouble-free handling solutions. The aim of this work is to assess the effect of the torrefaction and grinding conditions on the biomass flow behavior. A first part consists of an experimental study in which the flow properties of samples torrefied under different intensities were obtained using a ring shear tester. Flowability is correlated to the intensity of torrefaction, as measured by the global mass loss, for two different wood species. Particle shape seems to be the predominant parameter influencing flowability of powders in a consolidated state.

Characterization of non-consolidated flowability through avalanching analysis using an in-house rotating drum was also conducted. Correlations between particle characteristics and flow behavior are thus established. The modeling of biomass flow using the Discrete Element Method (DEM) constitutes a second major part of this research. Challenging aspects of biomass particle modeling are their submillimetric size, low density, elongated shape and cohesive behavior. A material DEM model is implemented using a simplified (multisphere) upscaled representation of particle shape, along with a cohesive contact model. A systematic calibration procedure results in an optimal set of DEM parameters. The experimental shear stress evolution and yield locus can then be realistically reproduced. The avalanching behavior of the powders is also well captured by simulations, both qualitatively and quantitatively. These results highlight the potential of DEM simulations to investigate the effect of particle characteristics, which are driven by torrefaction and grinding conditions, on the flow behavior of powdered biomass.